

NASA Contract Report - 195349

1N-20
34451
367P

Advanced Small Rocket Chambers Basic Program and Option II – Fundamental Processes and Material Evaluation

Final Report

Donald M. Jassowski
GenCorp Aerojet
Propulsion Division
Sacramento, California

September 1993

Prepared for
Lewis Research Center
Under Contract NAS3-25646

(NASA-CR-195349) ADVANCED SMALL
ROCKET CHAMBERS. BASIC PROGRAM AND
OPTION 2: FUNDAMENTAL PROCESSES AND
MATERIAL EVALUATION Final Report
(GenCorp Aerojet) 367 p

N95-18192

Unclas

NASA
National Aeronautics and
Space Administration

63/20 0034451

Contract NAS 3-25646

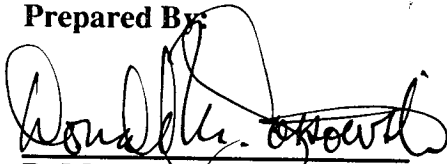
ADVANCED SMALL ROCKET CHAMBERS

Basic Program and Option II

September 1993


**Aerojet Propulsion Division
P.O. Box 13222
Sacramento, CA 95813-6000**

Prepared By:



**D. M. Jassowski
Project Engineer**

Approved By:



**B. Reimer
Program Manager**

Prepared For:

**NASA-Lewis Research Center
Cleveland, OH 44135**

REPORT DOCUMENTATION PAGE

1. Report No. NASA-CR-195349		2. Government Accession No.		3. Recipient's Catalog No.	
4. Title And Subtitle Advanced Small Rocket Chambers Basic Program and Option II Final Report				5. Report Date September 1993	
				6. Performing Organization Code	
7. Author(s) D.M. Jassowski				8. Performing Organization Report No.	
9. Performing Organization Name and Address Aerojet Propulsion Division P.O. Box 13222 Sacramento, CA 95813				10. Work Unit No.	
				11. Contract or Grant No. NAS 3-25646	
12. Sponsoring Agency Name and Address National Aeronautics and Space Administration Lewis Research Center Cleveland, OH 44135-3191				13. Type of Report and Period Covered Contractor Report Basic and Option II, Final	
				14. Sponsoring Agency Code	
15. Supplementary Notes Project Manager – Dr. Steven J. Schneider Space Propulsion Technology Division NASA Lewis Research Center					
16. Abstract <p>Propellants, chamber materials and processes for fabrication of small high performance radiation cooled liquid rocket engines were evaluated to determine candidates for eventual demonstration in flight-type thrusters. Both storable and cryogenic propellant systems were considered. The storable propellant systems chosen for further study were nitrogen tetroxide oxidizer with either hydrazine or monomethylhydrazine as fuel. The cryogenic propellants chosen were oxygen with either hydrogen or methane as fuel. Chamber material candidates were CVD rhenium protected from oxidation by CVD iridium for the chamber hot section, and film cooled wrought platinum-rhodium or regeneratively cooled stainless steel for the front end section exposed to partially reacted propellants.</p> <p>Laser diagnostics of the combustion products near the hot chamber surface and measurements at the surface layer were performed in a collaborative program at Sandia National Laboratories, Livermore, CA. A laboratory system to simulate the combustion environment in terms of gas and material temperature, composition and pressure up to 6 Atm, the Material Sample Test Apparatus, was developed for these studies.</p> <p>Rocket engine simulator studies were conducted to evaluate the materials under simulated combustor flow conditions, in the Diagnostic Test Chamber. These tests used the Exhaust Species Measurement System, a device developed to monitor optically species composition and concentration in the chamber and exhaust by emission and absorption measurements.</p>					
17. Key Words (Suggested by Author(s)) Rockets; Satellite Propulsion; Rhenium Thrusters; Iridium Coatings; Chemical Vapor Deposition; Bipropellants; Radiation Cooling; High Performance; High Temperature; Long Life			18. Distribution Statement Unclassified, Unlimited Subject Category 20		
19. Security Classif. (of this report) Unclassified	20. Security Classif. (of this page) Unclassified		21. No. of pages 352		22. Price

TABLE OF CONTENTS

	<u>Page</u>
1.0 Summary	1
2.0 Introduction	2
3.0 Conclusions and Recommendations	5
4.0 Technical Discussion	6
4.1 Material, Process and Propellant Selection	6
4.1.1 Materials	6
4.1.2 Processes	12
4.1.3 Propellant Selection	18
4.2 Test Sample Preparation	34
4.3 Design of Sample Test Facility	41
4.4 Sample Test Facility Fabrication, Installation, and Checkout	41
4.5 High Temperature Material Tests (Sandia)	52
4.5.1 Gas Phase Measurements	68
4.5.2 Surface Measurements	108
4.6 Diagnostic Thrust Chamber and Instrumentation Evaluation	188
4.6.1 Design	191
4.6.2 Fabrication	234
4.6.3 Testing	243
5.0 References	263
6.0 Bibliography – Reports Based on This Contract	264

APPENDICES

<u>Appendix</u>	A-1
A Materials Data	B-1
B Propellant Combustion Product Composition	

TABLE LIST

<u>Table</u>	<u>Page</u>
4.1-1 Task 1 Recommendations	8
4.1-2 Aerojet High Temperature Rocket Materials Test Data Base	10
4.1-3 Recent Significant Documents	11
4.1.2-1 Candidate Chamber Materials and Processes	15
4.1.2-2 Sources for Iridium Deposition	16
4.1.2-3 Fabrication Techniques	19
4.1.3-1 Propellant Screening – Oxidizer – Fuel	20
4.1.3-2 Liquid Propellants Used in Production Bipropellant Propulsion Systems	26
4.1.3-3 Equilibrium Composition of Candidate Bipropellant Combinations at Chamber Conditions ($P_c = 5 \text{ ATM}$)	27
4.2-1 MSTA and DTC Specimen Materials	40
4.2-2 Diagnostic Thrust Chamber Specimens Weight and Dimension Data	45
4.3-1 Materials Test Apparatus for Sandia Burner Operating Conditions	49
4.4-1 Material Sample Test Apparatus Checkout	62
4.5.1-1 Flow Conditions For the Computer Simulations	73
4.5.1-2 Experimental Conditions For Gas-Phase Profiles	80
4.5.2-1 Sandia Materials Tests – Summary of Experiments	114
4.5.2-2 MSTA Surface Measurements	173
4.6.1-1 Diagnostic Thrust Chamber Design Criteria	192
4.6.1-1A DTC Housing – Port Identification	197
4.6.1-2 Test Matrix for Task 6.0	200
4.6.1-3 Specimen Analysis Procedures	201
4.6.1-4 Curve Fit Constants for Pyrometer Data	226
4.6.1-5 Spectral Characteristics of Species of Interest	232
4.6.3-1 Instrumentation for Diagnostic Thrust Chamber	246
4.6.3-2 Test Matrix for Task 6.3 Diagnostic Test Chamber Testing at A-Area	248
4.6.3.3 DTC Test Log	249
4.6.3-4 Summary of DTC Results	251

FIGURE LIST

<u>Figure</u>		<u>Page</u>
2-1	Program Logic	3
2-2	Phase I Basic Program Schedule	4
4.1-1	Task 1 Program Logic	7
4.1-2	Melting Points of Candidate Materials	13
4.1-3	Ultimate Tensile Strength Versus Fraction of Melting Point Temperature	14
4.1.2-1	CVD Chamber Fabrication Steps	17
4.1.3-1	Normalized Isp ($N_2O_4/MMH = 1.0$)	22
4.1.3-2	Theoretical Isp vs MR for Various Oxidizer/Fuel Combinations	23
4.1.3-3	Mole Fraction Versus Mixture Ratio of Oxygen/Hydrogen at 5 Atm	29
4.1.3-4	Mole Fraction Versus Mixture Ratio for Oxygen/Methane at 5 Atm	30
4.1.3-5	Mole Fraction Versus Mixture Ratio for Nitrogen Tetroxide/Hydrazine at 5 ATM	31
4.1.3-6	Mole Fraction Versus Mixture Ratio for Nitrogen Tetroxide/Monomethylhydrazine at 5 Atm	32
4.1.3-7	$O_2/H_2/Cu$ Equilibrium	33
4.1.3-8	Estimated Corrosion Rate of Molybdenum in H_2O/H_2 Atmospheres	35
4.1.3-9	Laboratory Screening of Materials	36
4.1.3-10	Molybdenum Exposed to Oxygen-Ethane Combustion Products	37
4.1.3-11	Material Reaction Rate	38
4.2-1	DTC Specimen Assembly (Welded)	39
4.2-2	Welded Foil DTC Specimens	42
4.2-3	Electron Beam Welds on Platinum DTC Specimen	43
4.2-4	Electron Beam Welds on Rhenium DTC Specimen	44
4.3-1	Material Sample Test Apparatus (MSTA) System Block Diagram	46
4.3-2	Sample Test Facility – Combustion Apparatus Components	47
4.3-3	MSTA Burner/Combustion Chamber Assembly	48
4.3-4	MSTA Chamber Assembly	50
4.3-5	MSTA Schematic – 1 to 6 Atm System	51
4.4-1	Platelet Burner Assemblies	53
4.4-2	MSTA Burner for Task 5	54
4.4-3	MSTA Burner Face	55
4.4-4	6 Atm Vista Components	56
4.4-5	Specimen and Holder Components	57

FIGURE LIST (cont.)

<u>Figure</u>	<u>Page</u>
4.4-6 MSTA Specimen Holder Assembly	58
4.4-7 Specimen Holder Detail	59
4.4-8 MSTA Combustor Assemblies	60
4.4-9 MSTA Control Console	61
4.4-10 Overall 6-Atm MSTA System	63
4.4-11 View of 6-Atm MSTA Chamber	64
4.4-12 View of Combustion Zone Showing Burner Face and Igniter in Inserted Position	65
4.4-13 MSTA During Operation (the Injector is Positioned in the Middle of the View Port, the Specimen is at the Top)	66
4.4-14 Iridium Specimen Exposed to O_2/H_2 at $MR = 6$ for 45 min	67
4.5.1-1 Schematic of Experimental Apparatus For Simultaneous Laser Induced OH Fluorescence, Raman Scattering, and Rayleigh Scattering Measurements in Turbulent Jet Flames	69
4.5.1-2 Apparatus For Gas-Phase Raman Scattering and OH Fluorescence Measurements in the MSTA	70
4.5.1-3 Physical Processes of LIF and Raman Scattering	71
4.5.1-4 Laser Probe For OH in MSTA O_2/H_2 Combustion Zone With Heated Ir Specimen	72
4.5.1-5 Profile of the Axial Velocity For the Conditions Described in Table 4.5.1-1 With No Surface Reactions	75
4.5.1-6 Profile of the Temperature For the Conditions Described in Table 4.5.1-1 With No Surface Reactions	76
4.5.1-7 Profiles of the Predicted OH Mole Fraction (Solid Line With No Symbols) Compared With the OH Mole Fraction Calculated From Partial Equilibrium With O_2 and H_2 in Table 4.5.1-1 With No Surface Reactions	77
4.5.1-8 Profile of the Axial Velocity For the Conditions Described in Table 4.5.1-1 With High Radical Recombination Rates at the Surface	78
4.5.1-9 Calculated Profiles of T, OH, N_2 , H_2O Illustrate That Major Species Mole Fractions Can Be Expected to Change Very Little in the MSTA Gas Phase Boundary Layer, While Temperature and OH Fraction Can Change Significantly	79
4.5.1-10 Laser-Induced Fluorescence (LIF) Profiles in a Rich ($\Phi = 1.35$) Hydrogen/Air Flame. The Laser is Turned On a Off Resonance to Separate the OH Fluorescence Signal From Scattered Light From the Material Sample Source	84
4.5.1-11 OH LIF Profile in the Rich Hydrogen/Air Flame, With the Contribution From Scattered Light Subtracted	85

FIGURE LIST (cont.)

<u>Figure</u>		<u>Page</u>
4.5.1-12	Orientation of the Material Sample Relative to the Laser Beam For Gas-Phase Measurements	86
4.5.1-13	In the MSTA, the Cylindrical Metal Foil is Held at a 45° Angle to the Axis-of the Laser Beam For OH Fluorescence or Raman Scattering Measurements	87
4.5.1-14	Measured OH Fluorescence Profile in the Boundary Layer Adjacent to an Iridium Foil Sample at 2100°C in a Stagnation Flow of Combustion Products From a Hydrogen-Air Flame at MR = 6.5, 1-Atm	89
4.5.1-15	Profiles of Simultaneous Raman on LIF Signals For an Air-H ₂ Flame (MR = 6.5) With the Iridium Surface at 1400°C	91
4.5.1-16	Illustration of Modification of the Polychromator Entrance Aperture	93
4.5.1-17	OH Fluorescence Profiles Obtained in the MSTA With an Iridium Sample at a) 1400, b) 1600, c) 1800, d) 2000, and e) 2100°C Exposed to Hydrogen-Air Combustion Products at MR = 6.5	95
4.5.1-18	OH Fluorescence Profiles Obtained in the MSTA With an Iridium Sample at a) 1400, b) 1600, c) 1800, d) 2000, and e) 2100°C Exposed to Hydrogen-Air Combustion Products at MR = 5.5	96
4.5.1-19	OH Fluorescence Profiles With the Iridium Sample at 1670K For Three Laser-Excited Transitions: Δ -S ₂₁ (5), O-S ₂₁ (8), ∇ -S ₂₁ (11)	98
4.5.1-20	OH Fluorescence Profiles With the Iridium Sample at 2370K For Three Laser-Excited Transitions: Δ -S ₂₁ (5), O-S ₂₁ (8), ∇ -S ₂₁ (11)	99
4.5.1-21	Temperature Profiles Based on the OH Fluorescence Measurements (MR = 6.5, Iridium Sample at 1670K). Open Symbols Correspond to Temperature Determined From Eq. (2) For Pairs of Transitions: Δ S ₂₁ (5), S ₂₁ (8); O, S ₂₁ (11) ∇ , S ₂₁ (8)- S ₂₁ (11)	100
4.5.1-22	Temperature Profiles Based on the OH Fluorescence Measurements (MR = 6.5, Iridium Sample at 2370K). Open Symbols Correspond to Temperatures Determined From Eq. (2) For Pairs of Transitions: Δ , S ₂₁ (5) - S ₂₁ (8); O, S ₂₁ (5)-S ₂₁ (11); ∇ , S ₂₁ (8)-S ₂₁ (11)	101
4.5.1-23	Average Temperature Profiles For the Iridium Sample at 1670K (Closed) Symbols and 2370K (Open Symbols). The Curve is Provided as a Visual Aid to Represent the Undisturbed Gas Temperature	102
4.5.1-24	Profiles of OH Concentration and Temperature For MR = 6.5 Air/H ₂ Combustion Products With Iridium Specimen Surface Temperatures of 1670, 1970, 2270 and 2370K. Measurements Are Shown by the Open Symbols. The Curves in the OH Plots Show Equilibrium Concentration Profiles Based Upon Fits to the Temperature Profiles	103
4.5.1-25	Profiles of OH Concentration and Temperature for MR=5.5 Air/H ₂ Combustion Products with Iridium Specimen Surface Temperature of 1670, 1970, and 2270K. Measurements are Shown by the Open Symbols. The Curve in the OH Plots Show Equilibrium Concentration Profiles Based on Fits to the Temperature Profiles	106

FIGURE LIST (cont.)

<u>Figure</u>	<u>Page</u>
4.5.1-26 Equilibrium OH Concentration as a Function of Temperature For MR=6.5 and MR=5.5 Air/H ₂ Combustion Products	107
4.5.1-27 Profiles of OH Concentration and Temperature For a) MR = 6.5 and b) MR = 5.5 Air/H ₂ Combustion Products With a Platinum Specimen Surface Temperature of 1670K. Measurements Are Shown by the Open Symbols. The Curves in the OH Plots Show Equilibrium Concentration Profiles Based Upon Fits to the Temperature Profiles	107
4.5.1-28 Profiles of the Fluorescence Signal For Three Transitions S ₂₁ (5), S ₂₁ (8) and S ₂₁ (11) For the Case With an Iridium Sample and O ₂ /H ₂ Combustion Products at MR = 6.5	109
4.5.1-29 Profile of Temperature Determined From the OH Fluorescence Measurements Shown in Figure 4.5.1-25 For the Case With an Iridium Sample and O ₂ /H ₂ Combustion Products at MR = 6.5	110
4.5.1-30 Profiles of the Fluorescence Signal for Three Transitions S ₂₁ (5), S ₂₁ (8) and S ₂₁ (11) for the Case With an Iridium Sample and O ₂ /H ₂ Combustion Products at MR = 5.5	111
4.5.1-31 Profile of Temperature Determined From the OH Fluorescence Measurements Shown in Figure 4.5.1-27 for the Case With an Iridium Sample and O ₂ /H ₂ Combustion Products at MR = 5.5	112
4.5.2-1 Raman Surface Analysis System	116
4.5.2-2 Second Harmonic Generation Surface Analysis System	117
4.5.2-3 Raman Spectra – Oxide Standards	119
4.5.2-4 Raman Spectroscopy – A Surface Analytical Tool	120
4.5.2-5 Ir-After 15 Min/1000 C in Oxygen	121
4.5.2-6 SEM of Foil Surface After Heating in Oxygen to 1250C For One Hour	122
4.5.2-7 Sputter Depth Profiles Into Ir/O ₂ Surface	123
4.5.2-8 Auger Spectroscopy – A Surface Analytical Tool	124
4.5.2-9 Sputter Profiling Using Auger Spectroscopy	125
4.5.2-10 Auger Spectra – Ir Metal	126
4.5.2-11 Auger Spectra – Ir Metal After 1250C in O ₂	127
4.5.2-12 Depth Profile Before and After Heating	128
4.5.2-13 After Heating 1600 C/45 Min/Vacuum	129
4.5.2-14 Surface Morphology After Heating	130
4.5.2-15 Raman Spectra From Deposit Which Forms on Furnace Window When Heating Iridium in Oxygen. Comparison With Standard Spectra Shows That the Deposit is IrO ₂	132
4.5.2-16 Auger Sputter Profile of an Iridium Sample Heated to 1000C For 15 Min. in Oxygen at 1 Atmosphere	133

FIGURE LIST (cont.)

<u>Figure</u>	<u>Page</u>
4.5.2-17 Surface Raman Spectra of a Platinum Sample Heated to 1250C in 1 Atmosphere of Oxygen For 1 Hour Showing That There is no Formation of PtO ₂ on the Pt Metal	134
4.5.2-18 Surface Raman Spectra of an Iridium Sample Heated to 1250C for 1 Hour in 1 Atmosphere Oxygen, Showing Formation of IrO ₂ on the Ir Metal	136
4.5.2-19 Surface Raman Spectra of an Iridium Foil Heated For Two Hours in One Atmosphere of Oxygen at 650C. The 300C and RT Data Were Taken During Cooling From 650C	137
4.5.2-20 Raman Spectra of Iridium Foil Exposed to One Atmosphere Oxygen at 650C For Two Hours	138
4.5.2-21 Sputter Auger Depth Profile of the Iridium Dioxide Layer Formed on Iridium After 650C Anneal in Oxygen	139
4.5.2-22 X-Ray Diffraction Spectrum For the Oxide Formed on Iridium After Heating to 1250C in Oxygen	140
4.5.2-23 XRD Spectrum of an Iridium Coated Rhenium Foil Heated in Vacuum to 1400C For 45 Minutes	141
4.5.2-24 Auger Depth profile of Rhenium Coated With ~2.5μ of Ir, Heated to 1200°C For 45 Minutes. A Theoretical Fit to the Data is Shown (Solid Line). From This a Diffusivity 2.4×10^{-12} cm ² /sec is Calculated For T = 1200°C	143
4.5.2-25 Comparison of X-Ray Diffraction Spectra For Heated Ir-Re Pellet (Top), Heated Thin-Film Deposit (Middle), and as Deposited Thin-Film of Ir on Re (Bottom). This h.c.p. Solid Solution Phase is Identified By the Black Dots Above Each of Its Corresponding Peaks. The Re Peaks in the Heated Thin-Film (Middle-Spectra) Correspond to the Underlying Re Foil	145
4.5.2-26 Diffusion Constants Obtained as a Function of Temperature Plotted	146
4.5.2-27 Composition Profile Predicted For a 50μm Ir Coating on Re Annealed at 2000°C For 5 Hours	147
4.5.2-28 Geometry and Approximate Dimensions For Fracture Sample	149
4.5.2-29 Auger Spectra From Surface of Re Grain After Fracture. Total Vacuum Exposure After Fracture Was 23 Minutes With Less Than 2 Minutes of Electron Beam Exposure. Carbon Concentration is 23 Atomic % and Oxygen Concentration is 14 Atomic %	150
4.5.2-30 Atomic Compositions Measured From Freshly Sputtered Rhenium Surface During Exposure to Ambient Vacuum and Electron Beam	152
4.5.2-31 Cross-Section of CVD End Ring Polished Perpendicular to the Ir-Re Interface. Horizontal Bar at Lower Right of the Microphoto is Equal to 10 Microns	154
4.5.2-32 Cross-Section of CVD End Ring Polished Perpendicular to the Ir-Re Interface. Magnification of Figure 4.5.2-31	155

FIGURE LIST (cont.)

<u>Figure</u>		<u>Page</u>
4.5.2-33	Electron Microprobe Elemental Trace For Ir and Re Across the Diffusion Interface. The Sharp Elemental Cross Over Region Identifies the Diffusion Zone	156
4.5.2-34	Cross-Section of CVD End Ring Polished Perpendicular to the Ir-Re Interface. This Secondary Electron Image (SEI) Shows the Additional Structures Observed Within the Re Along the Ir-Re Interface	157
4.5.2-35	Micrograph of Iridium-Coated Rhenium End Ring Section After Vacuum Anneal For 14 hrs at 1400°C	158
4.5.2-36	Elemental Map For Rhenium in 1400°C Annealed End Ring Section	158
4.5.2-37	Elemental Map For Iridium in 1400°C Annealed End Ring Section	160
4.5.2-38	Elemental Map For Molybdenum in 1400°C Annealed End Ring Section	160
4.5.2-39	Iridium Concentration vs Depth For End Ring, P/N 7154-3-2-L-4	161
4.5.2-40	Micrograph of Iridium-Coated Rhenium End Ring Section After Vacuum Anneal For 8 Hours at 1700°C	162
4.5.2-41	Elemental Map For Rhenium in 1700°C Annealed End Ring Section	162
4.5.2-42	Elemental Map For Iridium in 1700°C Annealed End Ring Section	164
4.5.2-43	Elemental Map For Molybdenum in 1700°C Annealed End Ring Section	164
4.5.2-44	CVD Specimen MSTA	166
4.5.2-45	Iridium Concentration on Sample Annealed at 1900°C for 8 hr	168
4.5.2-46	Iridium Concentration on Samples Annealed at 1700°C For 8 hr	169
4.5.2-47	Iridium Concentration on Samples Annealed at 1400°C For 14 hr	170
4.5.2-48	Plot of Diffusion Coefficients as a Function of Reciprocal Temperature	172
4.5.2-49	Auger Spectra For CVD Ir/Re Specimen at 1900°C	176
4.5.2-50	Atomic Percent Ir and Re vs Time For CVD Ir/Re Specimen at 1900°C	177
4.5.2-51	Auger Peak Height Ratio (Re/Ir) as a Function of Time During 1730C Anneal in Ultrahigh Vacuum	179
4.5.2-52	Assumed Configuration of Rhenium on Surface of Iridium Coating After Extended Annealing in Ultrahigh Vacuum	181
4.5.2-53	Fraction of Rhenium Atoms in Top Layer of a 25µm CVD Coating After Extended Annealing in Ultrahigh Vacuum	181
4.5.2-54	Calculated Rhenium Profile After 20 Hr at 1550C in 0.5% O ₂ at 0.028 Atm	185
4.5.2-55	Calculated Rhenium Profiles After 40 Hr at 1550C in 0.5% O ₂ at 0.028 Atm	186
4.5.2-56	Calculated Rhenium Profile After 60 Hr at 1550C in 0.5% O ₂ at 0.028 Atm. Final Failure Occurs at 67 Hr	186

FIGURE LIST (cont.)

<u>Figure</u>	<u>Page</u>
4.5.2-57 Bulk Concentration in the Near Surface Region as Function of Time During 1730°C Anneal in Ultrahigh Vacuum	187
4.5.2-58 Bulk Concentration in the Near Surface Region as Function of Time During 2100°C Anneal in Ultrahigh Vacuum	189
4.6-1 Diagnostic Thrust Chamber Conceptual Design	190
4.6.1-2 Diagnostic Thrust Chamber	193
4.6.1-2A SEM of Portion of Rolled Injector Face After Electropolishing	194
4.6.1-3 Optical Temperature Measurement Approach	195
4.6.1-4 DTC Measurement Location	196
4.6.1-5 Exhaust Species Monitoring System Detector Head	199
4.6.1-6 DTC Specimen Temperature Control	203
4.6.1-7 DTC Propellant Flow vs Pc O ₂ /H ₂ (Nitrogen Flow = 0.0)	205
4.6.1-8 DTC Propellant Flow vs Pc O ₂ /H ₂ (Nitrogen Flow = 0.05 lb/sec)	206
4.6.1-9 DTC Chamber Wall Temperature vs Pc (Nitrogen Flow = 0.0)	207
4.6.1-10 DTC Chamber Wall Temperature vs Pc (Nitrogen Flow = 0.5 = Wp)	208
4.6.1-11 Mechanical Properties of Platinum vs Temperature	209
4.6.1-12 O ₂ /H ₂ Combustion Products Total Oxidizer Species	210
4.6.1-13 O ₂ /CH ₄ Combustion Products Total Oxidizer Species	211
4.6.1-14 Total Oxidizing Species vs MR/MR Stoichiometric	212
4.6.1-14A Chamber Assembly	213
4.6.1-14B Chamber Assembly	214
4.6.1-14C Chamber Assembly	215
4.6.1-14D Chamber Assembly	216
4.6.1-14E DTC Drilled Injector Design	217
4.6.1-15 Two-Color Temperature Measurement – Emission Ratio Versus Temperature, $\lambda_1 = 0.9\mu$; $\lambda_2 = 1.0\mu$	219
4.6.1-16 DTC Pyrometer Checkout and Calibration	221
4.6.1-16A Pyrometer Signals, S1 and S2, Versus Temperature Unit A: S1 = 0.9 μ ; S2 = 1.0 μ	222
4.6.1-17 Signal Ratio Cubed Versus Temperature T _{Lamp} : Mikron: Unit A and F, 9-7-90	223
4.6.1-18 Signal Ratio Cubed Versus Temperature T _{Lamp} : Mikron: Unit B, 9-10-90	224
4.6.1-19 Signal Ratio Cubed Versus Temperature T _{Lamp} : Mikron: Unit E, 9-10-90	225

FIGURE LIST (cont.)

<u>Figure</u>		<u>Page</u>
4.6.1-20	Pyrometer Fit Error Versus Temperature Unit A: $m = 677.1$; $b = 929.6$, $n = 3.000$	227
4.6.1-21	Pyrometer Fit Error Versus Temperature Unit B: $m = 893.5$; $b = 869.6$; $n = 3.000$	228
4.6.1-22	Pyrometer Fit Error Versus Temperature Unit E: $m = 716.3$; $b = 868.9$; $n = 3.000$	229
4.6.1-23	Pyrometer Fit Error Versus Temperature Unit F: $m = 576.0$; $b = 845.0$; $n = 3.000$	230
4.6.1-24	Pyrometer Error Due to Mixed Field Temperature: Percent Error for Equal Area at T1 and T2 (Unit A Calibration)	231
4.6.1-25	ESMS System Schematic	233
4.6.1-26	Exhaust Species Monitoring System – Detector Head	235
4.6.2-1	DTC Components	236
4.6.2-2	DTC Assembly	237
4.6.2-3	Drilled Injector and Platinum Specimen/Chamber	238
4.6.2-4	DTC Injector Face Detail	239
4.6.2-5	ESMS Detector Head	240
4.6.2-6	DTC With Exhaust Species Monitoring System (ESMS) Detector Head	241
4.6.2-7	DTC Injector Coolant Flowrate and Kw Versus Delta P Water Flow Coolant Circuits 9-14-90	242
4.6.3-1	DTC Facility Schematic	244
4.6.3-2	DTC Operating Sequence	245
4.6.3-3	Diagnostic Thrust Chamber Setup	247
4.6.3-4	DTC Mass Loss Rate Data, O ₂ Plus Fuel	252
4.6.3-5	DTC Absorption Measurements	253
4.6.3-6	DTC Plume Absorption and Emission	254
4.6.3-7	DTC Normalized Plume Absorption and Emission	255
4.6.3-8	DTC Plume Absorption and Emission	256
4.6.3-9	DTC Plume Absorption and Emission	257
4.6.3-10	DTC Plume Absorption and Emission	258
4.6.3-11	DTC Test #47 LIA Absorption and Emission vs Time	260
4.6.3-12	DTC 47 - Specimen Temperature vs Time	261
4.6.3-13	DTC Test #47 Emission at 488 nm vs Time	262

1.0 SUMMARY

This report documents Aerojet and Sandia/Livermore activity on the Basic and Option II 15-month initial portion of Contract NAS 3-25646, Advanced Small Rocket Chambers. The period covered is July, 1989 through September, 1990.

The purpose of this program is to advance the state-of-the-art of high temperature small rocket chambers significantly by: (1) examining fundamental propellant combustion processes, (2) selecting candidate propellants, materials and fabrication processes suitable for radiation-cooled thrusters, (3) evaluating materials in relevant environments, and (4) evaluating small rocket concepts by direct firing. Fundamental processes and material evaluation were conducted in the basic program and Option II; direct rocket engine firing was conducted in Options I and III, which have separate final reports.

Candidate propellants which were chosen for study after a screening process were two storable combinations – nitrogen tetroxide/monomethylhydrazine and nitrogen tetroxide/hydrazine, and two cryogenic propellant combinations—oxygen/hydrogen and oxygen/methane.

Candidate materials studied in this program were rhenium protected with iridium for the high temperature, radiation-cooled section of the chamber and platinum – 10% rhodium for use in film-cooled thruster front ends.

The fabrication processes chosen were chemical vapor deposition of the iridium and rhenium and conventional machining of the platinum alloy.

Aerojet provided the Material Sample Test Apparatus (MSTA) to Sandia for study of gas-phase reactions in oxygen-hydrogen near a surface at the Combustion Research Facility in Livermore, CA. Auger measurements of the surface of iridium-rhenium specimens exposed to high temperature in a vacuum furnace at Sandia show that this material system should have a life of over 40 hours based on diffusion of rhenium to the iridium surface.

Limited testing of the candidate material in a simulated rocket chamber in oxygen-hydrogen and oxygen-methane at Aerojet in the Diagnostic Thrust Chamber (DTC) gave relative mass loss data for these systems, concluding the Basic Program activities, Tasks 1 through 6. Option II, which was to cover Investigation of Storable Propellants in Laboratory Testing at Sandia in the MSTA and Simulated Rocket Chamber Tests at Aerojet in the DTC was initiated in February of 1990, and put on hold seven months later to conserve resources for Option III.

1.0, Summary (cont.)

The results of the Basic Program were used to demonstrate the understanding of combustion product/chamber material interaction for flight thrusters. Ir-Re 14 lbf and 110 lbf flight type thrusters were designed, built and tested with impressive results in Option I and Option III, respectively, as reported in References 1 and 2.

2.0 INTRODUCTION

The Advanced Small Rocket Chambers Program, NASA LeRC Contract NAS 3-25646 has as its goal the understanding of rocket chamber material/combustion interaction mechanisms for high temperature radiation-cooled rocket engines.

Program Logic

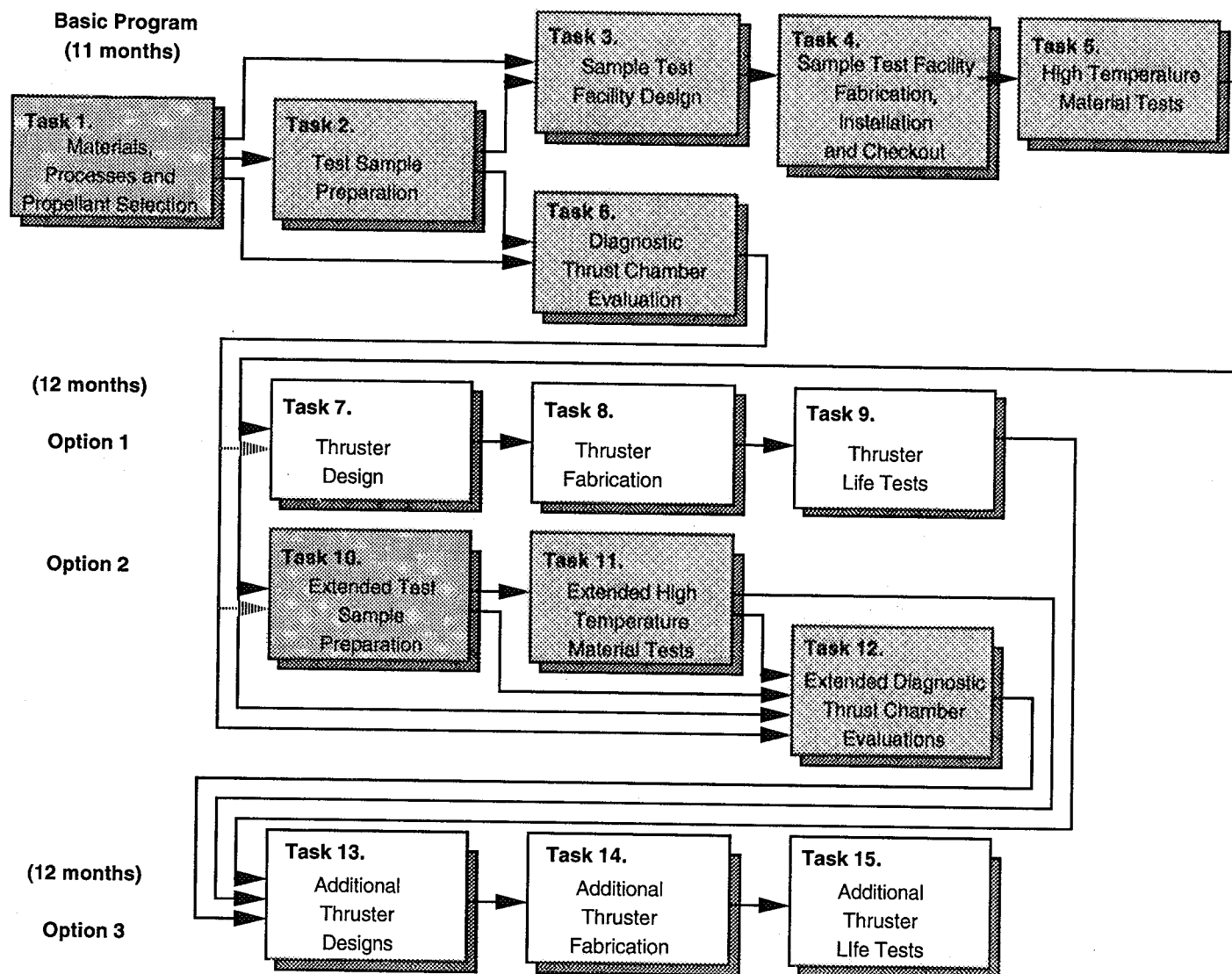
The logic to carry out this program is shown in Figure 2-1. The program is a basic program plus three options consisting of 15 tasks and reporting in Task 16. The Basic Program and Option 2, documented in this final report, included Tasks 1 through 6 and Tasks 10 through 12, which covered study and selection of materials, propellants and fabrication processes, basic combustion product/material interaction research in collaboration with Sandia/Livermore Combustion Research Facility using their advanced laser diagnostics techniques, and exposure of candidate chamber materials to simulated rocket engine conditions.

Activity on this part of the program began in July, 1989; technical activity at Aerojet was concluded in September 1990, to concentrate the program resources on Option III, technology demonstration of a 100 lbf Ir-Re thruster (Figure 2-2). The collaborative effort at Sandia, Task 5, High Temperature Material Tests, continued into 1991.

The purpose of this program was to significantly advance the state-of-the-art of high temperature small rocket chambers by:

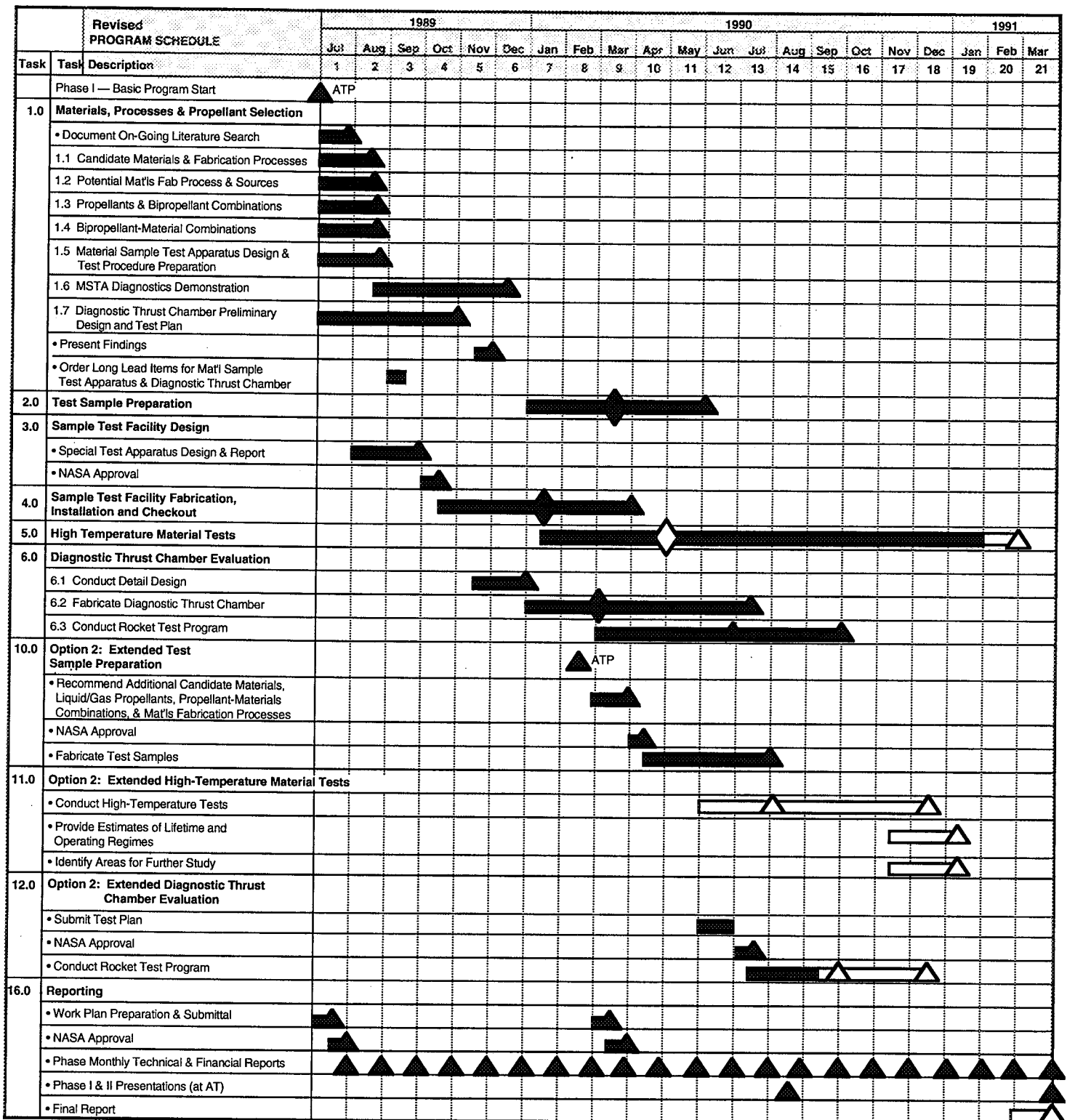
- examining fundamental propellant combustion processes
- evaluating materials in relevant environments
- and evaluating small rocket concepts by direct firing.

The program task schedule is shown in Figure 2-2. The basic program and Option 2 consisted of ten tasks, as follows:



14.30.07

Figure 2-1. Program Logic



M7/D20/ASRC-1
14.09.09

Figure 2-2. Phase I Basic Program Schedule

2.0, Introduction (cont.)

Task 1 – Material, Process and Propellant Selection

Task 2 – Test Sample Preparation

Task 3 – Design of Sample Test Facility (Material Sample Test Apparatus – MSTTA)

Task 4 – Sample Test Facility Fabrication, Installation and Checkout

Task 5 – High Temperature Materials Tests

Task 6 – Diagnostic Thrust Chamber Evaluation

Task 10 - Extended Test Sample Preparation

Task 11 - Extended High-Temperature Material Tests

Task 12 - Extended Diagnostic Thrust Chamber Evaluation

Task 16 – Reporting

The testing portions of these tasks concentrated on cryogenic propellants, oxygen/hydrogen and oxygen/methane in the basic program.

The Option II program, which was initiated in February 1990, was intended to extend the laboratory and simulated rocket chamber testing to the storable propellants nitrogen tetroxide/hydrazine and nitrogen tetroxide/monomethylhydrazine. Design and fabrication activities were begun but the work was put on hold in September, before storable propellant testing was conducted, in order to conserve funding for Option III, 100 lbf Thrust Technology Demonstration.

This program was a collaborative effort between Aerojet Propulsion Division, Sacramento, CA, and the Sandia National Laboratories at Livermore, CA. This work was reported jointly in the Advanced Small Rocket Chambers Monthly Technical reports. The Task 5 work described here is summarized from these reports. The gas-phase measurements were reported by John Hamilton. More recent work conducted for NASA after this collaboration is noted in Section 6.0, Bibliography.

3.0 CONCLUSIONS AND RECOMMENDATIONS

The selected materials and fabrication processes can provide chambers which, when properly applied, should have long life with the propellant systems considered.

Of the possible material systems which could provide significant improvement in small rocket engine performance by eliminating film cooling, only Ir-Re is believed to be a viable choice at this time.

3.0, Conclusions And Recommendations (cont.)

Two laboratory simulators of rocket engine operating conditions, the MSTA and DTC were demonstrated, along with the ESMs for chamber and exhaust plume diagnostics. These devices have significant potential for rapid screening of materials and processes for rocket chamber fabrication and should be utilized more extensively.

4.0 TECHNICAL DISCUSSION

The technical activities on the basic program centered on three areas. The first was choice of materials fabrication and propellants which was conducted in Task 1. The second involved basic materials studies at Sandia in the gas phase and on the chamber material surface, which were conducted in Task 5. Tasks 2, 3 and 4 supported this activity through design, fabrication and checkout of test specimen and experimental test apparatus. The third activity area was material evaluation in a combustion environment using a simulated rocket engine.

4.1 MATERIAL, PROCESS AND PROPELLANT SELECTION

Suitable combinations of materials and propellant combinations are essential for long duration operation at high temperature. The program logic for Task 1 is shown in Figure 4.1-1. The results of Task 1 are summarized in Table 4.1-1.

4.1.1 Materials

As part of the initial effort on the program, a literature search was conducted on the topic of high-temperature materials suitable for use in small rocket chambers. An earlier literature search and vendor survey had been conducted on the "High-Temperature, Oxidation-Resistant Thruster Research" program and is documented in the Final Report, Appendix A, Contract NAS 3-24643 (Ref. 3). The literature search done here was an update of the previous work done for that Report.

The search was conducted using materials, processes, and properties for descriptors. The materials searched included ceramic matrix composites, intermetallic composites, ceramics, platinum group metals, and rhenium. These were matched up with processes such as CVD, PVD, HIP, etc., and properties such as oxidation rate, diffusion data, etc.

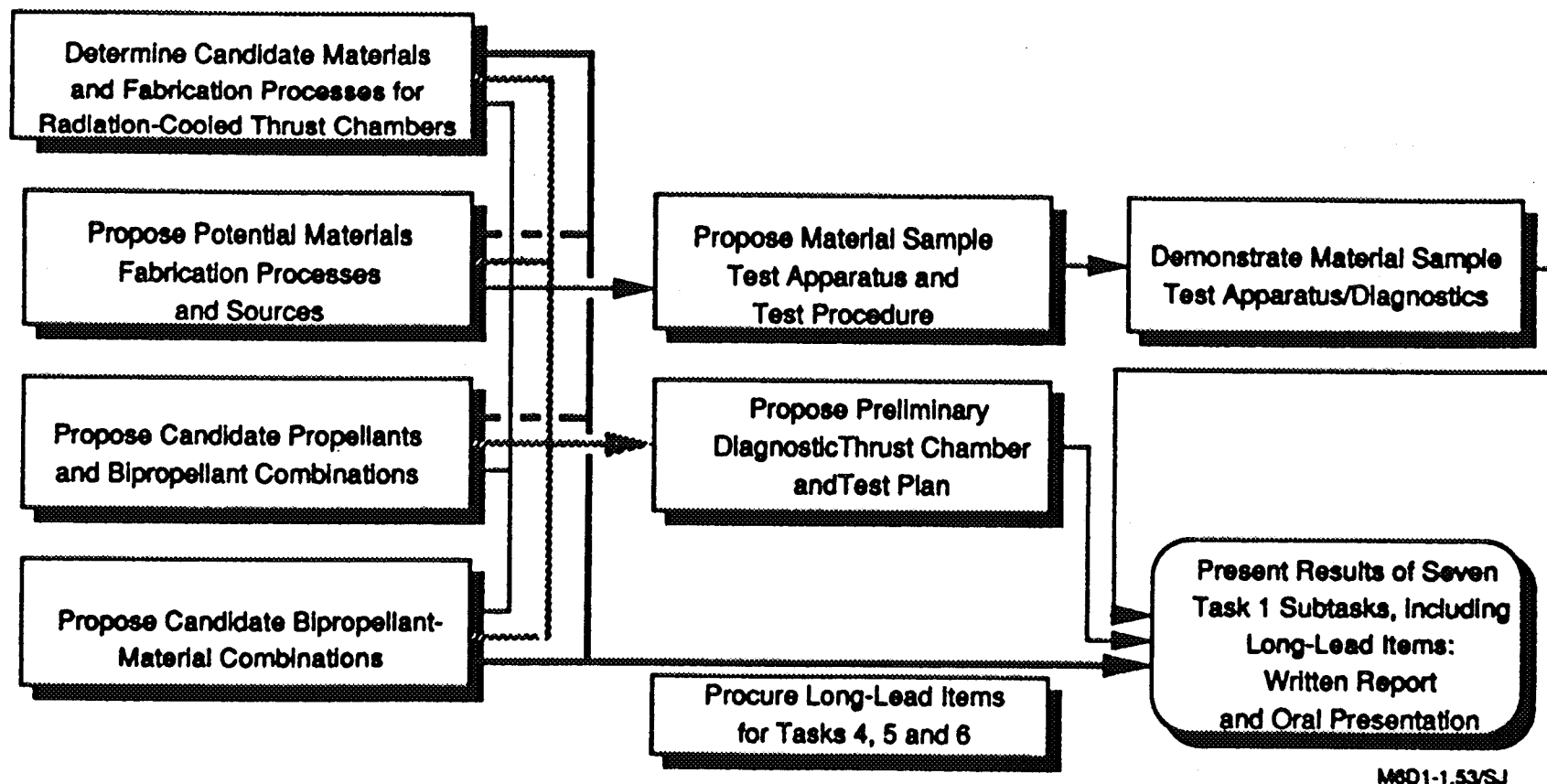


Figure 4.1-1. Task 1 Program Logic

Table 4.1-1. Task 1 Recommendations for Basic Program

Propellants	Oxygen/Hydrogen and Oxygen/Methane
Materials	Iridium – Very High Temperature Oxidation Resistant Coating
	Rhenium – Ultra High Temperature Structure
	Platinum – Very Oxidation Resistant Boundary Layer Trip Structure
Fabrication	
MSTA and DTC Specimens	Rolled Foil
Thruster	CVD Rhenium on CVD Iridium

4.1, Material, Process and Propellant Selection (cont.)

The specific descriptors searched were:

- (1) Oxidation models
- (2) Diffusion models
- (3) Intermetallic matrix composites
- (4) HfC/ceramic composites
- (5) Engel-Brewer compounds
- (6) Cermets
- (7) Carbon/Carbon/coatings/oxidation/since 1986
- (8) Ceramic matrix composites/SiC
- (9) Ceramic matrix composites/ZrO₂
- (10) Ceramic matrix composites/ZrC
- (11) Platinum group metals/since 1985
- (12) Rhenium/since 1985
- (13) Aluminum oxynitride

The data bases searched were NTIS, Compendix, Ceramics Abstracts, Sci-Search, Metadex. Some recent additions to the literature are listed in Table 4.1-3. Over 150 citations were located in the first search. The significant titles that appeared to be of interest were ordered and have been reviewed. No surprises were uncovered, based on previous studies of the literature.

Based on discussions with a fabricator of advanced materials (Comurhex) the recent literature was reviewed for data on aluminum oxynitride because of its potential for oxidation resistance and low cost. However, it has a relatively low melting point (2165°C/3930°F) and therefore did not meet the requirements of this program. It could be a candidate for lower temperature applications, such as a low cost replacement for silicide coated niobium if it can overcome the disadvantages it shares with other ceramics of potential for brittle failure.

A detailed presentation of the finding of the materials study is presented in Appendix A. A significant factor in material selection was previous Aerojet experience, listed in Table 4.1-2.

The materials chosen for study in the basic program were (1) rhenium for the chamber structure, (2) iridium, as a oxidation protection layer on the rhenium, and (3) platinum, for those thrusters where a trip is required in the head end. Other material systems which have

Table 4.1-2.
Aerojet High Temperature Rocket Materials Test Data Base

Material	Source	Chamber Type S/N	Thrust lbF	Temp Range, F	MR, NTO/MMH	Total Burn Time, Sec	Full Thermal Cycles	Total Starts	Throat ID Change, in.	Contract
Rhenium	SFL	85001	5	1,940 - 3,700	0.8 - 1.65	1,762	24	8,889	.028**	IR&D
Rhenium	SFL	85002	5	2,730 - 3,720	0.8 - 1.72	9009	34	1,207	0.002**	IR&D
Rhenium	Ultramet	85003	5	1,550 - 3,730	1.1 - 1.51	575	10	12	0.000	IR&D
Ir-Re	Ultramet	86001	5	3,400 - 4,200	1.2 - 2.18	31,363	37	3,638	Hole	IR&D
Ir-Re	Ultramet	86002	5	3,500 - 4,000	1.4 - 1.7	13,018	14	14	Hole	IR&D
HfO ₂ -Ir-Re	Ultramet	86005	5	3,540 - 4,100	1.4 - 1.6	1,232	5	5	HfO ₂ Spalled	IR&D
Ir-Re	Ultramet	86003	5	4,010 - 4,300	1.4 - 1.7	28,426	74	157	Hole	NASA
Ir-Re	Ultramet	86004	5	4,000 - 4,070	1.55 - 2.0	54,431	70	2,701*	0.000	NASA
Ir-Re***	Ultramet	86009	5	3,920	1.4	926	9	10	0.000	SBIR
Ir-Re	Ultramet	—	100	3,200 - 3,500	1.5 - 1.7	3,381	30	30	0.000	JPL
Ir-Re	Ultramet	86001	5	2,500 - 3,500	1.6	6,774		100,000	0.000	NASA
Ir-Re	Ultramet	—	100	3,200 - 3,500	1.5 - 1.7	15,000	33	33	0.000	JPL
Ir-Re***	Ultramet	—	5	2,000 - 3,000	1.8 - 2.8	7,800	29	29	0.004	IR&D
Ir-Re	Ultramet	—	5	Not tested						IR&D
ODS Pt	Englehard	—	5	Not tested						IR&D
ODS Pt	Englehard	—	5	2,000	1.8 - 2.8	3,000	15	15	0.000	IR&D
ZGSPt	JM****	85004	5	2,600 - 3,000	0.8	1,011	5	5	0.000	IR&D
ZGSPt	JM****	86005	5	2,600 - 3,000	0.8 - 2.0	2,237	25	43,158	0.000	IR&D
ACC4CC	Vought	86006	5	1,625 - 2,375	1.4 - 1.5	327	4	4	Hole	IR&D
ACC4CC	Vought	86007	5	Not tested						IR&D
HfC-CC	Ref Comp Inc	87001	5	2,880	1.59	105	1	1	Mechanical	IR&D
SiC K-Karb	Midland Mat	86008	5	1,340 - 1,800	1.4 - 1.7	222	3	3	0.0025	IR&D
C-103/R512E	HITemco	86008	5	2,200 - 2,610	0.8 - 2.1	4,170	16	16	0.001	IR&D
C-103	Thermocoore	Heatpipe	5	2,000	0.7 - 1.65	905	4	4	0.000	SBIR
Rhenium	Ultramet	—	25	2,000 - 4,000	O ₂ /H ₂ O ₂ /CH ₄	6,840 360	192 6	192 6	0.000 0.007	Test @ JPL

*Cycled 3,500 to 4,000 F

** Material Loss Encountered in Pulsing and When Operated at MR>1.5

***Iridium Thickness Two Times Nominal .002 in.

****Johnson Matthey

MS01-1.48/3J

Table 4.1-3. Recent Significant Documents

- Survey Reports
 - Hoppin III, G.S. and Danesi, W.P., "Future of Superalloys, Superalloys II High-Temperature Materials for Aerospace and Industrial Applications," Wiley, 1987.
 - Stephens, J.R. and Nathal, M.V., "Status and Prognosis for Alternative Engine Materials," NASA TM-100903, September 1988.
 - Stephens, J.R., "High-Temperature Metal Matrix Composites for Future Aerospace Systems, NASA TM-100212, October 1987.
- Properties
 - Luo, A., et al., "Tensile Properties of W-3.6% Re-0.4 HfC Above 0.5 TM," Scripta Met., Vol. 23, 1989.
- Metallic and Ceramic Coatings
 - Harding, J.T., et al., "Oxidation Resistance of CVD Coatings," AFRPL TR 86-099, February 1987.
 - Harding, J.T., et al., "Oxidation Resistant Coatings for Operation at 1650-2000° and Above," 11th Annual Conference on Composites and Advanced Ceramics, January 1987.
 - Anon, "HfO₂ and ZrO₂ Overcoating of SiC for Extending the Oxidation Protection of Carbon-Carbon Composites to 3500°F," Ultramet SBIR Phase I Report to Wright-Patterson AFB, May 1986.
 - Schoenman, L., "Rocket Engine Test Report – HfO₂ – Lined Ir/Re Chamber," Aerojet IR&D Internal Report, 25 June 1986.
- Ceramics and Composites
 - Yang, J.M., et al., "Development of Nickel Aluminide Matrix Composites," Materials Science and Engineering, January 1989.
 - Barr, F.A. and Page, R.J., "Slip Casting and Extruding Shapes of Rhenium With Metal Oxide Additives," NASA-CR-174970, April 1986.

4.1, Material, Process and Propellant Selection (cont.)

promise and which should be considered for subsequent development include (1) stabilized hafnia as an oxidation protection layer for the iridium, (2) molybdenum-rhenium alloys as a low density, machinable replacement for pure rhenium, and (3) tungsten-rhenium as a lower cost, machinable replacement for rhenium.

To be considered as a candidate the material must pass several gates. First, it must have good mechanical properties at the desired maximum operating temperature of 2200°C (4000°F). As a minimum, the melting point must be above this value. High melting point materials are shown in Figure 4.1-2. The combustion temperatures of a number of propellant combinations are also shown on the figure. These are the temperatures which would be achieved with an adiabatic chamber wall; actual temperatures are significantly lower because of radiation loss and gas side thermal resistance. A comparison of the ultimate tensile strengths of refractory materials as they approach their melting point is shown in Figure 4.1-3. Rhenium is clearly superior.

A second requirement is that the material be fabricable into the relatively complex shape required for a rocket engine, without degrading its desirable properties.

A third material criteria is that it have good resistance to chemical attack or be capable of being protected against attack by the combustion products. Oxidation resistance is a prime requirement, although material degradation by formation of carbides, hydrides, carbonyls or nitrides is a potential problem with some materials, propellants and operating conditions.

4.1.2 Processes

The objective of Task 1.2 was to select fabrication processes suitable for the high temperature chamber materials. Table 4.1.2-1 lists processes available for the fabrication of candidate materials and some of their characteristics. The CVD process for rhenium fabrication was chosen because of favorable experience with this technique in References 4.1.2-1 and 4.1.2-2. Techniques for preparing the protective iridium coating are shown in Table 4.1.2-2. Again, the CVD process was chosen because of prior experience.

The CVD fabrication process is shown schematically in Figure 4.1.2-1. A mandrel of the dimensions of the inside contour of the chamber is used as the basis for the CVD deposition. The iridium is deposited on the mandrel to the required thickness, and can be tested and examined as desired before proceeding with rhenium deposition. After buildup to the required minimum thickness the deposit can be ground to selectively reduce thickness and form

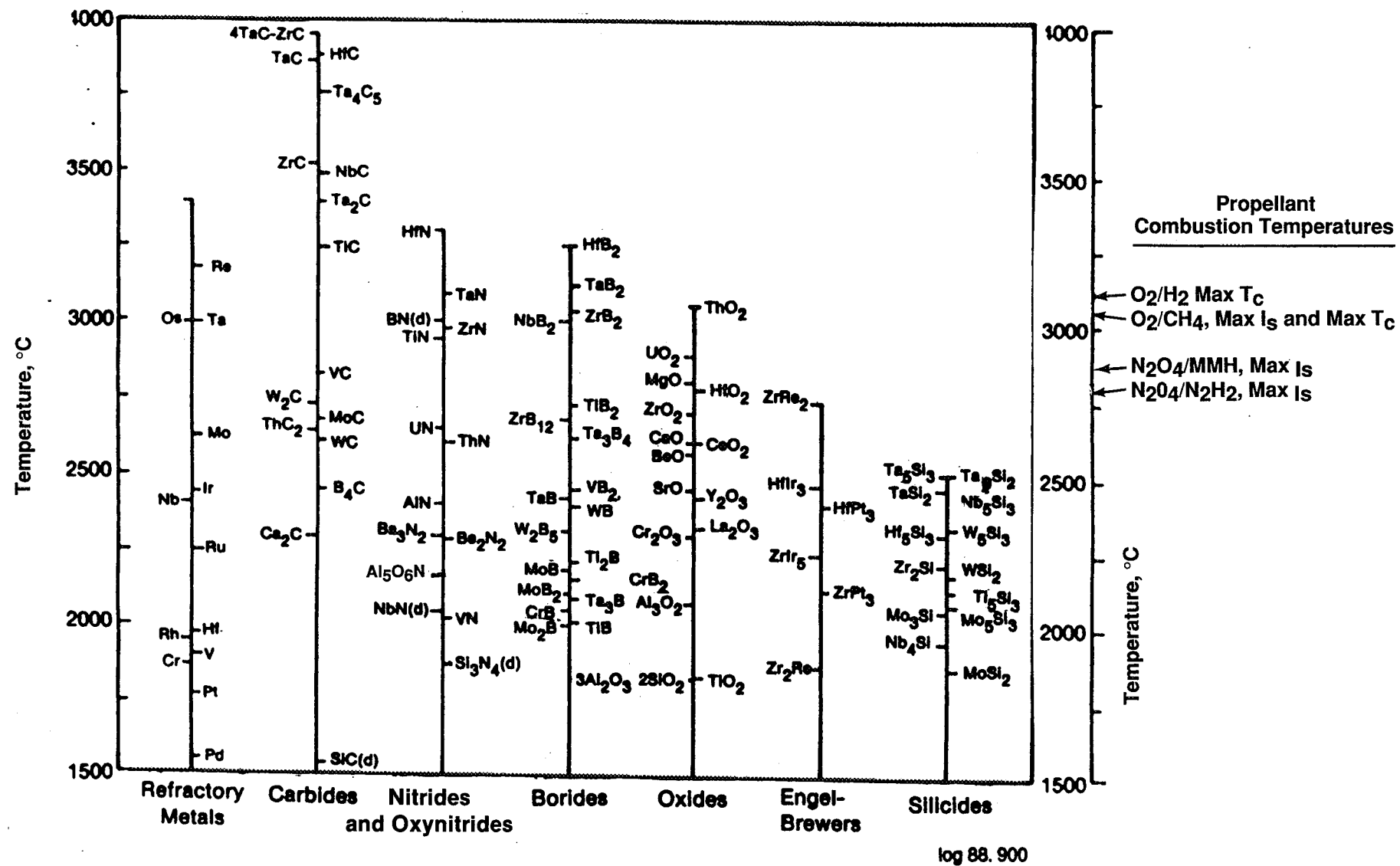


Figure 4.1-2. Melting Points of Candidate Materials

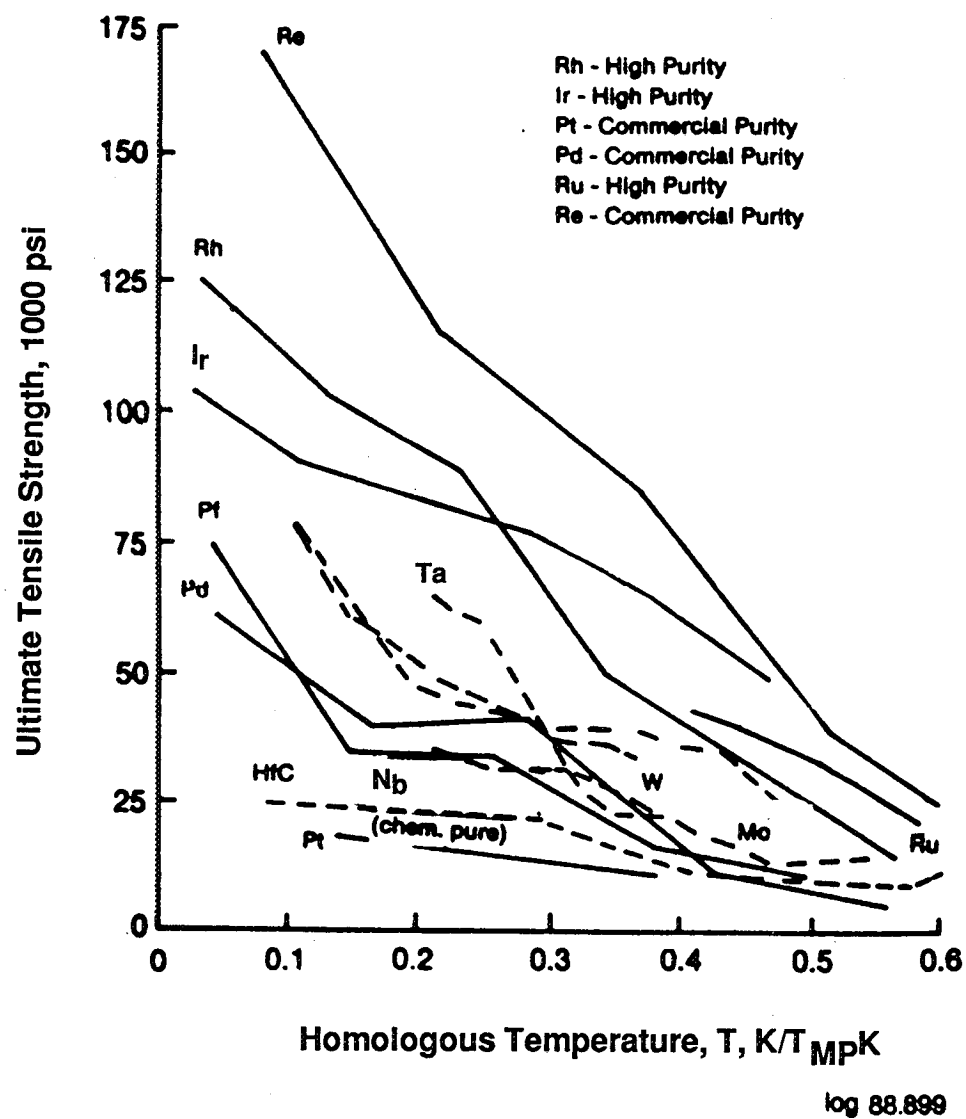


Figure 4.1-3. Ultimate Tensile Strength Versus Fraction of Melting Point Temperature.

Table 4.1-2-1. Candidate Chamber Materials and Processes

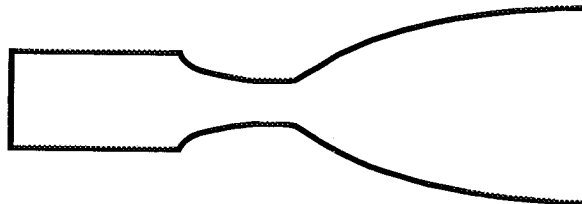
<u>Chamber Materials</u>	<u>Production Process</u>	<u>Suppliers</u>	<u>Propellant Application</u>	<u>Tm. °F</u>	<u>Key Properties Th. Cond (BTU*ft/hr*ft °F)</u>	<u>Ox Resist</u>	
<u>Hot Section Structural</u>							
Rhenium	CVD	Ultramet	ALL (Must Be Protected)	5760	44	Poor	
	PVD	Battelle					
G.S. Moly	P/M	R.J. Page Co.			4730	84.5	Poor
	P/M	Plansee					
Cb Alloys	Conventional	Wah Chang	Fluorinated Only	4470	30	Poor	
C-C Composites	Weave, Densify	ARC, Hitco, etc.			6420	15-25	Excellent
HfC/C Composites	Weave, CVI	RCI			7100/6420	7.5/15-25	Good
				All			
<u>Hot Section Coating</u>							
Iridium	CVD	Ultramet	All	4430	86	Excellent	
	See Table 4.1.2-2	See Table 4.1.2-2					
HfO ₂ /Iridium	CVD	Ultramet		5150/4430	1.5/86	Excellent	
	EB Sputter	Temescal					
HfO ₂ /Platinum	CVD	Ultramet		5150/3220	1.5/42	Excellent	
	EB Sputter	Temescal					
Iridium/Rhodium	EB Sputter	Temescal		4170	<86	Excellent	
<u>Front-End</u>							
Copper	Conventional	Several	H/O Only	1980	226	Fair	
Stainless Steel	Conventional	Several	All	2500	9	Good	
Platinum	Conventional	Johnson-Matthey	Storable Only	3220	42	Excellent	
Silver	Conventional	Johnson-Matthey			1763	244	Good

**Table 4.1.2-2.
Sources for Iridium Deposition**

Supplier	Location	Process	Deposition Efficiency	Recovery	Experience
Temescal	US	EB-VAP	40%	100%	YES
		SPUTTER	20%	100%	YES
Plansee	Austria	EB ION PL	10%	80%	YES
Battelle	US	SPUTTER	20%	?	YES
VaporTech	US	LT VAD	30%	?	NO
Comurhex	France	CVD	?	?	YES
Ultramet	US	CVD	?	?	YES
Aerojet	US	CVD	?	?	YES
Johnson-Matthey	US,UK	Fused Salt	100%	100%	YES
Westinghouse	US	Arc Deposition	?	?	NO

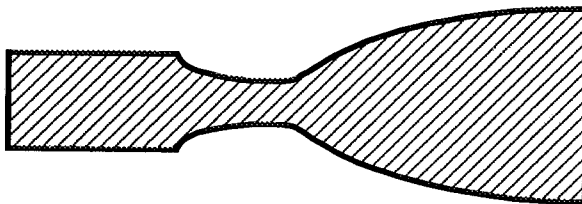
6.1.44-SJ

1. Mandrel



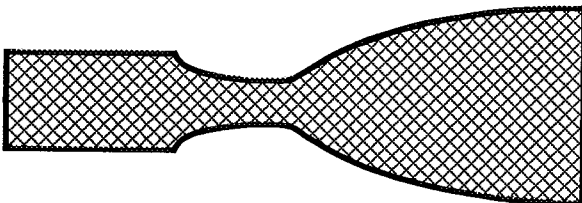
**Mandrel Plus Deposition Guides
Determine Deposit Uniformity**

2. CVD
Iridium
Deposit



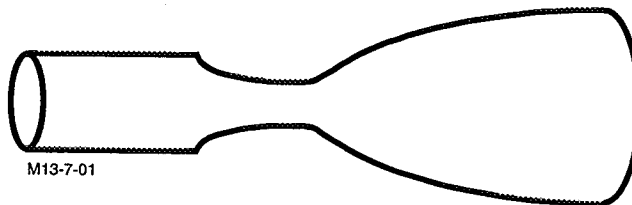
Heat Treat Deposit

3. CVD
Rhenium
Deposit



**Process Surface To Control
Emissivity If Required**

4. Remove
Mandrel



Free-Standing Chamber

Figure 4.1.2-1 CVD Chamber Fabrication Steps

4.1, Material, Process and Propellant Selection (cont.)

attachment sections. After overcoating with a high emissivity dentoid (tooth like) layer of Re, the mandrel is removed by etching.

The fabrication processes chosen for laboratory test specimens and flight thrusters are listed in Table 4.1.2-3.

4.1.3 Propellant Selection

The purpose of this task was to select the propellant combinations to be used in the experimental portions of the program. The selection was based on consideration of both the likely importance of the propellants in future missions and the logical development of a high-temperature materials technology base.

To assure that all reasonable propellant candidates were considered, potential propellants were screened by characteristics which are important to propulsion system applications. These characteristics include melting and boiling point, density, stability, toxicity, exhaust contamination, and application experience. The screening results are summarized in Table 4.1.3-1 with an assessment of whether the propellant should be considered further for this program. Three oxidizers passed this screen: hydrogen peroxide, nitrogen tetroxide, and oxygen. Ten fuels passed this initial screen: ammonia, diethyl hydrazine, dimethylhydrazine, ethane, hydrazine, hydrogen, methane, monomethyl hydrazine, propane and RP-1.

Further screening required assessment of the performance of the oxidizers and fuels as bipropellants and the possible application in which they will be employed.

The system applications considered included Space Station, Pathfinder, communication satellites, and other vehicles and spacecraft on which radiation-cooled thrusters are likely to be employed.

Specific impulse of many potential propellant combinations is shown in Figure 4.1.3-1, normalized to performance of the NTO/MMH propellant combination. The effect of mixture ratio on theoretical specific impulse for a selected group of propellants is shown in Figure 4.1.3-2.

From a performance standpoint ammonia loses out to hydrazine or MMH in combination with either oxygen or N_2O_4 , while hydrogen peroxide is inferior to nitrogen tetroxide in both specific impulse and density in combination with hydrazine or MMH.

**Table 4.1.2-3
Fabrication Technique**

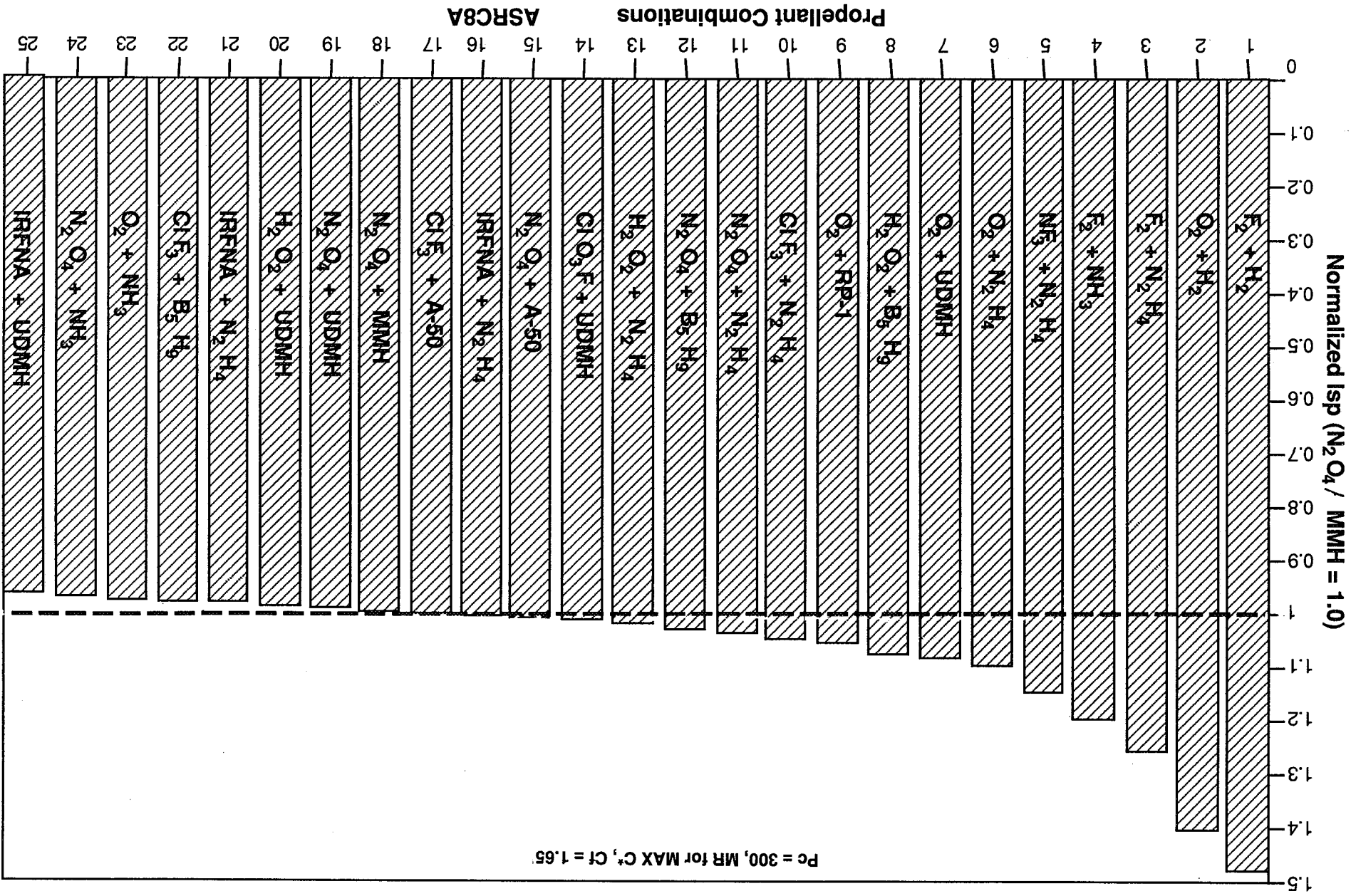
	Tasks 2, 5 MSTA Specimen	Task 6 DTC Specimen	Task 7 Thruster
Rhenium	Foil, 0.001 in. Thick	Foil, 0.004 in. Thick Roll and Weld Cylinder	CVD Re (0.02 to 0.03 in. Thick
Iridium	Foil, 0.001 in. Thick	Foil, 0.001 in. Thick Roll and Weld Cylinder	CVD Ir (.002 in. Thick)
Platinum	Foil, 0.001 in. Thick	Foil, 0.004 in. Thick Roll and Weld Cylinder	Machine Wrought Bar

Table 4.1.3-1
Propellant Screening - Oxidizers, Page 1 of 2

NAME	FORMULA	MELTING POINT, C	BOILING POINT, C	DENSITY	STORABILITY	STABILITY	TOXICITY	REACTIVITY	EXHAUST CONTAM.	EXPERIENCE	COST	AVAILA- BILITY	CONSIDER FOR ASAC?
CHLORINE PEROXIDE	C1207	-91.5	82	1.76	stable (cryo)	good	high	high	moderate	low	...	no	no
CHLORINE PENTAFLUORIDE	C1F5	-102	-13.7	1.76	stable (cryo)	good	high	high	moderate	moderate	...	no	no
CHLORINE DIOXIDE	C1O4			high	high	moderate	moderate	...	no	no
CHLOROTETROXY FLUORIDE	C1O4F	-163.7	-15.9	...		explosive	high	high	moderate	low		no	no
CHLORINE TRIFLUORIDE	C1F3	-83	11.3	1.77			high	high	moderate	moderate		no	no
CHLOROSYL TRIFLUORIDE	C1F3O	-163.5	-57	1.45(1) 1.91(6)			high	high	moderate	moderate		no	no
DIOXYGEN FLUORIDE	F2O2	-163.5	-57	1.31	stable (cryo)	stable	high	high	moderate	moderate		no	no
FLUORINE	F2	-219.6	-188.1	1.31	stable (cryo)	stable	high	high	moderate	moderate		no	no
FLUORINE DIOXIDE	F2O	-223.8	-144.8	1.45			high	high	moderate	moderate		no	no
HYDROGEN PEROXIDE	H2O2	-0.41	150.2	1.442	possible	decomposes	high	high	moderate	moderate		no	no
HYDRONIUM PENTACALBATE	HC164	-112	39	1.764	poor	unstable	high	high	moderate	moderate		yes	no
NITROGEN TETRAFLUORIDE	N2F4	-11.2	21.2	1.499	good	good	high	high	moderate	moderate		no	no
NITROGEN TETROXIDE	N2O4	-11.2	21.2	1.499	good	good	high	high	moderate	moderate		yes	no
NITROGEN TRIOXYFLUORIDE	N2O3F	-175	-45.9	1.507	decomposes	explosive	high	high	moderate	moderate		no	no
NITROGEN TRIOXIDE	N2O3			high	high	moderate	moderate		no	no
DIYBEN	N2	-218.4	-183.0	1.149	good; cryo.	good	low	moderate	moderate	extensive	low	good	yes
DIYBEN DIFLUORIDE	NF2	-223.8	-144.8	1.9	poor	unstable	high	high	moderate	moderate		no	no
DIYBEN	O2	-192.7	-111.9	1.614	poor	unstable	high	high	moderate	moderate		no	no
PENTACHLORYL FLUORIDE	Cl83F	-146	-46.8	1.39			high	high	moderate	moderate		no	no

Table 4.1.3-1
Propellant Screening – Fuels, Page 2 of 2

NAME	FORMULA	MELTING POINT, C	BOILING POINT, C	DENSITY	STORABILITY	STABILITY	TOXICITY	REACTIVITY	EXHAUST CONTAM.	EXPERIENCE	COST	AVAILA- BILITY	CONSIDER FOR ASRC?
FUELS													
ACETYLENE	C ₂ H ₂	-81.8	-83.6 (sub.)	0.618	poor	explosive	low	moderate	none	low	low	good	no
AMMONIA	NH ₃	-77.7	-33.4	0.771	good	good	low	low	none	extensive	low	good	yes
BUTYL LITHIUM	C ₄ H ₉ Li	150(d)	0.743					high				no
CARBON ADDITIVE	C (graph.)	3652 (SUB.)	4200	2.25		good	low	low	none	low	low	good	no
	C (diam.)	>3550	4827	3.51		good	low	low	none	none	high	poor	no
CARBON SUBOXIDE	C ₃ O ₂	-111.3	7.0	1.114					none				no
CYANOGEN	HCCN	-27.9	-20.7	2.335			highly toxic		none	low	moderate	moderate	no
CYCLOBUTANE	C ₄ H ₈	-50	12	0.720	good (cryo)							good	no
DIBORANE	B ₂ H ₆	-165.5	-92.5	0.447	good	good	moderate	low	high	moderate	high	moderate	no
DIETHYL HYDRAZINE	(C ₂ H ₅) ₂ N ₂	...	84-86	...	good	good		low	none	low	high		yes
DIMETHYL HYDRAZINE	(CH ₃) ₂ N ₂	...	81	0.827	good	good		low	none	low	high		yes
ETHANE	C ₂ H ₆	-183.3	-88.6	0.572	good	good	low	low	none	moderate	low	good	yes
HYDRAZINE	N ₂ H ₄	1.4	113.5	1.011	good	good	high	low	none	extensive	moderate	good	yes
HYDROGEN	H ₂	-259.1	-252.5	0.07	poor	good	low	low	none	extensive	low	good	yes
METAL ADDITIVES	VARIOUS	good (as gel)	moderate	varies	varies	high	moderate	moderate	good	no
METHANE	CH ₄	-182	-164	0.466	good	good	low	low	none	moderate	low	good	yes
MONOMETHYL HYDRAZINE	N ₂ H ₃ CH ₃	-32.4	87.7	0.879	good	good	high	low	none	extensive	high	good	yes
PENTABORANE	B ₅ H ₉	-46.8	58.4	0.66	good	good	high	low	high	low			no
PROPANE	C ₃ H ₈	-189.9	-44.5	0.589	good	good	low	low	none	low	low	good	yes
RP-1	*H/C=2	*-48	*217	0.807	good	good	low	low	none	extensive	low	good	yes

Figure 4.1.3-1. Normalized Isp ($N_2O_4 / MMH = 1.0$)

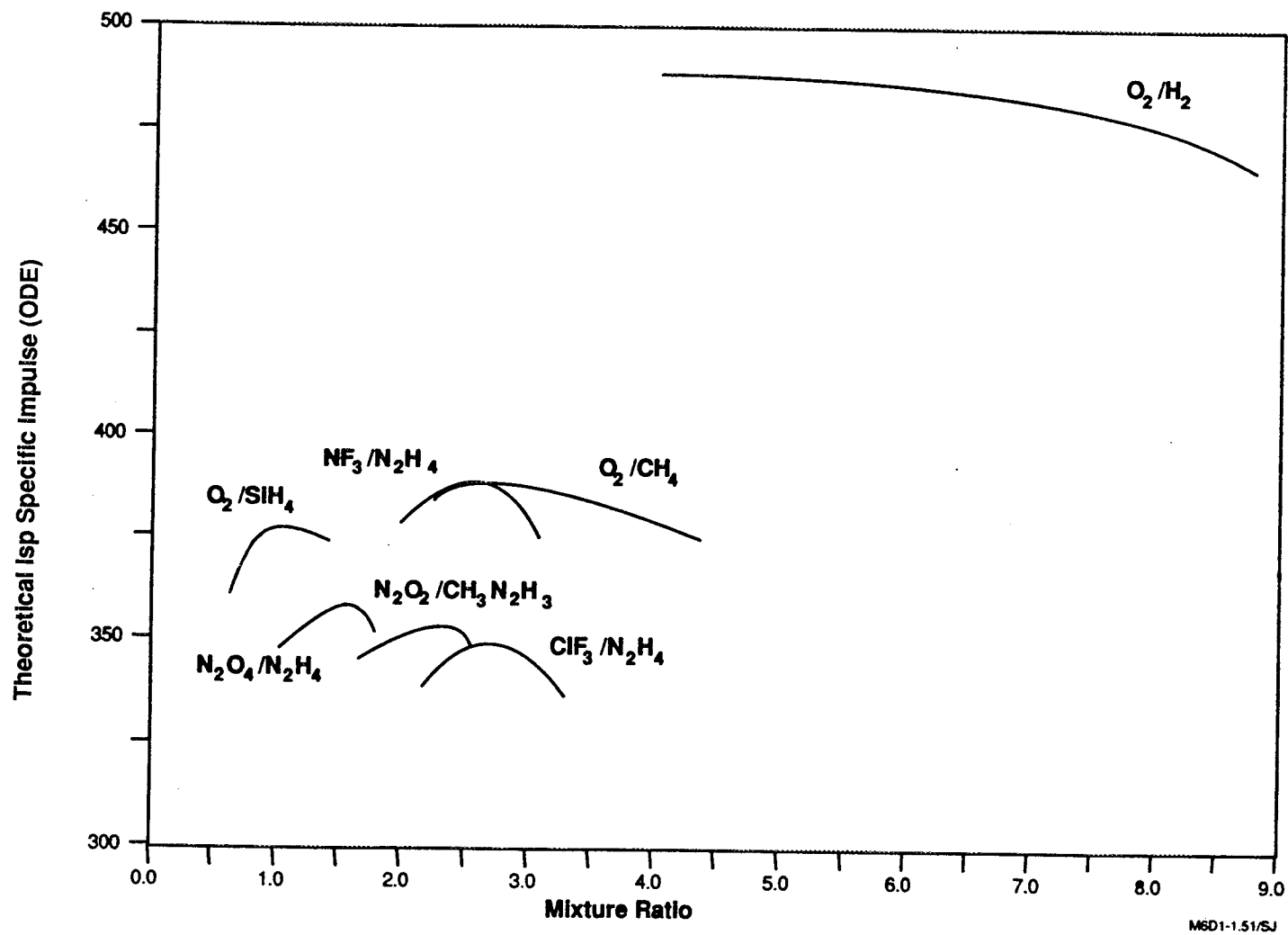


Figure 4.1.3-2. Theoretical Isp Vs. MR for Various Oxidizer/Fuel Combinations

4.1, Material, Process and Propellant Selection (cont.)

The choices for oxidizer condense to oxygen for applications which can tolerate cryogenic propellants and N_2O_4 for those that cannot. This has the proviso that hydrogen peroxide could be used, in applications where the toxicity of N_2O_4 is not acceptable, with a slight reduction in I_s and density, the penalty of a relatively high freezing point, and some reduction in long term storage life because of decomposition. The peroxide should retain the advantage of hypergolicity with either hydrazine or MMH.

For applications where cryogenic propellants are acceptable, hydrogen or methane with oxygen are the propellants of choice, $\text{O}_2\text{-CH}_4$ because of its high I_s , combined with its six-fold increase in density over hydrogen. Ethane, propane and RP-1 could have niches which depend on a tradeoff between I_s , density and storage temperature; from the standpoint of this program their chemistry is covered generically by methane. Of the remaining fuel possibilities, the chemistry of diethyl and dimethyl hydrazine is well represented by monomethyl hydrazine, which is very well understood and for which there is an extensive experience base. Hydrazine is a logical choice to accompany the MMH. It permits dual-mode operation which can be important in some applications and it gives a simpler chemistry to understand in advance of MMH experiments.

Systematic development of the materials technology base and the use of laser base and emission diagnostics dictated that the program begin with simple chemistry and progress to more complex chemistry. The program began with the least complex chemistry, i.e., that provided by the O_2/H_2 bipropellant combination. The program then proceeded with a three element system with the addition of a carbon-containing fuel, i.e., O_2/CH_4 and concluded with the most complex of the earth storable bipropellant combinations, i.e., $\text{N}_2\text{O}_4/\text{CH}_3\text{N}_2\text{H}_3$.

Consideration of present and future applications for radiation-cooled thrusters results in a similar list of bipropellant combinations. Space Station was based, in large part, on development of a "water economy". The on-board propulsion is based on the O_2/H_2 bipropellant combination. Pathfinder chemical transfer propulsion was based on O_2/H_2 , in conjunction with, or independent of, Space Station.

Both O_2/H_2 and O_2/CH_3 were considered for Advanced Launch System propulsion. Indeed a goal of ALS was to make this propulsion system "fuel transparent", i.e., to develop engines which operate equally well on O_2/H_2 and O_2/CH_4 .

Orbit transfer (ΔV) and on-orbit (RCS) propulsion systems for current and future satellites are being based more and more on the $\text{N}_2\text{O}_4/\text{CH}_3\text{N}_2\text{H}_3$ bipropellant combination, e.g., Intelsat 5, 6 and 7. The Mariner Mark II Bus uses $\text{N}_2\text{O}_4/\text{CH}_3\text{N}_2\text{H}_3$ as does the Orbit

4.1, Material, Process and Propellant Selection (cont.)

Maneuvering Vehicle. More recently, the use of N_2O_4/N_2H_4 for spacecraft has been discussed to improve performance and permit dual mode operation with simplified propulsion systems. Table 4.1.3-2 summarizes propellant application experience on a number of production propulsion systems.

For these considerations, it appears that the needs of (1) systematic development and (1) current and future applications can best be served by the study of four bipropellant combinations. In the order of complexity of chemistry these are O_2/H_4 , O_2/CH_4 , N_2O_4/N_2H_4 , and $N_2O_4/CH_3N_2H_3$.

Interactions between propellant combustion products and chamber material over the range of operating conditions were considered. Extent of reactive species in the combustion products and potential volatile reaction products with the wall impact wall life.

Major and minor species for six potential propellant combinations at a specified MR, are shown in Table 4.1.3-3, along with ODE specific impulse and combustion temperature.

The evaluation of the best combinations of propellants and materials included the most recent experience of Aerojet and others and considered thermochemical predictions of suitable operating regimes (MR, T_{wall} , Pc) for candidate material/propellant combinations.

The three materials recommended in Subtask 1.1 are potentially suitable for construction of thrusters for all four selected propellant combinations.

Given the recommended set of propellant combinations, it is practical to explore the expected combustion species to which the chamber materials will be exposed. Equilibrium composition calculations were performed for the following conditions.

<u>Propellant</u>	<u>MR Range</u>	<u>Pc Range, Atm</u>
O_2/H_2	to 10	1, 5 and 10
O_2/CH_4	2 to 5	1, 5 and 10
N_2O_4/N_2H_4	1 to 2	1, 5 and 10
$N_2O_4/CH_3 N_2H_3$	1 to 3	1, 5 and 10

Table 4.1.3-2
Liquid Propellants Used in Production Bipropellant
Propulsion Systems

Earth Storable Propulsion Systems	Bipropellant Combinations
Titan IV, Stages 1 and 2	N_2O_4 /AeroZINE-50 ^a
Medium Launch Vehicle, Stage 2	N_2O_4 /AeroZINE-50 ^a
Peacekeeper, Stage IV	N_2O_4 / $CH_3N_2H_3$
STS Orbiter, Maneuvering and Reaction Control	N_2O_4 / $CH_3N_2H_3$
Geostationary Satellites, Orbit Transfer and Station Keeping	N_2O_4 / $CH_3N_2H_3$
Cryogenic Propulsion Systems	
Medium Launch Vehicle, Stage 1	LO_2 /RP-1 ^b
STS SSME	LO_2 / LH_2
Centaur Upper Stage, RL-10	LO_2 / LH_2

^a AeroZine-50, $N_2H_4 + (CH_3)_2 N_2H_2$, 50-50 wt%

^b RP-1, $n-C_{12}H_{26}$ Kerosene Distillate Cut

M7D4/N4

Table 4.1.3-3.
Equilibrium Composition of Candidate Bipropellant
Combinations at Chamber Conditions (Pc = 5 atm)

	O ₂ /H ₂	O ₂ /CH ₄	O ₂ /SiH ₄	N ₂ O ₄ / N ₂ H ₄	N ₂ O ₄ / MMH	ClF ₃ / N ₂ H ₄
Mixture Ratio	4.35	3.39	0.88	1.40	2.34	2.84
Temperature	5493 R	5873 R	5121 R	5445 R	5603 R	6420 R
Isp (vac) @ 150:1	492 sec	394 sec	376 sec	358 sec	356 sec	352 sec
CO	—	0.18886	—	—	0.08323	—
CO ₂	—	0.10348	—	—	0.06498	—
Cl	—	—	—	—	—	0.09568
ClF	—	—	—	—	—	0.00002
Cl ₂	—	—	—	—	—	0.00010
F	—	—	—	—	—	0.01338
F ₂	—	—	—	—	—	—
H	0.05332	0.04687	0.02774	0.02067	0.02405	0.05523
HC	—	—	—	—	—	—
HCL	—	—	—	—	—	0.08594
HF	—	—	—	—	—	0.53212
H ₂	0.42144	0.10044	0.44946	0.07433	0.06005	0.03278
H ₂ O	0.50072	0.42115	0.19111	0.43399	0.34727	—
HO ₂	—	0.00003	—	0.00001	0.00002	—
N	—	—	—	—	0.00001	0.00006
NH	—	—	—	—	—	—
NO	—	—	—	0.01022	0.01328	—
N ₂	—	—	—	0.39592	0.31522	0.18468
O ₂	0.00172	0.02235	0.00014	0.00708	0.01242	—
OH	0.02192	0.07927	0.00345	0.04104	0.05052	—
O ₂	0.00083	0.03753	0.00002	0.01671	0.02894	—
SiO	—	—	0.27132	—	—	—
SiO ₂	—	—	0.00114	—	—	—
SiO ₂ (l)	—	—	0.05561	—	—	—
SiO ₂ (s)	—	—	0.00001	—	—	—

M7/D4/N3

4.1, Material, Process and Propellant Selection (cont.)

The mixture ratio ranges were chosen to bracket the nominal operating conditions so that composition data are available for off-MR conditions which can represent either poor mixing or film cooling and core flows. The chamber pressure ranges were selected to cover the range planned for the Sandia experiments, the thruster tests at Aerojet, and typical flight thruster conditions.

A representative set of composition data are given in Figures 4.1.3-3 through 4.1.3-6 for the four propellant combinations at 5 atmospheres. The complete set of composition data is given in Appendix B, in graphical form. Plots of combustion temperature and theoretical specific impulse ($\epsilon = 75$, vacuum) are given for the four propellant combinations as a function of MR. For convenience, these data are also tabulated, along with composition data, in the Appendix.

An equilibrium model of the interaction of chamber materials and combination products was evaluated as a way to correlate the data to be obtained in MSTA tests at Sandia and DTC tests at Aerojet. This approach is straightforward and represents a limiting bound for the process at the chamber wall. The process is represented by the reaction



where the metal/combustion product compounds can be oxides, hybrids, nitrides, carbides, carbonyls and the like.

To perform the calculations requires the availability of thermodynamic properties of the possible products as a function of temperature. A complete set was available for copper. The results of these calculations for copper are shown in Figure 4.1.3-7. The lower curve shows solid copper in equilibrium with copper vapor with chemical reactions suppressed; this represents the lower limit of the removal mechanism. The second curve shows the equilibrium conditions considering metal vapor, copper oxides, and hydride formation. In this example, at the extreme upper end of the range of copper wall temperature (1300°F on the hot surface), the mole fraction of reacted copper is about 5 orders of magnitude higher than that of the vapor without reaction.

In this form, this model can provide an indication of the temperature and MR range at which significant reaction of wall material will occur. Coupled with assumptions on

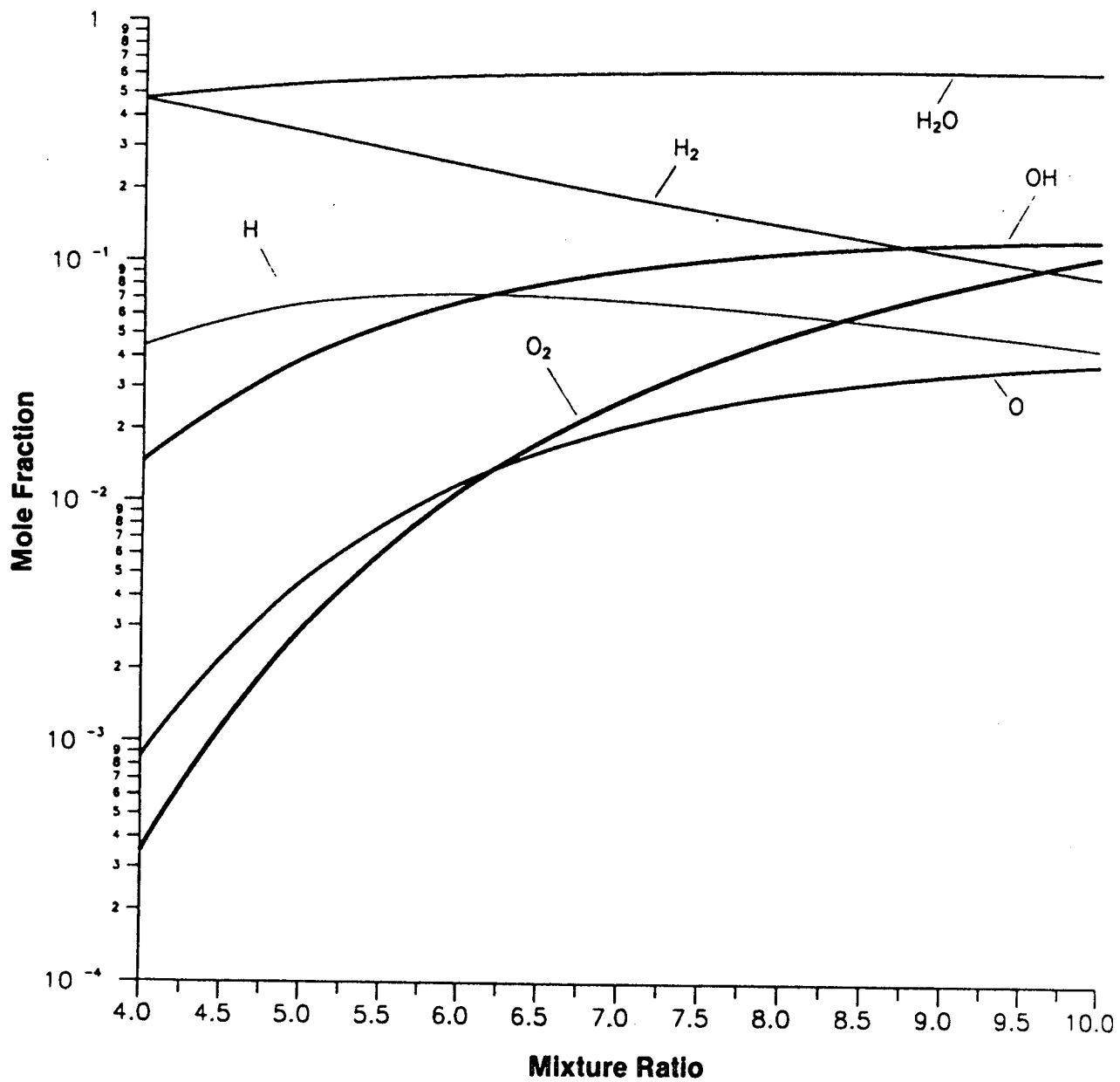


Figure 4.1.3-3. Mole Fraction Versus Mixture Ratio of Oxygen/Hydrogen at 5 atm

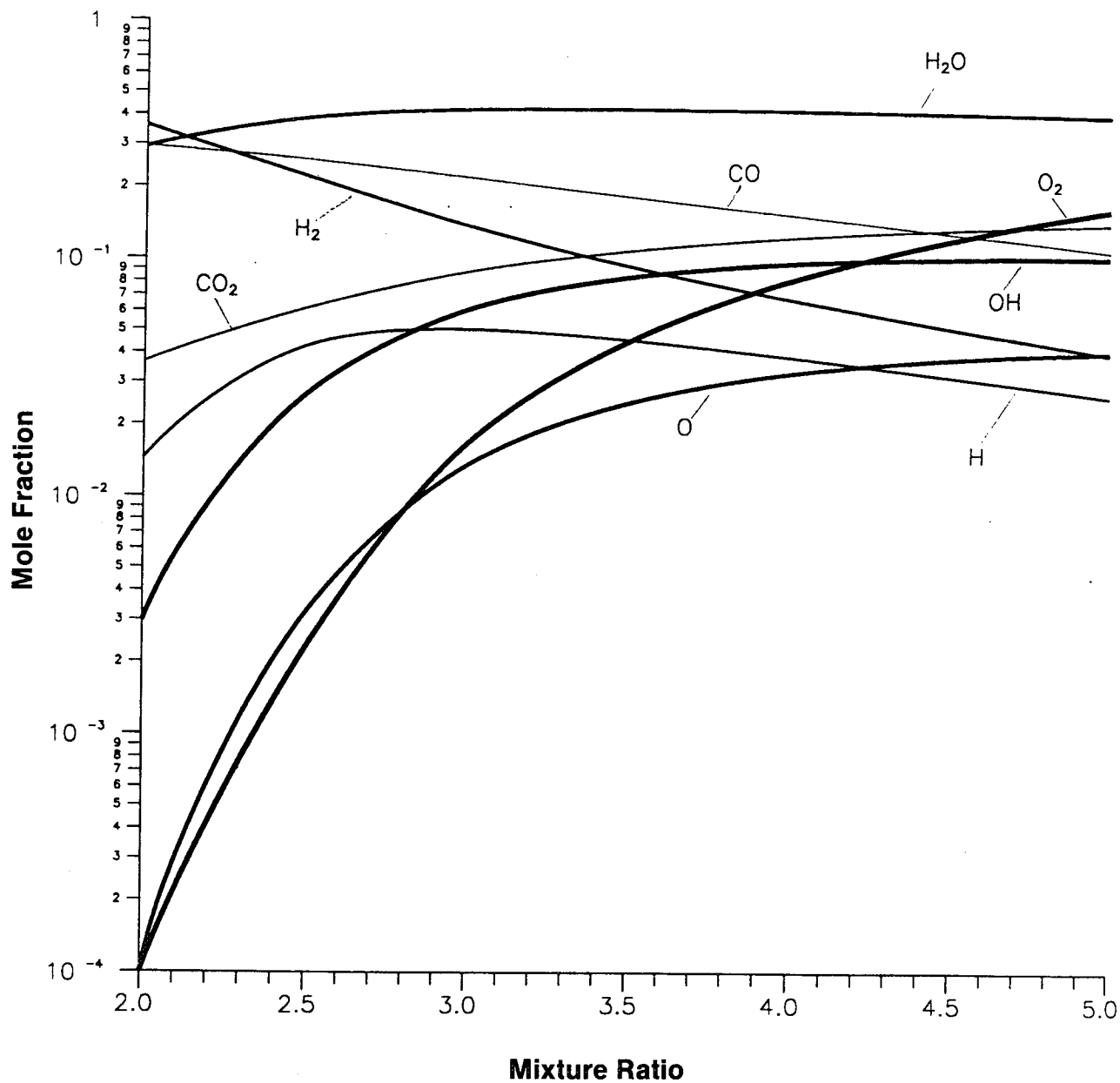


Figure 4.1.3-4. Mole Fraction Versus Mixture Ratio for Oxygen/Methane at 5 atm

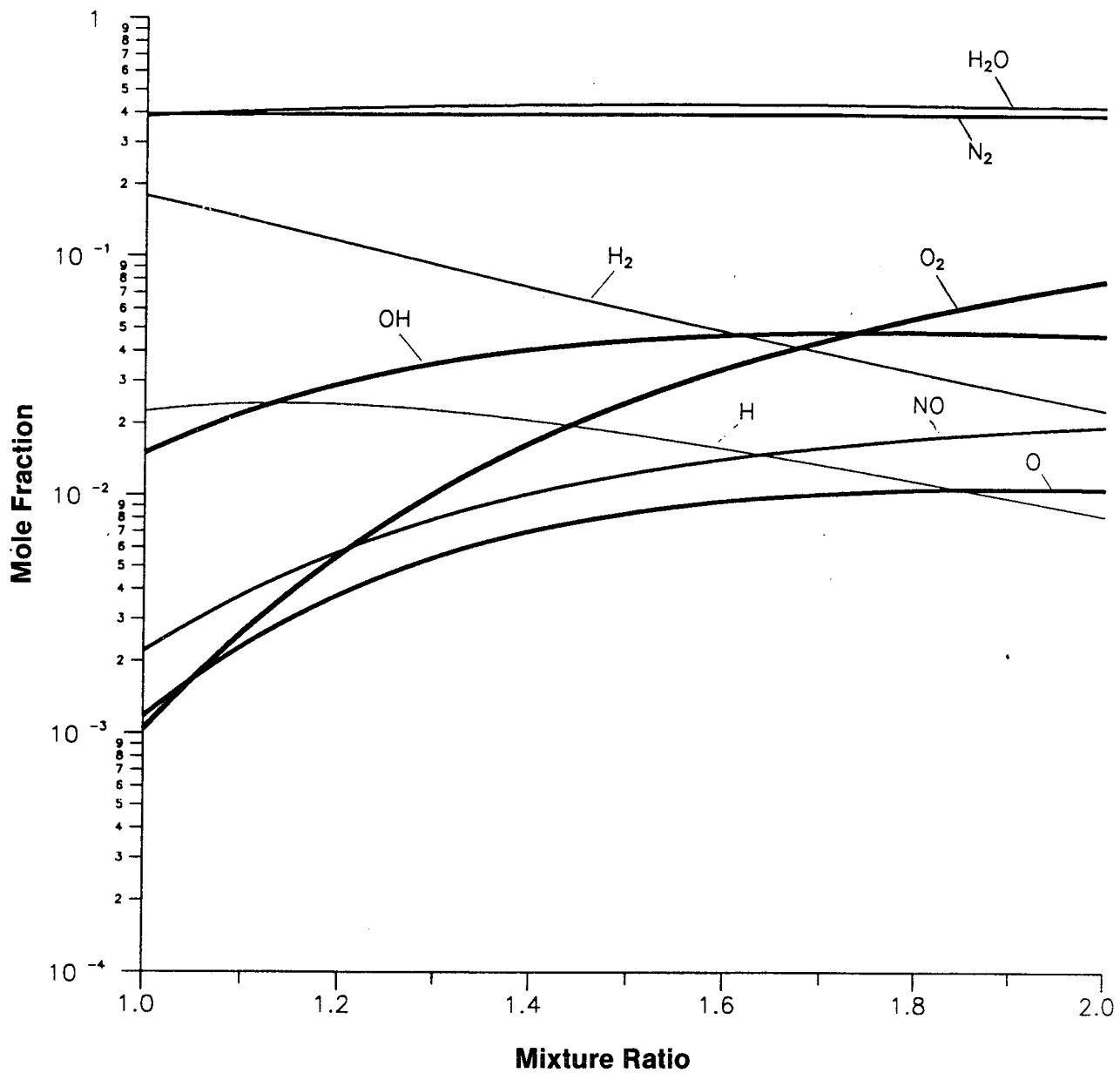


Figure 4.1.3-5. Mole Fraction Versus Mixture Ratio for Nitrogen Tetroxide/Hydrazine at 5 atm

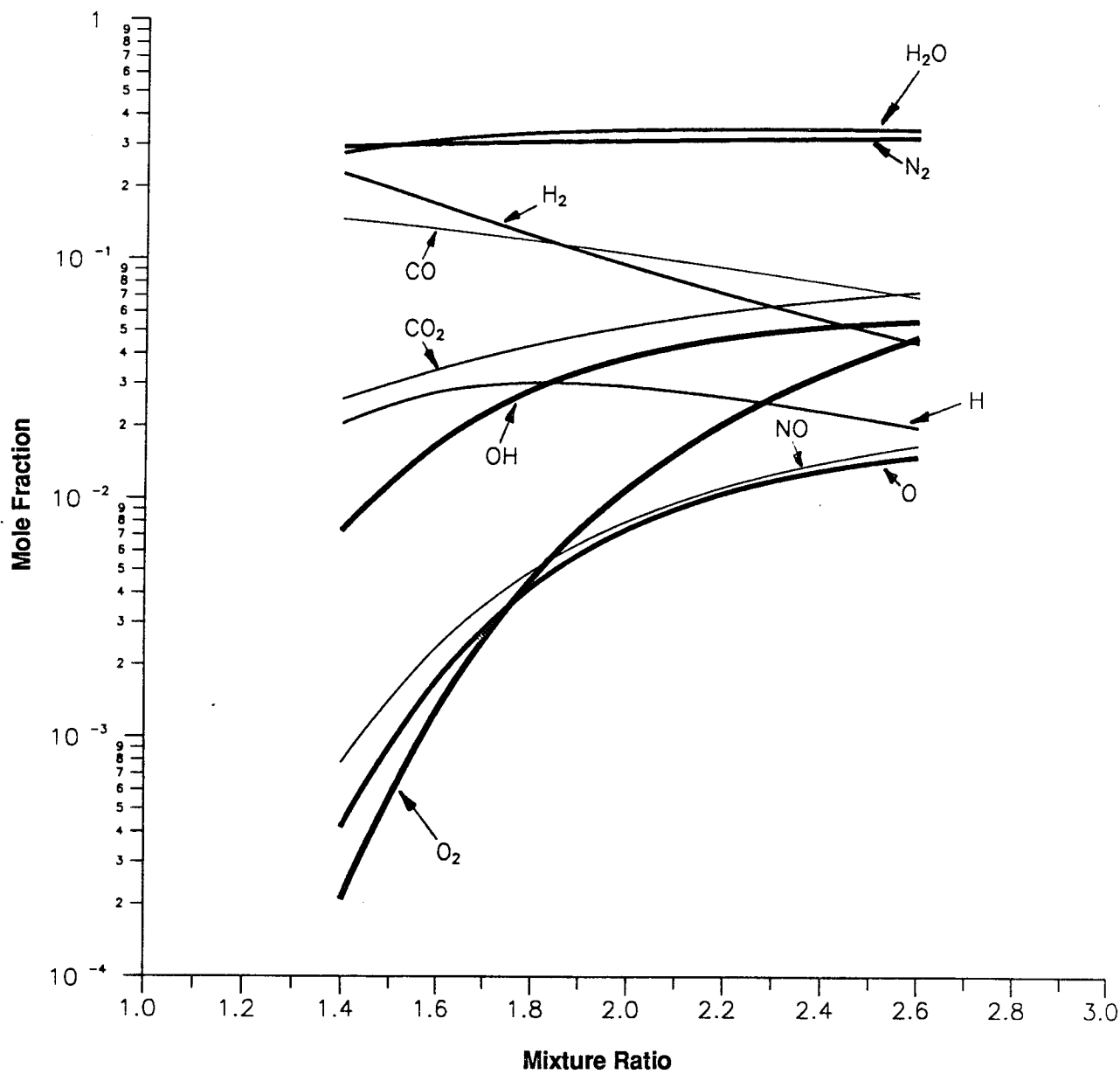


Figure 4.1.3-6. Mole Fraction Versus Mixture Ratio for Nitrogen Tetroxide/Monomethylhydrazine at 5 atm

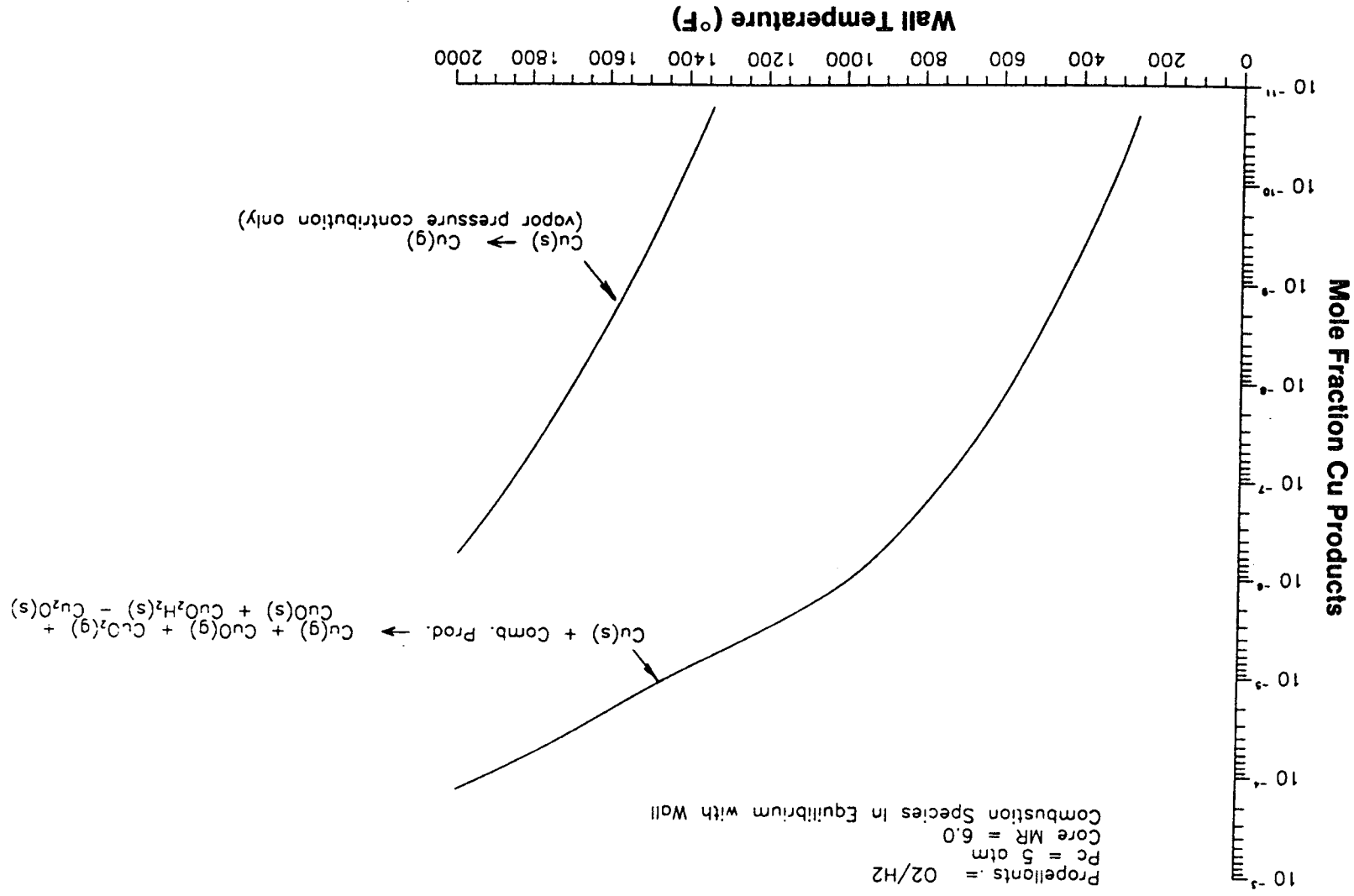


Figure 4.1.3-7. $O_2/H_2/Cu$ Equilibrium

4.1, Material, Process and Propellant Selection (cont.)

boundary layer conditions, loss rates can be predicted, as shown in Figure 4.1.3-8 from Reference 5 for molybdenum in O_2/H_2 combustion products.

The value of such analysis appears high and should be pursued. It requires (1) collection and/or generation of reasonable thermodynamic data for the possible reaction products and (2) inclusion of simple but reasonable correlations for boundary layer conditions to permit absolute wall regression rate prediction as a function of wall temperature and combustion conditions (propellant, MR, Pc).

An Aerojet-sponsored program was conducted to demonstrate an inexpensive laboratory approach for obtaining these data. Measurements were made of material reaction rates in Reference 6 using a simplified version of the material screening apparatus shown in Figure 4.1.3-9, in oxygen-ethane combustion products. These were exploratory tests to determine feasibility for obtaining chamber material reaction rate data on a simple wire specimen. A sequence of photomicrographs of a molybdenum specimen during a portion of a long duration exposure is shown in Figure 4.1.3-10. Reaction rate measurements made on molybdenum, columbium (niobium) and titanium are shown in Figure 4.1.3-11.

This approach can provide direct reaction measurements on simple, standardized, readily available specimens under defined temperature, composition and pressure conditions to use in providing inputs to and validation of chamber wall reaction rate models.

4.2 TEST SAMPLE PREPARATION

Material test specimens of iridium platinum and rhenium were designed and fabricated for use at Sandia in MSTA gas phase measurements and surface measurements and for use as simulated combustion chambers in the Diagnostic Thrust Chamber.

The MSTA specimens were rectangular approximately 1.0 by 1.75 inches. These were electrically heated by passing a current through the foil. To limit the heating current to about 500 amps required a 1 mil thick specimen. The DTC specimens, whose design is shown in Figure 4.2-1, were planned to be 4 mil thick. However, the iridium was only available in 1 mil foil. The specimens ordered for the study are listed in Table 4.2-1.

The specimens fabricated for the DTC used laser welding of the seam to form a cylinder. This was successful for the 4 mil Re and Pt but not for the 1 mil Ir.

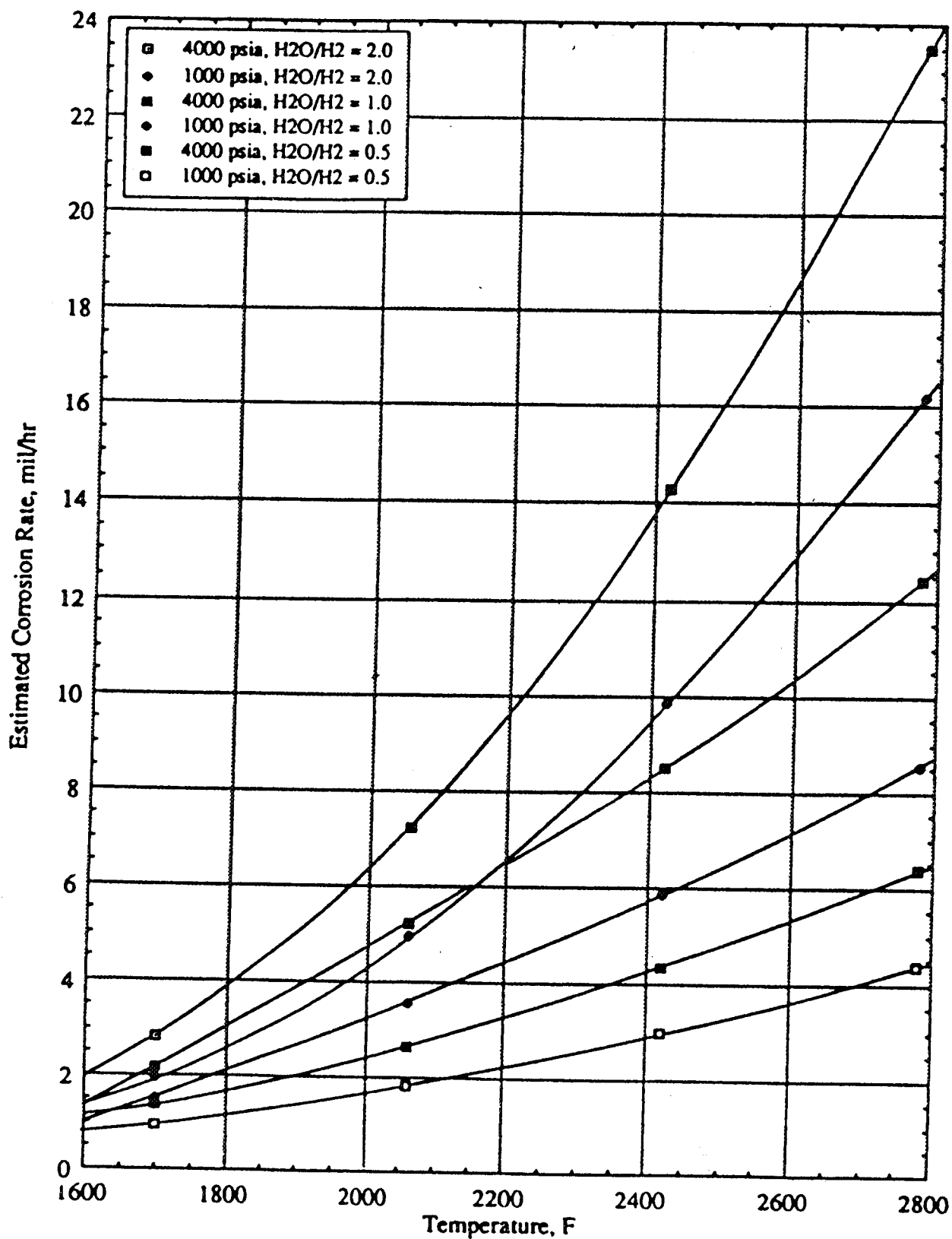


Figure 4.1.3-8. Estimated Corrosion Rate of Molybdenum in H₂O/H₂ Atmospheres

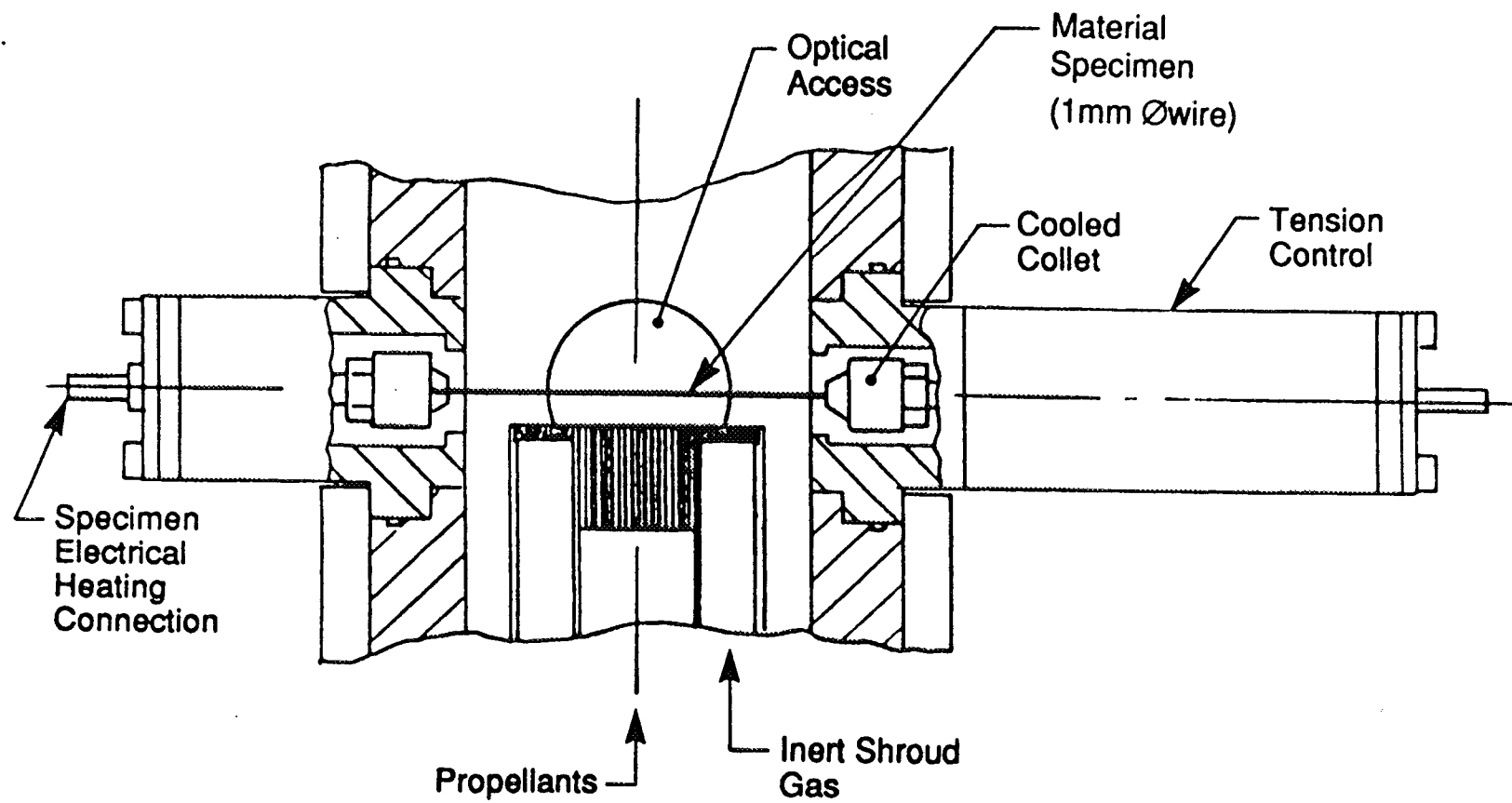


Figure 4.1.3-9. Laboratory Screening of Materials

MR = 3.0
P_c = 1 ATM
Specimen O.D. = 1.0 mm
Material Loss Rate = 201 Micron/hr

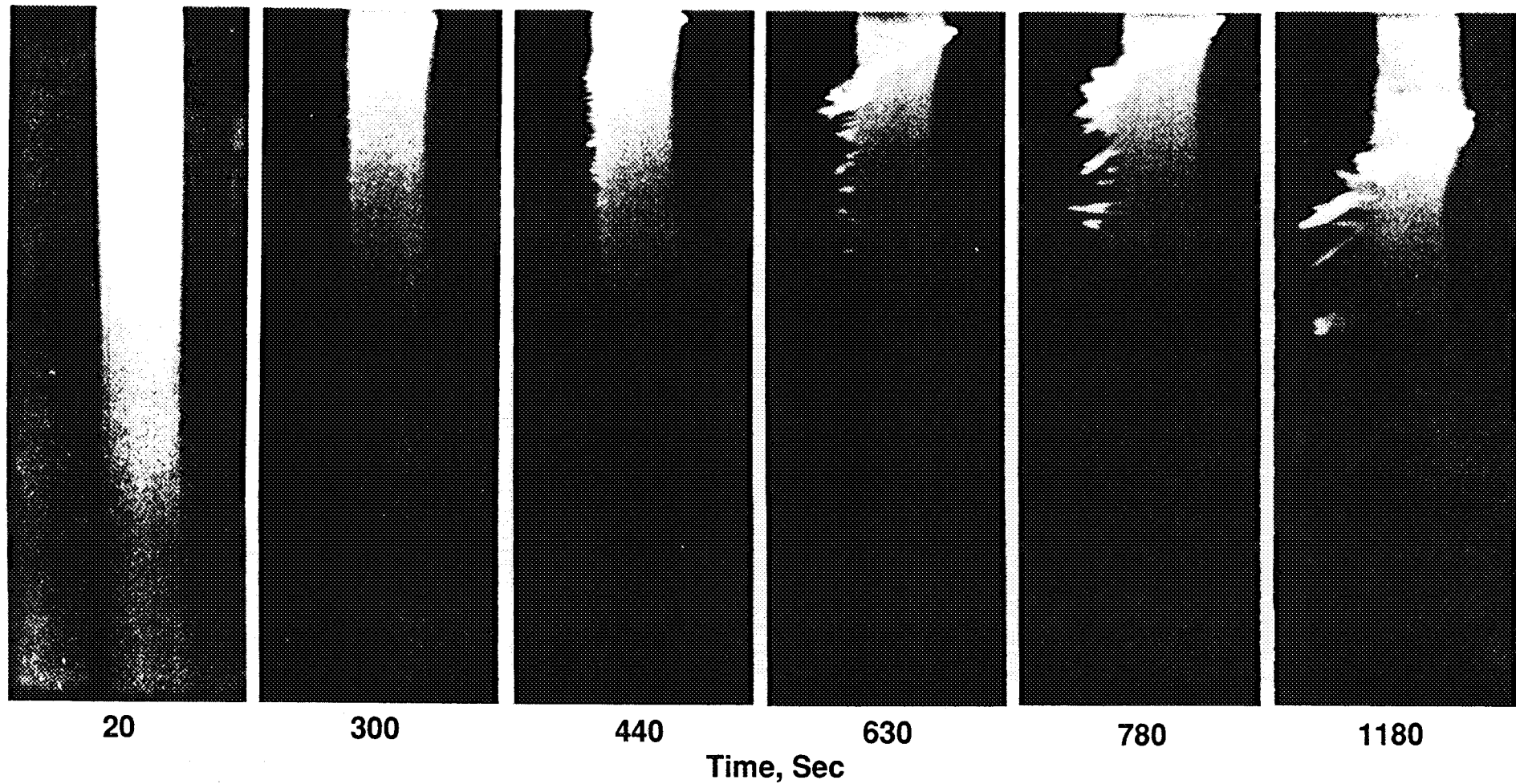


Figure 4.1.3-10. Molybdenum Exposed to Oxygen-Ethane
Combustion Products

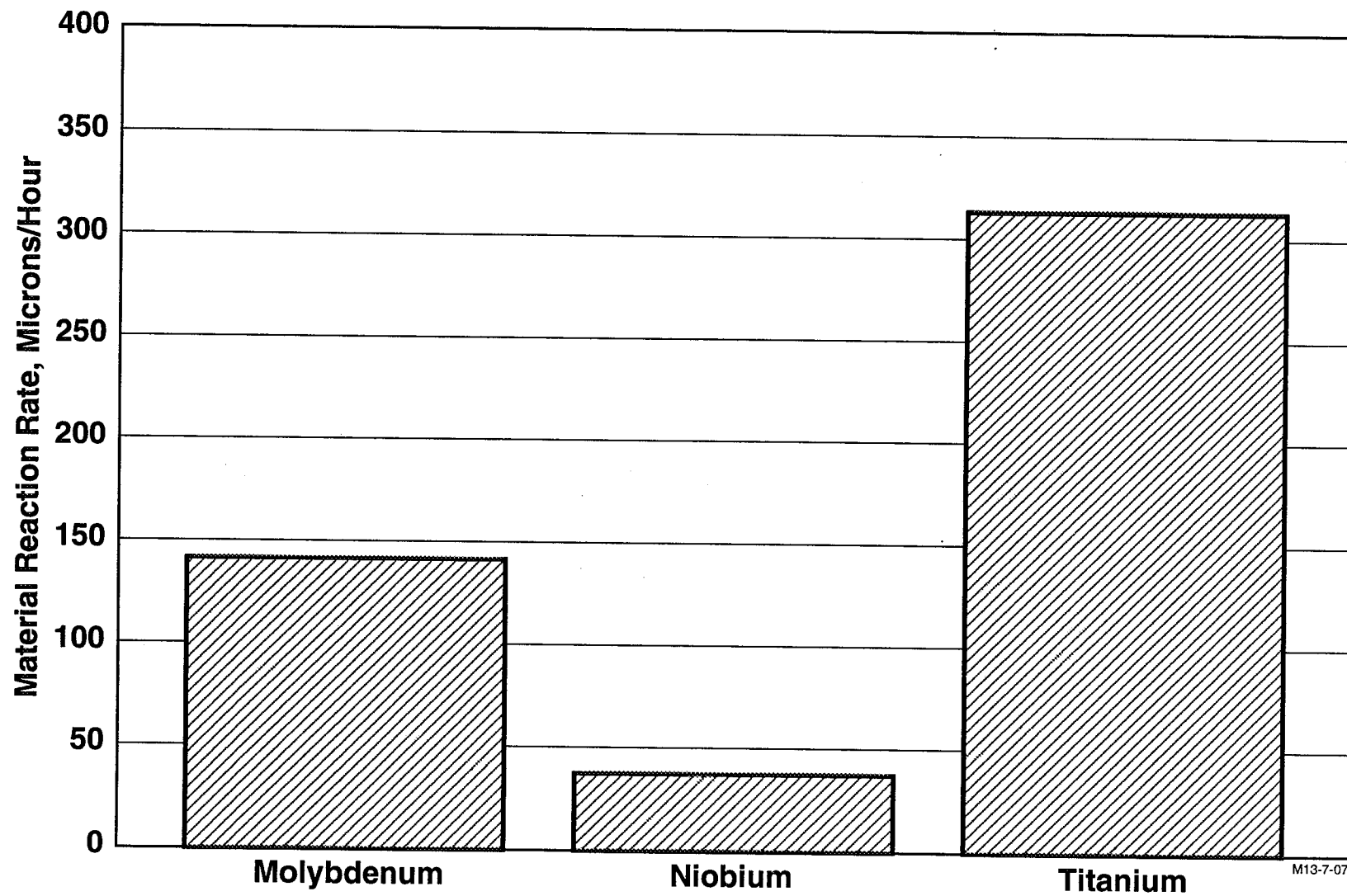


Figure 4.1.3-11. Material Reaction Rate – Oxygen/Ethane, MR = 3.0 1 Atm

[illegible]

YELLOW

>FB OR LASER WELD

STOCK

502 DIA 504

1.075

INFORMATION PRINT ONLY
 DO NOT FOLD HERE
 THIS INFORMATION PRINT IS
 TO BE USED TO IDENTIFY
 THE INFORMATION PRINT ONLY
 DATE

SPECIMEN

14915

000000 07001 104 00

D	05874
---	-------

Table 4.2-1 MSTA and DTC Specimen Materials

<u>Item No.</u>	<u>Quantity</u>	<u>Description</u>
1	10 each	Rhenium Foil, 99.9% or Better, 1.00 inch by 1.75 inch, by 0.001 inch thick
2	10 each	Rhenium Foil, 99.99% or Better, 1.88 inch by 2.0 inch, by 0.004 inch thick
3	10 each	Iridium Foil, 99.9% or Better, 1.00 inch by 1.75 inch, by 0.001 inch thick
4	8 each	Iridium Foil, 99.9% or Better, 1.88 inch by 2.0 inch by 0.001 inch thick
5	12 each	Platinum Foil, 99.9% or Better, 1.00 inch by 1.75 inch, by 0.001 inch thick
6	8 each	Platinum Foil, 99.9% or Better, 1.88 inch by 2.0 inch by 0.004 inch thick

Material must be free of creases, wrinkles or scratches.

Each item must be packaged separately to protect from shipping and handling damage.

4.2, Test Sample Preparation (cont.)

Photographs of DTC specimens are shown in Figure 4.2-2. SEM photos of a portion of the weld area of the platinum and rhenium DTC test specimens are shown in Figures 4.2-3 and 4.2-4, respectively. In the case of the platinum the weld and the surrounding surface are free of anomalies. Flaws are evident on the rhenium surface, but they are not associated with the weld. A pinhole was noted in one of the rhenium specimens near the start of the weld. A pinhole in this area, which slips over the DTC injector, is not a problem.

Weights, dimensions and comments for the fabricated DTC specimens are given in Table 4.2-2.

4.3 DESIGN OF SAMPLE TEST FACILITY

The Material Sample Test Apparatus (MSTA) is a laboratory reaction chamber used at the Sandia CRF for advanced laser diagnostics studies of gas-phase and surface combustion product material interactions. This system was provided to the program by Aerojet. Figure 4.3-1 is a schematic of the MSTA system. It consists of a combustion chamber with a premix platelet burner and a specimen holder. The combustion chamber has four 2-in. dia fused-silica ports for optical diagnostic access. The specimen holder permits electrical control of specimen temperature. Figure 4.3-2 is a pictorial representative of the system. The burner and combustor arrangement is shown in Figure 4.3-3. Table 4.3-1 summarizes design operating conditions for the MSTA. Two burner systems were provided to Sandia, one for the gas phase interactions experiments, operating in the chamber at one to six atmospheres, and a second burner and specimen holder operating in the high temperature interfaces experiment at one atmosphere. Only the 1 atmosphere system was used at Sandia.

A cross-section of the assembled chamber is given in Figure 4.3-4, showing the relation of the specimen holder to the burner and the adjustable cooled pintle for chamber pressure control. Figure 4.3-5 is a schematic of the 6 atmosphere system, as it was setup at Aerojet for checkout.

4.4 SAMPLE TEST FACILITY FABRICATION, INSTALLATION AND CHECKOUT

The MSTA premixed burner was fabricated with Zr-Cu platelets to provide a combustion gas flow, shroud gas flow and internal water cooling.

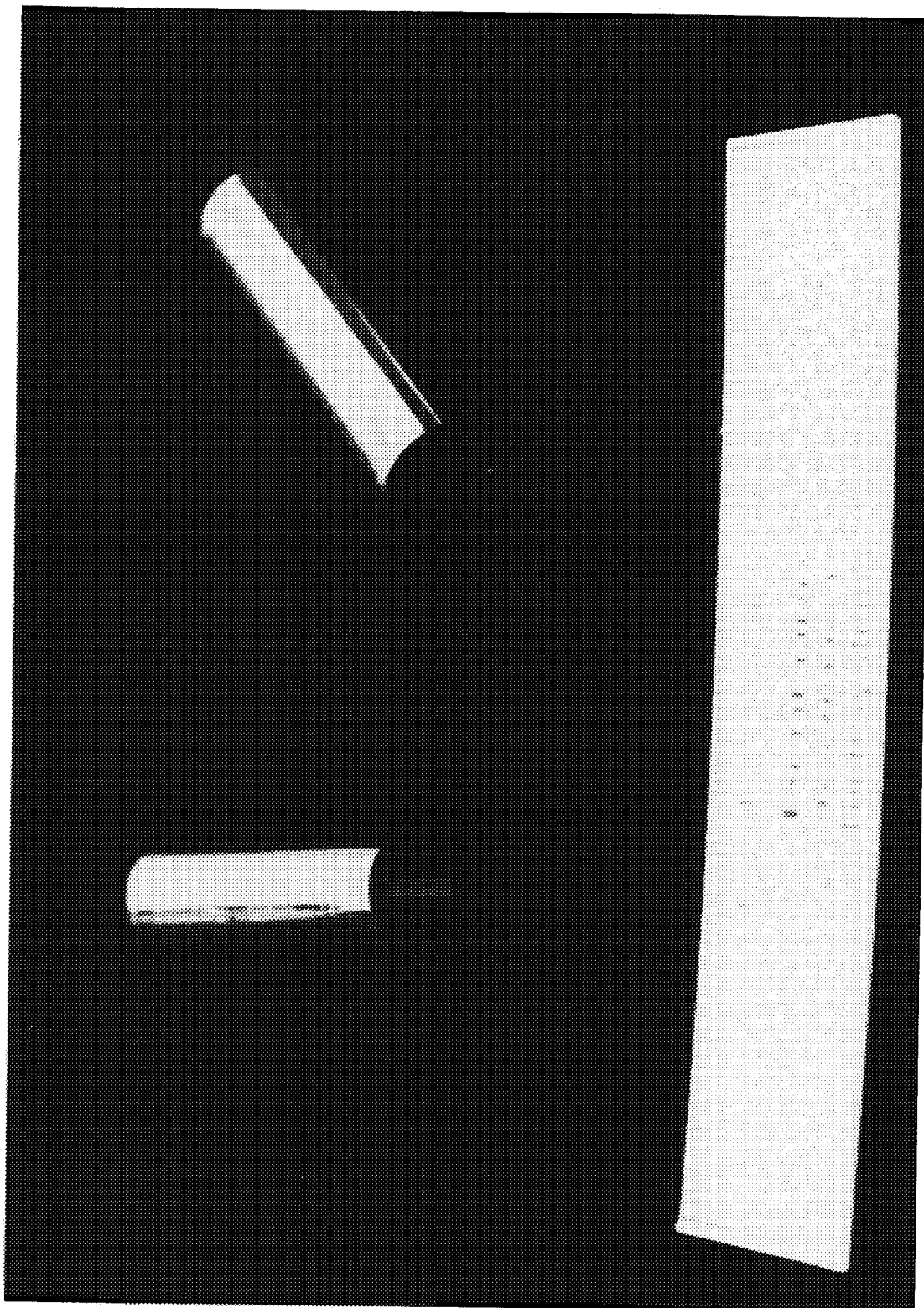


Figure 4.2-2. Welded Foil DTC Specimens

[illegible]

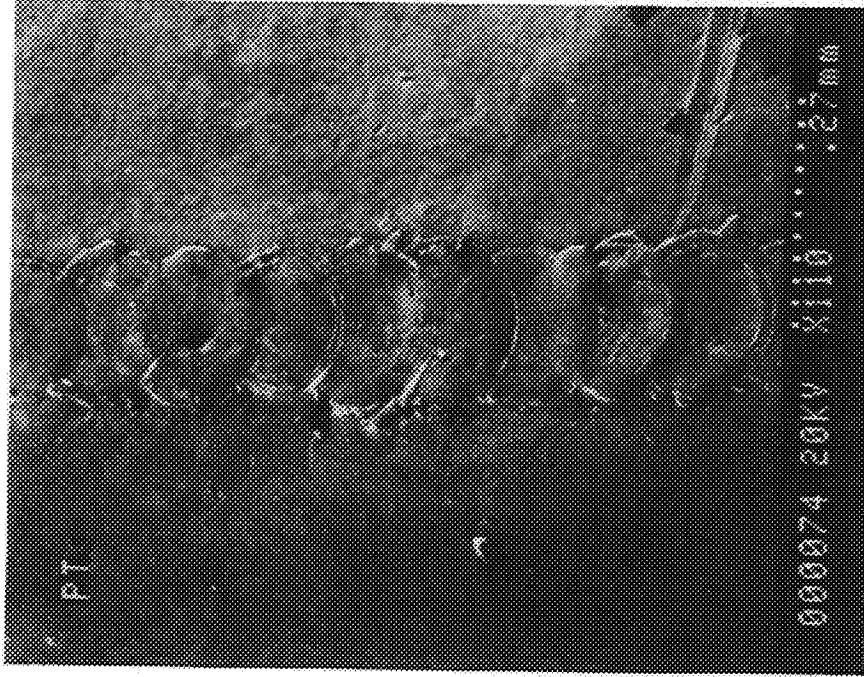
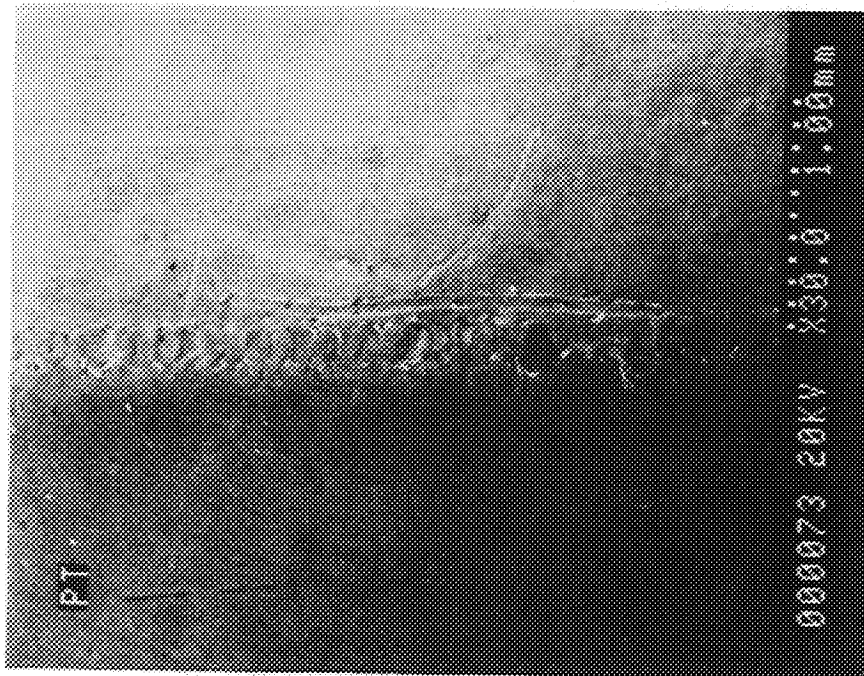


Figure 4.2-3. Electron Beam Welds on Platinum DTC Specimen

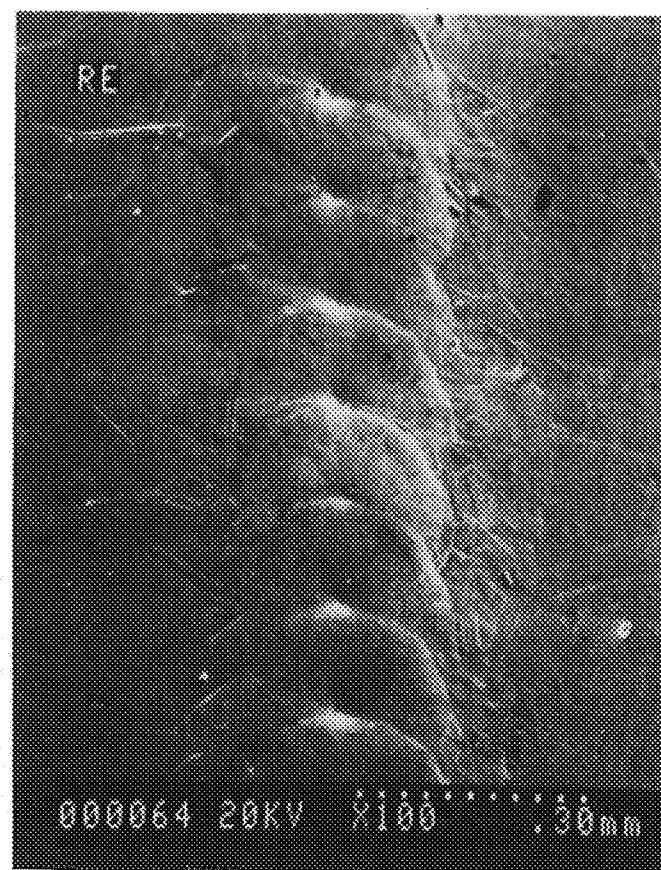
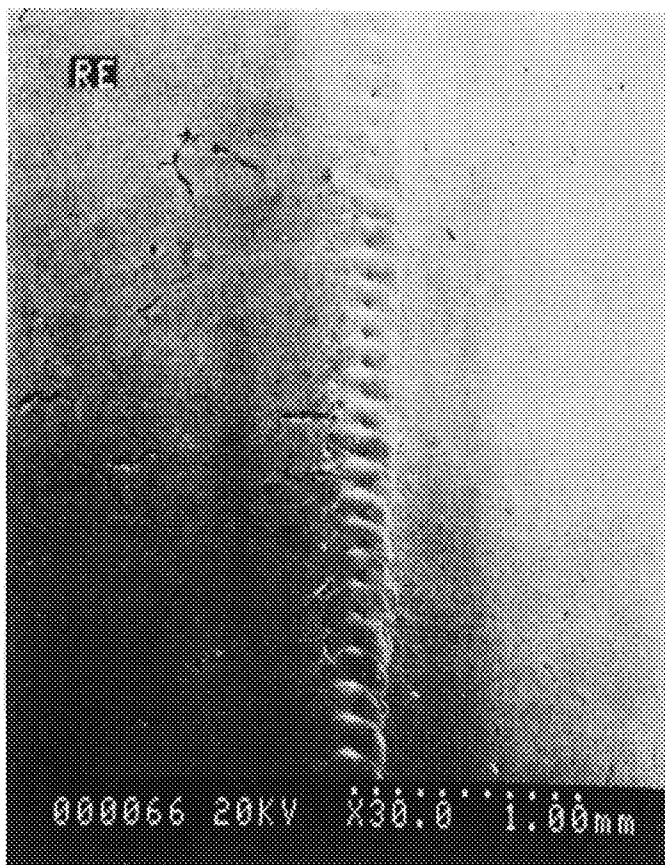


Figure 4.2-4. Electron Beam Welds on Rhenium DTC Specimen

**Table 4.2-2. Diagnostic Thrust Chamber Specimens –
Weight and Dimension Data**

<u>Specimen</u>	<u>Weight GMS</u>	<u>Approx. Length, in.*</u>	<u>Internal dia, in.</u>	<u>Comment</u>
DTC-Re-001	4.09025	1.877	.500 Go; .501 Go One End	
DTC-Re-002	3.88218	1.770	.503 Go	Slight Flare One End
DTC-Re-003	4.20697	1.885	.502 Go; .503 Partial	Flare One End
DTC-Re-004	4.20606	1.885	.501 Go; .502 Partial	Flare One End
DTC-Re-005	4.11346	1.873	.500 Go Snug	**
DTC-Re-006	4.25764	1.889	.502 Go; .503 Partial	Flare One End
DTC-Re-007	4.07526	1.863	.500 Go Snug	**; Several Weld Irregularities; Pinhole at ~0.4 In.
DTC-Re-008	4.13179	1.882	.503 Snug	
DTC-Re-009	4.22615	1.873	.503	Slight Flare Both Ends
DTC-Re-010	4.26846	1.886	.502 Snug	Flares, Rough End
DTC-Pt-001	4.02030	1.872	.502 Go; .503 Partial	Offset One End
DTC-Pt-002	4.08634	1.870	.502 Go; .503 Partial	
DTC-Pt-003	4.06592	1.869	.503 Go	
DTC-Pt-004	4.01384	1.863	.502 Go; .503 Partial	
DTC-Pt-005	3.99790	1.870	.502 Go; .503 Partial	
DTC-Pt-006	4.00437	1.869	.501 Go; .502 Partial	Weld Irregularities
DTC-Pt-007	4.13724	1.869	.502 Go; .503 Partial	Weld Irregularities One End. Pinhole at 0.35 In.
DTC-Pt-008	4.09410	1.865	.503 Go	Weld Irregularities; offset Both Ends
DTC-Pt-009	3.98220	1.865	.503 Go	
DTC-Pt-010	4.08702	1.869	.501 Go; .502 Partial	

* Ends Not Necessarily Square

** Injector dia to be .499/.501; May Not Fit

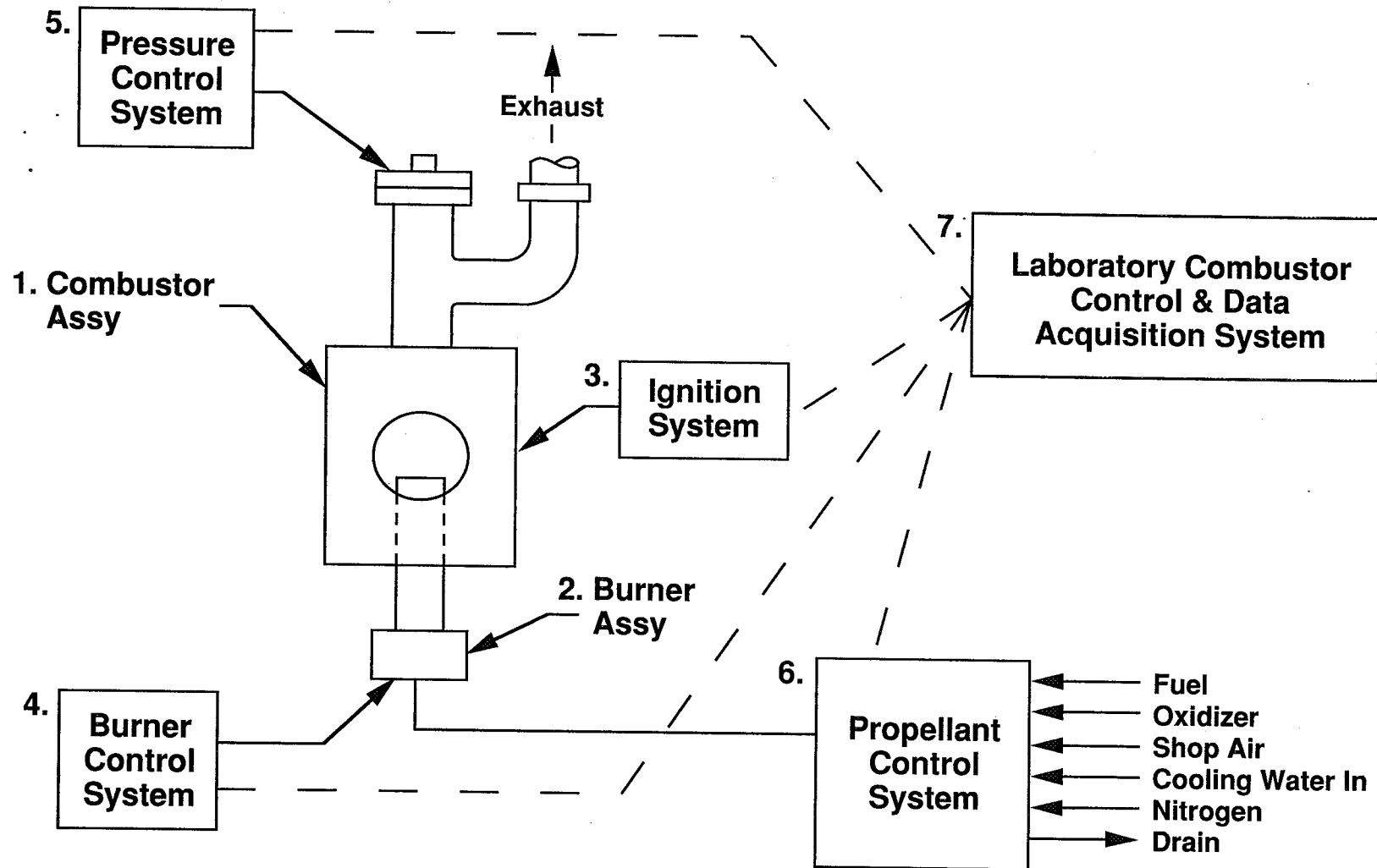
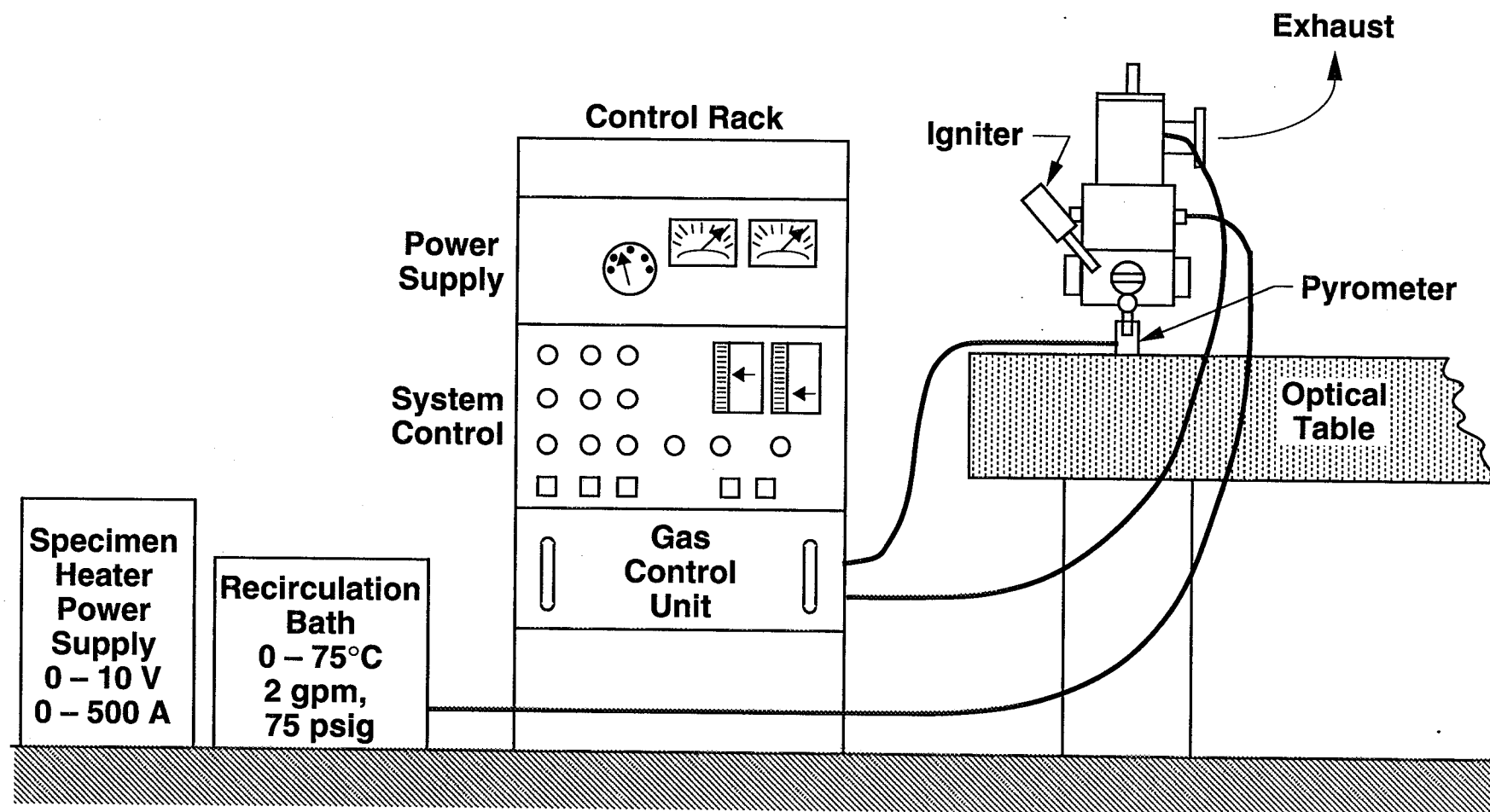


Figure 4.3-1. Material Sample Test Apparatus (MSTA) System Block Diagram



M13-7-04

Figure 4.3-2. Sample Test Facility – Combustion Apparatus Components

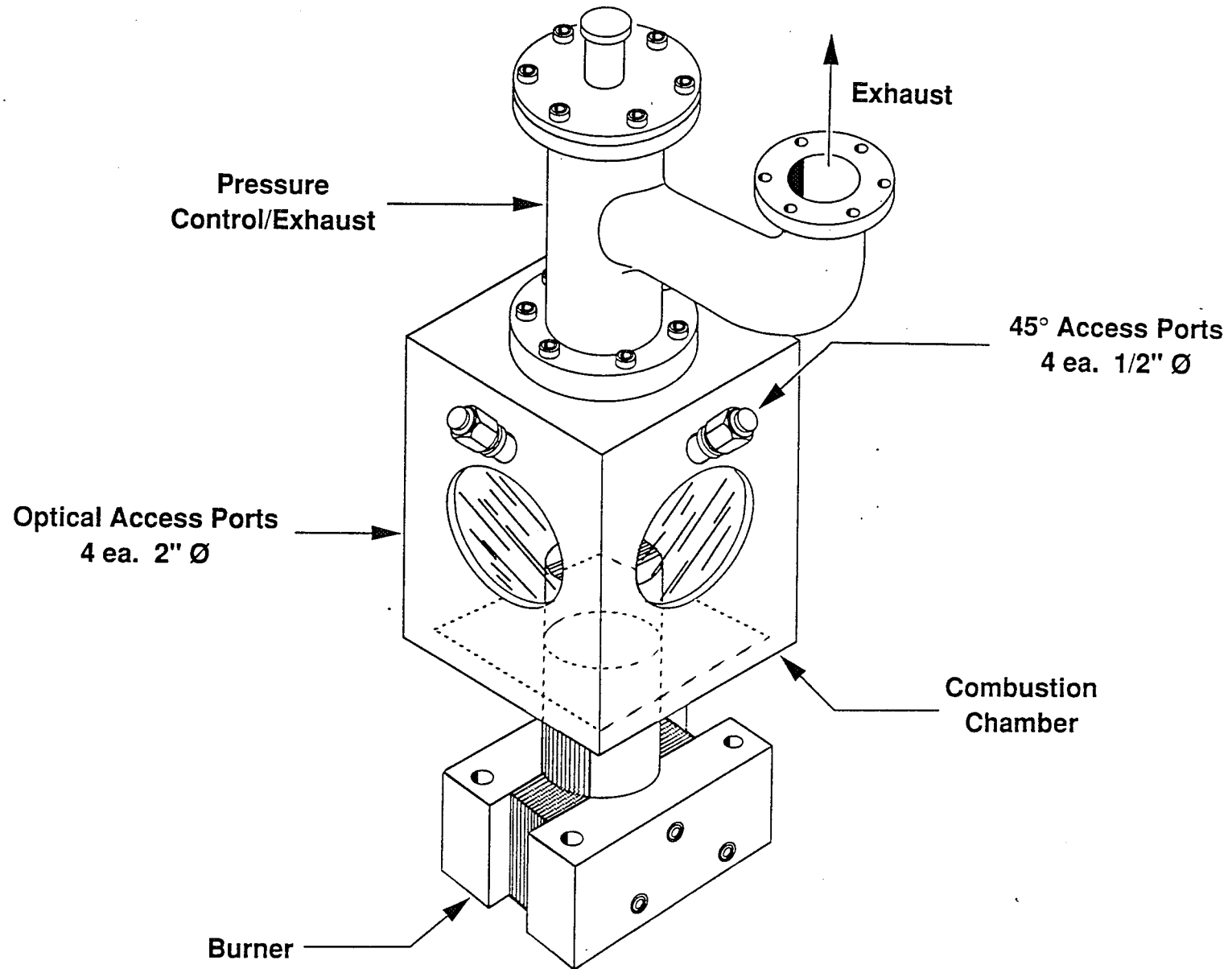


Figure 4.3-3. MSTA Burner/Combustion Chamber Assembly

Table 4.3-1
Materials Test Apparatus for Sandia
Burner Operating Conditions

Propellants	O ₂ /H ₂ and O ₂ /CH ₄
Nominal Flow Rate	0.1 gm/sec
Chamber Pressure	1 to 6 atm
MR: O ₂ /H ₂	2 to 12
O ₂ /CH ₄	3 to 6
<u>Burner</u>	Platelet, premixed, with GN ₂ shroud and water cooling
Propellant Elements	180 ea 0.008 x 0.017 in.
N ₂ Elements	420 ea 0.008 x 0.017 in.
Heat Release	Approximately 5 kw
Burner Water Cooling	Approximately 0.5 gpm

M7D4/N8

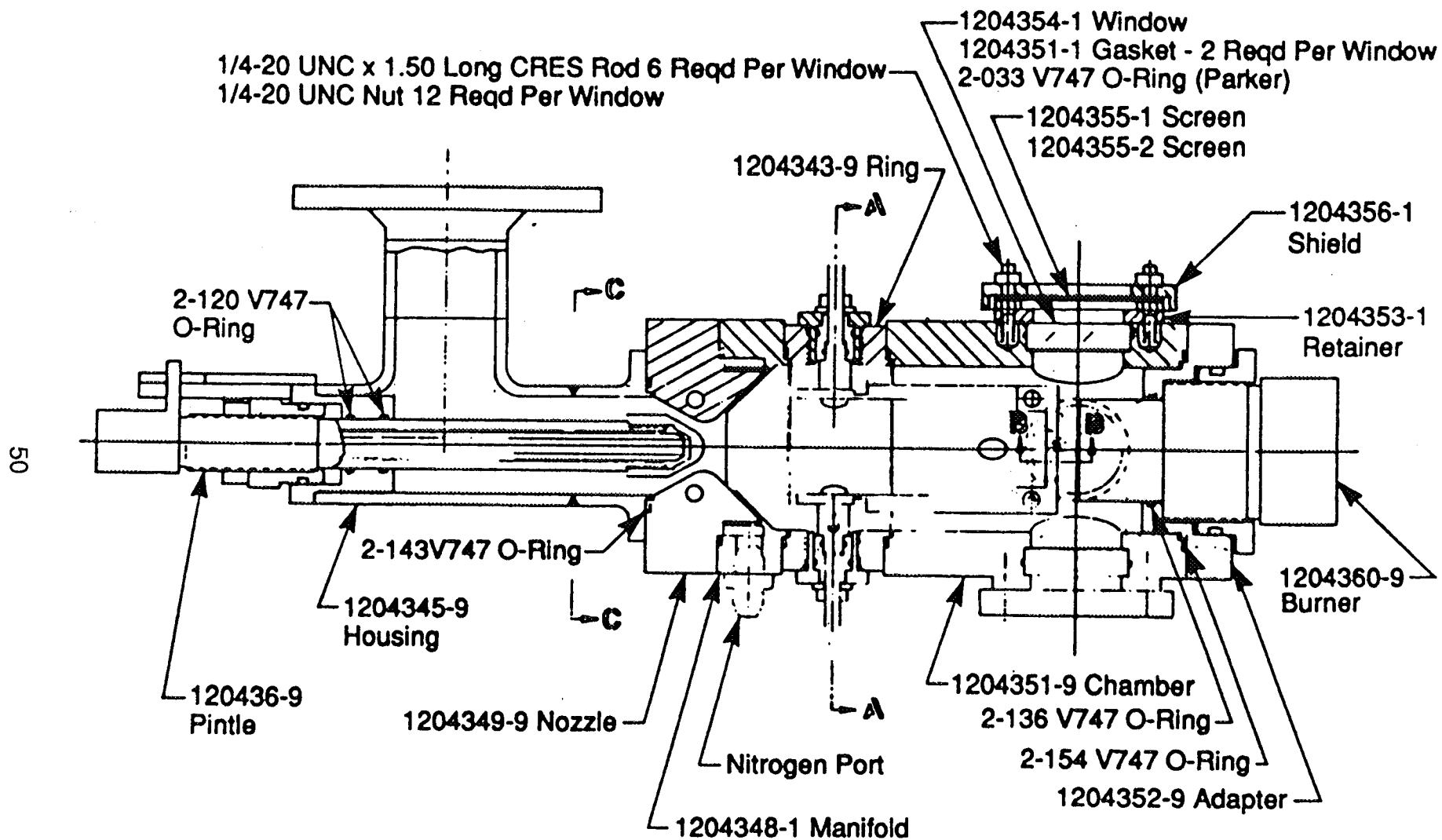


Figure 4.3-4. MSTA Chamber Assembly

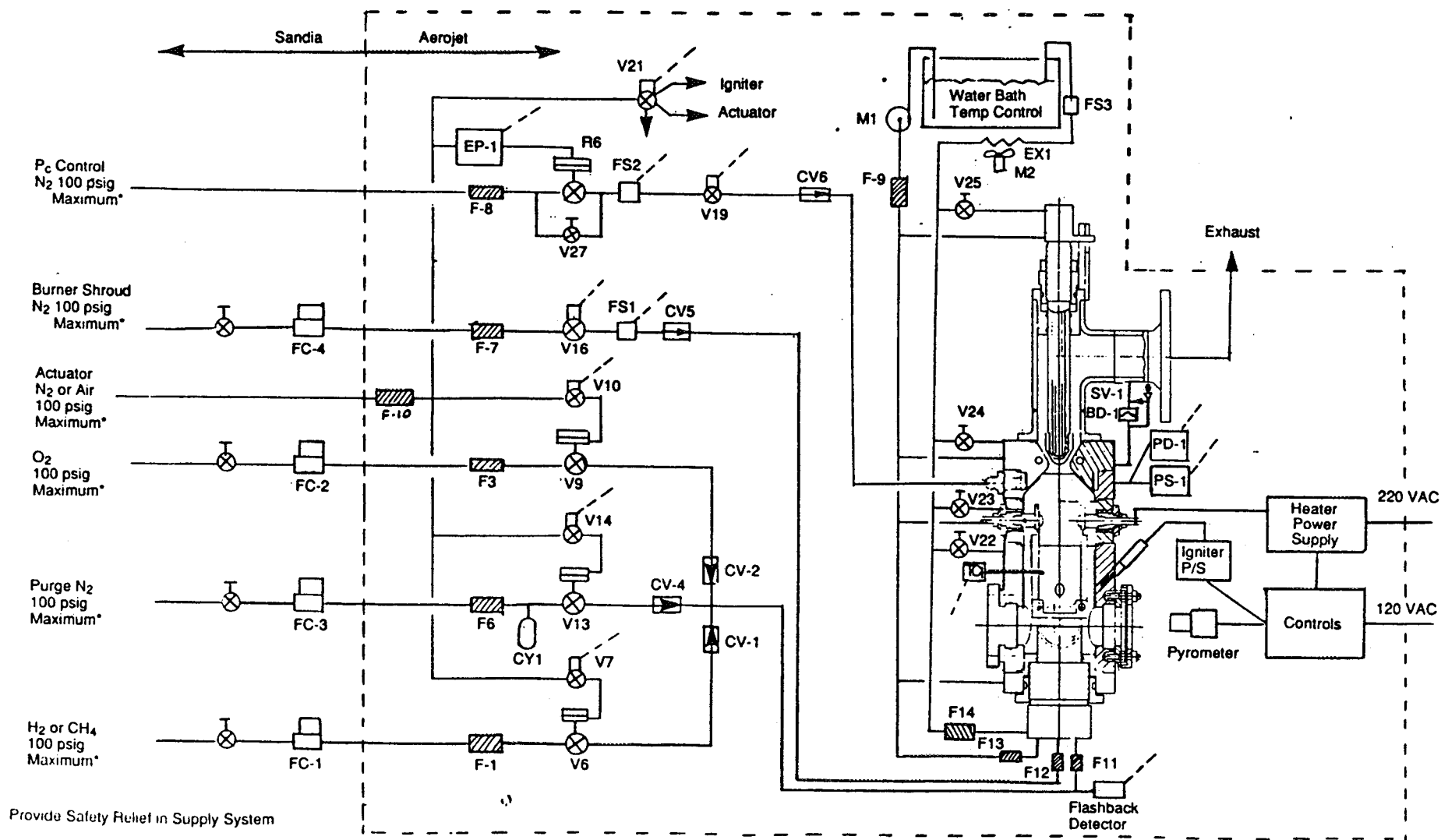


Figure 4.3-5. MSTa Schematic - 1 to 6 ATM System

4.4, Sample Test Facility Fabrication, Installation and Checkout (cont.)

Four units were fabricated, three for use at Sandia (one for gas phase experiments, one for surface experiments, and a spare). The burner assemblies are shown in Figure 4.4-1. Figure 4.4-2 identifies the burner gas and cooling circuits. The face section of the burner is shown in Figure 4.4-3.

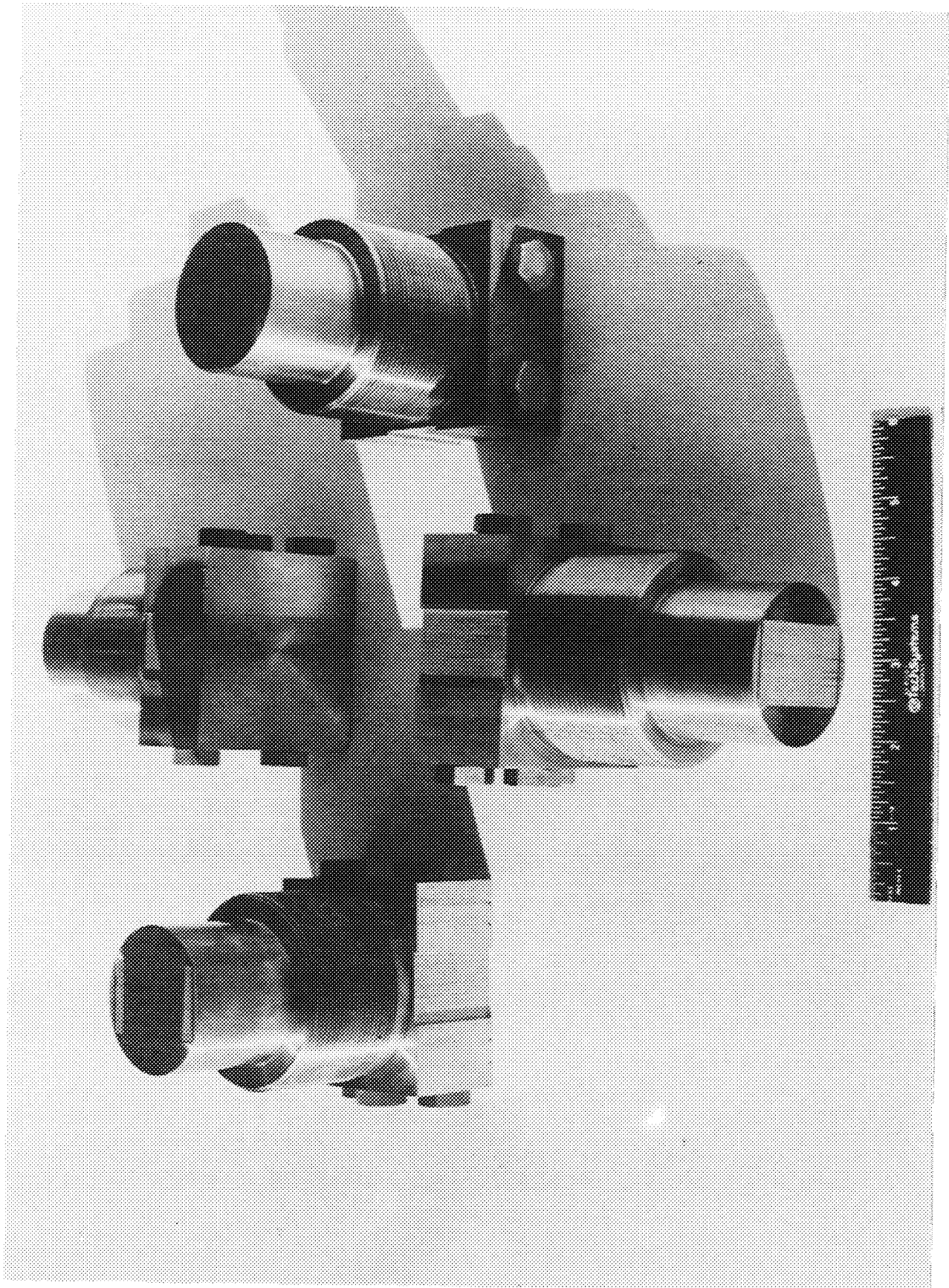
The MSTA 6-ATM components are shown in Figure 4.4-4. Specimen and holder components are shown in Figure 4.4-5. The specimen holder is shown assembled in Figure 4.4-6 and with a 0.00254 in. thick rhenium foil installed (Figure 4.4-7). The 6- and 1-ATM MSTA units are shown assembled in Figure 4.4-8. The MSTA control console (6-ATM) is shown in Figure 4.4-9.

The tests conducted to checkout the MSTA are listed in Table 4.4-1. First, the burner and chamber were proof and leak checked. The burner was then operated at full gas flow with oxygen-hydrogen and oxygen-methane using the 6-Atm recirculating hot water cooling system. When operated near stoichiometric mixture ratio the burner face darkened. After about two hours of operation the face was cleaned with a moist cotton swab. SEM examination showed that the nickel flash used to promote platelet bonding had reacted. The underlying copper surface was unaffected. The nickel was removed from the burner surface to eliminate a possible contamination source.

After checkout of the control system and gas delivery system the 6-Atm system was installed at Aerojet and checked as an assembly. Operation was demonstrated at 4-Atm using oxygen and hydrogen, with an iridium specimen heated to 3600°F. Figure 4.4-10 shows the overall system; Figure 4.4-11 shows the combustion chamber. A view of the chamber showing the burner with the igniter inserted is shown in Figure 4.4-12. The system during operation is shown in Figure 4.4-13; a closeup of the iridium specimen being exposed to O₂/H₂ at MR 6 while being electrically heated is shown in Figure 4.4-14. As part of assembly and checkout, an MSTA Operations Manual was prepared for use at Sandia (Ref. 7).

4.5 HIGH TEMPERATURE MATERIALS TESTS (SANDIA)

Basic laboratory studies of gas- and surface-phase interactions of propellant combustion products with materials for radiation-cooled chambers were conducted at the Sandia National Laboratories, Livermore, CA. This work used the advanced laser diagnostics capability of the Combustion Research Facility and Surface Science Laboratory in a collaborative effort



C1189 6406

Figure 4.4-1. Platelet Burner Assemblies

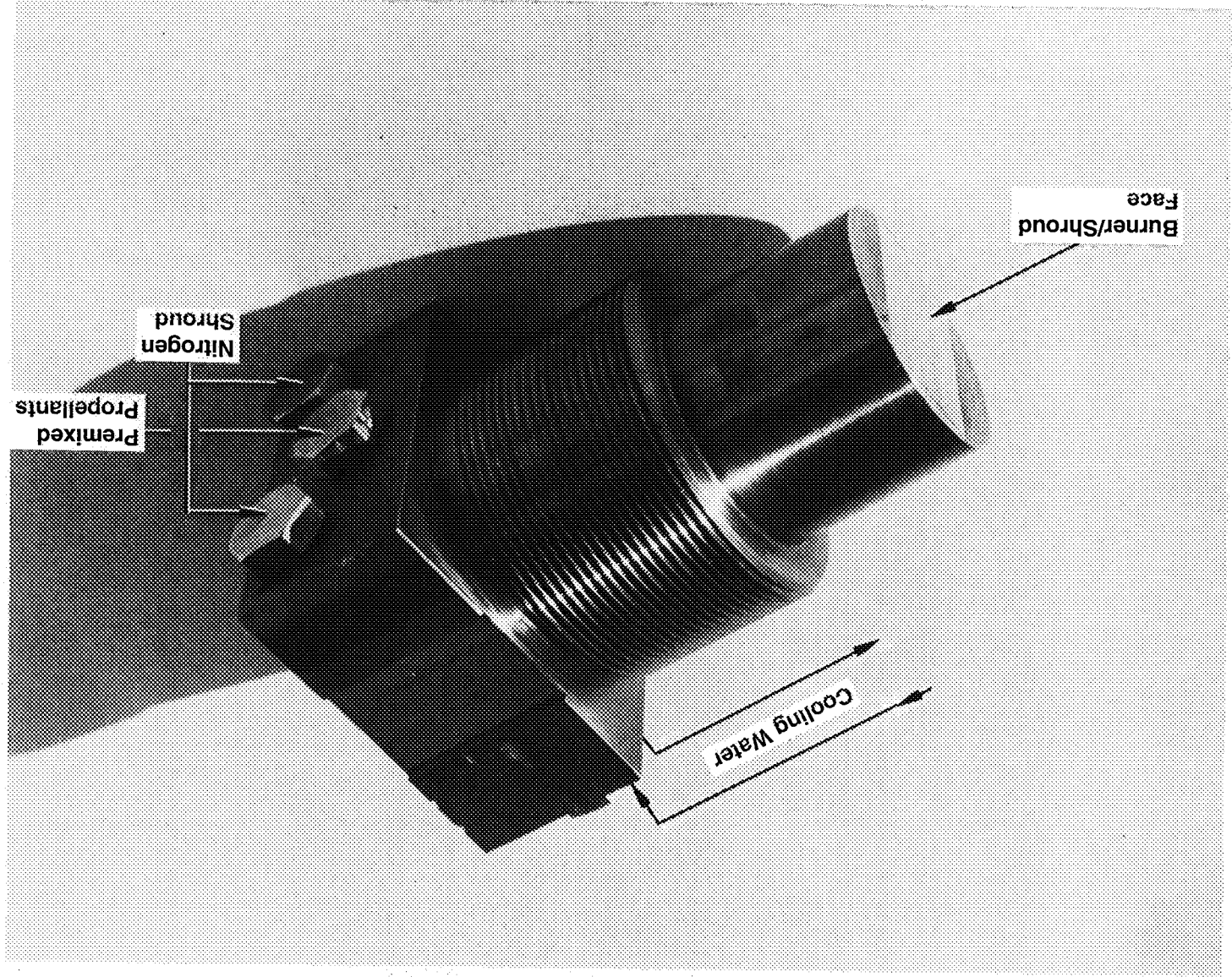
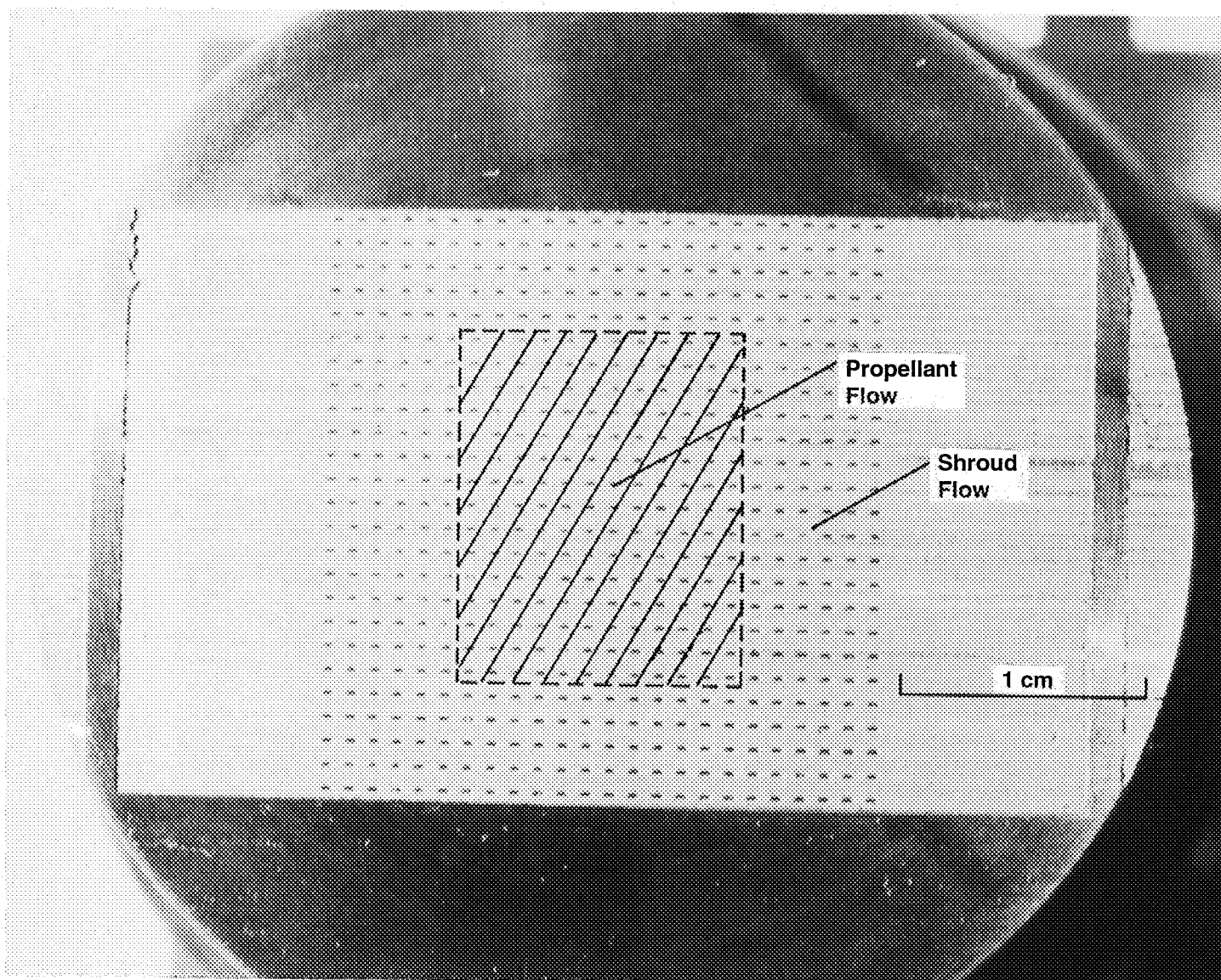


Figure 4.4-2. MST-A Burner for Task 5.0

C1189 6403



C1189 6405

Figure 4.4-3. MSTA Burner Face

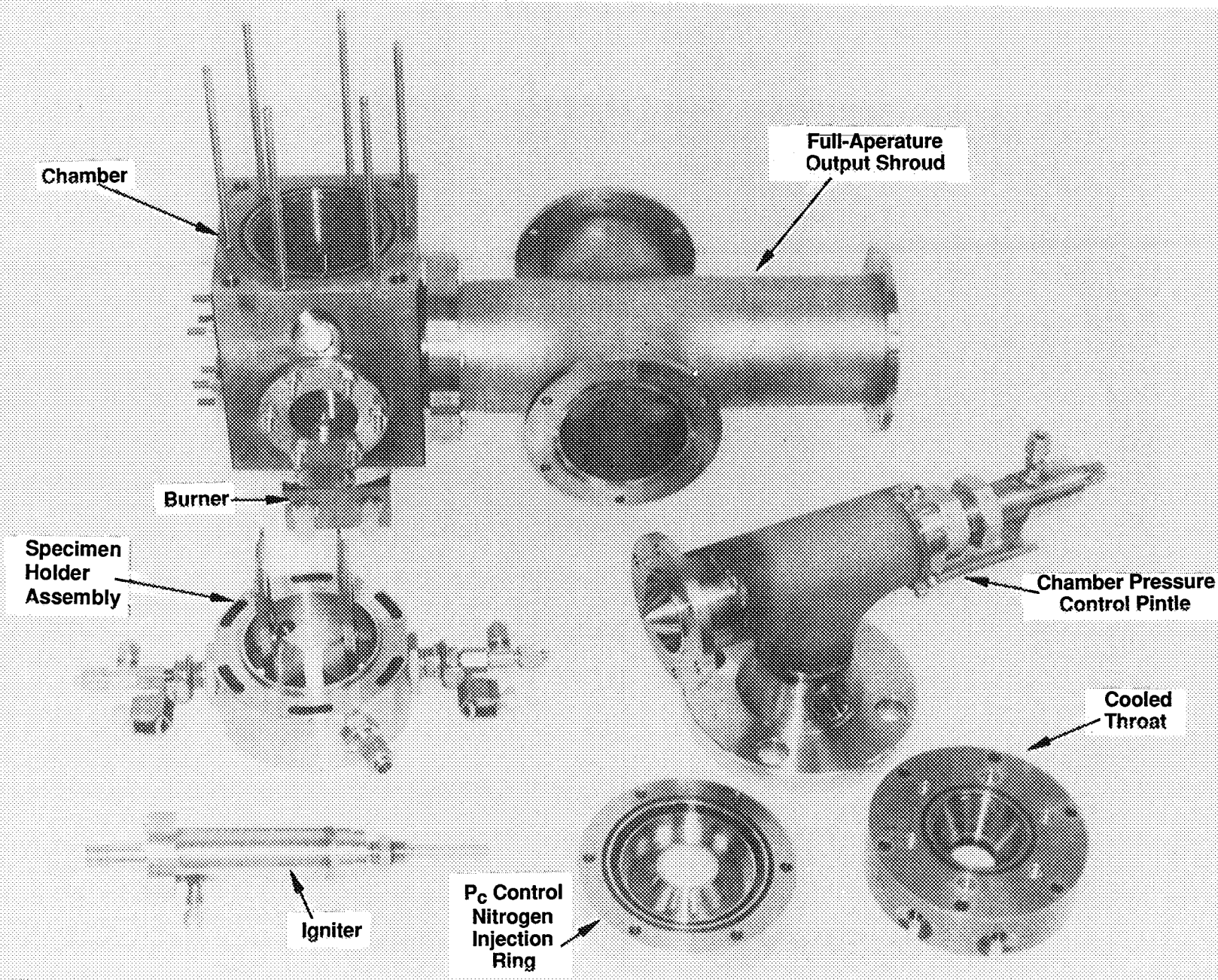


Figure 4.4-4. 6 ATM MSTA Components

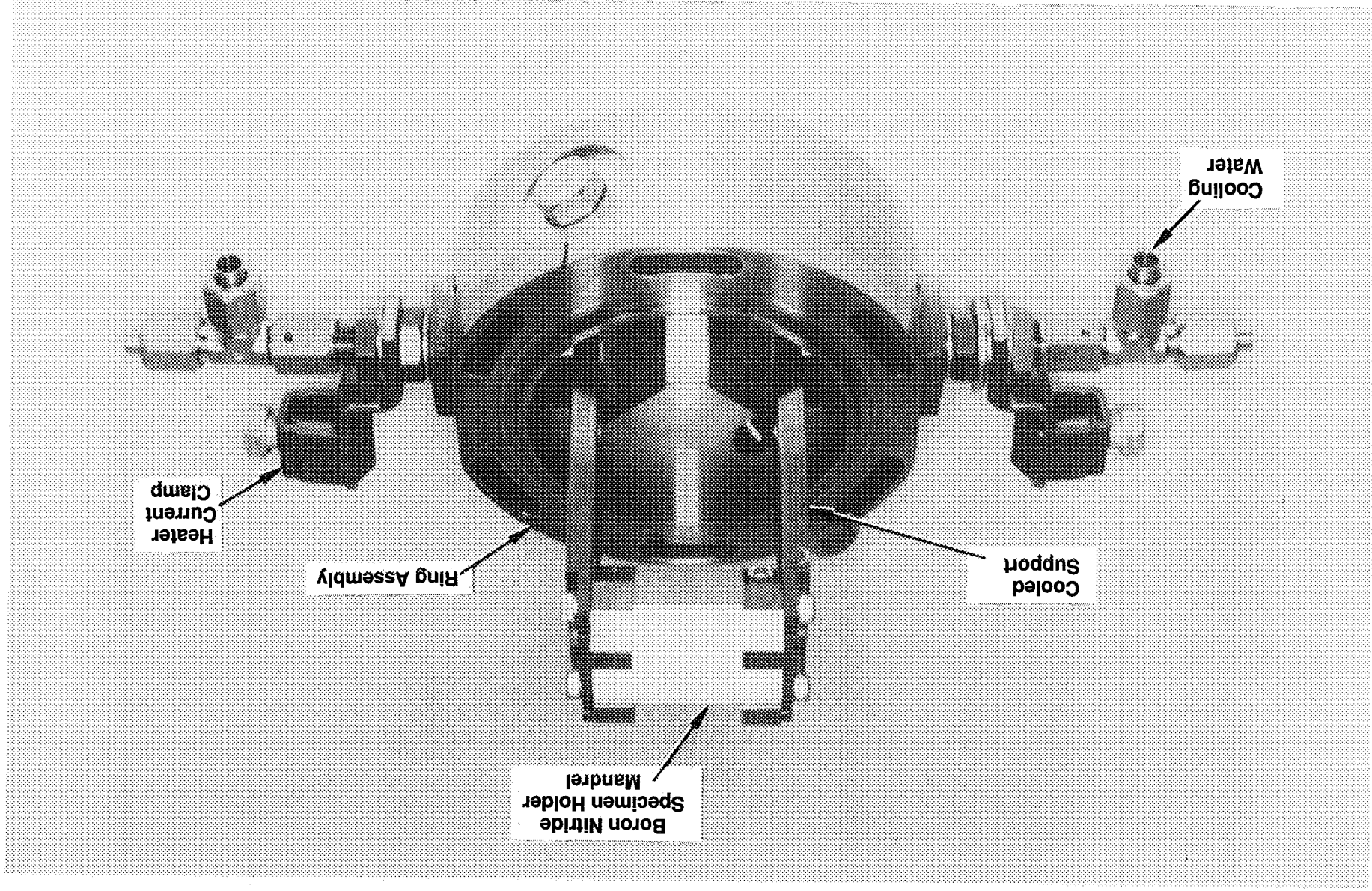
C0290 0471

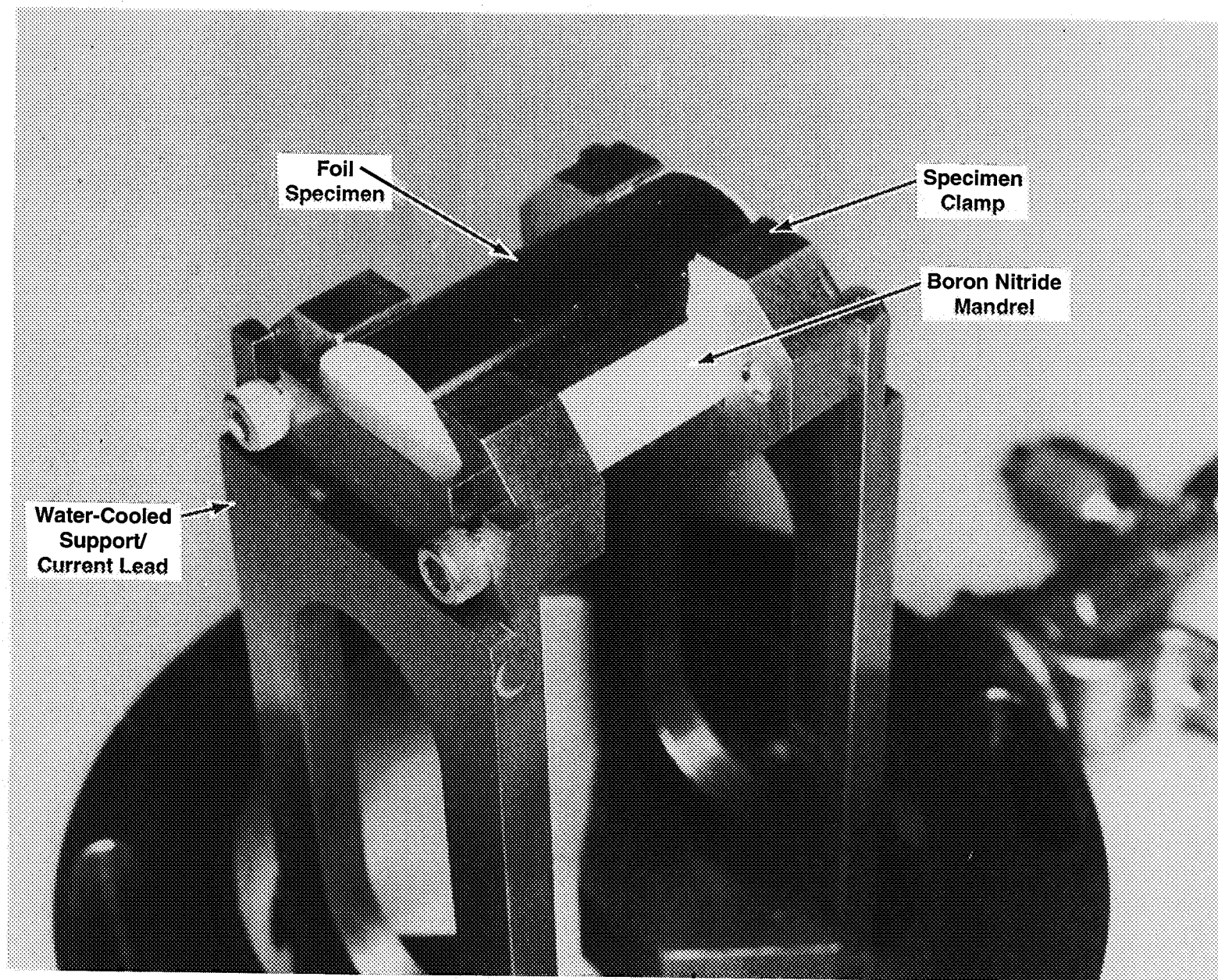


Figure 4.4-5. Specimen and Holder Components

C0290 0480

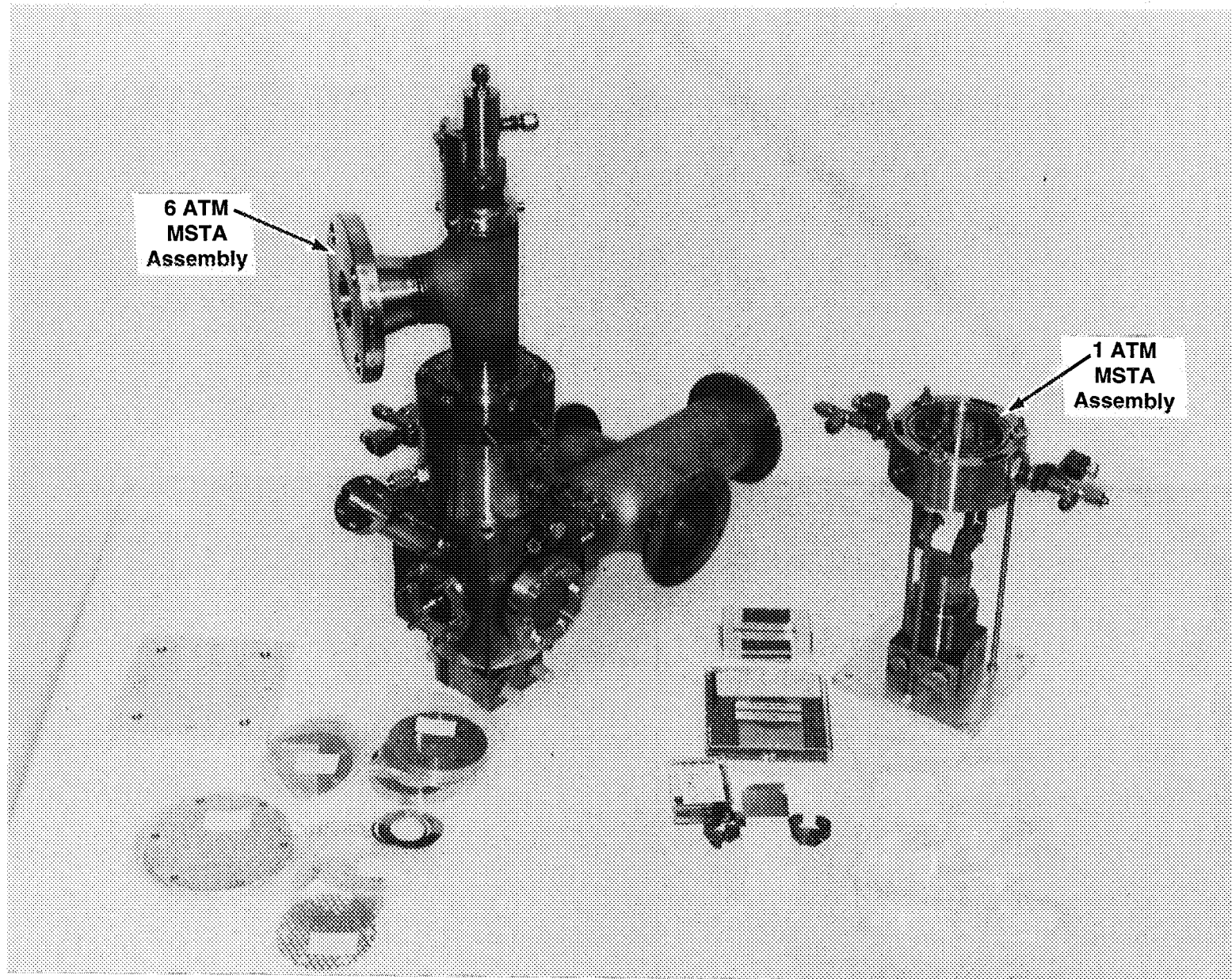
Figure 4.4-6. MSTA Specimen Holder Assembly





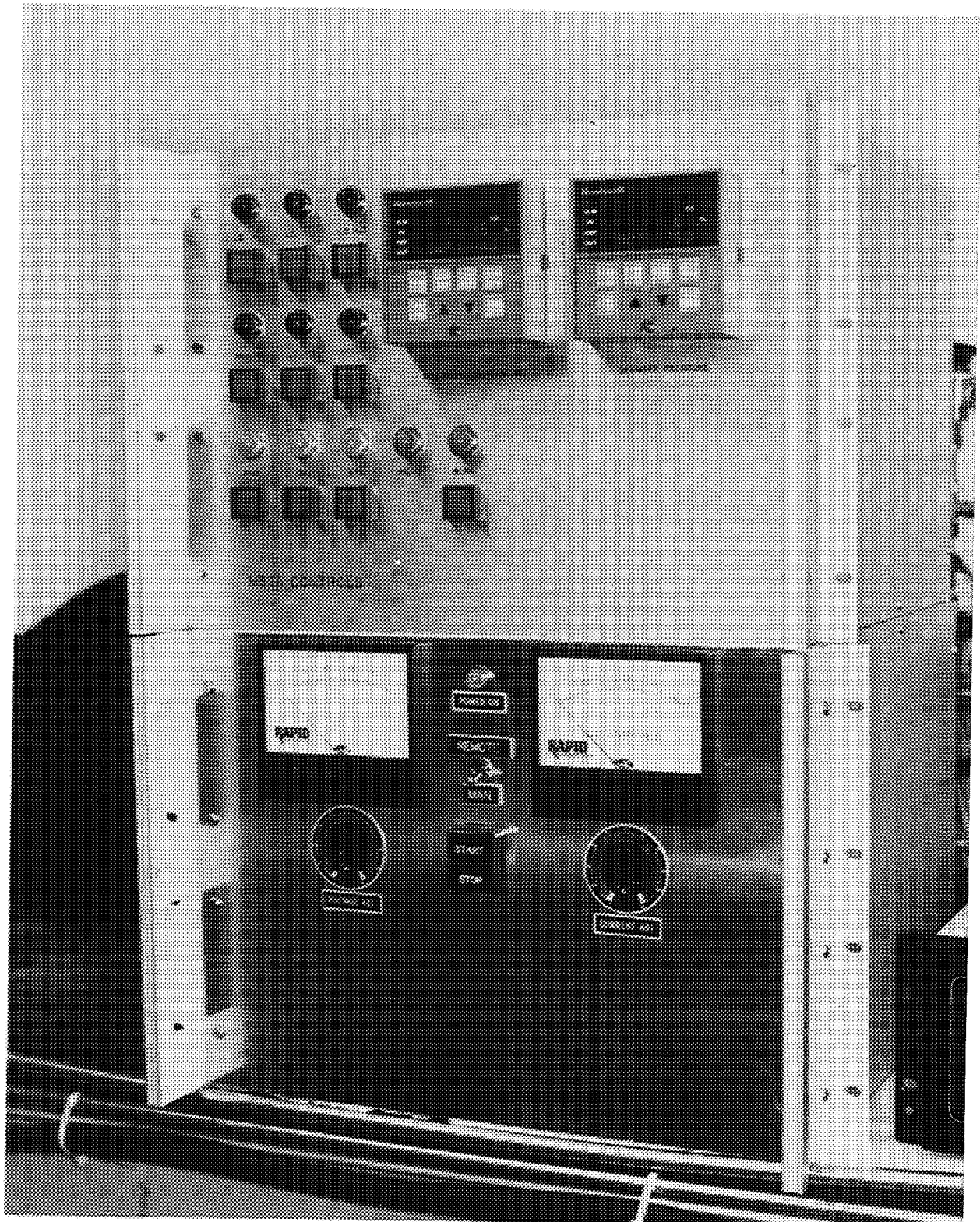
C0290 0477

Figure 4.4-7. Specimen Holder Detail



C0290 0474

Figure 4.4-8. MSTA Combustor Assemblies



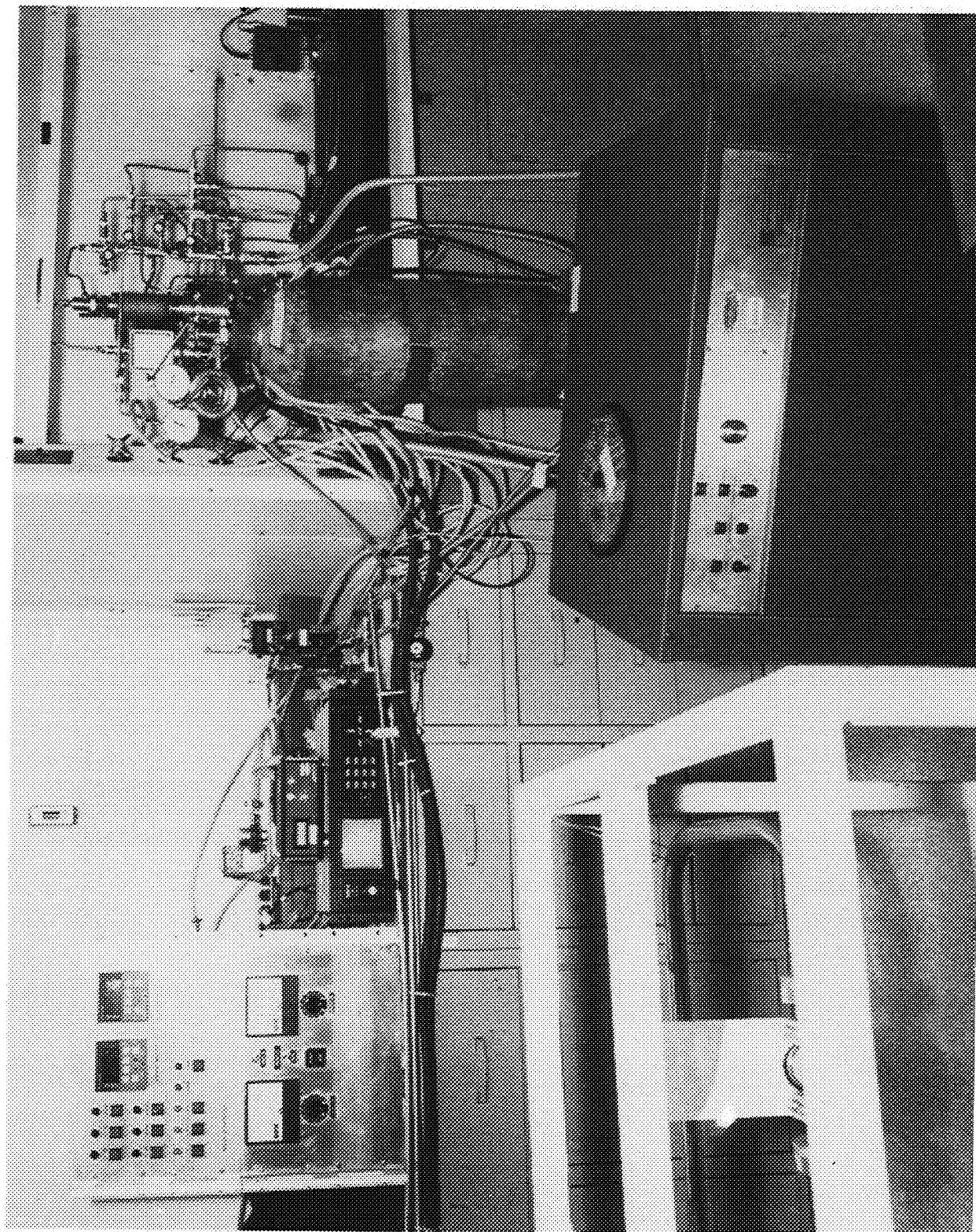
C0490 1322

Figure 4.4-9. MSTA Control Console

Table 4.4-1. Material Sample Test Apparatus Checkout

<u>Location</u>	<u>Type</u>	<u>Material</u>	<u>Propellant</u>	<u>Mixture Ratio (mass oxidizer/ mass fuel)</u>	<u>Chamber Pressure, Atmospheres</u>	<u>Specimen Temp. K</u>	<u>Objective</u>
Aerojet	Proof	—	GN ₂	—	32	—	Determine Design Adequacy
	Leak	—	GN ₂	—	7	—	Determine Design Adequacy
	Controls Operation	—	GN ₂	—	1 to 6	—	Determine Design Adequacy
	Burner Operation	—	O ₂ /H ₂	2 to 12	1 to 6	—	Determine Design Adequacy
	Specimen Heater Operation	Iridium	O ₂ /H ₂	2 to 12	1 to 6	1000, 2200	Determine Design Adequacy

ORIGINAL PAGE
BLACK AND WHITE PHOTOGRAPH



C0490 1319

Figure 4.4-10. Overall 6-ATM MSTA System

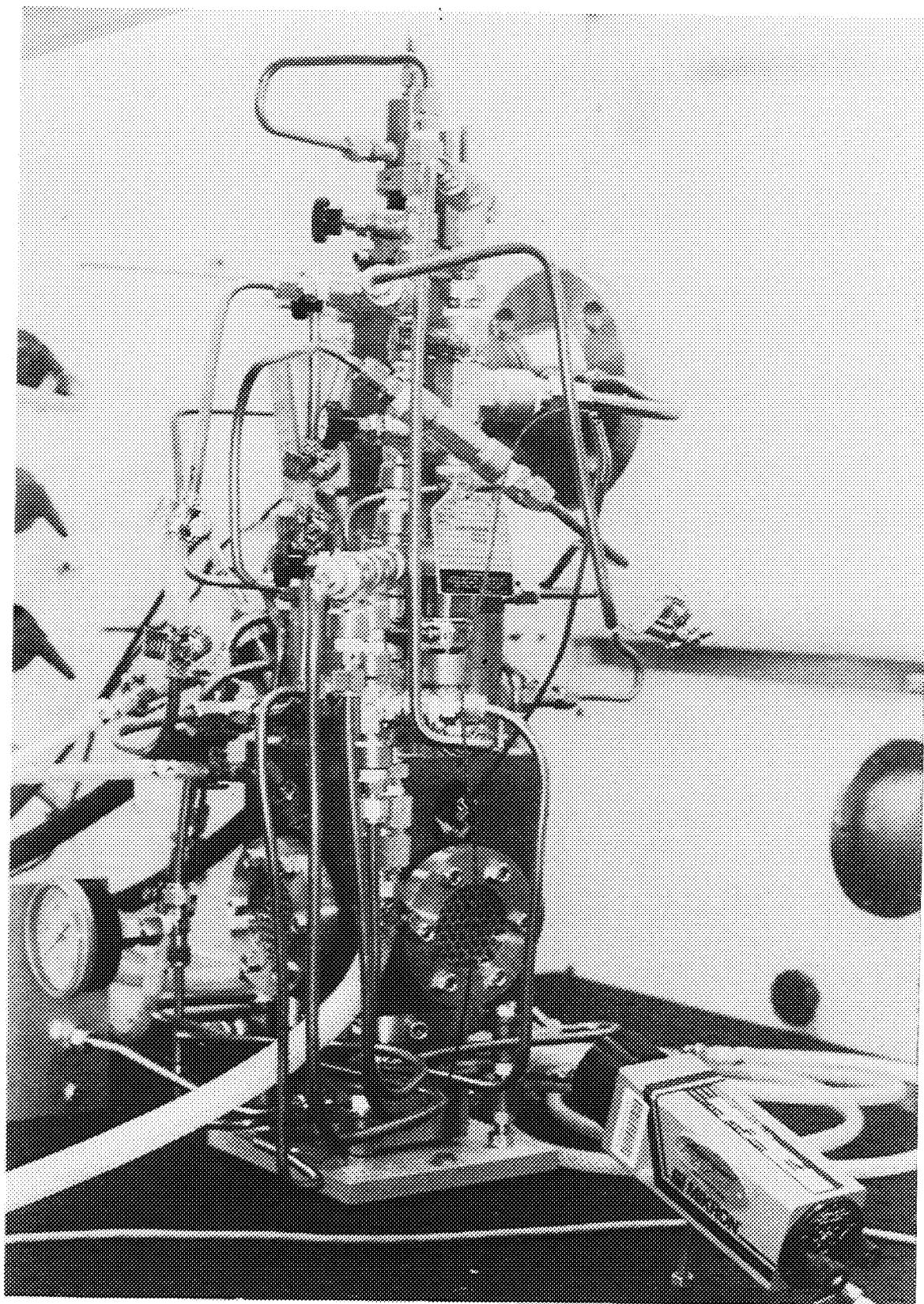
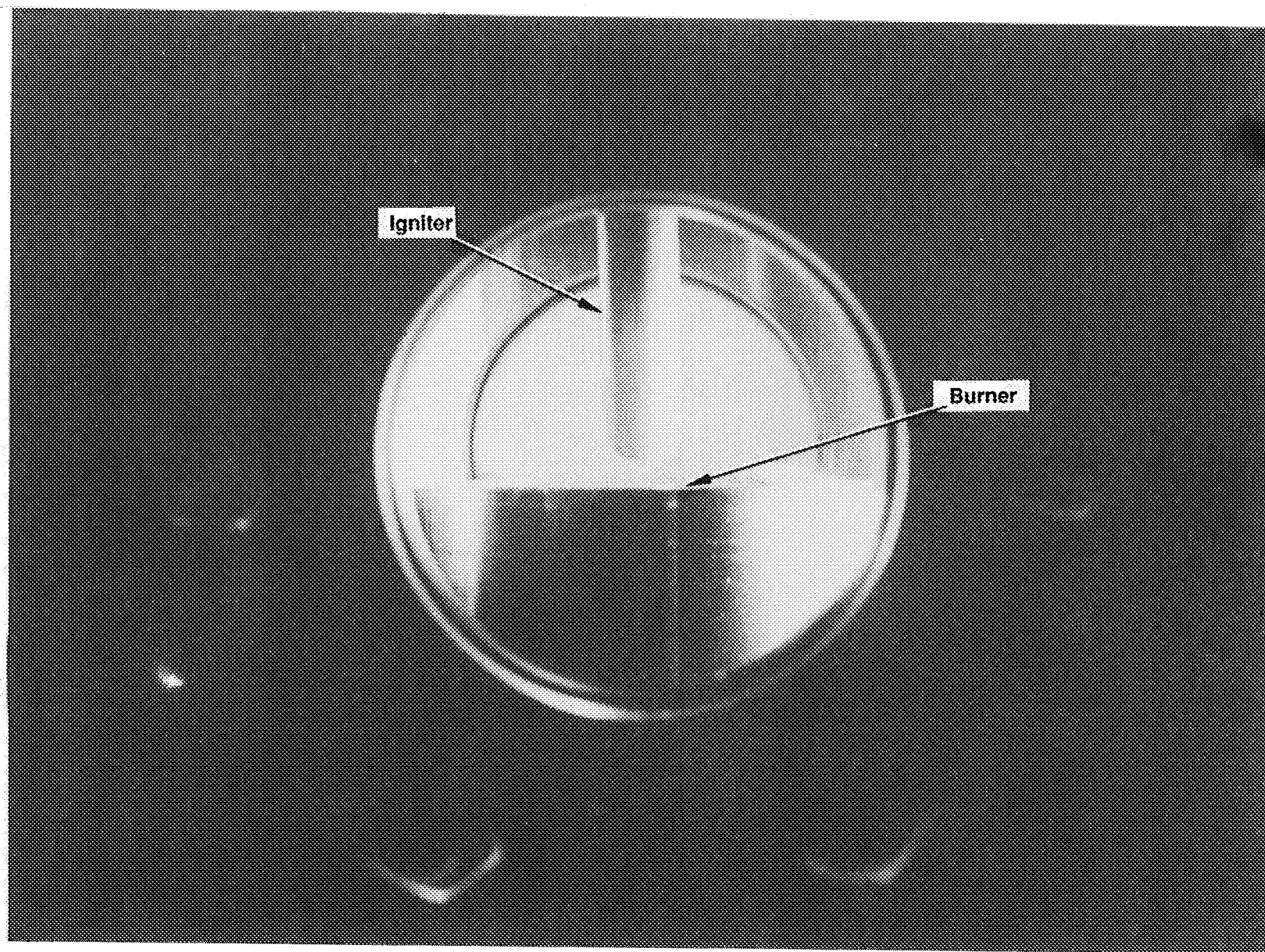


Figure 4.4-11. View of 6-ATM MSTA Chamber



C0290 0475

Figure 4.4-12. View of Combustion Zone Showing Burner Face and Igniter in Inserted Position

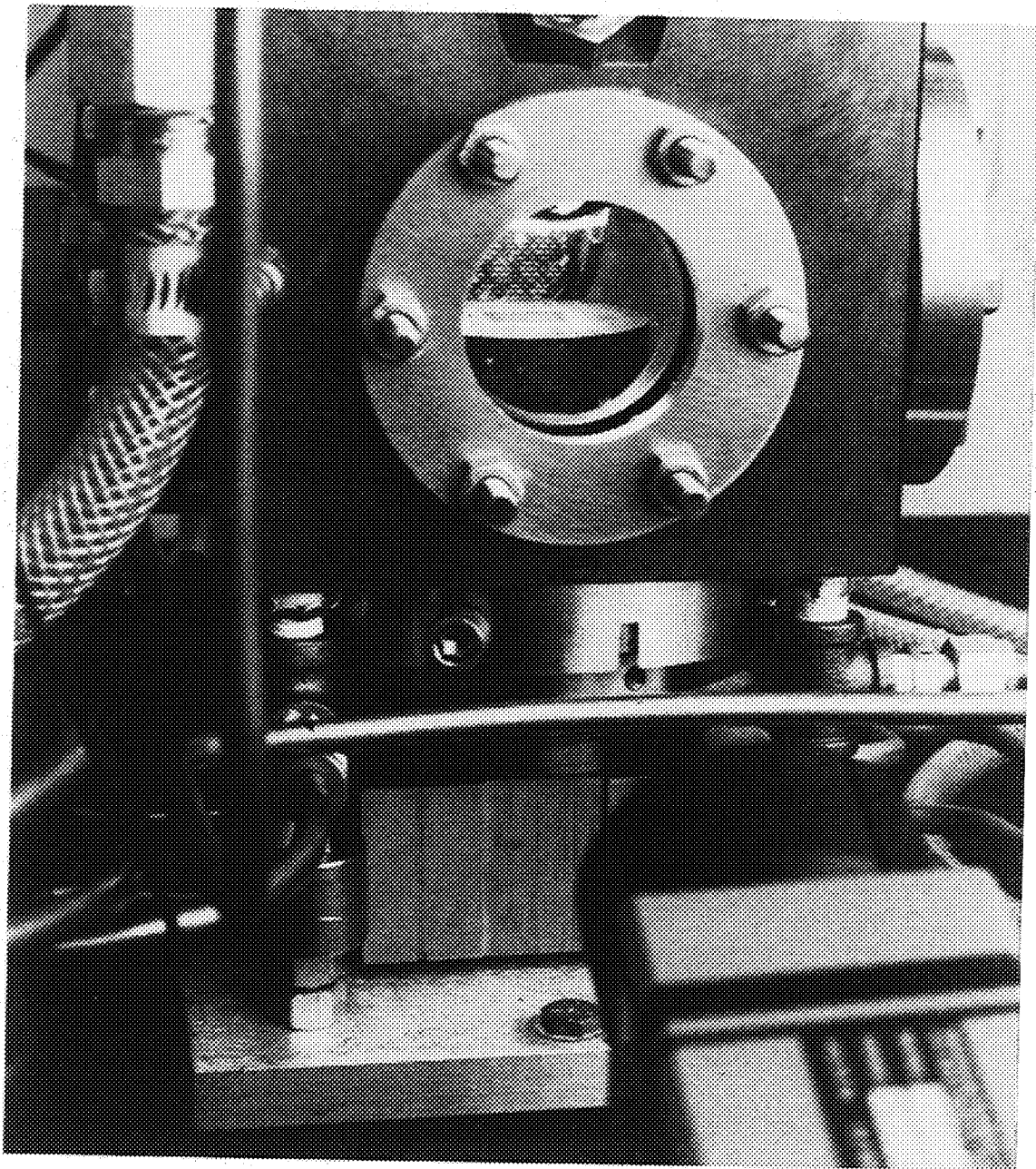
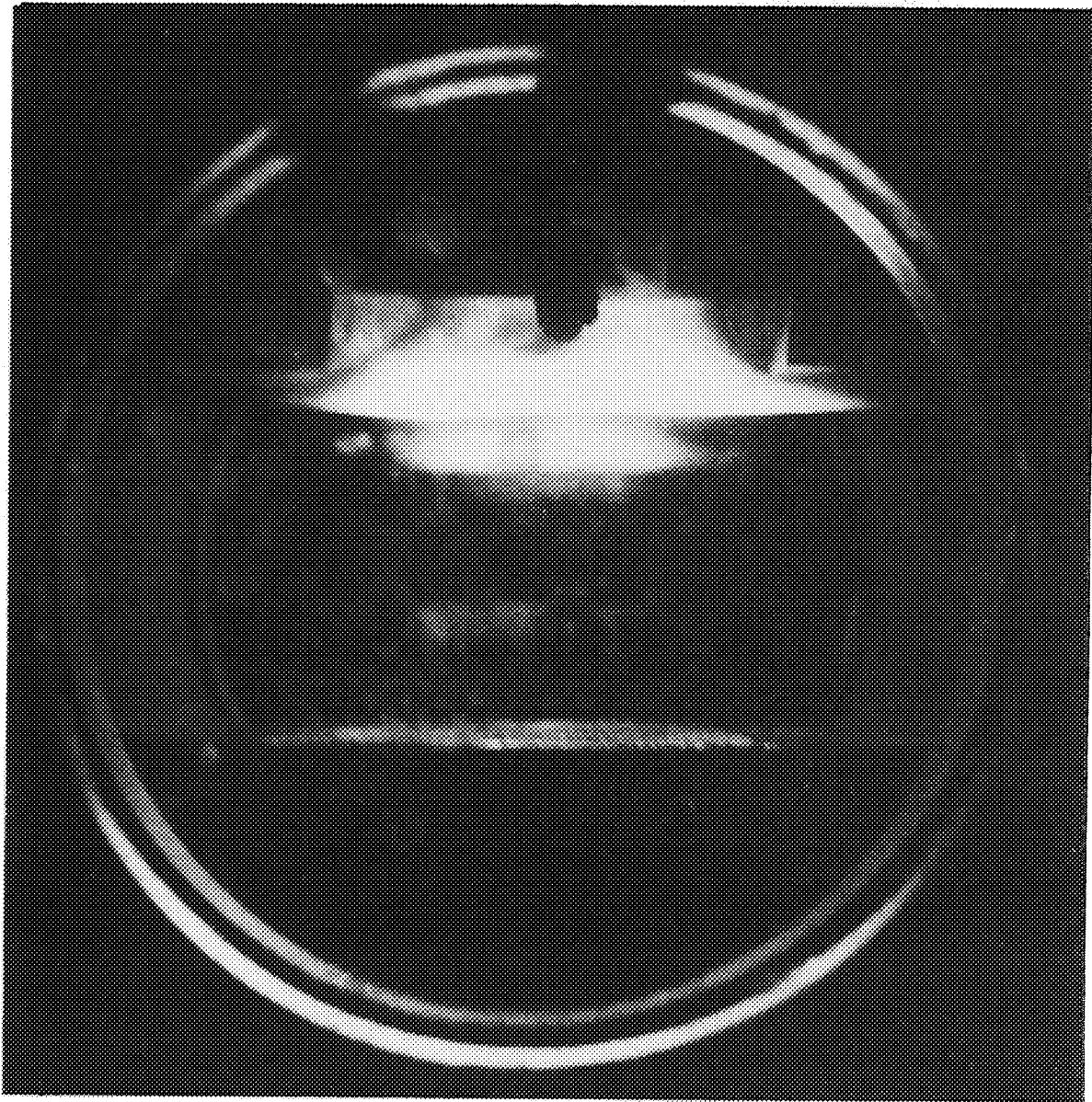


Figure 4.4-13. MSTA During Operation (The Injector is Positioned in the Middle of the View Port. The Specimen is at the Top)

ORIGINAL PAGE
BLACK AND WHITE PHOTOGRAPH



CO290

Figure 4.4-14. Iridium Specimen Exposed to O_2/H_2 at $MR = 6$ for 45 min.

4.5, High Temperature Materials Tests (Sandia) (cont.)

with Aerojet. This work was reported jointly in the Advanced Small Rocket Chambers Monthly Technical reports. The work described here is summarized from those reports. The gas-phase measurements were reported by Bob Lucht and Bob Barlow; the surface measurements were reported by John Hamilton. More recent work conducted for NASA after this collaboration is noted in Section 6.0.

The objective of the gas phase studies was to quantify the gas properties downstream of the reaction zone as the gas approaches a hot surface representative of the inner wall of a radiation-cooled chamber.

The surface studies were used to measure optical characteristics of surface oxide layers for Ir, Pt and Re, and to characterize the Ir-Re diffusion couple under the high temperature of a radiation-cooled rocket engine.

4.5.1 Gas Phase Measurements

Gas phase measurements were performed in the Turbulent Diffusion Flame Facility (TDFF) using our existing simultaneous Raman-OH laser-induced fluorescence (LIF) system and the 1-atm MSTA as the combustion source. Figure 4.5.1-1 is a schematic diagram of the system; Figure 4.5.1-2 is a pictorial representation of the system.

The physical processes of LIF and Raman scattering are shown schematically in Figure 4.5.1-3. Figure 4.5.1-4 is a photograph of the laser probe for OH in the MSTA combustion zone with a heated Ir specimen.

The gas-phase measurements were carried out using the 1-atm MSTA. In anticipation of these experiments, computer simulations were run to obtain an estimate of the thickness of the boundary layer adjacent to the cylindrical sample. The SURFACE-CHEMKIN computer code used for this simulation was developed by Sandia for numerical modeling of CVD processes. For the conditions listed in Table 4.5.1-1, the boundary layer thickness was predicted to be approximately 6 mm. This can be resolved using our current OH fluorescence system.

OH concentration and temperature are the two most important quantities required to determine the effect of the material surface on gas phase chemistry. Specifically, we wish to determine whether the heated surface acts as a catalyst to increase the concentrations of

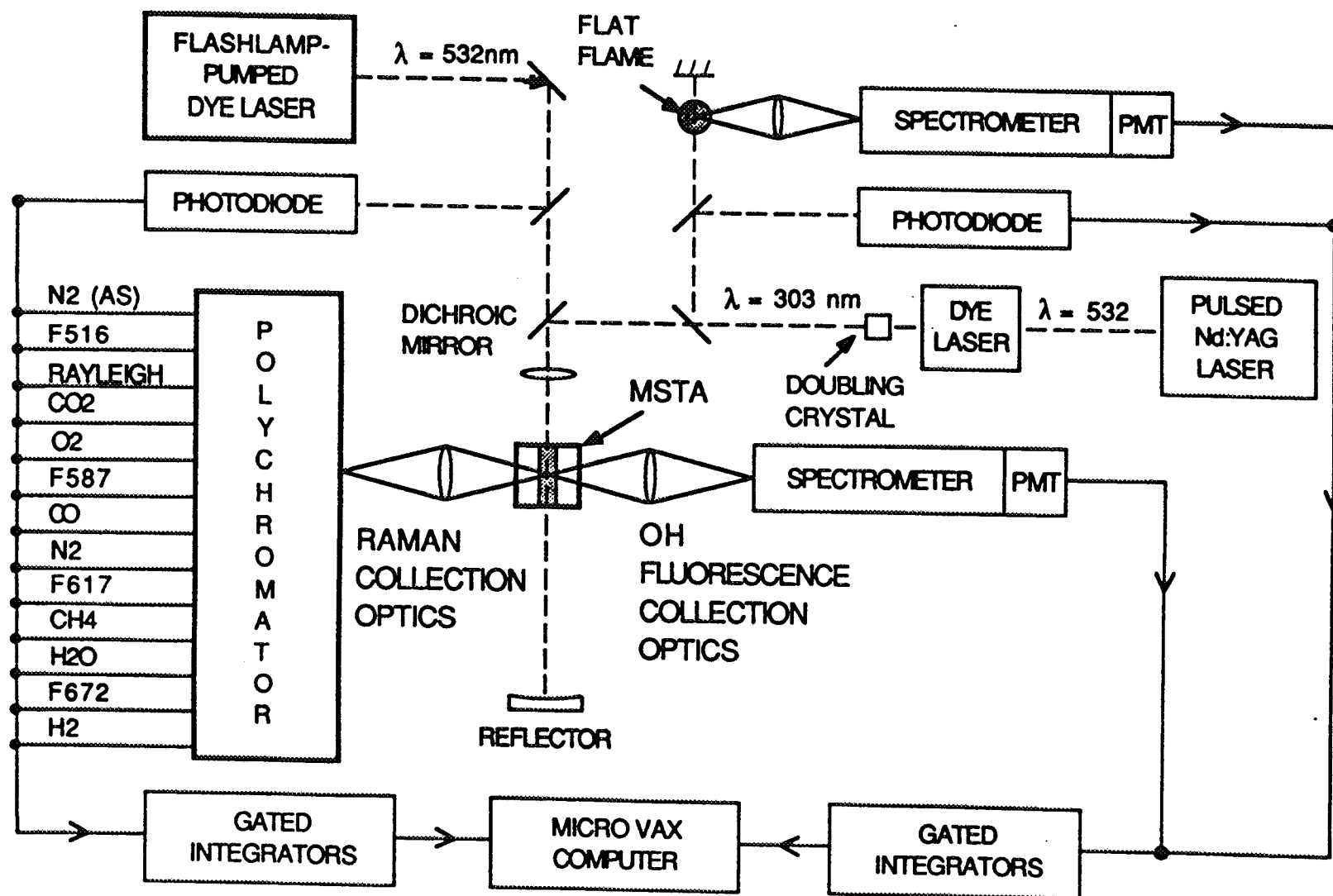


Figure 4.5.1-1. Schematic of Experimental Apparatus for Simultaneous Laser Induced Fluorescence, Raman Scattering, and Rayleigh Scattering Measurements in Turbulent Jet Flames

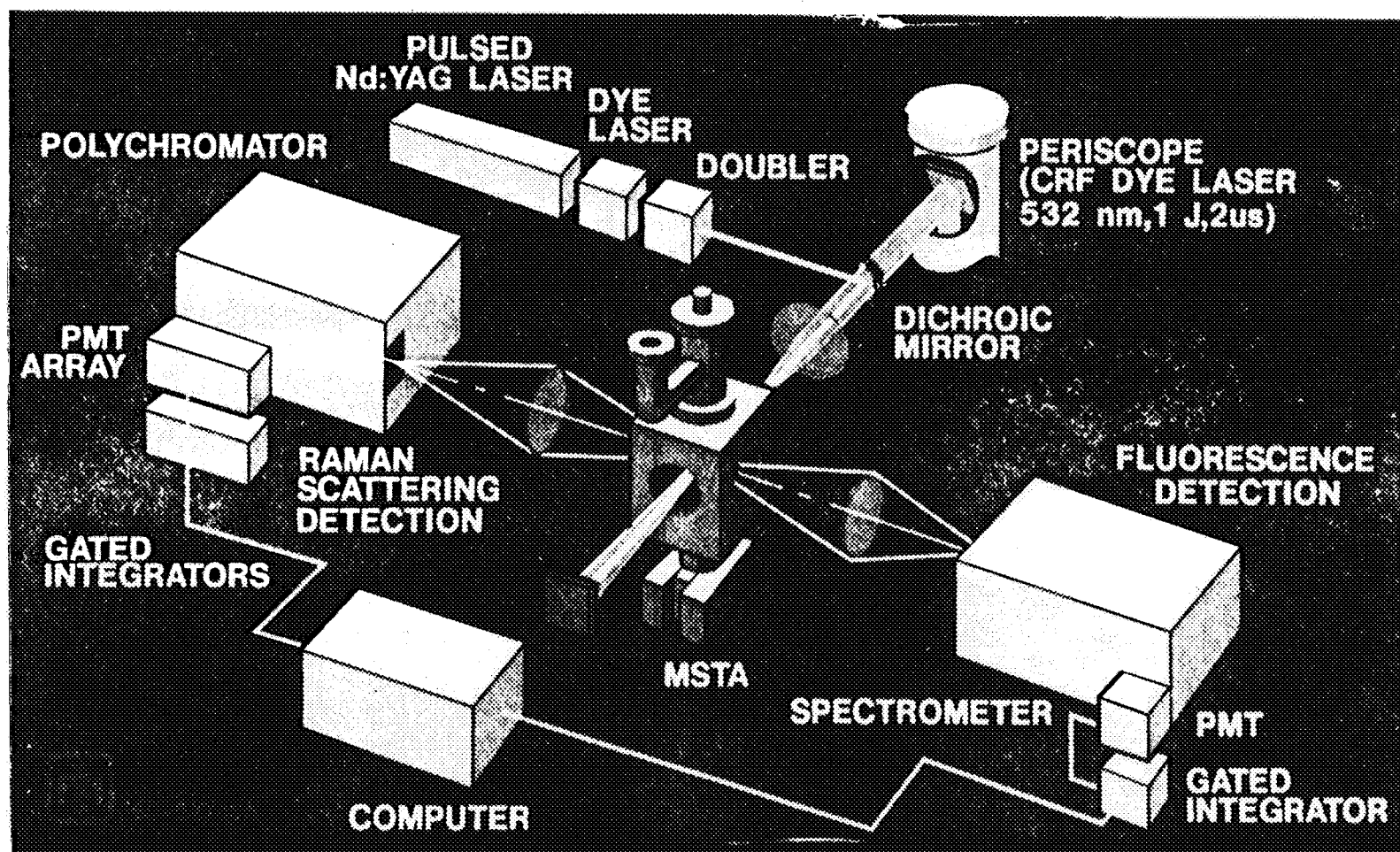
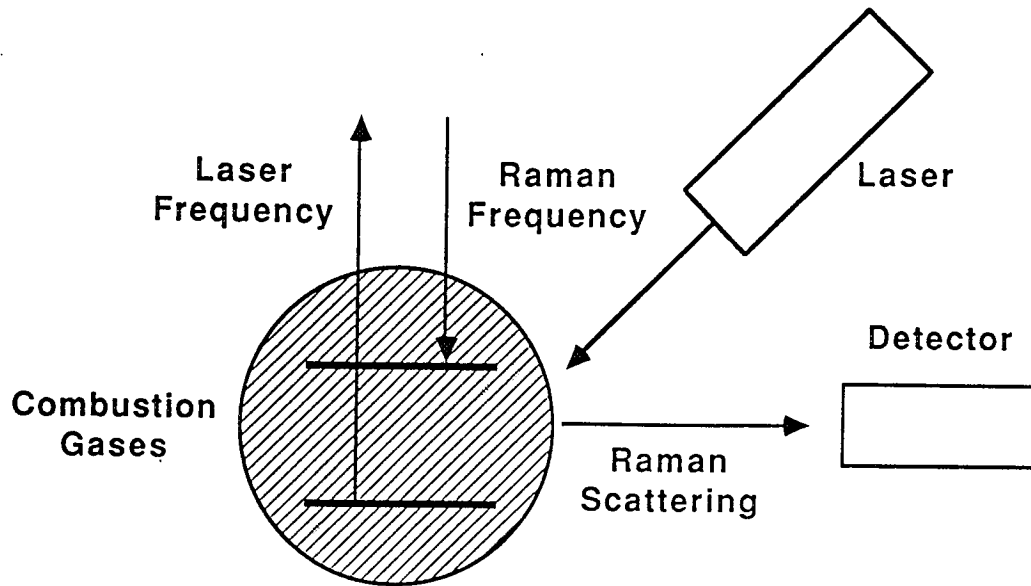


Figure 4.5.1-2. Apparatus for Gas-Phase Raman Scattering and OH Fluorescence Measurements in the MST

Spontaneous Raman Scattering Measurements



Laser-Induced Fluorescence (LIF) Measurements

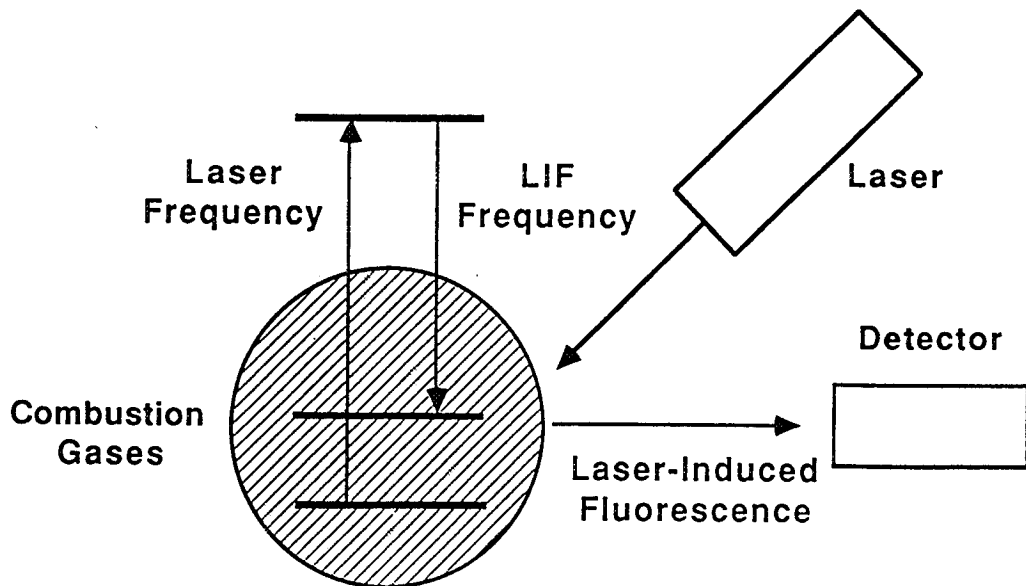


Figure 4.5.1-3. Physical Processes of LIF and Raman Scattering

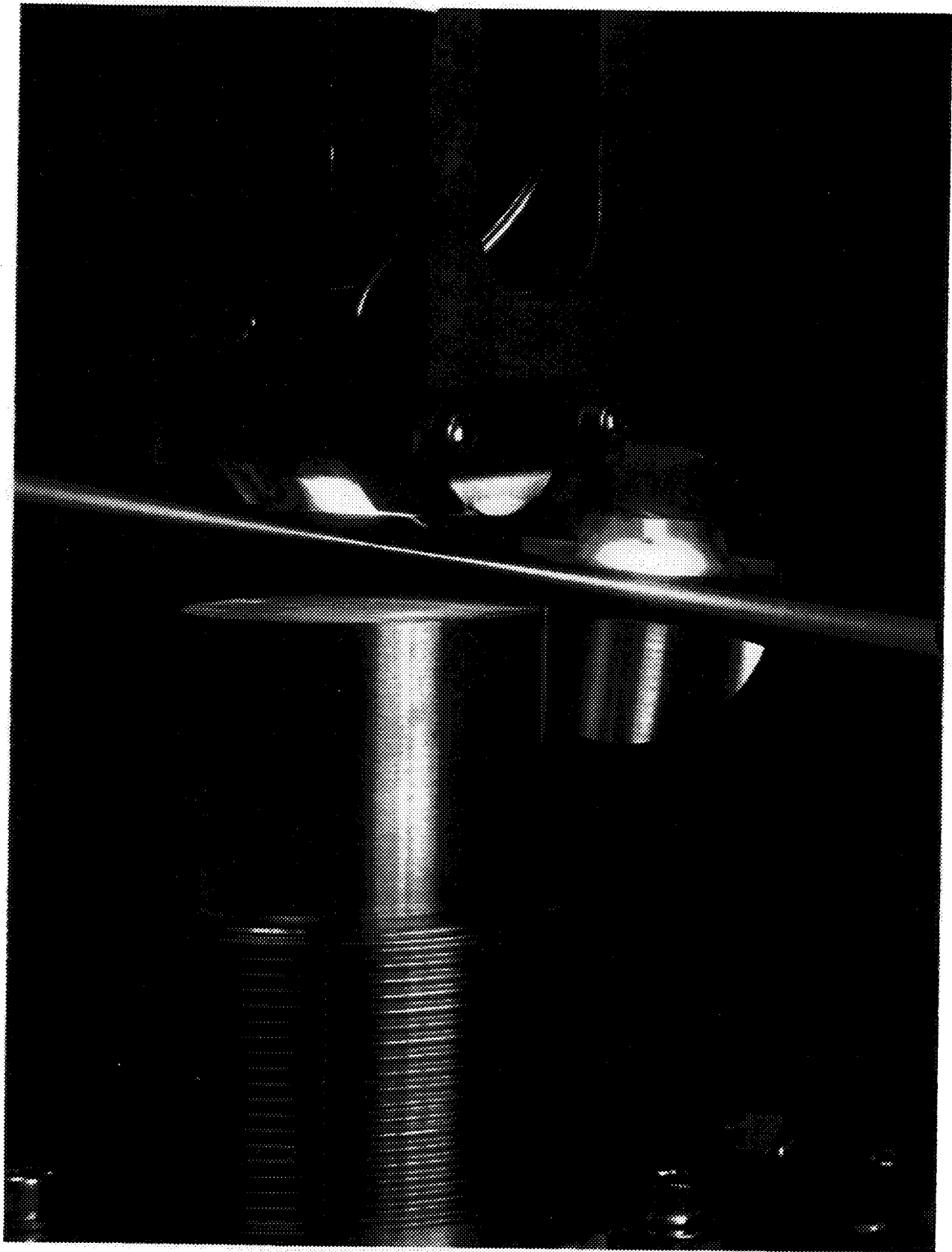


Figure 4.5.1-4. Laser Probe for OH in MSTA O₂/H₂ Combustion Zone with Heated Ir Specimen

Table 4.5.1-1. Flow Conditions For the Computer Simulations

Pressure	1 atm
Free Stream Composition	Equilibrium Products of H ₂ -Air Combustion
Free Stream Temperature	2090 K
Free Stream Velocity	11.9 m/s
Surface Temperature	2000 K

4.5, High Temperature Materials Tests (Sandia) (cont.)

flame radicals above the gas-phase equilibrium levels or as an efficient third body to facilitate recombination reactions and reduce the radical concentrations below the gas-phase equilibrium. Temperature profiles were determined in two ways using the Raman scattering system; 1) from the ratio of the Stokes and anti-Stokes nitrogen signals, and 2) from the total number density of major species in combination with the perfect gas law. Because we were working with combustion products from a premixed burner in the MSTA, the major species mole fractions were expected to change very little in the boundary layer, while the temperature and OH mole fraction may change significantly.

Representative results from two simulations are included in this report, one with no reactions at the surface and the second with high radical recombination rates at the surface. Profiles of axial velocity, temperature, and the OH mole fraction for the case with no surface chemistry are shown in Figures 4.5.1-5, -6, and -7, respectively. Corresponding profiles for the second case, where radical concentrations are forced to zero at the surface, are shown in Figures 4.5.1-8 and -9.

An important result obtained from the simulations is that the OH concentration throughout the boundary layer in the case with no surface chemistry is in partial equilibrium with the H_2 and O_2 concentrations, as shown in Figure 4.5.1-7. This demonstrates that residence times in the boundary layer are long enough to allow the rapid bimolecular reactions of the oxygen-hydrogen system to achieve equilibrium at the local temperature. Figure 4.5.1-9 shows that partial equilibrium holds through the outer part of the boundary layer in the case with high recombination rates at the surface. However, because the radical concentrations are pulled to zero at the surface, partial equilibrium cannot be achieved near the surface, and the OH concentration drops below that corresponding to partial equilibrium of OH, O_2 , and H_2 .

Experimental conditions for the boundary-layer measurements that have been completed in the atmospheric pressure MSTA are summarized in Table 4.5.1-2. Profiles of temperature and OH concentration were obtained using the laser-induced fluorescence techniques described below.

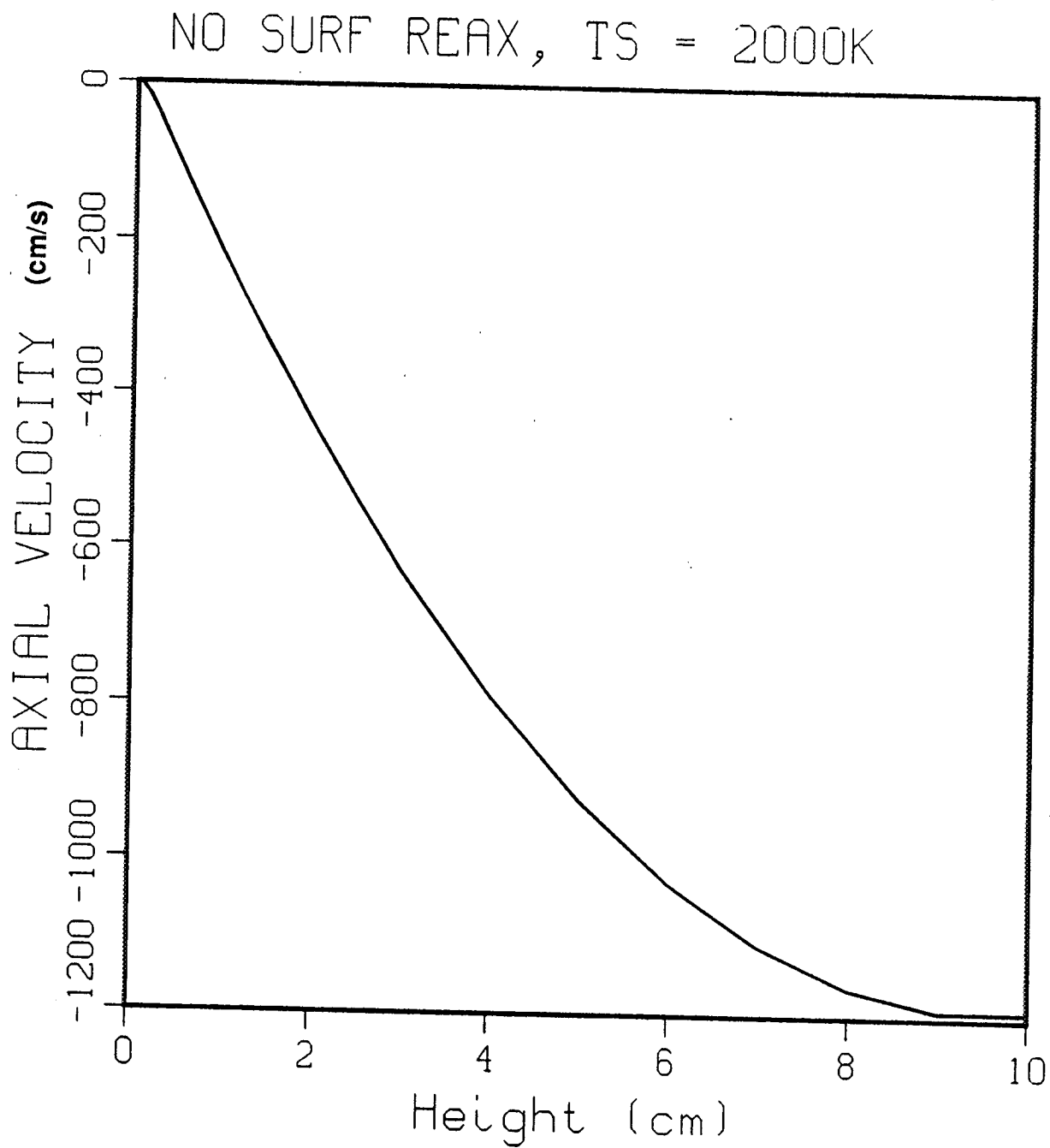


Figure 4.5.1-5. Profile of the Axial Velocity for the Conditions Described in Table 4.5.1-1 with No Surface Reactions

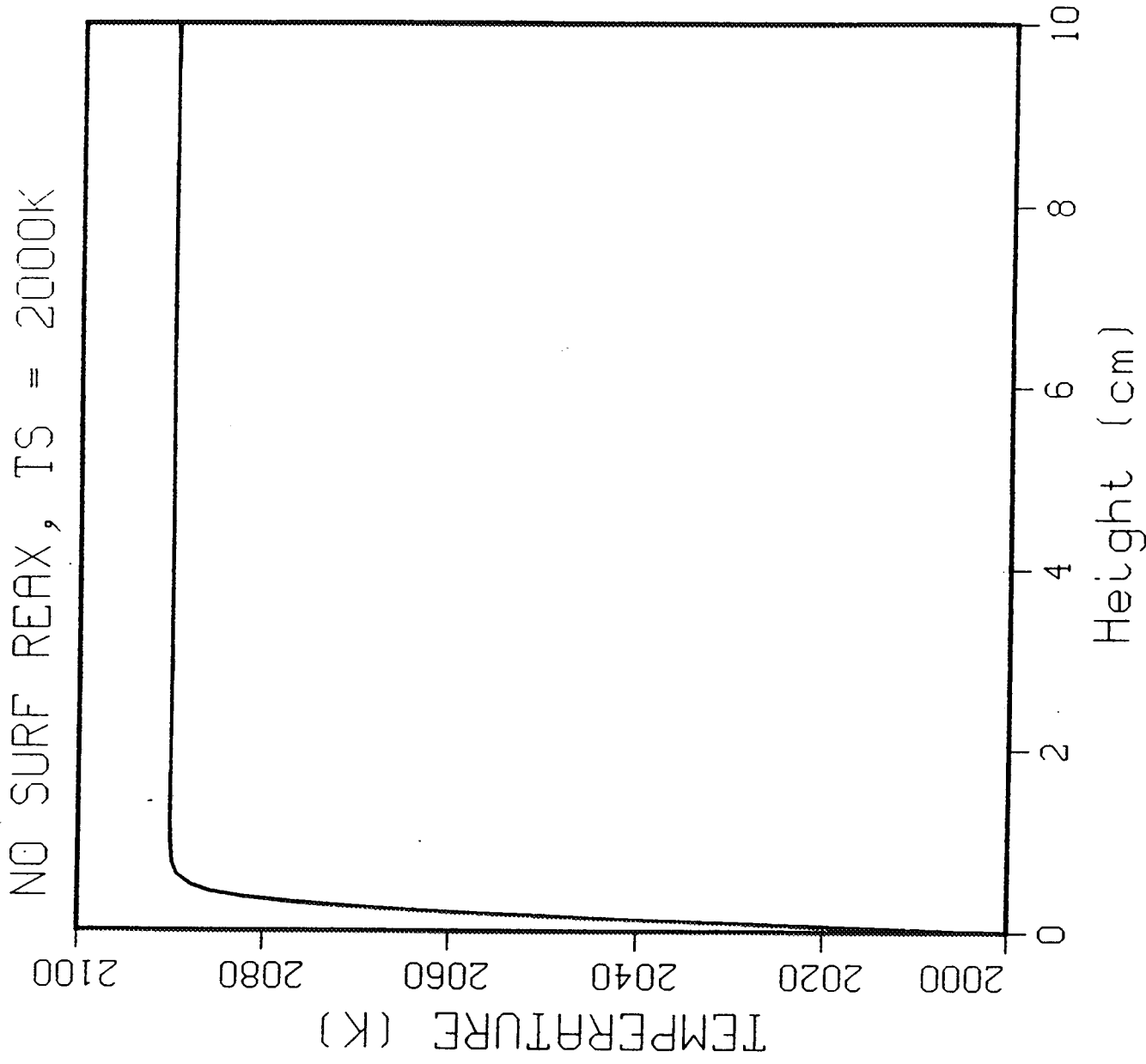


Figure 4.5.1-6. Profile of the Temperature for the Conditions Described in Table 4.5.1-1 With No Surface Reactions

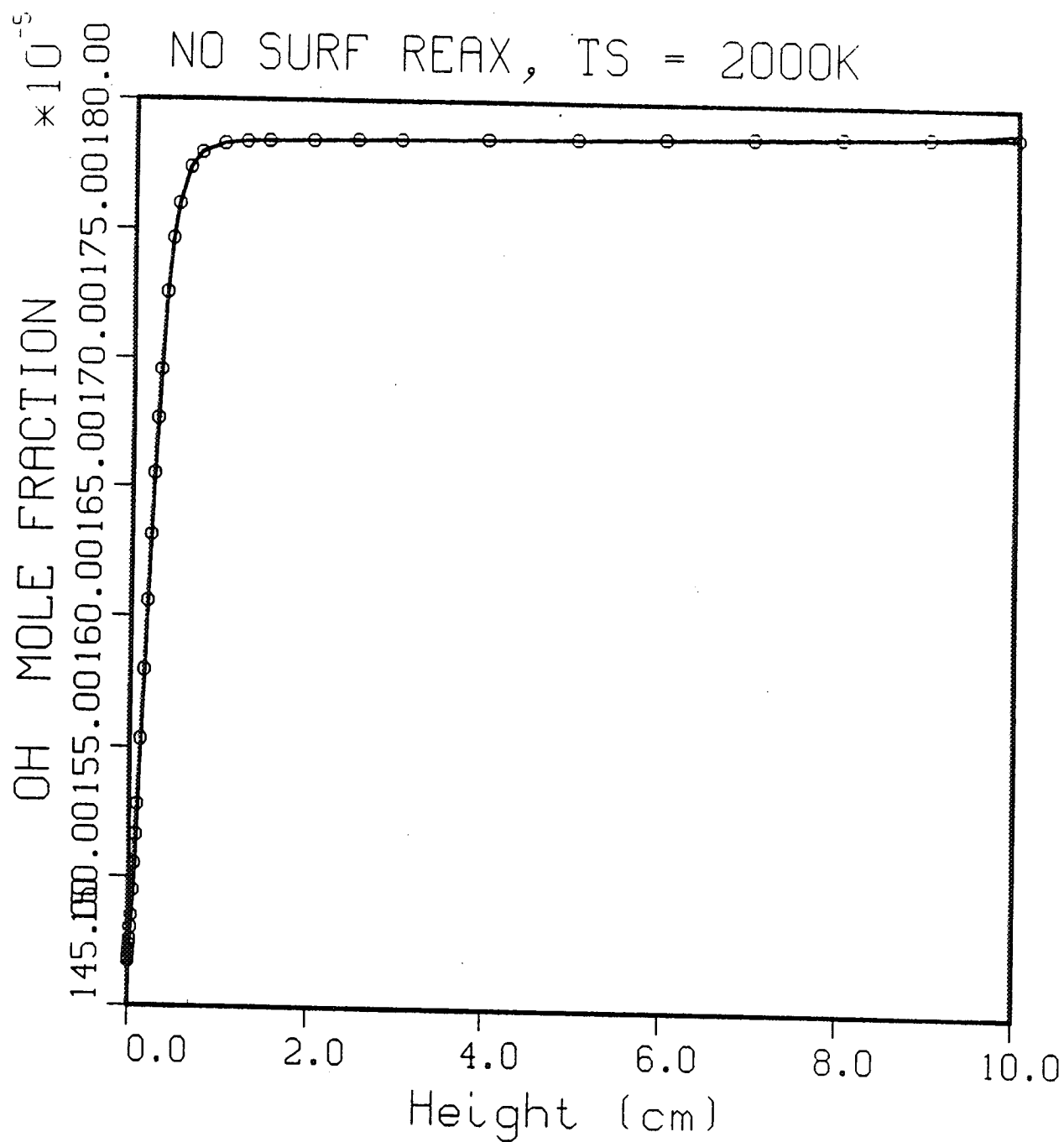


Figure 4.5.1-7. Profiles of the Predicted OH Mole Fraction (Solid Line with No Symbols) Compared with the OH Mole Fraction Calculated from Partial Equilibrium with O_2 and H_2 Conditions Described in Table 4.5.1-1 with No Surface Reactions

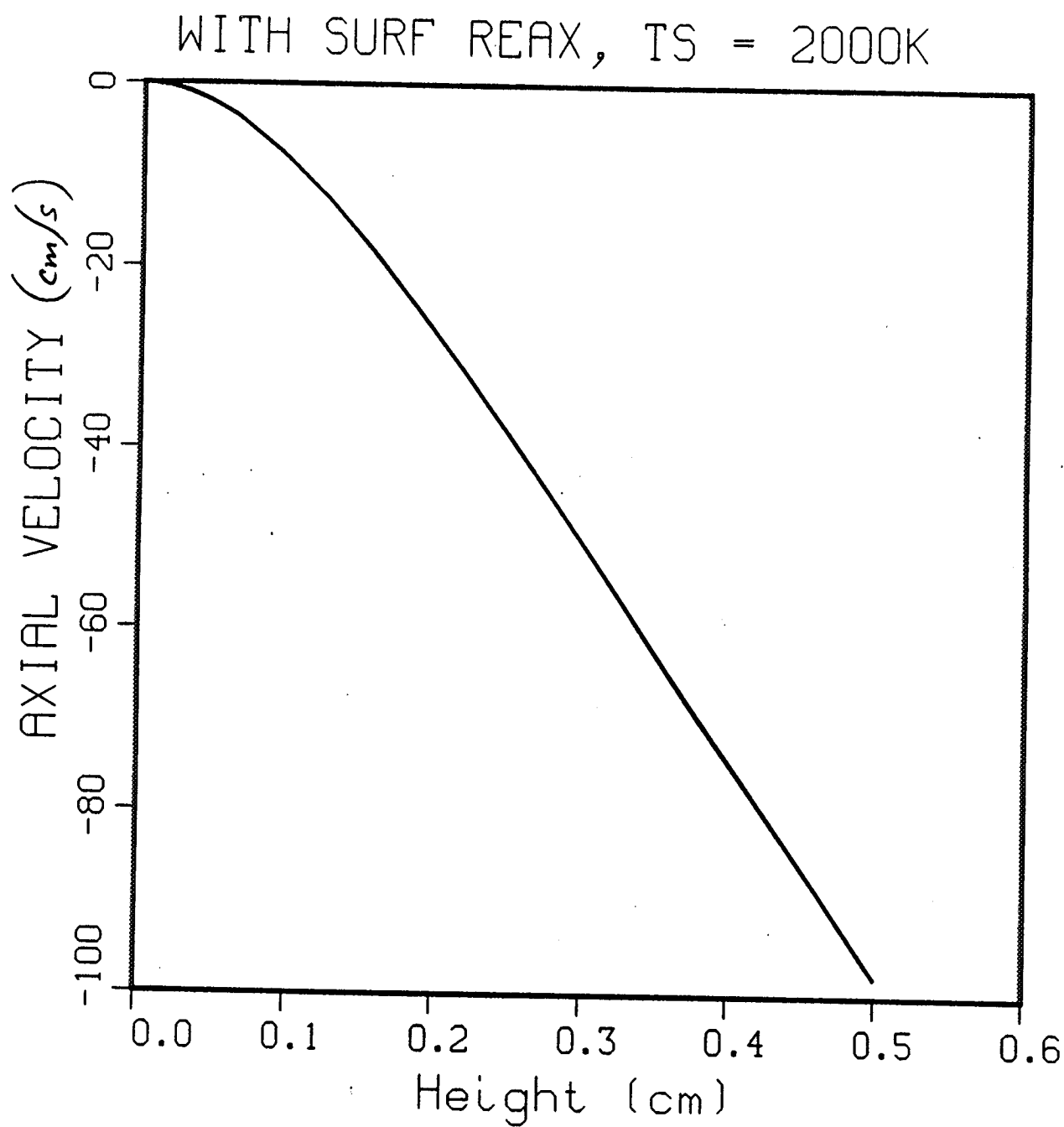


Figure 4.5.1-8. Profile of the Axial Velocity for the Conditions Described In Table 4.5.1-1 with High Radical Recombination Rates at the Surface

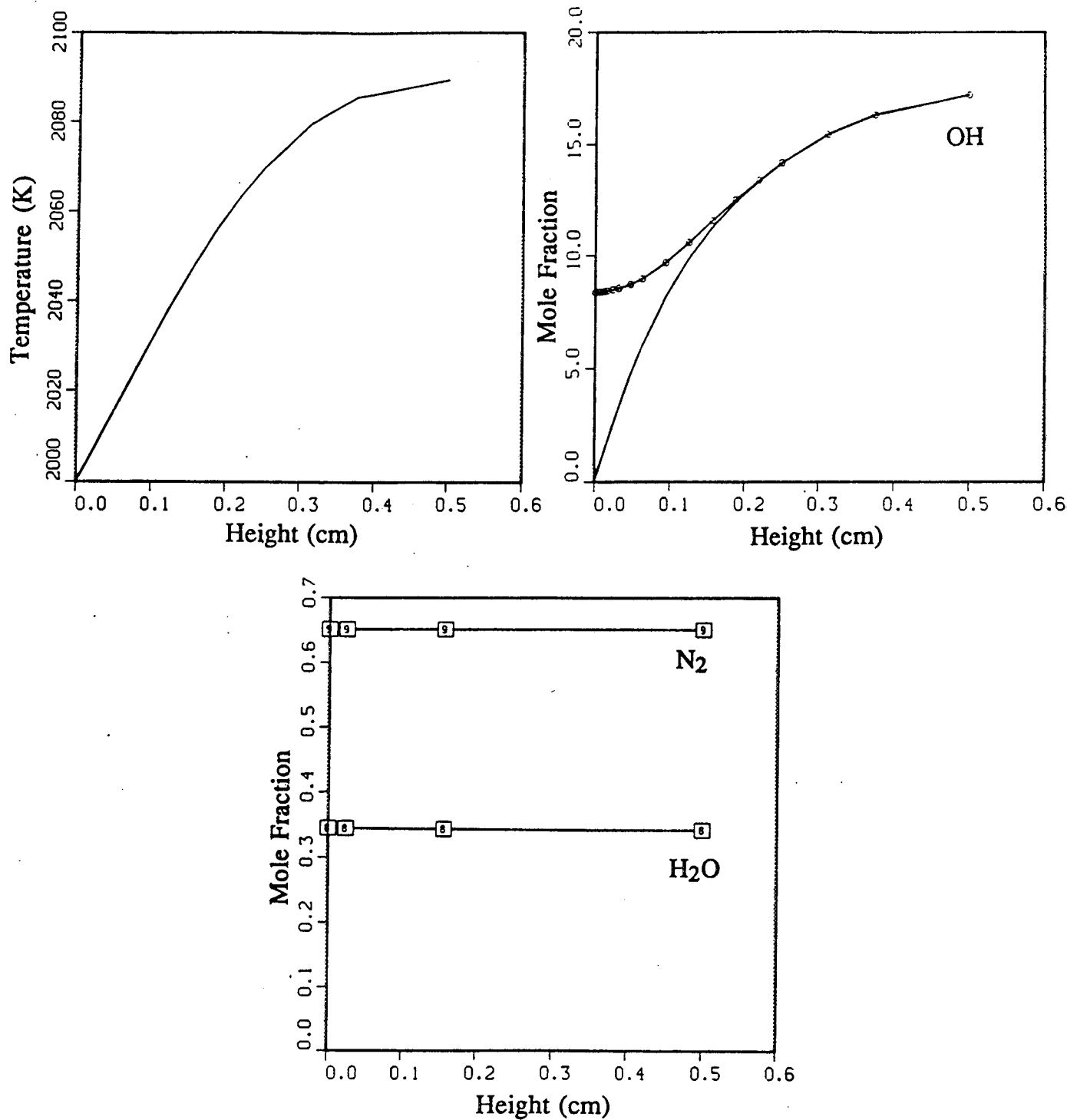


Figure 4.5.1-9. Calculated Profiles of T, OH, N₂, H₂O Illustrate That Major Species Mole Fractions Can Be Expected to Change Very Little in the MSTA Gas Phase Boundary Layer, While Temperature and OH Mole Fraction Can Change Significantly

4.5, High Temperature Materials Tests (Sandia) (cont.)

Table 4.5.1-2. Experimental Conditions For Gas-Phase Profiles

Foil	T ₅ (K) [†]	Reactants	MR
Ir	1670	H ₂ -air	6.5
Ir	1970	H ₂ -air	6.5
Ir	2270	H ₂ -air	6.5
Ir	2370	H ₂ -air	6.5
Ir	1670	H ₂ -air	5.5
Ir	1970	H ₂ -air	5.5
Ir	2270	H ₂ -air	5.5
Pt	1670	H ₂ -air	6.5
Pt	1670	H ₂ -air	5.5
Ir	1990	H ₂ -O ₂	6.5
Ir	2100	H ₂ -O ₂	5.5

[†]T₅ is the specimen surface temperature measured by the two-color pyrometer.

OH Concentration Measurements

For the OH concentration measurements, as well as the temperature measurements, the laser diagnostic system is operated in the linear fluorescence regime. Fluorescence signal is normalized by laser energy and averaged for 300 shots at each location in the boundary layer. OH concentration is calculated from the averaged data according to Eq. (1),

$$[\text{OH}] = C_{\text{ref}} C_Q C_f C_{\text{trap}} F \quad (1)$$

where F is the average value of the normalized fluorescence signal, C_{ref} is a calibration constant referenced to measurements above a calibration burner, C_Q is the correction factor accounting for variation of the collisional quenching rate, C_f corrects for variation with temperature of the Boltzmann fraction in the ground-state rotational level, and C_{trap} is a function of distance from the sample surface that corrects for the effect of fluorescence trapping in the MSTA.

Fluorescence trapping refers to the absorption of some of the fluorescent light by OH molecules in the combustion gases between the laser probe volume and the collection lens. C_{trap} was determined for several locations (1, 2, 4, and 8 mm from the surface) by measuring fluorescence profiles along the optical axis of the collection lens (tangent to the sample surface) and calculating the integrated absorption effect for each profile. A curve fit to

4.5, High Temperature Materials Tests (Sandia) (cont.)

these data was then used to obtain C_{trap} as a function of distance from the surface for each value of the mixture ratio.

The quenching correction factor C_Q is the most important correction factor for the present experiments. The quenching rate can be written as

$$Q = \bar{\sigma} n_o \sqrt{\frac{8kT}{\pi m_{\text{OH}}}} \quad (2)$$

where n_o is the total number density, and the species-averaged quenching cross section is

$$\bar{\sigma} = \sum_p \chi_p \sigma_p(T) \sqrt{\frac{m_p}{m_{\text{OH}}}} \quad (3)$$

Here, the summation is over the OH collision partners, with X_p and σ_p being the mole fractions and collisional quenching cross sections of the collision partners. Species-averaged quenching cross sections were calculated by Philip Paul (Sandia National Laboratories, Reacting Flow Division, 8351) as functions of temperature for air/H₂ mixture ratios of 6.5 and 5.5. These calculations were based upon the equilibrium concentrations of major species at each value of temperature. This analysis showed that the species-averaged quenching cross sections for both the MR = 6.5 and MR = 5.5 cases scale very nearly as $T^{-1/2}$ within the temperature range of interest for the present hydrogen/air experiments (1600 to 2400K). Consequently, the overall quenching rate is proportional to $1/T$ and C_Q can be approximated as T_{ref}/T to good accuracy.

Temperature Measurements

Gas-phase temperature at each location in the boundary layer was determined by measuring the OH fluorescence signal for three transitions corresponding to three values of the ground-state rotational quantum number. We have used the $S_{21}(5)$, $S_{21}(8)$, and $S_{21}(11)$ transitions for $v' = v'' = 0$. Assuming that the collisional quenching rate of the excited OH molecules is independent of rotational levels at the high temperatures of interest here, the ratio of fluorescence signals for any pair of transitions is related to the local temperature according to Eq. (4).

$$\frac{F_i}{F_j} = \frac{B_i(2J_i + 1)}{B_j(2J_j + 1)} \exp\left(\frac{-\Delta E_{ij}hc}{kT}\right) \quad (4)$$

4.5, High Temperature Materials Tests (Sandia) (cont.)

where F is the linear fluorescence signal normalized by laser energy and averaged over 300 laser shots, B is the Einstein coefficient, $J = N + 1/2$, the subscripts i and j refer to the ground-state rotational level ($N = 5, 8$, or 11), ΔE is the energy difference between the two ground-stage levels in question, and h , c , and k are physical constants. By rearranging Eq. (4) we obtain Eq. (5), which is solved to determine temperature from each pair of fluorescence measurements at a given spatial location.

$$T_{ij} = \left(\frac{hc}{k} \right) \frac{-\Delta E_{ij}}{\ln \left(\frac{F_i}{B_i(2J_i + 1)} \right) - \ln \left(\frac{F_j}{B_j(2J_j + 1)} \right)} \quad (5)$$

Temperatures reported here are averages of the three temperatures obtained from Eq. (5) at each spatial location.

For measurements close to the surface, scattering of the laser beam off the surface interferes with the fluorescence measurements. To account for this, measurements of the background scattering signal for each transition were made by tuning the laser off the OH line and subtracting the off-resonant signal from the fluorescence signal obtained with the laser at line center.

In system operation tests a hydrogen-air flame was stabilized on the burner over a range of stoichiometries from fuel-lean to fuel-rich. The hydrogen-air flame was visible with the laboratory lights turned low and the flow appeared to be quite stable. Slight problems initially were experienced with the instability of the nitrogen shroud flow; the shroud flow line was modified so that the mass flow controller stabilized the flow rate.

The MSTA sample holder/electrical heating system was also tested successfully. An iridium foil was used for the test-run. A pyrometer was used to measure the temperature of the iridium surface. The measurements confirmed that the temperature of the sample could be increased significantly by electrical heating. After the test run, it was observed that the iridium foil was wrinkled and had a whitish haze, possibly from an oxide coating. The flame stoichiometry had been varied significantly during the test and it is not clear at what stoichiometry the surface reactions had occurred.

4.5, High Temperature Materials Tests (Sandia) (cont.)

Initial measurements were made of OH profiles in the burner for rich and stoichiometric hydrogen/air flames. We performed vertical scans from the burner surface to the surface of the material sample, and also measured OH fluorescence profiles in a horizontal plane 2 mm below the material surface.

The vertical OH profile in the rich flame is shown in Figures 4.5.1-10 and -11. Figure 4.5.1-10 shows the raw fluorescence profile. The data were recorded by tuning the frequency-doubled, Nd: YAG-pumped dye laser to the OH $S_{21}(8)$ rotational transition of the $A^2\Sigma^+-X^2\Pi(0,0)$ electronic transition. This line was selected for its temperature insensitivity. The spectrometer bandpass was set to collect the entire R-branch of the $A^2\Sigma^+-X^2\Pi(0,0)$ electronic transition. This fluorescence excitation and detection scheme is identical to that used for turbulent flame measurements.

As can be seen from Figure 4.5.1-10, scattered light is significant both at the burner surface and when the beam is within 1 mm of the material sample surface. We performed scans with the laser detuned from the OH resonance near the material sample surface (open circles in Figure 1) to determine the proportion of the signal due to scattered light. The scattered light was then subtracted from the total signal to give the profile shown in Figure 4.5.1-11.

Figure 4.5.1-11 suggests that OH concentration is increasing near the burner surface, although large error bars (on the order of 20-40%) should be assigned to the two points closest to the burner surface. This increase is the opposite of what would be expected from recombination of OH at the surface. The surface may be inert for fuel rich stoichiometries, in which case the OH concentration is observed to decrease slightly near the burner surface for the stoichiometric case, indicating that recombination may be more important at leaner conditions.

The computer simulations indicated that the thickness of the temperature-species boundary layer is 5 mm or less for the 1-atm test conditions and that the inner 1 to 2 mm will be most affected by surface reactivity. Therefore, high spatial resolution and good accuracy near the surface are essential. Spatial resolution is primarily determined by the diameter of the laser beam at the waste, which is $\sim 100\mu\text{m}$, allowing good resolution of the boundary layer.

Figures 4.5.1-12 and -13 show the orientation of the laser beam relative to the sample. The axis of the cylindrical sample is at 45° to the laser beam, and fluorescence is detected at 90° to the laser beam. This orientation allows measurements close to the surface and

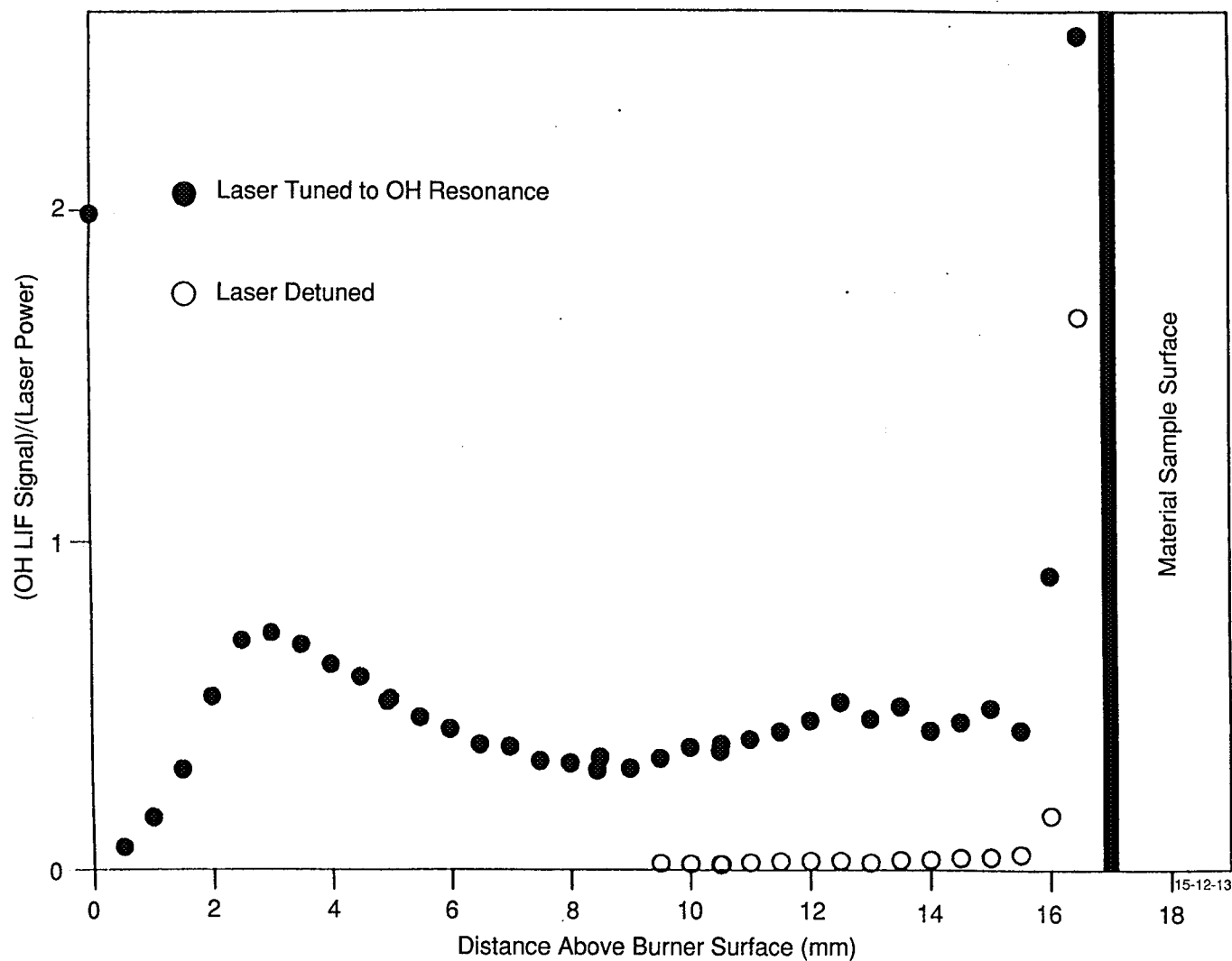


Figure 4.5.1-10. Laser-Induced Fluorescence (LIF) Profiles in a Rich ($\Phi = 1.35$) Hydrogen/Air Flame. The Laser is Turned On and Off Resonance to Separate the OH Fluorescence Signal From Scattered Light From the Material Sample Source

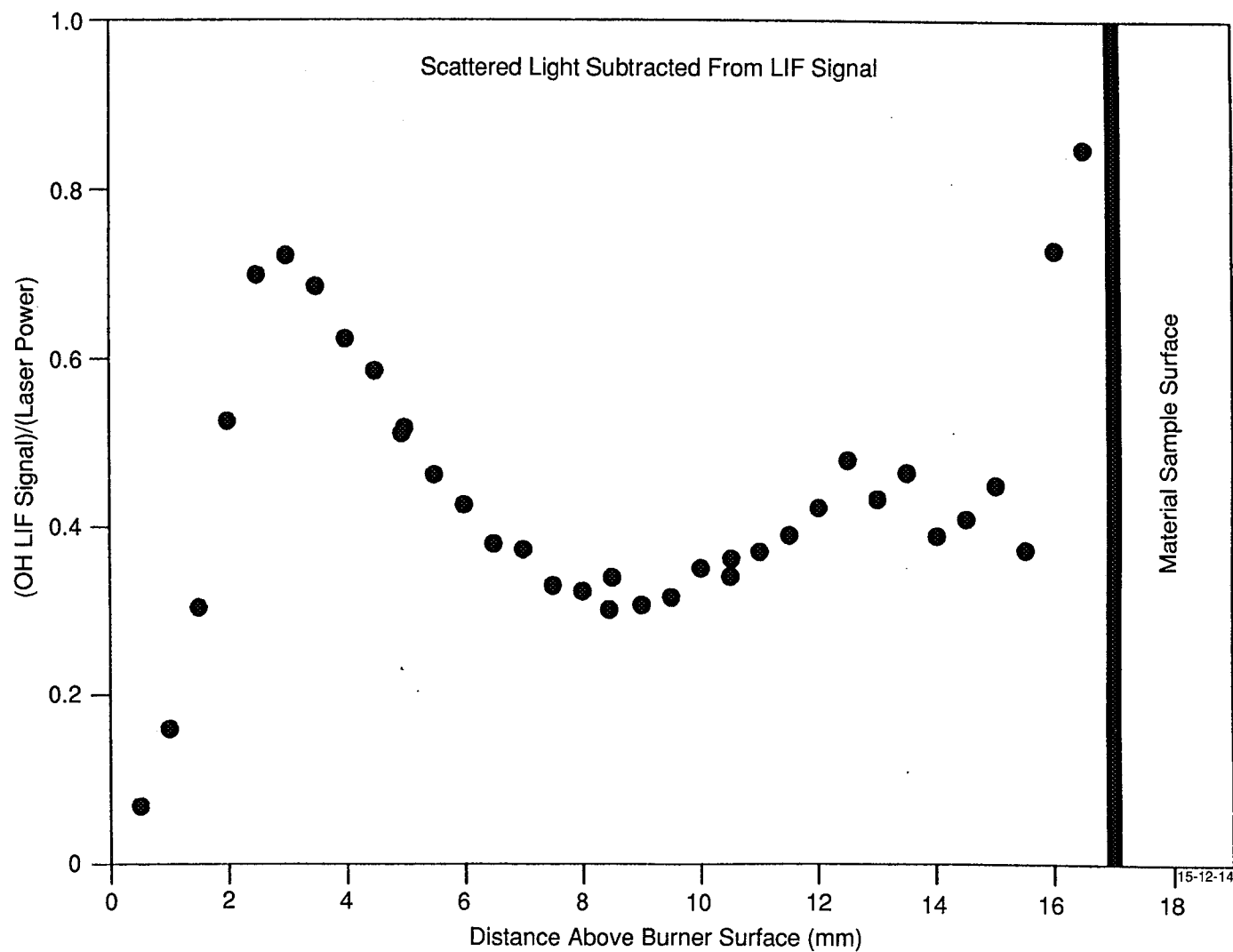


Figure 4.5.1-11. OH LIF Profile in the Rich Hydrogen/Air Flame, With the Contribution From Scattered Light Subtracted

Atmospheric Pressure Material Sample Test Apparatus

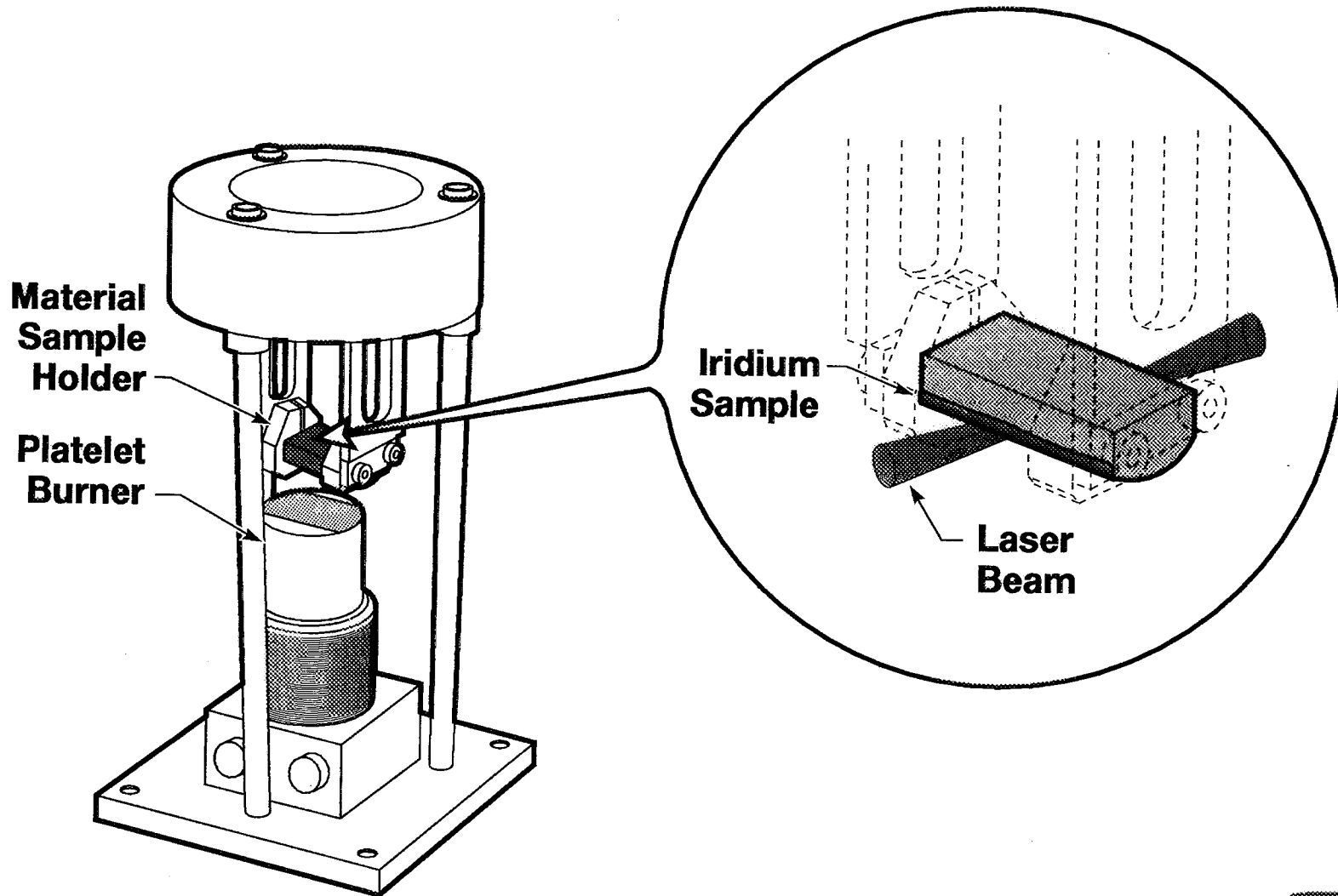


Figure 4.5.1-12. Orientation of the Material Sample Relative to the Laser Beam for Gas-Phase Measurements

Geometry of LIF Diagnostics in the MSTA

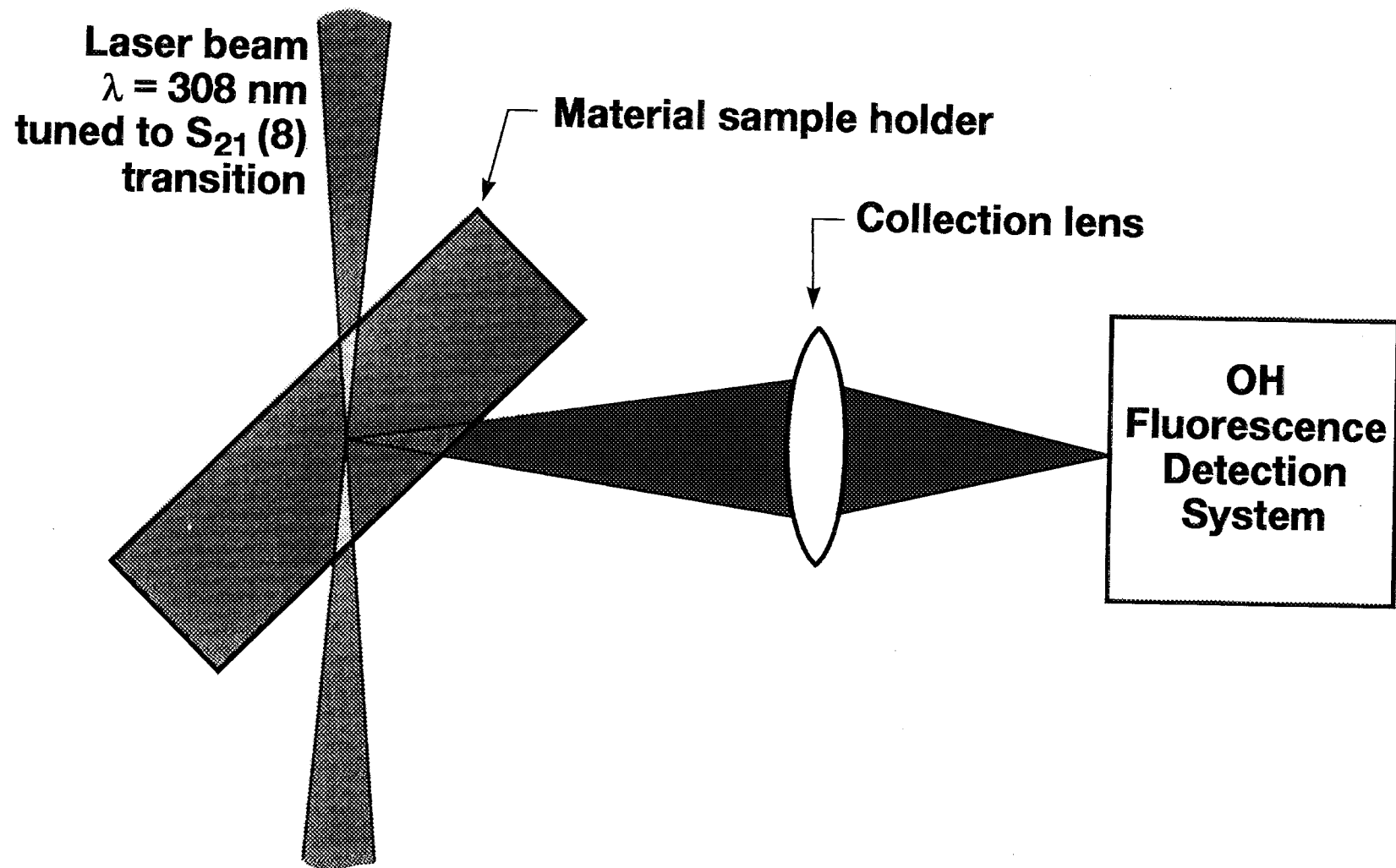


Figure 4.5.1-13. In the MSTA, the Cylindrical Metal Foil is Held at a 45° Angle to the Axis of the Laser Beam for OH Fluorescence or Raman Scattering Measurements

4.5, High Temperature Materials Tests (Sandia) (cont.)

avoids obscuration of either the laser beam or the collection cone of the fluorescence detection system.

Accuracy within 1 mm of the surface is affected by the relative magnitudes of the true OH fluorescence signal and the signal due to scattering of the laser light from the surface. We have developed a strategy that optimizes the ratio of these signals. Residual effects due to scattering from the surface are removed by repeating the boundary layer profile with the laser tuned off the OH transition and subtracting the resulting profile of scattered light intensity from the profile that includes both the fluorescence signal and the scattering signal.

Figure 4.5.1-14 shows the measured OH fluorescence signal vs distance from the iridium surface for a 1-atm, $MR = 6.5$, hydrogen-air flame. Here, the OH signal decreases linearly in the region from 3 mm to 1 mm from the surface. This decrease is due to radical recombination in the post flame gases. The OH concentration boundary layer for this operating condition is only 1 mm thick. Within the boundary layer the OH fluorescence profile deviates significantly from the linear trend and drops rapidly toward a near zero value at the surface. This suggests that the surface serves to catalyze radical combination reactions, as assumed in one of the computer simulations, pulling the radical concentrations to low values near the surface. It is important to note that the surface temperature for the profile in Figure 4.5.1-14 was 2100°C. Black body radiation from this high temperature surface did not cause interference on the OH fluorescence measurements.

The Raman scattering system used a doubled Nd: YAG laser (532 nm) rather than the CRF flashlamp-pumped dye laser. The dye laser, with its high energy and long pulse duration (2J, 3 μ s), is required for single-shot measurements in turbulent flames. However, the Nd:YAG provides a higher quality beam that can be focused down to the small diameter required for good spatial resolution in the MSTA boundary layer. Signals from the laminar MSTA flame are averaged over many laser shots to obtain accurate concentration profiles.

Measurements made using a pulsed Nd:YAG laser show that laser light scattering from the material surface does not interfere with the Raman signals. Even the relatively weak nitrogen anti-Stokes signal appears to be free of interference. These are important results in themselves because they indicate that it should be possible to obtain temperature measurements in two ways: (1) from the nitrogen anti-Stokes to Stokes ratio, and (2) from the total

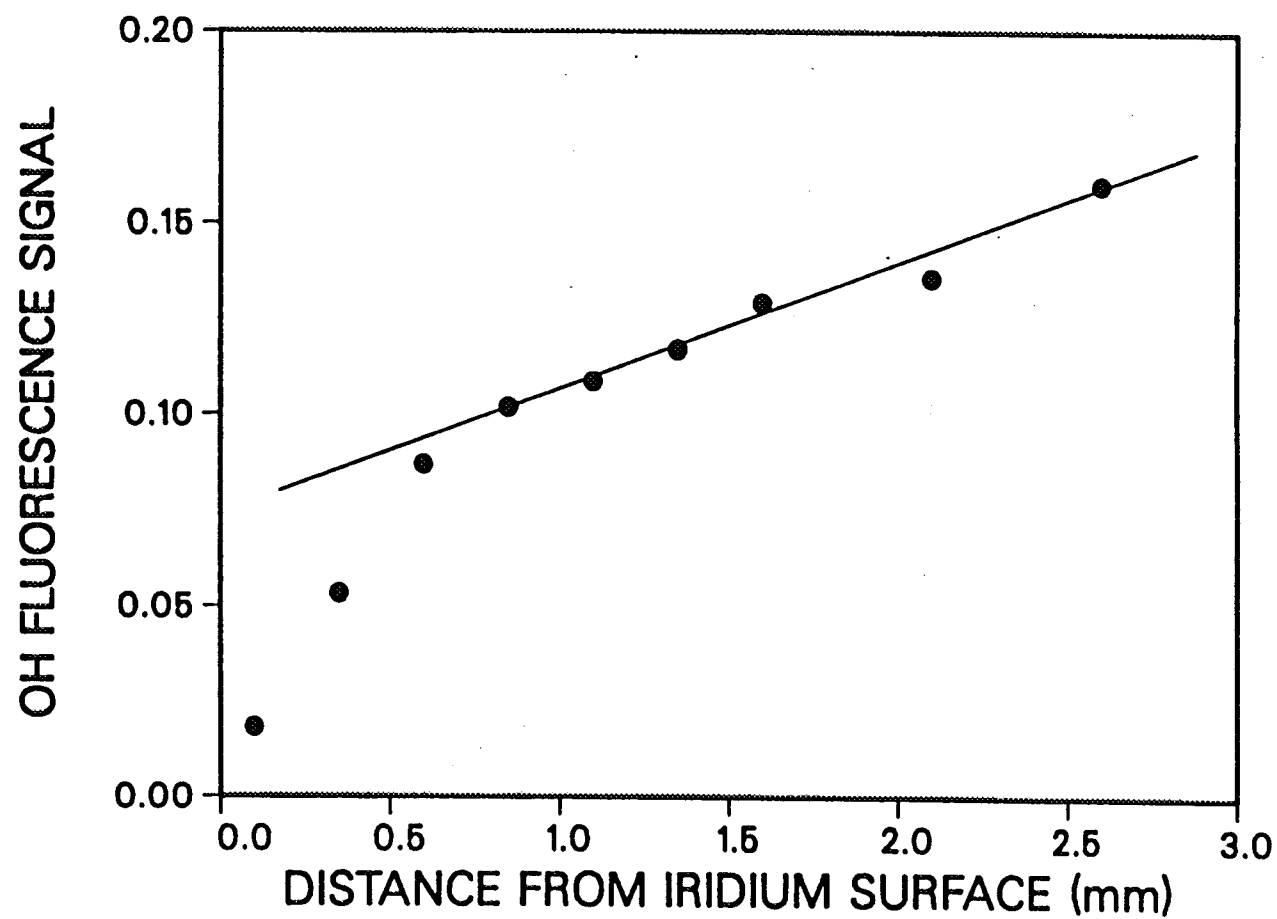


Figure 4.5.1-14. Measured OH Fluorescence Profile in the Boundary Layer Adjacent to an Iridium Foil Sample at 2100°C in a Stagnation Flow of Combustion Products from a Hydrogen-Air Flame at $MR=6.5$, 1-Atm

4.5, High Temperature Materials Tests (Sandia) (cont.)

number density of the measured species, using the perfect gas law. Accurate temperature profiles will be important in interpreting the OH concentration profiles and in evaluating the reactivity of the material surface.

Measurements of the concentration profiles of major species (H_2 , O_2 , N_2 , and H_2O) and the OH radical in the boundary layers below heated metal foil samples in the MSTA were made. Examples of the measured Raman and LIF profiles for an air- H_2 ($MR = 6.5$) flame with the surface temperature at $1400^\circ C$ are shown in Figure 4.5.1-15. Some features of these data are discussed below.

Modifications to the laser diagnostics system were required for simultaneous measurement of Raman scattering and laser-induced fluorescence (LIF) to facilitate measurements of concentration profiles very close to the high temperature material sample. These modifications included: tailoring the dimensions of the laser probe volume, masking the collection lenses, and altering the entrance aperture of the Raman polychromator.

Tailoring the laser probe volumes: The beam focusing optics were modified to produce measuring volumes for the Raman and LIF systems that are elongated in the direction tangent to the material surface and compressed in the direction normal to the surface. The resulting beam profiles are approximately $100\ \mu m \times 500\ \mu m$ at the measurement location. Concentration gradients in the boundary layer are steep only in the direction normal to the surface. The spatial resolution of the measurements is, therefore, determined by the height of the probe volume. The elongated Raman probe volume allows the use of higher laser energies before gas breakdown occurs. This provides higher Raman scattering signal levels. The elongated LIF probe volume allows higher laser energies before saturation of the OH transition becomes significant. This also provides higher signal levels.

Masking the collection lenses: The profiles shown in Figure 4.5.1-15 were obtained using the full collection lens apertures ($f/2$ for the Raman system, $f/2.5$ for the LIF system). The N_2 and H_2O profiles are nearly constant until the probe volume is within approximately 1 mm of the surface where we enter the thermal boundary layer. The temperature decreases toward the surface, which is at $1400^\circ C$, and the Raman signals increase as the local gas density increases. Within $500\ \mu m$ of the surface, however, the Raman signals drop off sharply due to partial obscuration of the probe volume by the cylindrical material sample. (The view of

H₂-Air Flame, MR=6.5, TS=1400°C

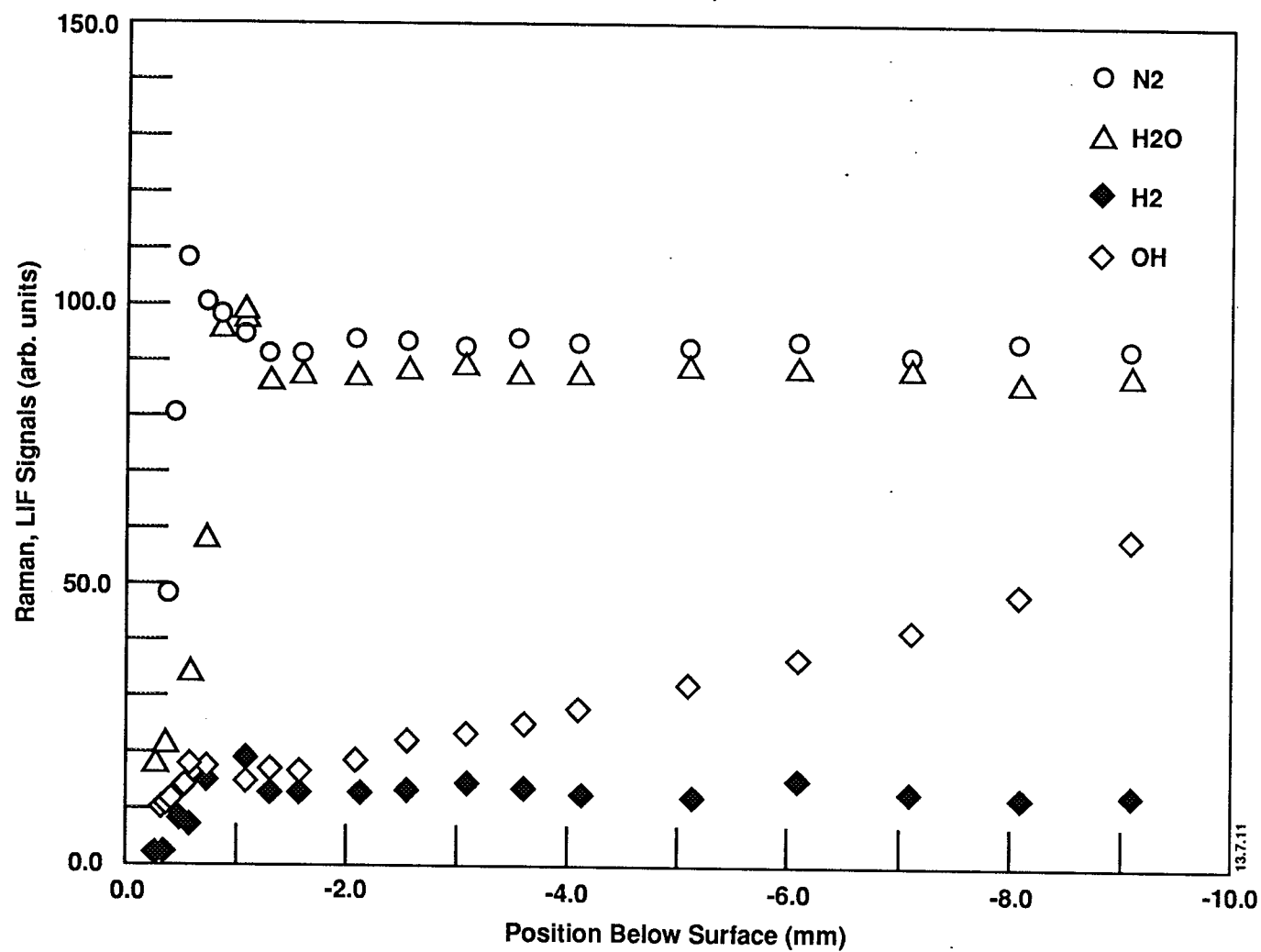


Figure 4.5.1-15. Profiles of Simultaneous Raman and LIF Signals for an Air-H₂ Flame (MR=6.5) With the Iridium Surface at 1400°C.

4.5, High Temperature Materials Tests (Sandia) (cont.)

the probe volume from the top portion of the Raman collection lens becomes blocked.) By masking a portion of the upper half of each collection lens (Raman and LIF), we obtain measurements closer to the surface before the signals are affected by this partial obscuration.

Modifying the polychromator aperture: In the standard setup for measurements in turbulent flames, the entrance to the polychromator is a vertical slit perpendicular to the image of the laser beam. When the MSTA is operated with the surface at a high temperature (e.g., 2000°C), radiation from the surface interferes with the Raman signals. (Measurements with the surface at 1400°C show no measurable interference.) Consequently, the entrance to the polychromator has been changed from a slit to a rectangular aperture, as illustrated in Figure 4.5.1-16.

In addition, radiation from the material surface interferes with the Raman signals when the MSTA is operated with the surface at a high temperature (e.g., 2000°C). The current produced in the photomultiplier tubes by this background radiation exceeds the continuous current capability of the tubes/power supply, causing the gain of the tubes to drop significantly. Masking of the collection lens and the polychromator entrance slit are not sufficient to eliminate this interference when measurements are made very close to the surface, as required for the present experiments. Consequently, the detection system was gated with a Uniblitz mechanical shutter installed in the Raman detection system. The photomultiplier tubes are thus mechanically gated, and exposed to the surface emission for only a few msec/sec. In spite of these modifications, with the heated material surface at 2000°C, the background radiation exceeds the Raman signal on the nitrogen channel (the strongest Raman channel) by nearly an order of magnitude at a distance of 1 mm from the surface. Boundary layer profiles must extend to within 100 to 200 μm of the surface to be useful. Therefore, laser-induced fluorescence techniques were used for subsequent measurement of temperature profiles, as well as OH concentration profiles in the boundary layer. Temperatures were determined from Boltzmann plots of LIF signals corresponding to transitions from several different ground-state rotational levels. Corrections were applied to account for the dependence of collisional quenching rates on rotational level.

In preparation for the LIF measurements of temperature, a new frequency doubling system (Lumonics HyperTrak-1000) was installed that allows computer controlled scans over several OH transitions. Previously, the LIF system was set up to operate at a fixed wavelength.

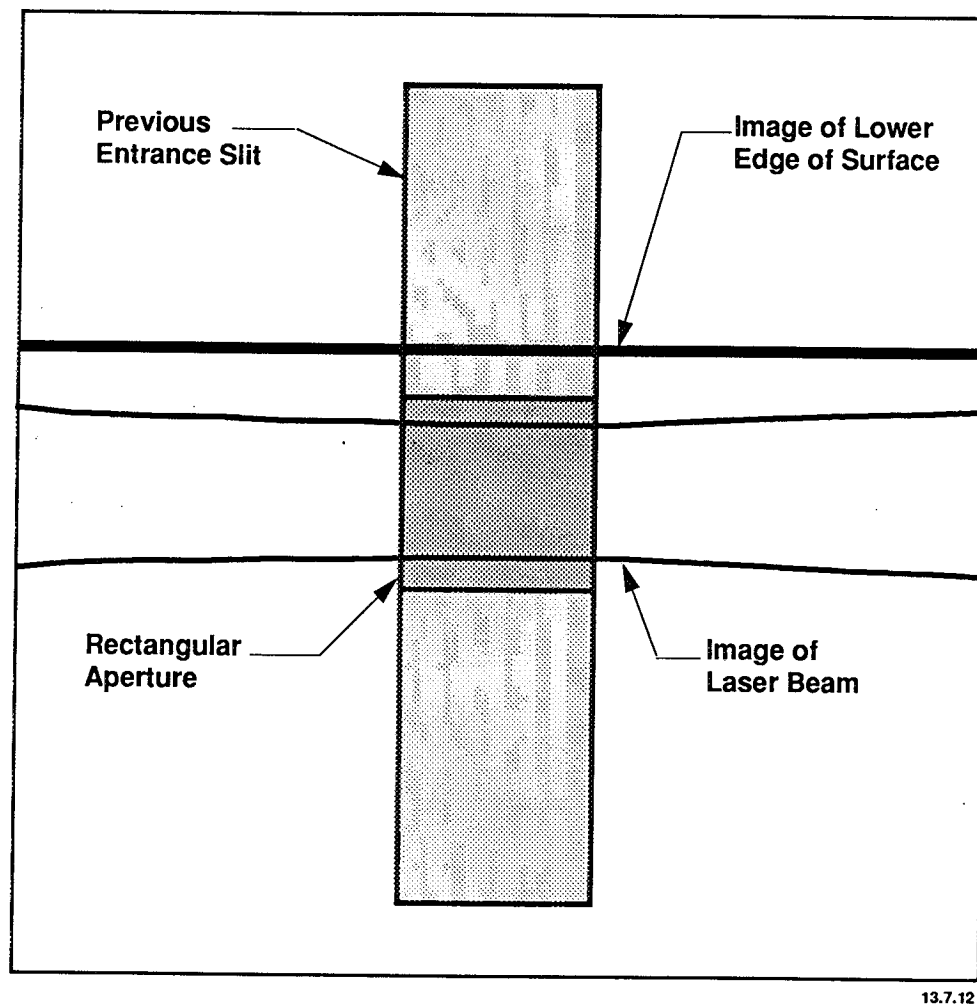


Figure 4.5.1-16. Illustration of Modification of the Polychromator Entrance Aperture.

4.5, High Temperature Materials Tests (Sandia) (cont.)

Using the modified laser diagnostics system, OH fluorescence profiles were obtained with an iridium foil sample at several surface temperatures between 1670 and 2370 K (1400°C and 2100°C). The one-atm MSTA was operated with hydrogen-air flames at mixture ratios of 6.5 and 5.5. Linear OH fluorescence measurements were made by exciting the S_{21} (8) ($v'=v''=0$) transition of OH at 303.3 nm and detecting R-branch fluorescence between 306 and 307.5 nm. The ground state population fraction for this transition varies by only a few percent over the temperature range of interest, and the change in the collisional quenching rate is small for the conditions studied here. Therefore, the fluorescence profiles are relative OH concentration profiles. Conversion of these data to absolute OH concentration profiles were carried out using calibration measurements that have been made in our standard flame.

Figure 4.5.1-17 includes five OH fluorescence profiles at MR = 6.5 for iridium surface temperatures of $T_s = 1400, 1600, 1800, 2000,$ and 2100°C . Figure 4.5.1-18 includes corresponding profiles at MR = 5.5. In both cases the measured profiles extend to a distance of 10 mm from the surface, and the burner is located 13 mm below the surface. Profiles in Figures 4.5.1-17 and -18 are characterized by relatively flat regions between 5 mm and 10 mm. The OH fluorescence signal (relative OH concentration) begins to drop significantly for distances from the surface of less than 5 mm. These overall features of the outer portion of the measured profiles are characteristics of the MSTA burner and are not associated with the boundary layer adjacent to the sample surface. (This boundary layer is approximately 1.4 mm thick, as shown by the temperature profiles discussed below.) The MSTA burner produces a matrix of high speed pre-mixed jets of fuel and oxidizer. Combustion occurs over a relatively broad reaction zone that is observed visually to extend 3-5 mm from the burner surface. Radicals (OH, H-atom, and O-atom) can be expected to be produced in super equilibrium concentrations via rapid binary shuffle reactions throughout this reaction zone, resulting in the observed broad region of high and nearly constant OH fluorescence signal. Beyond this initial reaction zone the OH concentration begins to decay toward equilibrium via the relatively slow three-body recombination reactions. This decay toward equilibrium is still in progress as the combustion gases reach the boundary layer near the sample surface, making it difficult to distinguish the boundary layer thickness from the OH profiles alone. For both mixture ratios, the measured OH fluorescence signals at locations closest to the surface increase as the surface temperature increases.

Temperature profiles were measured with an iridium sample for a mixture ratio of 6.5 and surface temperatures of 1670 K and 2370 K (1400°C and 2100°C). To determine

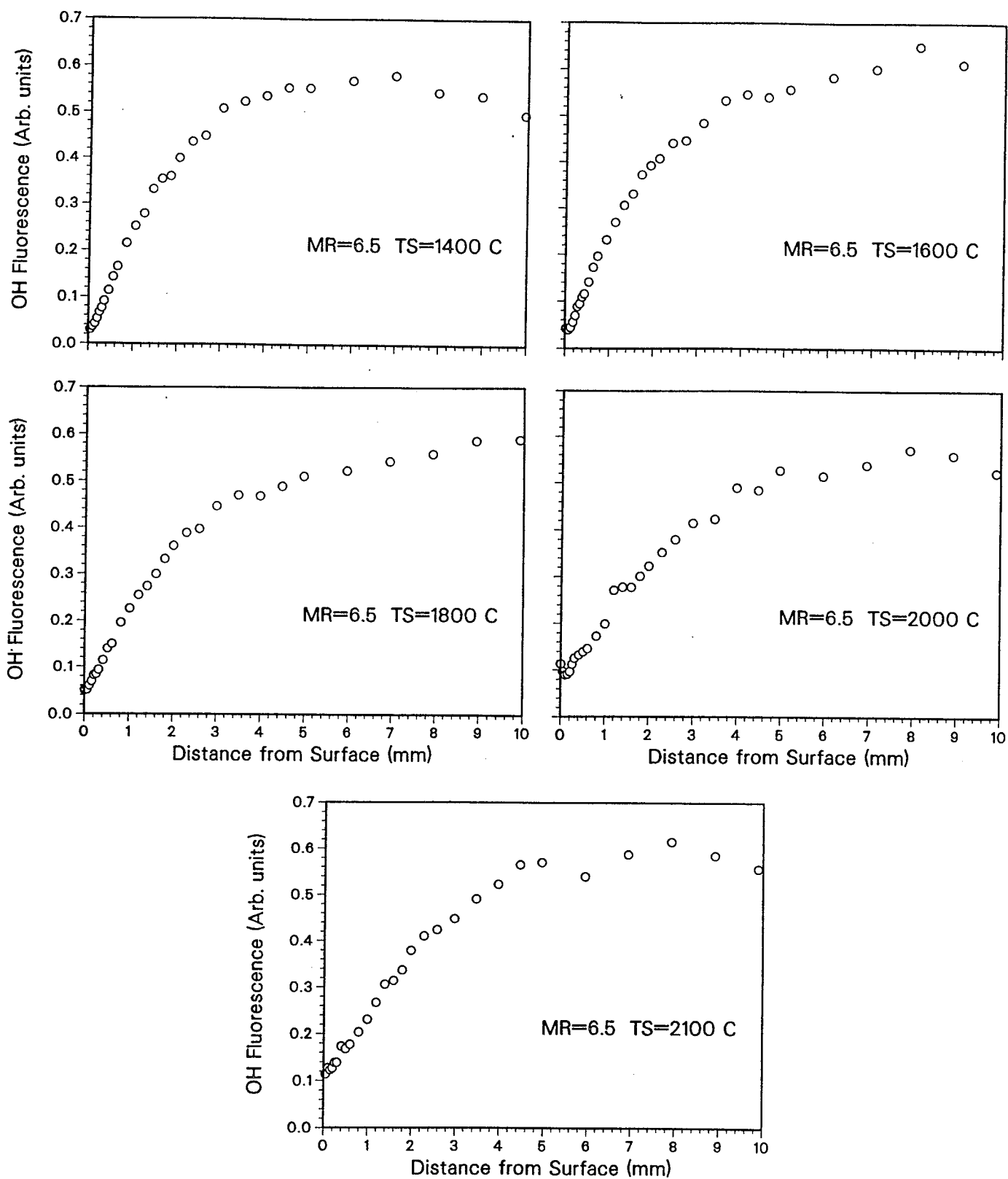


Figure 4.5.1-17. OH Fluorescence Profiles Obtained in the MSTa with an Iridium Sample at a) 1400, b) 1600, c) 1800, d) 2000 and e) 2100°C Exposed to Hydrogen-Air Combustion Products at MR = 6.5.

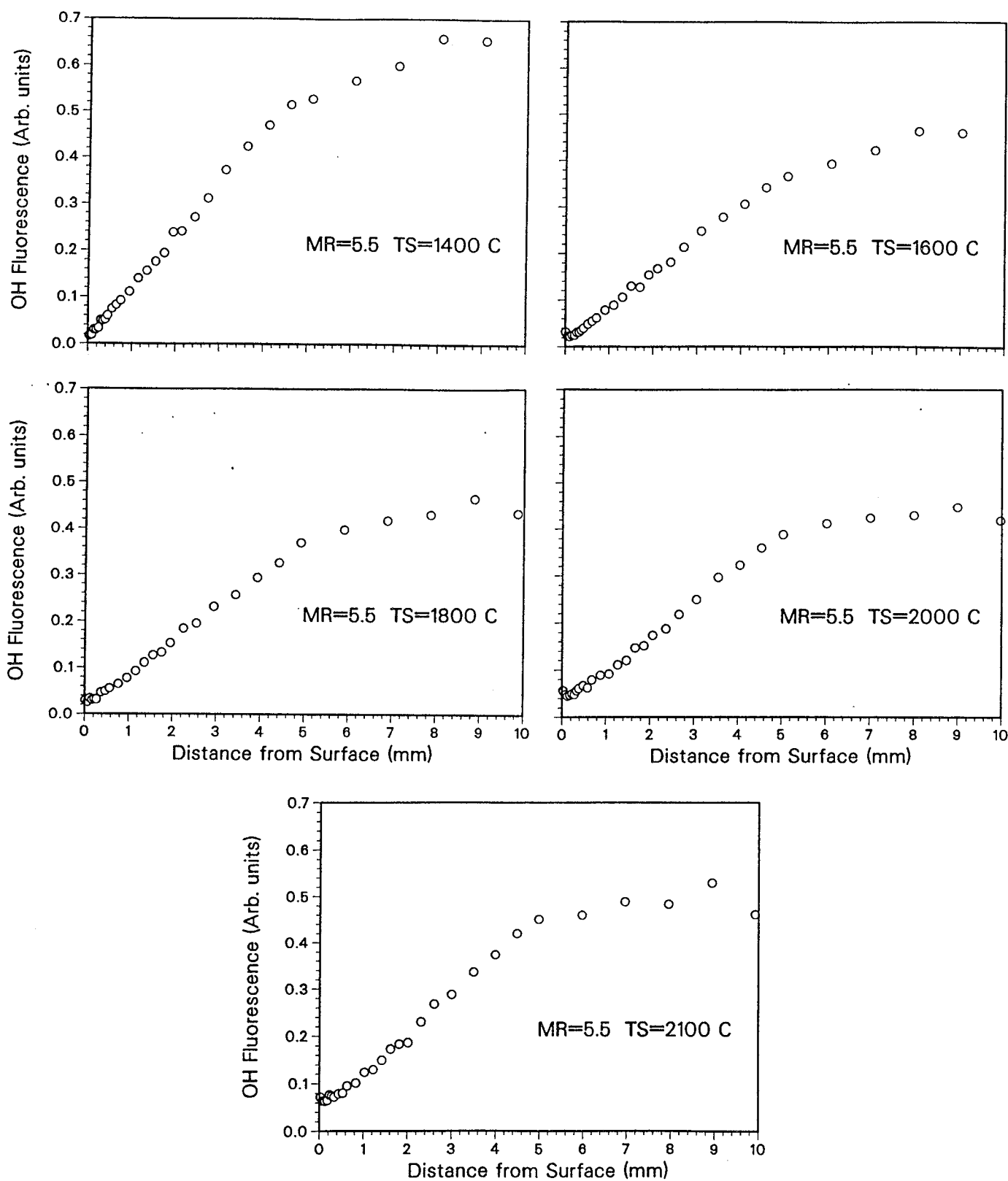


Figure 4.5.1-18. OH Fluorescence Profiles Obtained in the MSTA with an Iridium Sample at a) 1400, b) 1600, c) 1800, d) 2000 and e) 2100°C Exposed to Hydrogen-Air Combustion Products at MR = 5.5

4.5, High Temperature Materials Tests (Sandia) (cont.)

temperature, OH fluorescence was measured for three transitions corresponding to three values of the ground-state rotational quantum number, the $S_{21}(5)$, $S_{21}(8)$, and $S_{21}(11)$ transitions. As mentioned above, the fluorescence profile for $S_{21}(8)$ excitation may be treated as a relative OH concentration profile under the present experimental conditions.

Fluorescence profiles for each of the three transitions are shown in Figures 4.5.1-19 and -20 for surface temperatures of 1670 K and 2370 K, respectively. Figures 4.5.1-21 and -22 show the resulting temperature profiles, with the open symbols corresponding to temperatures derived from each pair of fluorescence measurements, and the solid circles corresponding to the average of the three values at each location. The outer portion of the profiles shows a gradual increase in temperature as the laser probe volume moves away from the burner (toward the iridium surface). This corresponds to energy release in the initial hydrogen-air reaction zone followed by additional energy release due to the slower radical recombination process. At locations close to the surface, the uncertainty in measured temperature can be large because the OH fluorescence signals themselves become small close to the surface, and the signal-to-noise ratio decreases. Nevertheless, the presence of a thermal boundary layer is readily apparent ($T_s = 1670$ K). The thermal boundary layer is less apparent in Figure 4.5.1-22 ($T_s = 2370$ K) because the surface temperature is comparable to the equilibrium temperature that the gas is approaching. This is a particularly interesting case because an inert surface at this temperature would allow the OH concentration to continue its approach toward equilibrium.

The thickness of the thermal boundary layer can be determined more easily from Figure 4.5.1-23, which includes only the average temperatures for two conditions in Figures 4.5.1-21 and -22. As a visual aid, a smooth curve has been drawn to represent the expected behavior of the gas phase temperature in the absence of a solid surface. From Figure 4.5.1-23 the thermal boundary layer is estimated to be approximately 1.4 mm thick.

Results for H_2 /Air Cases

Figure 4.5.1-24 shows boundary-layer profiles of OH concentration and temperature for a mixture ratio of 6.5 with an iridium foil at temperatures of 1670, 1970, 2270, and 2370K (3010, 3545, 4090, and 4270 R). In each case the outer portion of the temperature profile shows a gradual increase as the laser probe volume moves away from the burner and toward the specimen. This temperature increase occurs outside the boundary layer and can be explained as follows. When the MSTA is operated with hydrogen and air, the primary reaction

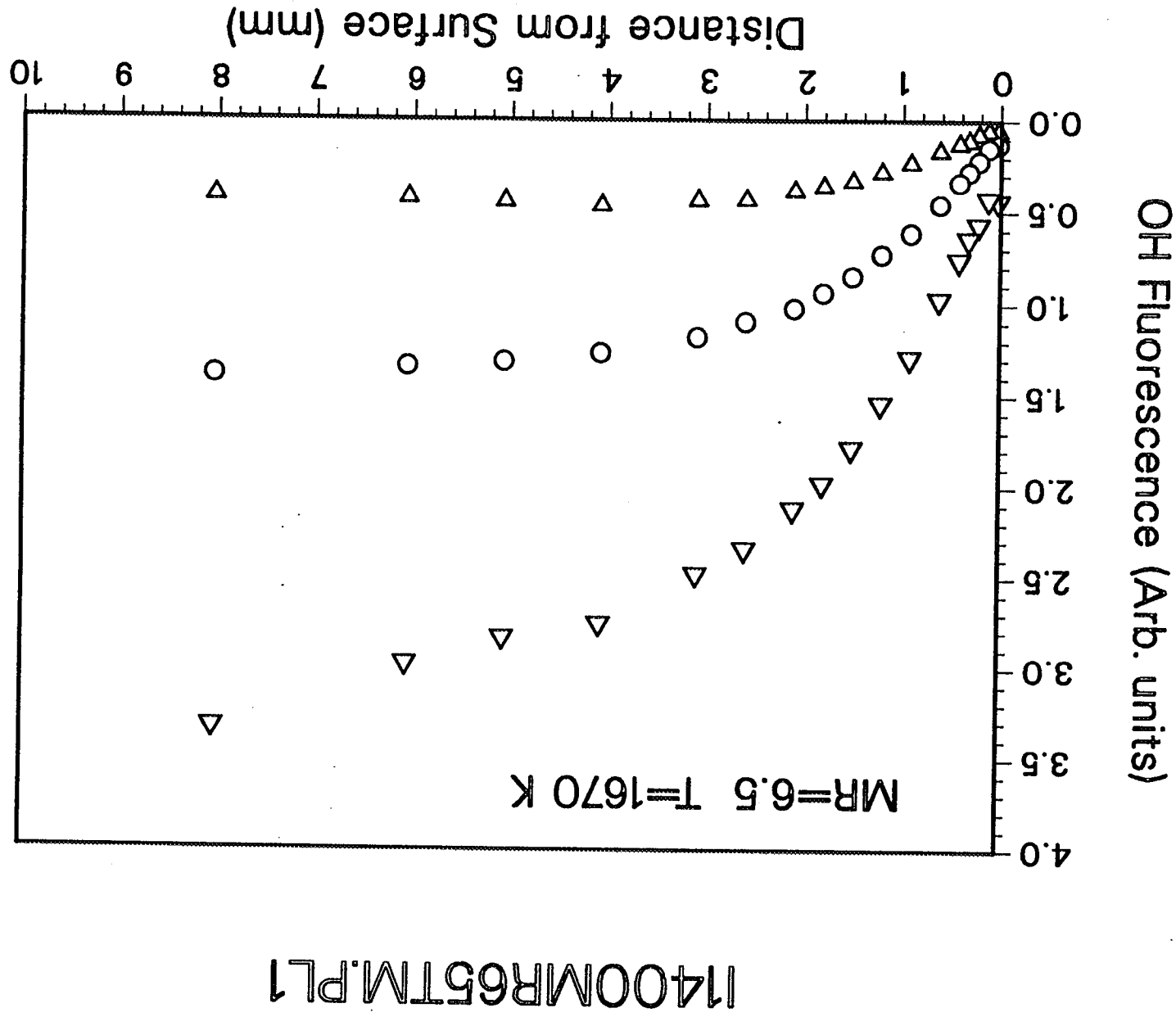
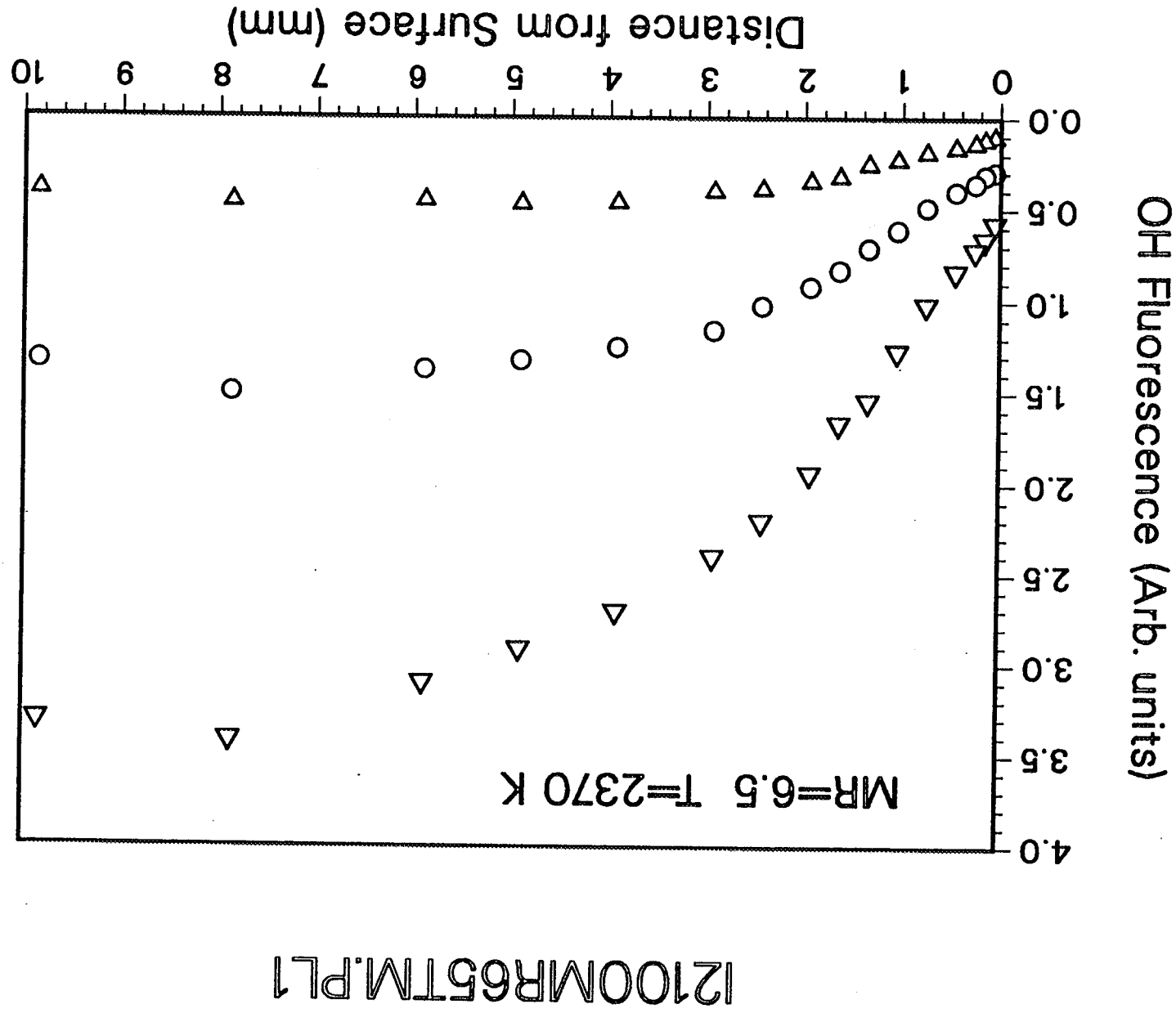


Figure 4.5.1-19. OH Fluorescence Profiles with the Iridium Sample at 1670 K for Three Laser-Excited Transitions: $\Delta-S^{21}$ (5), $O-S^{21}$ (8), $\nabla-S^{21}$ (11).



I1400MR65TM.PL1

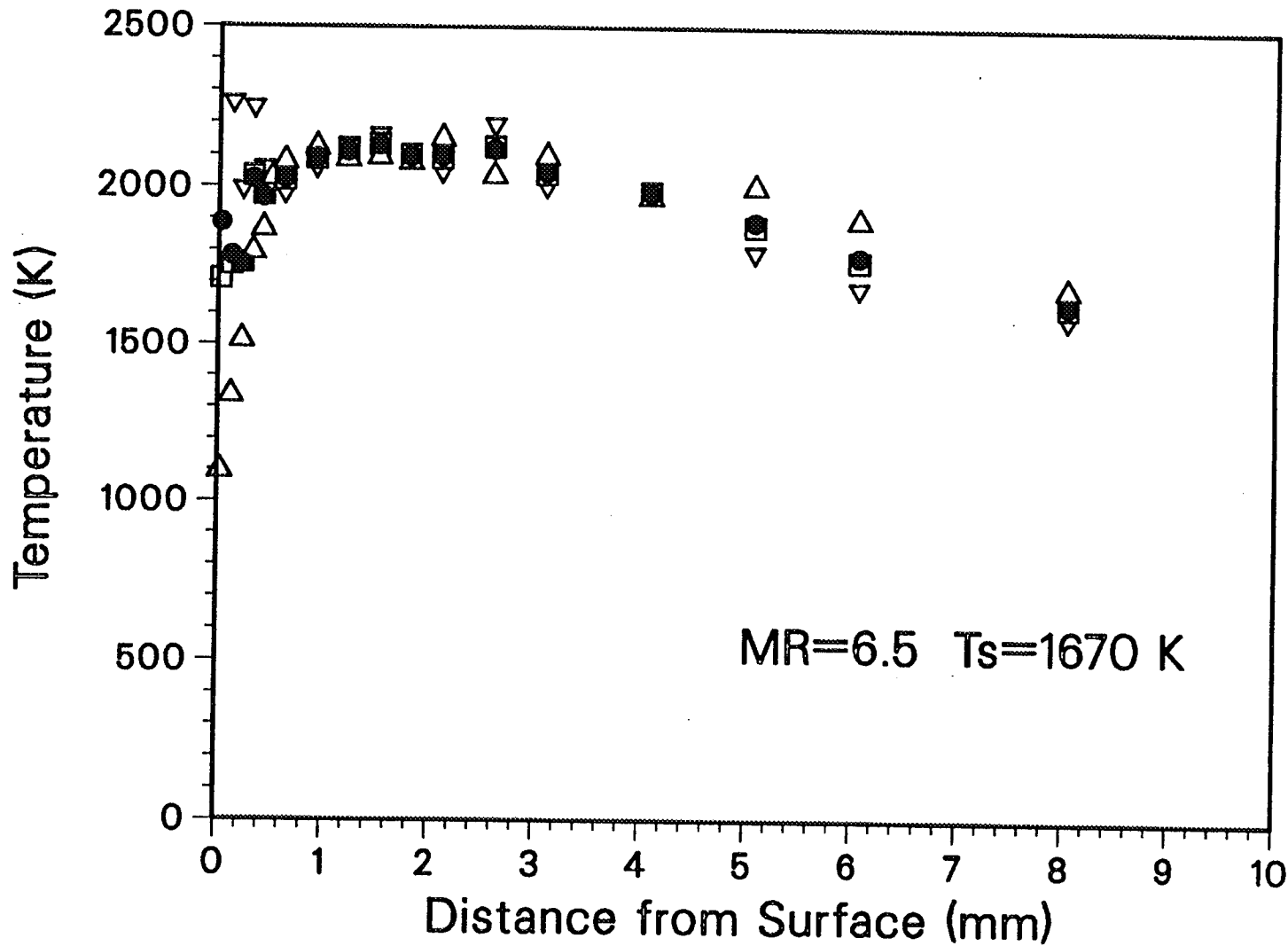


Figure 4.5.1-21. Temperature Profiles Based on the OH Fluorescence Measurements (MR = 6.5, Iridium Sample at 1670K). Open Symbols Correspond to Temperatures Determined from Eq. (2) for Pairs of Transitions: Δ , S21 (5)-S21 (8); \circ S21 (5)-S21 (11); ∇ , S21(8)-S21 (11). The Solid Circles are Averages of the Three Values.

I2100MR65TM.PL1

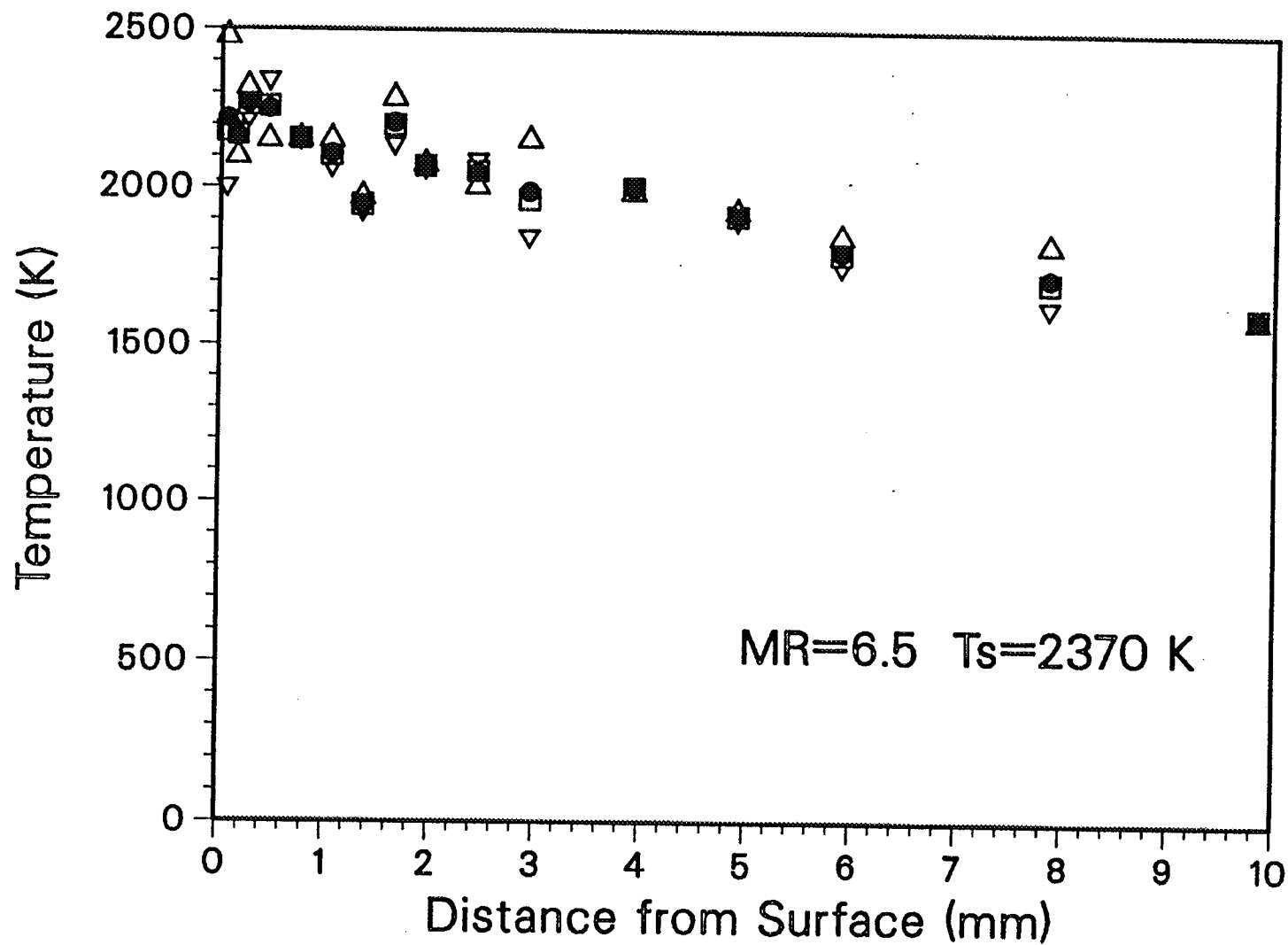


Figure 4.5.1-22. Temperature Profiles Based on the OH Fluorescence Measurements (MR =6,5, Iridium Sample at 2370K). Open Symbols Correspond to Temperatures Determined from Eq. (2) for Pairs of Transitions: Δ , S21 (5)-S21 (8); \circ , S21 (5)-S21 (11); ∇ , S21 (8)-S21 (11). The solid Circles are Averages of the Three Values at Each Location.

I1400MR65TM.PL1

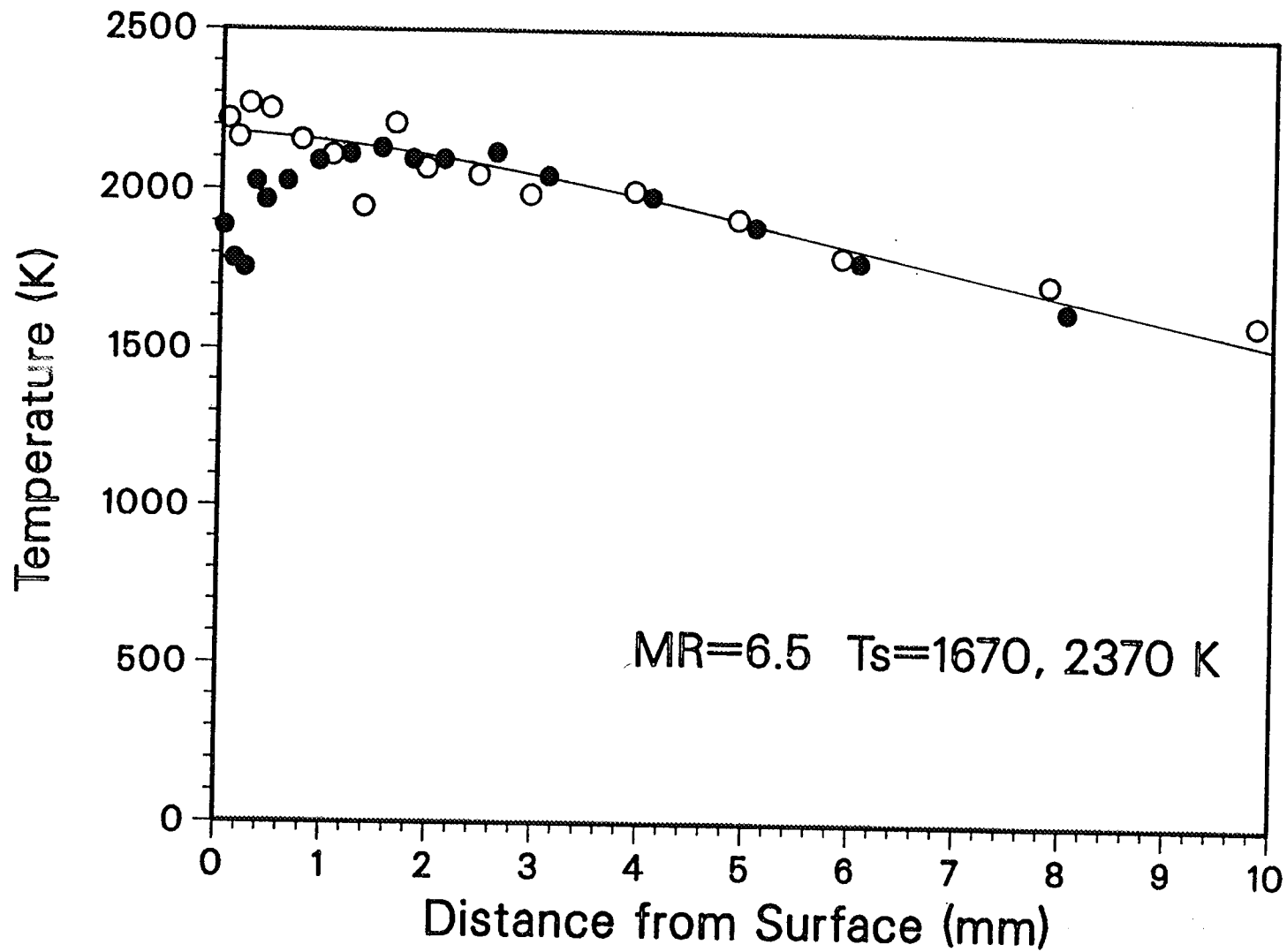


Figure 4.5.1-23. Average Temperature Profiles for the Iridium Sample at 1670 K (Closed Symbols) and 2370 K (Open Symbols). The Curve is Provided as a Visual Aid to Represent the Undisturbed Gas Temperature.

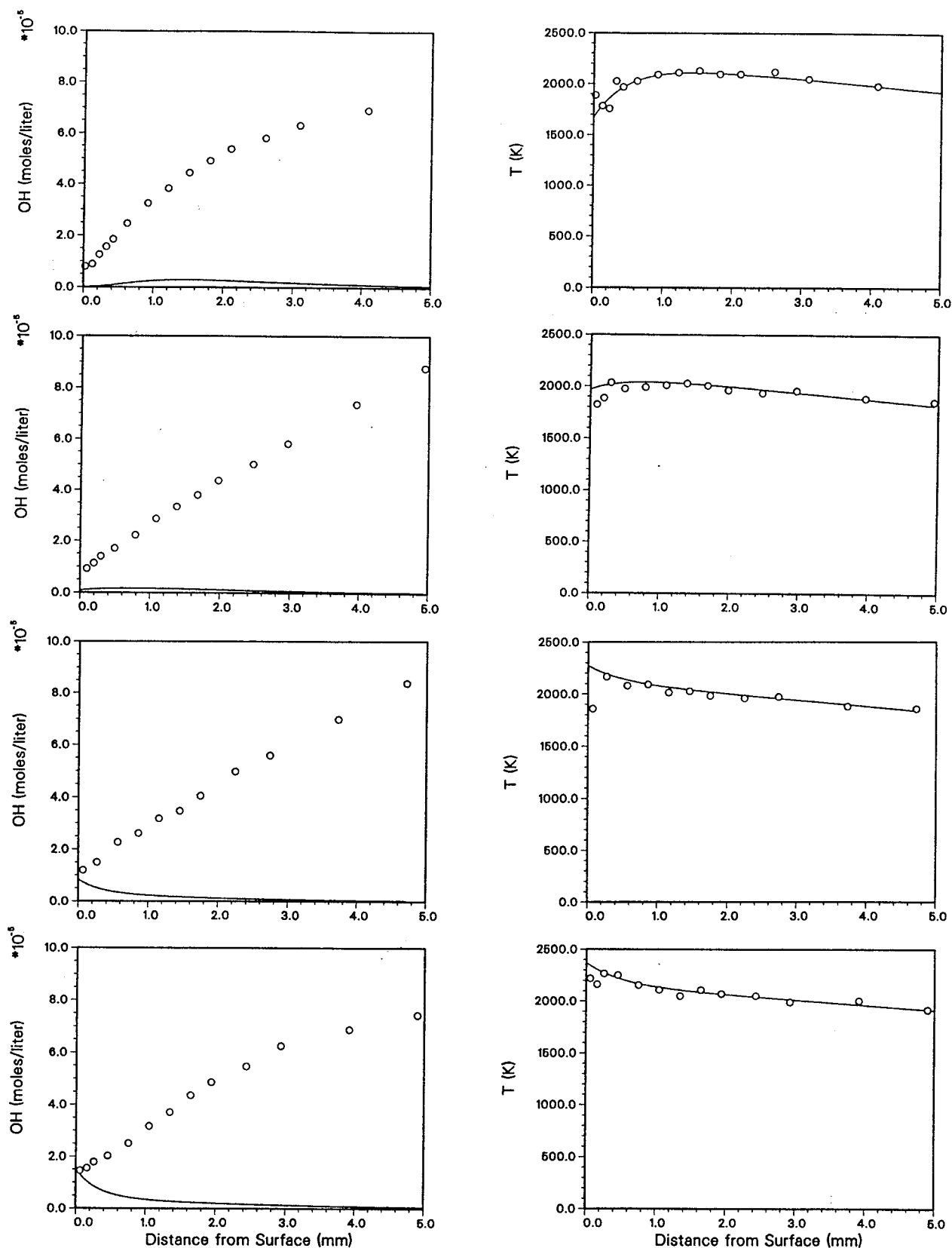


Figure 4.5.1-24. Profiles of OH Concentration and Temperature for MR=6.5 Air/H₂ Combustion Products with Iridium Specimen Surface Temperatures of 1670, 1970, 2270 and 2370K. Measurements are Shown by the Open Symbols. The Curves in the OH Plots Show Equilibrium Concentration Profiles Based upon Fits to the Temperature Profiles.

4.5, High Temperature Materials Tests (Sandia) (cont.)

zone is observed to extend 3-5 mm from the burner, which is 13 mm below the specimen. The concentrations of radicals (OH, H-atom, and O-atom) reach their maxima in this primary reaction zone. These radicals recombine to form H_2O via relatively slow three-body reactions, and the temperature continues to increase as the radical concentrations decay toward equilibrium. The profiles of OH concentration show a corresponding decrease with increasing distance from the burner. The thickness of the boundary layer near the sample surface can be determined from the temperature profile for the case with $T_s = 1670\text{K}$, which shows a distinct deviation from the temperature trend beginning approximately 1.4 mm from the surface. The boundary layer is less apparent in the OH profiles, which decrease monotonically in all cases due to the radical recombination process.

At locations close to the surface the OH fluorescence signals become small, and the signal-to-noise ratio decreases, causing the uncertainty in measured temperature to increase. Consequently, we have calculated the correction factors C_Q and C_f in Eq. (1) using the results represented by the solid curve in each temperature plot. Each curve combines a linear fit to the data outside the boundary layer with an exponential term that brings the profile to the measured surface temperature at $x = 0$. Recall that surface temperature is measured using a two-color pyrometer.

Based upon these fitted temperature profiles, *equilibrium* OH concentration profiles were calculated and are shown as solid lines in the concentration plots of Figure 4.5.1-24. With the exception of the near-wall points in the cases with iridium surface temperatures of 2270 and 2370K, the measured OH concentrations are significantly above equilibrium. The super equilibrium OH concentrations within the boundary layer result from the fact that the convective time between the primary reaction zone and the outer edge of the boundary layer is not sufficiently long to allow the radical concentrations to reach full equilibrium. It is reasonable to assume that the rapid binary reactions are in partial equilibrium everywhere for the present experimental conditions because the characteristic chemical kinetic time scale for these reactions is of order $20\ \mu\text{s}$, which is small compared to the convective flow times in the MSTA. (A possible exception occurs for the near-surface locations in the profile with $T_s = 1670\text{K}$, because the binary reaction rates are strongly temperature dependent.) Therefore, the super equilibrium OH concentrations of H-atoms and O-atoms are also significantly above equilibrium.

4.5, High Temperature Materials Tests (Sandia) (cont.)

Profiles of OH concentration and temperature for the air/H₂, MR = 5.5 cases with iridium surface temperatures of 1670, 1970, and 2270K are shown in Figure 4.5.1-25. Due to the richer condition of the flame, the measured OH concentrations are lower than for the corresponding MR = 6.5 cases. However, measured OH concentrations are again significantly above equilibrium, with the exception of the near-surface data for the highest surface temperature case, T_S = 2270K.

For both MR = 6.5 and MR = 5.5 the measured OH concentrations at locations closest to the surface increase as the surface temperature increases. However, the relative increase is much less than that for the equilibrium OH concentrations based upon the measured surface temperatures. Figure 4.5.1-26 shows the temperature dependence of the equilibrium OH concentration for air/H₂ (MR = 6.5 and 5.5) at atmospheric pressure. For MR = 6.5 the equilibrium concentration increases by a factor of nine between 1970 and 2270K, while the measured concentration at the points closest to the surface increases by less than 50 percent. This result suggests that the radical recombination process dominates the characteristics of the OH concentration profile and that the influence of surface chemistry is secondary.

Experiments were also carried out with platinum foil samples in the MSTA. When the 1-mil platinum foil was firmly clamped, it buckled immediately upon exposure to the flame due to thermal expansion. Consequently, profiles were obtained with the specimen loosely held around the boron nitride mandrel, and the electrical heating system was not used. Figure 4.5.1-27 includes profiles of OH concentration and temperature for air/H₂ combustion at MR = 6.5 and MR = 5.5 with the platinum surface at the radiative equilibrium temperature of 1670K (3010 R). These profiles are similar to those obtained with the iridium samples. This result indicates either that there is not a significant difference in surface reactivity for these two metals under the present experimental conditions or that, as suggested above, the OH concentration profile is determined primarily by the radical recombination process.

Results for H₂/O₂ Cases

Boundary-layer measurements were obtained for an iridium foil sample exposed of H₂/O₂ combustion products at mixture ratios of 6.5 and 5.5. In the absence of N₂, the rotational energy transfer rate for OH in the combustion product stream decreases significantly. Consequently, saturation effects in the fluorescence measurements become important at lower laser energies in the H₂/O₂ flames than in the H₂/air flames. (The fluorescence signal is no

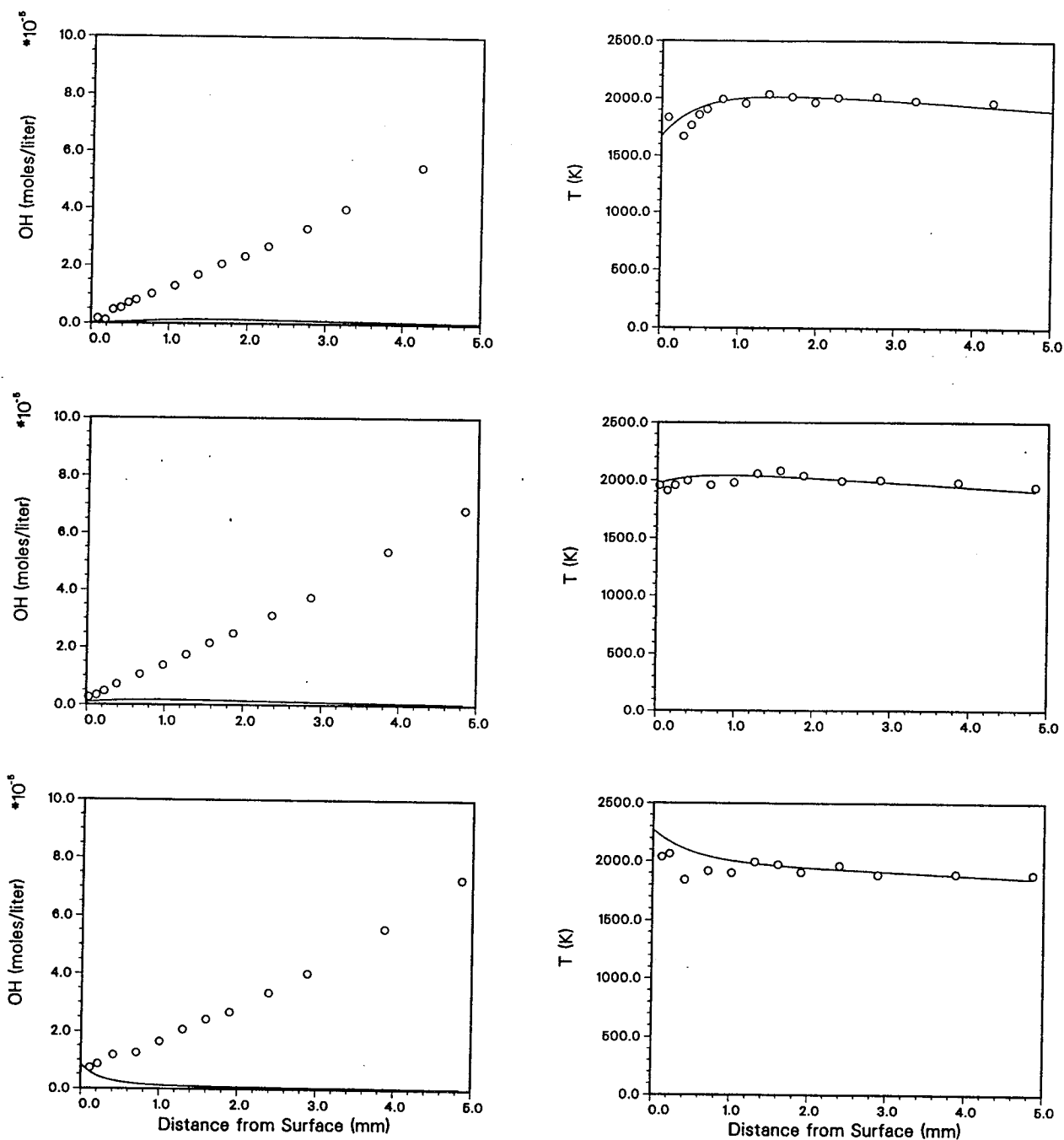


Figure 4.5.1-25. Profiles of OH Concentration and Temperature for MR=5.5 Air/H₂ Combustion Products with Iridium Specimen Surface Temperatures of 1670, 1970 and 2270K. Measurements are shown by the Open Symbols. The Curves in the OH Plots Show Equilibrium Concentration Profiles Based on Fits to the Temperature Profiles.

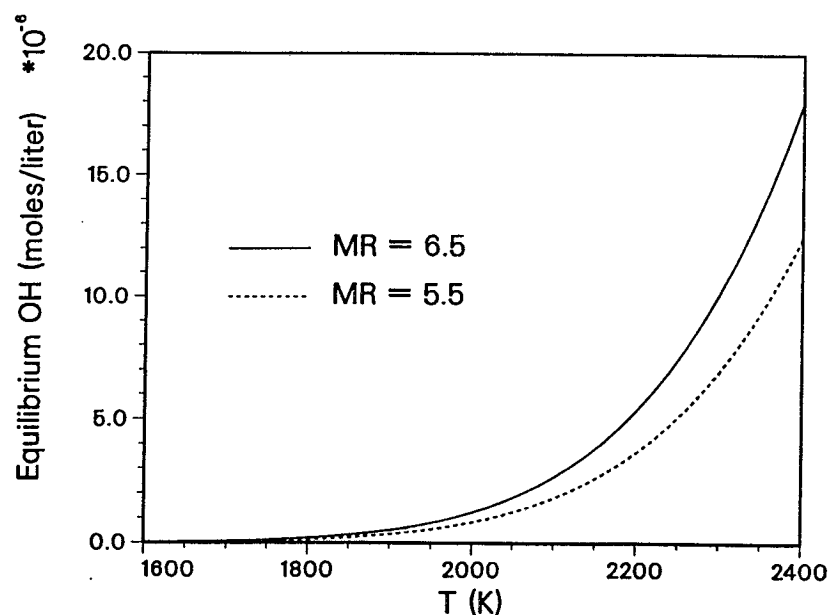


Figure 4.5.1-26. Equilibrium OH Concentration as a Function of Temperature for MR=6.5 and MR= 5.5 Air/H₂ Combustion Products.

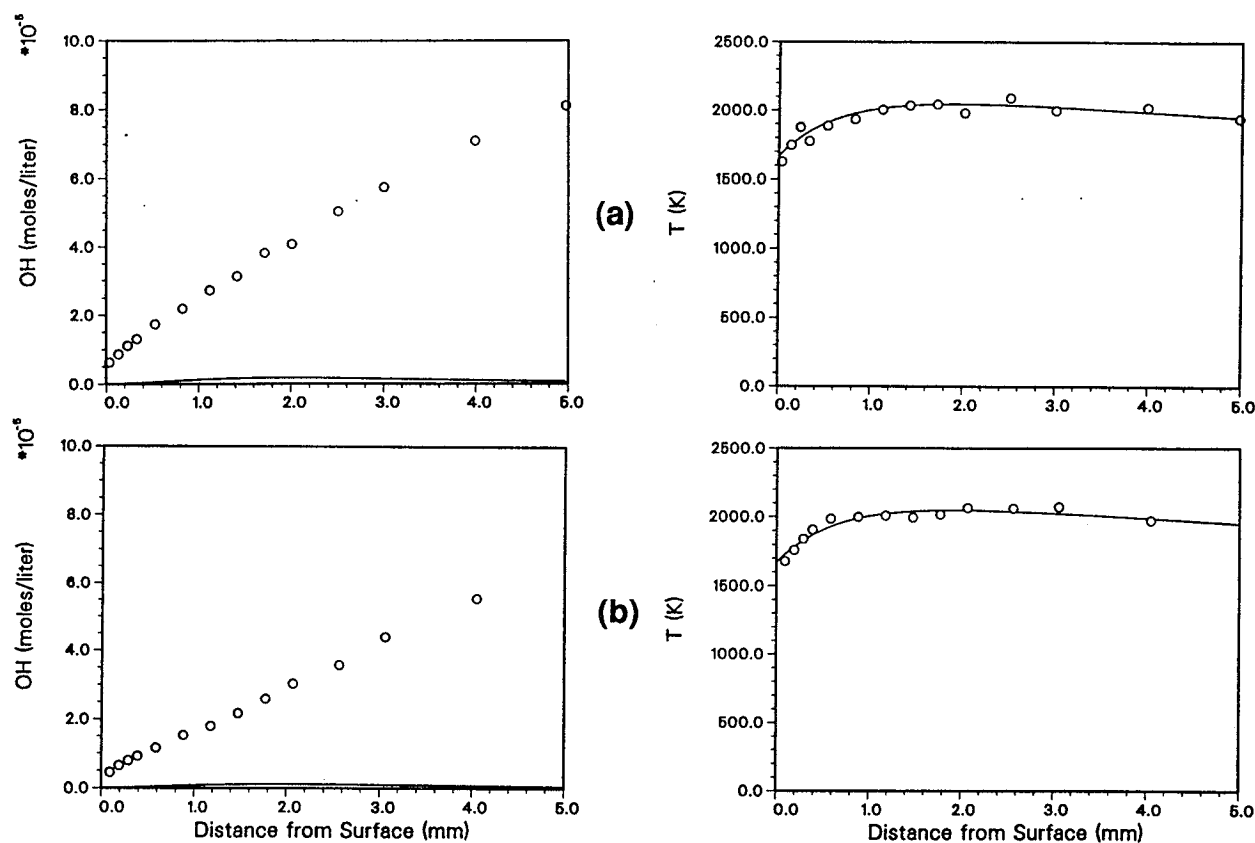


Figure 4.5.1-27. Profiles of OH Concentration and Temperature for a) MR=6.5 and b) MR=5.5 Air/H₂ Combustion Products with a Platinum Specimen Surface Temperature of 1670K. Measurements are Shown by the Open Symbols. The Curves in the OH Plots Show Equilibrium Concentration Profiles Based upon Fits to the Temperature Profiles.

4.5, High Temperature Materials Tests (Sandia) (cont.)

longer linearly related to the laser energy in the probe volume unless a very low laser intensity is used.) Due to this complication, calibration measurements in our standard H_2/air reference flame cannot be used to convert the fluorescence profiles in the H_2/O_2 cases to OH concentration profiles. It may be possible to use the fluorescence trapping profiles measured in the flames to determine OH concentration. However, in this report we include only the relative fluorescence profiles and temperature profiles. We note that this saturation effect in the H_2/O_2 flames has only a small effect upon the temperature obtained from the fluorescence measurements.

Figures 4.5.1-28 and -29 show results for the $\text{MR} = 6.5$ case with an iridium specimen at the radiative equilibrium temperature of 1990K. Figure 4.5.1-28 shows the boundary layer profiles of OH fluorescence for the three transitions used in the temperature measurements. The corresponding temperature profile is shown in Figure 4.5.1-29. In contrast to the results for the H_2/air cases, this temperature profile shows a gradual decrease between 8 mm and 3 mm, as the laser probe volume moves away from the burner and toward the sample surface. This decrease most likely results from energy loss due to radiation from the high-temperature ($\sim 3000\text{K}$) combustion products being greater than the energy gain from radical recombination. The edge of the thermal boundary layer is not well resolved. However, the OH fluorescence profiles display a significant change in slope just inside the 1 mm location that is clearly a boundary-layer effect.

Results for the iridium foil with $\text{MR} = 5.5$ are shown in Figures 4.5.1-30 and -31. The temperature profile is similar to that for $\text{MR} = 6.5$, and the fluorescence levels are lower, as would be expected for the lower mixture ratio. An unexpected result is that the surface temperature measured by the two-color pyrometer is significantly higher for the $\text{MR} = 5.5$ case (2100 vs 1990K for $\text{MR} = 6.5$).

4.5.2 Surface Measurements

A wide range of advanced diagnostics was used to obtain data to aid in modeling the processes involved in the interaction of high temperature chamber materials and the rocket engine environment. These techniques have been developed and used by Sandia extensively to characterize materials and combustion products and their interactions.

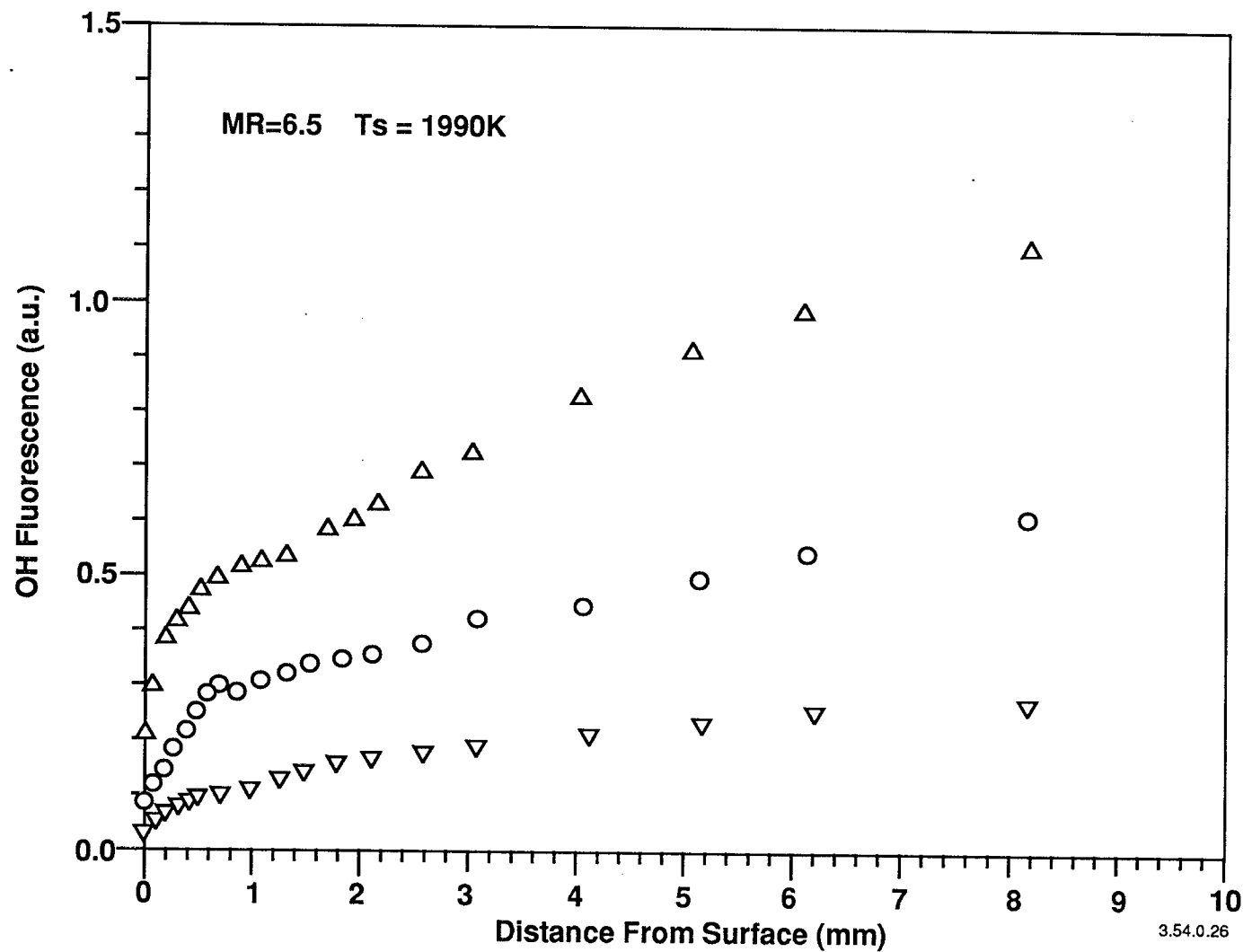


Figure 4.5.1-28. Profiles of the Fluorescence Signal for Three Transitions S21 (5), S21 (8) and S21 (11) for the Case with Iridium Sample and O_2/H_2 Combustion Products at $MR = 6.5$

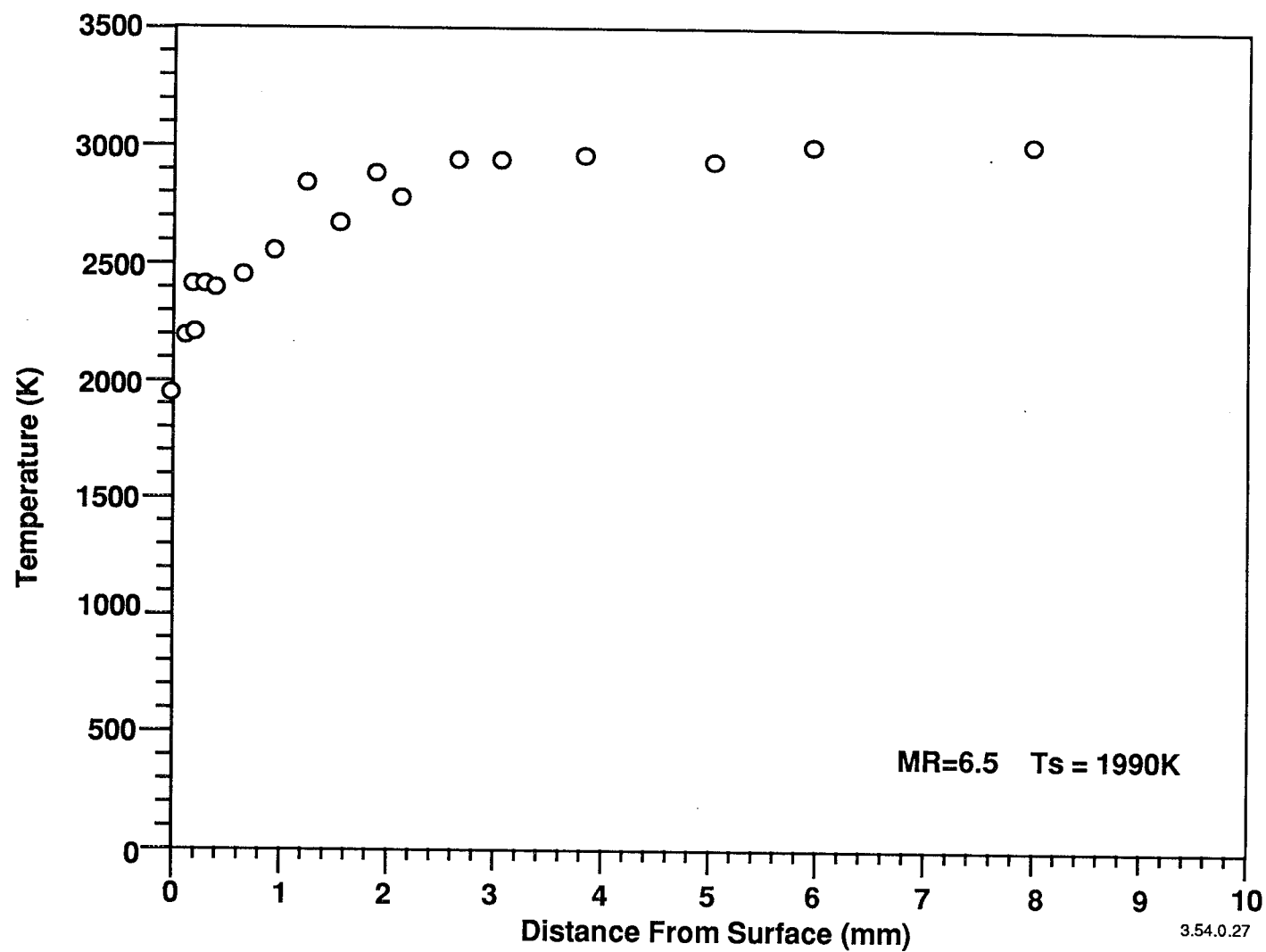


Figure 4.5.1-29. Profile of Temperature Determined from the OH Fluorescence Measurements Shown in Figure 4.5.1-25 for the Case with an Iridium Sample and O_2/H_2 Combustion Products at $\text{MR} = 6.5$

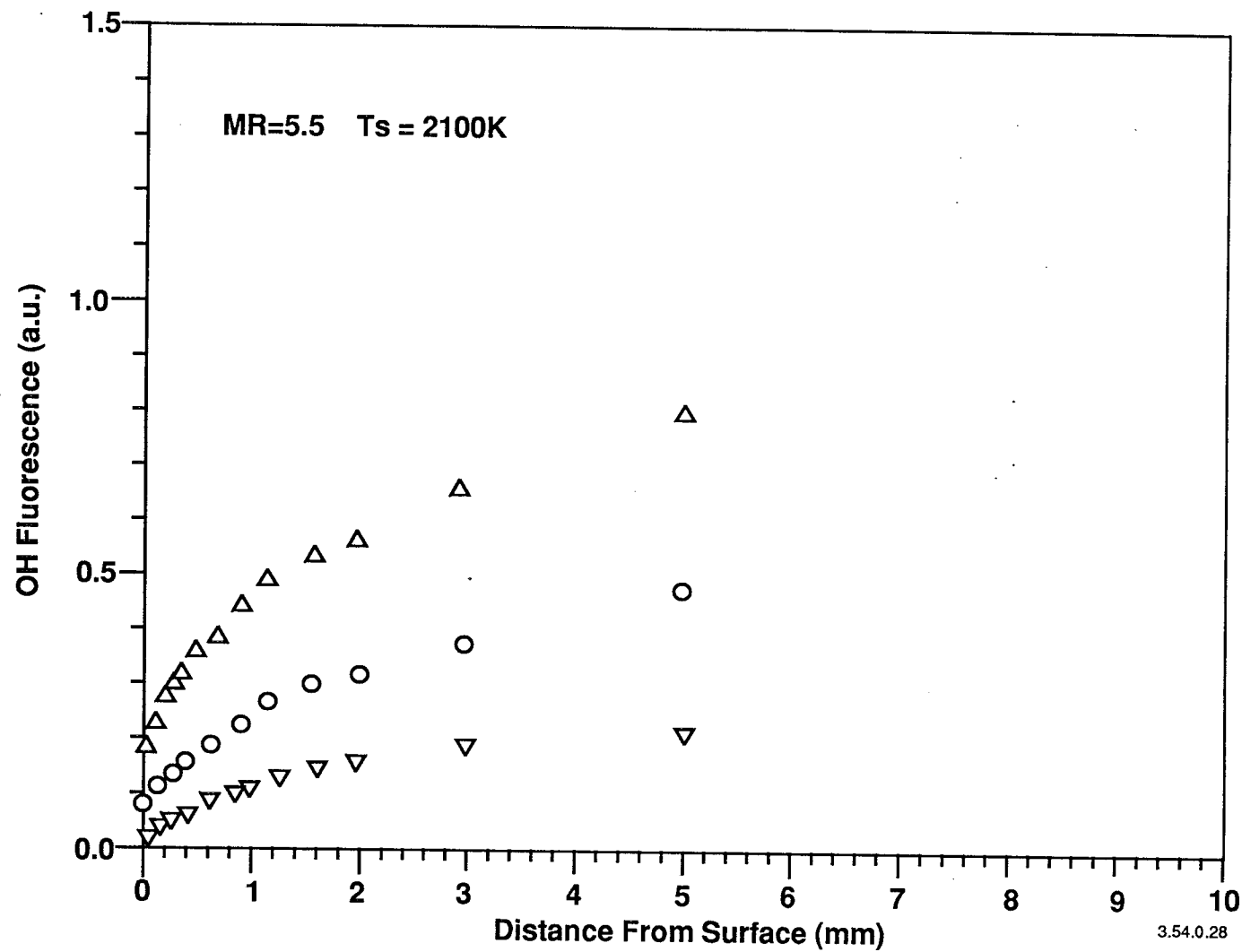


Figure 4.5.1-30. Profiles of the Fluorescence Signal for Three Transitions $S_{21}(5)$, $S_{21}(8)$ and $S_{21}(11)$ for the Case with an Iridium Sample and O_2/H_2 Combustion Products at $MR=5.5$

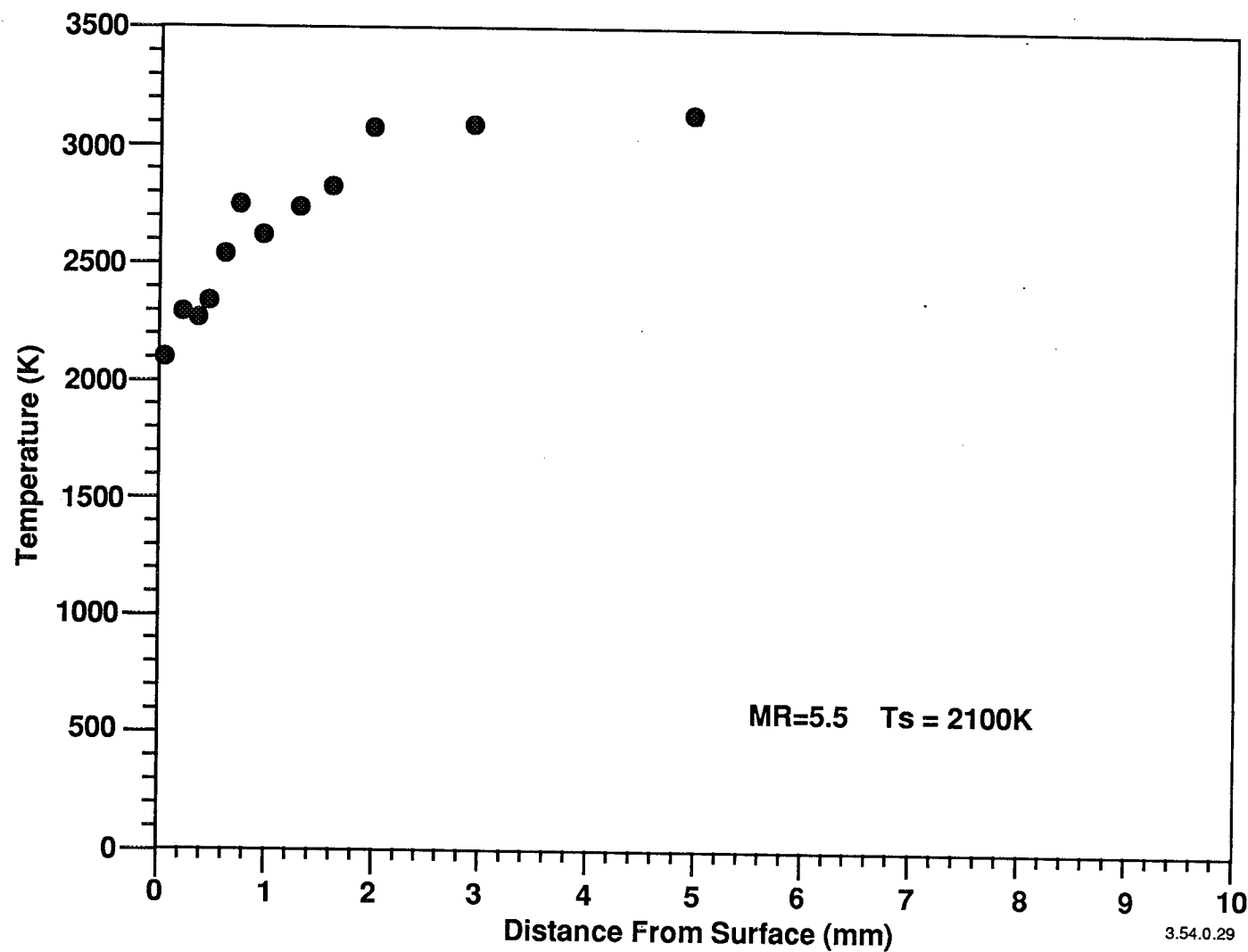


Figure 4.5.1-31. Profile of Temperature Determined from the OH Fluorescence Measurements Shown in Figure 4.5.1-27 for the Case with an Iridium Sample and O_2/H_2 Combustion Products at $\text{MR}=5.5$

4.5, High Temperature Materials Tests (Sandia) (cont.)

The range of the experimental program conducted during this portion of the contract is shown in Table 4.5.2-1. This table shows the specimen material, the type of diagnostic technique used, and the experimental conditions in terms of temperature, exposure time, and atmosphere.

The experimental conditions and results are described in the following section, along with the development of models to aid in interpreting and extending the results. The specific measurements listed in the table are keyed to the figures or table where the results are shown.

Techniques investigated at Sandia for specimen surface monitoring included Raman surface scattering and Second Harmonics Generation (SHG). The Raman analysis is a linear effect which can identify oxide phases on iridium and rhenium surfaces under high temperature, hostile conditions. The technique is simple, rapid, and non-perturbing. The setup for demonstration of the Raman analysis capability is shown schematically in Figure 4.5.2-1. The experimental setup consists of a high temperature furnace for controlling specimen temperature, an argon ion laser for probing the surface, and optics to image scattered light from the surface on to a detection system consisting of a spectrograph coupled to a diode array.

The SHG system utilizes nonlinear, second-order optical effects, and can detect oxide layers less than one atom deep on high temperature surfaces. The technique has fast time response and can monitor kinetic processes, such as diffusion through a barrier layer. Figure 4.5.2-2 is a schematic showing the major components of the system. In this case the surface is illuminated with the output of a turnable dye laser driven by a neo-dynium-YAG laser. For checkout purposes, the specimen is mounted in a vacuum chamber. This permits calibration of the SHG system with conventional Auger spectroscopy which requires high vacuum operation.

This task consisted of the demonstration of advanced laser and surface diagnostics for the characterization of relevant material surfaces before, during, and after high temperature exposure. While Sandia has had extensive experience using surface Raman to examine a wide variety of materials, spectra have not been reported previously for the materials of interest. The demonstration of diagnostic technique required first obtaining phase pure samples of the oxides of platinum, rhenium, and iridium for the purpose of developing a data base of standard spectra for later comparison with high temperature experiments.

ASRC628

Table 4.5.2-1. Sandia Materials Test - Summary of Experiments

9-29-93

SUMMARY OF EXPERIMENTS

<u>SPECIMEN</u>	<u>TECHNIQUE</u>	<u>TEMP</u> oC	<u>EXPOSURE</u> <u>TIME</u>	<u>ATMOS-</u> <u>PHERE</u>	<u>REFER TO</u> <u>FIGURE</u>
					<u>4.5.2-</u>
IrO2 POWDER	RAMAN	AMBIENT	--	--	-3
ReO3	RAMAN	AMBIENT	--	--	-3
PtO2	RAMAN	AMBIENT	--	--	-3
Ir FOIL	RAMAN	1000	15 MIN	O2	-5
Ir FOIL	SEM	1250	1 HR	O2	-6
Ir FOIL	SPUTTER AUGER	POST-EXPOSURE			-7
Ir	AUGER SPECTRA				-10
Ir+O2	AUGER SPECTRA	1250			-11
Ir+Re	SPUTTER AUGER	PRE-EXPOSURE			-12
Ir+Re	SPUTTER AUGER	1600	45 MIN	VACUUM	-13
Ir+Re	SEM	POST-EXPOSURE			-14
IrO2	RAMAN	WINDOW DEPOSIT			-15
Ir+O2	SPUTTER AUGER	1000	15 MIN	O2/1 ATM	-16
Pt	RAMAN	1250	1 HR	O2/1ATM	-17
Ir FOIL	RAMAN	1250	1 HR	O2/1ATM	-18
Ir FOIL	RAMAN	650	2 HR	O2/1 ATM	-19
Ir FOIL	RAMAN	650	2 HR	O2/1 ATM	-20
Ir FOIL	SPUTTER AUGER	650	2 HR	O2/1 ATM	-21
Ir FOIL	XRD	1250	1 HR	O2/1ATM	-22
Ir+Re FOIL	XRD	1400	45 MIN	VACUUM	-23
Re+Ir	SPUTTER AUGER	1200	45 MIN	VACUUM	-24
Ir+Re PELLET	XRD	1500		VACUUM	-25
Ir FILM ON Re	XRD	1500		VACUUM	-25
Ir FILM ON Re	XRD	AS-DEPOSITED			-25

Table 4.5.2-1 (cont.)

<u>SPECIMEN</u>	<u>TECHNIQUE</u>	<u>TEMP</u> oC	<u>EXPOSURE</u> <u>TIME</u>	<u>ATMOS-</u> <u>PHERE</u>	<u>REFER TO</u> <u>FIGURE</u> <u>4.5.2-</u>
Ir-Re END RING	FRACTURE AUGER	AMBIENT	--	VACUUM	-29
Ir-Re END RING	ELECTRON MICROPROBE	AMBIENT	90 MIN	VACUUM	-30
Ir-Re END RING	SEM	AMBIENT			-31
Ir-Re END RING	SEM				-32
Ir-Re END RING	ELECTRON MICROPROBE				-33
Ir-Re END RING	SEM				-34
Ir-Re END RING	SEM	1400	14 HRS	VACUUM	-35
Ir-Re END RING	ELECTRON MICROPROBE				-36
Ir-Re END RING	ELECTRON MICROPROBE				-37
Ir-Re END RING	ELECTRON MICROPROBE				-38
Ir-Re END RING	ELECTRON MICROPROBE				-39
Ir-Re END RING	SEM	1700	8 HRS	VACUUM	-40
Ir-Re END RING	ELECTRON MICROPROBE				-41
Ir-Re END RING	ELECTRON MICROPROBE				-42
Ir-Re END RING	ELECTRON MICROPROBE				-43
Ir-Re END RING	ELECTRON MICROPROBE	1900	8 HRS	VACUUM	-45
Ir-Re END RING	ELECTRON MICROPROBE	1700	8 HR	VACUUM	-46
Ir-Re END RING	ELECTRON MICROPROBE	1400	14 HR	VACUUM	-47
CVD Ir/Re	AUGER SPECTRA	1900	9 HR	VACUUM	-49
CVD Ir/Re	SPUTTER AUGER	1730	50 HR	VACUUM	-57
CVD Ir/Re	SPUTTER AUGER	2100	15 HR	VACUUM	-58
CVD Ir/Re-1-2-1	MSTA EXPOSURE	1400	8 HR	H2/O2 COMB.	T-4.5.2-2
CVD Ir/Re-1-2-1	MSTA EXPOSURE	1800	4 HR	H2/O2 COMB.	T-4.5.2-2
CVD Ir/Re-1-2-1	MSTA EXPOSURE	1800	4 HR	H2/O2 COMB.	T-4.5.2-2
CVD Ir/Re-1-2-1	MSTA EXPOSURE	1900	3 HR	H2/O2 COMB.	T-4.5.2-2

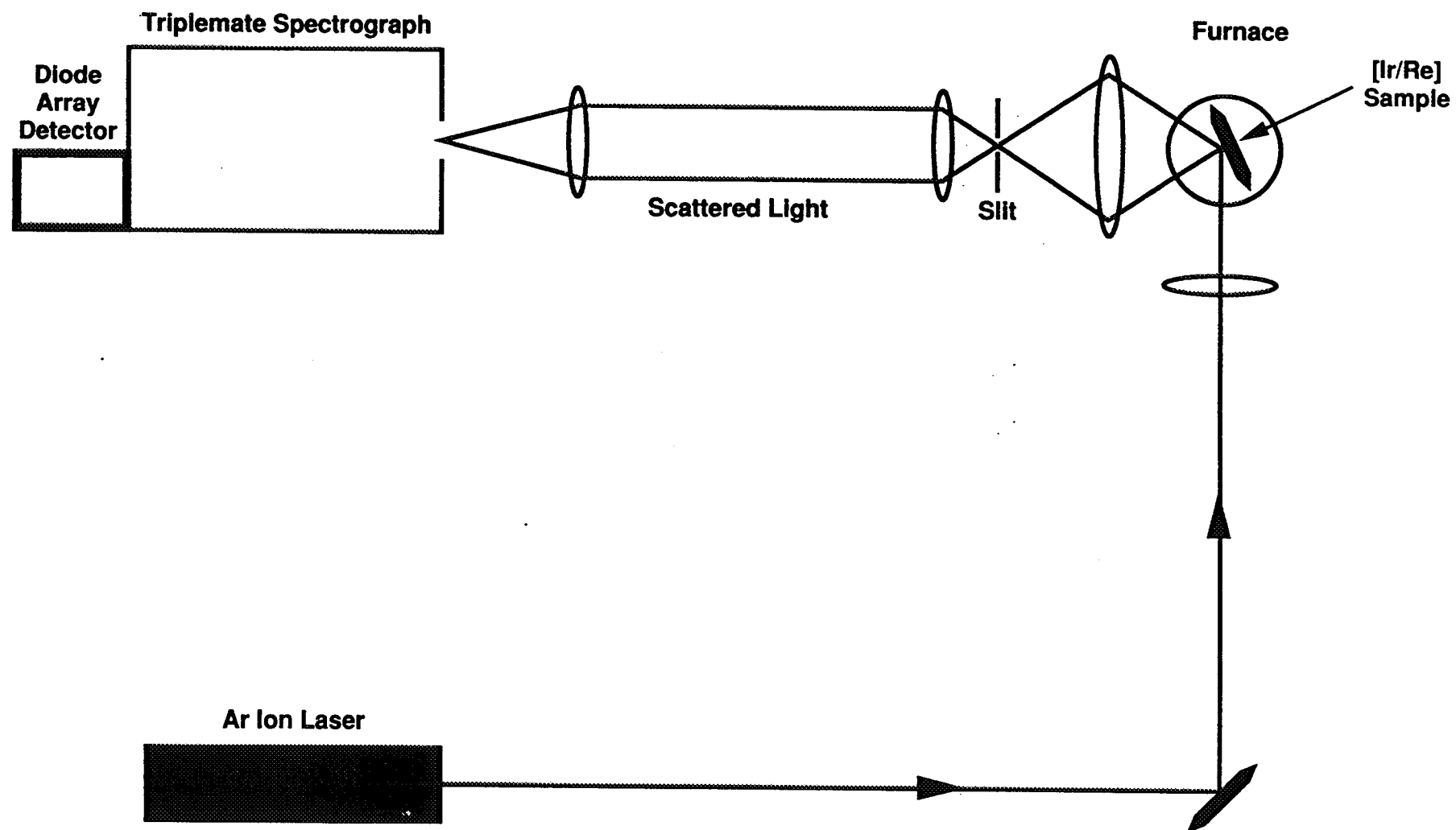


Figure 4.5.2-1. Raman Surface Analysis System

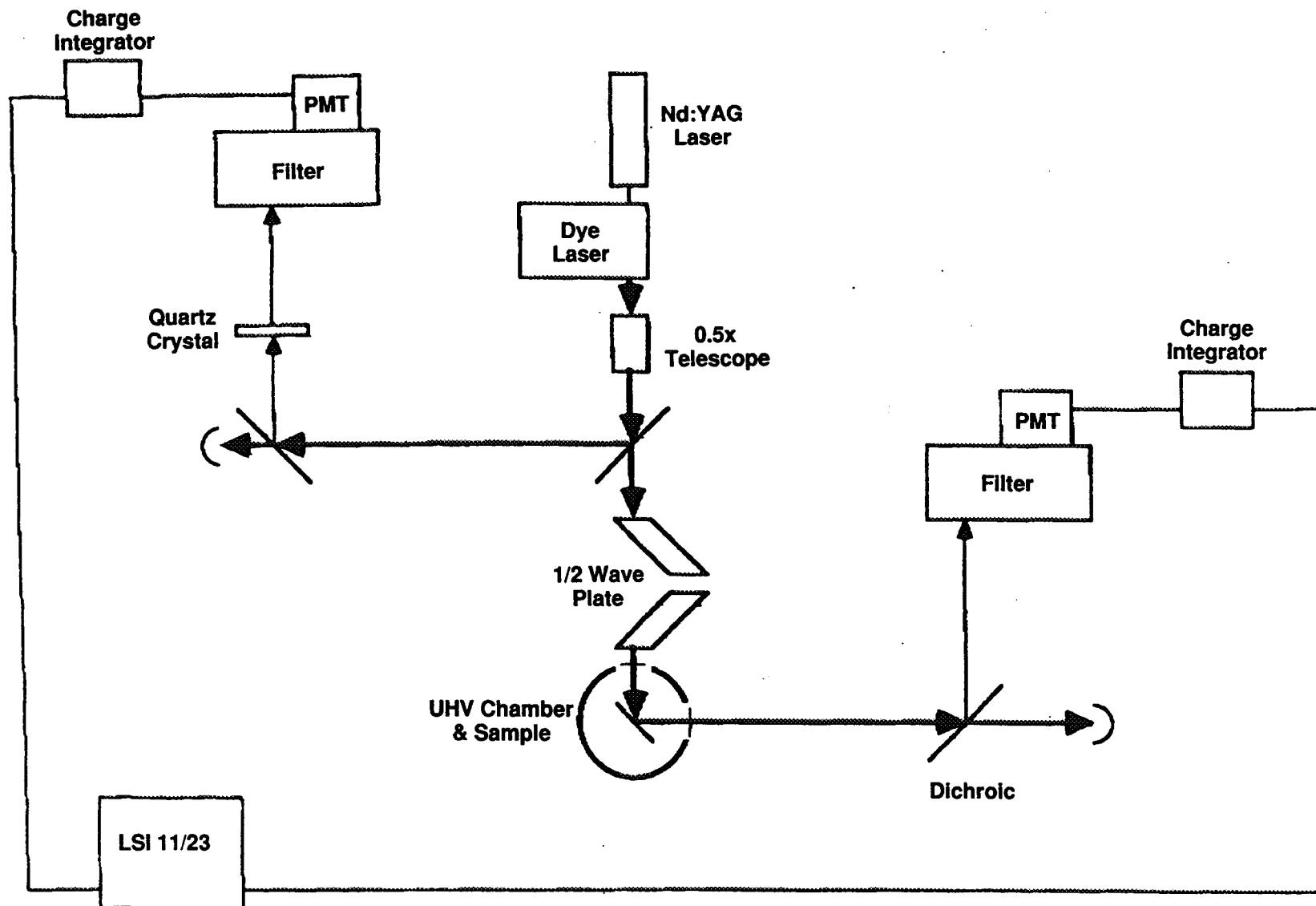


Figure 4.5.2-2. Second Harmonic Generation Surface Analysis System

4.5, High Temperature Materials Tests (Sandia) (cont.)

X-ray diffraction data have been obtained on powder samples of IrO_2 , ReO_3 , and PtO_2 to verify that the oxide phase is what the manufacturer claimed it to be. For some samples there was significant metallic contamination rendering them useless as standards. Figure 4.5.2-3 shows Raman spectra for power samples deemed reasonably phase pure by X-ray diffraction. These spectra form the basis of a data set of oxide standards relevant to our research. The Raman spectroscopy system is shown conceptually in Figure 4.5.2-4.

As a second step in demonstrating surface Raman spectroscopy, Ir foil was heated in oxygen while optical spectra were recorded. Figure 4.5.2-5 shows the results of heating to 1000°C in oxygen for 15 min. Four spectra are shown, one of the foil prior to heating and three taken at elevated temperature during cooling from 1000°C . They clearly demonstrate detectable oxide formation at temperature. The success of this experiment was crucial to demonstrating that the next phase of the research using the MSTA would be feasible. Figure 4.5.2-6 shows a SEM of the foil surface after heating in oxygen to 1250°C for one hour. What used to be a smooth featureless surface has been transformed into a rough oxide with a morphology exhibiting crystallographic features.

The laser Raman work was followed by post exposure characterization using Auger and sputter Auger analysis. Figure 4.5.2-7 is a sputter depth profile into the IrO_2 surface. Assigning an accurate depth scale is difficult due to the rough morphology and unknown sputter rate. The data are plotted in terms of sputter time which is roughly linearly proportional to depth. For comparison, tantalum oxide is sputtered detected at a rate of $167 \text{ \AA}/\text{min}$ under these same conditions. The apparatus used for these measurements are shown conceptually in Figures 4.5.2-8 and -9. Auger spectra for pure Ir metal and Ir after exposure at 1250°C to O_2 are shown in Figures 4.5.2-10 and -11.

Coating experiments were conducted to examine fundamental materials properties such as oxidation and interdiffusion under high temperature oxidizing environments. A 1.4 micron thick Ir coating was sputter deposited on top of a rhenium foil and heated in vacuum to 1600°C for 45 min. The depth profile before and after heating is shown in Figures 4.5.2-12 and -13, respectively. Prior to heating, there is a well defined interface between the Ir coating and Re substrate. After heating, the depth profile shows complete interdiffusion between the two materials forming a mixed zone which has approximately an equal composition of Ir and Re and is twice as thick as the original Ir layer. The surface morphology after heating, shown in Figure 4.5.2-14, is no longer mirror-like, but is rough indicating possible formation of a second phase.

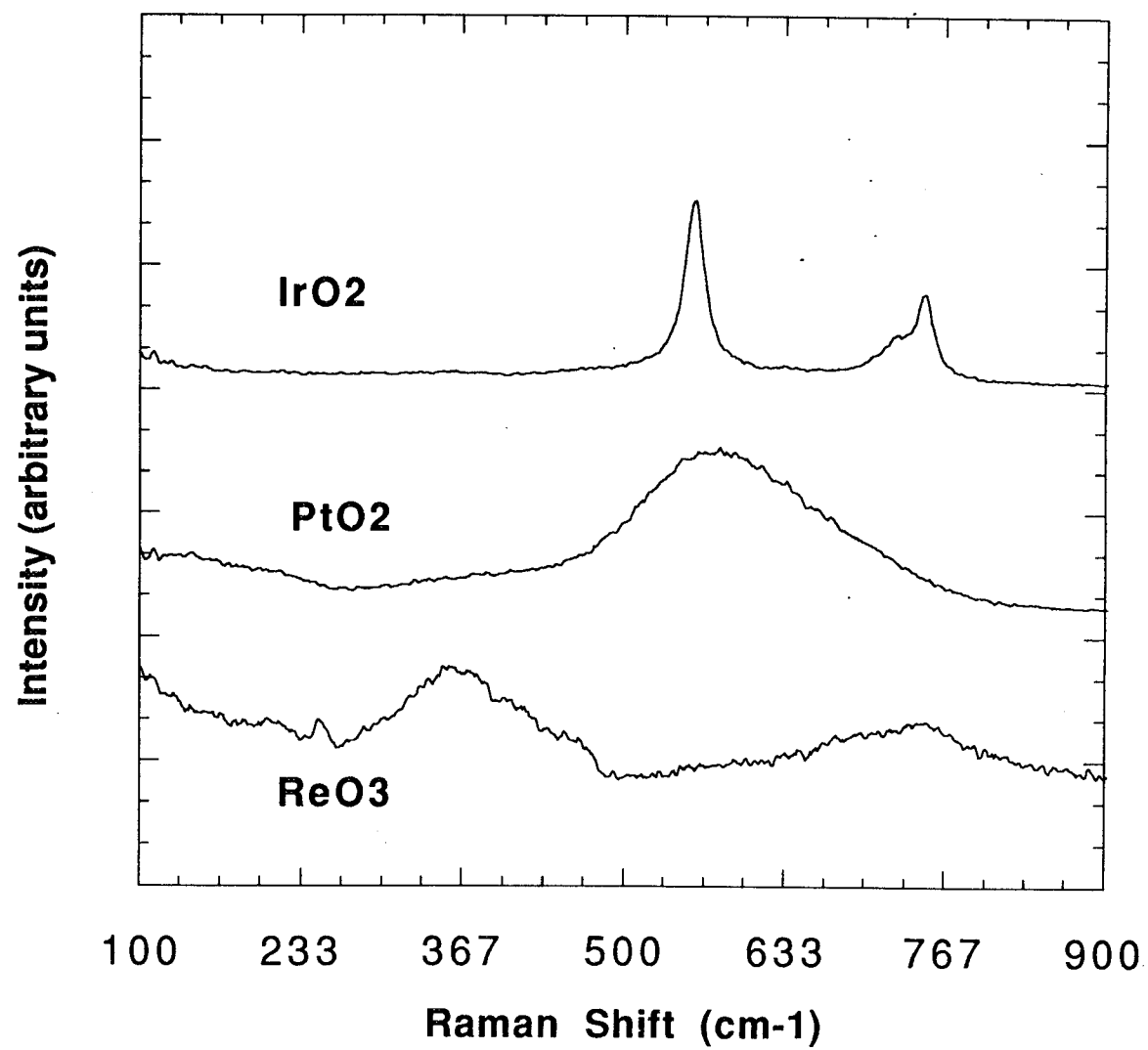


Figure 4.5.2-3. Raman Spectra - Oxide Standards

Raman Spectroscopy : A Surface Analytical Tool

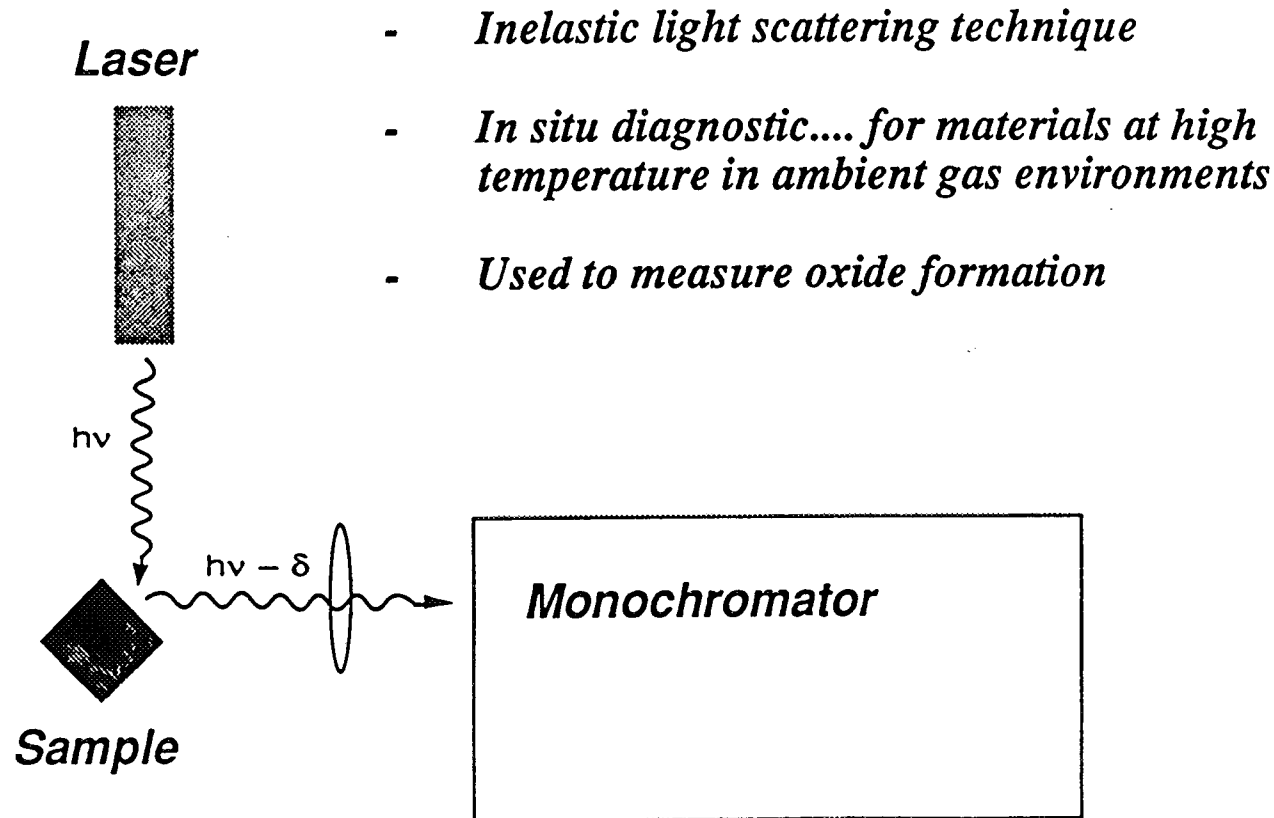


Figure 4.5.2-4. Raman Spectroscopy - A Surface Analytical Tool

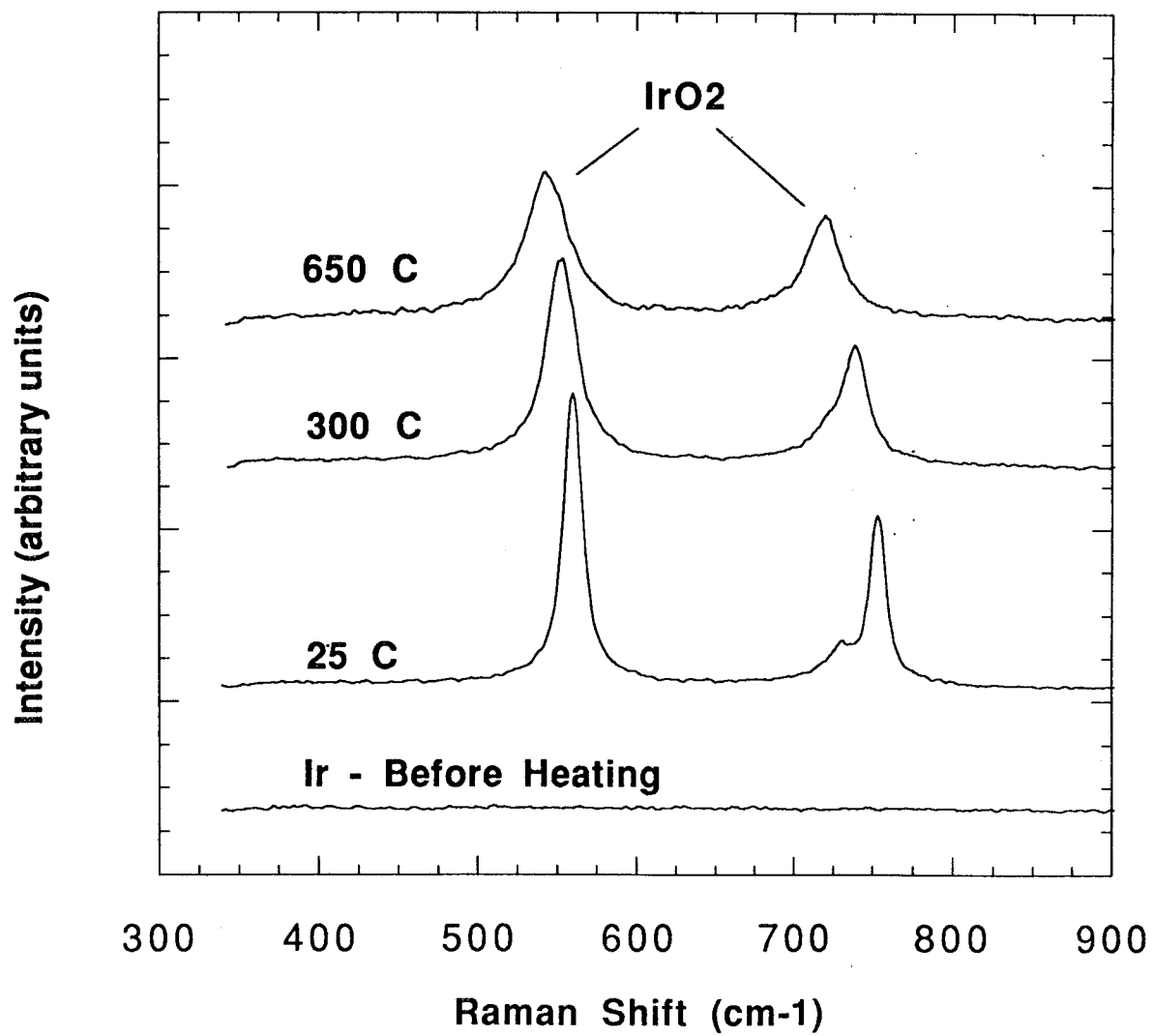


Figure 4.5.2-5. Ir - After 15 Min/1000 c in Oxygen

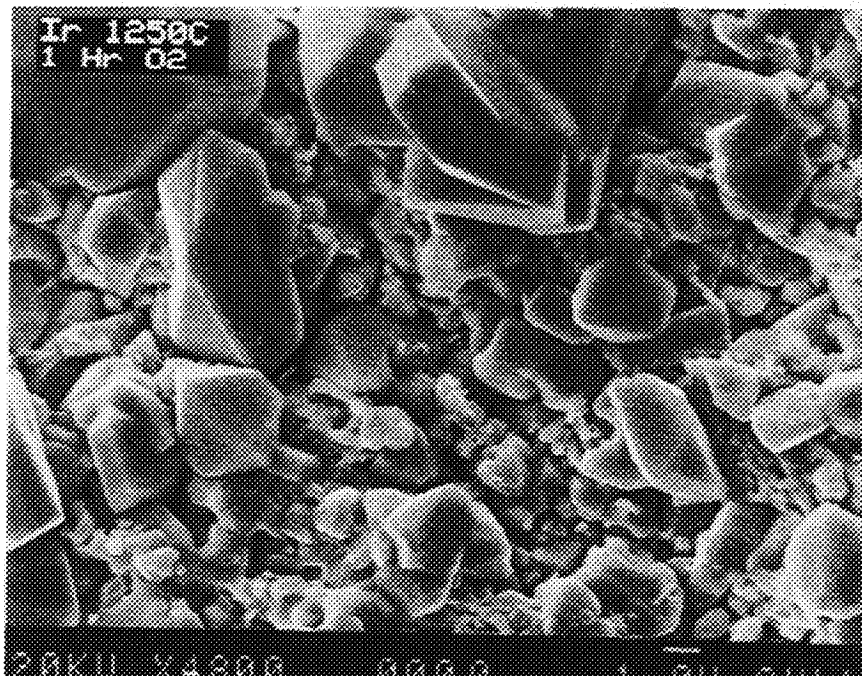


Figure 4.5.2-6. SEM of Foil Surface After Heating in Oxygen to 1250C for One Hour

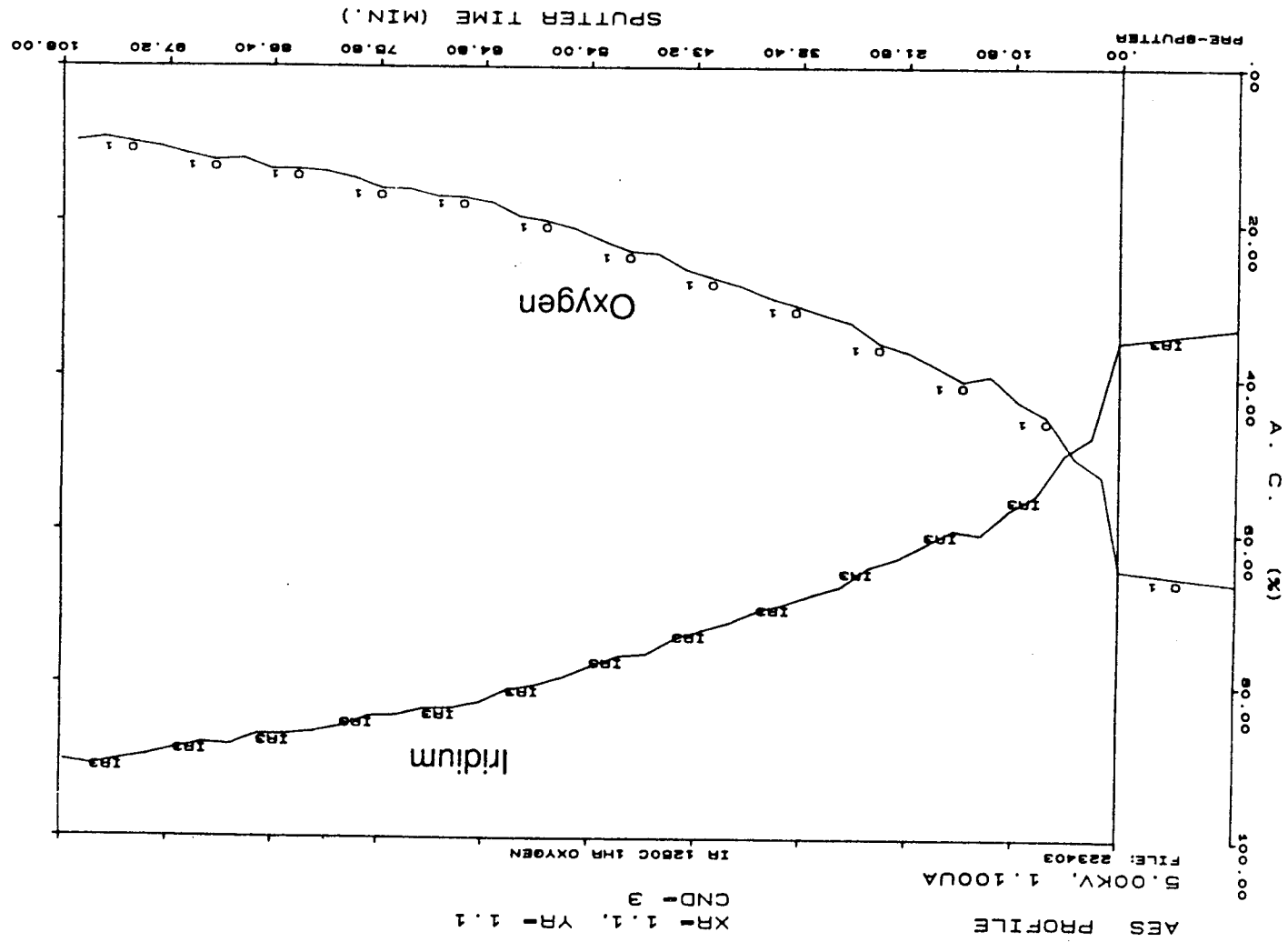


Figure 4.5.2-7. Sputter Depth Profile into the Ir/O₂ Surface

- *Electron spectroscopy — probes $\sim 10 \text{ \AA}$ depth*
- *Ultra high vacuum technique*
- *Gives spatially resolved compositional map*
- *Can be used for high-resolution depth profiling*

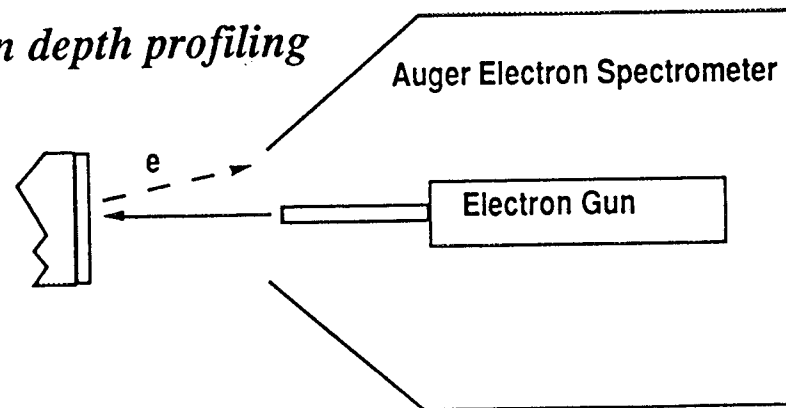


Figure 4.5.2-8. Auger Spectroscopy - A Surface Analytical Tool

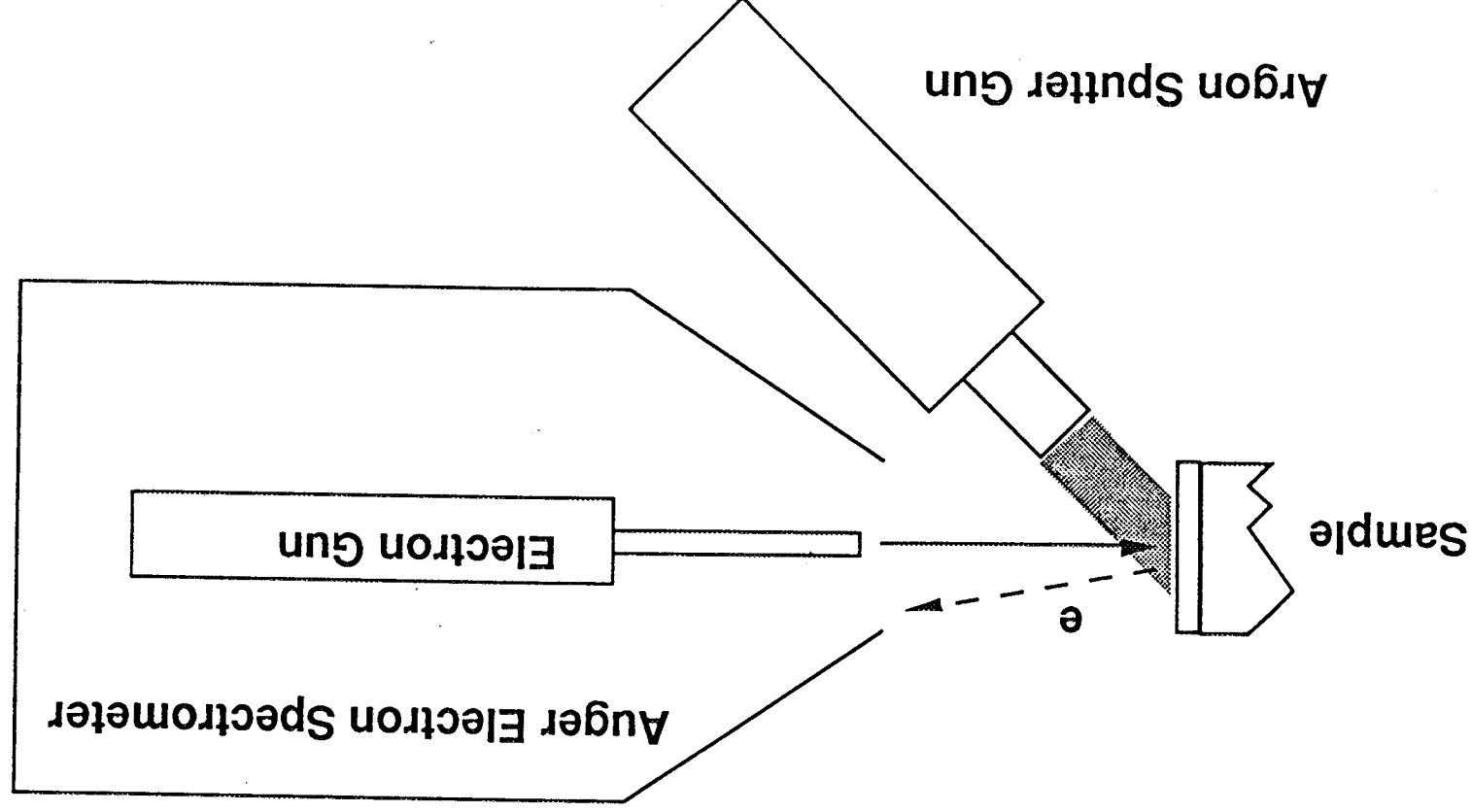


Figure 4.5.2-9. Sputter Profiling Using Auger Spectroscopy

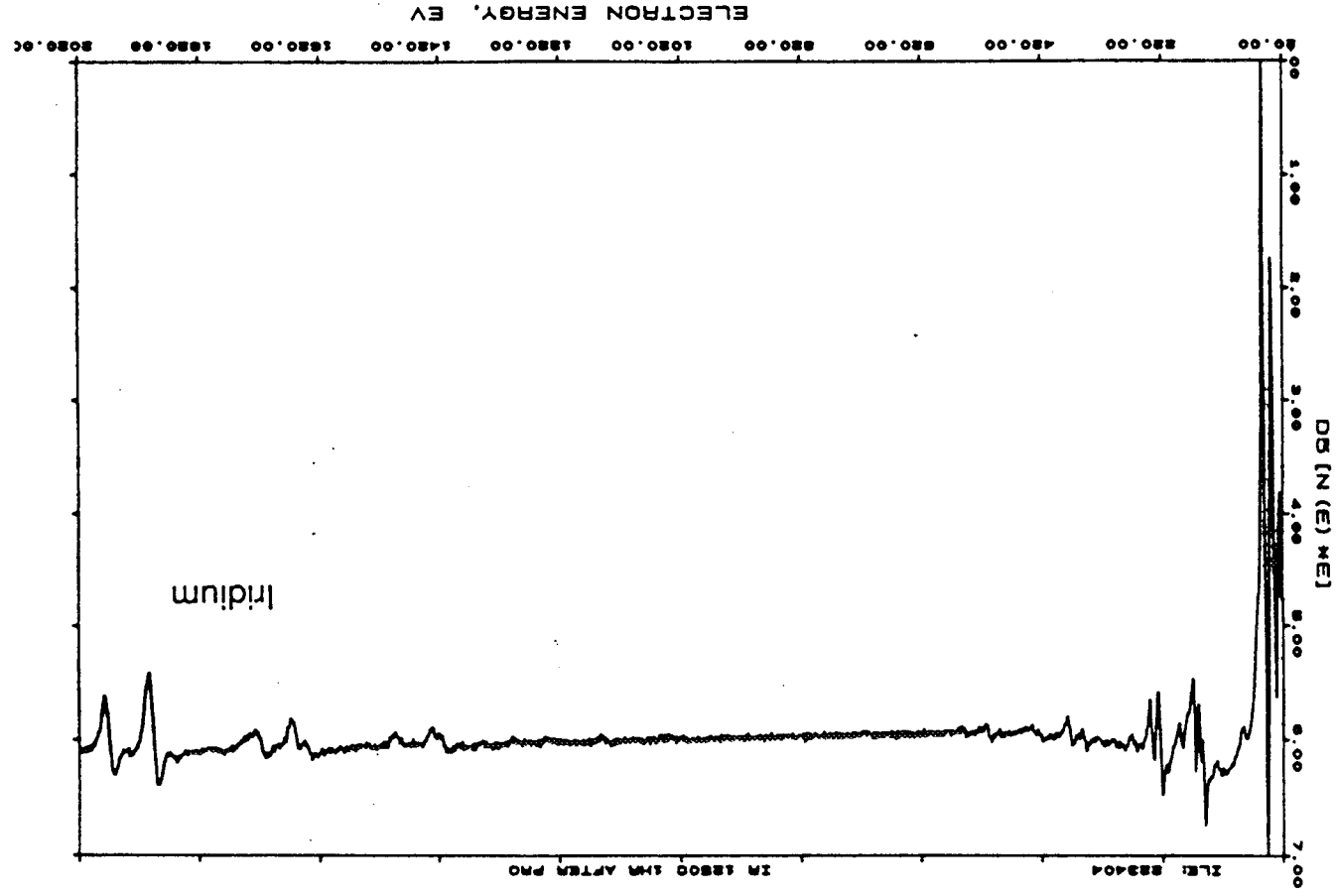


Figure 4.5.2-10. Auger Spectra - Ir Metal

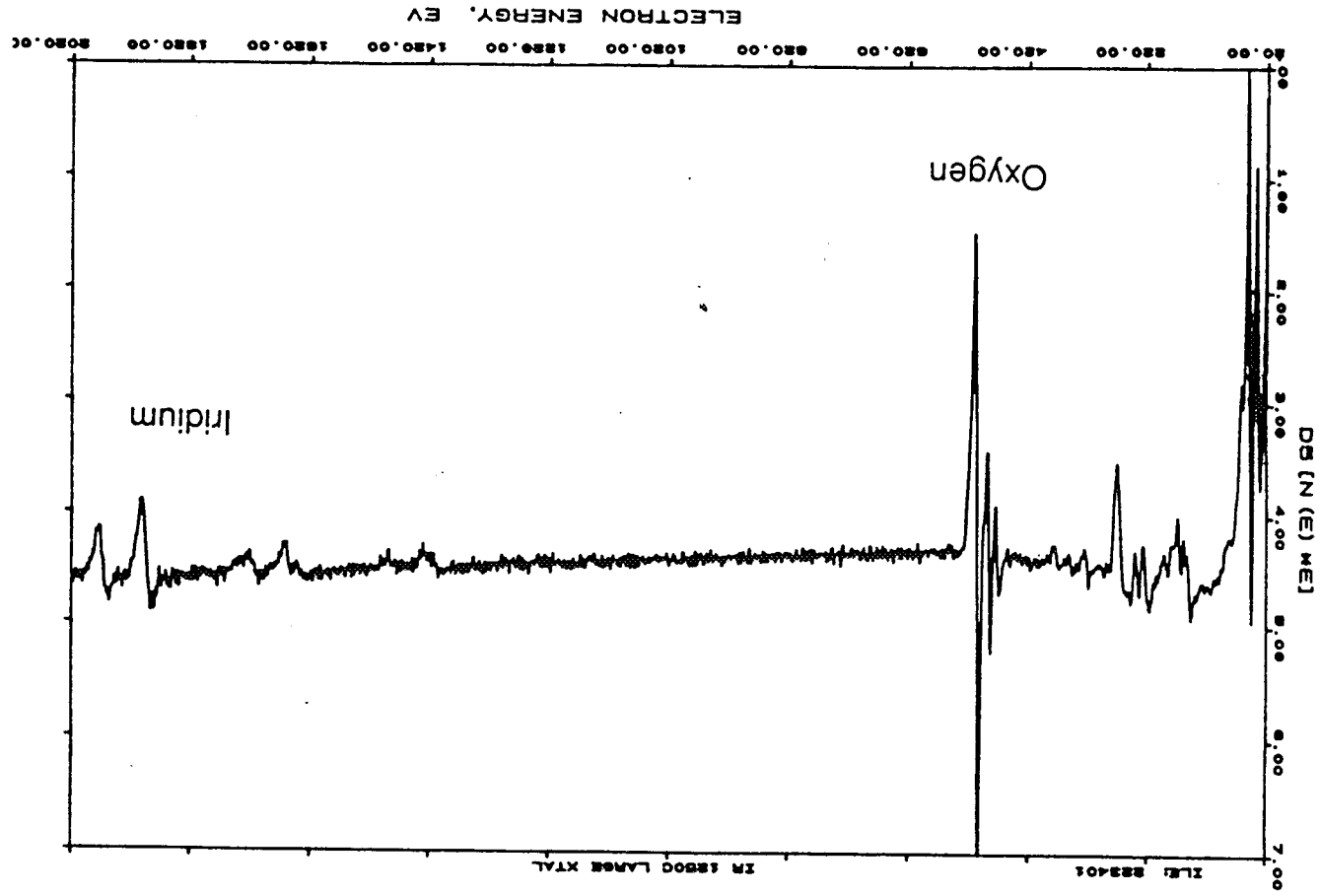


Figure 4.5.2-11. Auger Spectra - Ir Metal After 1250 c in O₂

AES PROFILE

XR= 1.1, YR= 1.1

CND= 3

5.00KV, .600UA

FILE: 223502

IR RE NO1 A

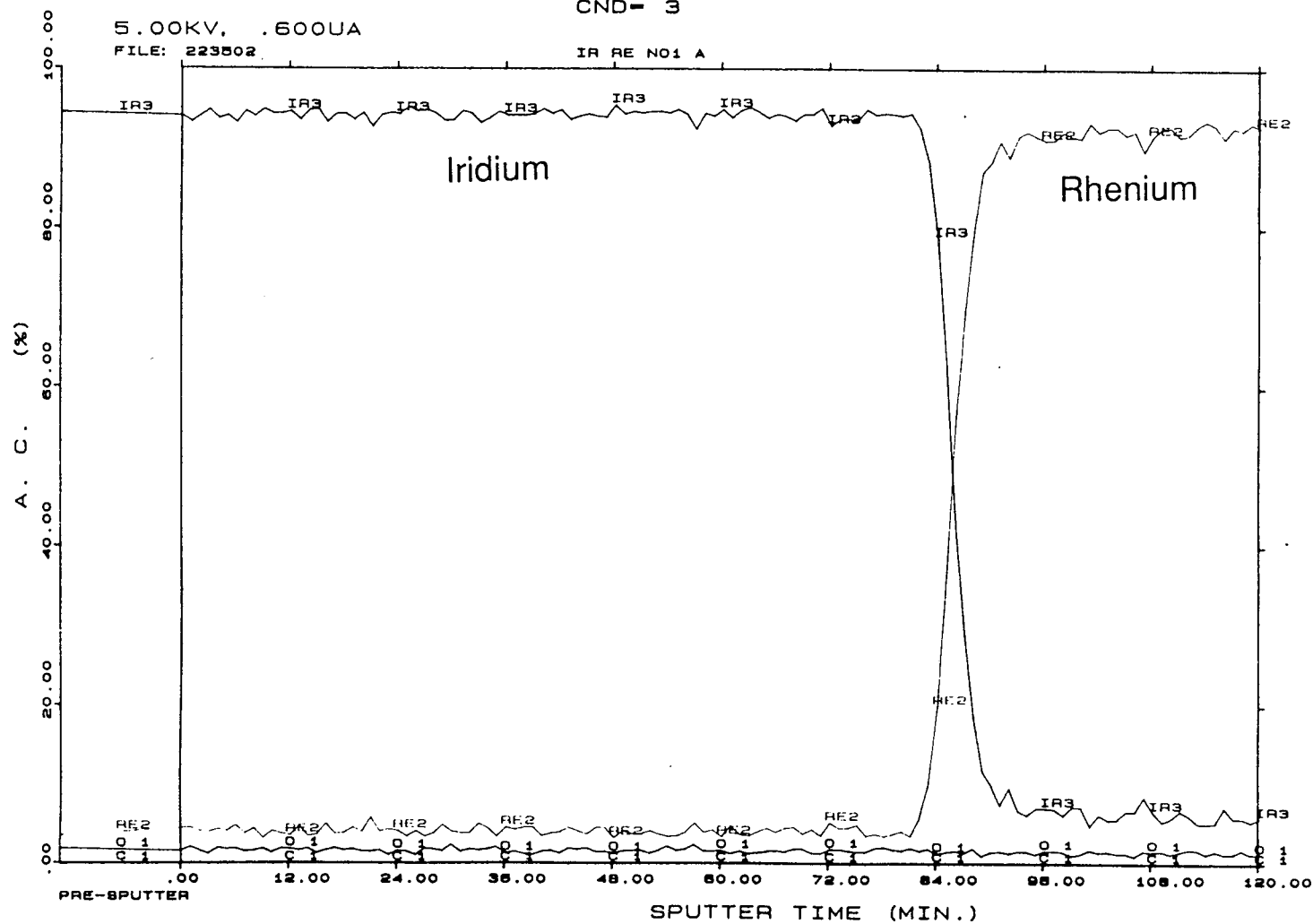


Figure 4.5.2-12. Depth Profile Before and After Heating

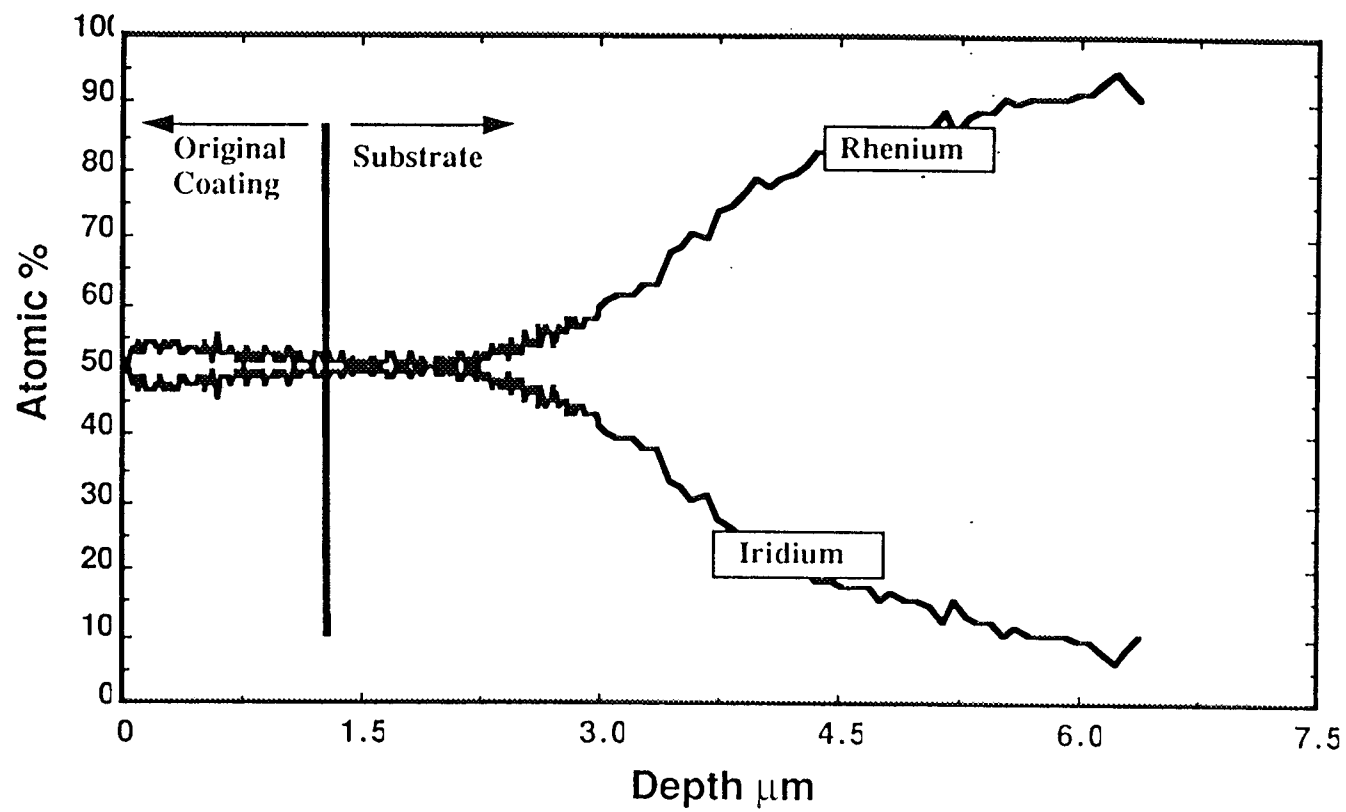


Figure 4.5.2-13. After Heating -1600 C/45 Min/Vacuum

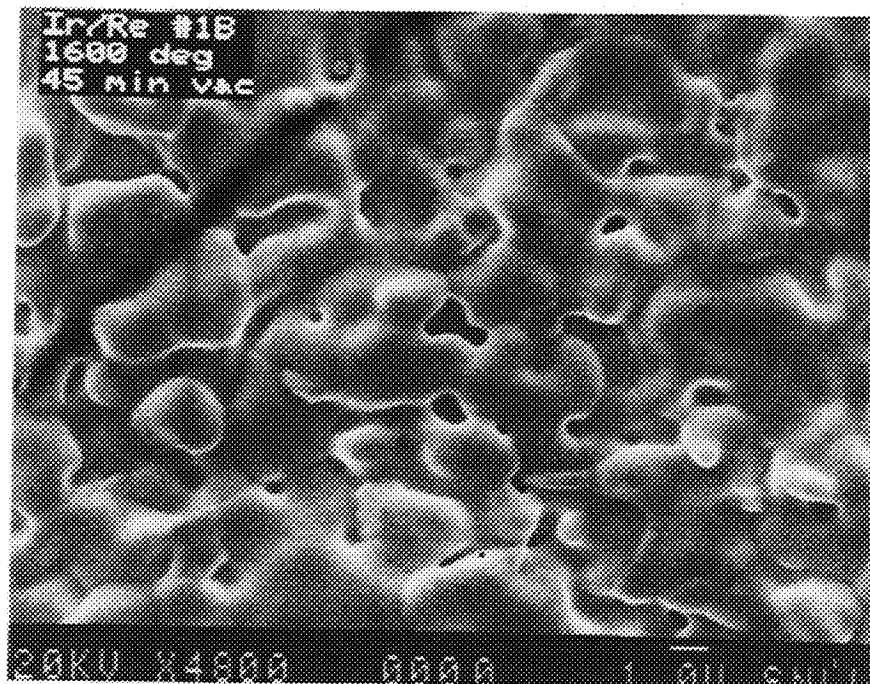


Figure 4.5.2-14. Surface Morphology After Heating

4.5, High Temperature Materials Tests (Sandia) (cont.)

These results were surprising as they suggest that Ir should not work as a protective film. However, Aerojet has demonstrated that Ir works under real operating environments. For the materials used in those tests, the Ir coatings on the rocket engines are ~35 times thicker than what we have used here so that it will take longer for the Re to reach the surface than in our case. If diffusion is the "rate limiting" step, then the time to failure for these engines may have an incubation period that would be related to the thickness of the Ir coating. Alternatively, we may speculate that the reaction of the alloy surface with the hot exhaust gases is appreciably different than that for the pure Re or Ir metals. Clearly we need to understand more about both the solid state diffusion of the two metals and the reactivity of the Ir-Re alloys surface formed at high temperature with the oxidizing environment.

It has been demonstrated that it is possible to detect IrO_2 using a Raman probe on an iridium sample at elevated temperatures in an oxygen environment. During the course of these measurements it was found that the windows of the Raman cell gradually become darkened with a deposit, presumably a result of the reaction of iridium with oxygen. Raman spectra of these products show that the window deposit is in fact stoichiometric IrO_2 . Figure 4.5.2-15 shows a comparison of the Raman spectra for the deposit and the Raman spectra taken on the IrO_2 standard. These results confirm the picture of material loss through the volatilization of stoichiometric metal oxide during high-temperature exposure to oxygen.

An Auger sputter depth profile of an iridium surface after 1000 C exposure to oxygen is shown in Figure 4.5.2-16. This is an extension of the previous work at 1250 C which showed oxide formation following 1 hr exposures in 1 atm oxygen. The data in Figure 4.5.2-16 shows that there is considerable oxide growth on an iridium sample held at a lower temperature, 1000 C, after only 15 min. The calibration of the depth scale is taken from sputtering experiments on tantalum oxide standards and should be considered as only approximate due to surface morphology effects.

Platinum is used for the BLT. It does not see excessively high temperatures. In order to examine the oxidation resistance of Pt, specimens have been exposed to O_2 at near atmospheric pressure. The data plotted in the lower curve in Figure 4.5.2-17 were taken on a Pt coupon after exposing it at 1250 C to oxygen for a one-hour period. The data plotted in the top curve in this figure are for the PtO_2 standard. It is clear from these spectra that there is no evidence for growth of platinum oxide under these conditions. These results are quite striking when

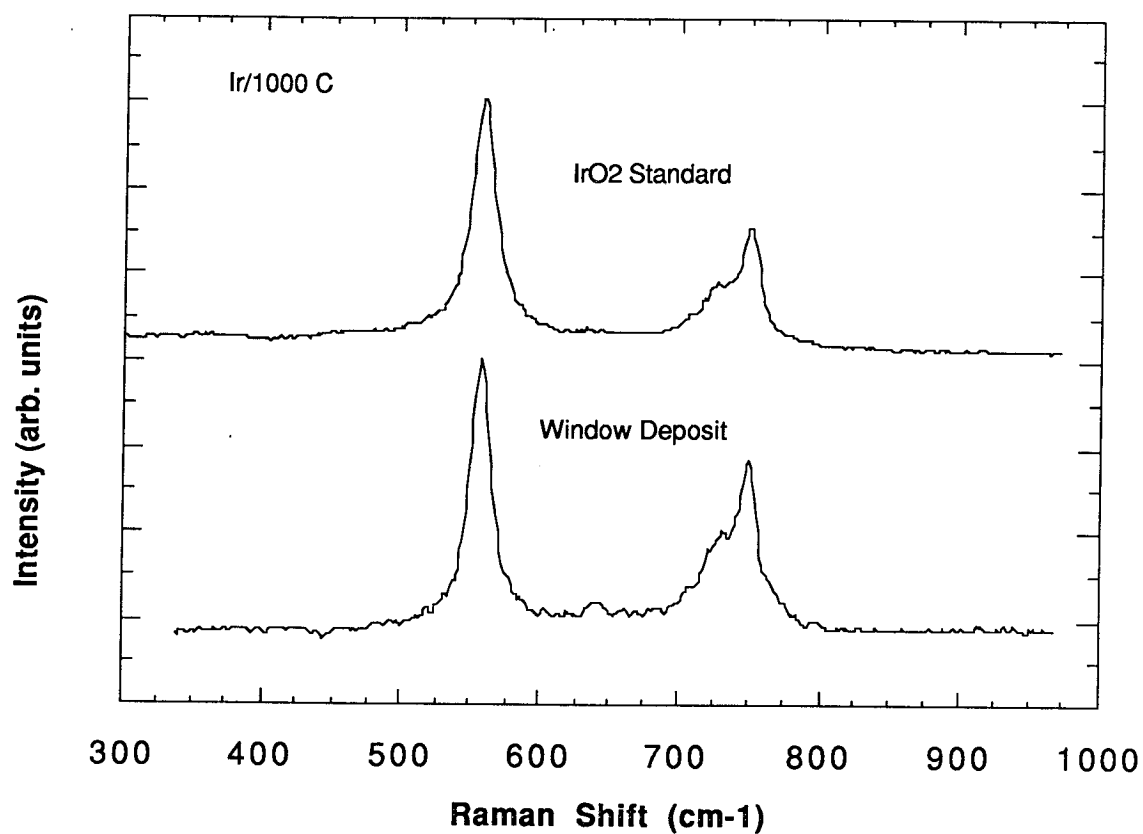


Figure 4.5.2-15. Raman Spectra from Deposit which Forms on Furnace Window when Heating Iridium in Oxygen. Comparison with Standard Spectra Shows that the Deposit is IrO₂

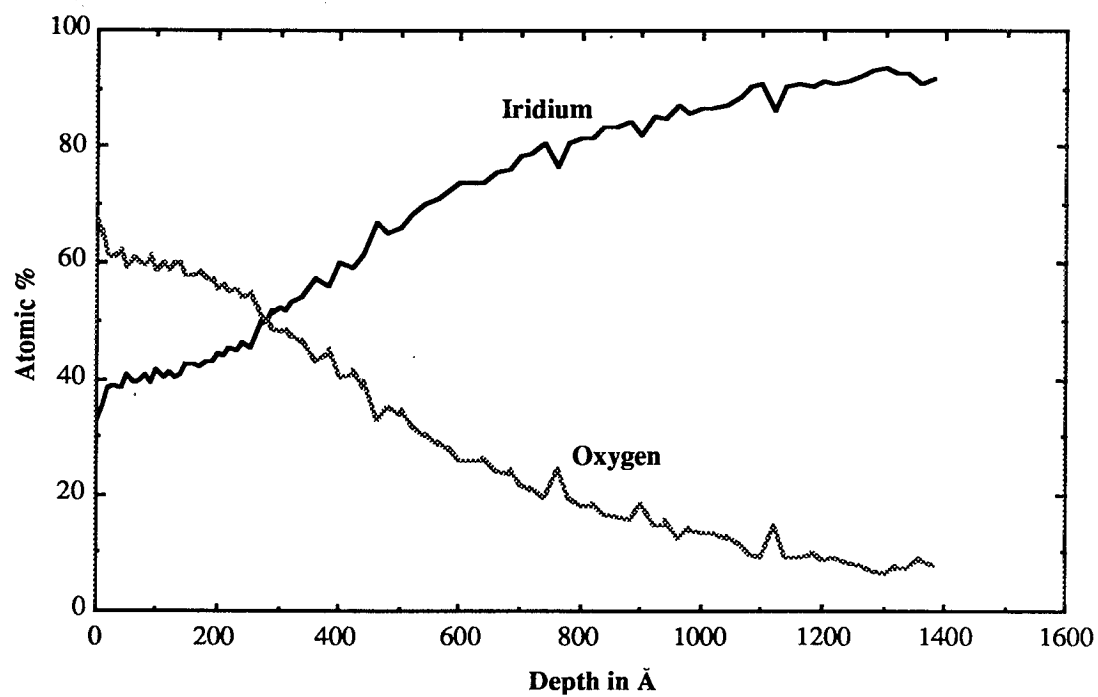


Figure 4.5.2-16. Auger Sputter Profile of an Iridium Sample Heated to 1000 C for 15 min. in Oxygen at 1 Atmosphere

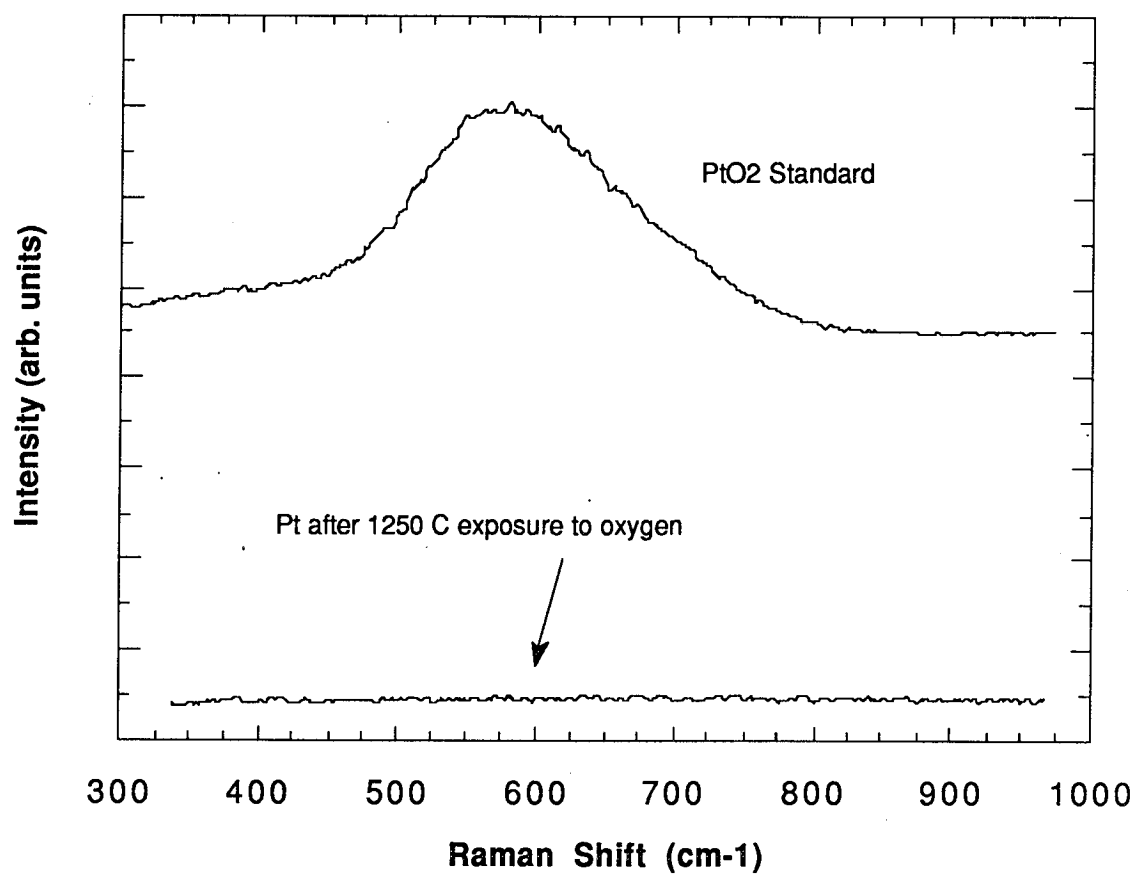


Figure 4.5.2-17. Surface Raman Spectra of a Platinum Sample Heated to 1250 C in 1 Atmosphere of Oxygen for 1 Hour Showing that there is no Formation of PtO₂ on the Pt Metal

4.5, High Temperature Materials Tests (Sandia) (cont.)

compared to similar data for Ir (Figure 4.5.2-18). It is clear that Pt is not nearly as vulnerable to oxygen attack as is either Ir or Re.

Additional Raman studies were made to characterize the low temperature onset of IrO₂ formation. Figure 4.5.2-19 shows Raman spectra taken on Ir samples held at 650 C in one atm of O₂ for two hours. The initial spectra show that an IrO₂ layer can be seen forming in the furnace environment even at these relatively low temperatures. In addition, there is a large change in the Raman shift for both peaks of IrO₂ as a function of temperature. This is quite interesting as it is indicative of either a phase change or a change in stoichiometry as a function of temperature.

Figure 4.5.2-20 shows the surface Raman spectrum of these samples at room temperature after removal from the furnace. This latter spectrum is taken to eliminate any artifacts which may arise from scattering from the furnace windows.

Figure 4.5.2-21 shows the Auger depth profile from this oxide. It should be compared with the depth profile taken for a 1250 C exposure shown in Figure 4.5.2-7. The approximate oxide thickness for this specimen is ~200 Å for the 1250 C exposure. What is remarkable here is that the Raman technique is sensitive to such a thin layer of iridium oxide, an indication of the large strength of the scattering cross section in this material.

X-Ray Diffraction Measurements

X-ray diffraction (XRD) methods have been initiated to study the thin films formed on Ir and Re after high-temperature exposure to oxygen. Analysis of an Ir foil that was heated to 1250 C in O₂ for one hour shows the formation of the tetragonal phase IrO₂ (Figure 4.5.2-22). Diffraction peaks corresponding to both the oxide (starred peaks) and the underlying Ir metal are observed in the XRD spectra.

XRD measurements were also made on Ir coated Re heated to 1400 C in vacuum (~10⁻⁶ Torr) for 45 minutes. Previous Auger depth profiles have shown that there is complete intermixing of the two components after heating to 1600 C in vacuum (Figure 4.5.2-13). XRD spectra show peaks corresponding to the Ir coating and the Re foil substrate as well as unidentified peaks which are thought to result from an Ir-Re solid-solution or intermetallic phase of unknown stoichiometry, see Figure 4.5.2-23. There are no reported Ir-Re phases in the XRD standard database.

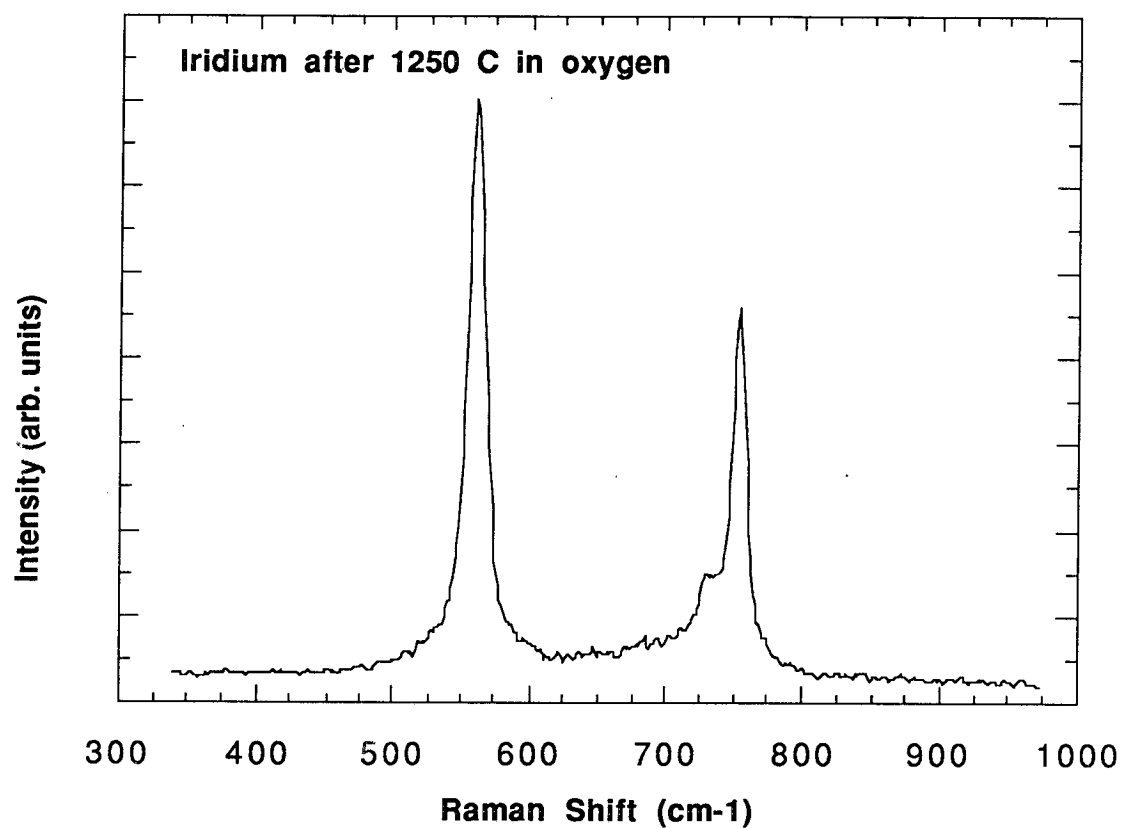


Figure 4.5.2-18. Surface Raman Spectra of an Iridium Sample Heated to 1250 C for 1 Hour in 1 Atmosphere Oxygen, Showing Formation of IrO₂ on the Ir Metal

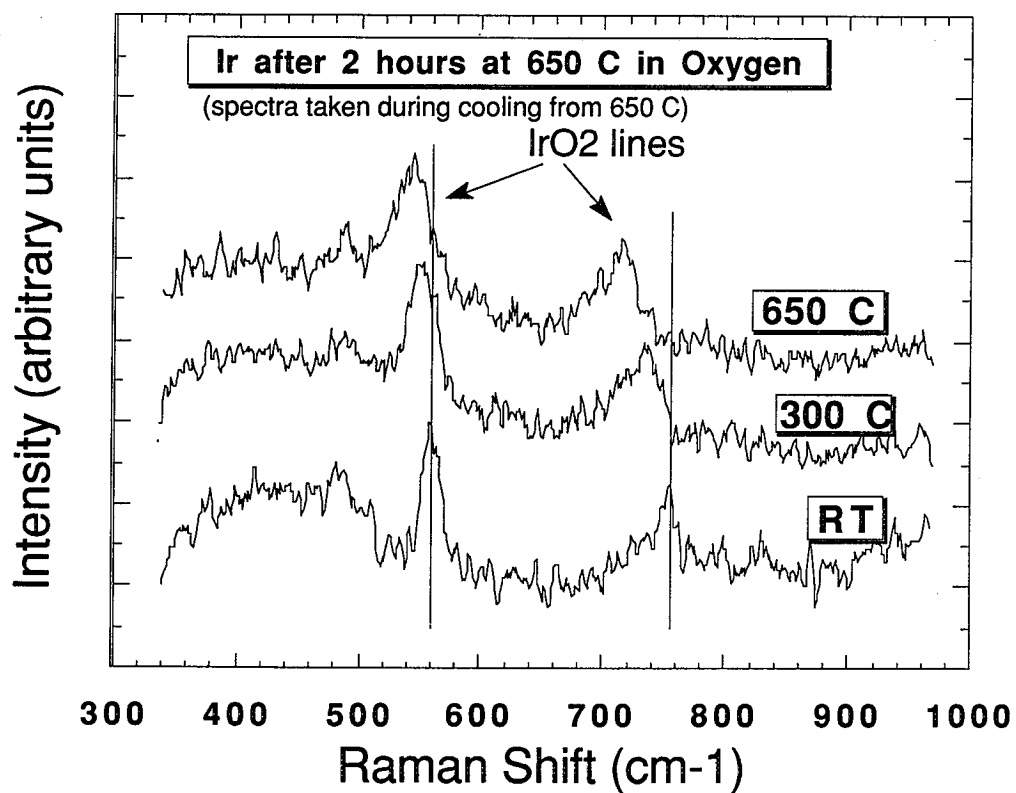


Figure 4.5.2-19. Surface Raman Spectra of an Iridium Foil Heated for Two Hours in One Atmosphere of Oxygen at 650 C. The 300C and RT Data were Taken During Cooling from 560 C

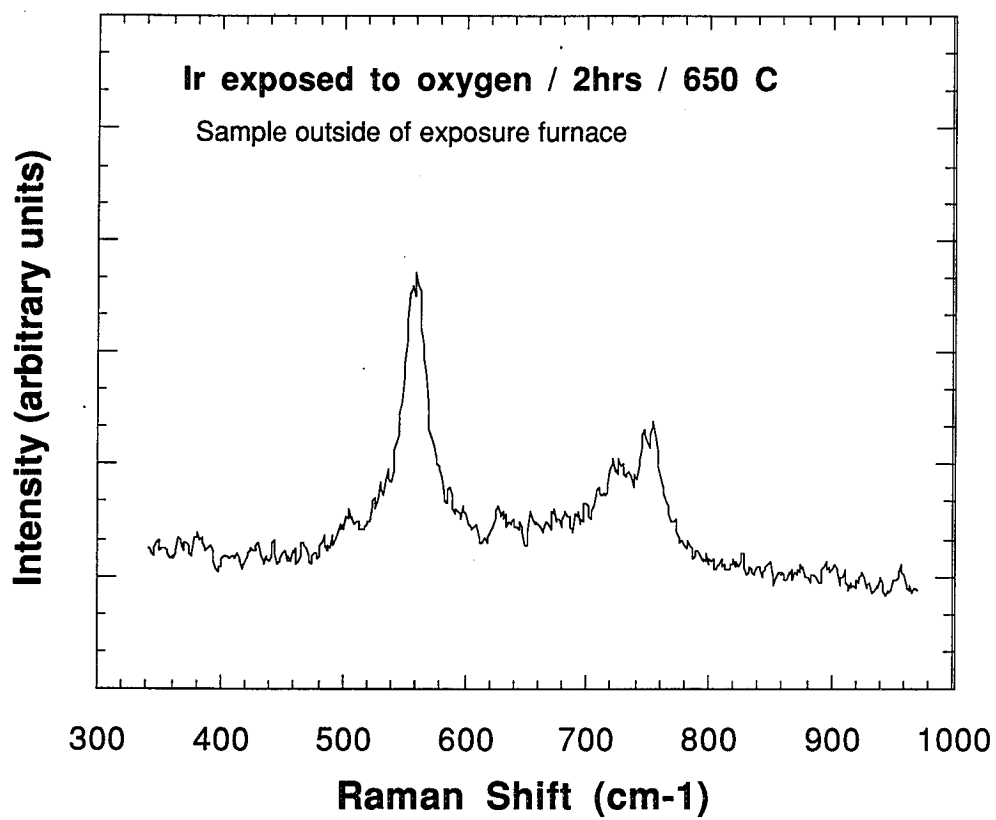


Figure 4.5.2-20. Raman Spectra of Iridium Foil Exposed to One Atmosphere Oxygen at 650 C for Two Hours

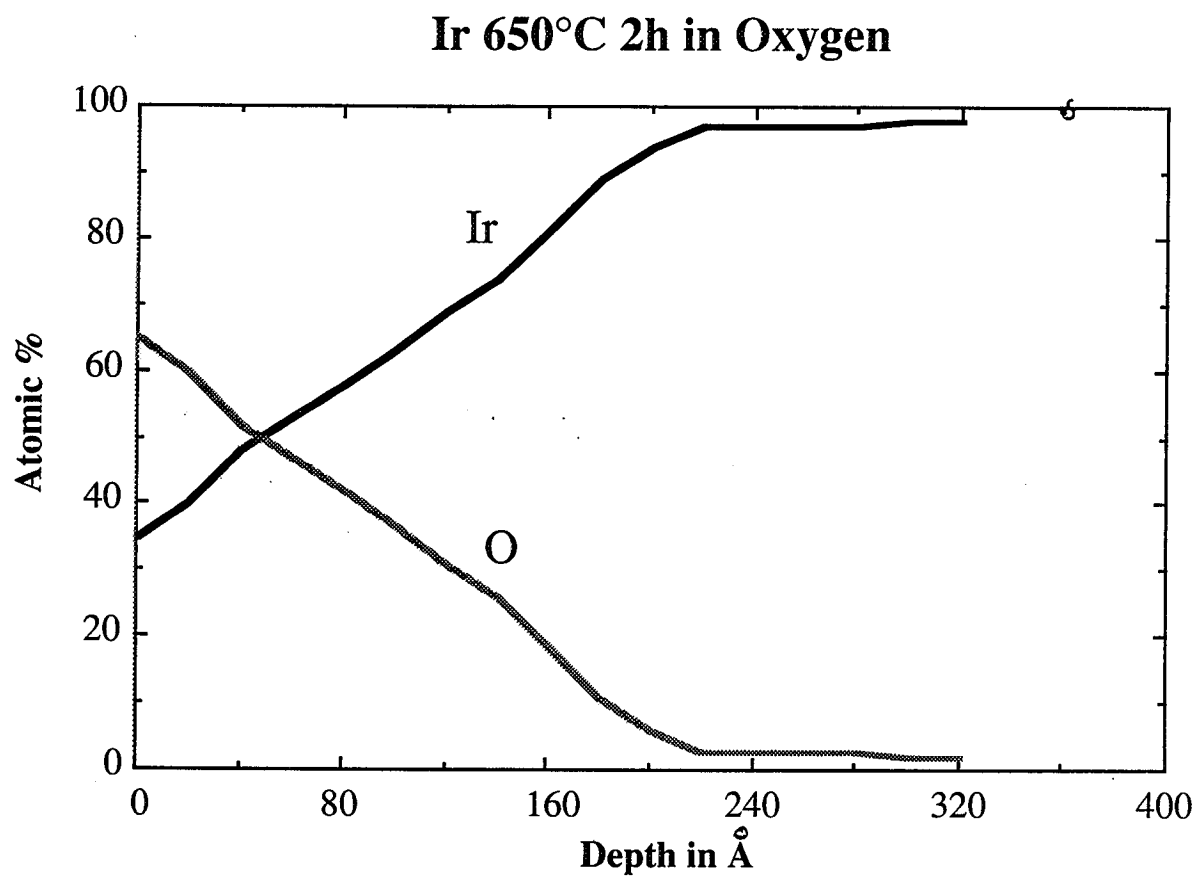


Figure 4.5.2-21. Sputter Auger Depth Profile of the Iridium Dioxide Layer Formed on Iridium after 650 C Anneal in Oxygen

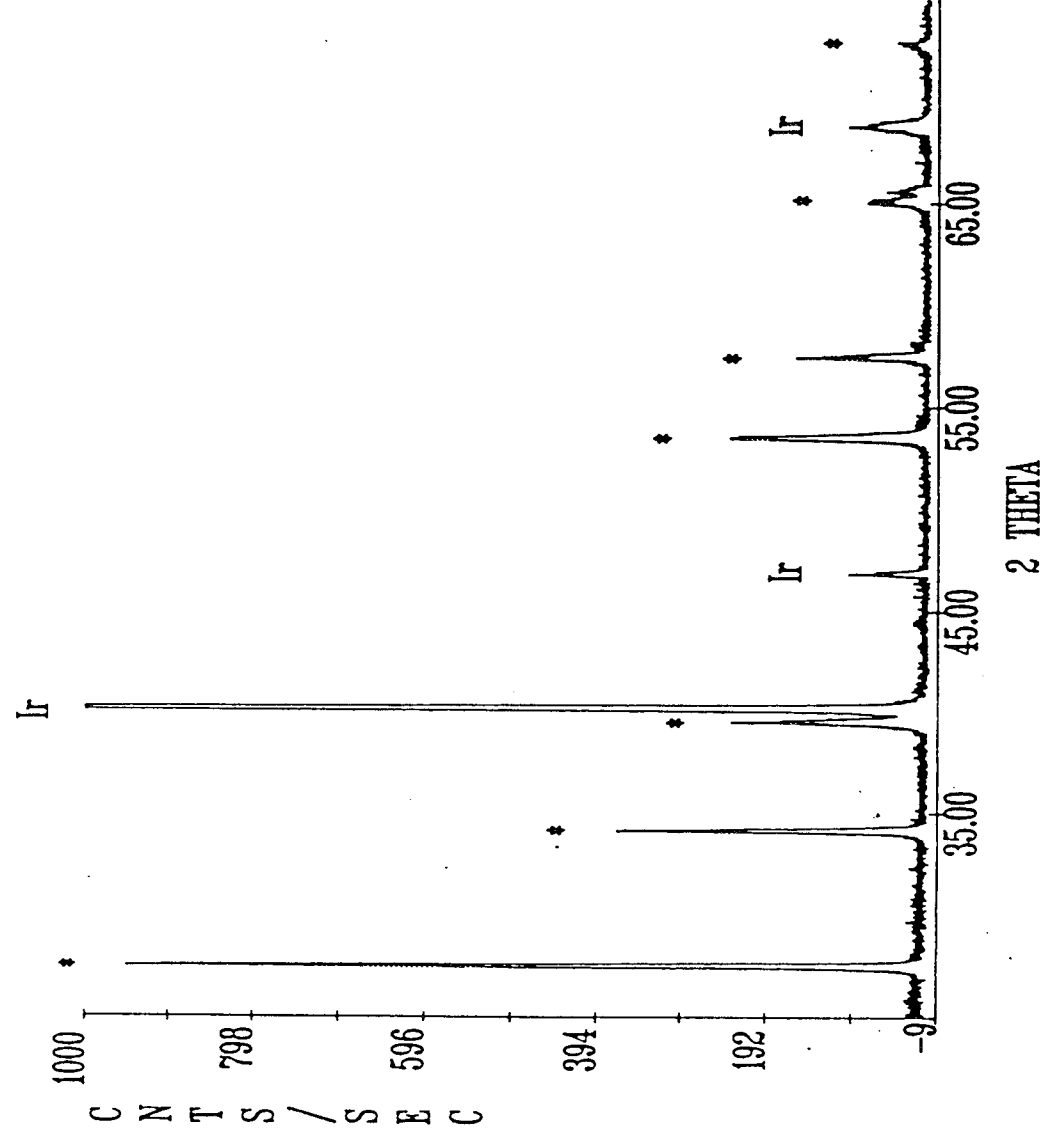


Figure 4.5.2-22. X-Ray Diffraction Spectrum for the Oxide Formed on Iridium after Heating to 1250 C in Oxygen

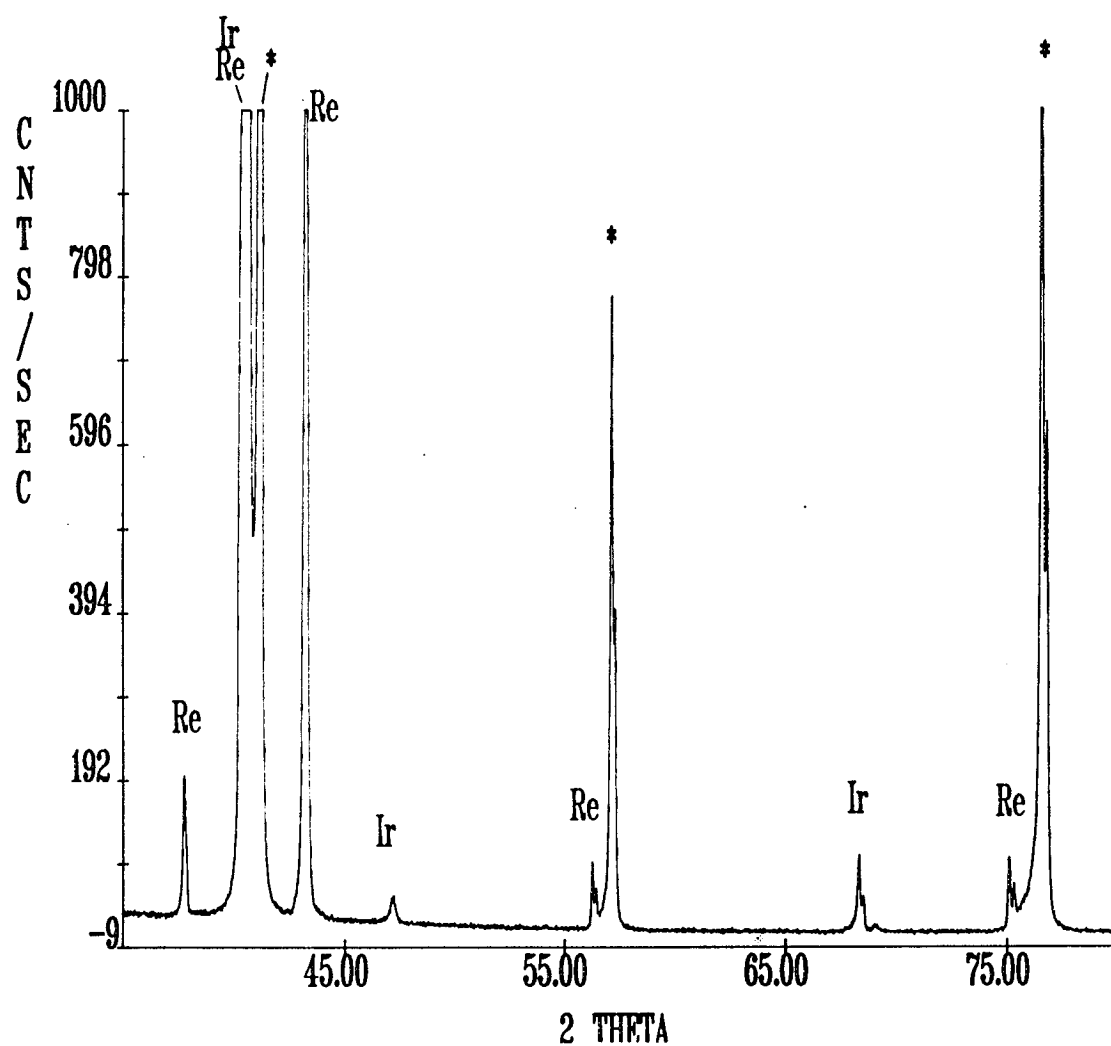


Figure 4.5.2-23. XRD Spectrum of an Iridium Coated Rhenium Foil Heated in Vacuum to 1400 C for 45 Minutes

4.5, High Temperature Materials Tests (Sandia) (cont.)

Ir-Re Diffusion

The data in Figure 4.5.2-13 show that after heating a Re sample coated with ca. 1.5 microns of Ir to 1600 C for 45 min in vacuum, the surface composition is nearly equal in Ir and Re. The interdiffusion of these two species is extremely important for life predictions of coated nozzles, because as the Re breaks through to the surface, it can be lost from the sample through the formation of volatile oxides. In order to make a predictive model to calculate expected coating life under different oxidizing environments at appropriate operating temperatures, we made a series of measurements aimed at quantifying the diffusion constant relevant to the Ir/Re system. Our first measurements are shown in Figure 4.5.2-24 along with a 1-D theoretical fit.

The data shown in this figure were obtained using the technique of sputter Auger depth profiling. The Re specimen was initially coated with ca. 2.5 microns of Ir using Sandia's sputter deposition apparatus. The sample was heated in vacuum to 1200 C for 45 min and then depth profiled. Only Ir and Re were found to be present in the Auger spectra (the data in the figure show only the Ir concentration vs depth). The experimental data were fit to a theoretical expression for diffusion of an extended source of limited extent (Ref. 8).

$$C = \frac{1}{2} C_o \left(\operatorname{erf} \frac{h-z}{2\sqrt{Dt}} + \operatorname{erf} \frac{h+x}{2\sqrt{Dt}} \right)$$

Here C is concentration as a function of time and distance, C_o is the concentration at time equal zero, h is the depth of the Ir coating on Re, t is the time, x is the distance, and D is the diffusion coefficient. From the theoretical fit we obtain a value for the diffusion coefficient at 1200 C of $D = 2.4 \times 10^{-12} \text{ cm}^2/\text{sec}$. The X-ray diffraction data indicate that Ir is diffusing preferentially into the Re but do not provide a value for the activation energy and pre-exponential. This required a plot of the diffusivity vs $1/T$ which gives an activation energy, E_a , once D has been measured at a number of different temperatures above and below 1200 C.

X-ray diffraction analyses were carried out on sintered pellets consisting of pressed powders of Ir and Re in order to understand further the corresponding studies of thin-film coatings of Ir on Re. Pellets weighing approximately 5 g were pressed from 50:50 mixes (atomic %) of pure Ir and Re powders. The pellets were heated up to 1800 C in vacuum. The resulting diffraction spectra were identical to spectra observed for heated thin-films of Ir and Re

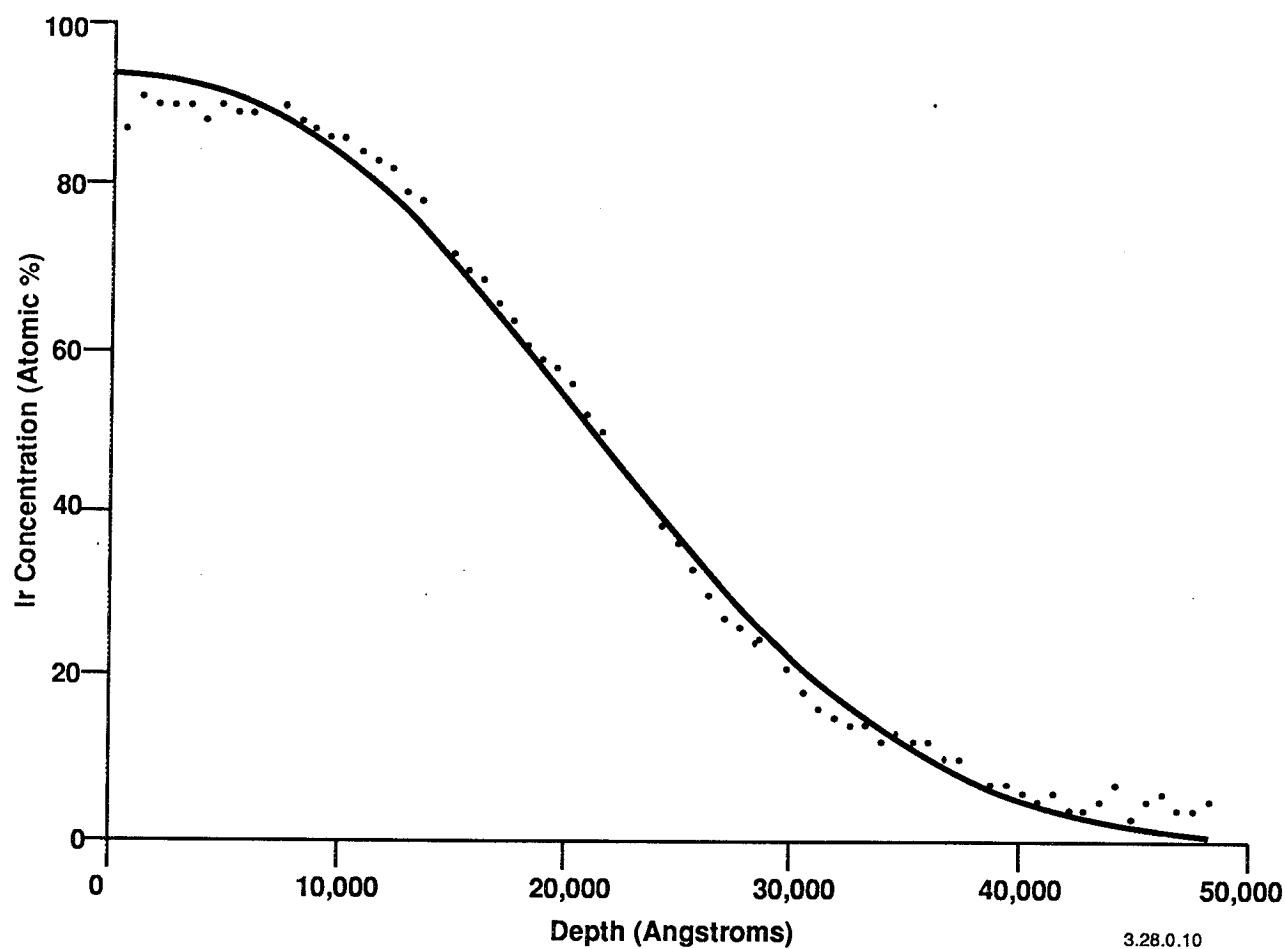


Figure 4.5.2-24. Auger depth profile of rhenium coated with $\sim 2.5 \mu$ of Ir, Heated to 1200°C for 45 minutes. A theoretical fit to the data is shown (solid line). From this a diffusivity $2.4 \times 10^{-12} \text{cm}^2/\text{sec}$ is calculated for $T=1200^\circ\text{C}$.

4.5, High Temperature Materials Tests (Sandia) (cont.)

powders. The pellets were heated up to 1800 C in vacuum. The resulting diffraction spectra were identical to spectra observed for heated thin-films of Ir on Re foils. Figure 4.5.2-25 compares X-ray diffraction spectra for a pressed pellet and a thin-film specimen (peaks that do not appear in the pellet spectra result from a small Ta contamination from the furnace). The combination of thin-film and pressed pellet studies indicate that, upon heating, the Ir-Re reaction produces a solid solution phase of hexagonal close packed (h.c.p.) structure with lattice parameters similar to those of pure Re. These data correspond to earlier studies of h.c.p. noble metal alloys (Ref. 9). The lattice parameters calculated for the characteristic phase produced in the thin-film and pressed pellet samples correspond to a atomic composition of approximately Re-40% Ir, based on data reported in the earlier studies of these materials. In Figure 4.5.2-26 the diffusion constants obtained as a function of temperature are plotted.

Diffusion is generally modeled as an activated process

$$D = D_0 e^{-E/kT}$$

where E is the activation energy for diffusion, T is the temperature, and k is Boltzmann's constant. Based on the fit shown in the figure an activation energy of 1.85 eV is measured. This activation energy is roughly half of the estimated self diffusion energy for iridium or rhenium. Activation energies of this magnitude are typical of grain boundary diffusion. This is the most likely diffusion mechanism in this case.

These measurements of the activation energy allow the prediction of diffusion rates at thruster operating temperatures. The composition profile predicted for a 50 μ m Ir coating on Re annealed at 2000°C for 5 hours is shown in Figure 4.5.2-27. For these exposure conditions, ~20% Re is predicted at the surface. Diffusion of this magnitude would likely lead to failure by volatilization of rhenium oxides at the surface. Fortunately, measurements of CVD coatings at Aerojet indicate a much slower diffusion rate with an interdiffusion zone on the order of 8 μ m thick after two hour vacuum anneal at 2200°C. For sputter-deposited coatings at temperatures >1500°C, we have also observed slower diffusion than predicted using 1.85eV activation energy. This discrepancy was clarified by subsequent re-evaluation of the diffusion process as one of diffusion into a semi-infinite medium where the boundary is kept at a constant concentration.

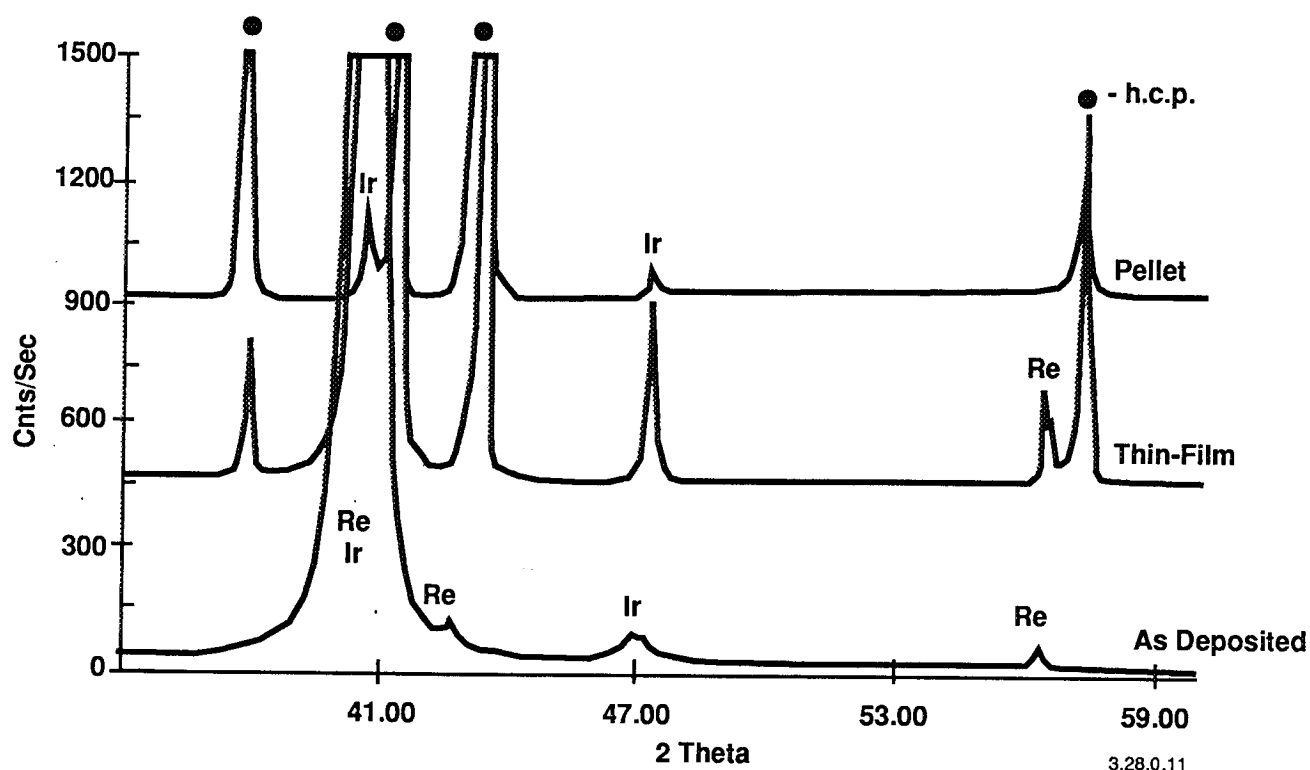


Figure 4.5.2-25. Comparison of X-ray diffraction spectra for heated Ir-Re pellet (top), heated thin-film deposit (Middle), and as deposited thin-film of Ir on Re (bottom). The h.c.p. solid solution phase is identified by the black dots above each of its corresponding peaks. The Re peaks in the heated thin-film (middle-spectra) correspond to the underlying Re foil.

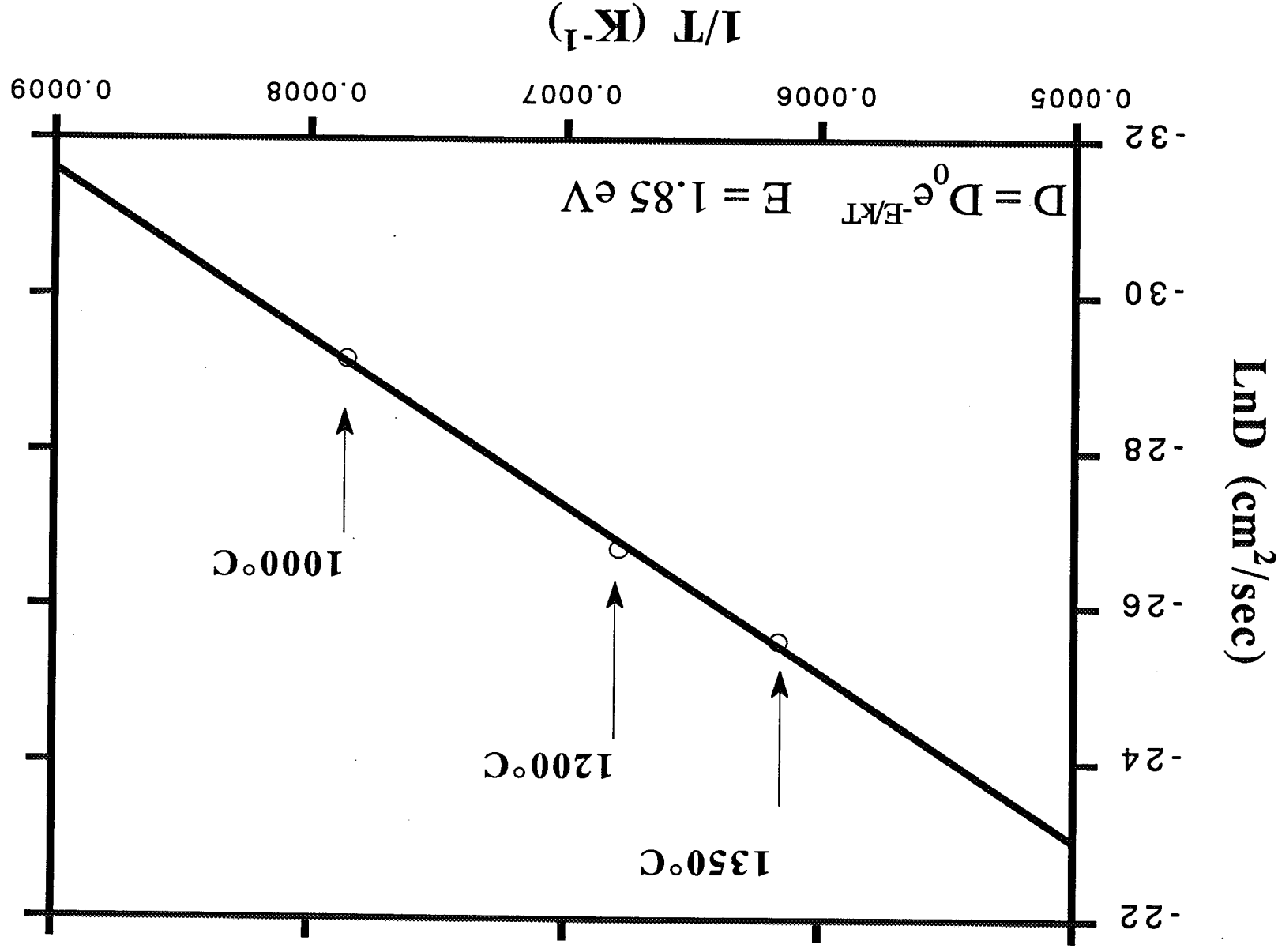


Figure 4.5-2-26. Diffusion Constants Obtained as a Function of Temperature Plotted

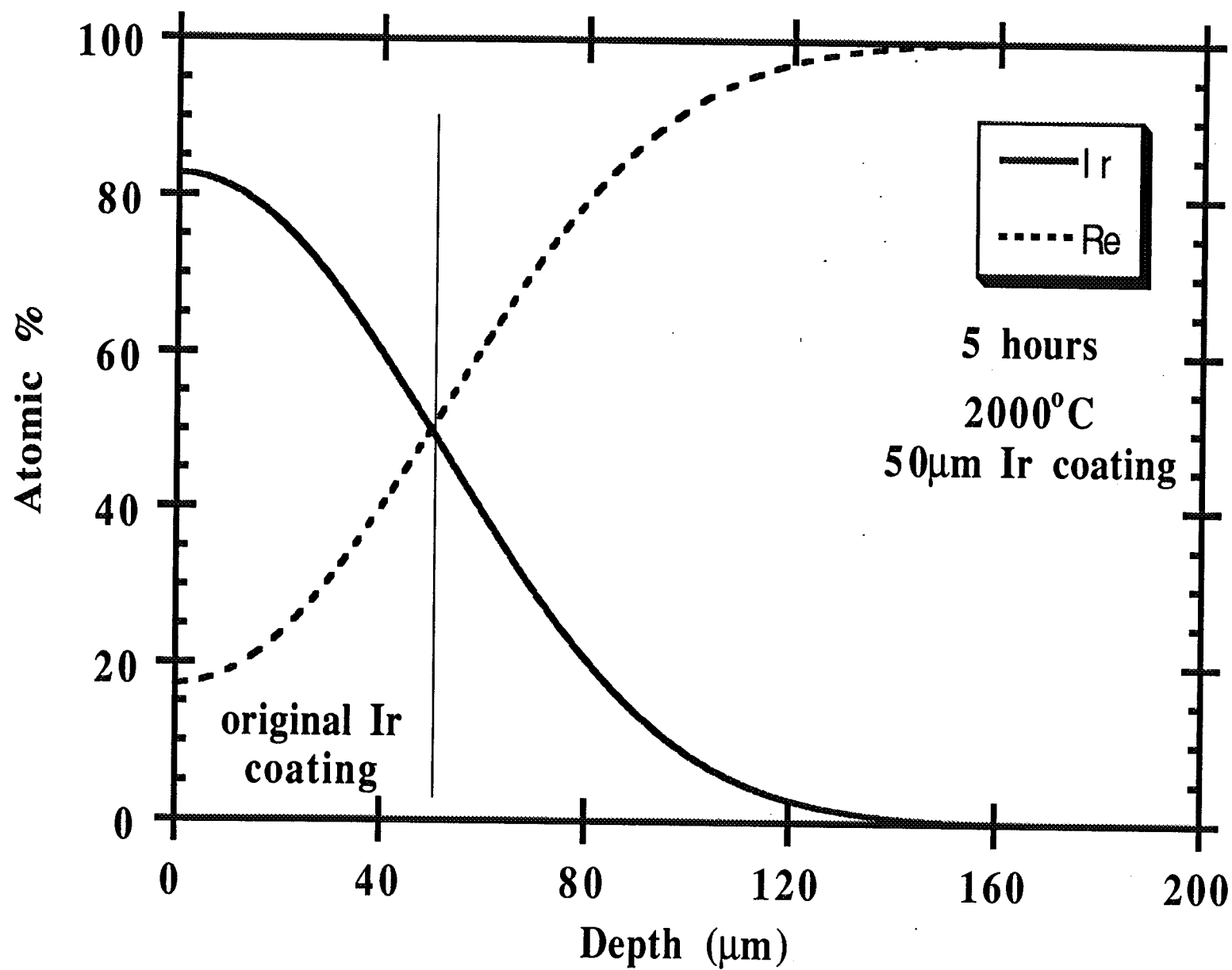


Figure 4.5.2-27. Composition Profile Predicted for a 50μm Ir Coating on Re Annealed at 2000°C for 5 Hours

4.5, High Temperature Materials Tests (Sandia) (cont.)

In order to better understand the mechanisms of diffusion in CVD Ir-Re an end ring sample was fractured in ultra high vacuum and then analyzed using scanning Auger microscopy. This technique is invaluable since it provides information on grain boundary composition which cannot be obtained by other methods. Since grain boundary diffusion is much more rapid than bulk diffusion it generally dominates the overall diffusion process in engineering materials. Obviously the rate of grain boundary diffusion can be affected by impurities which concentrate preferentially at grain boundaries due to segregation or precipitation from the bulk.

A fracture sample was prepared from Ultramet CVD Ir/Re cut from an end ring, part no. 7154-3-2-L-4 dated 8/8/90. Notches were cut in a small rectangular sample which serve to initiate fracture with the fracture plane containing a cross section of the Ir/Re interface. This geometry allows examination of freshly fractured Ir, Re, and of the interdiffusion zone formed during CVC processing at temperature. See Figure 4.5.2-28. The sample was cooled to about -150°C in order to insure low ductility during fracture. The sample was fractured inside the Auger vacuum system at a pressure of 2×10^{-10} torr. During fracture some delamination was observed, resulting in a fissure. This delamination is probably related to the delamination observed at this interface in some previous CVD samples. One must bear in mind that the process of fracture imposes severe stresses on the material which do not occur in normal use. Thus this delamination is probably not significant for normal operation of the thrusters. The Ir layer and the Ir/Re interdiffusion zone fractured intergranularly while the Re layer had a mixed fracture mode with some grains breaking and exposing bulk material during the fracture process.

Working quickly in order to minimize contamination from the background gases in the vacuum system, Auger spectra were collected from various points along the fracture to determine grain boundary composition. Figure 4.5.2-29 shows Auger spectra from the surface of a rhenium grain. The rhenium grain boundaries showed carbon with a carbidic peak shape. The carbon concentration was between 20 and 23 atomic % (this is an average value for the outer several atomic layers). These results are consistent with a model having approximately two monolayers of rhenium carbide in the grain boundary. The rhenium grain boundaries also showed an oxygen concentration of 11 to 15 atomic %, consistent with submonolayer concentrations of oxide at the fracture surface.

Since carbon (from background CO) and oxygen (from background CO and H_2O) are common contaminants in vacuum systems which easily form on freshly cleaned or

Approximate Dimensions:

Length: $\frac{3}{4}$ inch

Width: $\frac{1}{10}$ inch

Height: $\frac{1}{10}$ inch

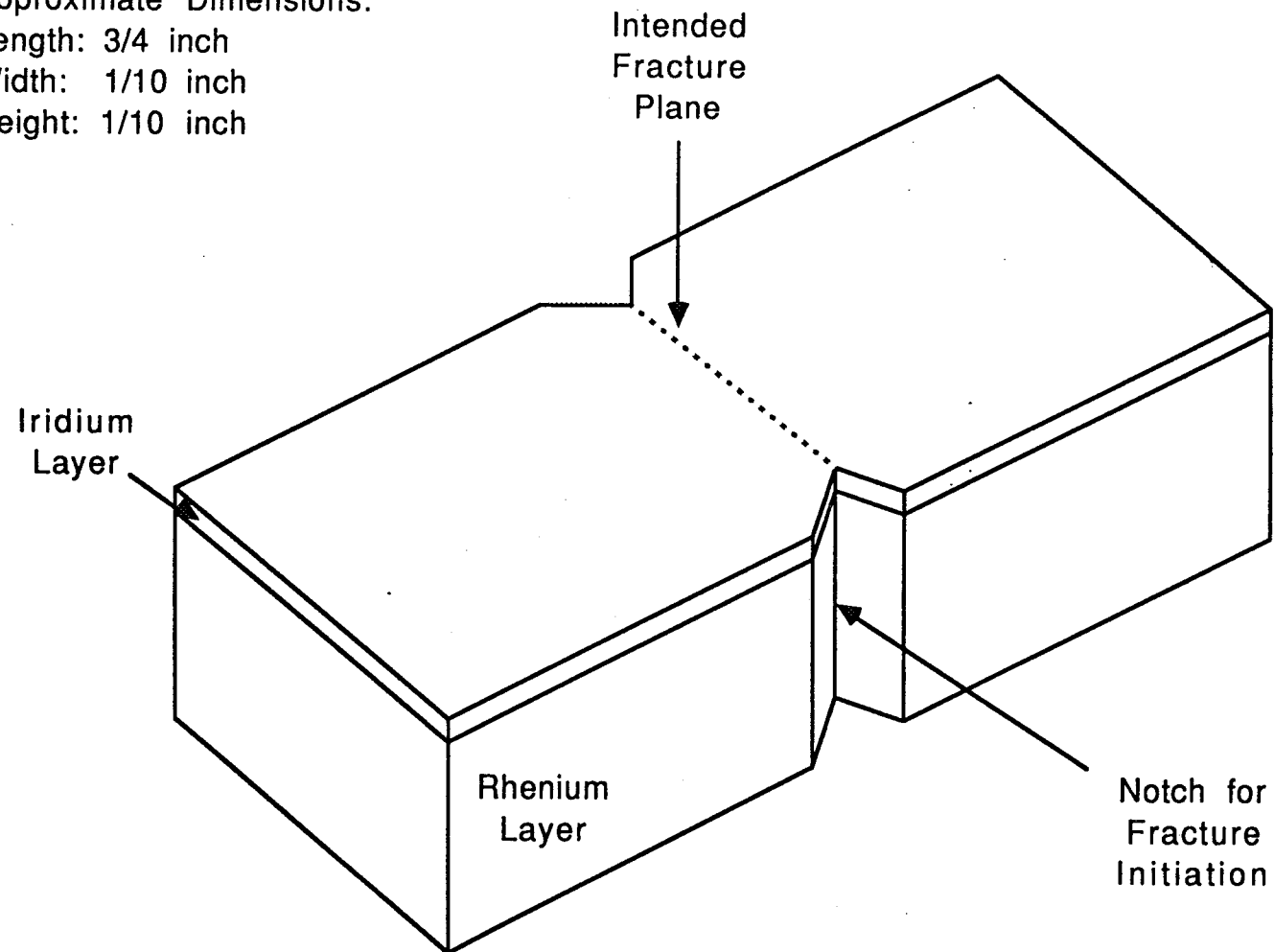


Figure 4.5.2-28 Geometry and Approximate Dimensions for Fracture Sample

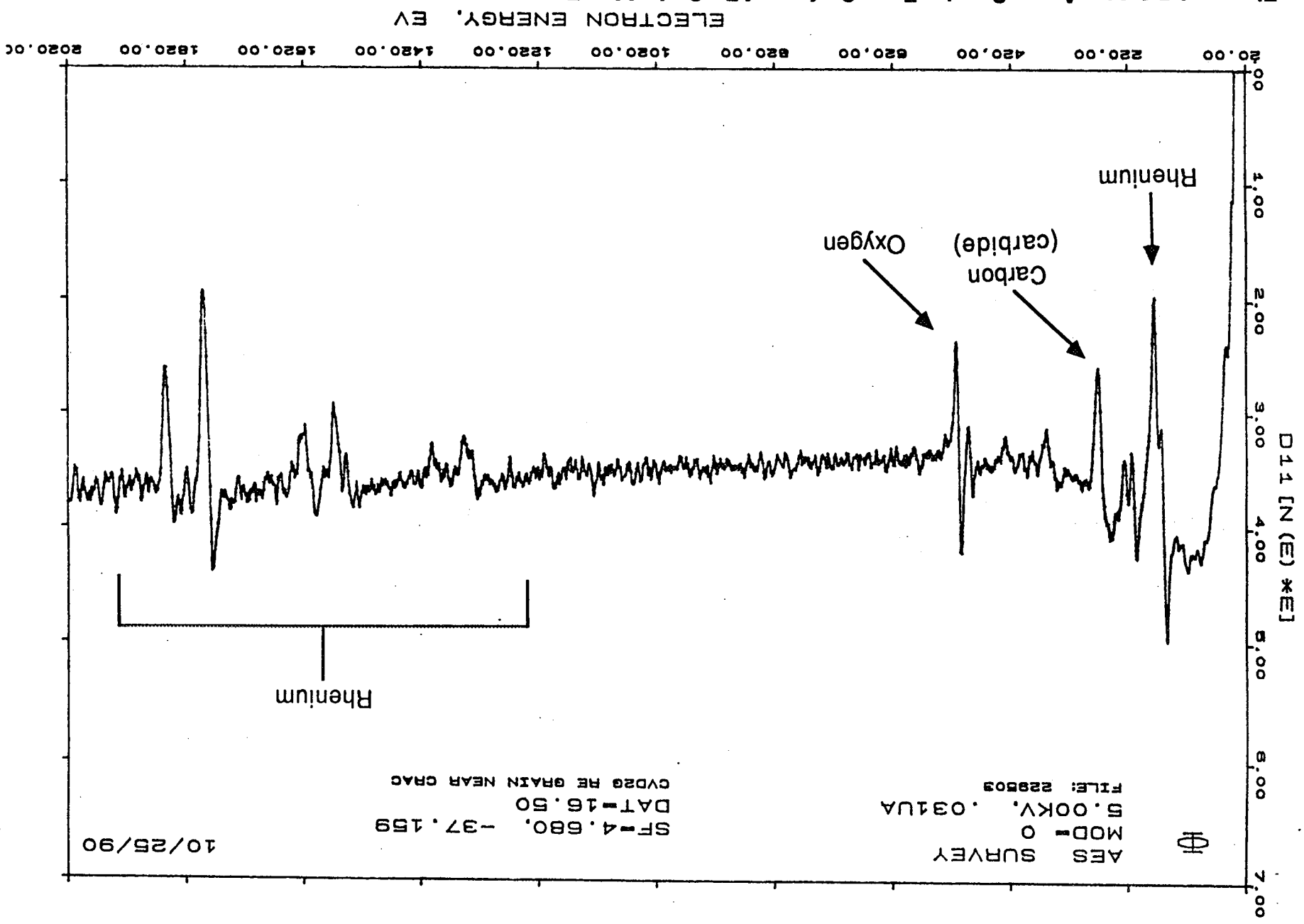


Figure 4.5.2-29. Auger Spectra From Surface of Re Grain After Fracture. Total Vacuum Exposure After Fracture was 23 Minutes With Less Than 2 Minutes of Electron Beam Exposure. Carbon Concentration is 23 Atomic % and Oxygen Concentration is 14 Atomic %

4.5, High Temperature Materials Tests (Sandia) (cont.)

fractured surfaces, experiments were also conducted to determine the maximum level of contamination that could possibly have occurred from the background. After completing the above analysis, the fracture surfaces were cleaned by sputtering and then exposed to the background vacuum gases at 2×10^{-10} torr. Figure 4.5.2-30 shows the atomic % for carbon and oxygen observed as a function of time during exposure to background and electron beam. After vacuum and electron beam exposures similar to those experienced during the analysis of freshly fractured samples, carbon and oxygen levels grew to about 6 atomic % on rhenium. The peak shape for the carbon was carbidic indicating the propensity of rhenium to form carbide. On iridium, 3 atomic % of graphitic carbon was observed with no oxygen after comparable background and beam exposure. These results allow us to be confident that the carbon and oxygen observed on the fractured surfaces are largely due to grain boundary species which form preferentially by segregation or precipitation from the bulk.

In addition to examination of the grain boundaries in Re and Ir, the material in the interdiffusion zone where delamination had occurred during fracture was studied. The material on the rhenium side after delamination of the iridium showed a 2:1 atomic ratio for Ir:Re indicating substantial interdiffusion as expected. The analysis confirms that delamination had in fact occurred in the interdiffusion zone.

The presence of rhenium carbide in the grain boundaries could clearly affect the rate of interdiffusion for these thrusters. Suggestions have been made at JPL that efforts should be made to eliminate all carbon from these materials assuming it to be a deleterious contaminant. We would urge caution until the harmful effect of carbon is demonstrated. It is conceivable that the carbon may slow diffusion. Further studies of the effect of carbon in these oxidation resistant coatings are desirable.

Interdiffusion of iridium and rhenium occurs slowly in Ultramet CVD end ring samples compared to diffusion couples prepared by sputtering iridium onto rhenium foil at Sandia. This relatively slow interdiffusion rate is critical to the successful operation of thrusters since rapid diffusion of rhenium through iridium would result in catastrophic failure due to vaporization of volatile rhenium oxides. In order to understand this slow interdiffusion, we have examined end ring sections using electron microprobe analysis (EMPA) and X-ray diffraction (XRD). Since Ir and Re are chemical vapor deposited at elevated temperature, some interdiffusion occurs during thruster manufacture. End ring sections were also annealed at high temperatures to determine if further interdiffusion and/or grain growth occurs during thruster operation.

Contamination of Clean CVD Rhenium
by Background Vacuum and Electron Beam

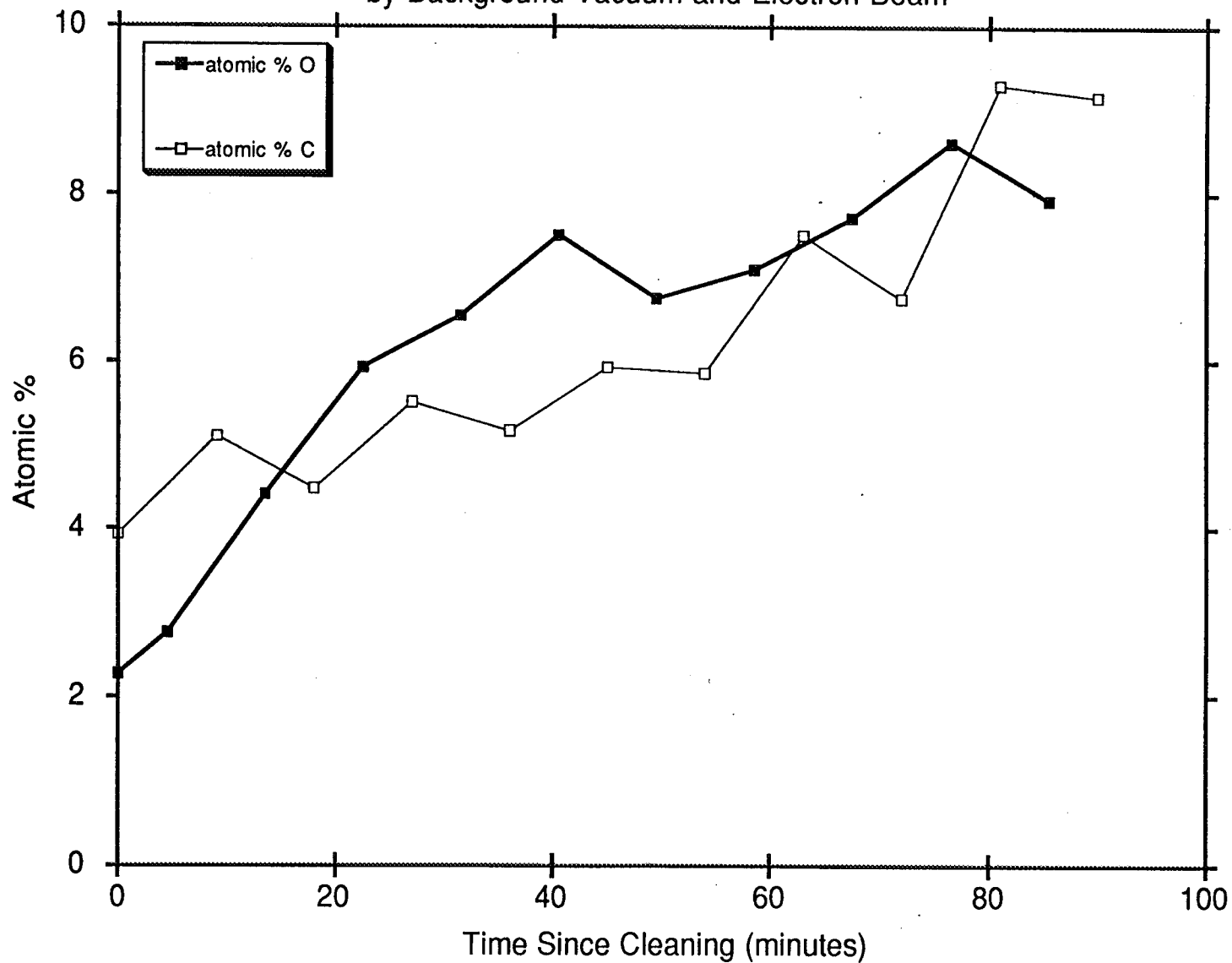


Figure 4.5.2-30. Atomic Compositions Measured From Freshly Sputtered Rhenium Surface During Exposure to Ambient Vacuum and Electron Beam

4.5, High Temperature Materials Tests (Sandia) (cont.)

A sample was cross sectioned from an end ring, Part No. 7154-3-2-L-4, and polished perpendicular to the Ir-Re interface. Figures 4.5.2-31 and 4.5.2-32 are microphotographs of this cross-section. The Ir surface (to be exposed to combustion gases during operation) shows two Ir-Mo interdiffusion layers with a total thickness of 2-3 μm . X-ray analysis identifies these layers as IrMo and Ir₃Mo, presumably formed by reaction between Ir and the Mo mandrel used for fabrication. Similar results have been seen for the inner Ir surface of all CVD samples analyzed at Sandia.

Also visible in Figures 4.5.2-31 and 4.5.2-32 is a narrow Ir-Re interdiffusion region less than 3 μm thick. Figure 4.5.2-33 shows electron microprobe analysis of the elemental composition as a function of distance across this interdiffusion region. X-ray diffraction identifies a diffusion layer phase with approximate composition Ir₆₀Re₄₀. This composition is estimated based upon lattice parameter calculations and other investigations of the Ir-Re solid solution system reported in the open literature. A similar composition has also been seen at the Ir/Re interface of diffusion couples produced at Sandia by sputter deposition of Ir on Re foil with subsequent vacuum annealing. The formation of a stable composition in the interdiffusion layer appears to occur for all Ir/Re interdiffusion systems studied to date and suggests the possibility of a blocking layer which acts as a diffusion barrier.

Figure 4.5.2-31 also shows a 40 μm zone in the Re adjacent to the Ir/Re interface which contains small microvoids. These microvoids are presumably formed as Re is removed by diffusion into the Ir overlayer. These voids occur randomly and are not associated with grain boundaries. The absence of voids near the grain boundaries would argue in favor of bulk diffusion as the dominant mechanism for interdiffusion during formation of these coatings. In addition to the microvoids, second phase particles and structures were observed in the Re adjacent to the Ir/Re interface (see Figure 4.5.2-34). Examination of the remainder of the CVD rhenium revealed four distinct Re layers with varying grain size and morphology. The layers showed progressively larger grain size and equiaxed grains toward the Ir/Re interface.

A sample was cut from an end ring, Part No. 7154-3-2L-4, and annealed in an alumina boat in a vacuum furnace. After cooling, the sample was cut in half and polished perpendicular to the Ir-Re interface. Figure 4.5.2-35 shows a micrograph of this cross section. The grain structure in the iridium coating is clearly visible at this magnification. The average iridium grain size is about 10 μm . A different magnification shows the average grain size in the rhenium layer to be about 400 μm . The grain structure is essentially identical to that observed and

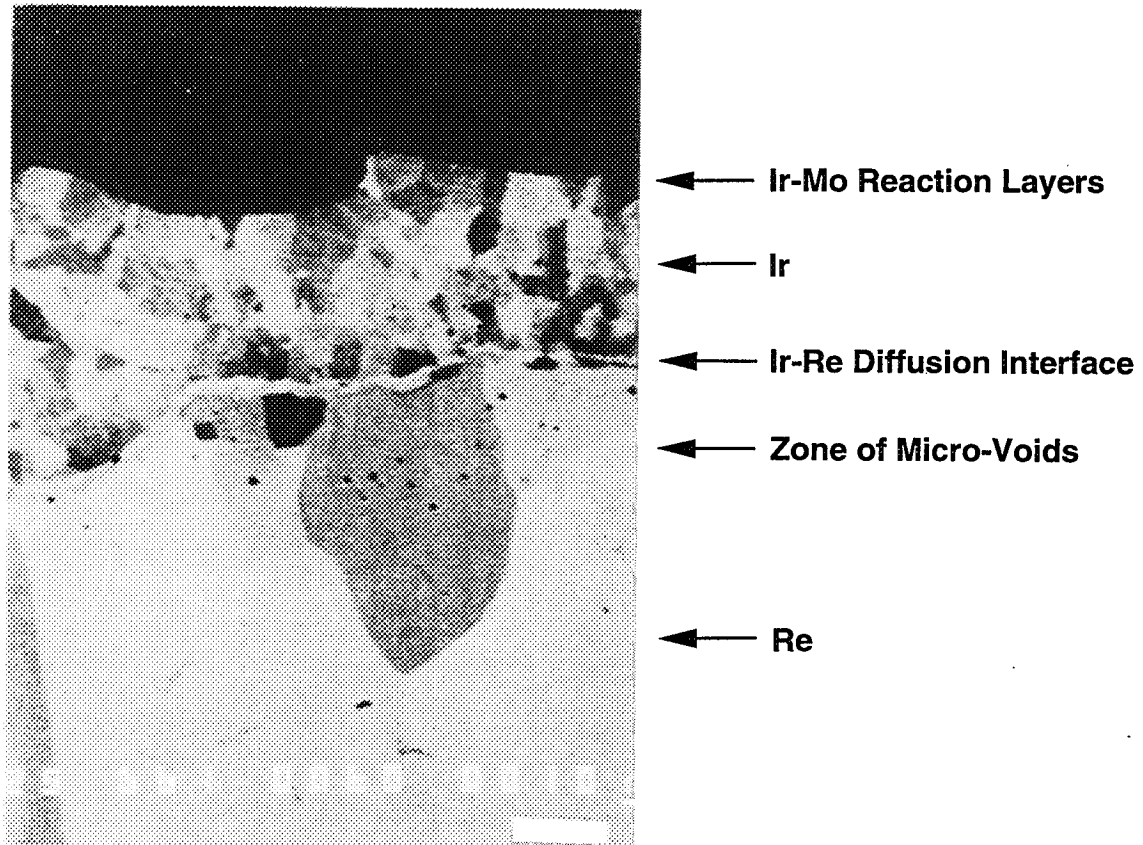


Figure 4.5.2-31. Cross-Section of CVD End Ring Polished Perpendicular to the Ir-Re Interface. Horizontal Bar at Lower Right of the Microphoto is Equal to 10 Microns

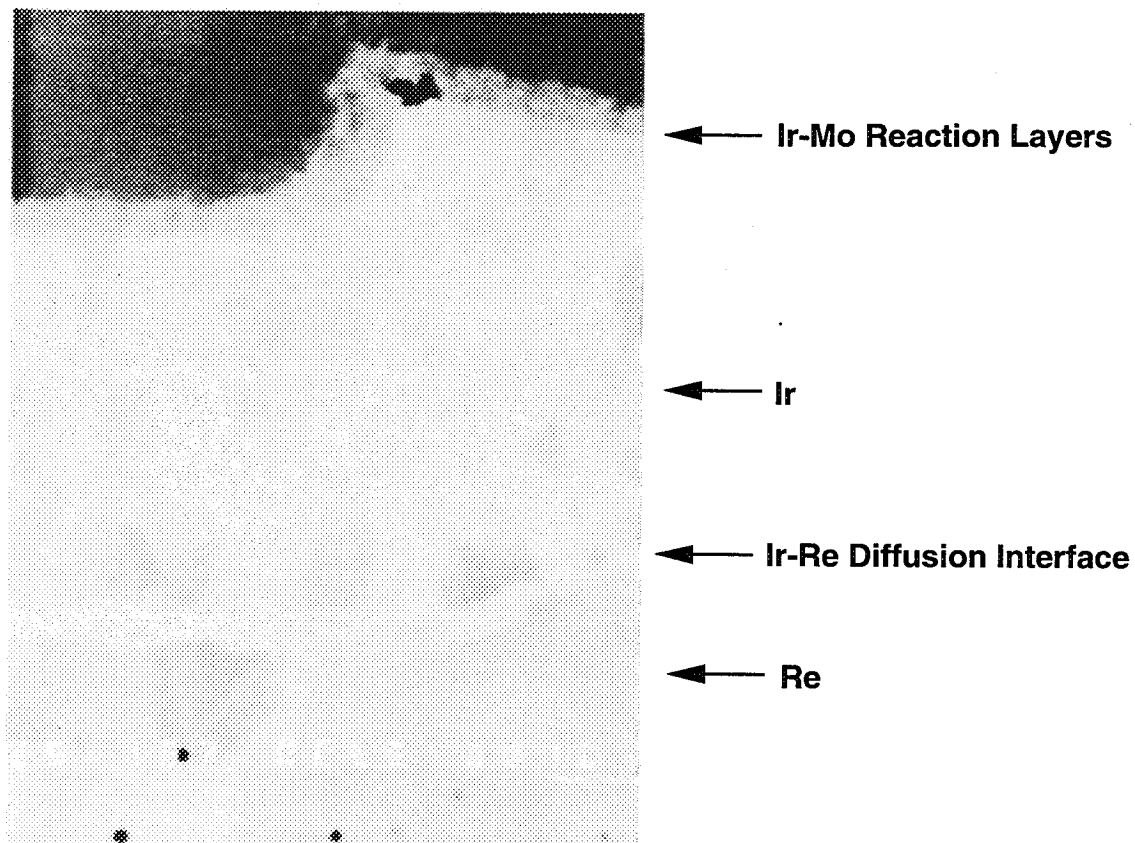


Figure 4.5.2-32. Cross-Section of CVD End Ring Polished Perpendicular to the Ir-Re Interface. The Magnification from Figure 4.5.2-31 Clearly Shows the Narrow Ir-Re Interface and the Ir-Mo Layers on the Ir

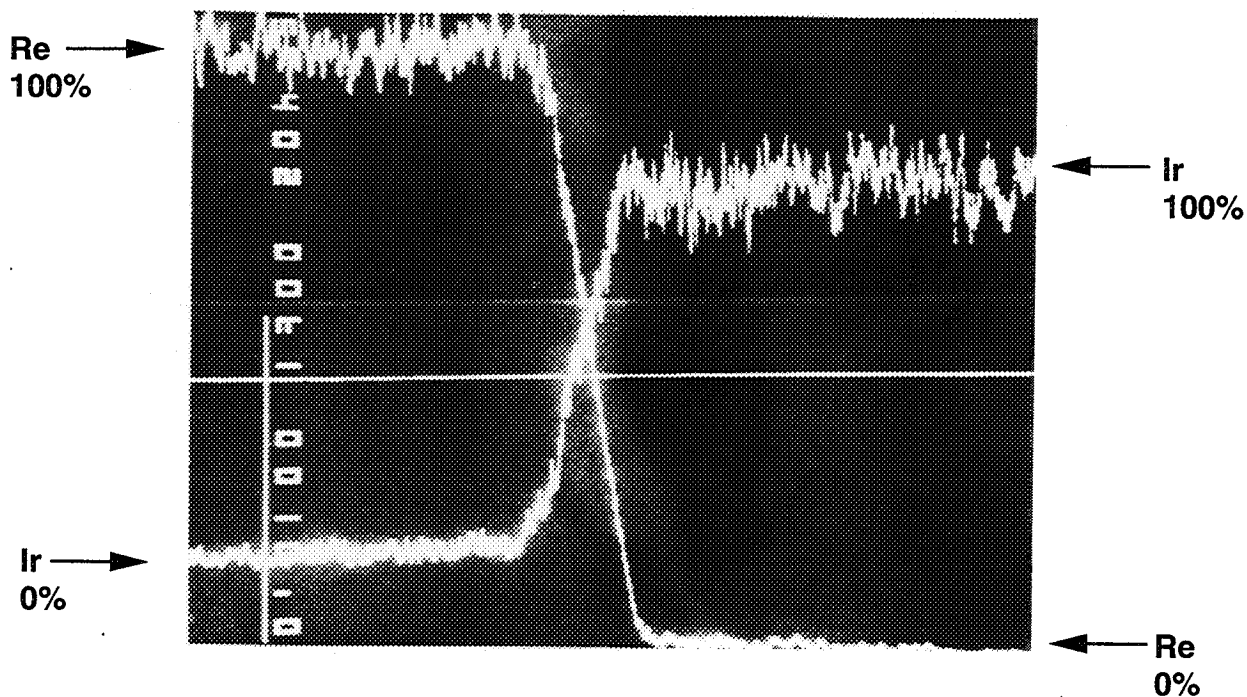


Figure 4.5.2-33. Electron Microprobe Elemental Trace for Ir and Re Across the Diffusion Interface. The Sharp Elemental Cross Over Region Identifies the Diffusion Zone

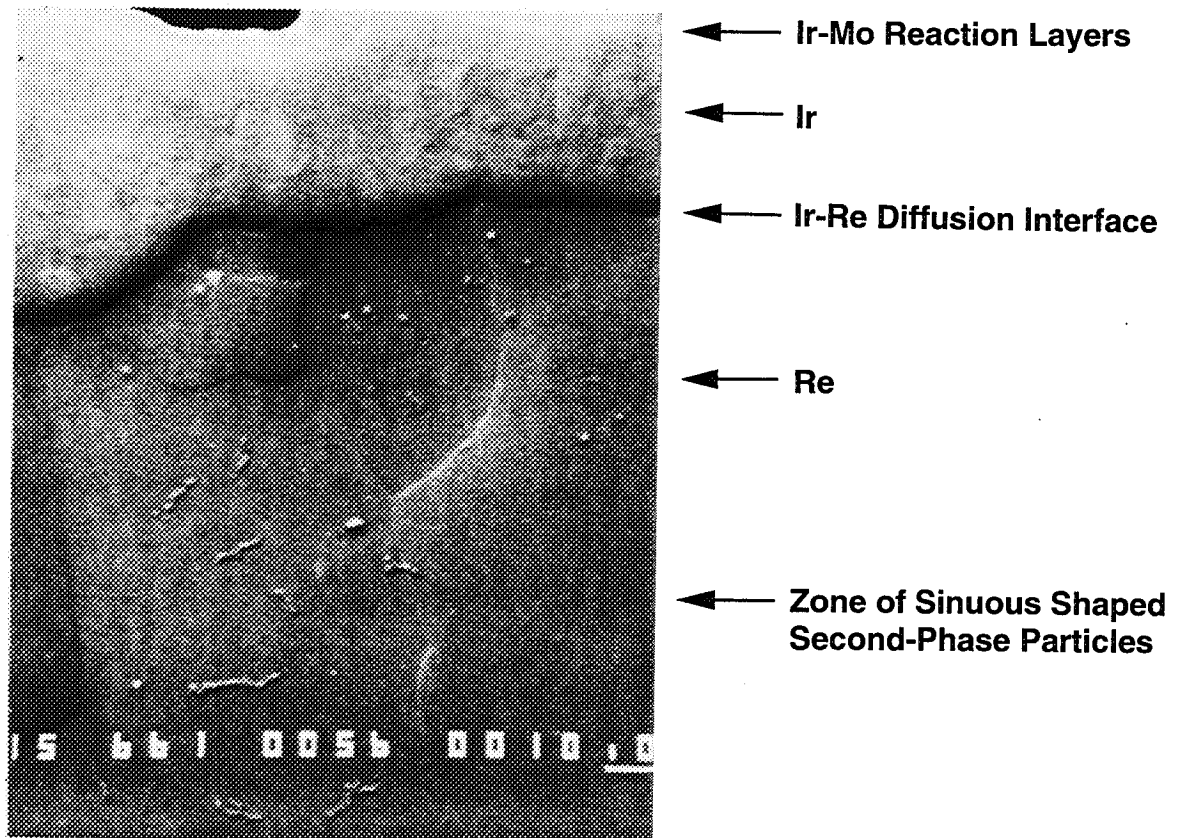
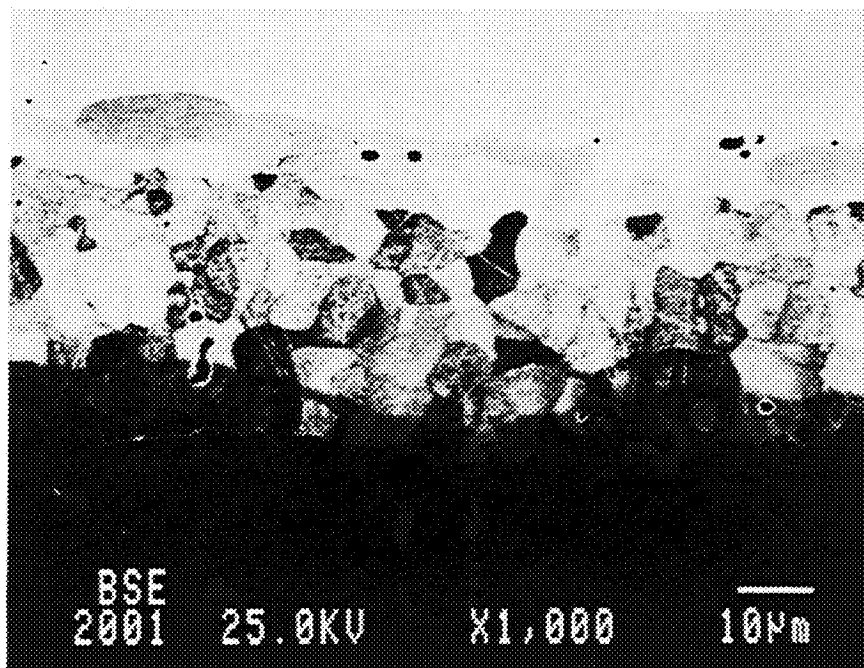
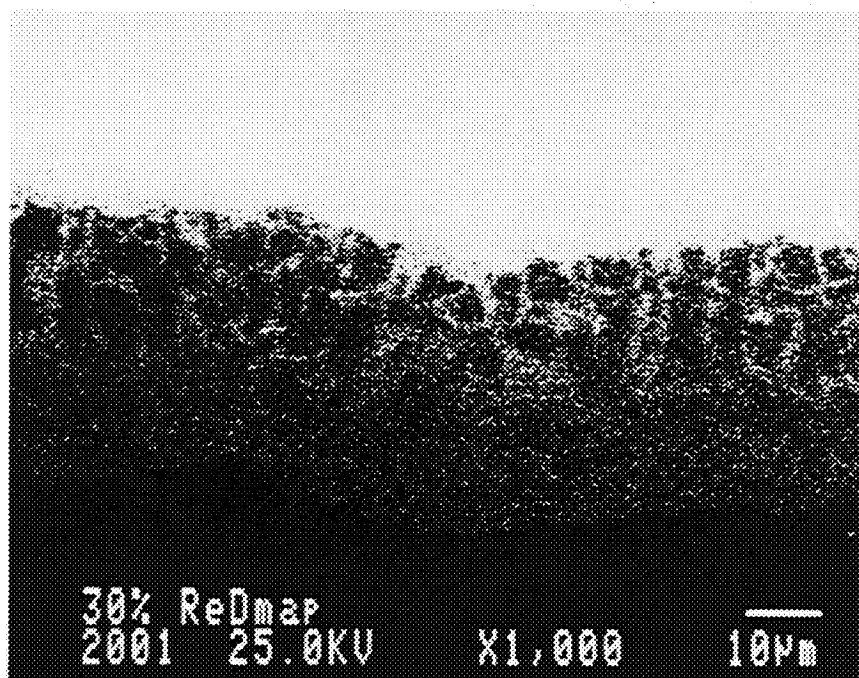


Figure 4.5.2-34. Cross-Section of CVD End Ring Polished Perpendicular to the Ir-Re Interface. This Secondary Electron Image (SEI) Shows the Additional Structures Observed Within the Re Along the Ir-Re Interface



**Figure 4.5.2-35. Micrograph of Iridium-Coated Rhenium End Ring Section
After Vacuum Anneal for 14 hrs at 1400°C**



**Figure 4.5.2-36. Elemental Map for Rhenium in Annealed
End Ring Section**

4.5, High Temperature Materials Tests (Sandia) (cont.)

reported previously for the as deposited coatings. We conclude that no grain growth occurs during extended anneals at 1400°C.

Figures 4.5.2-36, -37, and -38 show elemental maps for Re, Ir, and Mo respectively in this sample. From these figures, we can draw several conclusions regarding diffusion in these CVD materials. The Re map shows considerable Re diffusion along grain boundaries with Re penetrating approximately 25 μ m into the Ir coating. Clearly grain boundary diffusion is much faster than bulk diffusion for this sample. The Ir map shows little or no diffusion of Ir into the Re by bulk or grain boundary diffusion. The Mo map shows that Mo has diffused from the surface into the Ir. The Mo diffusion is similar to the Re diffusion in that grain boundary diffusion dominates and Mo has penetrated a substantial fraction of the total Ir coating thickness. We note that the Mo concentration in the grain boundaries is considerably smaller than that of Re as might be expected because only a relatively small quantity of Mo was present on the surface prior to annealing. (A total thickness of 2-3 μ m of Ir-Mo compounds was previously reported for the as deposited sample prior to annealing.)

Figure 4.5.2-39 shows a line scan for the Ir concentration as a function of distance perpendicular to the Re-Ir interface. Dips in the Ir concentration which are only a few μ m wide are due to the scan crossing a grain boundary where Re is present. Ignoring these dips the width of the interdiffusion zone is about 10 μ m. A preliminary theoretical fit is also shown in this figure. For these data, the diffusion coefficient D is 1.5×10^{-12} cm²/s. Another line scan resulted in a diffusion coefficient D of 2.2×10^{-12} cm²/s. The difference is an indication of the accuracy of this measurement. This value can be used to predict diffusion for longer times. It tends to underestimate the effect of grain boundary diffusion, however.

Based on these diffusion measurements it appears that these thrusters should provide excellent lifetimes (much greater than 14 hr) in service at 1400°C. (Note that a hot-fire time of 15 hr has been demonstrated on a single Ir-coated Re chamber.)

Additional diffusion measurements were made for a thruster end ring section annealed in vacuum for 8 hr at 1700°C. A sample was cut from the end ring, Part No. 7154-3-2-L-4, and annealed in an alumina boat in a vacuum furnace. After cooling, the sample was cut in half and polished perpendicular to the Ir-Re interface. Figure 4.5.2-40 shows a micrograph of this cross section. The grain structure in the iridium coating is clearly visible at this magnification. The average iridium grain size is about 10 μ m. A different magnification shows the

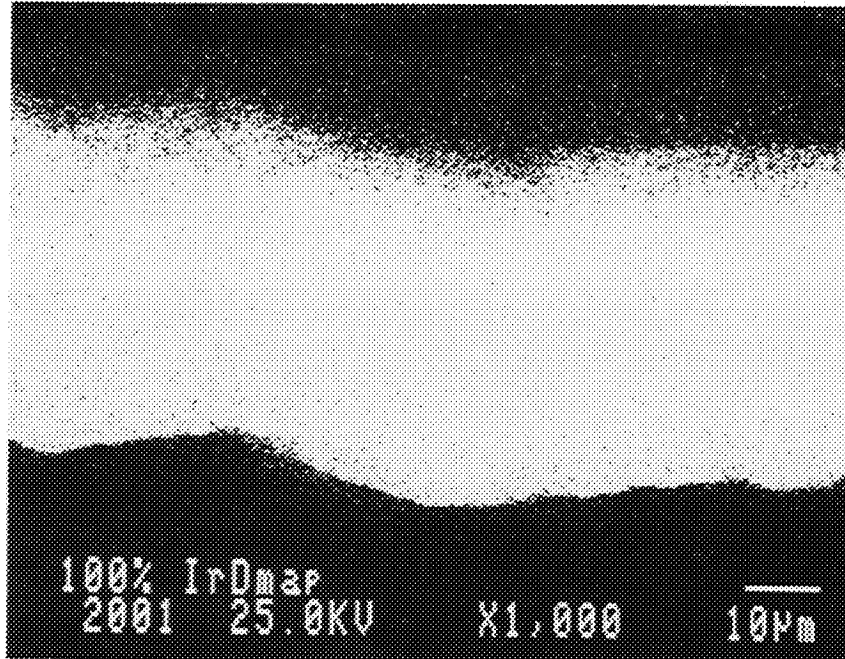


Figure 4.5.2-37. Elemental Map for Iridium in Annealed End Ring Section

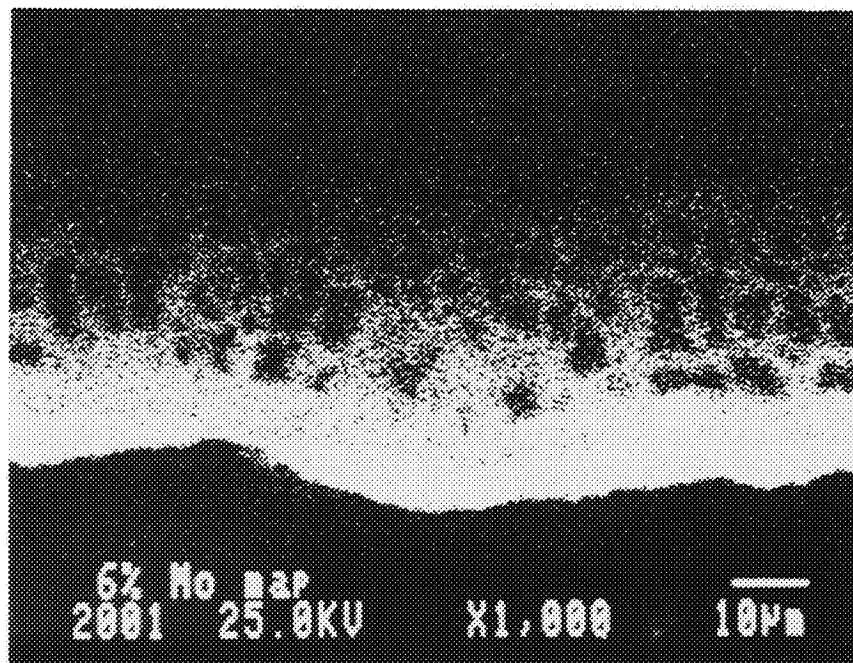


Figure 4.5.2-38. Elemental Map for Molybdenum in Annealed End Ring Section

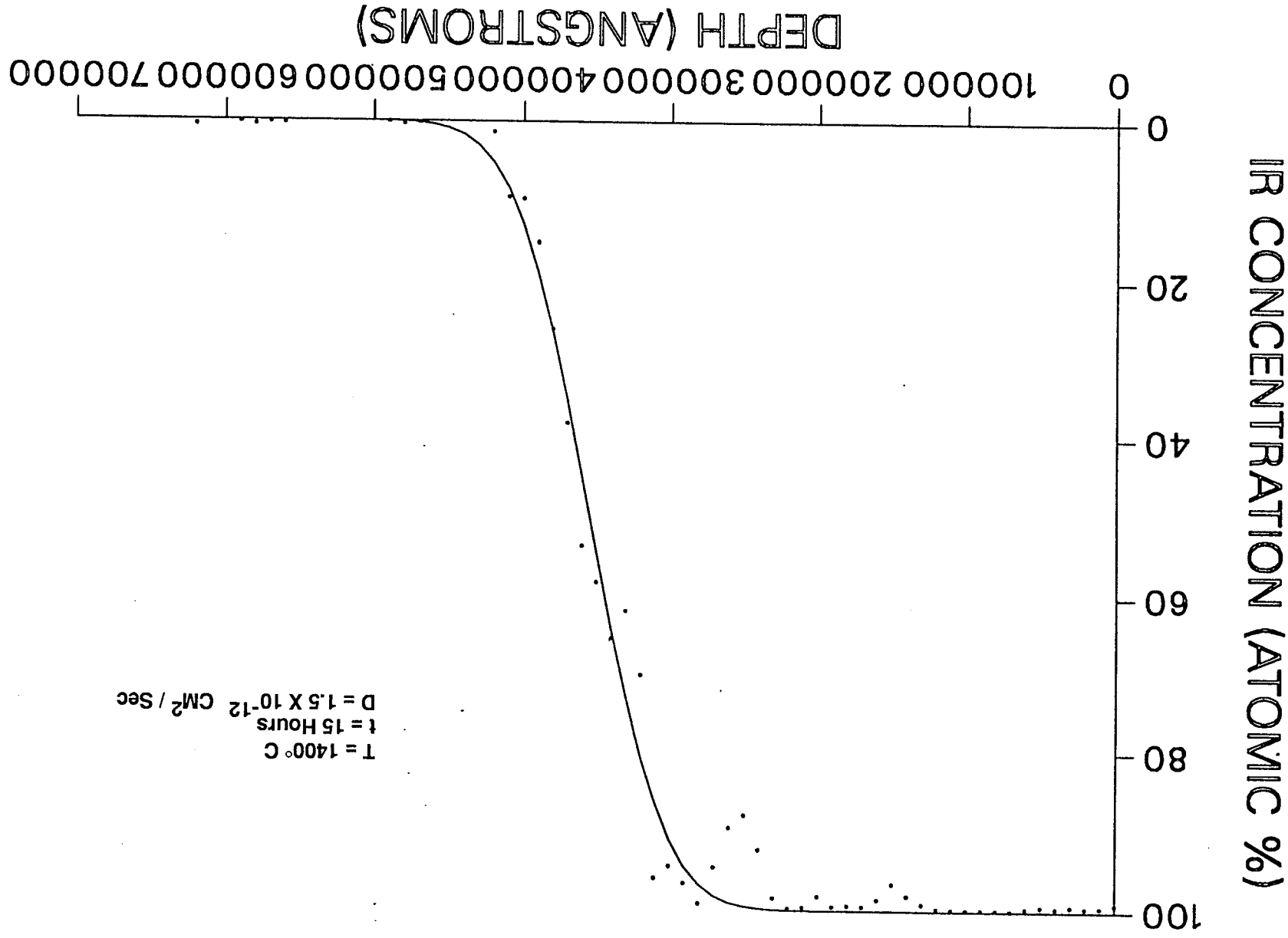


Figure 4.5.2-39. Iridium Concentration versus Depth for End Ring, P/N 7154-3-2-L-4

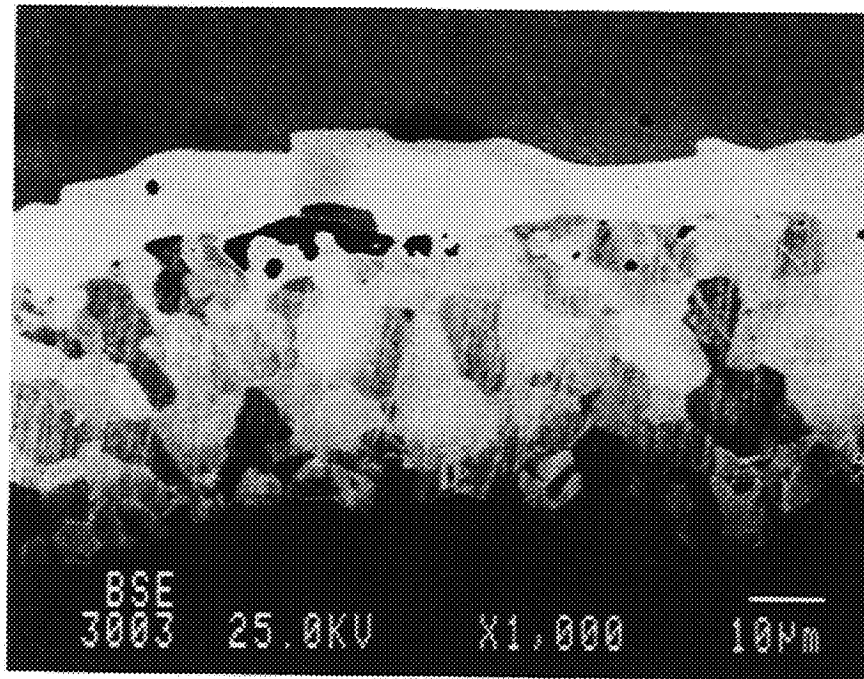


Figure 4.5.2-40. Micrograph of Iridium-Coated Rhenium End Ring Section After Vacuum Anneal for 8 Hours at 1700°C.

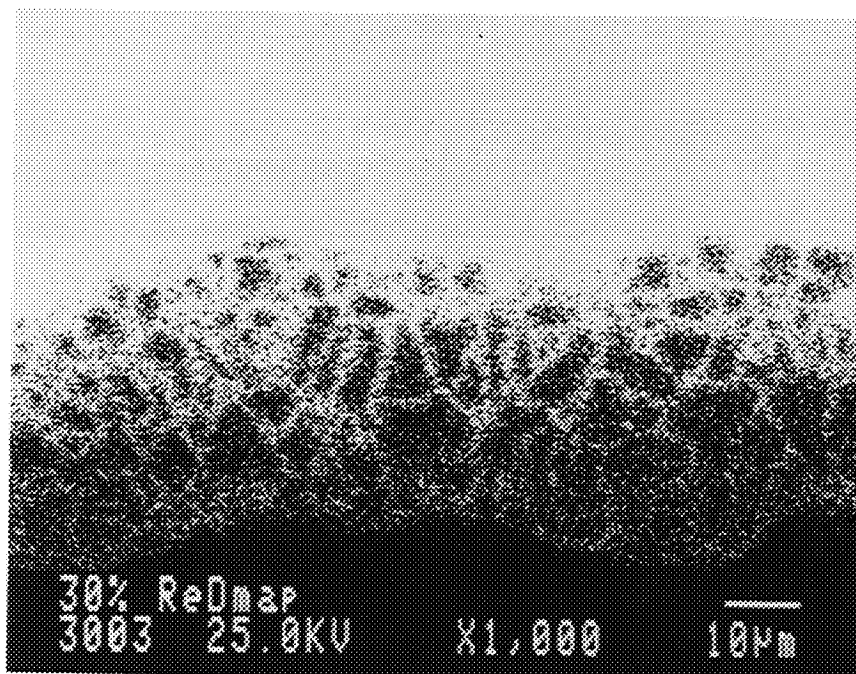


Figure 4.5.2-41. Elemental Map for Rhenium in 1700°C Annealed End Ring Section.

4.5, High Temperature Materials Tests (Sandia) (cont.)

average grain size in the rhenium layer to be about 400 μm . The grain structure is essentially identical to that observed and reported previously for the as-deposited coatings. We conclude that no grain growth occurs during extended anneals at 1700°C.

Figures 4.5.2-41, -42, and -43 show elemental maps for Re, Ir, and Mo in this sample. From these figures we can draw several conclusions regarding diffusion in these CVD materials. The Re map shows considerable rhenium diffusion along grain boundaries with rhenium penetrating approximately 35 μm into the Ir coating, 10 μm farther than at 1400°C. Clearly, grain boundary diffusion is much faster than bulk diffusion for this sample. Otherwise, the results are qualitatively similar to those at 1400°C.

A line scan for the iridium concentration as a function of distance perpendicular to the rhenium-iridium interface shows dips in the iridium concentration which are only a few μm wide are due to the scan crossing a grain boundary where rhenium is present. Ignoring these dips, the width of the interdiffusion zone is about 20 μm (Figure 4.5.2-46)

Examination of the microprobe photographs and of the line scans of the diffusion data for 1700°C and 1400°C annealed samples clearly indicates that diffusion of rhenium into the iridium coating predominates with very little diffusion of iridium into the rhenium. For this case, the equation for diffusion into a semi-infinite medium where the boundary is kept at a constant concentration, C_0 , would be more appropriate than diffusion of an extended source of limited extent as was initially assumed (Ref. 7). By keeping the boundary at a concentration of 100% rhenium, only diffusion of rhenium into iridium is modeled. The appropriate equation is:

$$C = 0.5 C_0 \operatorname{erfc} (x-h)/2\sqrt{Dt} \quad x-h>0 \quad (2)$$

Here C is concentration as a function of time and distance, C_0 is the fixed boundary condition (100% rhenium), h is the depth of the Ir coating on Re, t is the time, x is the distance, and D is the diffusion coefficient.

We have used equations (1) and (2) to fit the line scan data. The theoretical fits to the experimental profile and the resulting diffusion coefficients have been determined. It is clear that allowing only diffusion of rhenium into iridium (i.e., equation 2) provides a much better fit to the experimental data. Compare Figure 4.5.2-39 with Figure 4.5.2-47.

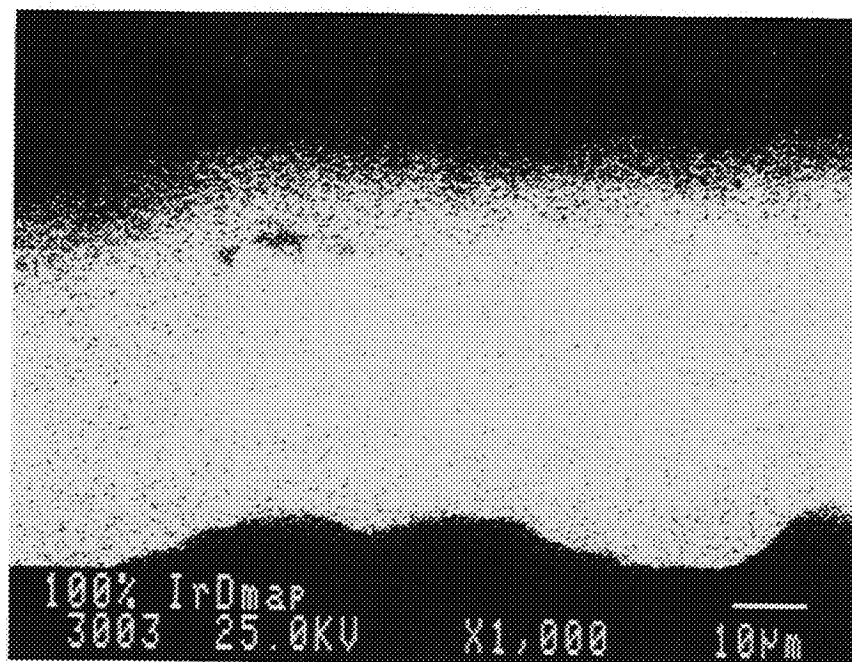


Figure 4.5.2-42. Elemental Map for Iridium in 1700°C Annealed End Ring Section.

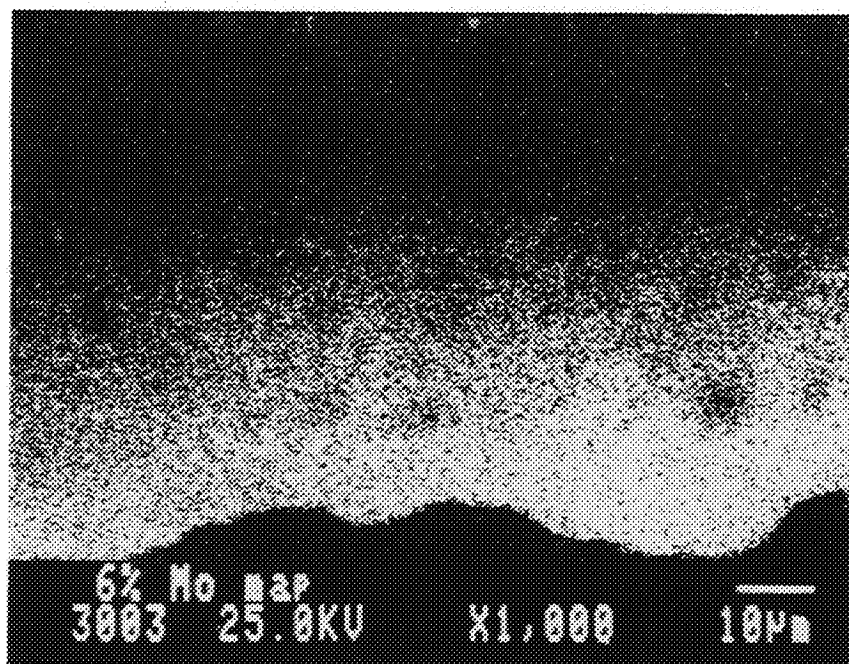


Figure 4.5.2-43. Elemental Map for Molybdenum in Annealed End Ring Section.

4.5, High Temperature Materials Tests (Sandia) (cont.)

Using equation (2), the best fit diffusion coefficient $D(1700^{\circ}\text{C})$ is $2.9 \times 10^{-11} \text{ cm}^2/\text{s}$ (Figure 4.5.2-46). Another line scan resulted in a diffusion coefficient $D(1700^{\circ}\text{C})$ of $2.1 \times 10^{-11} \text{ cm}^2/\text{s}$. The difference is an indication of the accuracy of this measurement. This value can be used in order to predict diffusion for longer times. For these materials with grain size large compared to the probe volume, it is difficult to measure and model grain boundary diffusion properly. Since the grain boundaries are only a small fraction of the measurement volume, their effect on the least square fit for the diffusion constant is minor. Their effect on the overall diffusion process is critical however, as they can provide a short circuit path to the surface. Thus, these diffusion equations and model fits may underestimate the concentration of rhenium at the surface. We are presently working to improve our observations and modeling of grain boundary diffusion. This should substantially improve the accuracy of lifetime predictions.

Using equation (2) to recalculate the diffusion coefficient for the 1400°C sample gives values for the diffusion coefficient from two different line scans of $D(1400^{\circ}\text{C}) = 7.0 \times 10^{-12} \text{ cm}^2/\text{s}$ (Figure 4.5.2-47) and $D(1400^{\circ}\text{C}) = 5.9 \times 10^{-12} \text{ cm}^2/\text{s}$. These values may be compared with the previous method which used equation (1), giving $D(1400^{\circ}\text{C}) = 2.2 \times 10^{-12} \text{ cm}^2/\text{s}$ and $1.5 \times 10^{-12} \text{ cm}^2/\text{s}$ (Figure 4.5.2-39).

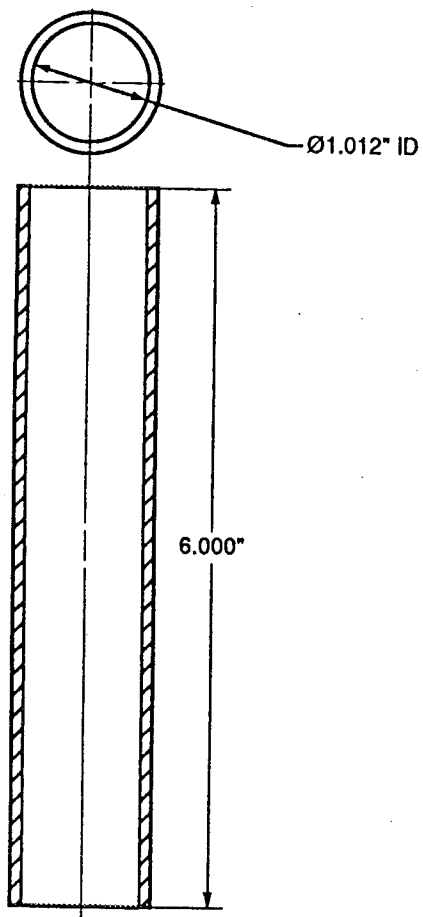
Surface Measurements in MSTA

Iridium coated rhenium test samples were prepared with dimensions appropriate for use in the Materials Sample Test Apparatus (MSTA). This test rig, designed and built by Aerojet and installed at the Sandia Combustion Research Facility, allows materials tests in flame environments simulating an operating thruster. The samples are heated by a hydrogen/oxygen flame and by supplementary electrical resistance heating. These samples will provide a better understanding of oxidation of CVD materials in flame environments.

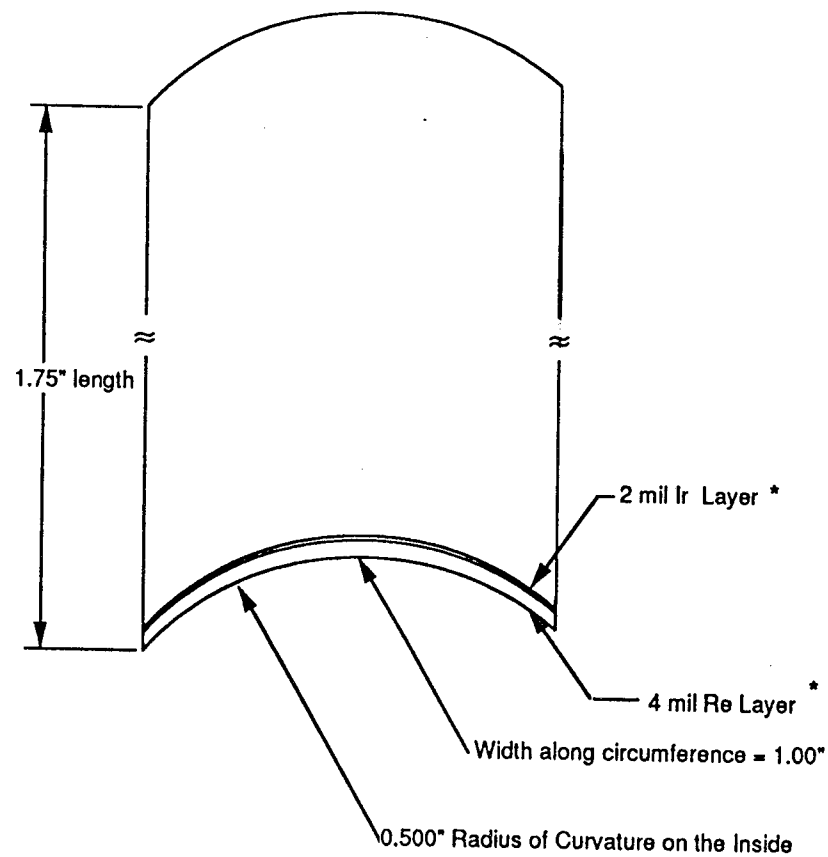
The samples are prepared by coating the interior of a molybdenum tube first with 2 mils of iridium and then 4 mils of rhenium. The tube is then cut to produce curved test specimens as shown in Figure 4.5.2-44. The molybdenum is then removed, leaving a specimen with iridium on the outer curved surface. The coating thicknesses were chosen to produce a sample with suitable resistivity for electrical heating.

Molybdenum Mandrel Tube

To be CVD Coated on the Inside.
with 2mils of Ir then 4 mils of Re



Ir/Re Test Specimens ~Scale 5 to 1



* Layer thicknesses are not to scale
(Exaggerated)

Figure 4.5.2-44. CVD Specimen for MSTA

4.5, High Temperature Materials Tests (Sandia) (cont.)

These specimens are designed to be tested at temperatures in the range 1700-2100C, with examination of the samples postexposure in the microprobe to determine the extent of rhenium diffusion into the iridium and the extent of iridium removal by oxidation.

Analysis of Additional Ir-Re Diffusion Data For Thruster End Ring Material

Diffusion data obtained for end ring sections annealed in vacuum at temperatures of 1400, 1700, and 1900°C are reported. The data for 1400 and 1700°C have been reported previously. The 1900°C data and the temperature dependence of the diffusion rate are new. All three test samples were cut from an end ring, part no. 7154-3-2-L-4, and annealed in alumina boats in a vacuum furnace. After cooling the samples were cut in half and polished perpendicular to the Ir-Re interface. Electron microprobe analysis was used to obtain line scans as a function of distance from the iridium surface. In all cases the predominant diffusion mechanism was rhenium diffusion into the iridium and grain boundary diffusion was the rapid diffusion process (see microprobe photographs presented in previous reports).

Figure 4.5.2-45 shows a line scan for the iridium concentration as a function of distance perpendicular to the rhenium-iridium interface for the 1900°C 8 hr annealed sample. The dots represent experimental data points. Dips in the iridium concentration which are only a few μm wide are due to the scan crossing a grain boundary where rhenium is present. Ignoring these dips the width of the interdiffusion zone is about 40 μm . Figures 4.5.2-46 and -47 present similar data for samples annealed at 1700°C for 8 hr and 1400°C for 14 hr.

The line scans indicate that diffusion of rhenium into the iridium coating predominates with very little diffusion of iridium into the rhenium. For this case, the equation for diffusion into a semi-infinite medium where the boundary is kept at a constant concentration, C_0 , can be used to fit the iridium concentration profile. By keeping the boundary at a concentration of 100% rhenium, only diffusion of rhenium into iridium is modeled. The appropriate equation is:

$$C = C_0 \operatorname{erfc} (x-h)/2\sqrt{Dt} \quad x-h>0 \quad (3)$$

Here C is concentration as a function of time and distance, C_0 is the fixed boundary condition (100% rhenium), h is the depth of the Ir coating on Re, t is the time, x is the distance, and D is the diffusion coefficient.

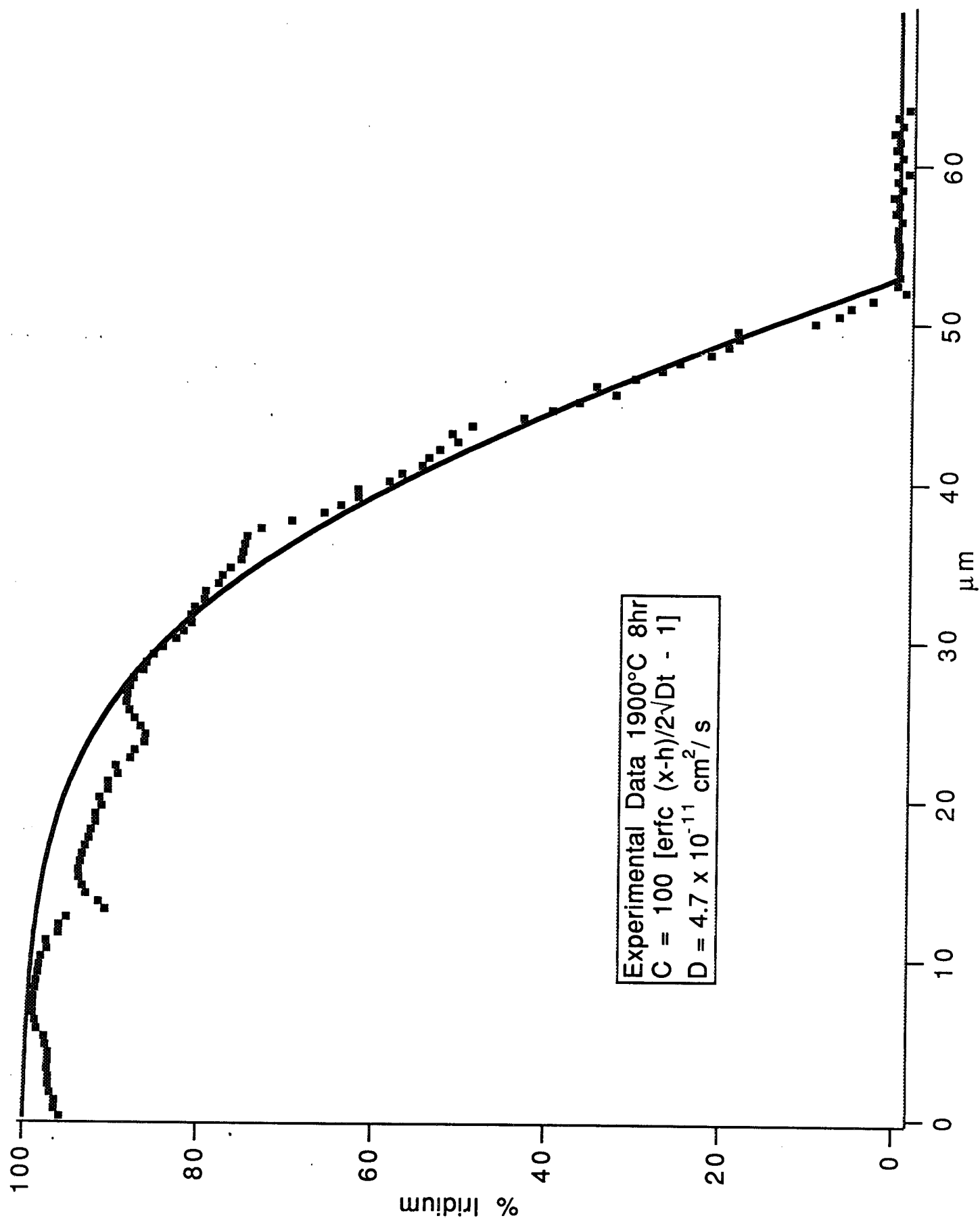


FIGURE 15-3-15

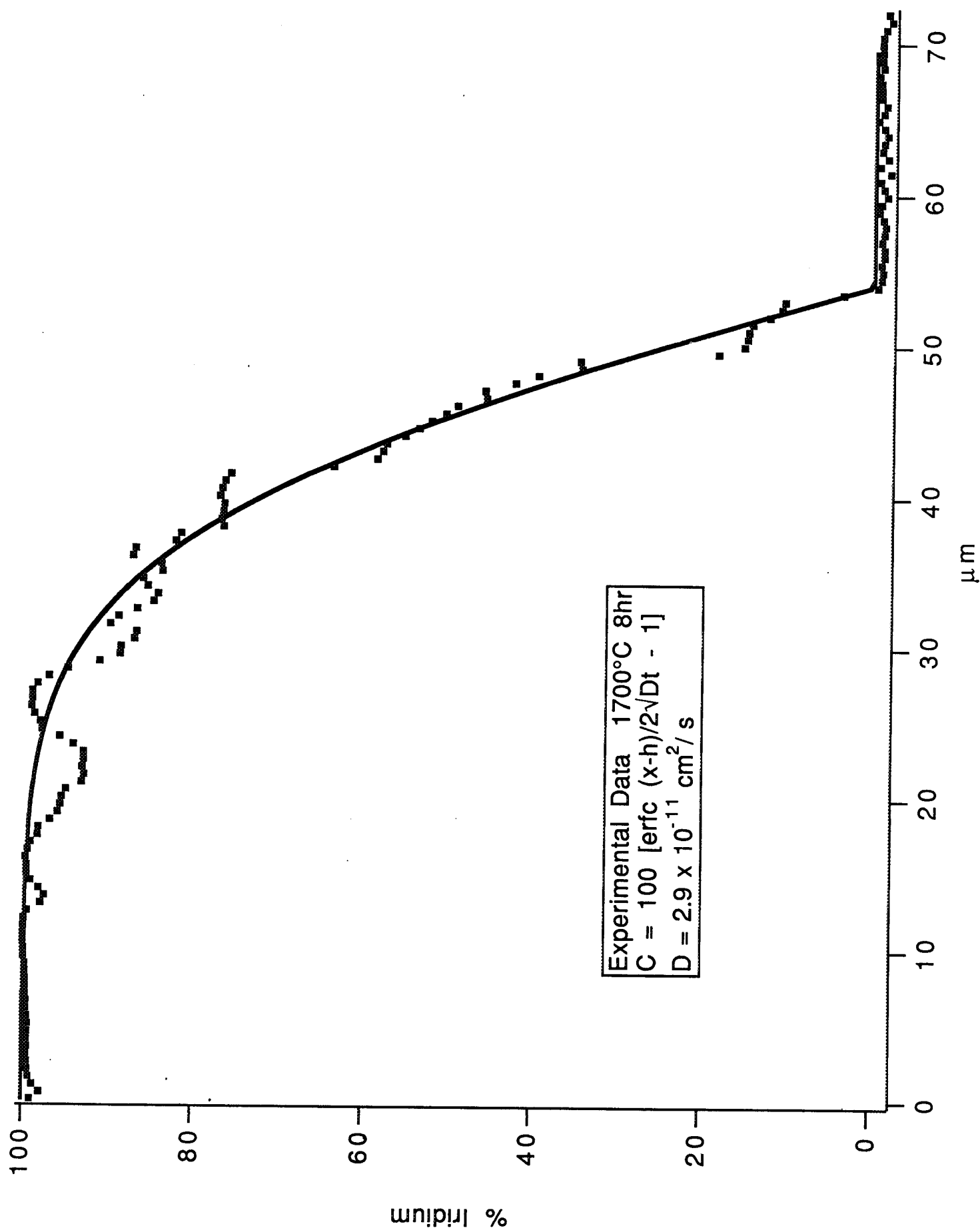
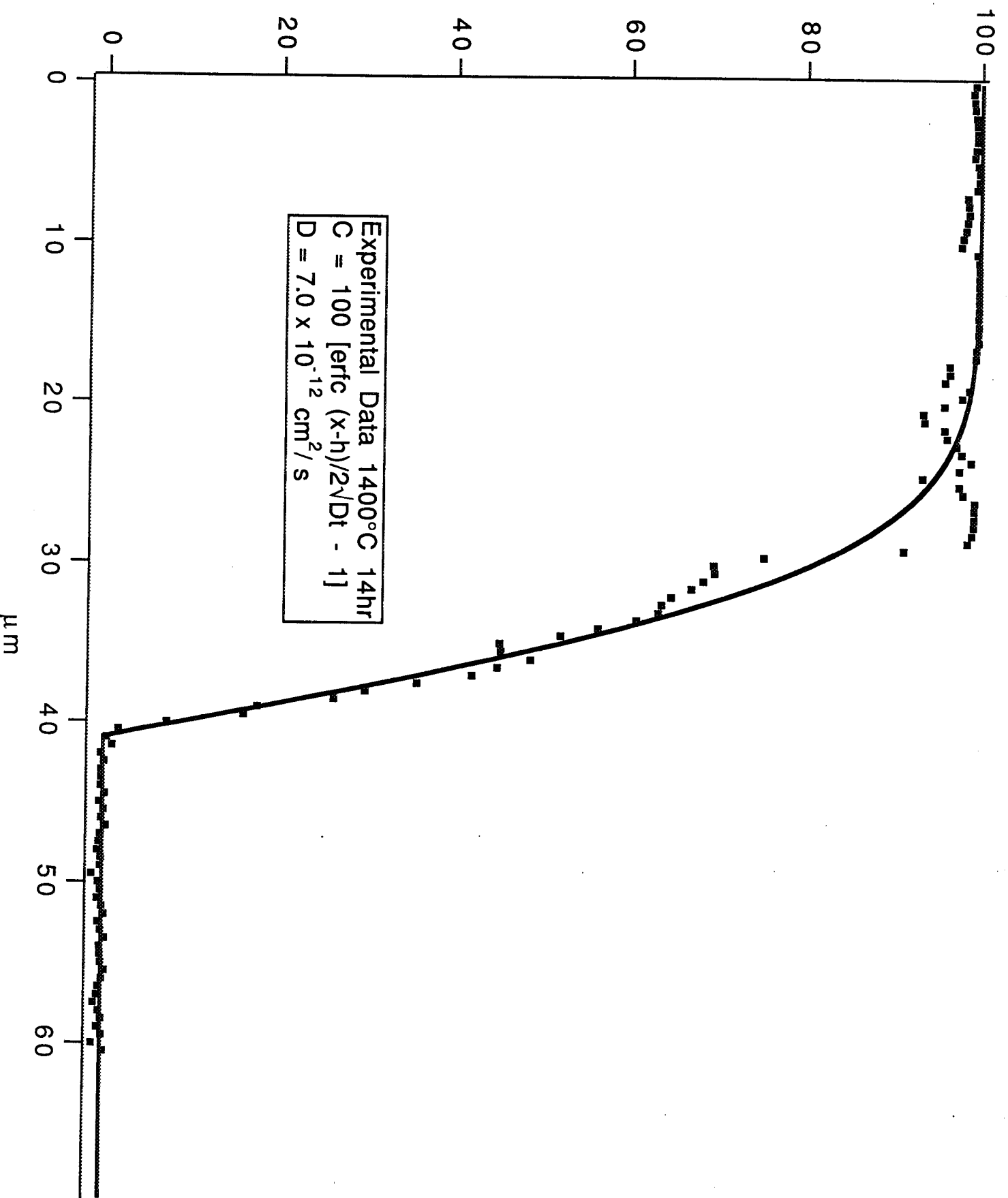


Figure 4.5.2-46.

170
% Iridium



4.5, High Temperature Materials Tests (Sandia) (cont.)

We have used equation (3) to fit the line scan data shown in Figures 4.5.2-45 through -47. The theoretical fits to the experimental profile and the resulting diffusion coefficients are shown. Allowing only diffusion of Re into Ir (i.e., equation 3) provides an excellent fit to the experimental data. For each sample, two line scans were taken and fit, giving two values for the diffusion constant at each temperature. These two values provide an indication of the precision of the measurement. Figure 4.5.2-48 gives a plot of these diffusion coefficients as a function of reciprocal temperature. The diffusion coefficients have an Arrhenius dependence and can be fit to an equation of the form:

$$D = D_0 e^{-E/kT} \quad (4)$$

The line plotted in the figure is equation (4) with $D_0 = 3.14 \times 10^{-8} \text{ cm}^2/\text{s}$ and $E/k = 1.42 \times 10^4 \text{ }^\circ\text{K}$. This fit to the data gives an activation energy for diffusion, E , of 1.23 eV. Based on an empirical relationship between melting point and self-diffusion, one would expect the activation energy for bulk diffusion to be approximately 4 eV. Typically activation energies for grain boundary diffusion are about half of those for bulk diffusion. Thus our measured activation energy provides additional evidence supporting grain boundary diffusion as the dominant mechanism in the CVD materials. Figure 4.5.2-48 also includes data points from previous studies of sputter-deposited Ir on Re performed under this contract. The diffusion constants measured in the CVD materials are consistent with the previous measurement for sputtered materials at lower temperatures.

The model presented here using equations (3) and (4) to predict Re concentrations will allow prediction of thruster lifetimes when combined with measured recession rates of Ir in appropriate oxidizing environments. We caution that these equations may tend to underestimate the effect of grain boundary diffusion. For these materials with grain size large compared to the probe volume, it is difficult to measure and model grain boundary diffusion properly, since the real diffusion process appears to be a combination of comparatively rapid diffusion along grain boundaries with slower bulk diffusion from grain boundaries or from bulk Re into the Ir grains. In the line scans, dips are observed as the line crosses a grain boundary. Since the grain boundaries are only a small fraction of the measurement volume, their effect on the least-square fit for the diffusion constant is minor. Their effect on the overall diffusion process is critical however, since they can provide a short circuit path to the surface. Thus these diffusion equations and model fits will tend to underestimate the concentration of Re at the surface. Further studies will attempt to better quantify grain boundary diffusion.

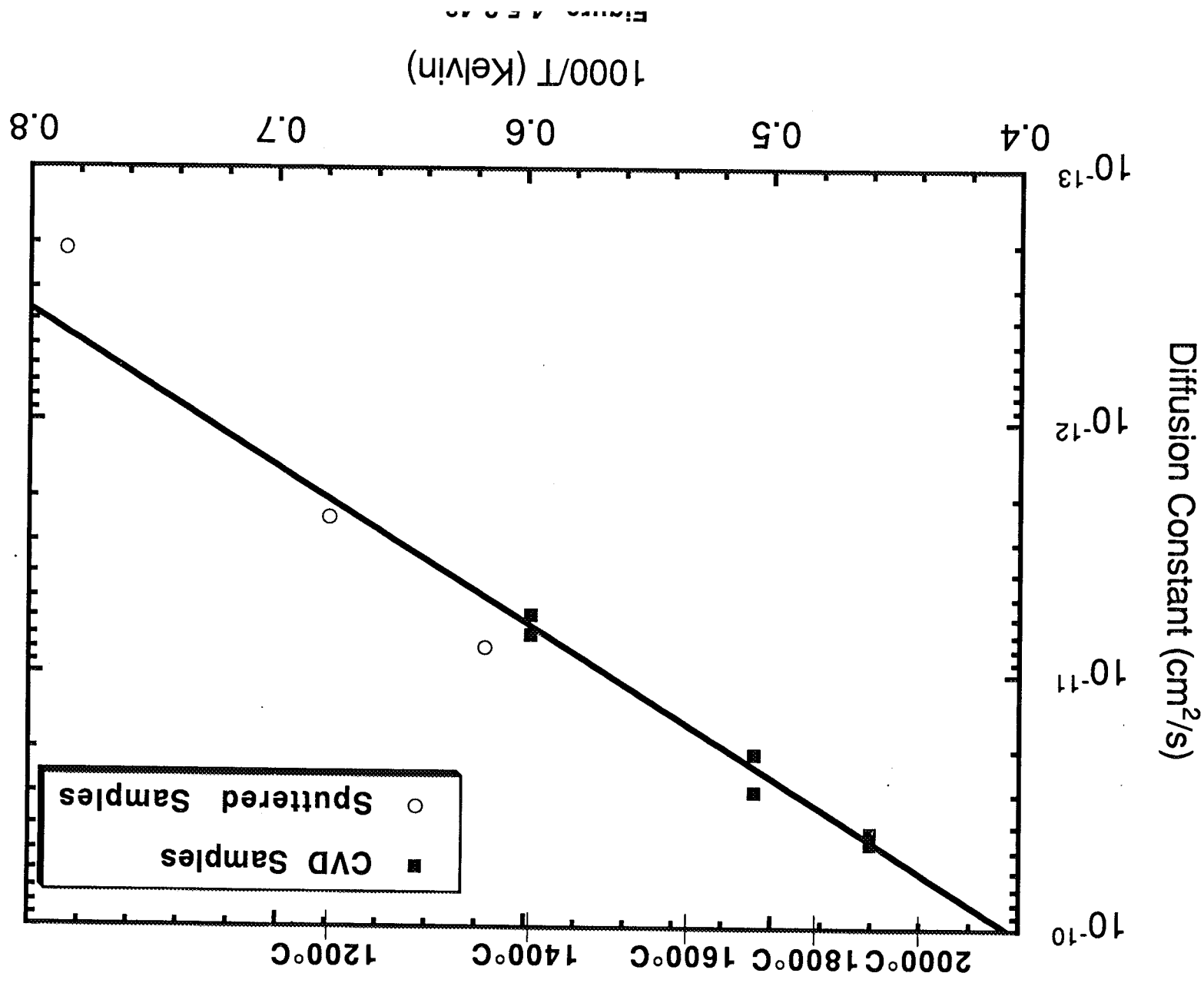


Figure 7.5.10

4.5, High Temperature Materials Tests (Sandia) (cont.)

MSTA Burner Measurements

CVD Ir-Re test samples from Ultramet were tested in the MSTA burner at the combustion Research Facility. In order to reduce entrainment of oxygen into the flame, a quartz shroud was placed around the burner and nitrogen flow as introduced on the sides of the shroud. Steel wool was placed between the burner and the shroud to disperse the nitrogen flow. A nitrogen purge was used on the back side of the samples to reduce oxidation of the rhenium side to a minimum. Four different foil samples were tested. Table 4.5.2-2 gives the iridium and rhenium thicknesses (measured by Ultramet), the exposure temperature and time, and mixture ratio. The measured sample weights as a function of exposure time are also included. These weight losses must not be used to calculate iridium loss because considerable attack of the rhenium side may have occurred due to imperfect purging. The attack of the iridium side was not uniform due to the variation in sample temperature and oxidizing conditions across the flame region.

Table 4.5.2-2. MSTA Surface Measurements

Sample #	Ir mils	Re mils	Temp °C	Mix Ratio	Test Duration hrs	Initial Weight gms	Weight After 1 hr	Weight After 2 hr	Weight After 3 hr	Weight After 4 hr	Weight After 8 hr
1-2-1	1.0	3.8	1400	6	8	2.738	--	--	--	2.712	2.681
1-3-4	1.5	2.8	1800	6	4	--	3.324	--	-3.253		
1-3-5	2.8			4	3.418	--	3.354	--	3.273		
1-3-1	2.0	3.5	1900	10	3	3.067	2.962	2.808	2.698		

When samples were removed from the burner for weighing, a Kevex machine was used to determine the composition in a centered area on the front and back faces. The faces were iridium on the front and rhenium on the back for all exposure times and conditions, indicating that both surfaces were largely intact at the center of the sample. Visual inspection revealed some pin holes in sample #1-3-1 after 3 hr exposure. However, these pinholes were located near the corners of the sample. They are not representative of the burner conditions. We speculate that the attack was by entrained oxygen from the air surrounding the burner.

4.5, High Temperature Materials Tests (Sandia) (cont.)

Auger Measurement of Grain Boundary Diffusion

Equipment was setup to study the grain boundary diffusion of CVD Re through CVD Ir in ultra high vacuum. A copper sample mount which could handle the 50 to 100 amps required to heat a specimen to 1900°C in vacuum was designed and constructed. This was installed in the vacuum system containing the Auger spectrometer along with the necessary high current feedthroughs and conductors.

The heating arrangement was tested with a 0.003 in. thick Mo foil in place of the Re/Ir sample. It was found that the Mo foil could be heated to 1700°C using a current of 70 amps which was the limit of the power supply available. The sample was hottest in the center and cooler near the supports. The test verified that the copper supports remained relatively cool and would not melt or vaporize under the test conditions. Temperatures were measured with a W-5% Re and W-26% Re thermocouple and agreed reasonably well with readings from a two-color optical pyrometer. The thermocouple failed during the test, however, when it shorted to a heater lead due to warping of the sample.

A test was performed to determine whether the high sample temperatures would interfere with the operation of the Auger Spectrometer. With the sample heated to approximately 1600°C, an Auger spectrum of the sample could still be recorded. The spectrum was more noisy than the room temperature spectrum and exhibited other changes such as loss of carbon and oxygen impurities. This demonstrates that Auger spectra can be recorded with the sample at elevated temperatures.

Two different sample mounts have been built and tested. Initial tests used these mounts to heat molybdenum foil in ultrahigh vacuum. The first mount held the sample rigidly at both ends. Thermal expansion during heating caused the sample to warp. The resulting stresses could potentially crack or strain the protective iridium coating on Ir/Re samples.

A second mount was designed which holds one end rigidly and uses a flexible conductor to carry current on the other end thus allowing the sample to expand freely during testing. This mount was tested with a 0.003 inch thick molybdenum foil. The foil was heated to 2000°C and Auger spectra obtained at this temperature. No buckling of the molybdenum foil was observed using this mount.

4.5, High Temperature Materials Tests (Sandia) (cont.)

A CVD Ir/Re sample was heated in ultrahigh vacuum and the arrival time of Re on the Ir surface was observed using Auger spectroscopy. The first experiment was successful. The sample was ~1 mil CVD Ir on ~3 mil CVD Re. The sample was mounted in ultrahigh vacuum and resistively heated to about 1900 C using 50 amps of direct current. The composition of the Ir face was monitored using Auger spectroscopy to determine atomic percentages of Ir and Re. The Auger spectra were obtained while the sample was at temperature. Auger scans each took approximately 5 minutes providing excellent temporal resolution for Re arriving at the surface.

Figure 4.5.2-49 shows Auger spectra recorded at the start of the heating period and after 9 hours of heating. The starting spectra show only iridium on the surface. After 9 hours of heating additional peaks due to rhenium are clearly visible in the Auger spectra. These peaks represent a surface concentration of about 3 atomic percent rhenium.

Figure 4.5.2-50 shows the atomic percentages as a function of time observed during this run. Rhenium is visible on the surface after about 3 hours heating and rises gradually to the 3 atomic percent level after 9 hours heating.

DIFFUSION MODEL

A computer code that models the combined effects of diffusion and oxidation was written and debugged. The diffusion rate model used in the code is based on measurements previously made at Sandia using CVD material. The oxidation rate model is based on measurements previously made at Aerojet.

The measurement of surface rhenium concentrations was extended on another sample to a total heating time of 50 hours. Rhenium concentrations were also measured during the heating of this ~1 mil CVD Ir on ~3 mil CVD Re sample. The sample was mounted in ultrahigh vacuum and heated to about 1730 C using 50 amps of direct current. Figure 4.5.2-51 shows the Auger peak height ratio of Re to Ir as a function of time during heating. The increase in this ratio is caused by the diffusion of Re through the Ir layer, predominantly by grain boundary diffusion.

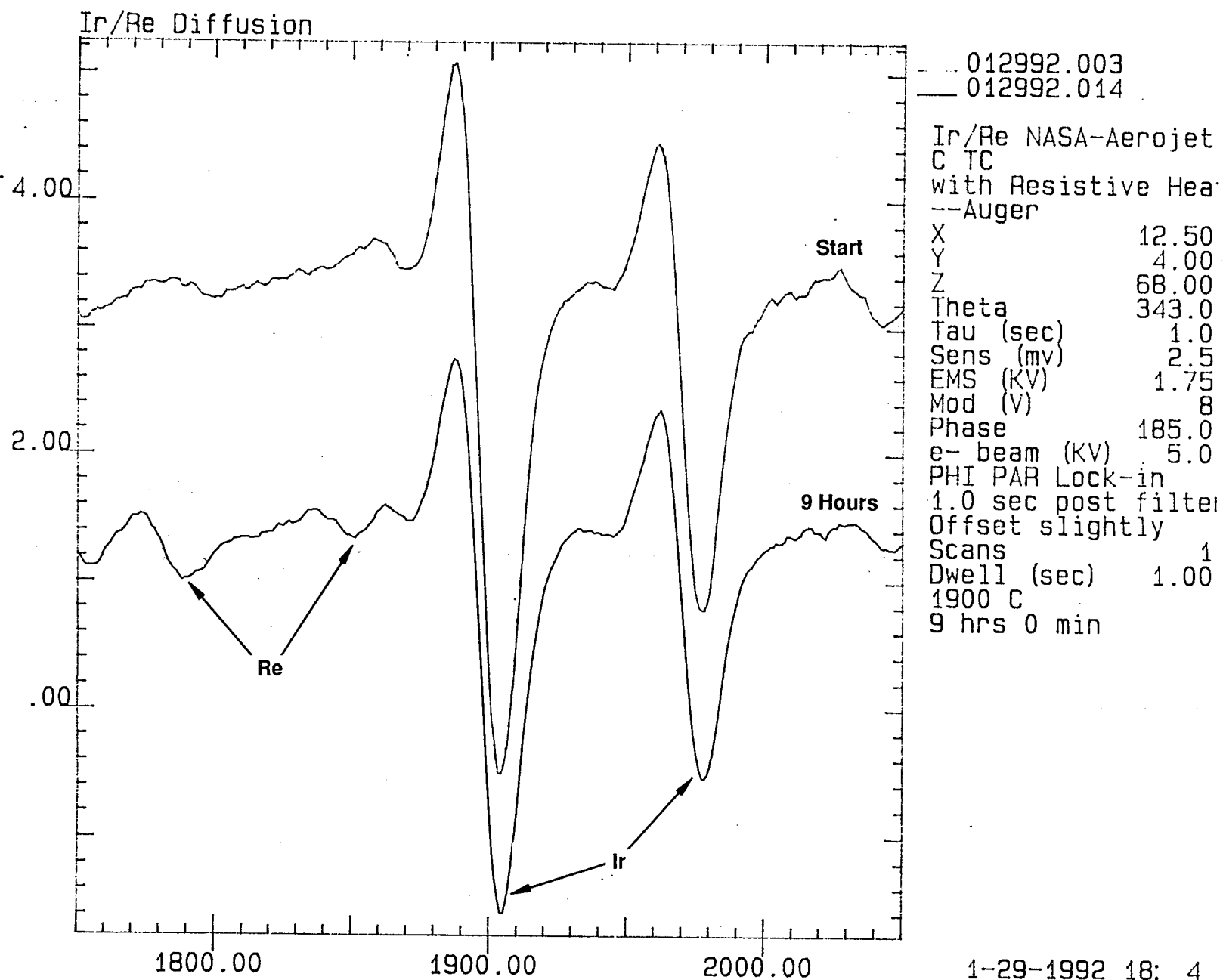


Figure 4.5.2-49. Auger Spectra for CVD Ir/Re Specimen at 1900°C

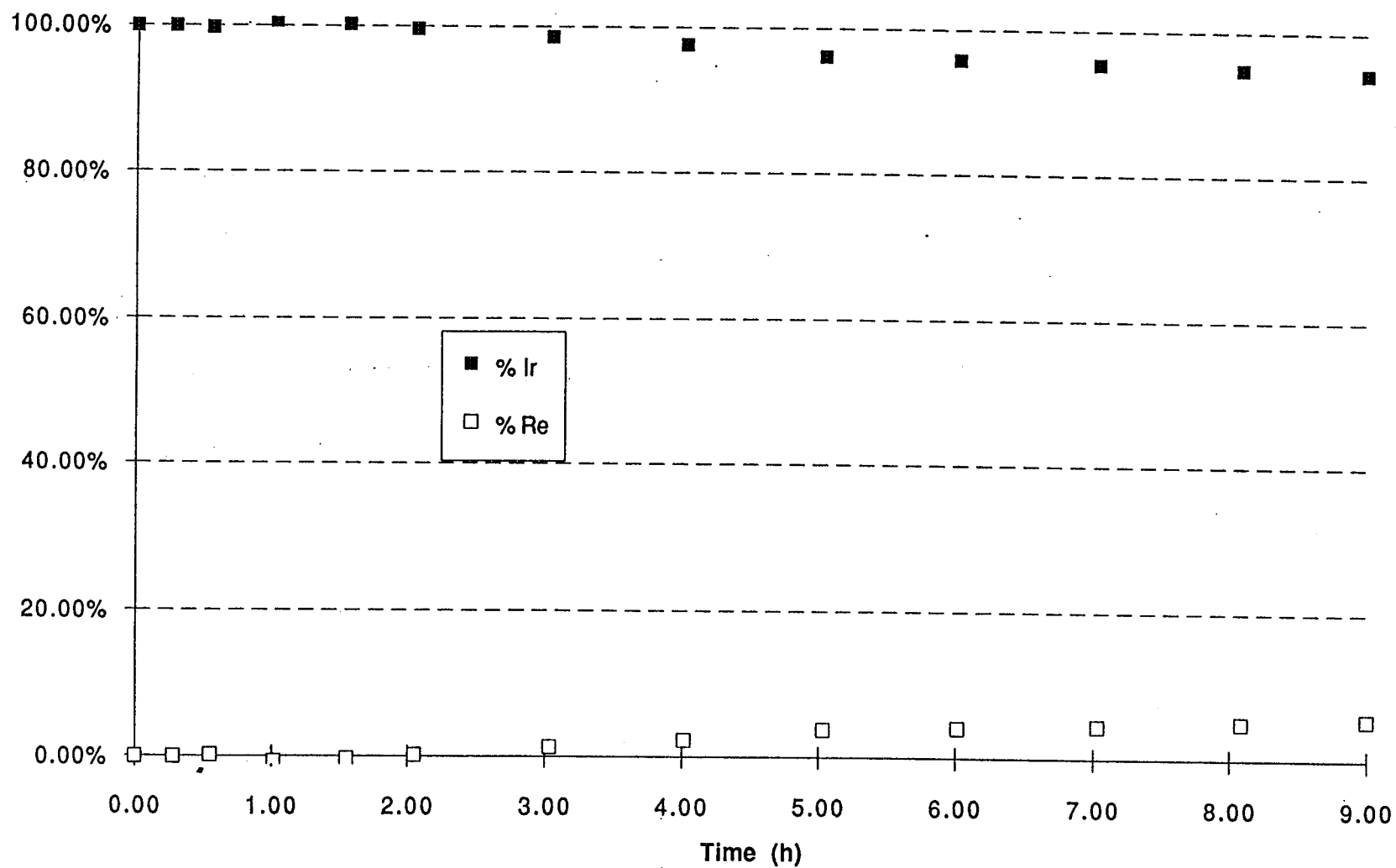


Figure 4.5.2-50. Atomic Percent Ir and Re Versus Time for CVD Ir/Re Specimen at 1900°C

4.5, High Temperature Materials Tests (Sandia) (cont.)

Calculation of Surface Rhenium Concentrations From Auger Data

Interpretation of the data shown in Figure 4.5.2-51 requires calculating the surface Re coverage from the Auger peak height ratios. This calculation requires knowledge of the relative elemental sensitivities for Re and Ir. These sensitivity factors are discussed and tabulated in Ref. 10. Some assumption regarding the spatial distribution of Re and Ir in the near surface region must also be made. The saturation Re Auger peak height is much less than the Ir peak height as seen by the final peak height ratio of about 0.22. In order to explain this relatively small final ratio, we have assumed that Re diffuses to the surface up the grain boundaries and spreads over the surface to form a saturation coverage of one monolayer. If the activity of a Re monolayer is close to that of bulk Re, there would be little driving force for further diffusion of rhenium. This assumption is consistent with the experimental data as the following calculation demonstrates:

The probability, P , that an Auger electron will escape to the surface of a solid from an atom at a particular depth, z , is

$$P = \exp\left(\frac{-z}{\lambda}\right) \quad (1)$$

where λ is the mean free path of the electrons which depends upon their energy. The Auger transitions for Re and Ir are at 1799 eV and 1908 eV, respectively. These values are both roughly 2000 eV for which the mean free path is approximately 20 Å based upon the data summarized by Ref. 11. Although this reference does not have data specifically for Ir or Re, it does present data for Au ($Z=79$) and W ($Z=74$) which are close to the same atomic number, Z , as Ir ($Z=77$) and Re ($Z=75$).

For a layered solid, the overall intensity of the Auger signal is related to the sum of the probabilities that electrons from each layer will reach the surface. (This analysis ignores the atomic sensitivity factors which are handled separately.) Therefore, for Ir and Re, the intensity of the Auger signals is proportional to

$$I_{\text{Ir}} = \sum_{\text{Ir layers}} P_{\text{Ir}} = \sum_{\text{Ir layers}} \exp\left(\frac{-z}{\lambda}\right) \text{ and } I_{\text{Re}} = \sum_{\text{Re layers}} P_{\text{Re}} = \sum_{\text{Re layers}} \exp\left(\frac{-z}{\lambda}\right) \quad (2)$$

respectively. These summations can be approximated by integrals, for example,

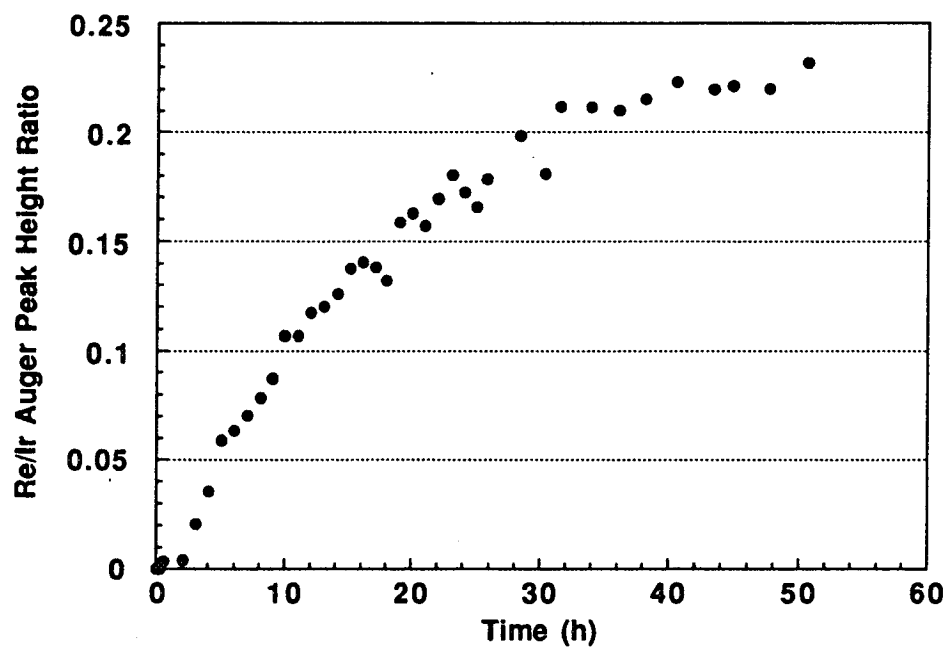


Figure 4.5.2-51. Auger Peak Height Ratio (Re/Ir) as a Function of Time During 1730C Anneal in Ultrahigh Vacuum

4.5, High Temperature Materials Tests (Sandia) (cont.)

$$I_{\text{Re}} = \int_{\text{Re layers}} \text{Re layers} \exp\left(\frac{-z}{\lambda}\right) dz = -\lambda \exp\left(\frac{-z}{\lambda}\right)_{\text{Re layers}} \quad (3)$$

The result of the integral will have units of distance which can be interpreted as the thickness of an ideal solid from which an equivalent Auger signal would be detected if the probability for detection of Auger electrons from all layers in the ideal solid were unity. For example, the integral for a purge semi-infinite solid from $z = 0$ to $z = \infty$ evaluates to simply λ , the mean free path. Thus, the Auger signal from a pure real solid is equivalent to the Auger signal from an ideal solid of thickness λ if all the Auger electrons in the ideal solid escaped to the surface.

The effect of a thin Re layer on top of Ir can now be evaluated. Assume that at the end of the diffusion experiment that there is a single layer of Re on top of a semi-infinite Ir solid as shown in Figure 4.5.2-52.

The nearest-neighbor distances for Ir and Re are approximately 2.75\AA . Thus, the relative intensities of the Ir and Re Auger singles are:

$$I_{\text{Re}} = \int_0^{2.75\text{\AA}} \exp\left(\frac{-z}{\lambda}\right) dz = -\lambda \exp\left(\frac{-z}{\lambda}\right) \Big|_{z=0\text{\AA}}^{z=2.75\text{\AA}} = 2.57\text{\AA} \quad (4a)$$

$$I_{\text{Ir}} = \int_{2.75\text{\AA}}^{\infty} \exp\left(\frac{-z}{\lambda}\right) dz = -\lambda \exp\left(\frac{-z}{\lambda}\right) \Big|_{z=2.75\text{\AA}}^{z=\infty} = 17.4\text{\AA} \quad (4b)$$

Using sensitivity factors for Ir and Re, the Auger peak height ratio can be written in the form:

$$R_{\text{Re/Ir}} = S_{\text{Re}} I_{\text{Re}} / S_{\text{Ir}} I_{\text{Ir}} \quad (5)$$

For a single layer of Re on Ir, the calculated Auger peak height ratio is 0.21 which is in good agreement with the observed peak height ratio after long annealing, as measured here. This suggests that the assumption of a monolayer of Re on Ir as the saturation concentration is reasonable. Similar analysis to that presented above can be used to convert the measured peak height ratios into surface Re concentrations. These surface Re concentrations as a function of annealing time are presented in Figure 4.5.2-53. Also shown are computer calculations of surface Re concentrations. These calculations are discussed in the following sections.

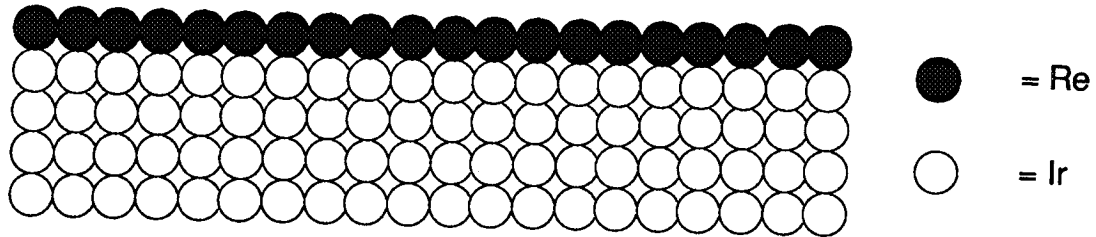


Figure 4.5.2-52. Assumed Configuration of Rhenium on Surface of Iridium Coating After Extended Annealing in Ultrahigh Vacuum

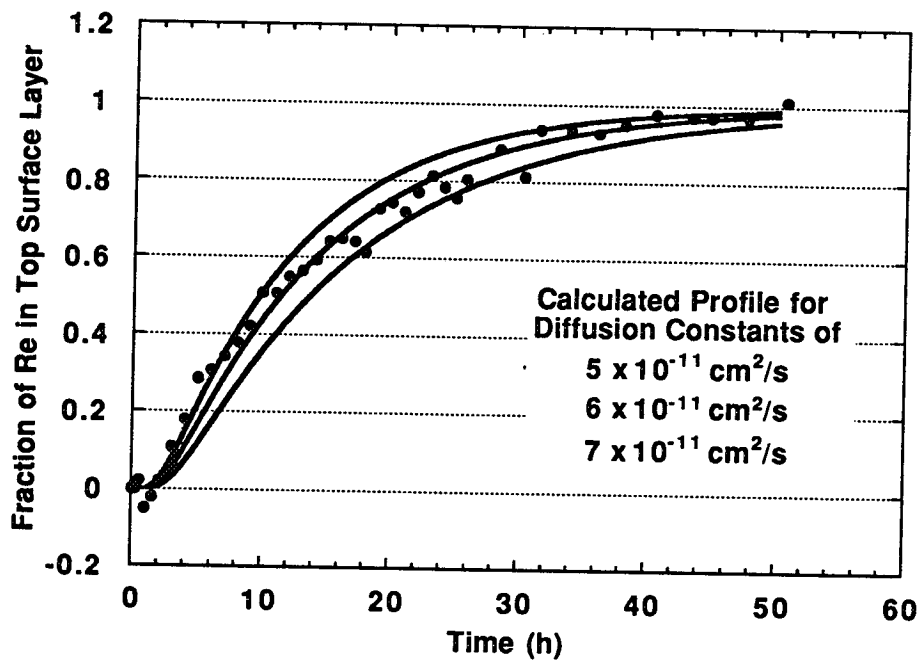


Figure 4.5.2-53. Fraction of Rhenium Atoms in Top Layer of a 25 μm CVD Coating After Extended Annealing in Ultrahigh Vacuum. Diffusion Profiles Are Calculated Using The Model Described Below

4.5, High Temperature Materials Tests (Sandia) (cont.)

Theoretical Treatment of Grain Boundary Diffusion

The Auger technique used for determination of the diffusion rate is discussed in a review article in Ref. 12.

The technique is known as the surface accumulation method. In particular, a theoretical analysis by Hwang and Balluffi is presented which is useful for analysis of our Auger data. Their model assumes that the bulk diffusion rate is negligible compared to the grain boundary diffusion rate. Huang and Balluffi use a geometric model for permeation and combined surface spreading. They present a general solution which can be simplified by assuming that surface diffusion is much more rapid than bulk diffusion. If one further assumes that the capacity of the Ir grain boundaries for Re is much larger than that of the Ir surface and that the surface concentration of Re equals that at the top of the grain boundaries (i.e., no segregation effects), the model is equivalent to the computer calculation described as follows:

Computer Model of Diffusion for CVD Iridium on Rhenium

To date, the diffusion has been modeled by representing the Ir layer as a semi-infinite slab. This is a good approximation for cases in which very little Re has diffused far enough to reach the Ir surface. Thus, it is appropriate for extracting diffusion constants from relatively short anneals in which the surface Re concentration reaches only 1 or 2%. The Auger measurements in ultrahigh vacuum involve much larger surface Re concentrations. For these situations, a numerical solution to the diffusion equation is required as follows:

$$\frac{\delta C}{\delta t} = D \frac{\delta^2 C}{\delta x^2} \quad (6)$$

Here C represents the concentration of the diffusing species, i.e., Re. The choice of boundary conditions depends upon the assumptions regarding directions of material diffusion and what happens to Re when it reaches the Ir surface. On the basis of previous observations that Re diffuses into Ir but that there is very little diffusion of Ir into Re, C is set to 1.0 at the Re/Ir interface. For the case of annealing in vacuum, zero flux is assumed at the Ir/vacuum surface.

Following the numerical solution outlined in Ref. 13, we use the Crank-Nicholson differencing scheme;

4.5, High Temperature Materials Tests (Sandia) (cont.)

$$\frac{C_j^{n+1} - C_j^n}{\Delta t} = \frac{(C_{j+1}^{n+1} - 2C_j^{n+1} + C_{j-1}^{n+1}) + (C_{j+1}^n + C_{j-1}^n)}{\Delta x^2} \quad (7)$$

Here Δx is the spatial step used for solution and Δt is the time step used for solution. The superscripts represent the time in units of the time step and the subscripts represent the spatial position in units of the spatial step. The boundary conditions become $C_0 = 1$ and $C_{N+1} = C_N$. Here N is the total number of spatial steps. Thus the coating thickness is $N\Delta x$.

These equations result in a tridiagonal system of linear equations which is solved using the algorithm in Section 2.6 of the reference. We have written the code using a Macintosh graphics program called IGOR. Macros and functions in IGOR are written in a subset of the programming language "C."

The experimental data were modeled using the diffusion program to determine the diffusion constant. Figure 4.5.2-53 shows the results of several calculations of the surface concentration vs time obtained using the diffusion program. The best overall fit was obtained for a diffusion constant of $6 \times 10^{-11} \text{ cm}^2/\text{sec}$. Overall, the fit is quite reasonable. It is likely that the fit would be even better with more precise temperature control. There was some uncertainty in the temperature, but it averaged 1730 C. The diffusion constant predicted by the previous model at this temperature would be $2.6 \times 10^{-11} \text{ cm}^2/\text{sec}$ compared to the $6 \times 10^{-11} \text{ cm}^2/\text{sec}$ obtained from the fit. Thus, the appearance of Re at the surface is somewhat faster than predicted by the previous diffusion model. As expected, grain boundary diffusion appears to be somewhat faster than the previous measurements of combined bulk and surface diffusion. It is encouraging that the grain boundary diffusion is not dramatically faster which leads us to conclude short circuit diffusion up the grains should not represent a major problem.

A modification of the diffusion code has been written which allows for oxidative removal of iridium and rhenium at the surface of the coating. This computer model represents a first quantitative attempt to combine the effects of diffusion and oxidation to yield a lifetime prediction. We assume that oxidation removes material in the same ratio of composition as the composition at the surface of the alloy, i.e., there is no preferential oxidation of Re or Ir. The data regarding oxidation loss rates for iridium-rhenium alloys are very limited. We have used the oxidation loss rates measured at Aerojet for Ir, 80% Ir/20% Re, and 60% Ir/40% Re in 0.5% O_2 in Ar at 1550 C and 0.0278 atm. For intermediate compositions, we used a linear interpolation to estimate oxidation rates. The diffusion rate used at 1550 C was 1.3×10^{-11}

4.5, High Temperature Materials Tests (Sandia) (cont.)

cm²/sec based on our previous measurement of diffusion. Under these conditions, we predict a lifetime of 67 hr for a 50μm coating of CVD Ir on Re. Figures 4.5.2-54, -55, and -56 show the calculated composition profile after 20, 40, and 60 hr of oxidation for a 50μm coating at 1550 C in 0.5% O₂. The sharp falloff to the right side of the 40 and 60 hr graphs represents the surface of the Ir coating which is receding due to oxidation.

It is easy to extrapolate our measurements of diffusion rates to other temperatures. The lack of information on oxidation rates preclude applying this model for other temperatures and gas stream compositions. This model clearly demonstrates the necessity for further studies of oxidation rates and mechanisms if more accurate lifetime predictions are to be obtained.

Sputter depth profiling of the elemental composition of a CVD iridium on rhenium sample after annealing for 50 hours in vacuum at 1730°C was performed. The surface composition was representative of the bulk concentration in the near surface region, requiring a change in the interpretation of the data based on previous testing. Sample annealing in ultrahigh vacuum was extended to 2100°C.

Figure 4.5.2-51 showed the ratio of the Re to the Ir peak to peak Auger signals as a function of time during 1730°C anneal in ultrahigh vacuum. In order to convert the Auger peak height ratio to atomic composition, additional information regarding the spatial distribution of rhenium and iridium in the near surface region is required. In order to obtain this information, after the 50 hours of heating to 1730°C, the sample was removed from the chamber which has Auger and DC resistive heating. Then it was mounted in a scanning Auger apparatus with provision for depth profiling by ion milling. The rhenium concentration was found to be independent of position across the surface and also normal to the surface. Thus we believe that the data shown in Figure 4.5.2-51 is representative of the bulk concentration in the grains in the near surface region. With this assumption, the data can be converted into data for composition as a function of time as shown in Figure 4.5.2-57.

An interesting feature seen in this figure is that the rhenium concentration appears to saturate at about 15 atomic %. This observation can be explained by reference to the phase diagram for the iridium/rhenium system. The solubility limit for rhenium in iridium is nominally about 30% (this phase boundary is not well determined by the original research). We suggest that the saturation corresponds to the solubility limit for rhenium in iridium.

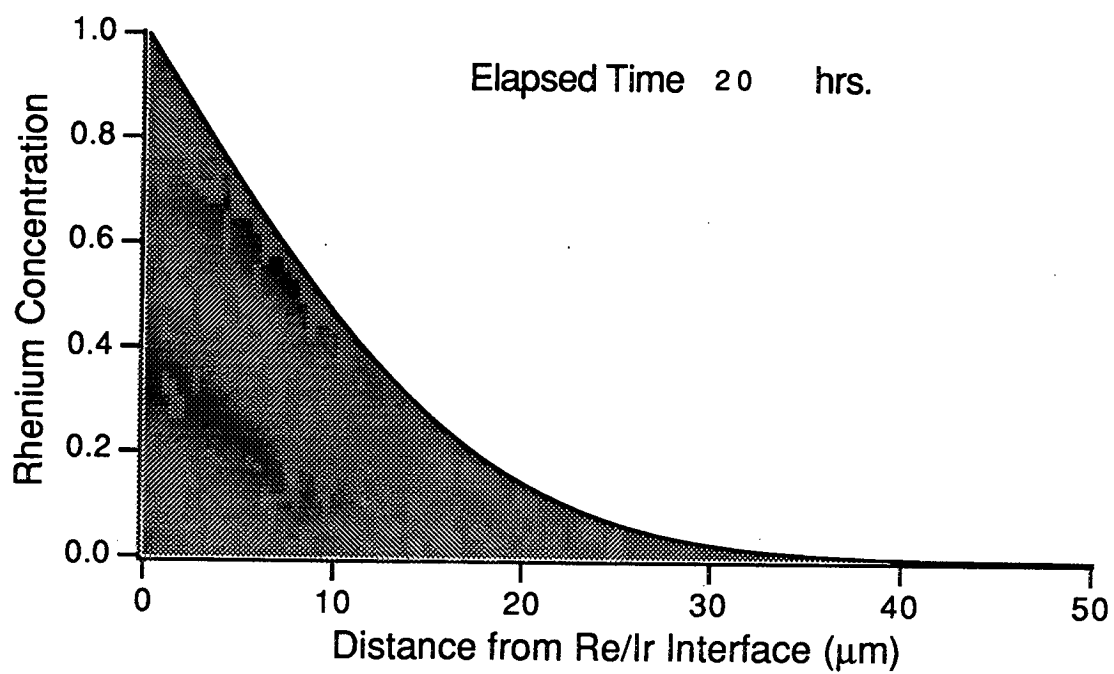


Figure 4.5.2-54. Calculated Rhenium Profile After 20 Hr at 1550 C in 0.5% O₂ at 0.028 atm

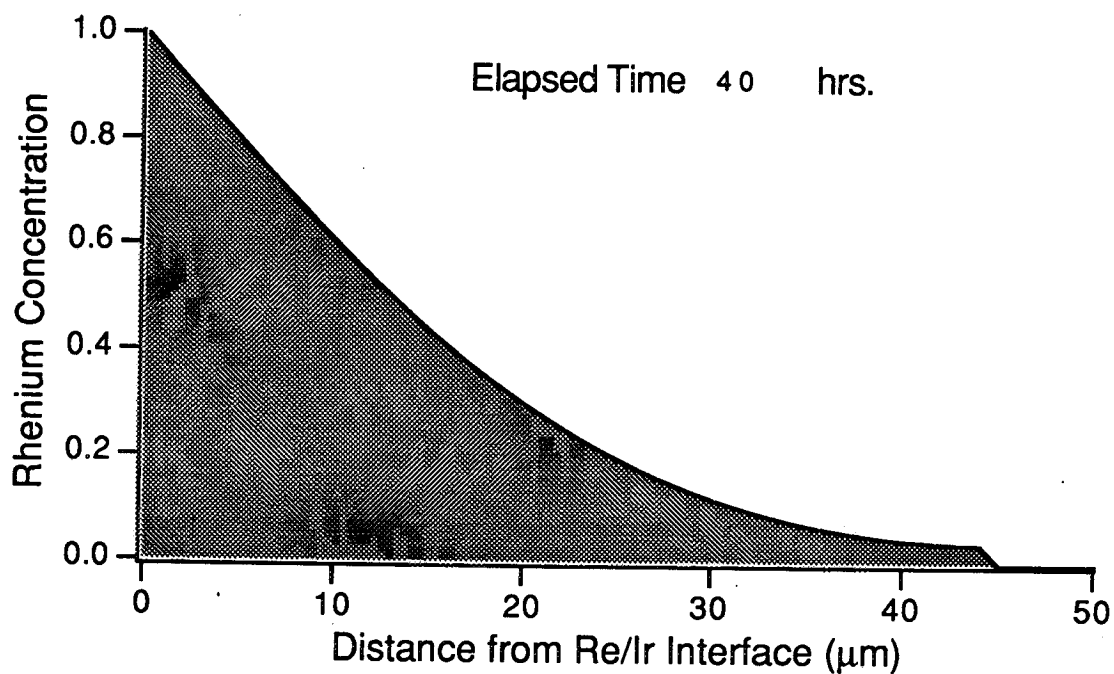


Figure 4.5.2-55. Calculated Rhenium Profile After 40 Hr at 1550 C in 0.5% O₂ at 0.028 atm

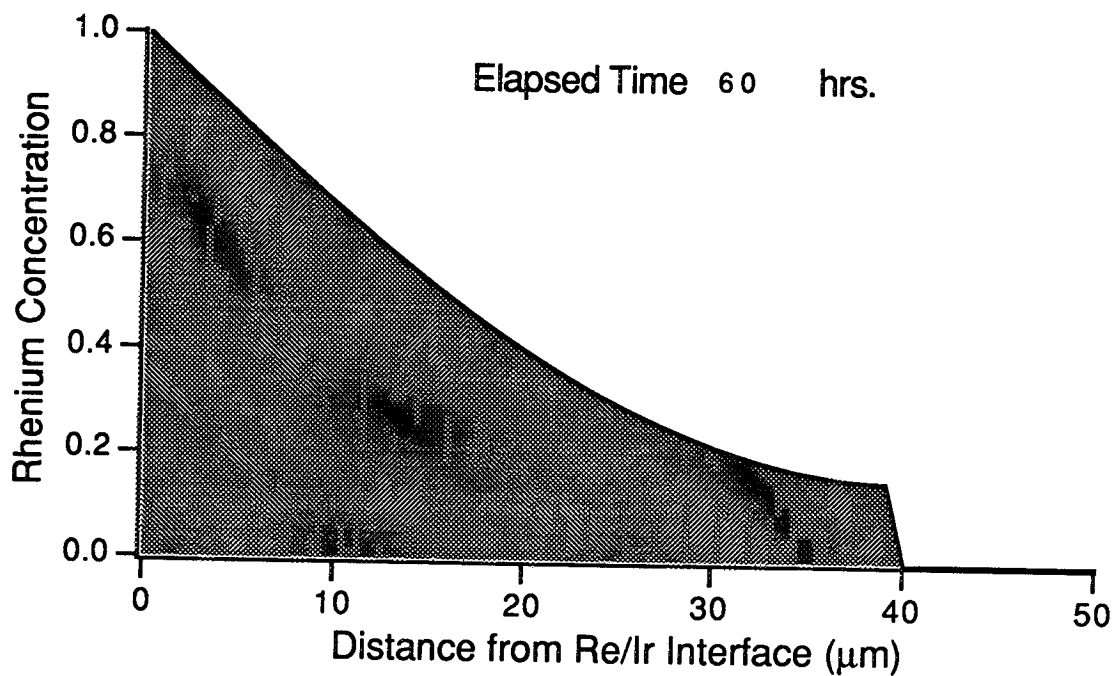


Figure 4.5.2-56. Calculated Rhenium Profile After 60 Hr at 1550 C in 0.5% O₂ at 0.028 atm. Final Failure Occurs at 67 Hr.

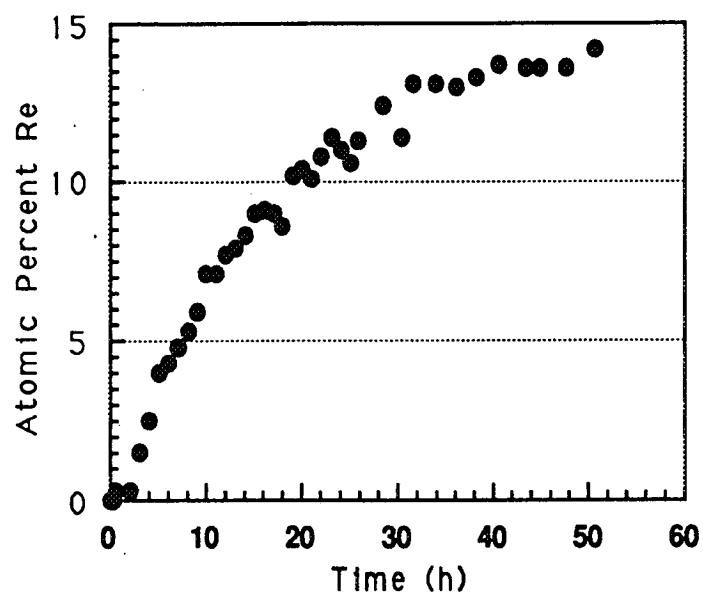


Figure 4.5.2-57. Bulk Concentration in the Near Surface Region as Function of Time During 1730°C Anneal in Ultrahigh Vacuum

4.5, High Temperature Materials Tests (Sandia) (cont.)

It is clear that for very long annealing times, the final composition of the whole sample should be identical and be rhenium with about 20% iridium in solution (i.e., the average composition of the original sample). Thus we would expect that the rhenium has not really saturated, but will eventually rise to a final level of 80%. To investigate this question, a new sample was mounted and the experiment repeated using an annealing temperature of 2100°C. At this temperature the diffusion is much faster allowing the experiment to be completed more rapidly. The resulting near surface concentration as a function of time is shown in Figure 4.5.2-58. This is qualitatively in accord with the above description in that the rhenium concentration initially rises to the solubility limit for rhenium in iridium. This value is a plateau and with further heating the rhenium concentration eventually rises further.

4.6 DIAGNOSTIC THRUST CHAMBER AND INSTRUMENTATION EVALUATION

Task 6 had as its objective the testing of the candidate chamber materials with the candidate propellant combinations under simulated rocket chamber conditions. The goal of these tests was to determine the effect of combustion products on chamber material performance at high temperature. To do this the Diagnostic Thrust Chamber was designed, built and tested. To provide optical measurements of the exhaust plume Aerojet provided design, fabrication, and calibration of the Exhaust Species Monitoring System (ESMS).

The conceptual design of the DTC is shown in Figure 4.6-1. The device is intended to permit testing of a material specimen of simple, low cost design under conditions identical to those found in a radiation-cooled thruster. The major features considered in the design were:

Injector:	Premix vs heterogeneous Drilled vs platelet Cooled vs uncooled
Specimen:	Exact dimensions Installation/mounting detail Temperature control design
Chamber:	Cooling design Optical access detail

In addition, the DTC interfaces with the Exhaust Species Monitoring System (ESMS).

Completion of the DTC task was deferred to permit concentration of resources on the 100 lbf engine development. Therefore only sufficient time was available to conduct a 1-week

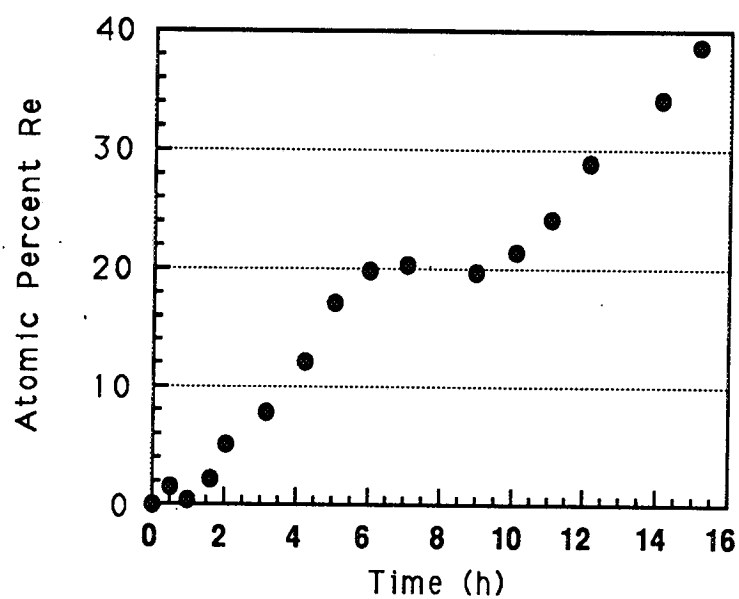


Figure 4.5.2-58. Bulk Concentration in the Near Surface Region as Function of Time During 2100°C Anneal in Ultrahigh Vacuum

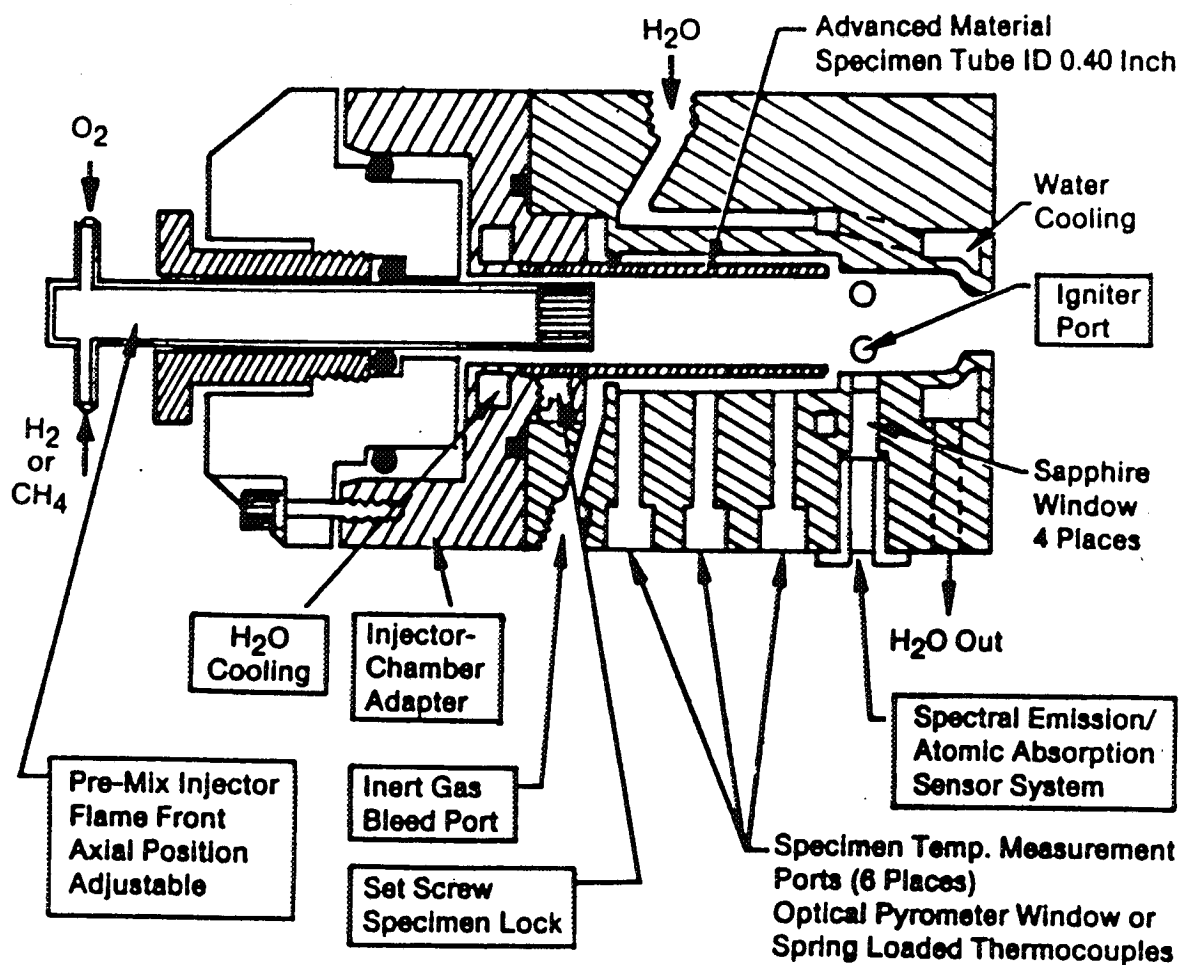


Figure 4.6-1. Diagnostic Thrust Chamber Conceptual Design

4.6, Diagnostic Thrust Chamber and Instrumentation Evaluation (cont.)

test campaign to characterize the test apparatus and obtain preliminary material compatibility data.

4.6.1 Design

The design criteria for the specimen, injector and chamber are listed in Table 4.6.1-1.

The design approach selected is shown in Figure 4.6.1-2. The specimen is a metal foil rolled into a cylinder to form the chamber wall. The foil can be the material under test or can serve as a substrate for material deposited by CVD or other process. Fabrication of an injector designed to eliminate flashback under all conditions was unsuccessful. This injector was intended to be a platelet premix 0.0013 cm (0.0005 inch) orifice injector. It was to be fabricated from etched foil, wrapped around a bonding fixture and diffusion bonded at 1450 F for 2 hours in a vacuum bonding furnace. Examination of the rolled injector face after electropolishing (Figure 4.6.1-2A) showed regions of disbond at creases formed during squeeze of the part during bonding. Incomplete or irregular opening of the orifices and deposits from the electropolish process are also evident. Two additional rolled foil injectors bonded at 1600 F showed similar evidence of disbonding, therefore a conventional drilled injector design which met most of the injector criteria was used.

The injector is a drilled, premix design with very small element 0.041 cm (0.016 in.) critical diameter and high injection velocity to eliminate flashback under most operating conditions. The chamber provides a nitrogen purge which protects the backside of the specimen and which can be used to control its temperature. Since specimen temperature is a critical parameter, provision was made for multiple temperature measurements. Multiple two-color pyrometer measurements were made using the setup shown schematically in Figure 4.6.1-3. This permits measurements along the length and circumference of the specimen. The specimen chamber is shown "unwrapped" in Figure 4.6.1-4 to map the location of the optical measuring points which are 0.25 in. dia fused silica windows. Rows Nos. 1 through 6 are provided for temperature measurement. Row No. 7 is used for emission and absorption measurements from the gas just downstream of the specimen. The ports are identified in detail in Table 4.6.1-1A.

Table 4.6.1-1. Diagnostic Thrust Chamber Design Criteria

A. SPECIMEN

1. Fabricate easily from all candidate materials
2. Permit use of formed or deposited (CVD or other) materials
3. Permit easy examination of exposed surface
4. Low cost

B. INJECTOR

1. Premixed
2. No flashback over full operating range of propellants, mixture ratio and pressure
3. Water-cooled
4. Fit within approximately 0.5 in. dia specimen
5. Traverse approximately 1.0 in. length of specimen
6. Uniform flow distribution at face
7. Minimum no-flow zone at wall

C. CHAMBER

1. Provide thermally isolated support for specimen
2. Provide rapid access for specimen exchange
3. Accommodate different specimen thicknesses
4. Provide control for specimen temperature
5. Provide chamber pressure control
6. Provide multiple locations for measurement of specimen temperature
7. Provide optical access for emission and absorption measurements of metal species in chamber gas by interfacing with Exhaust Species Measurement System (ESMS)

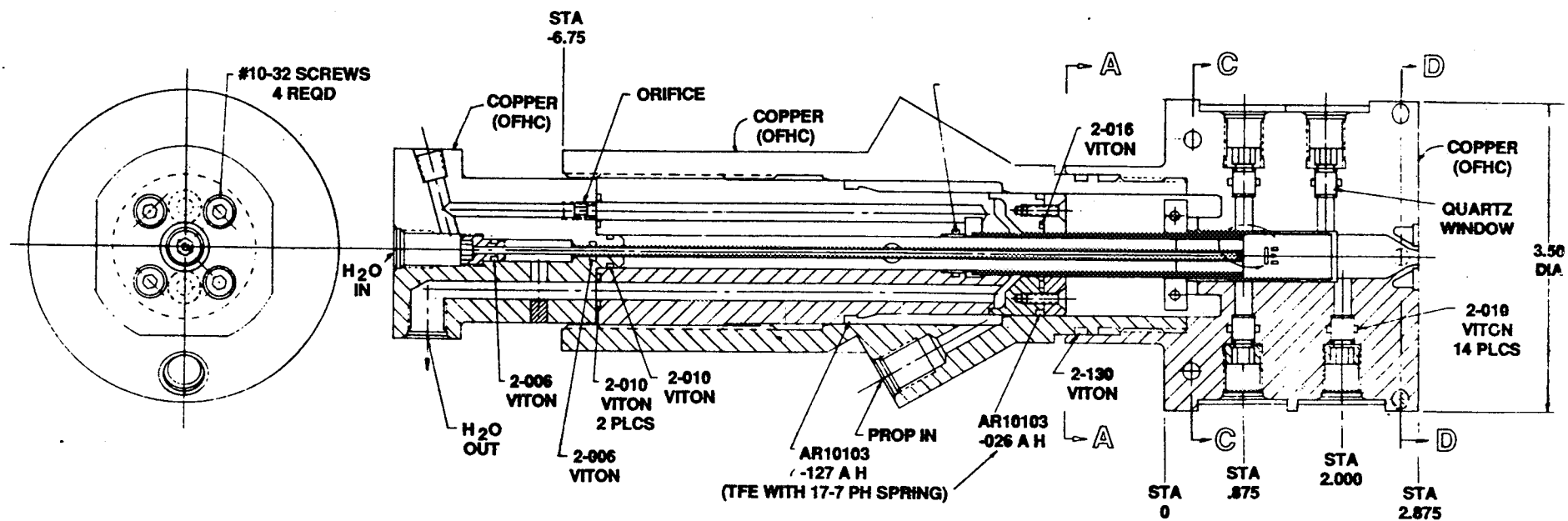


Figure 4.6.1-2. Diagnostic Thrust Chamber

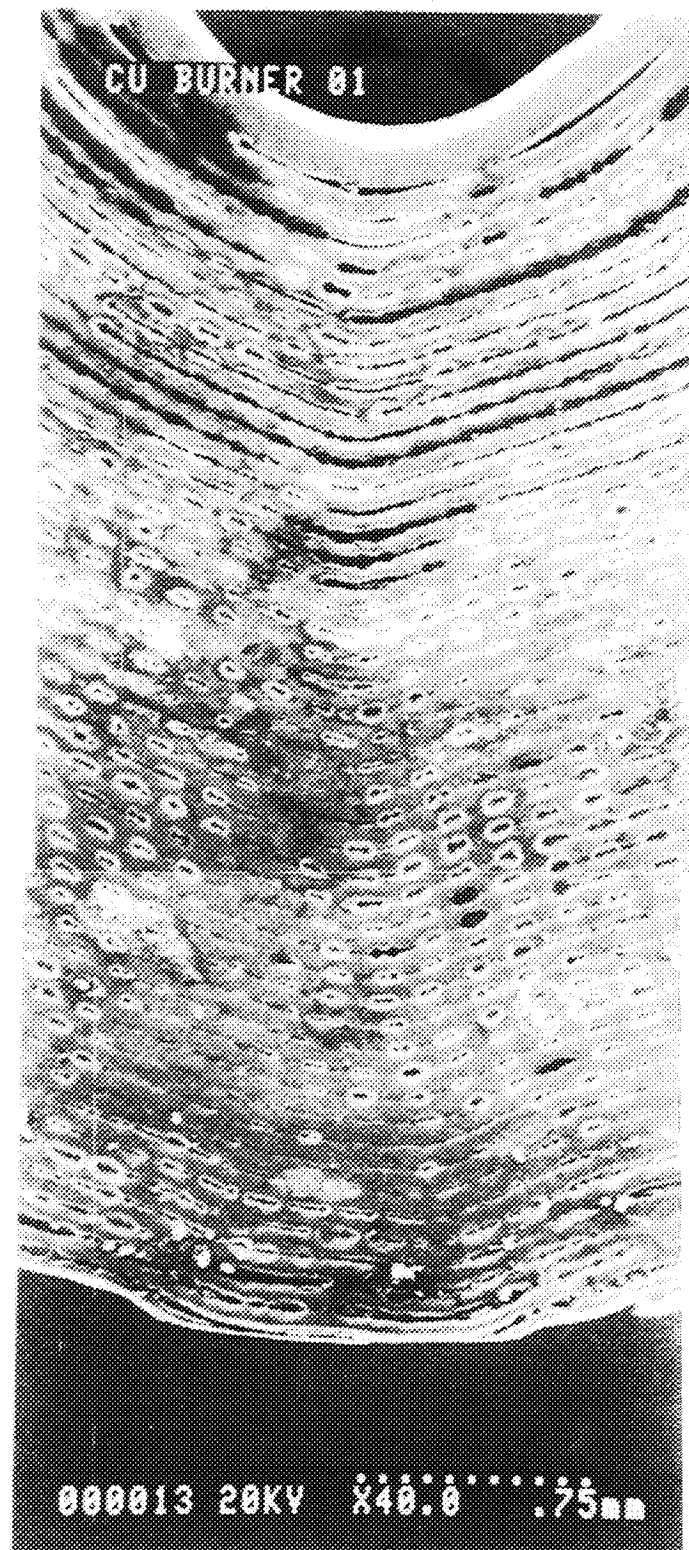


Figure 4.6.1-2A. SEM of Portion of Rolled Injector Face After Electropolishing

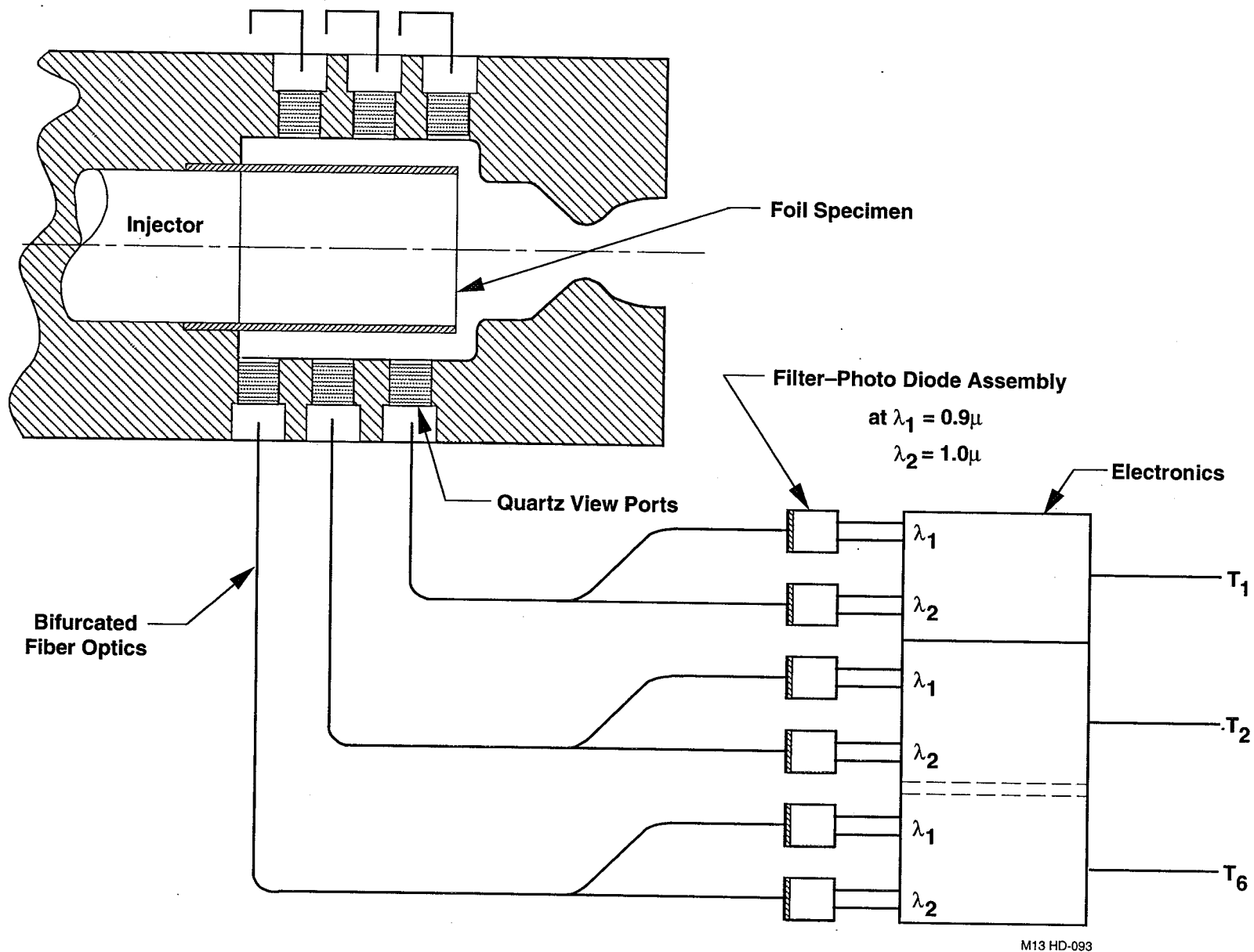


Figure 4.6.1-3. Optical Temperature Measurement Approach

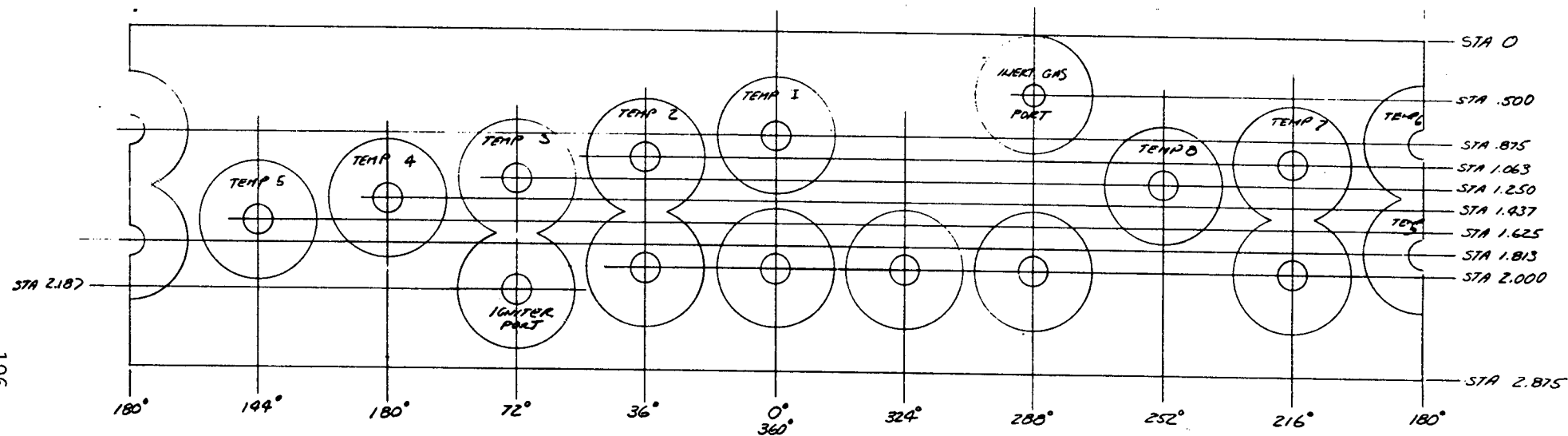


Figure 4.6.1-4. DTC Measurement Location

Table 4.6.1-1A. DTC Housing – Port Identification

Configuration: "A"

Run Number(s): Initial setup on stand 9-20-90 for fit and leak check

<u>Port ID</u>	<u>Axial Location, Inches (Note 1)</u>	<u>Circumf. Location, Degrees</u>	<u>Type</u>	<u>Use</u>
A1	2.375	45.0	Gas Port	Nitrogen input for specimen cooling
B1	2.000	0.0	Window	
B2	2.000	180.0	Window	
C1	1.750	135.0	Window	Pyrometer "A"
C2	1.750	315.0	Window	
D1	1.500	90.0	Window	
D2	1.500	270.0	Window	Pyrometer "B"
E1	1.250	45.0	Window	
E2	1.250	225.0	Window	Alternate video port
F1	1.000	0.0	Window	Pyrometer "F"
F2	1.000	180.0	Window	Pyrometer "E"
G1	0.875	22.5	Gas Port	Spark igniter
G2	0.875	67.5	Gas Port	Nitrogen input for Pc control
G3	0.875	112.5	Window	
G4	0.875	157.5	Window	
G5	0.875	202.5	Window	
G6	0.875	247.5	Gas Port	Nitrogen input for Pc control
G7	0.875	292.5	Window	
G8	0.875	337.5	Window	Video closeup

Note 1: 0.00 in. equals specimen exit plane

4.6, Diagnostic Thrust Chamber and Instrumentation Evaluation (cont.)

The windows in Row No. 7 match the optical paths of the ESMS whose detector head is shown schematically in Figure 4.6.1-5. It contains detectors and optics for two narrow band emissions measurements, one atomic absorption measurement, and one wide-band optical multichannel analyzer (OMA) measurement. In addition, the ring contains an optical temperature measuring port which matches Row No. 6 since the aft end optical ports are blocked when the ring is in place over the chamber ports. When the ESMS detector ring is used at the DTC nozzle exit, all the chamber ports are available for measurement.

The testing planned for DTC is shown in Table 4.6.1-2. It consisted of a group of system checkout tests and then an array of tests exploring the two propellant combinations, oxygen-hydrogen and oxygen-methane, the three materials, rhenium, iridium and platinum, over a range of mixture ratio, chamber pressure and wall temperature. A further parameter whose effect could be explored is distance from the injector face to the end of the chamber wall, which represents distance from the reaction zone and, is related to the life times of transient species formed during the reaction process.

Data obtained from the DTC tests are optical plume composition and surface temperature measurements during the exposure which indicate onset and extent of chamber wall reaction, and measurements made on the specimen before and after exposure. Table 4.6.1-3 describes the measurement techniques available for study of the materials to be used where appropriate.

In order to have a base comparison of the test sample material interaction, the as-received and tested sample materials must be characterized thoroughly. The pre- and posttest metallurgical evaluation consisted of a microstructure examination, surface mechanical characterization, and chemical composition determination.

Microstructure examination is necessary in order to characterize the base grain size, grain shape, and possible texturing of the sample materials. If this portion of the program was continued, samples of the materials of interest would be mounted, polished, and etched for metallographic examination using standard techniques. While platinum and iridium are difficult to metallographically etch, several techniques which are described in the literature can be employed in order to optimize the process. Techniques for etching rhenium have been developed and pose no problem. The grain size and shape of the materials would be

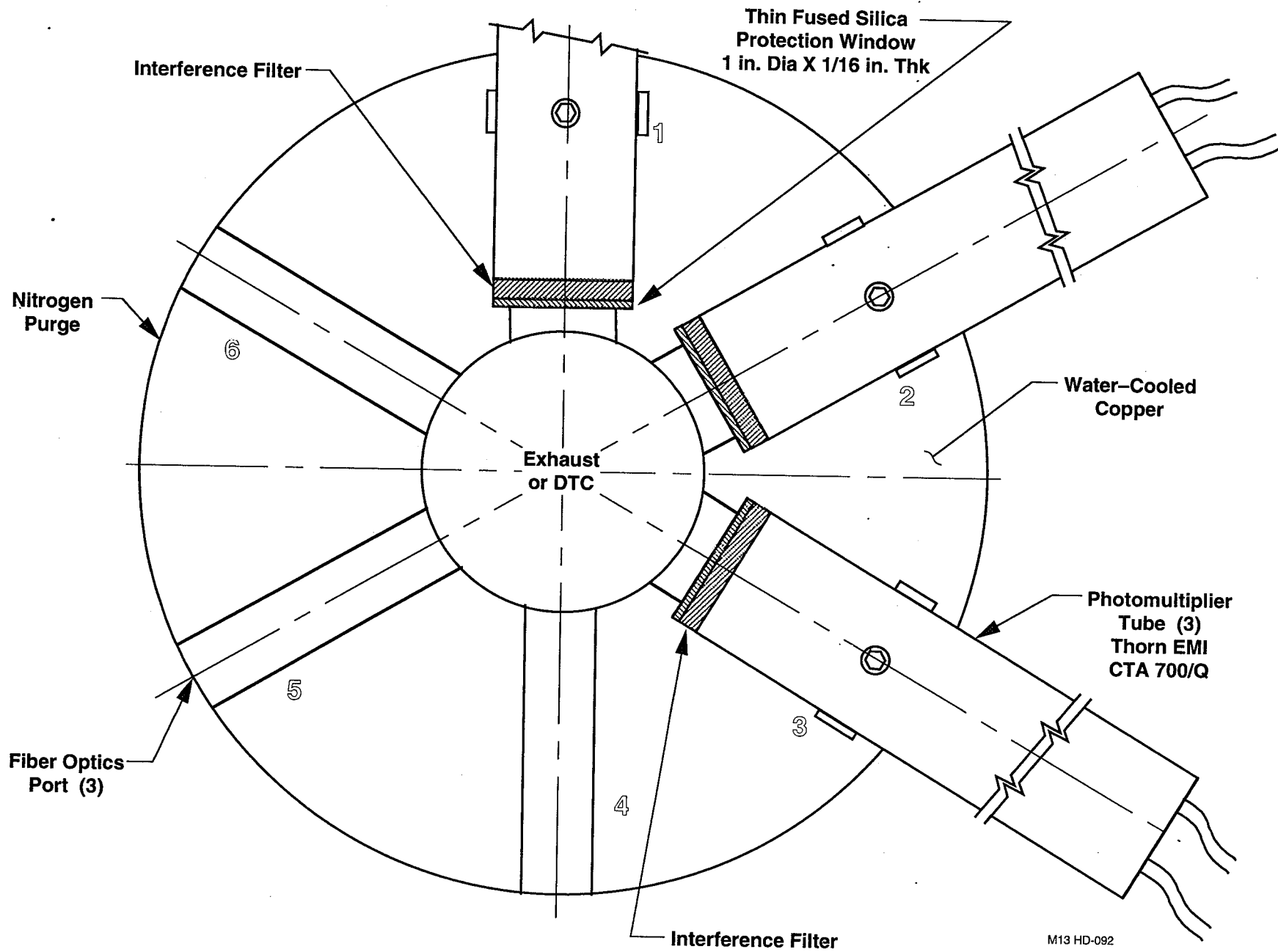


Figure 4.6.1-5. Exhaust Species Monitoring System Detector Head

Table 4.6.1-2
Test Matrix for Task 6.0

TEST TYPE	TEST OBJECTIVE	PR
CHECKOUT	PROOF	6N
"	LEAK	6N
"	FLOW BALANCE	O2
"	IGNITION	O2 MICRO-METALLOGRAPHIC ANALYSIS, DIMENSIONAL CHANGES
"	DIAGNOSTICS	O2 " " " "
MATERIAL INTERACTION	DETERMINE EFFECTS OF COMBUSTION PRODUCTS	MICRO-METALLOGRAPHIC ANALYSIS, DIMENSIONAL CHANGES
"	"	" " " "
"	"	" " " "
"	"	MICRO-METALLOGRAPHIC ANALYSIS, DIMENSIONAL CHANGES
"	"	" " " "
"	"	" " " "

Table 4.6.1-3. Specimen Analysis Procedures

<u>Procedure</u>	<u>Purpose</u>	<u>Results</u>
1. Optical Metallography	Characterize Microstructure	Grain size, grain shape, texture, substructure
2. Scanning Electron Microscopy (SEM)	Surface and Microstructure Characterization	Surface condition, surface damage, erosion, deposition, observation of microconstituents
3. Energy and/or Wavelength Dispersive X-ray Spectroscopy (EDS and WDS)	Chemical Composition of Microconstituents	Composition of secondary phases or contaminants before and after testing
4. Spark Emission Spectroscopy	Determine Chemical Composition	Identification of any impurities before and after testing
5. Roughness Measurements	Surface Roughness	Changes in surface conditions as a result of testing. Quantitative evaluation of material removed or deposited.
6. X-ray Diffraction	Crystallographic Orientation	Determination of texture and texture changes as a result of testing

4.6, Diagnostic Thrust Chamber and Instrumentation Evaluation (cont.)

characterized for comparison with samples after testing. This would provide a basis for determining if any microstructural changes have taken place during testing. It is not known what changes in microstructure and texture may take place during testing or what effects these changes may have on the chemical interaction of the specimens and the test environment. Both platinum and iridium are face centered cubic (FCC) materials and when these materials are heavily rolled, as they would be in thin foils, sharp textures can be formed upon recrystallization. In the case of heavily rolled rhenium, which has a hexagonal structure, basal plane slip may also result in a highly textured structure. Also, when rhenium is formed by chemical vapor deposition (CVD), it has a very ordered structure which has been observed to change dramatically during exposure to high temperatures. There is massive grain growth and an apparent reordering of the structure. Early indications are that rhenium is preferentially attacked on the basal planes and grain boundaries. Reordering and grain growth may slow the rate of attack by presenting an alternate crystallographic orientation and fewer grain boundaries for attack. If a major structural change is found to occur, it would be useful to determine the before and after texturing of the sample materials by using X-ray diffraction techniques. This helps to quantify observed microstructural changes and provides some insight into the chemical attack mechanisms.

Surface evaluation is necessary in order to determine the surface condition of the material being used for the test samples. Such features as rolling marks, surface flaws, cracks or other features that may be the result of a CVD process should be noted and photographed. Microscopic examination of the surface roughness and surface roughness measurements should be taken. These measurements and observations should be compared with the posttest surfaces. This would allow the determination of any localized erosion of (or deposition on) the surface. If there are any preferential areas of attack, such as grain boundaries, these can be observed as well.

Chemical composition of the samples can be used to determine any change in the samples during testing. Spark emission, energy dispersive X-ray, and wavelength dispersive X-ray spectra should be taken of as-received material. These spectra should be used as standards in order to determine if any chemical changes have taken place. Contamination species may be diffused into the specimens either from the surface or through the grain boundaries. These changes of chemical composition should be noted and their effects on the chemical interactions assessed.

The design approach for control of chamber pressure and specimen temperature is shown schematically in Figure 4.6.1-6. Total chamber pressure can be controlled

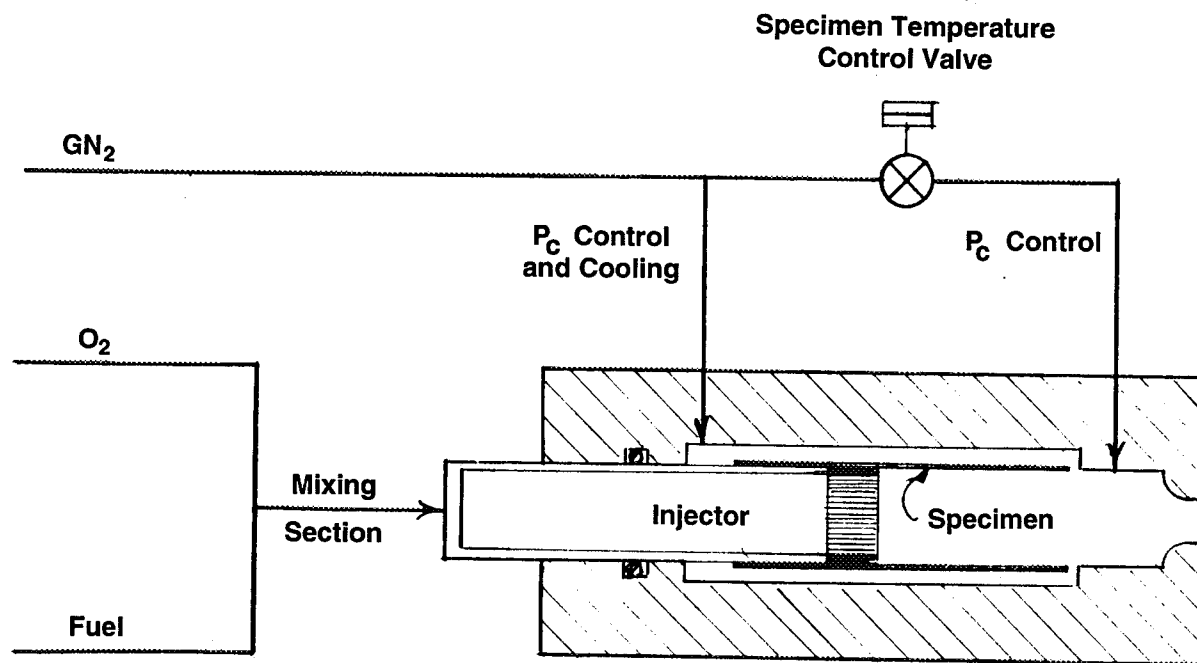


Figure 4.6.1-6. DTC Specimen Temperature Control

4.6, Diagnostic Thrust Chamber and Instrumentation Evaluation (cont.)

independently of propellant flows by control of the nitrogen flow added downstream of the specimen and upstream of the DTC throat. In addition, this total nitrogen flow can be split between cooling the backside of the specimen and direct injection into the chamber.

The effect the control nitrogen flow on propellant flow and chamber pressure is shown in Figures 4.6.1-7 and -8, where propellant flow of premixed O_2/H_2 is shown plotted versus chamber pressure, first for no added nitrogen and then with 0.05 lbf/sec. The effect of the nitrogen cooling on specimen temperature is shown in Figures 4.6.1-9 and -10, where calculated temperatures are shown for a specimen with emissivity of 1.0, for rhenium, and for iridium and platinum. As can be inferred from the latter figure, the nitrogen flow required to keep platinum specimens below their melting temperature must be a sizable fraction of propellant flow for chamber pressures above 40 psia. Because of its relatively low melting point, operating conditions are most difficult to maintain for platinum. Based on its mechanical properties at elevated temperature, Figure 4.6.1-11, the specimen should be kept below about 2600°F to assure mechanical integrity.

The primary interaction between the combustion products and the chamber wall is expected to be attack by oxidizing species, whose concentrations are a strong function of mixture ratio and propellant combination. Total oxidizing species mole fraction is shown plotted against mixture ratio for O_2/H_2 and O_2/CH_4 in Figures 4.6.1-12 and -13. These data are shown normalized to stoichiometric mixture ratio in Figure 4.6.1-14. The top curve on the figure shows the ratio of oxidizing species for the methane fuel relative to hydrogen. For example, the oxidizing species are about equal for O_2/H_2 operating at $MR = 6.0$ and O_2/CH_4 operating at $MR = 3.0$ (0.75* Stoichiometric).

The final design of the Diagnostic Thruster is shown in Figures 4.6.1-14A, -14B, -14C, -14D and -14E which are the fabrication drawings for the chamber and injector.

Specimen Temperature Measurement System

Since material reaction rate is expected to be a strong function of specimen temperature, a reliable means for its measurement was required. Non-contact two-color radiation pyrometers were used to avoid the operational difficulties of multiple high temperature thermocouples bonded to the foil. A small, fiberoptic-based two-color pyrometer was designed that could permit use of up to 6 measurement locations on the specimen.

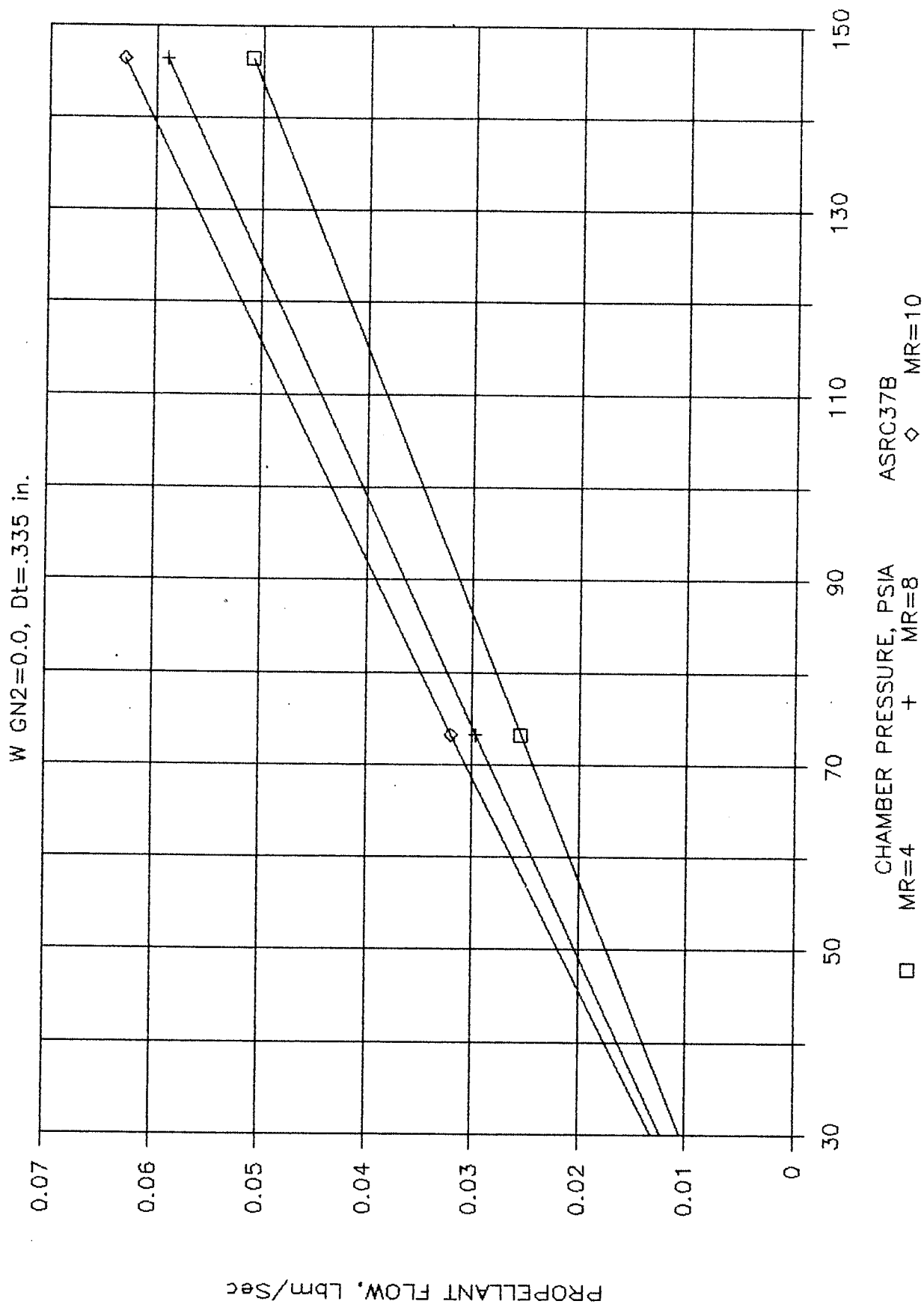


Figure 4.6.1-7. DTC Propellant Flow vs. P_c , O_2/H_2 (Nitrogen Flow = 0.0)

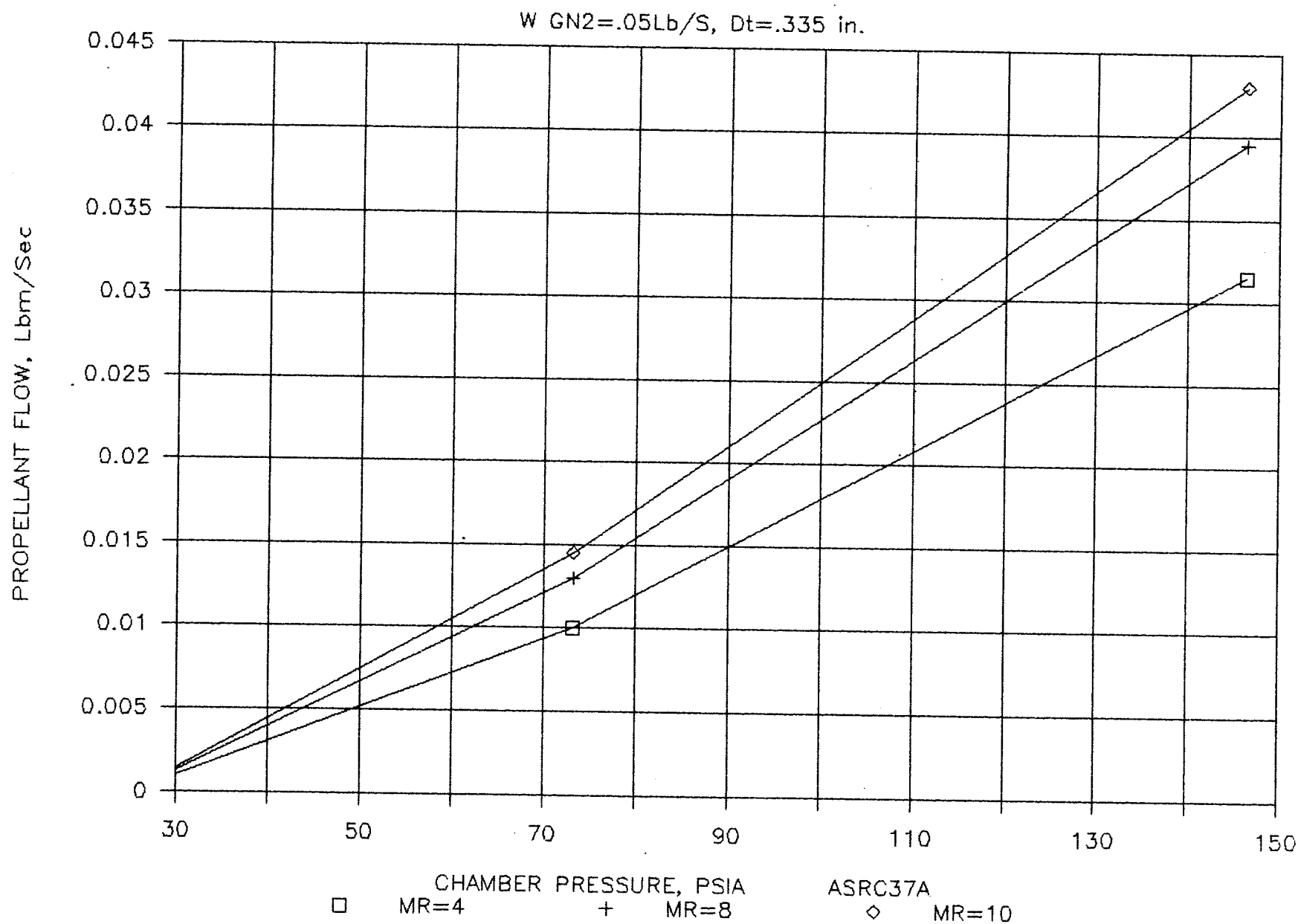


Figure 4.6.1-8. DTC Propellant Flow vs. P_c , O_2/H_2 (Nitrogen Flow = 0.05 lb/sec.)

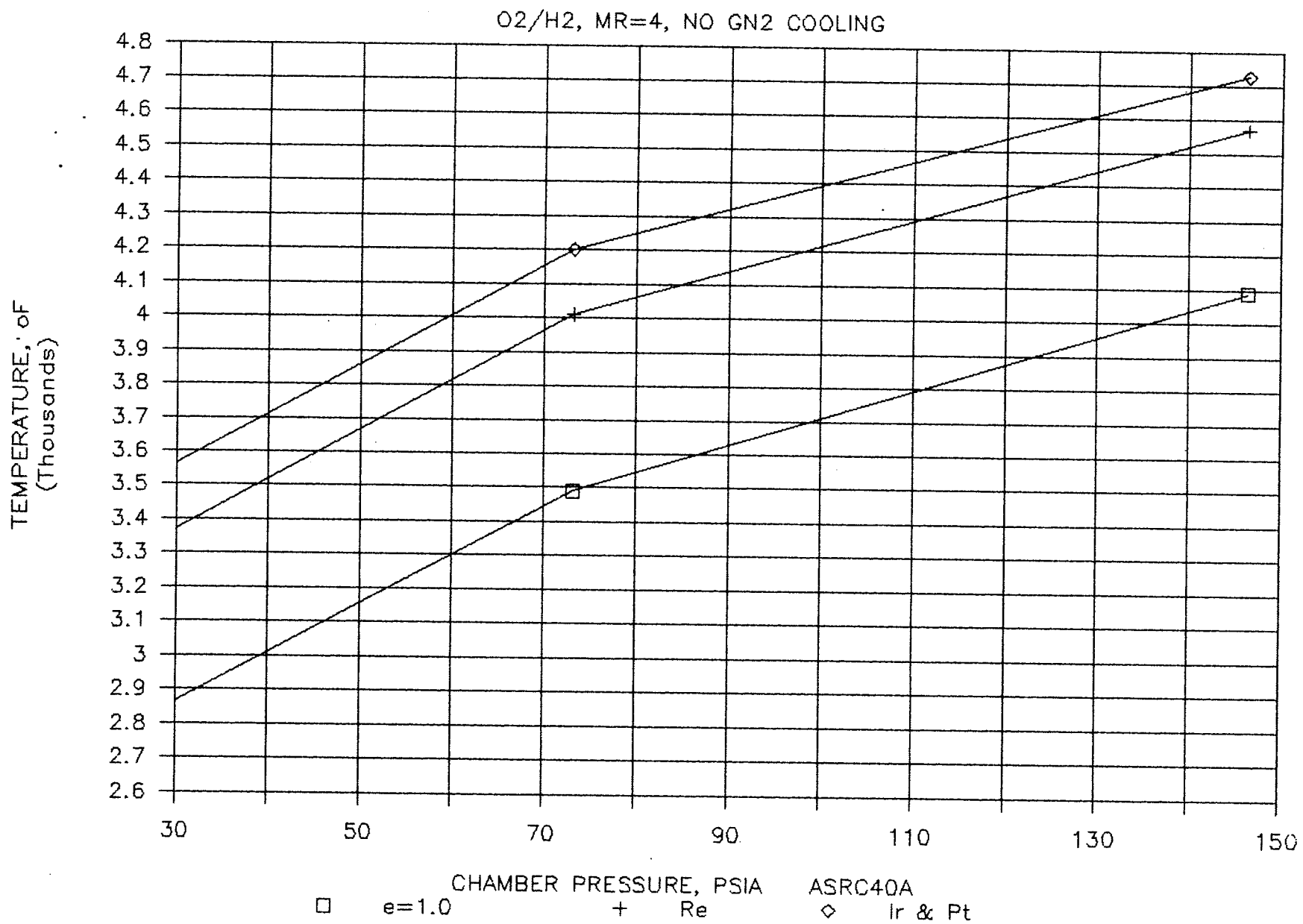


Figure 4.6.1-9. DTC Chamber Wall Temperature Vs. Pc (NitrogenFlow = 0.0)

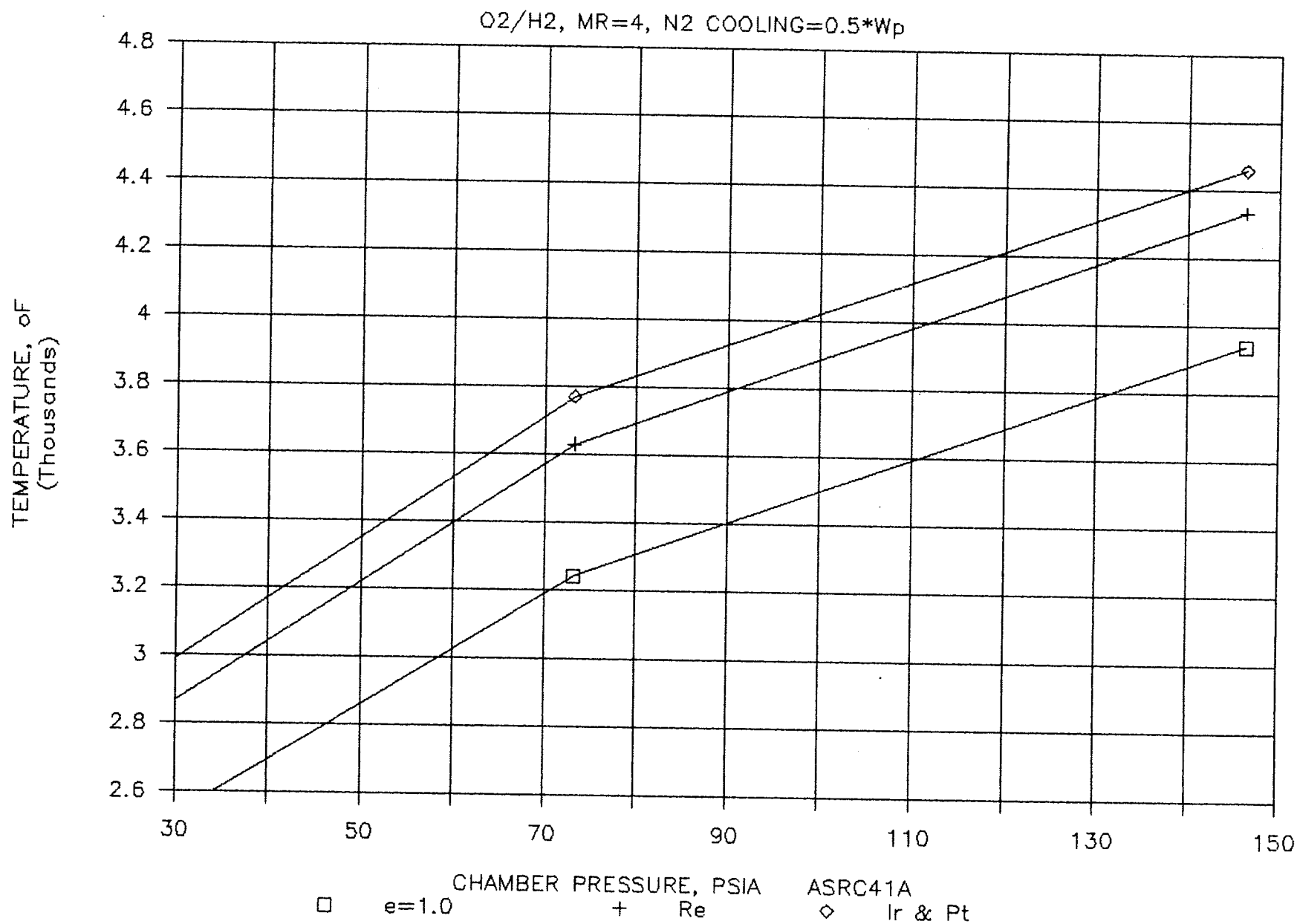


Figure 4.6.1-10. DTC Chamber Wall Temperature vs P_c (Nitrogen Flow = 0.5 = W_p)

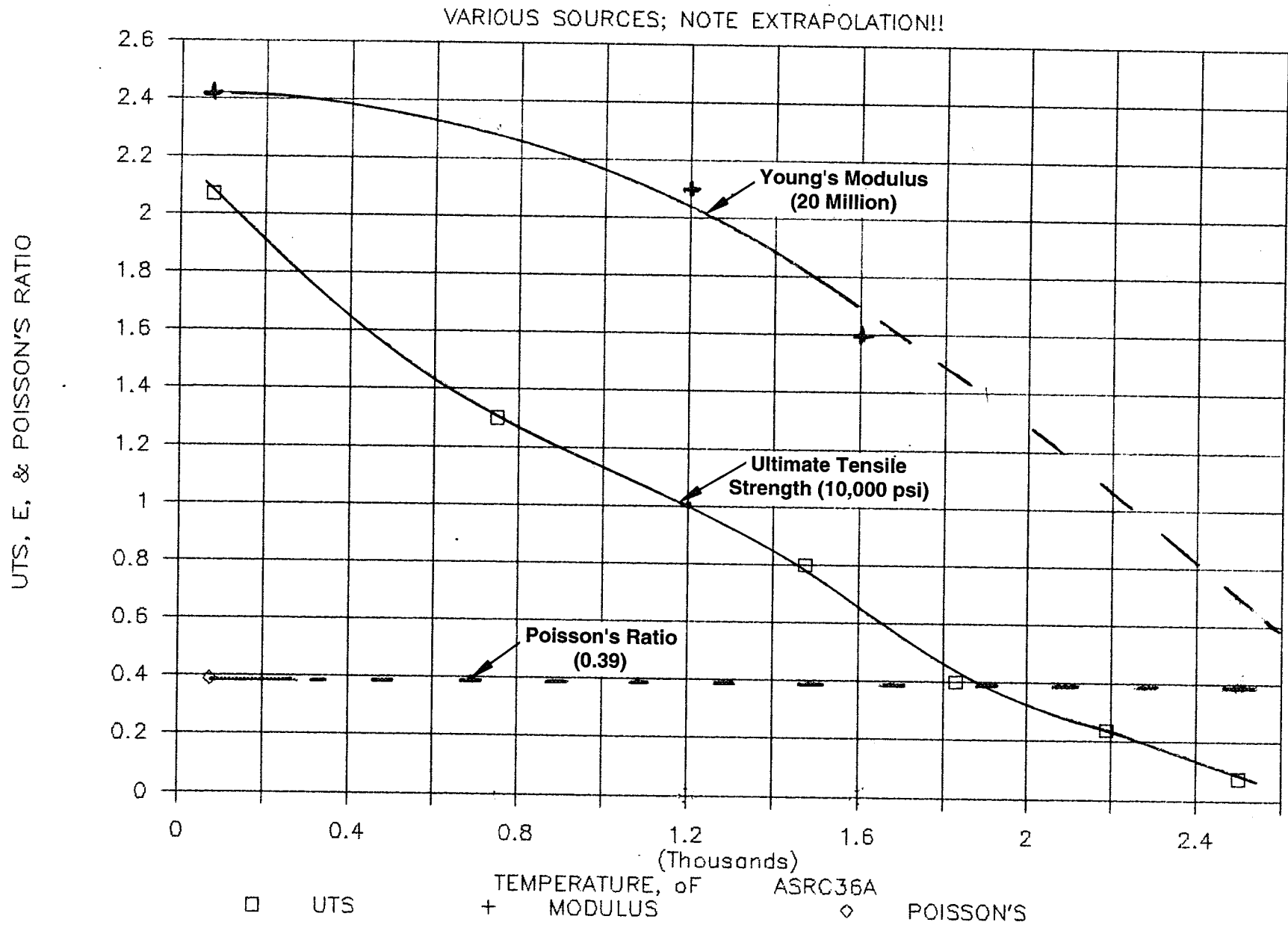


Figure 4.6.1-11. Mechanical Properties of Platinum Vs. Temperature

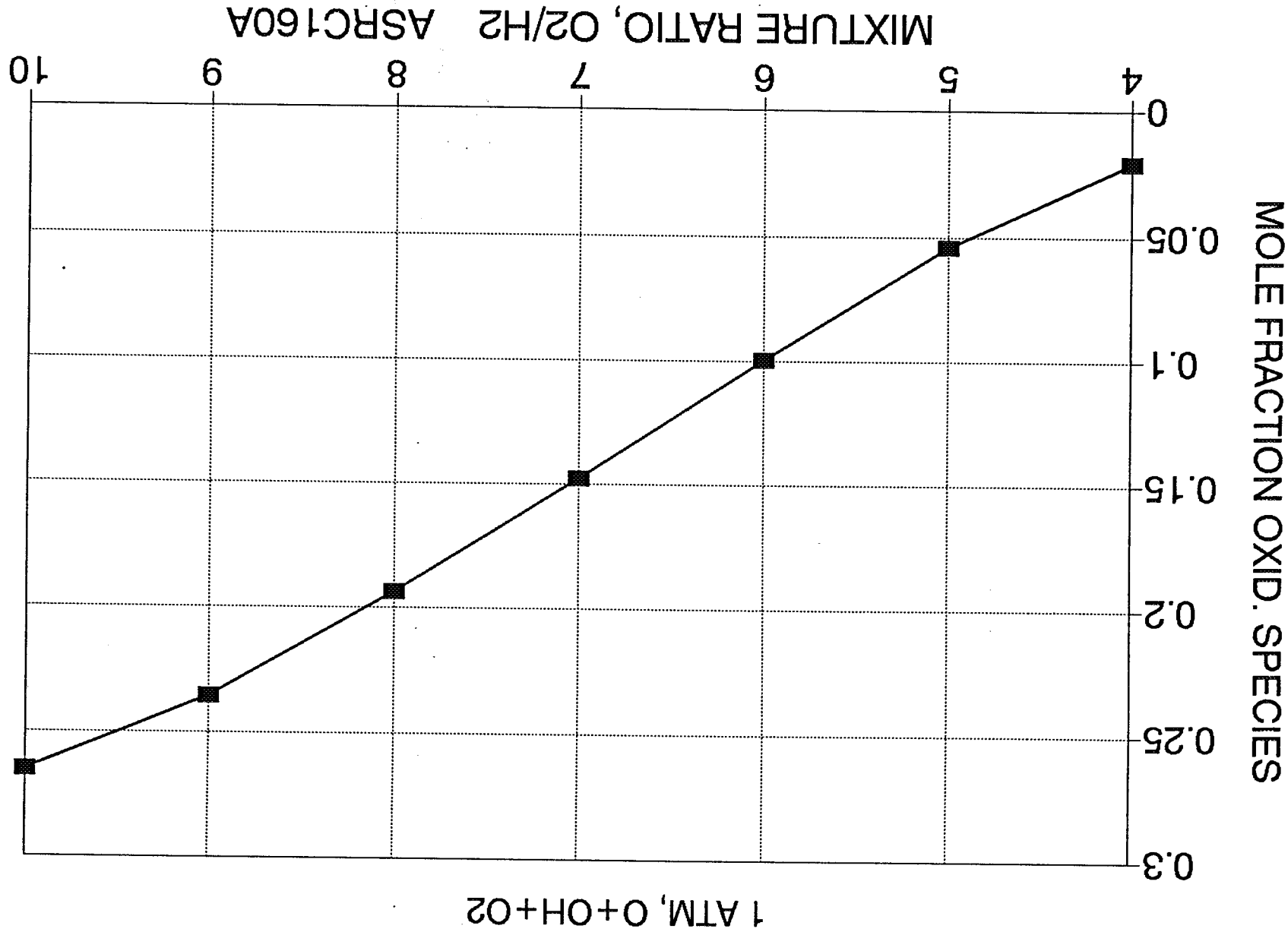


Figure 4.6.1-12. O₂/H₂ Comb. Prod. Total Oxid Species

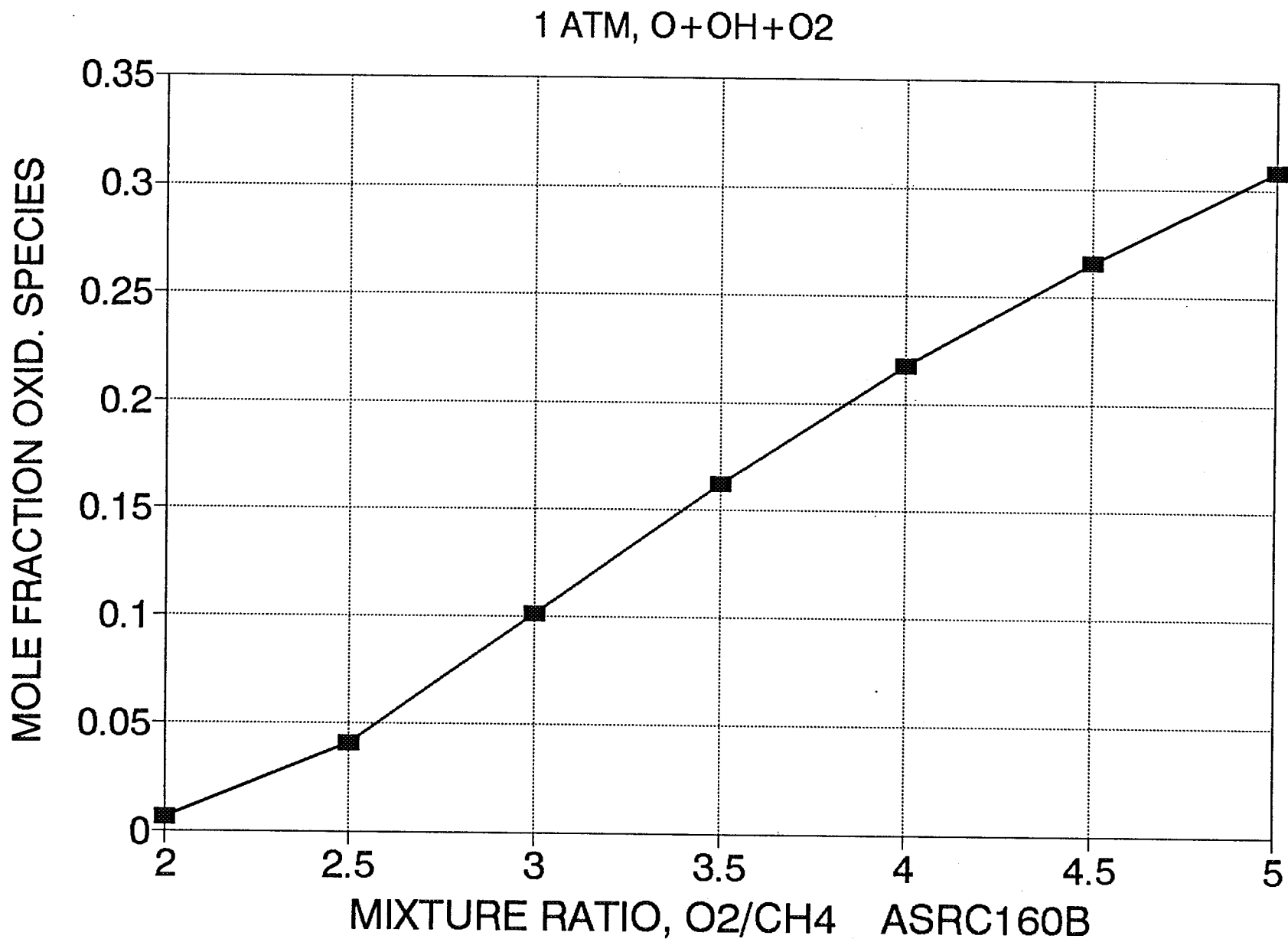


Figure 4.6.1-13. O₂/CH₄ Comb. Prod. Total Oxid Species

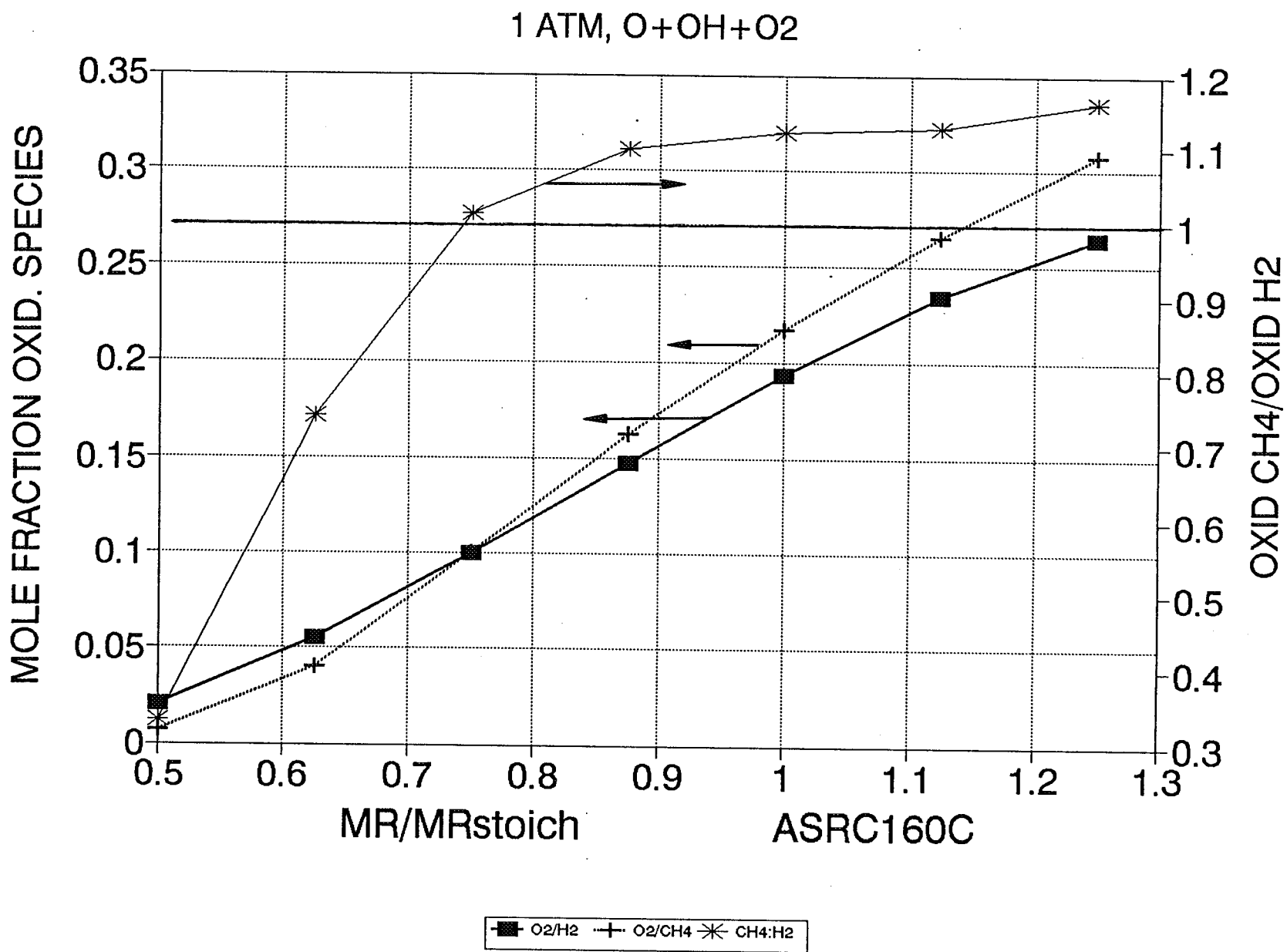
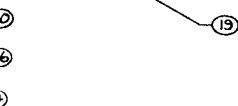


Figure 4.6.1-14. Total Oxidizing Species Vs. MR/MR_{stoich}



**INFORMATION PRINT ONLY
DO NOT FABRICATE
SAME CONFIGURATION PRINT MAY
REVEAL DIFFERENT INFORMATION
LATEST UNRELEASED REVISION
DATE**

213

FOLDOUT FRAME

H

NOTES:

1. INTERPRET DRAWING PER ATC-STD-4926
2. GTAW PER ATC-46351
3. PENETRANT INSPEC ALL WELDS PER ATC-STD-4942
TYPE I, METHOD A, ACCEPTANCE CRITERIA PER
ATC-STD-4005, CLASS II
4. MARK PER AS 478-2 WITH 1204391 AND
APPLICABLE DASH NO.
5. ITEM 13 OR 14 OR 15 IS AN ACCEPTABLE
SUBSTITUTE FOR ITEM 16
6. CLEANLINESS PER ATC-STD-4940, LEVEL 200
ON THE INTERNAL SURFACE OF ITEM 7 AND 29.
LEVEL VC ON ALL OTHER SURFACES.

G

F

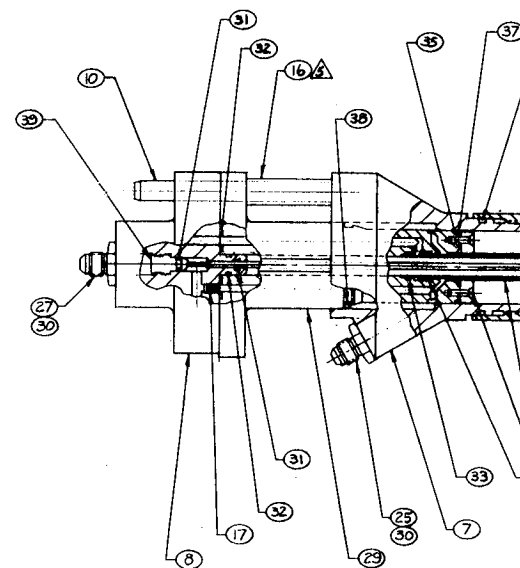
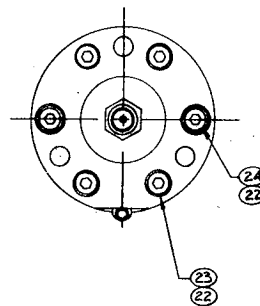
E

D

C

B

A



8

7

6

5

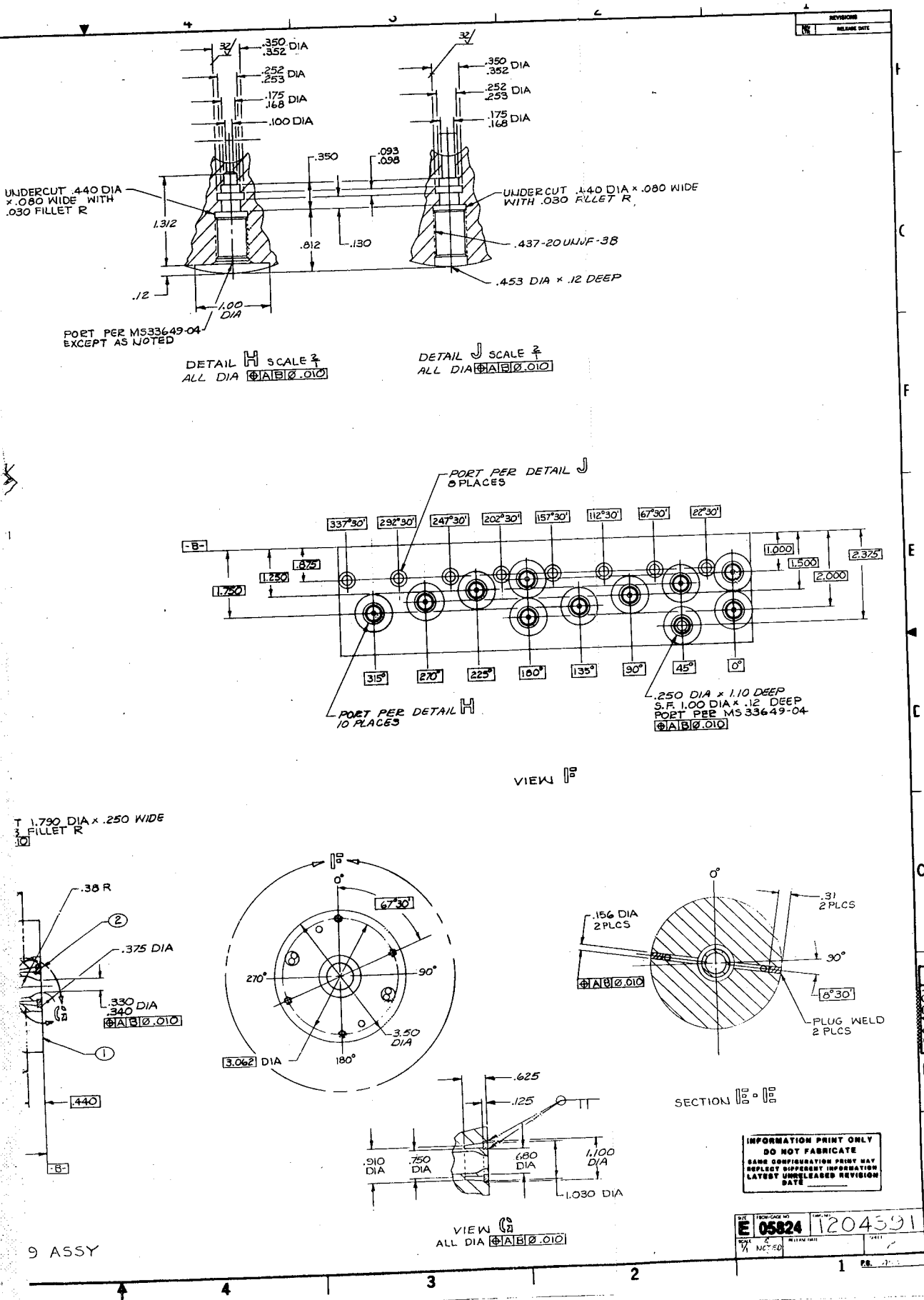
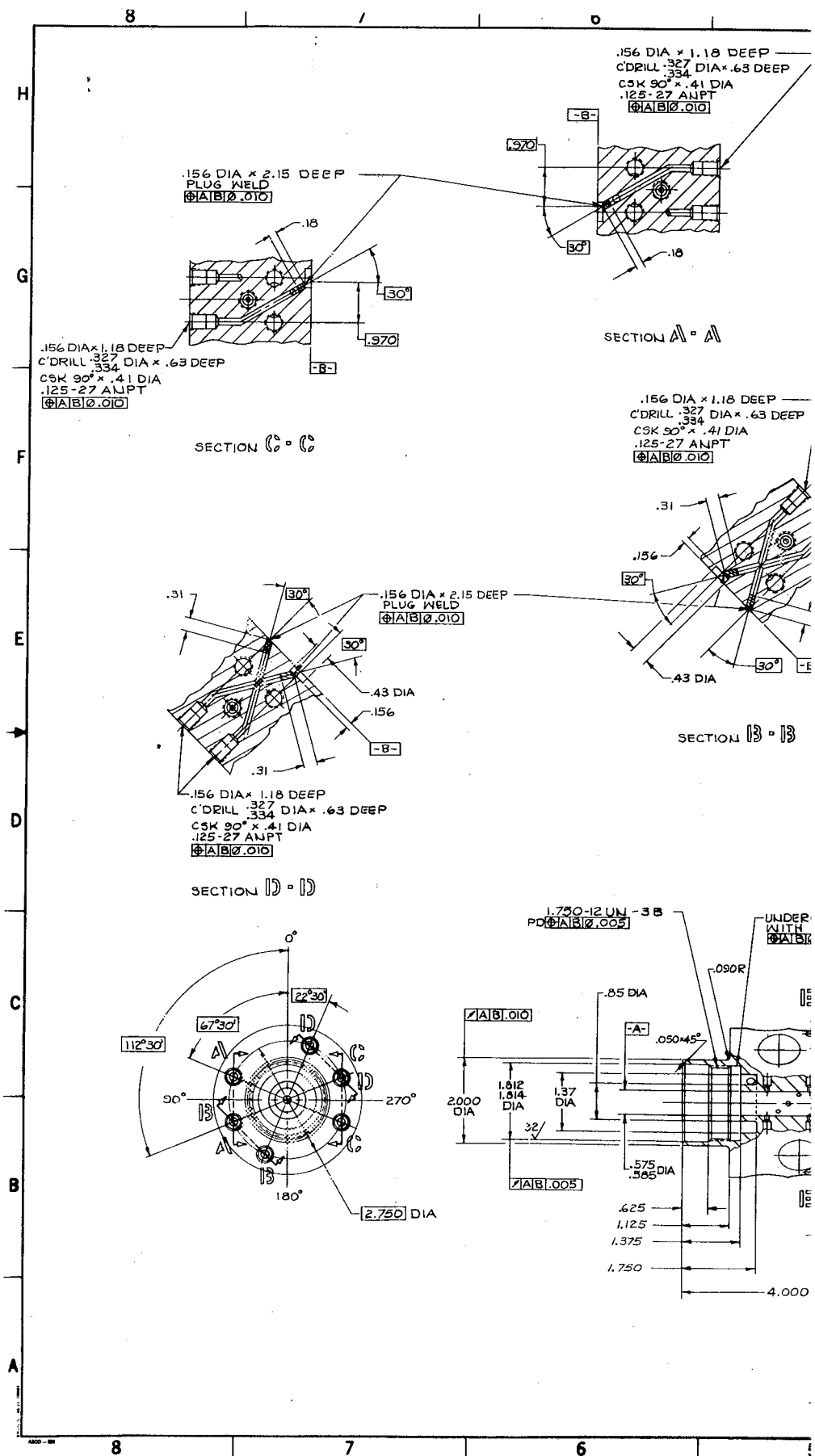


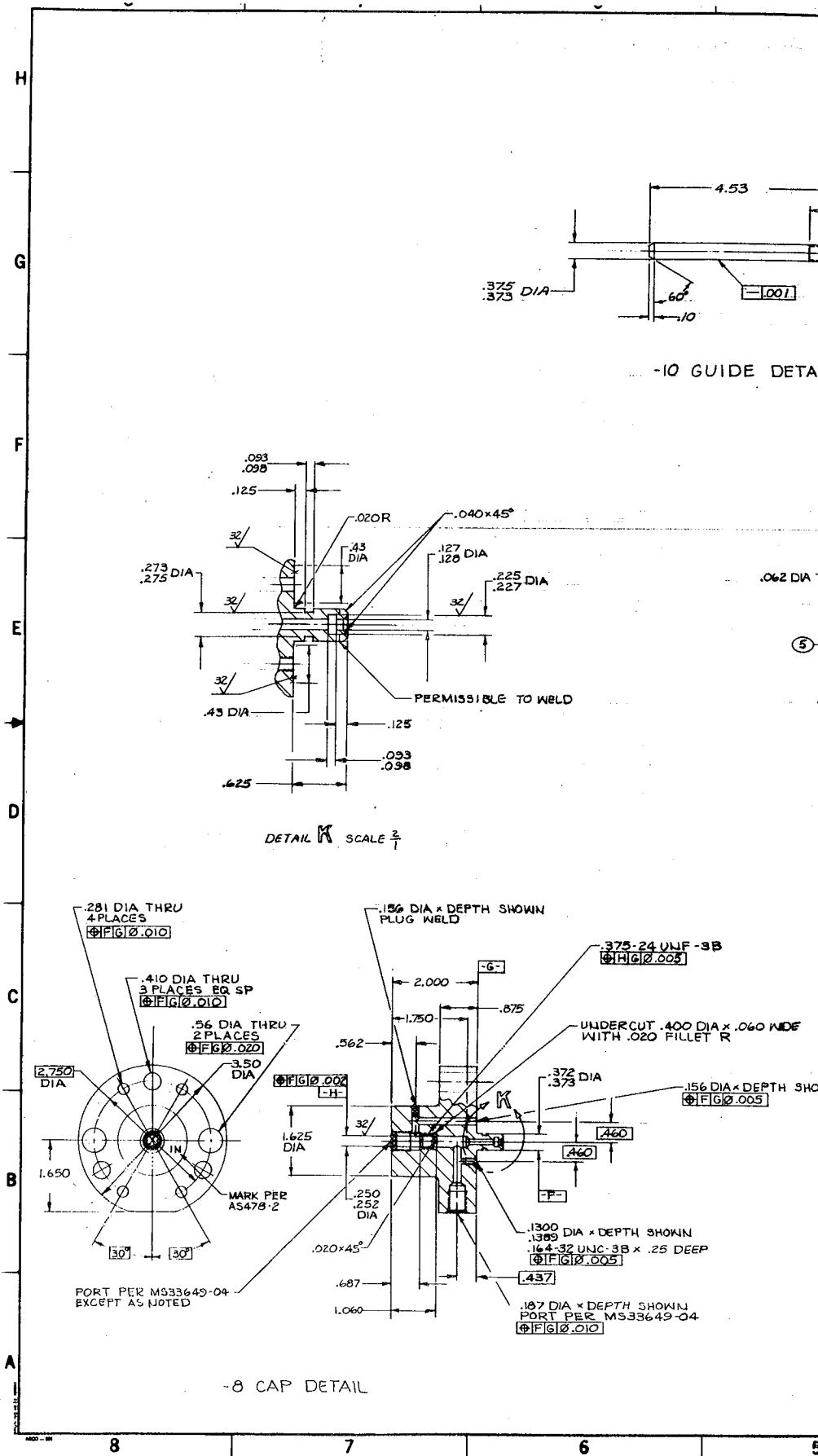
Figure 4.6.1-14B Chamber Assembly

FOLDOUT FRAME





1.





216

WELDOUT FRAME

H

G

F

E

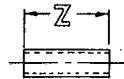
D

C

B

A

DASH NO	Z
-13	.875
-14	1.125
-15	1.375
-16	1.625



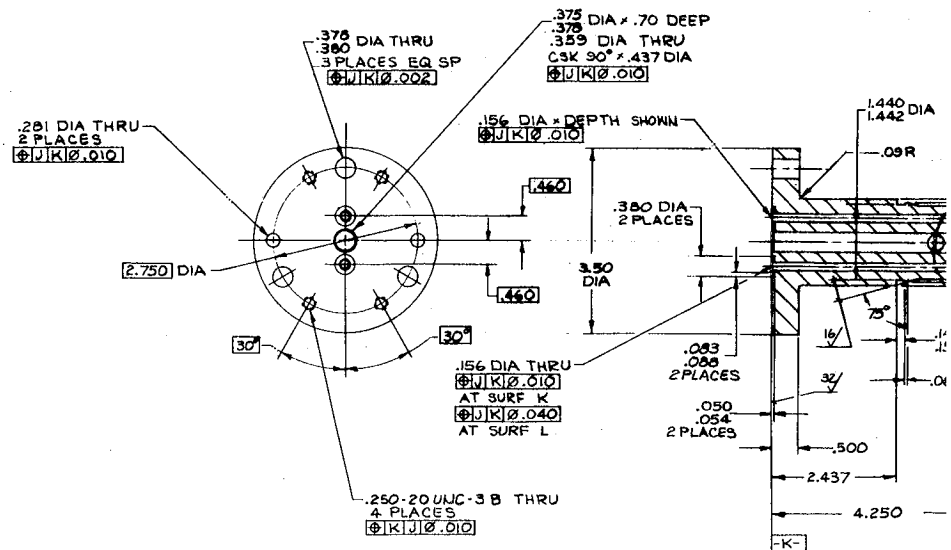
-13,-14,-15,-16 SLEEVE DETAIL

.032 DIA THRU

-17 ORIFICE DETAIL
SCALE 3/4

1.617
1.619
DIA REF

3



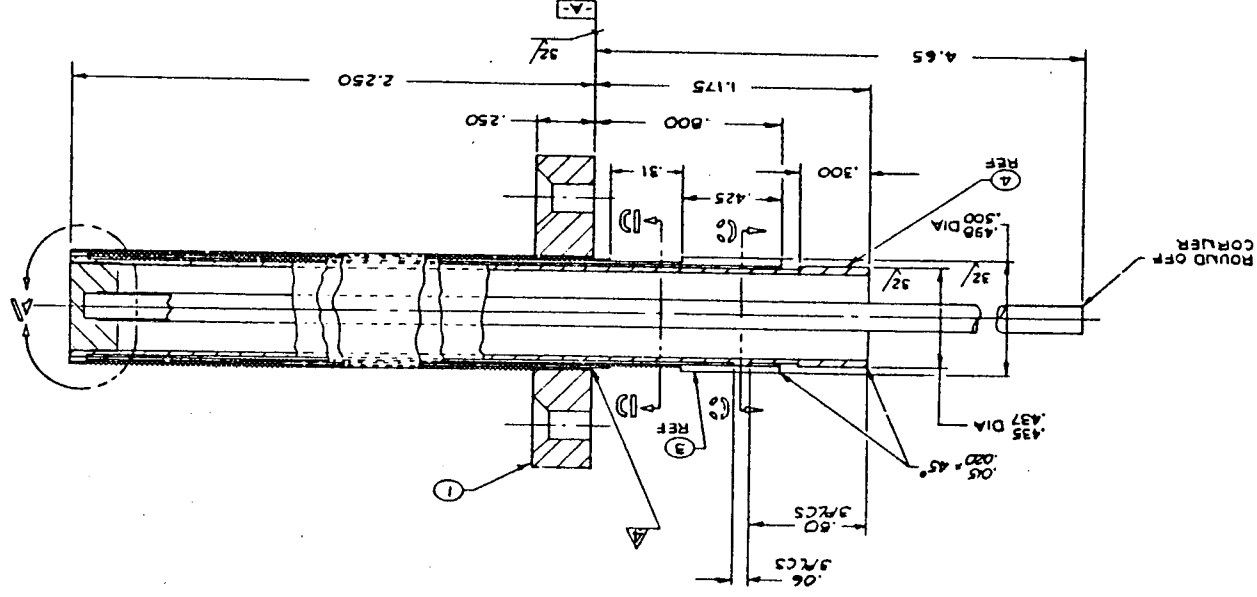
-3 MANIFOLD DETAIL

8

7

6

5



4.6, Diagnostic Thrust Chamber and Instrumentation Evaluation (cont.)

The pyrometer consisted of two EG&G DFA-XXXX photodiodes coupled to the optical ports on the DTC with bifurcated fiber optics. Individual sensor modules held the sensors and their electronics. The six modules were powered by a common power supply.

The sensors had integral narrow pass interference filters centered at 0.9 and 1.0 micron.

The specimen temperature is a function of the ratio of the two emission signals; the theoretical value for each signal is given by:

$$S_i = C_1 \lambda_i^{-5} [\exp(C_2/\lambda_i T) - 1]^{-1}$$

where

S_i = spectral radiance at λ_i and T , watt cm^{-1} micron $^{-1}$

C_1 = first radiation constant = $2\pi C^2 h = 3.741 \times 10^{12}$ watt cm^2

C_2 = second radiation constant = $hck^{-1} = 1.439$ cm°K

c = velocity of light = 2.9979×10^{14} micron sec^{-1}

h = Planck's constant = 6.625×10^{-34} watt sec^2

k = Boltzman's constant = 1.380×10^{-23} watt $\text{sec}^\circ\text{R}^{-1}$

The theoretical value of this ratio is shown in Figure 4.6.1-15 for $\lambda_1 = 0.9$ micron and $\lambda_2 = 1.0$ micron. However, the experimental value is dependent on factors such as the relative spectral transmission of the interference filters, spectral sensitivity of the diodes, view factor and transmission differences between the two optical paths, and differences in gains of the system electronics. Therefore, individual calibration is required.

To permit the required on-line setting of specimen temperature during a test, the measured temperature must be displayed in convenient form. For this purpose the calibration data have been fit as:

$$T_i = m_i \left(\frac{S_1}{S_2} \right)^n + b_1$$

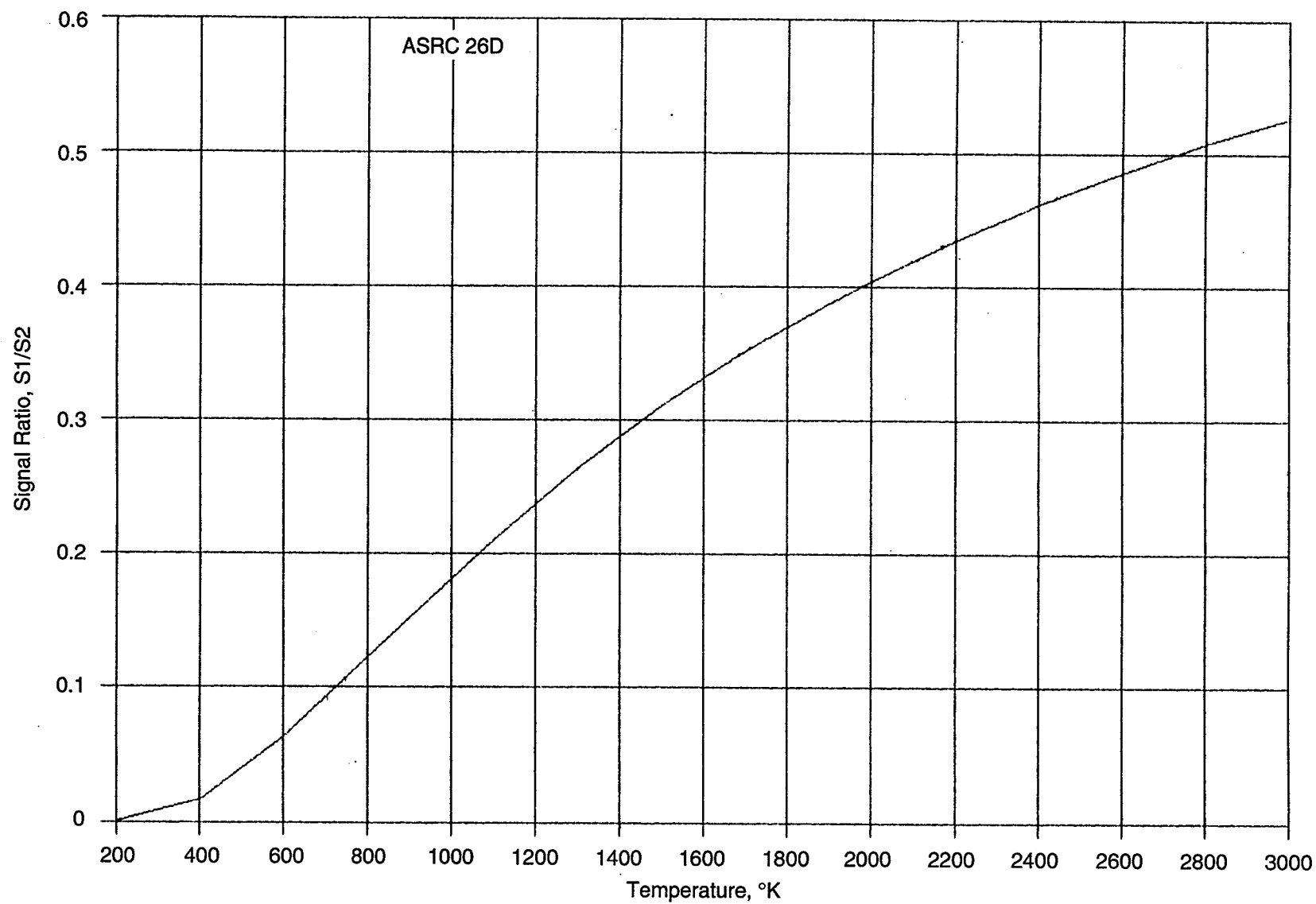


Figure 4.6.1-15. Two-Color Temperature Measurement - Emission Ratio Vs. Temperature, $\lambda_1 = 0.9\mu$; $\lambda_2 = 1.0\mu$

4.6, Diagnostic Thrust Chamber and Instrumentation Evaluation (cont.)

The individual pyrometers were calibrated using the setup shown in Figure 4.6.1-16. Absolute output signal for pyrometer Unit A is shown in Figure 4.6.1-16A. The calibration data are plotted for the units in Figures 4.6.1-17, 18, and -19 for $n = 3.00$, which gives a good fit to the data over the range of interest (1600 to 2500°C). The calibration parameters are listed in Table 4.6.1-4; deviation of the fit from the measured values is shown in Figures 4.6.1-20, -21, -22, and -23 for the four units used in testing. During calibration it was noted that because of the individual sensor optics, calibration was sensitive to distance from the sample surface.

An advantage of two-color radiation temperature measurement is relative insensitivity to signal level changes caused by clouding of windows, smoke or emissivity changes, as long as they are not wave length dependent. Also, in the presence of temperature gradients the measurements tend to indicate the highest temperature from which radiation is received. An example of this is shown in Figure 4.6.1-24 for a surface with equal areas at T_1 and T_2 where, with half the surface at 2400°C and half at 1000°C, the error in reading the higher temperature is less than 10%.

Exhaust Species Measurement System

The exhaust species of primary interest in the DTC tests are from the metallic specimen. These, along with some other species which could be present are shown in Table 4.6.1-5. This table also shows emission and absorption wave lengths and relative intensities. For a specific species and set of test conditions (e.g., temperature, concentration), either absorption or emission could be the preferred measuring technique. The ESMS was designed to provide great flexibility in making these measurements.

The ESMS consists of a 8-position detector head and associated electronics and instrumentation. The overall system is shown schematically in Figure 4.6.1-25. The detector head mounts at the thruster, either indexed to the view ports in the DTC or at the exhaust of a small thruster. The water-cooled detector head is coupled by cable and fiber optics to a Local Equipment Rack which can be up to 3 meters from the head. This rack contains reference/calibration lamps, OMA system, power supplies and electronics to interface to the operating equipment rack by coax and/or fiber optics data lines. The operating equipment rack is located in the control room and is connected to local displays and the control data acquisition system.

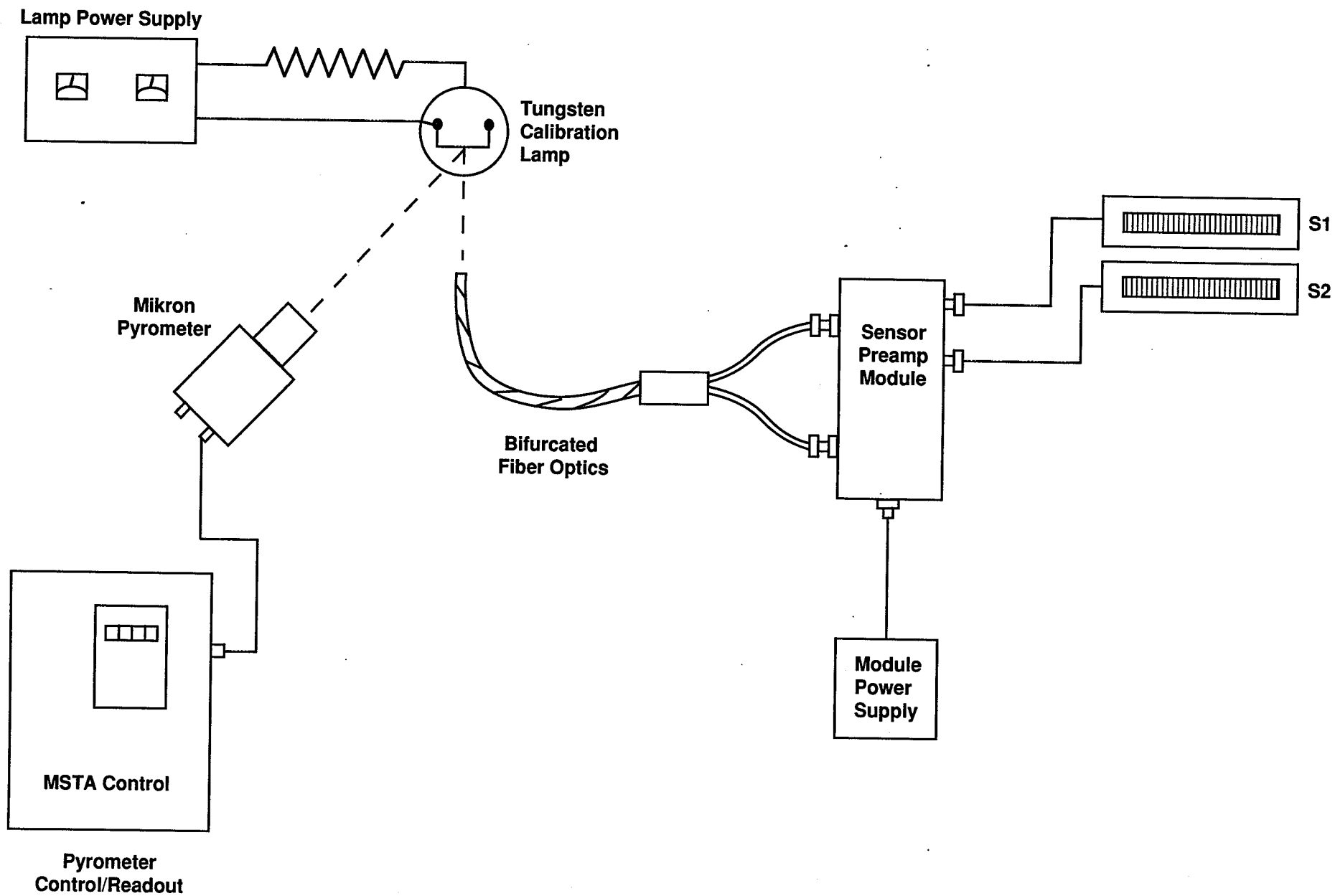


Figure 4.6.1-16. DTC Pyrometer Checkout and Calibration

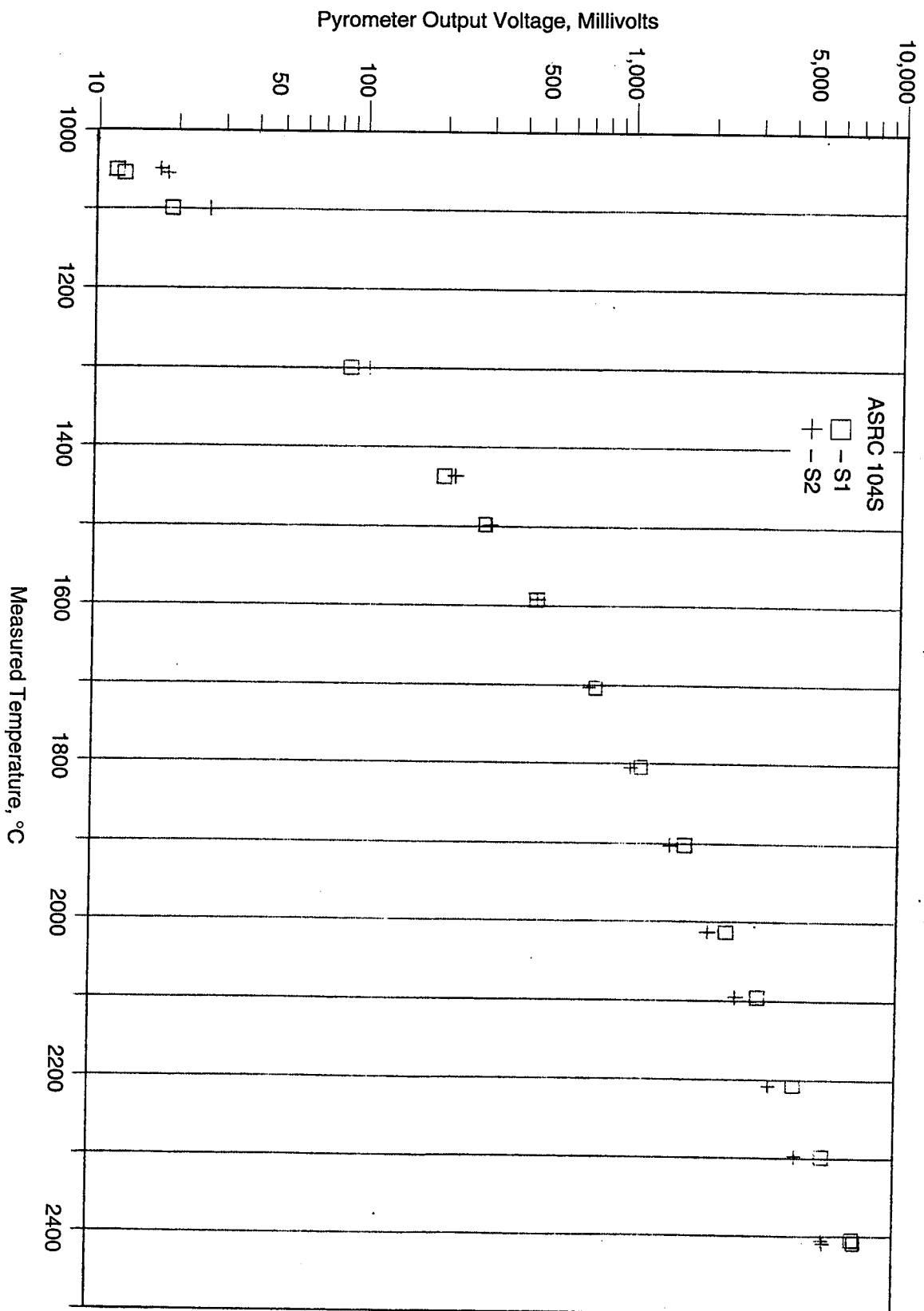


Figure 4.6.1-16A. Pyrometer Signals, S1 and S2, versus Temperature
 Unit A, S1 = 0.9 μ ; S2 = 1.0 μ

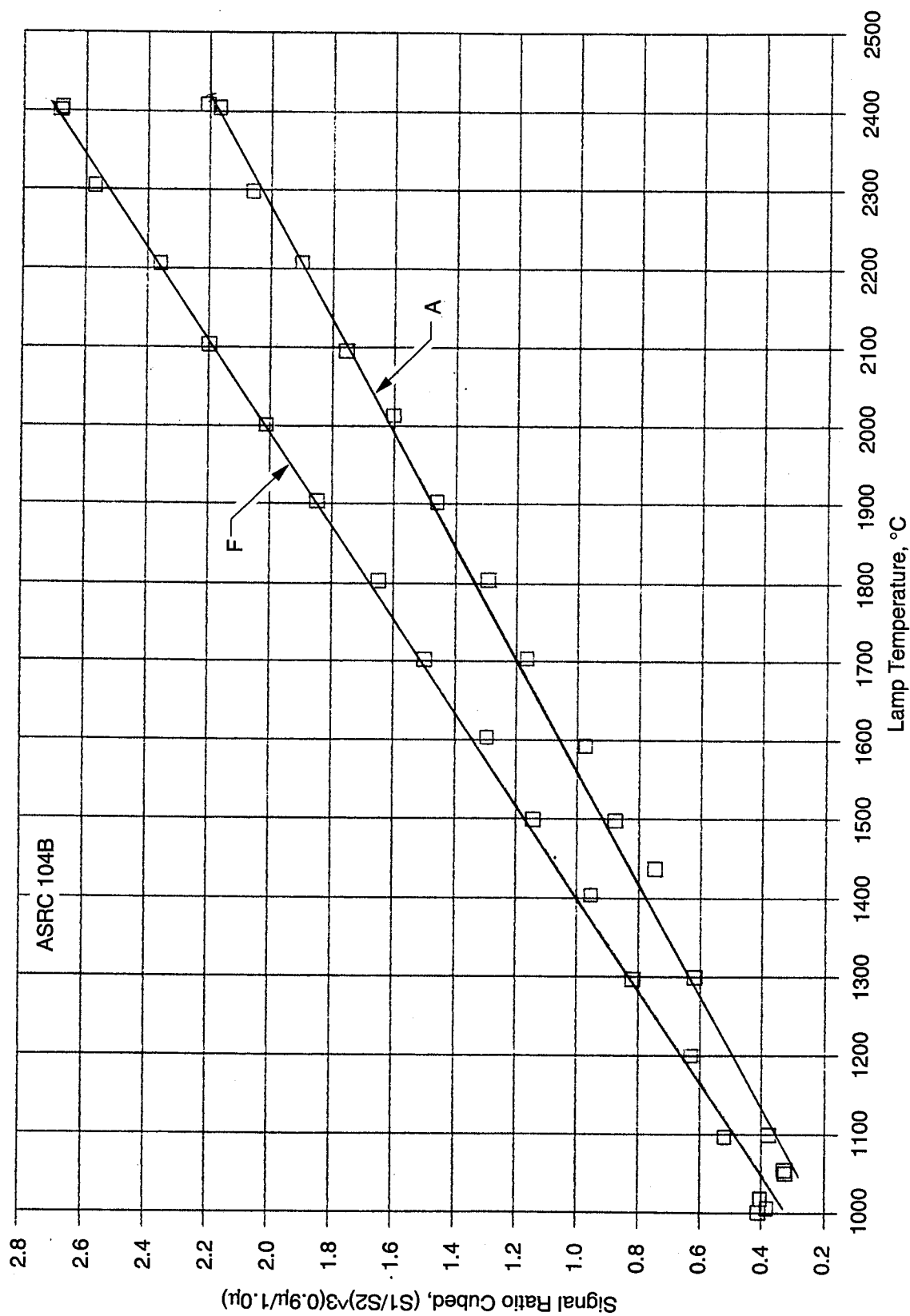


Figure 4.6.1-17. Signal Ratio Cubed versus Temperature
 T_{Lamp} : Micron; Unit A & F, 9-7-90

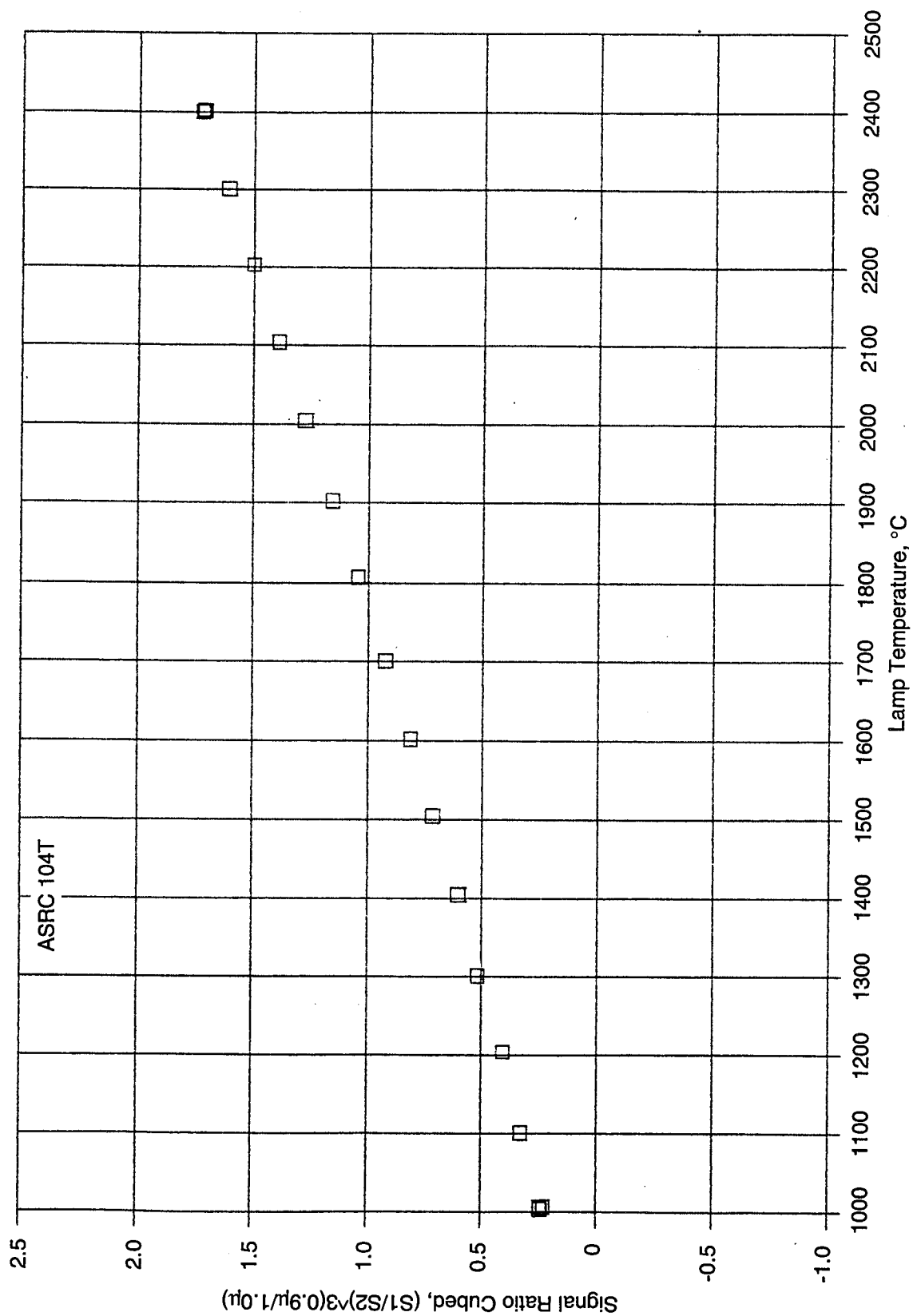


Figure 4.6.1-18. Signal Ratio Cubed versus Temperature
 T_{Lamp} : Micron; Unit B, 9-10-90

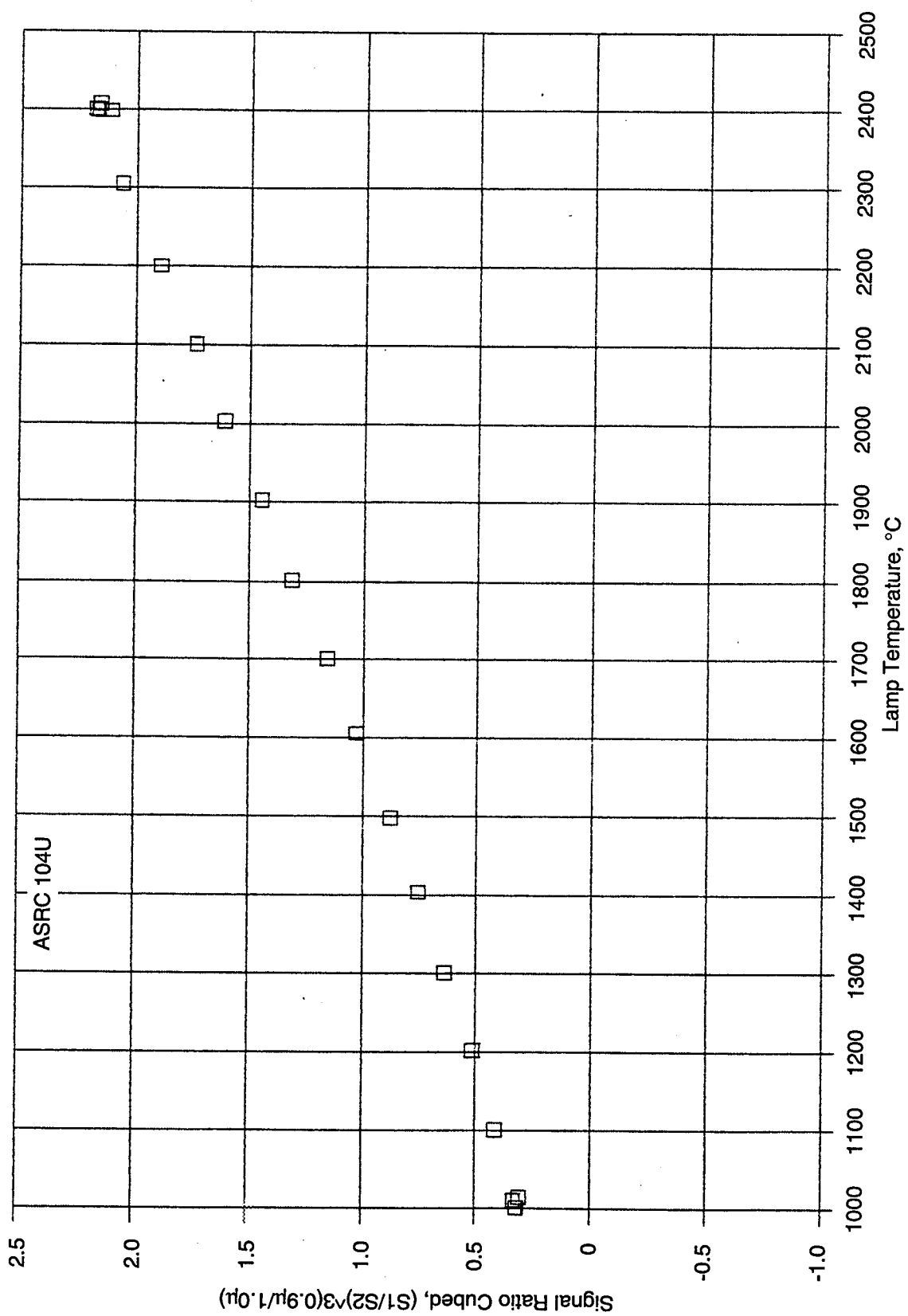


Figure 4.6.1-19. Signal Ratio Cubed versus Temperature
 T_{Lamp} : Micron; Unit E, 9-10-90

Table 4.6.1-4. Curve Fit Constants for Pyrometer Data

Fit: $T_x = m_x \left(\frac{S_1}{S_2} \right)^n + b_x$

<u>X = Unit ID</u>	<u>m_x</u>	<u>b_x</u>	<u>n</u>
A	677.1	929.6	3.000
B	893.5	869.6	3.000
C	N/A	—	—
D	N/A	—	—
E	716.3	868.9	3.000
F	576.0	845.0	3.000

T_x in °C

S_1, S_2 in millivolts

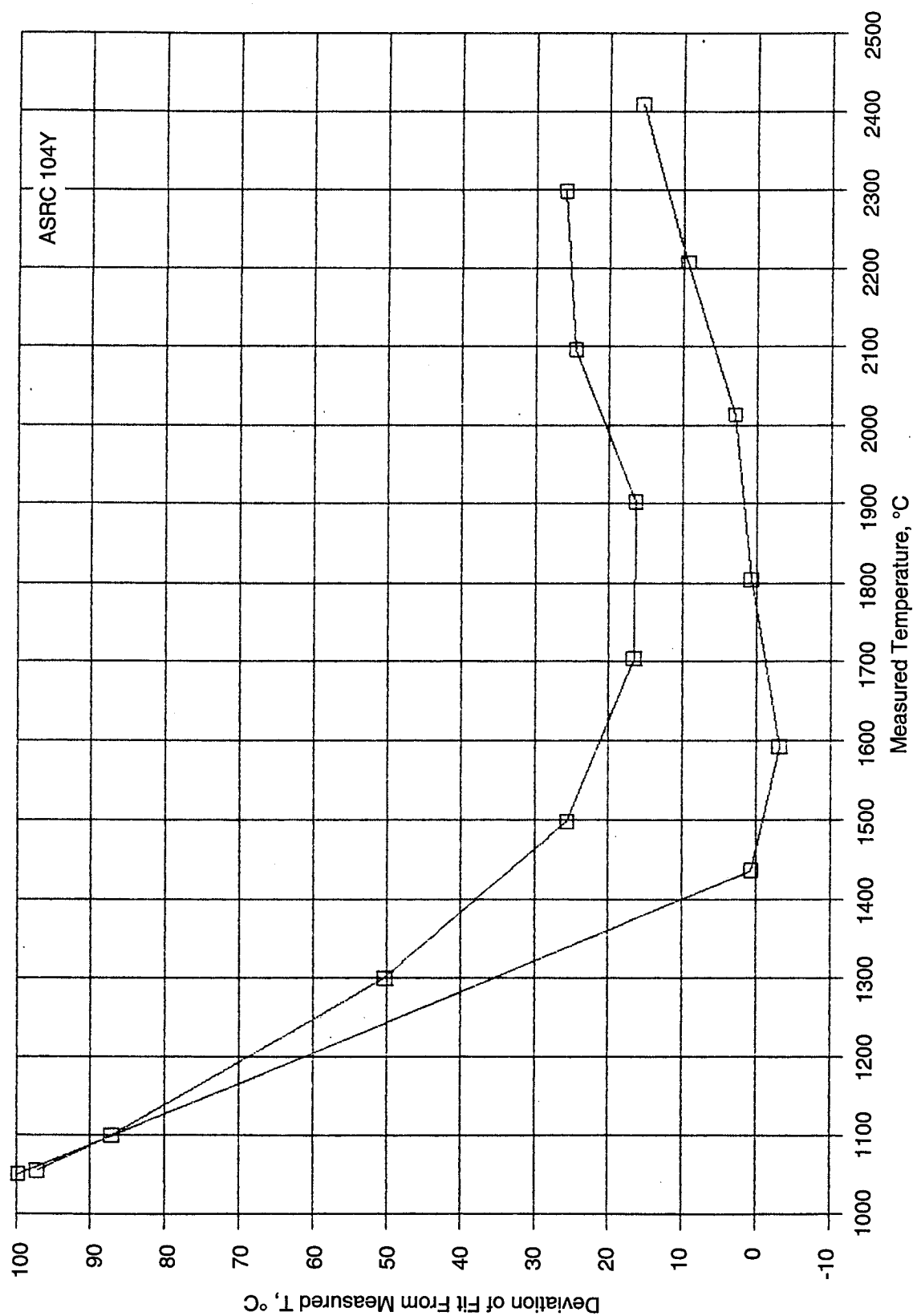


Figure 4.6.1-20. Pyrometer Fit Error versus Temperature
Unit A: $m = 677.1$; $b = 929.6$; $n = 3.000$

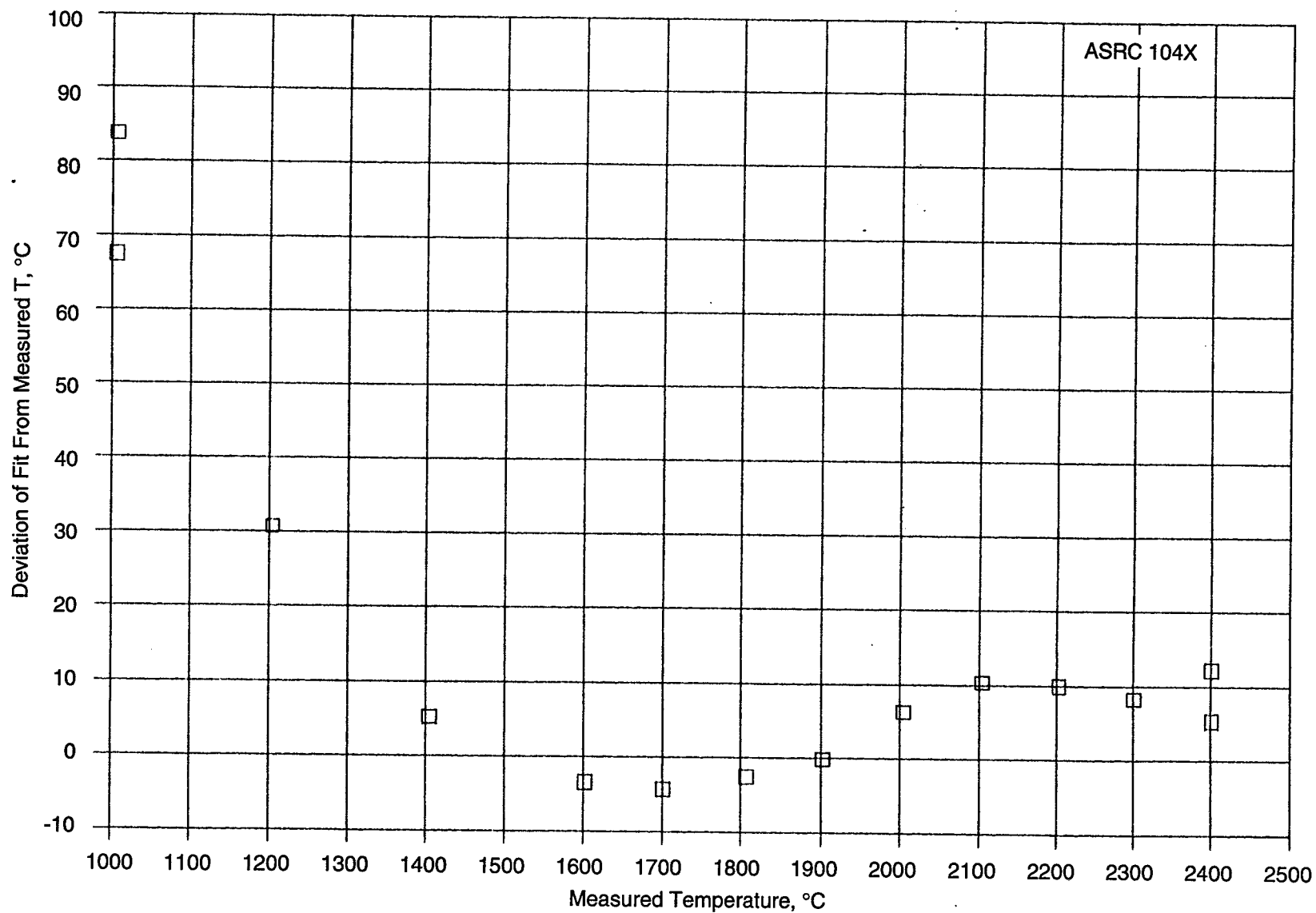


Figure 4.6.1-21. Pyrometer Fit Error versus Temperature
Unit B: $m = 893.5$; $b = 869.6$; $n = 3.000$

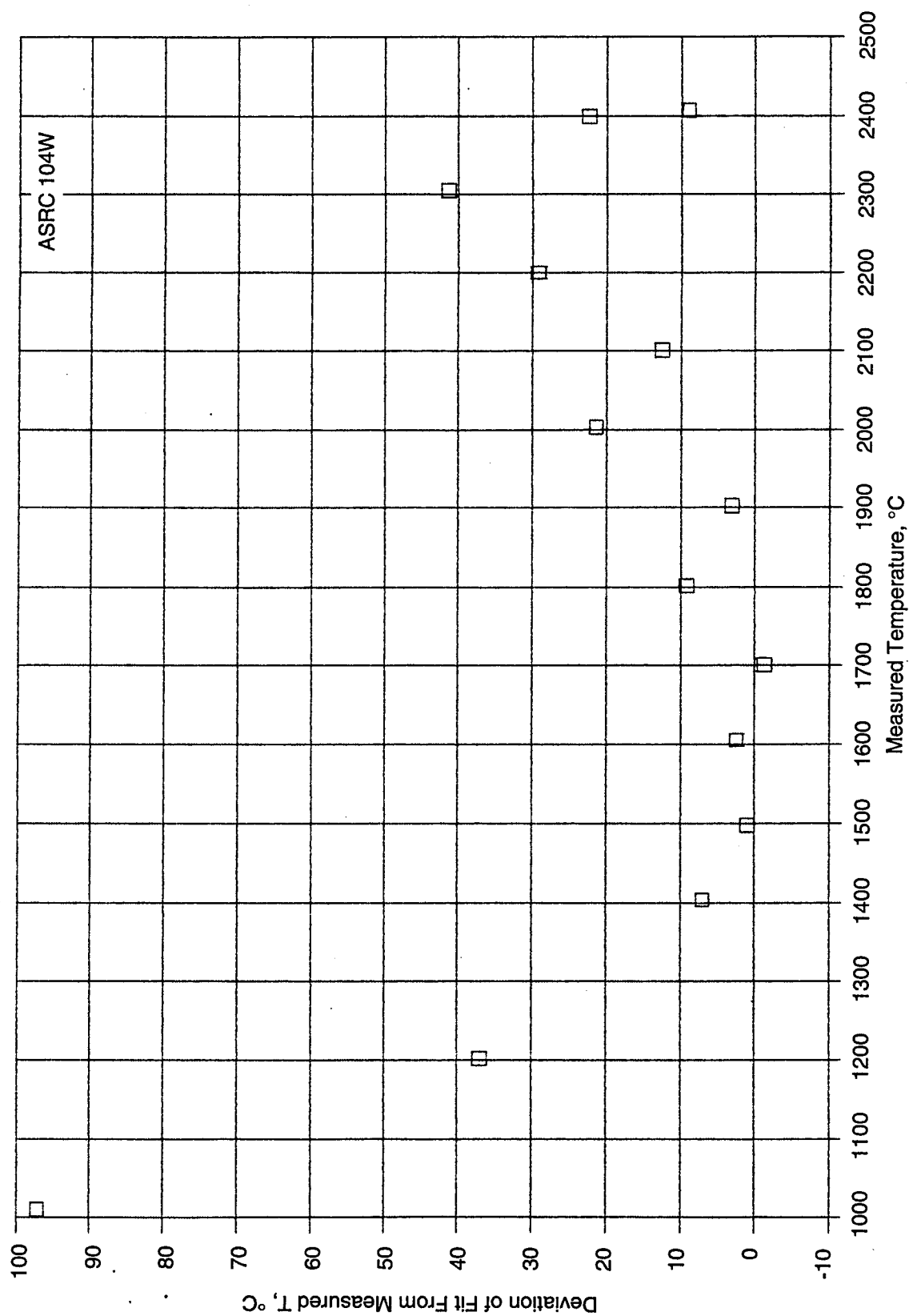


Figure 4.6.1-22. Pyrometer Fit Error versus Temperature
Unit E: $m = 716.3$; $b = 868.9$; $n = 3.000$

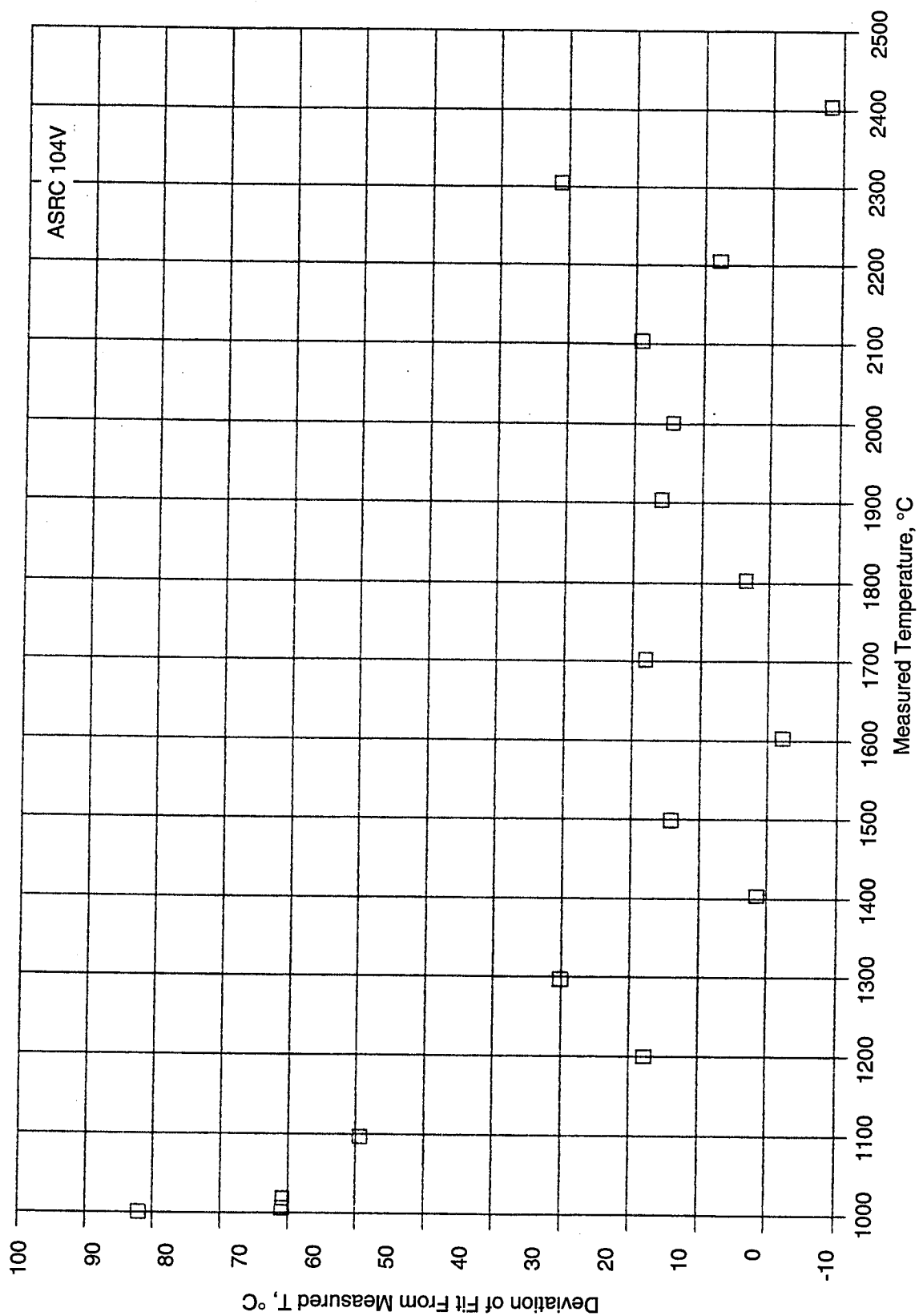


Figure 4.6.1-23. Pyrometer Fit Error versus Temperature
Unit F: $m = 576.0$; $b = 845.0$; $n = 3.000$

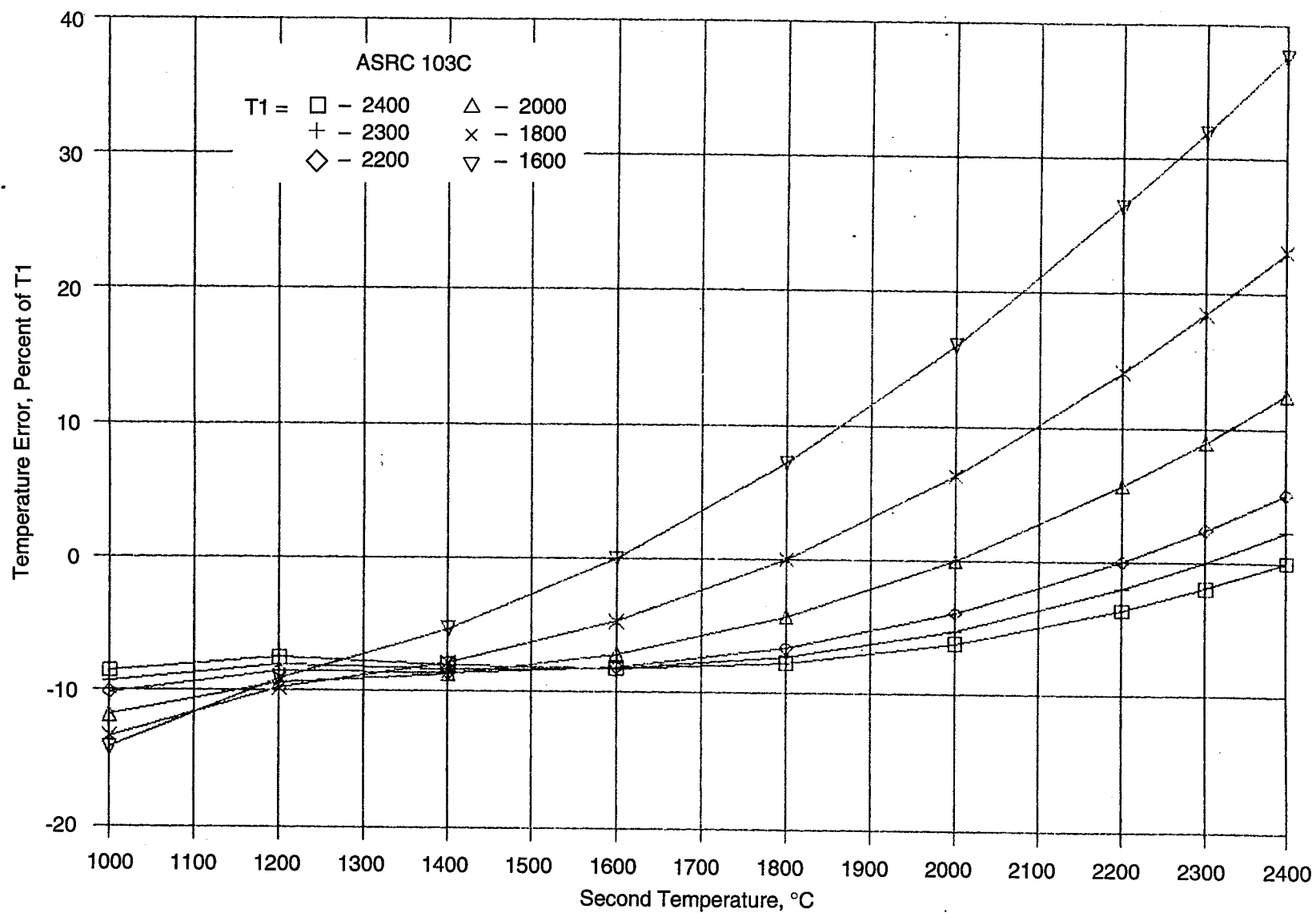


Figure 4.6.1-24. Pyrometer Error Due to Mixed Field Temperature
 Percent Error for Equal Area at T1 and T2
 (Unit A Calibration)

Table 4.6.1-5. Spectral Characteristics of Species of Interest

<u>Species</u>	<u>Measurement Type</u>	<u>Wave Length, mm</u>	<u>Relative Emission⁽¹⁾ Intensity (O/H Flame)</u>	<u>Absorption Detection Limit, PPB</u>
Rhenium	Emission	488.9	0.1	—
Rhenium	Absorption	346.1	—	TBD
Iridium	Emission	380.0	~0.15	—
Iridium	Absorption	266.5	—	TBD
Hydroxyl	Emission	310.0	(Depends on MR and ϵ (0) 100	—
Copper (Ref.)	Emission/Absorption	327.4	100	1.2
Nickel (Ref.)	Emission/Absorption	341.5	80	TBD

(1) Relative intensity on a scale where sodium = 50,000 counts.

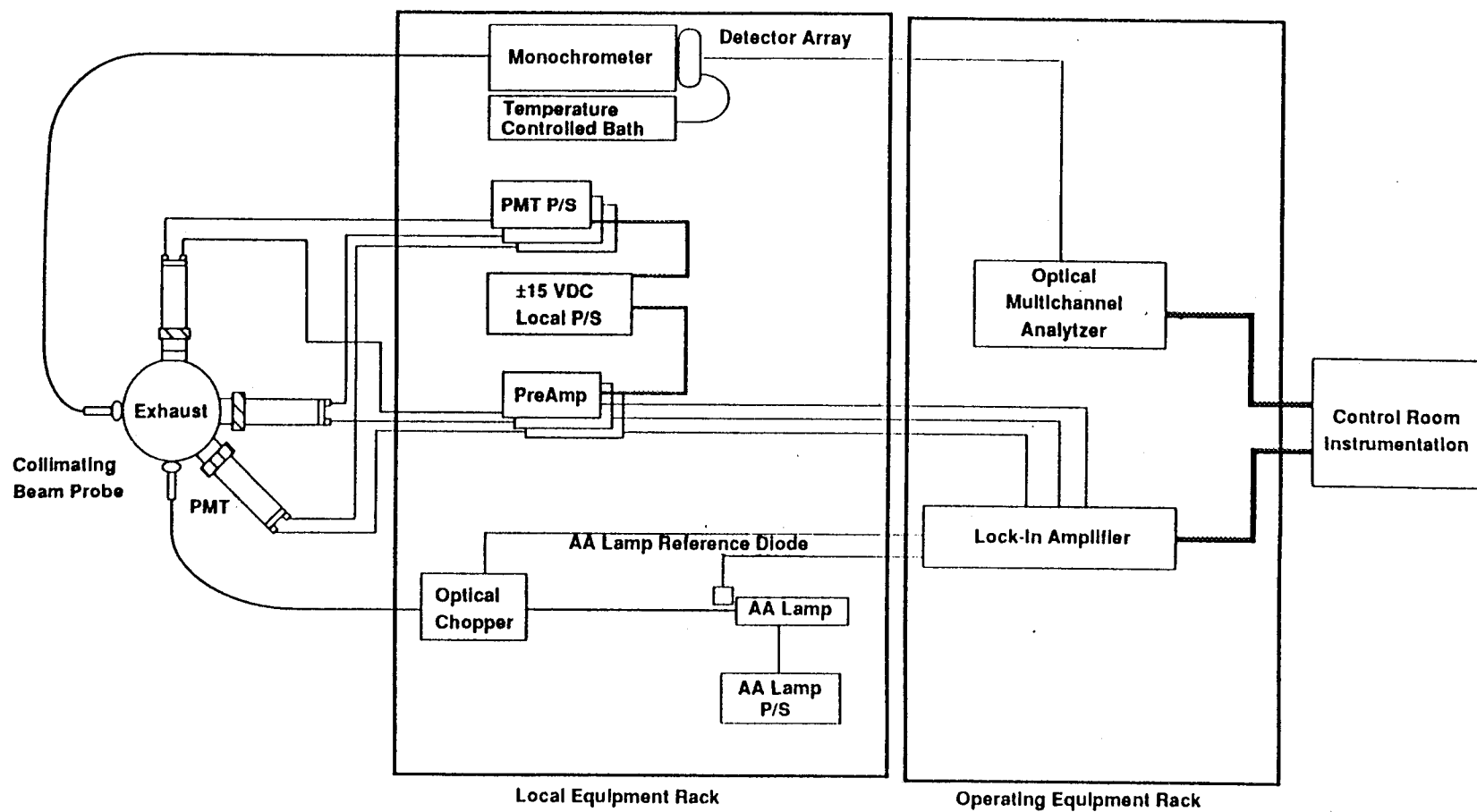


Figure 4.6.1-25. Schematic of ESMS

4.6, Diagnostic Thrust Chamber and Instrumentation Evaluation (cont.)

The detector head has provisions for eight one in. dia measuring ports at one axial station. These ports can accommodate close-coupled photomultiplier tubes (Thorn EMI Mod No. 96260) with narrow pass interference filters which can be used for either emission or absorption measurements. The eight stations can also accommodate fiber optic probes. These are used for wide-band spectral measurement with the EG&G OMA 1461 system or as inputs for a chopped reference beam for absorption measurements using an EG&G 5210 lock-in amplifier and AA absorption hollow-cathode spectral sources.

The detector head is cooled to permit operation adjacent to exhaust plumes while maintaining the temperature-sensitive photomultipliers at constant temperature. Figure 4.6.1-26 shows the installation of the detector head on the DTC. The mount can be reversed so the optical axes are on the DTC exhaust plume.

4.6.2 Fabrication

The DTC was fabricated using the drawings shown in the previous section.

The DTC is shown disassembled in Figure 4.6.2-1 and assembled in Figure 4.6.2-2. The injector assembly with a specimen/chamber liner installed is shown in Figure 4.6.2-3; the injector face detail is shown in Figure 4.6.2-4.

The water-cooled ESMS detector head, with eight stations for photomultiplier or fiber optic detectors is shown in Figure 4.6.2-5. The detector head is shown mounted on the DTC housing in Figure 4.6.2-6.

The Diagnostic Thrust Chamber housing welds were proof and leak tested. The DTC injector cooling circuit braze joints were leak checked with GN_2 and then flow checked with water (Figure 4.6.2-7). The DTC igniter was fabricated, assembled, and electrically tested to 3 KV, the normal breakdown voltage at the tip in air. The DTC was assembled with the windows, igniter, and optical instrumentation in place and installed on the stand in Chem Bay 5 for fitup and leak check.

During fitup, the pyrometers and Exhaust Species Monitoring System (ESMS) detector head were mounted on the DTC. The chamber measurement configuration for the initial setup was shown in Table 4.6.1-1A. For this testing, the ESMS detector head was

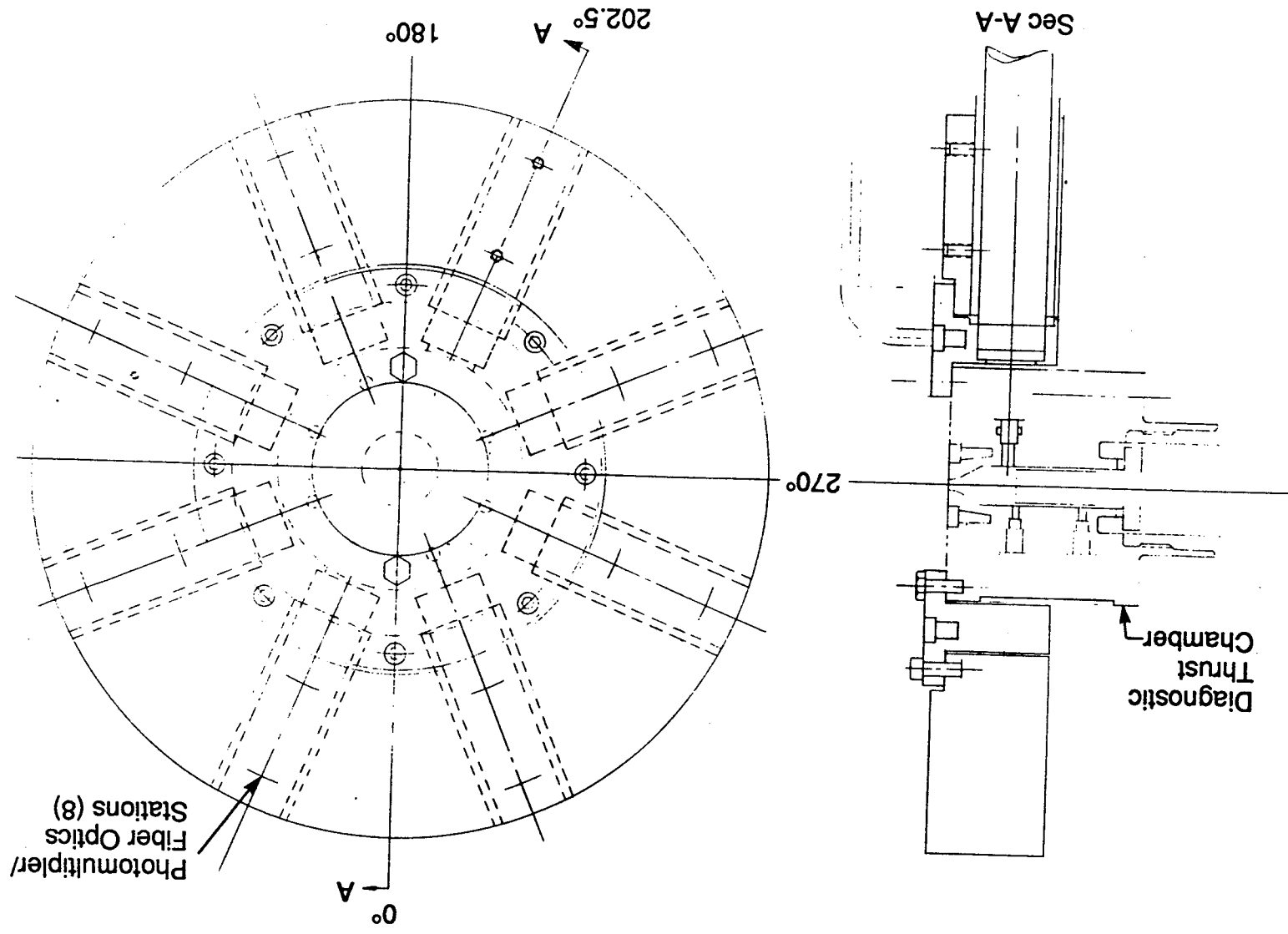


Figure 4.6-1-26. Exhaust Species Monitoring System - Detector Head

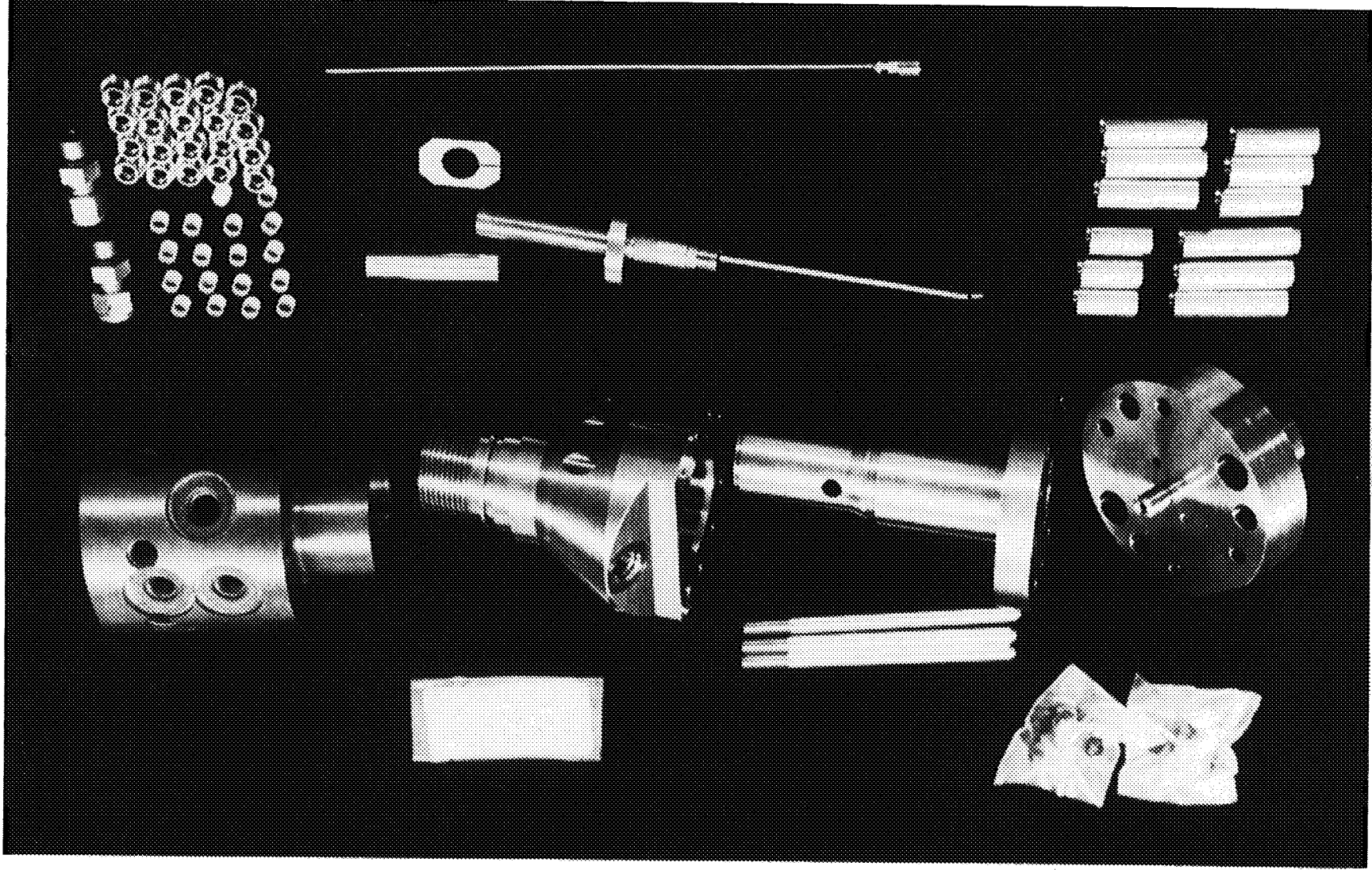
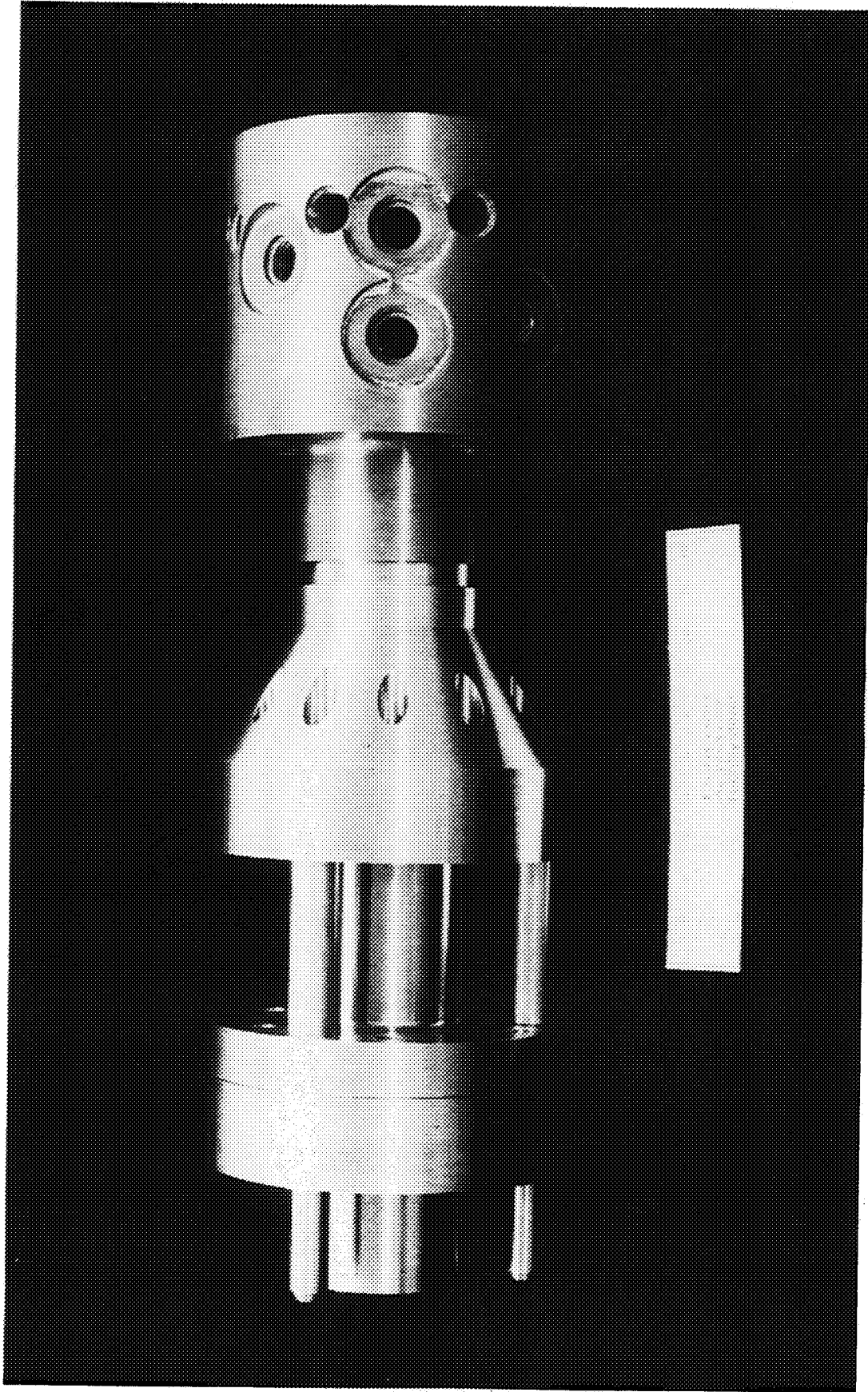


Figure 4.6.2-1. DTC Components

CO890 3577



CO890

Figure 4.6.2-2. DTC Assembly

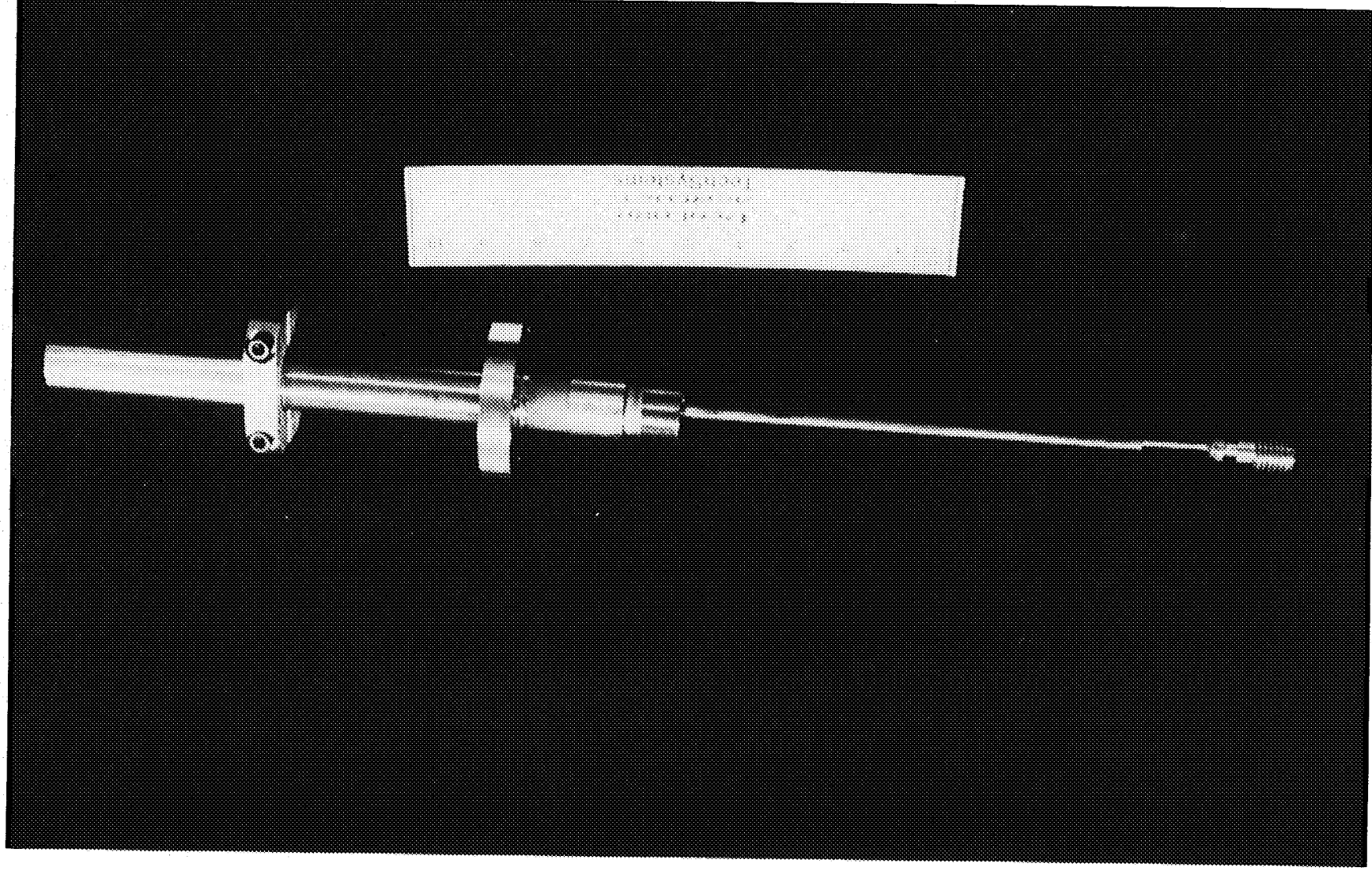
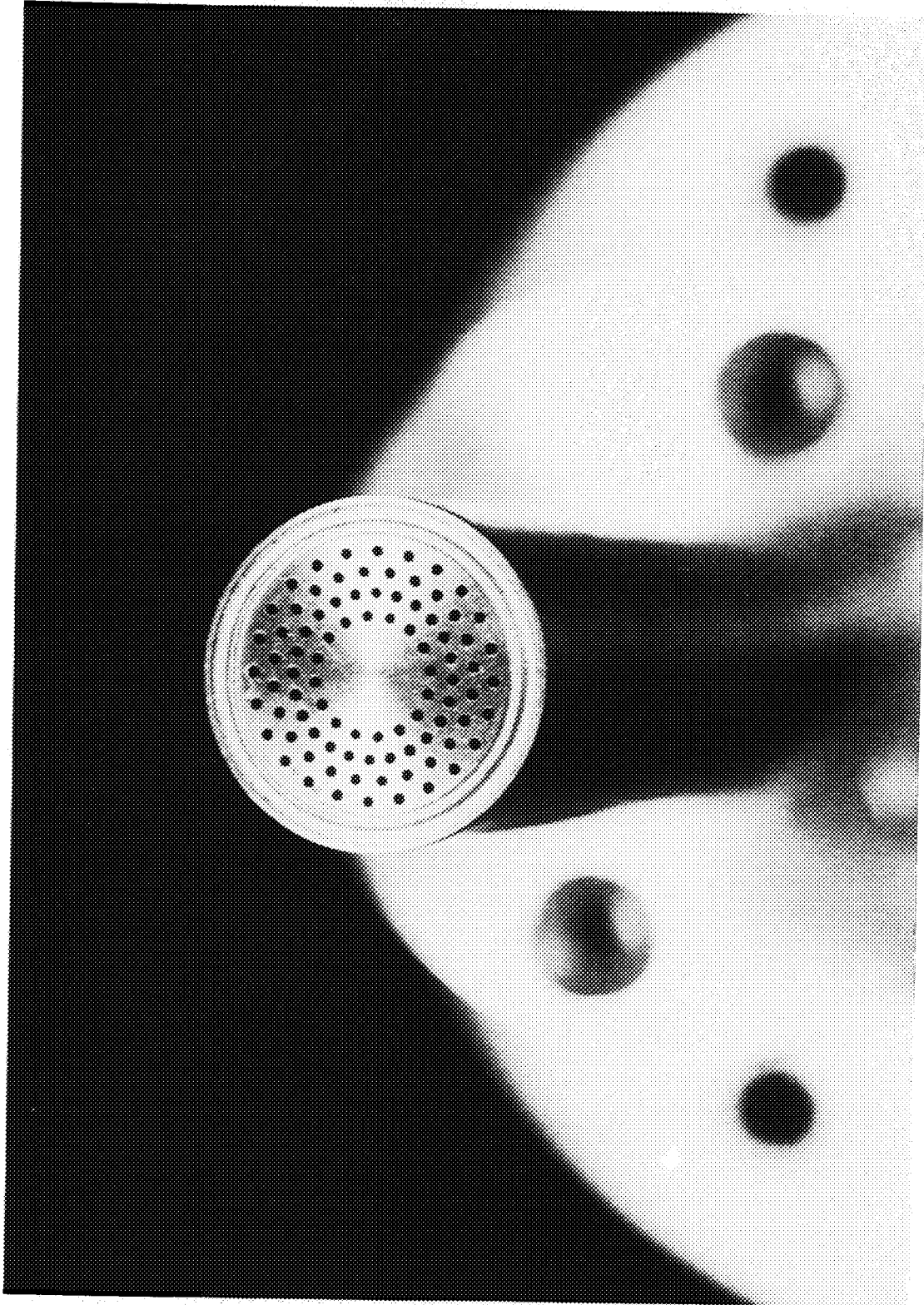


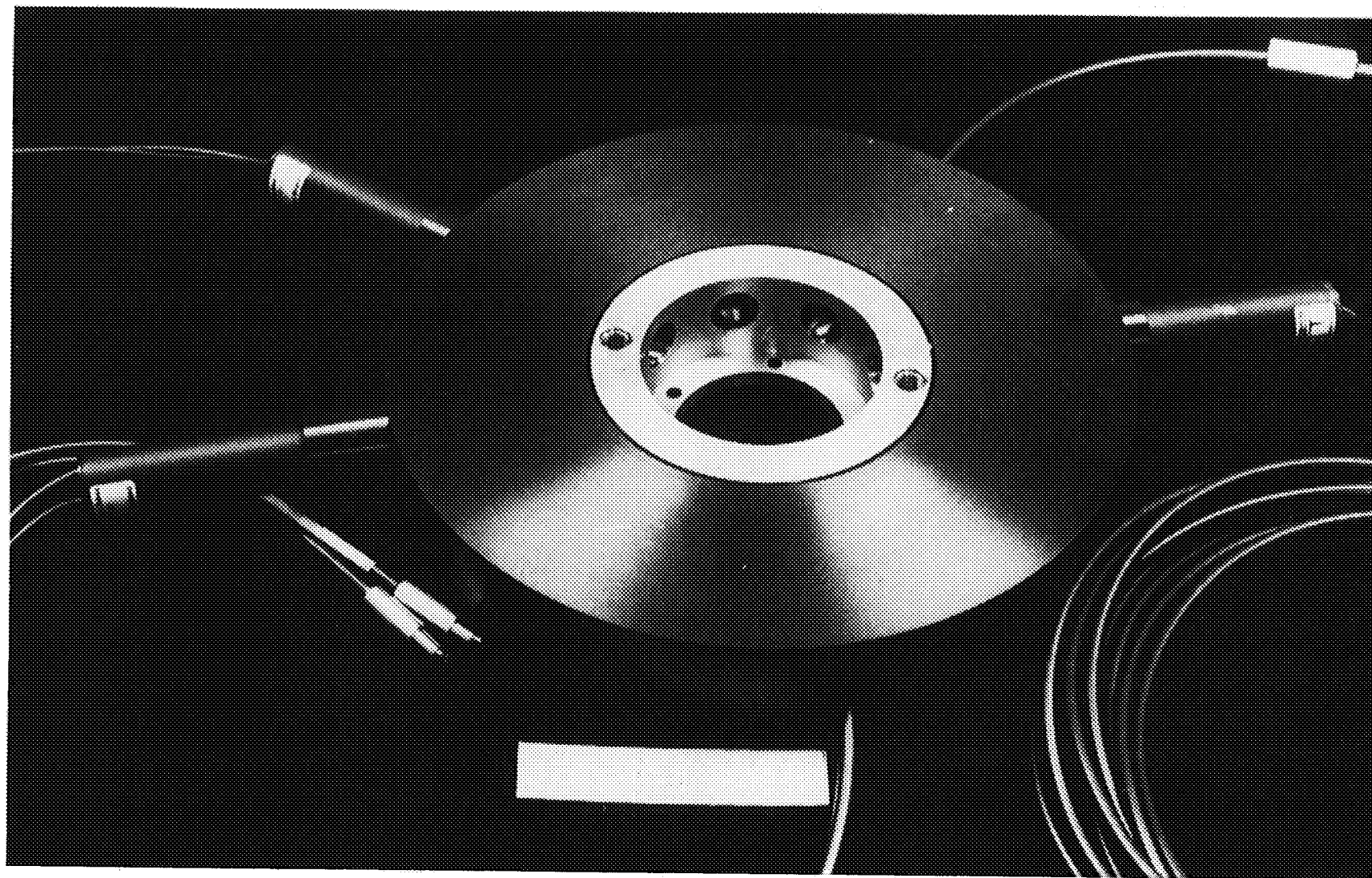
Figure 4.6.2-3. Drilled Injector and Platinum Specimen/Chamber

CO890



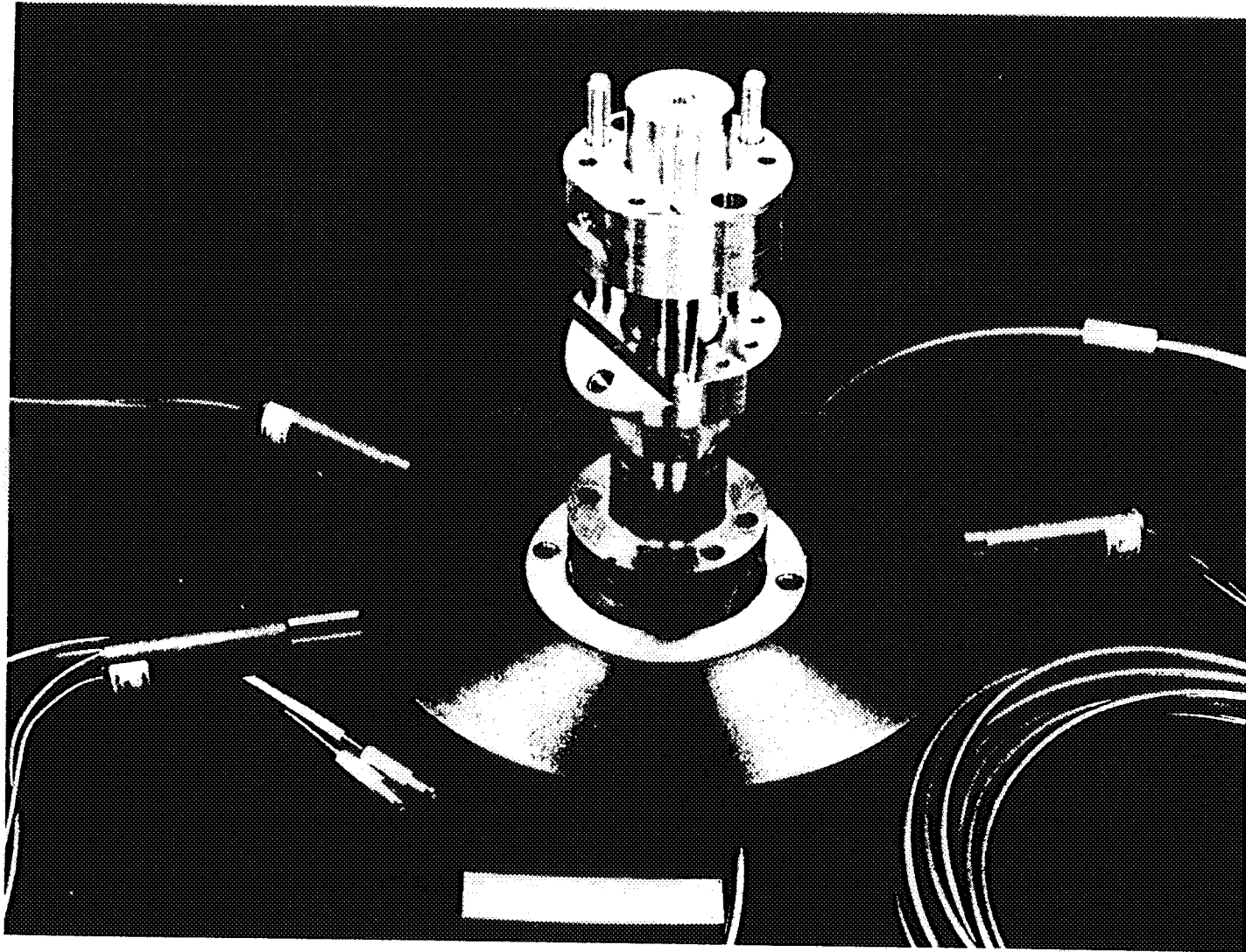
CO890

Figure 4.6.2-4. DTC Injector Face Detail



CO890

Figure 4.6.2-5. ESMS Detector Head



CO890

Figure 4.6.2-6. DTC with Exhaust Species Monitoring System (ESMS) Detector Head

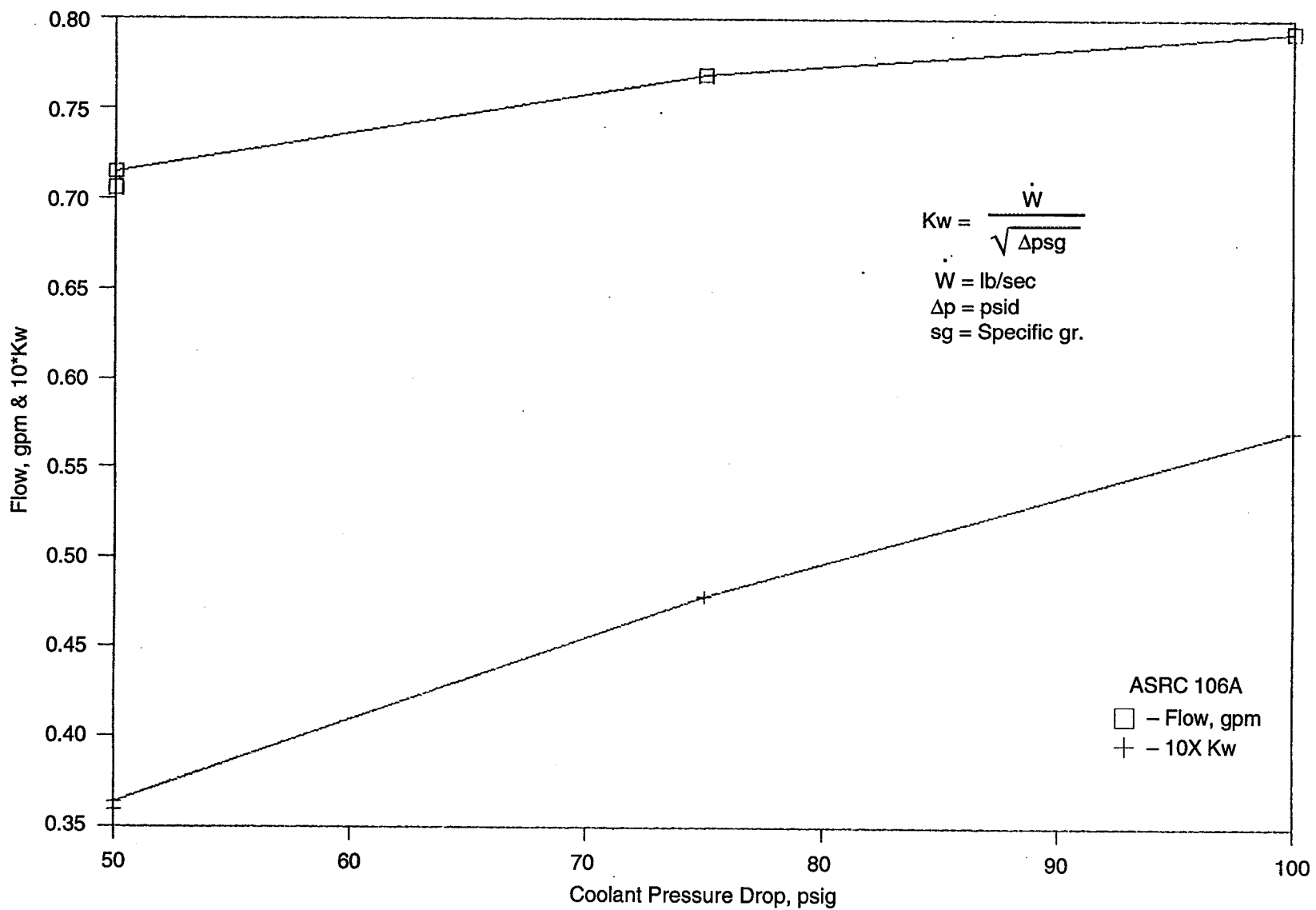


Figure 4.6.2-7. DTC Injector Coolant Flowrate and Kw versus Delta P
Water Flow Coolant Circuits 9-14-90

4.6, Diagnostic Thrust Chamber and Instrumentation Evaluation (cont.)

mounted at the chamber exit location as this permits the most flexibility in choice of specimen temperature measurement location.

4.6.3 Testing

The facility setup for the DTC testing is shown schematically in Figure 4.6.3-1. It consisted of the oxidizer supply, gaseous oxygen; the fuel supply, gaseous hydrogen or methane; and their controls. The chamber was cooled with hot recirculating water to prevent condensation of moisture from the combustion products. The gas supplies were interlocked with a flashback fuse which terminated the test if flashback occurred in the premixed gases entering the injector.

The operating sequence, depicted in Figure 4.6.3-2 was chosen to minimize the possibility of flashback. The measurements taken to define test conditions and to control operation are shown in Table 4.6.3-1. Figure 4.6.3-3 shows the DTC setup in the test bay with the ESMS and the optical pyrometer.

A limited, one-week test campaign was conducted to characterize the DTC operation with O_2/H_2 and O_2/CH_4 . The planned operating conditions are shown in Table 4.6.3-2. Tests of up to 10 minutes duration were conducted. With suitable operating conditions it appears that chamber loss rates are very low and that the system can be operated for hours at a time if desired. Table 4.6.3-3 shows the tests conducted.

Much of the test time was devoted to developing the startup technique for the system. A difficult balance had to be achieved between providing good ignition conditions at start while still cooling the specimen adequately to prevent its damage through overheating or excessive loss during the start transient. Generally, start-up was most difficult with platinum because of its relative low melting point. Most of the tests were conducted with O_2/H_2 .

One day was allotted to checkout with O_2/CH_4 . Most of the time was spent on obtaining a stable ignition sequence. This was not completely successful; operation for about 8 sec duration was achieved. The start procedure used was to begin with about 25% of nominal propellant flow and then to increase to full flow while at the same time increasing nitrogen flow to cool the specimen. It was not practical to control this process manually.

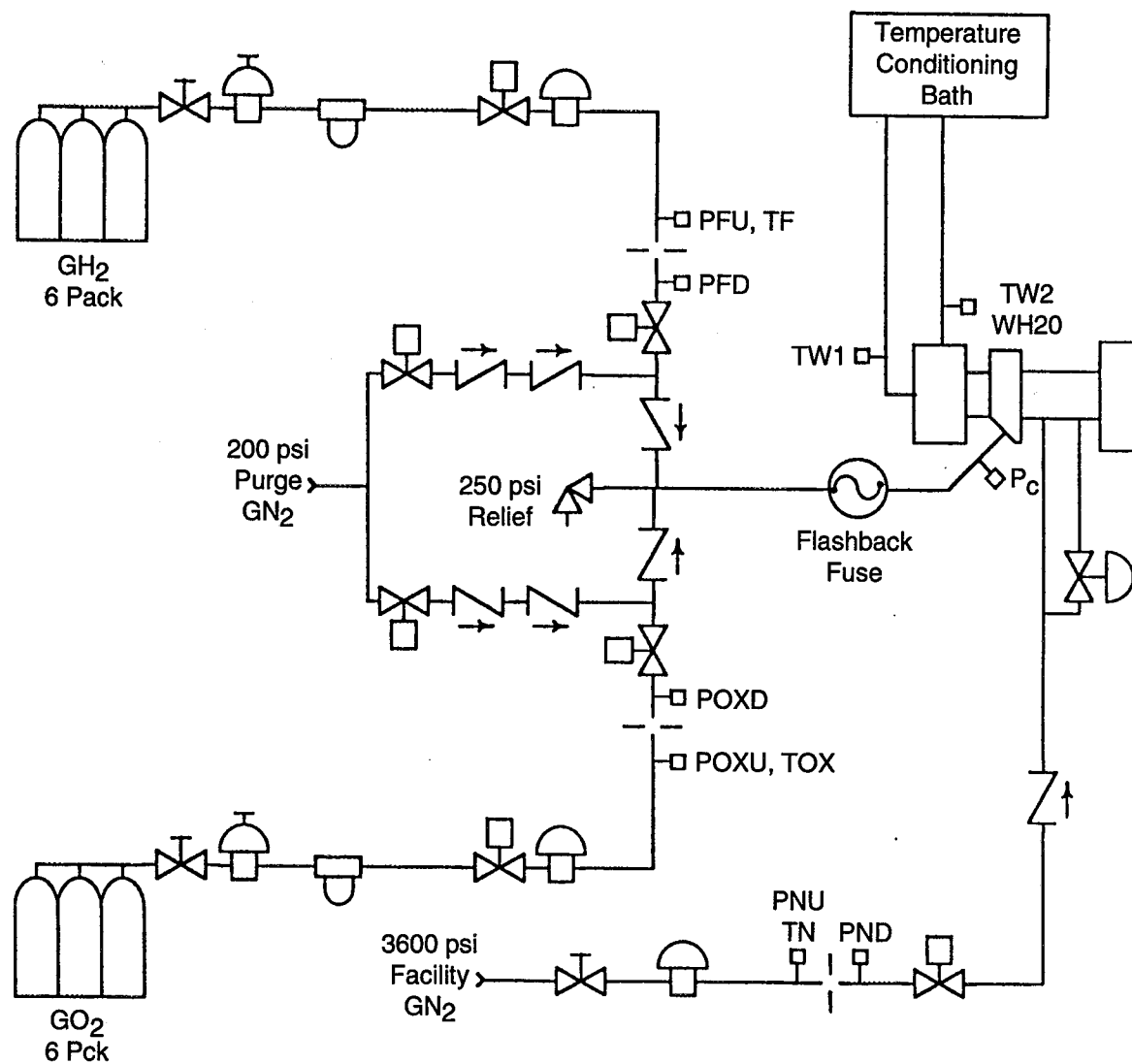


Figure 4.6.3-1. DTC Facility Schematic

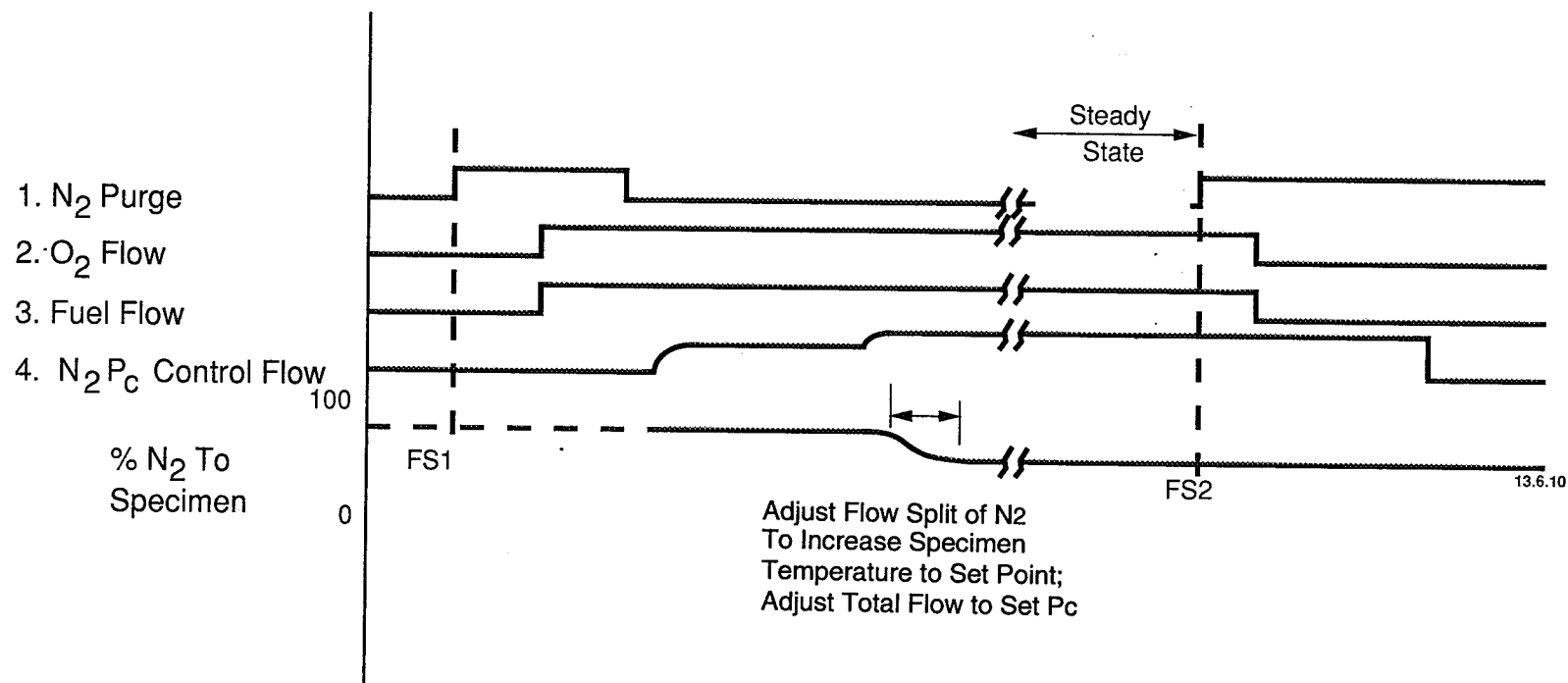


Figure 4.6.3-2. DTC Operating Sequence

Table 4.6.3-1. Instrumentation for Diagnostic Thrust Chamber

	<u>Function</u>	<u>Range</u>
VTCV	Propellant Valve Voltage	30V
POXU	Ox Orifice Upstream Pressure	500 psia
POXD	Ox Orifice Downstream Pressure	200 psia
TOX	Ox Orifice Upstream Temperature	C/A T/C
PFO	Fuel Orifice Upstream Pressure	500 psia
PFD	Fuel Orifice Downstream Pressure	200 psia
TF	Fuel Orifice Upstream Temperature	C/A T/C
PN2U	Nitrogen Orifice Upstream Pressure	500 psia
PN2D	Nitrogen Orifice Downstream Pressure	200 psia
TN2	Nitrogen Orifice Upstream Temperature	C/A T/C
PC	Chamber Pressure	200 psia
S ₁ (I), S ₂ (I)	6 Each Optical Pyrometer Voltage	0 - 5 V
TW ₁	Water Inlet Temperature	C/A T/C
TW ₂	Water Discharge Temperature	C/A T/A
WH2O	Injector Water Flowrate	0 - 1 GPM

ORIGINAL PAGE
BLACK AND WHITE PHOTOGRAPH

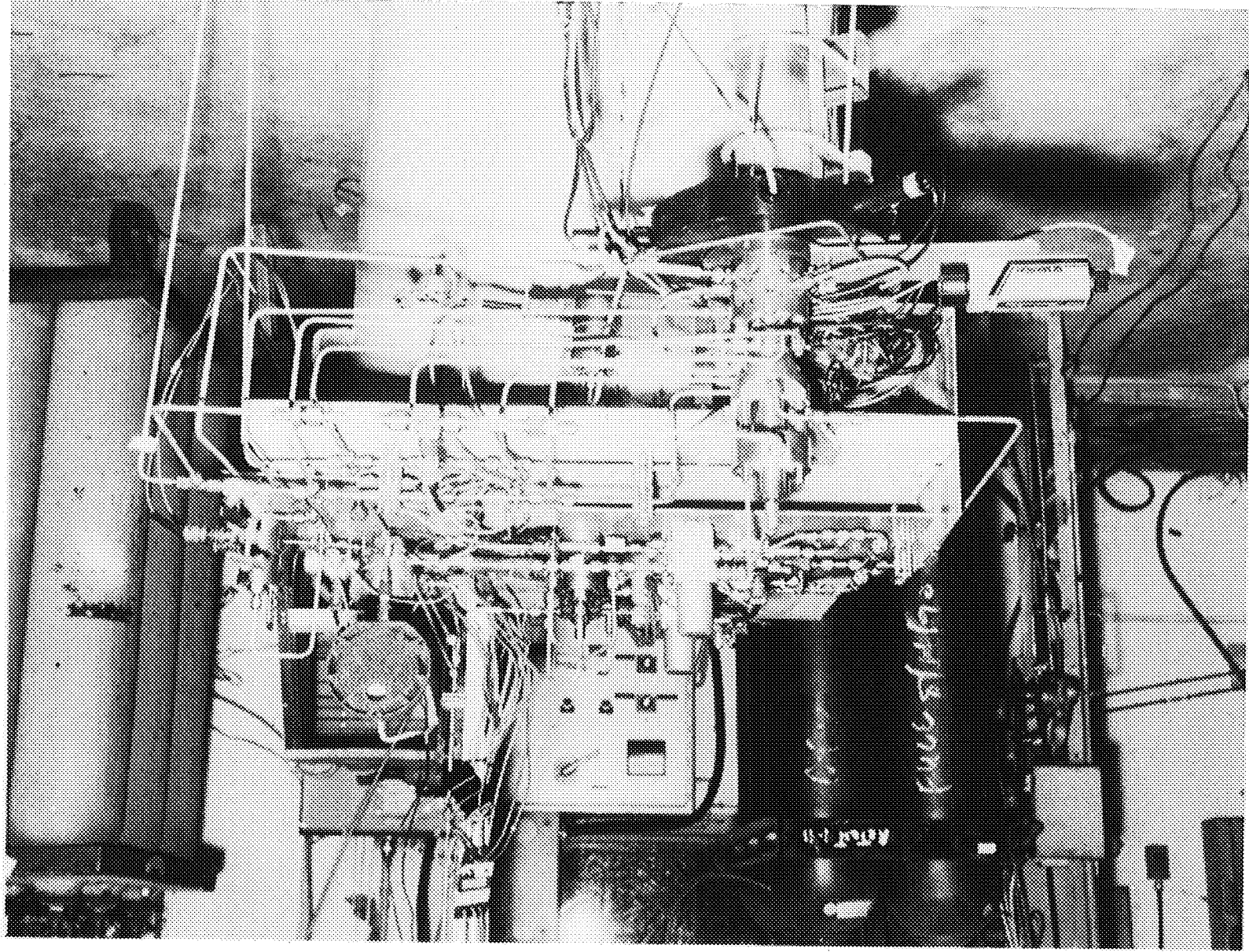


Figure 4.6.3-3. Diagnostic Thrust Chamber Set Up

C1190-5299

Table 4.6.3-2.
Test Matrix for Task 6.3 Diagnostic Test
Chamber Testing at A-Area

TEST TYPE	TEST OBJECTIVE	PROPELLANT	MATERIAL	MIXTURE RATIO	CHAMBER PRESSURE PSIA	EXPOSURE, 1.0-L/Lc	DURATION, MINUTES	DIAGNOSTICS (1)
CHECKOUT	PROOF	GN2	--	--	2 X MAX WORKING	--	--	--
"	LEAK	GN2	--	--	MAX WORKING	--	--	--
"	FLOW BALANCE	O2/H2 & /CH4	--	OPERATING RANGE	OPERATING RANGE	--	--	--
"	IGNITION	O2/H2 & /CH4	RHENIUM	OPERATING RANGE	OPERATING RANGE	1.0	1	--
"	DIAGNOSTICS	O2/H2 & /CH4	RHENIUM	OPERATING RANGE	OPERATING RANGE	1.0	1 TO 10	2 CHAMBER & EXIT
MATERIAL INTERACTION	DETERMINE EFFECTS OF COMBUSTION PRODUCTS	O2/H2	RHENIUM	2 TO 12	50 TO 150	1.0 TO .33	60 OR TO OPTICAL SIGNAL	2 CHAMBER & EXIT
"	"	O2/H2	IRIDIUM	2 TO 12	50 TO 150	1.0 TO .33	60 OR TO OPTICAL SIGNAL	2 CHAMBER & EXIT
"	"	O2/H2	PLATINUM	2 TO 12	50 TO 150	1.0 TO .33	60 OR TO OPTICAL SIGNAL	2 CHAMBER & EXIT
"	"	O2/CH4	RHENIUM	3 TO 6	50 TO 150	1.0 TO .33	60 OR TO OPTICAL SIGNAL	2 CHAMBER & EXIT
"	"	O2/CH4	IRIDIUM	3 TO 6	50 TO 150	1.0 TO .33	60 OR TO OPTICAL SIGNAL	2 CHAMBER & EXIT
"	"	O2/CH4	PLATINUM	3 TO 6	50 TO 150	1.0 TO .33	60 OR TO OPTICAL SIGNAL	2 CHAMBER & EXIT

(1) PRE & POST SEM & EDS, COMPARISON MICRO-METALLOGRAPHIC ANALYSIS, DIMENSIONAL CHANGES

Table 4.6.3-3. DTC Test Log

From Page No.		Specimen	Propellants	Pc, psia	MR	Time, sec	Comments
Date	DTC No.						
10/26/90	-001	Ir 001	O ₂ /H ₂	30	4.0	2	Specimen end is fractured
10/26/90	-002	Ir 003	O ₂ /H ₂	43		30	
10/29/90	3, 4, 5, 6	Pt 001	O ₂ /H ₂	40	4	—	Melted off
10/29/90	7, 8, 9, 10	Pt 002	O ₂ /H ₂	50	4	—	Start problems
10/30/90	11, 12	Pt 002	O ₂ /H ₂	50	4	~5	Melted off
10/30/90	13, 14	Pt 003	O ₂ /H ₂	50	4	19.4	Melted off
10/31/90	15, 16	Re 001	O ₂ /H ₂	50	4	60	Hole in specimen
10/31/90	17, 18, 19	Re 002	O ₂ /H ₂	50	4	—	Flashbacks
10/31/90	20	Re 002	O ₂ /H ₂	50	4	60	Specimen looks good
10/31/90	21, 22	Re 002	O ₂ /H ₂	50	4	600	Specimen looks good
10/31/90	23, 24, 25	Re 003	O ₂ /H ₂	150	4	360+	Specimen broke in two
11/1/90	26	Re 004	O ₂ /H ₂	50	6	~20	Burnout during startup
11/1/90	27	Re 004	O ₂ /H ₂	50	6	600	
11/1/90	28	Pt 004	O ₂ /H ₂	50	4	~3	Went out
11/1/90	29	Pt 004	O ₂ /H ₂	50	4	60	Holes; high on MR
11/1/90	30	Pt 005	O ₂ /H ₂	50	4	—	Went out
11/1/90	31	Pt 005	O ₂ /H ₂	50	4	453	Crease
11/1/90	32	Pt 006	O ₂ /H ₂	50	6	42	Large holes
11/2/90	33	Re 006	O ₂ /CH ₄	50	1.8	—	No ignition
11/2/90	34-38	Re 005	O ₂ /CH ₄	50	2.3	0.1	Ignition, goes out
11/2/90	39-43	Re 005	O ₂ /CH ₄		Various		More pops
11/2/90	44-45	Re 005	O ₂ /CH ₄		Various		Pops, etc.
11/2/90	47A, B, C, etc.	Re 005	O ₂ /CH ₄			8+	Raw 8 sec, went out

4.6, Diagnostic Thrust Chamber and Instrumentation Evaluation (cont.)

Table 4.6.3-4 is a summary of data from the tests; further analyses of the data was deferred to permit conduct of the 14 lb Ir-Re thruster testing.

The mass loss rate data for the successful tests are plotted in Figure 4.6.3-4 as a function of test duration. There is a general tendency towards lower mass loss rates at longer durations, consistent with high loss rates during the start transient.

Before resuming DTC testing, the gas flow control hardware should be modified so that the required start transient can be obtained without manual intervention to avoid frequent damage to the specimen during the long start transient.

Optical Measurements

Optical data from selected tests are described here. Measurements shown are representative of the types of data that can be obtained with the ESMS emission/absorption system.

Test DTC-002

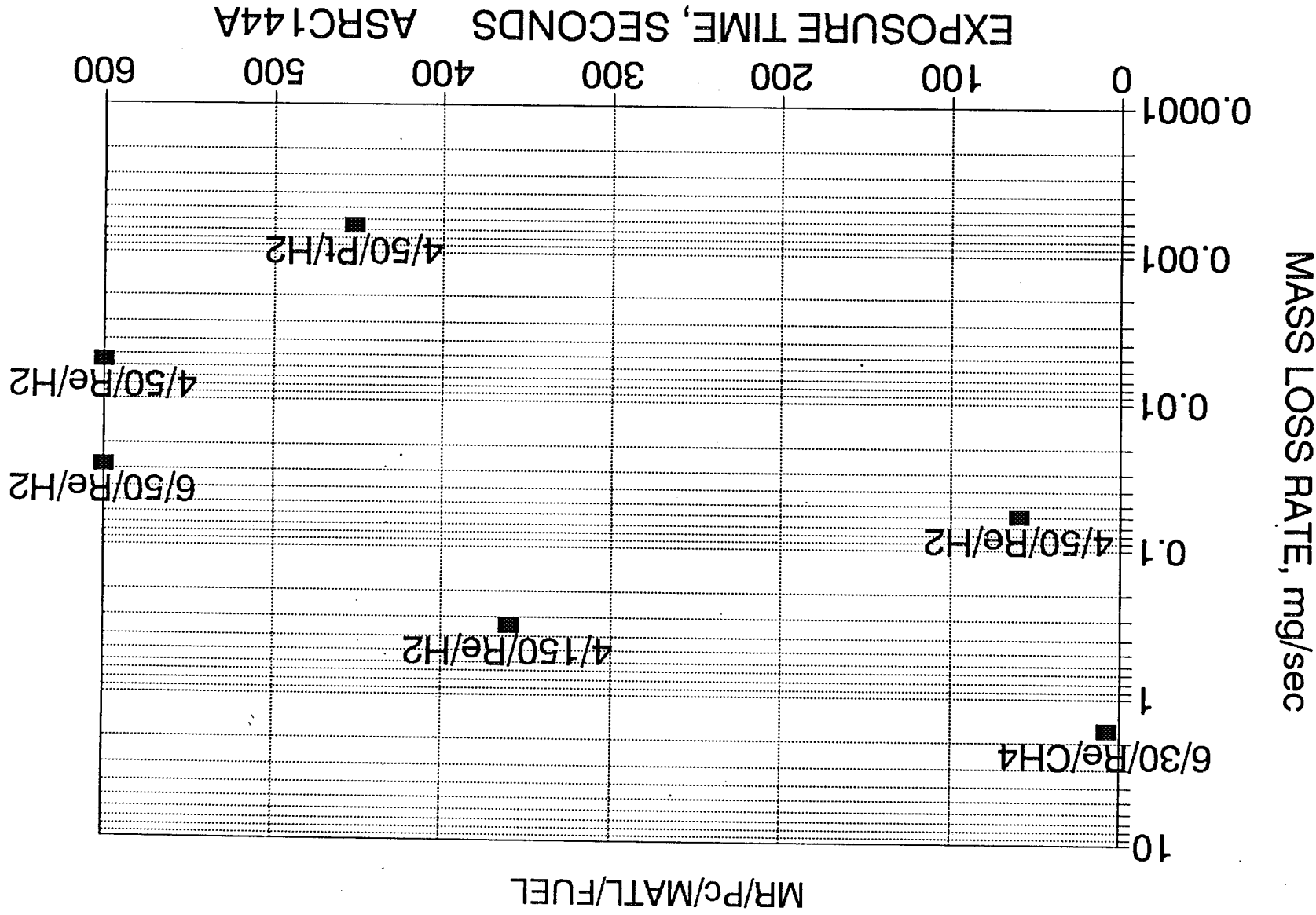
This test exposed Ir chamber specimen Ir 003 to O_2/H_2 combustion products. The absorption signal, Figure 4.6.3-5 indicated average value of about zero for the 30-sec duration. The initial and final weights of the specimen were the same, 1.1045 gm.

Test DTC-032

In this test chamber specimen Pt 006 was exposed to O_2/H_2 combustion products at $P_c = 50$ psia and $MR = 6$ for a duration of 42 sec. Holes were melted in the specimen, so no valid mass loss data were available. Absorption measurements were made at 270 nm, and emission measurements were made at 260, 270 and 310 nm. These measurements are plotted in raw form on a linear scale for the full test in Figure 4.6.3-6. There is an initial period of high absorption/emission of about 8 sec, during the start transient, followed by about 20 seconds of nearly baseline emission and absorption. At about 27 sec emission and absorption gradually increased until FS-2. Normalized absorption at 270 and emission at 260 nm are shown in Figure 4.6.3-7. They show direct correlation with each other throughout the firing. Figures 4.6.3-8 through -10 show the start, steady and shutdown optical measurements. These measurements are consistent with the major damage experienced by the chamber specimen.

**Table 4.6.3-4.
Summary of DTC Results**

RUN #	DATE	SPECIMEN	PROPEL- LANTS	MR O/F	Pc psia	RUN TIME, sec	MASS LOSS, mg	MASS LOSS RATE, mg/hr
DTC-020	10-31-90	Re-002	O2/H2	4	50	60	3.5	210.0
DTC-022	10-31-90	Re-002	O2/H2	4	50	600	3.3	19.8
DTC-025	10-31-90	Re-003	O2/H2	4	150	360	122.8	1228.0
DTC-027	11-1-90	Re-004	O2/H2	6	50	600	17.0	102.0
DTC-031	11-1-90	Pt-005	O2/H2	4	50	453	0.3	2.384
DTC-047	11-2-90	Re-005	O2/CH4	6	30	8	13.0	5850.0

Figure 4.6.3-4. DTC Mass Loss Rate Data, O₂ + Fuel

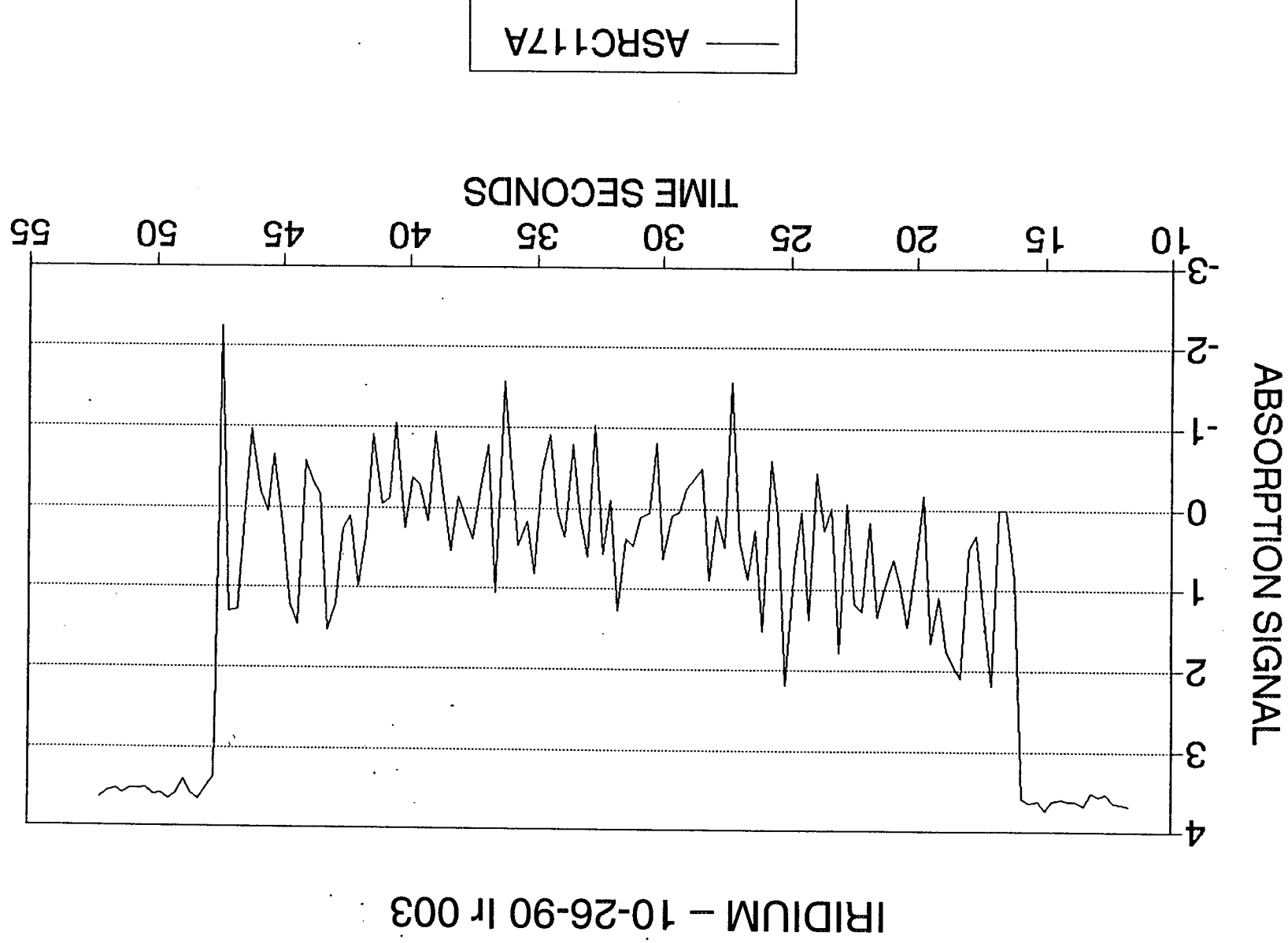


Figure 4.6.3-5. DTC Absorption Measurement

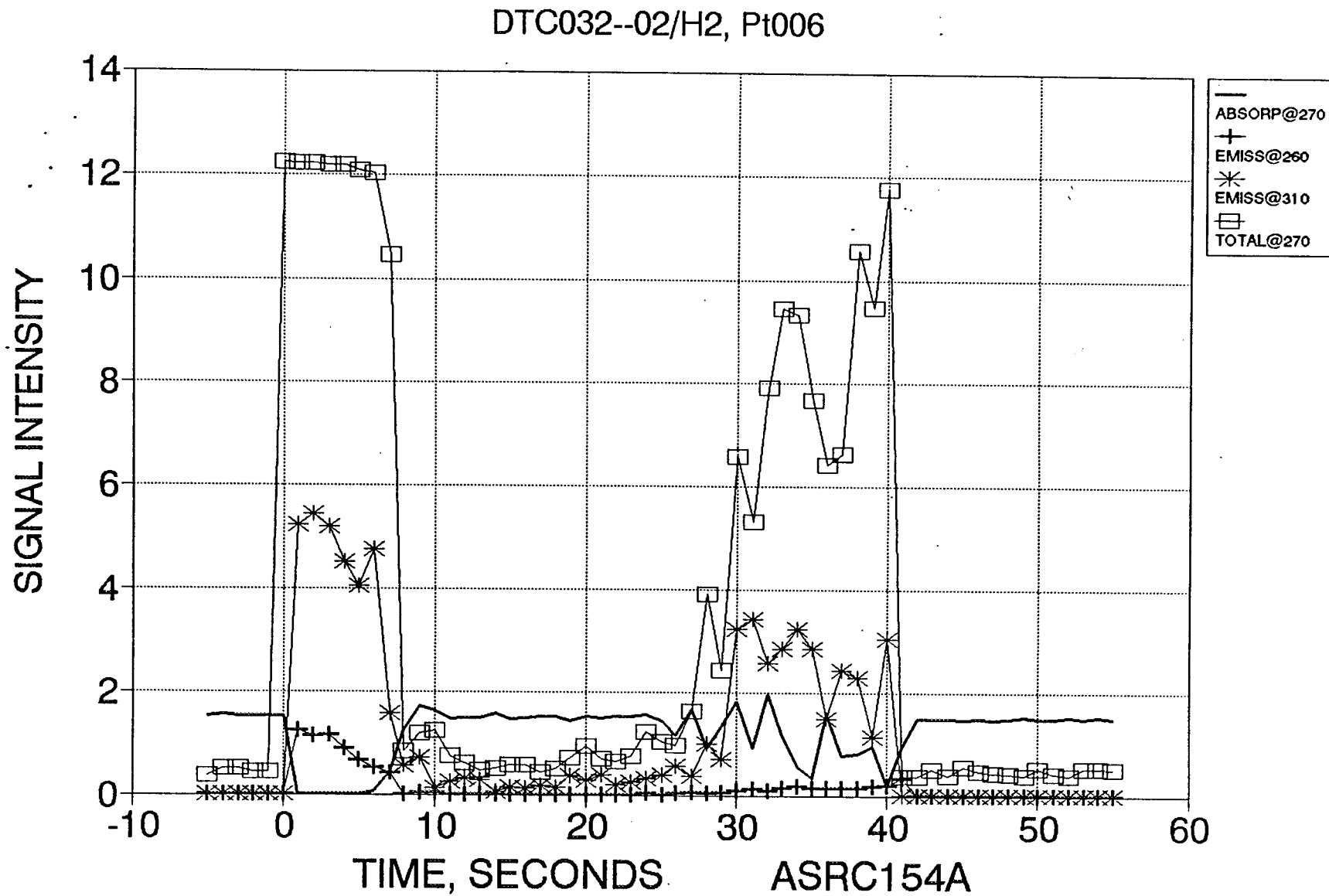


Figure 4.6.3-6. DTC Plume Absorption and Emission

DTC032--02/H2, Pt006

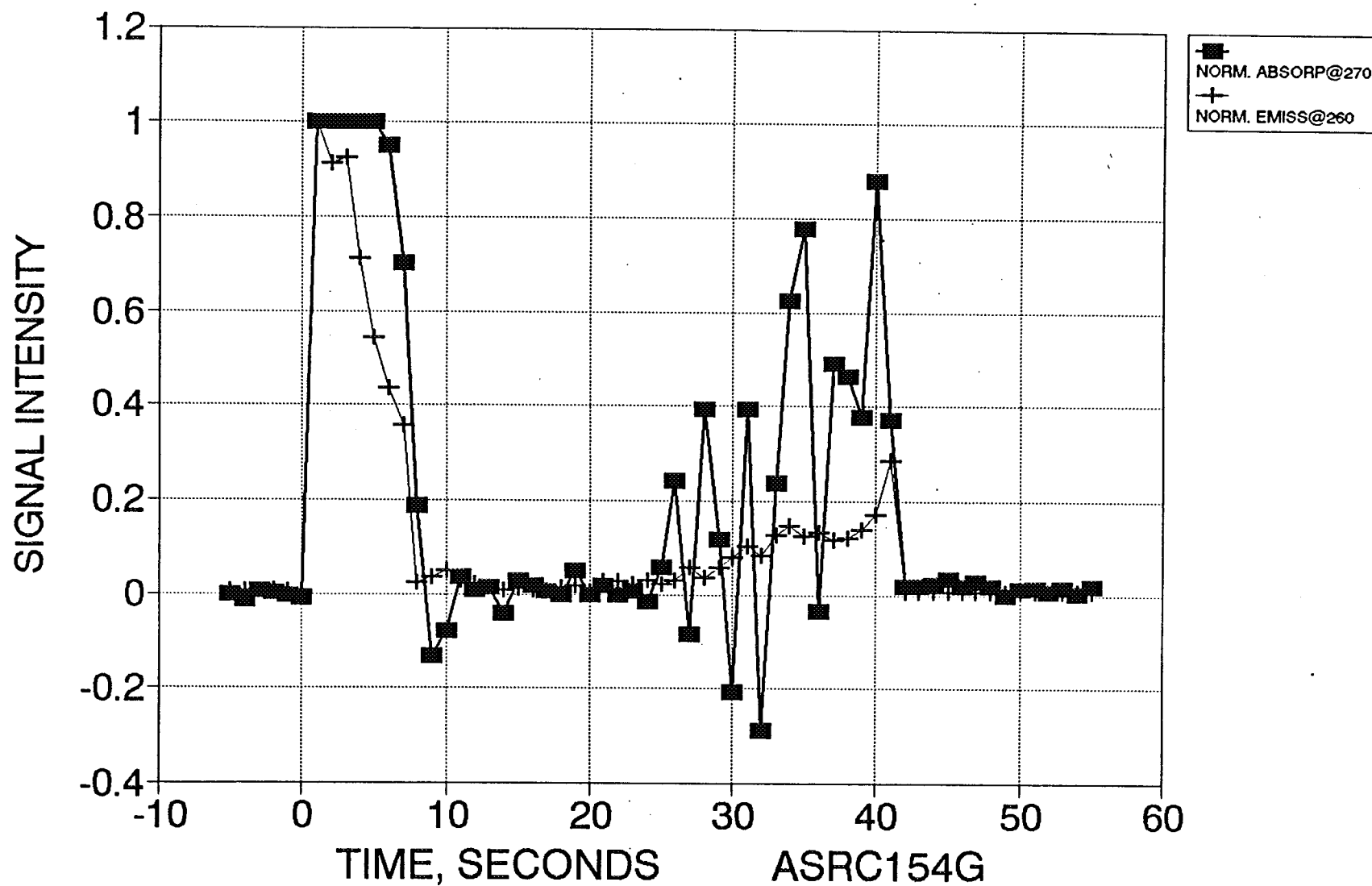


Figure 4.6.3-7. DTC Normalized Plume Absorption and Emission

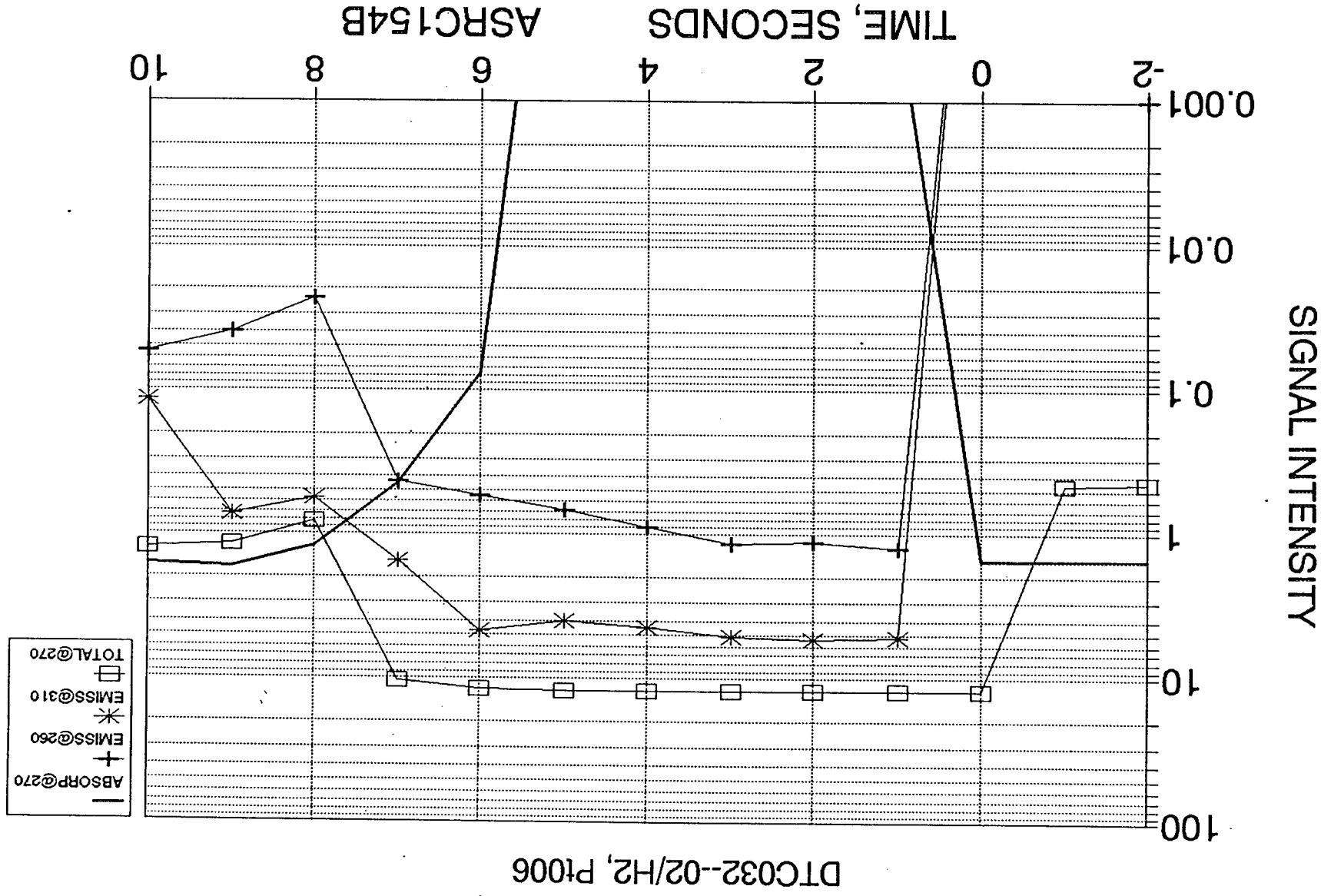


Figure 4.6.3-8. DTC Absorption and Emission

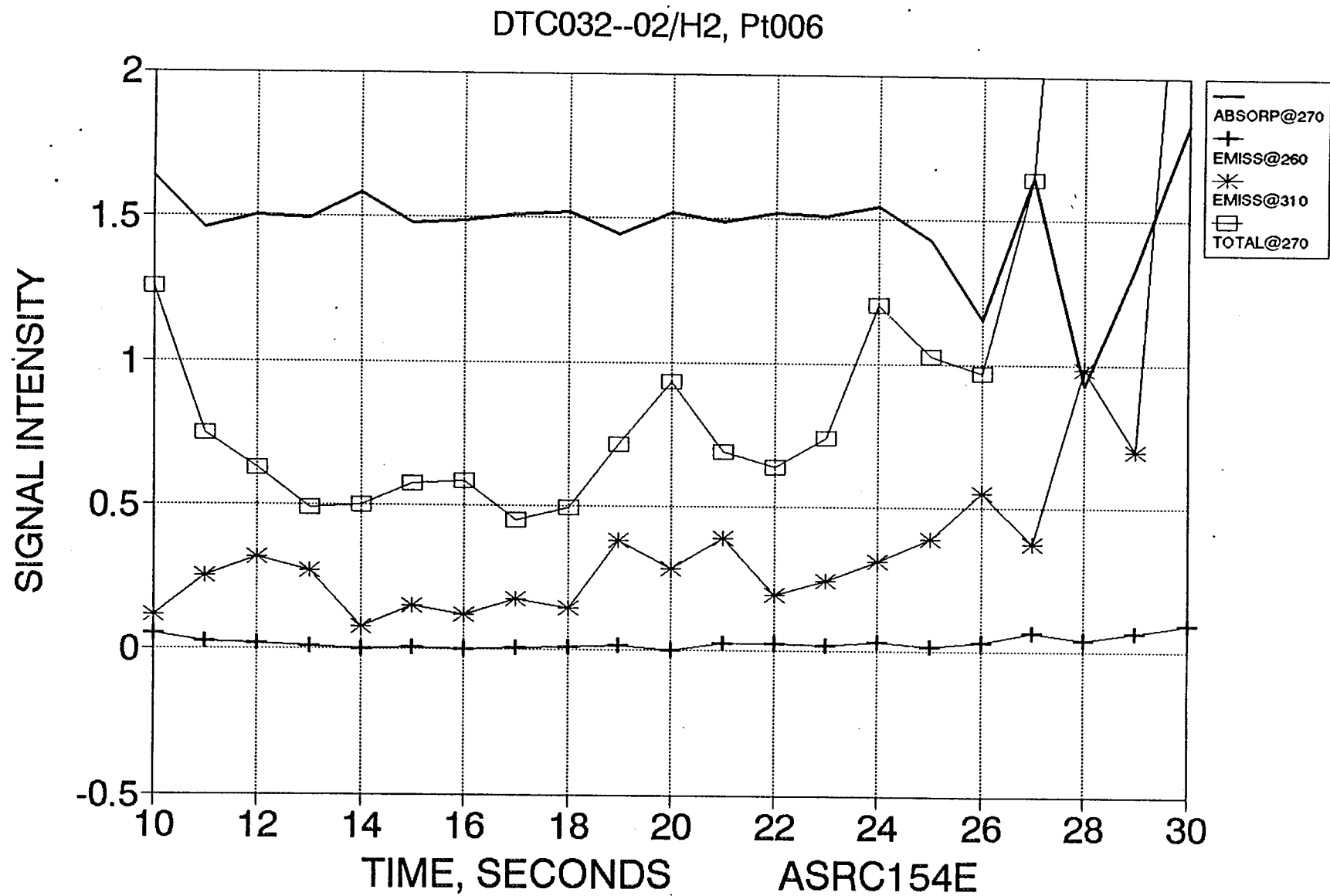


Figure 4.6.3-9 DTC Absorption and Emission

DTC032--02/H2, Pt006

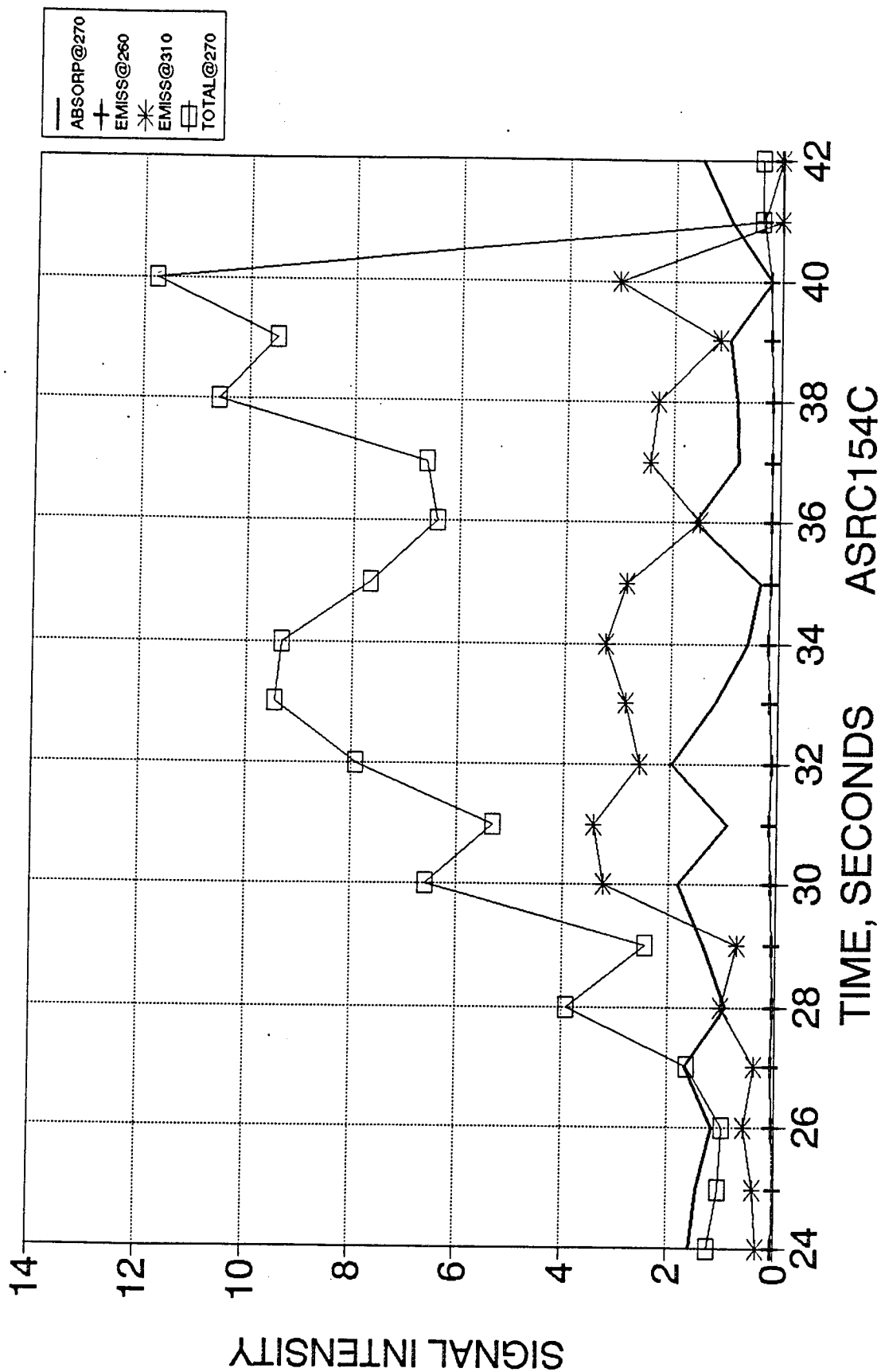


Figure 4.6.3-10. DTC Plume Absorption and Emission

4.6, Diagnostic Thrust Chamber and Instrumentation Evaluation (cont.)

Test DTC-047

This chamber specimen, Re 005, was exposed to O_2/CH_4 combustion for approximately 8 sec after several ignition attempts (Figure 4.6.3-11). Mixture ratio and wall temperature at three locations are shown in Figure 4.6.3-12. Nominal MR was steady but very high at about 6.0 (stoichiometric is 4.0) for the first 6.5 sec and then rose to nearly 10. Indicated temperature at the first station went to zero as the MR increased, probably because of burn through at this point. Emission at 488 nm (Re) shows a large peak at about 2 sec and another near shutdown (Figure 4.6.3-13).

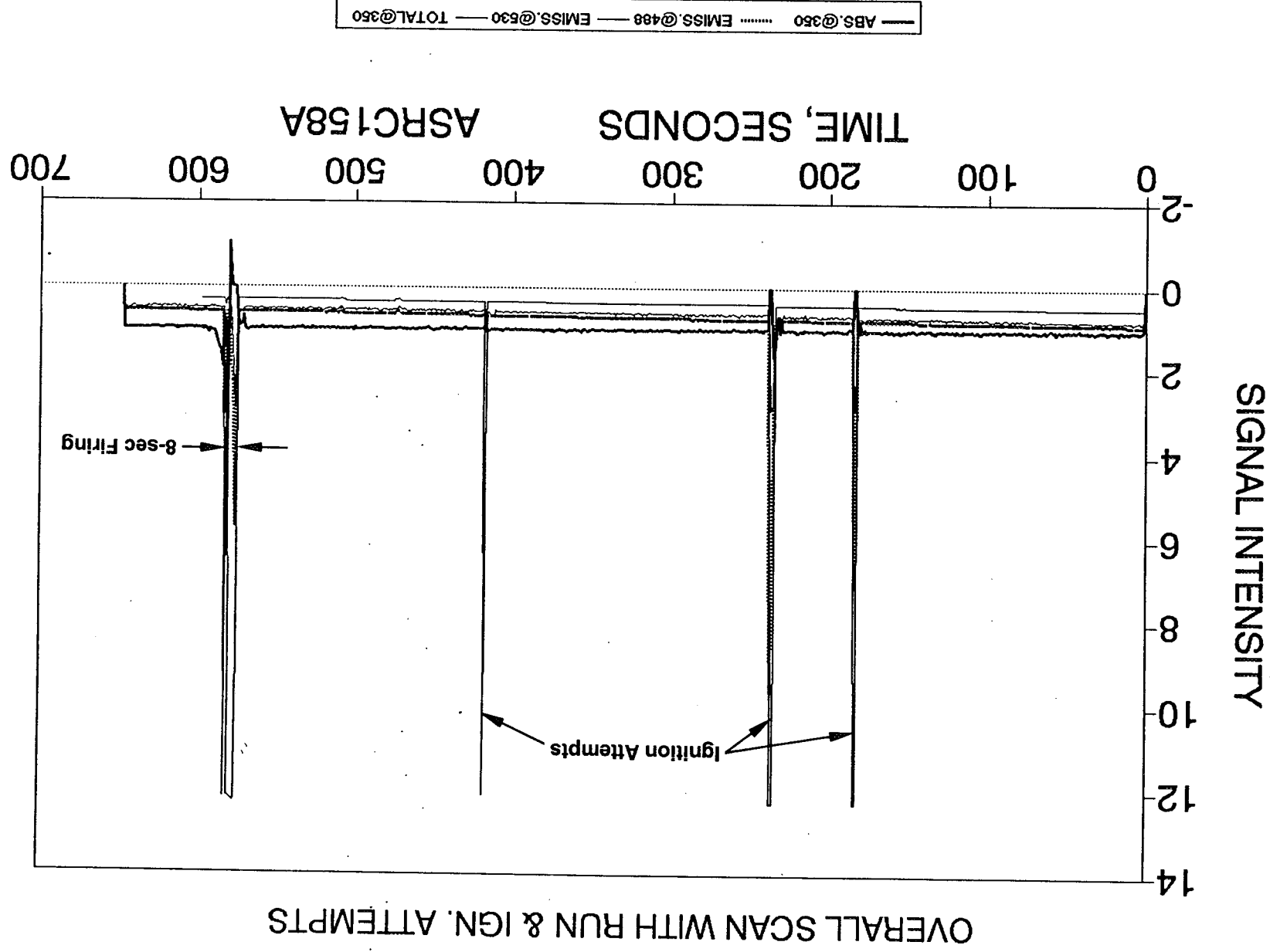


Figure 4.6.3-11. DTC Test No. 47 LIA Absorption and Emission Vs. Time

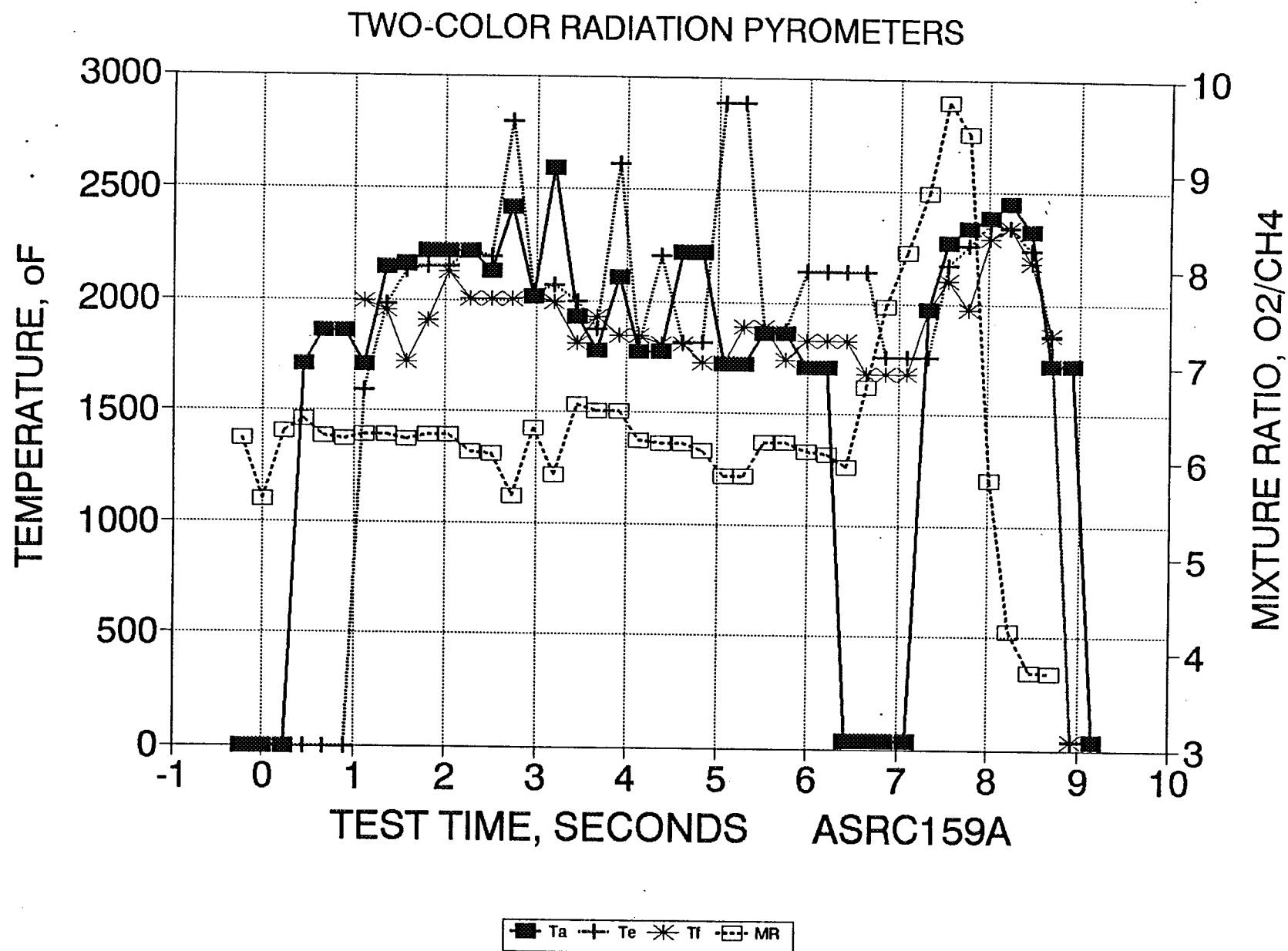


Figure 4.6.3-12. DTC47 – Specimen Temperature Vs. Time

RAW SIGNALS--NOT NORMALIZED

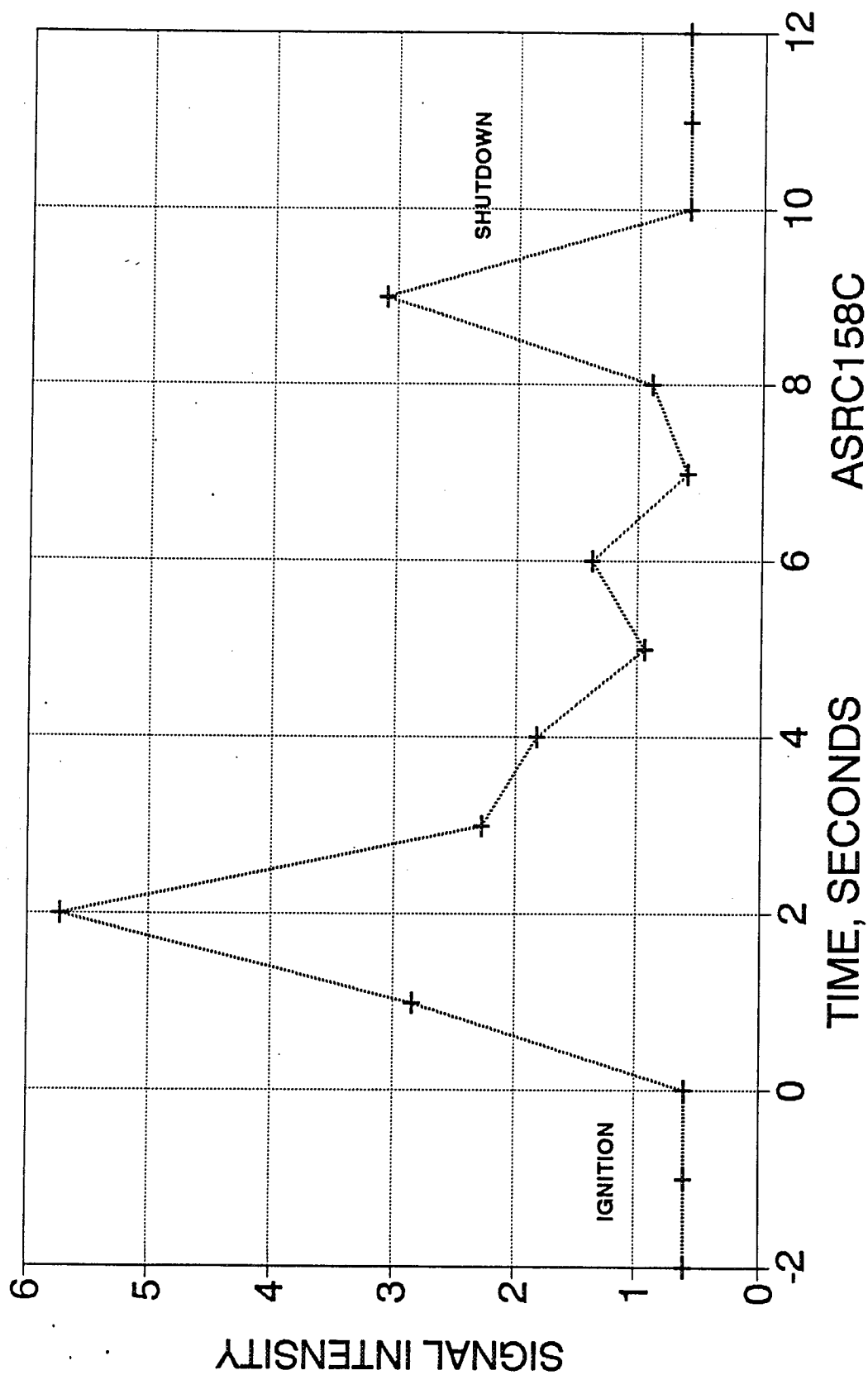


Figure 4.6.3-13. DTC Test No. 47 Emission at 488nm Vs. Time

5.0 REFERENCES

1. Jassowski/ D.M. and Gage, M.L., "Advanced Small Rocket Chambers, Option 1 – 14 lbf Ir-Re Rocket," Final Report, NASA Contract Report 191014, Lewis Research Center Contract NAS 3-25646.
2. "Advanced Small Rocket Chambers, Option 3 – 110 lbf Ir-Re Flight-Type Thruster." Final Report Contract NAS3-25646 to be published.
3. Lansaw, P.T. and Wooten, J.R., "High Temperature Oxidation-Resistant Thruster Research," NASA CR 185233, February 1990.
4. Schoenman, L., Franklin, J. and Lansaw, P.T., "Feasibility Demonstration of a High-Performance 100 lbf Rocket Engine," JPL Contract 957882, Final Report, January 1989.
5. "Corrosivity of O₂/H₂ Reaction Products Towards Molybdenum," R.E. Anderson to J.A. Mellish/R.G. Spenser, Internal Memo 9512:3782, 13 June 1988.
6. ATC89-07, Thermodynamics/Combustion Research, Aerojet TechSystems Independent Research and Development, 1989.
7. MSTA Operations Manual, Version 1.01, April, 1990.
8. Crank, J. The Mathematics of Diffusion, Clarendon Press, 1975, p. 15.
9. Rudman, P.S., J. Less-Common Metals, 12 (1967) p. 79-81.
10. Handbook of Auger Electron Spectroscopy, Physical Electronics Industries, Inc., 1976.
11. Powell, C.J., Surf. Sci. 44, 29 (1974).
12. Gupta, D., Cambell, D.R. and Ho, P.S., "Grain Boundary Diffusion" in Thin Films – Interdiffusion and Reactions, Eds. Poate, J.M., et al, John Wiley and sons, NY, 1978.
13. Press, W.H., Teukolsky, S.A. and Vettering, W.T., Numerical Recipes – The Art of Scientific Computing, Cambridge University Press, 1986.

6.0 REPORTS BASED ON THIS CONTRACT

Rosenberg, S.D. and Jassowski, D.M., "Combustion Interaction With Radiation-Cooled Chambers," AIAA 90-2121, July 1990.

Rosenberg, S.D. and Schoenman, L., "A New Generation of High Performance Engines for Spacecraft Propulsion," AIAA 91-2039, June 1991.

Hamilton, J.C., et al, Sandia and Franklin, L., APD, "Diffusion Mechanisms in Ir-Coated Re for High-Temperature, Radiation Cooled Rocket Thrusters, AIAA 91-2215, June 1991. Also Metallurgical Transactions A, Vol. 23A, pp 851-855, Material.

Barlow, R.S. and Lucht, R.P., Sandia CRF and Jassowski, D.J., Rosenberg S.D., APD, "Gas-Phase Measurements of Combustion Interaction With Materials For Radiation-Cooled Chambers," AIAA 91-2216, June 1991.

Jassowski, D., Makel, D. and Sakabu, R., "Rocket Engine Condition Monitoring and Characterization With Non-Intrusive Optical Techniques," AIAA 91-2523, June 1991.

Barlow, R., Jassowski, D. and Prast, T., "Measurements of Interaction of Combustion Gases with materials for Sandia Radiation-Cooled Rocket Chambers," Sandia Combustion Research Program Technical Review, 1992.

Knight, B.L., "Rhenium-Foil Witness Cylinders," NASA Tech Brief, January 1992.

Rosenberg, S., Schoenman, L. and Jassowski, D., "High Performance Storable Bipropellant orbit Transfer Engine, IAF-92-0672, August 1992.

Schoeman, L., Rosenberg, S. and Jassowski, D., "Test Experience, 490 N High Performance [321 Sec Isp] Engine," AIAA 92-3800, July 1992.

Jassowski, D.M., Rosenberg, S.D. and Schoeman, L., "Durability Testing of the AJ10-221 490N High Performance (321 Sec Isp) Engine," AIAA 93-2130, June 1993.

Schoenman, L., "4000°F Materials For Low Thrust Rocket Engines," AIAA 93-2406, June 1993.

Outka, D.A., Hamilton, J.C., Clift, W.M. Yang, N.Y., and Boehme, D.R., "High Temperature Diffusion in CVD Iridium Coatings on CVD Re," 182nd Annual Meeting of Electrochemical Society, October 1992.

APPENDIX A

MATERIALS DATA

Task 1.1 Candidate Materials and Fabrication Process Selection

1.0 Objective

The objective of Task 1.1 is to select material candidates for evaluation in Phase I of the program. The candidate materials must be capable of operating for many hours at temperatures above 3500 F, and preferably above 4000 F, in a sonic flow stream where the stream composition may vary from reducing to mildly oxidizing. Furthermore, the material system must have sufficient thermal shock resistance to withstand at least 10^5 engine pulses, many of which may be full thermal cycles.

2.0 Background

A large number of high-temperature material systems have been evaluated for use in low-thrust chemical propulsion by the propulsion industry. Most of these systems have been of the carbon-carbon composite type with metal carbide coatings, e.g., HfC, SiC, etc. Over the past five years, Aerojet has purchased and tested several types of advanced materials using our Rocket Materials Tester shown in Figure 1. The testing (References 1, 2, 3, and 4), summarized in Table I, included both metallic and nonmetallic materials. Thus far, it has been clearly established that a chemical vapor deposited (CVD) layered-wall chamber, comprised of a 0.002-in.-thick liner of iridium, overlaid with a thicker structural layer of rhenium, is superior to all other materials when measured by operating temperature and time. A single unit has operated 15 hours at nominal temperatures of 4000 F, using the test device shown in Figure 1. Other test articles of identical design have accumulated firing durations of 8 or more hours and a 20X scale-up, i.e., 100-lbF thrust test chamber of the same materials, has demonstrated 4 hours at ~3200-3500 F without failure. Because no other material system has approached these demonstrated capabilities, the iridium-lined rhenium chamber has been selected as the baseline high-temperature material to be used for comparison with other advanced high-temperature, oxidation-resistant material systems.

The only other materials which have demonstrated oxidation resistance superior to iridium are platinum and alloys of platinum and rhodium. these systems, however, are limited to ~3000 F operation.

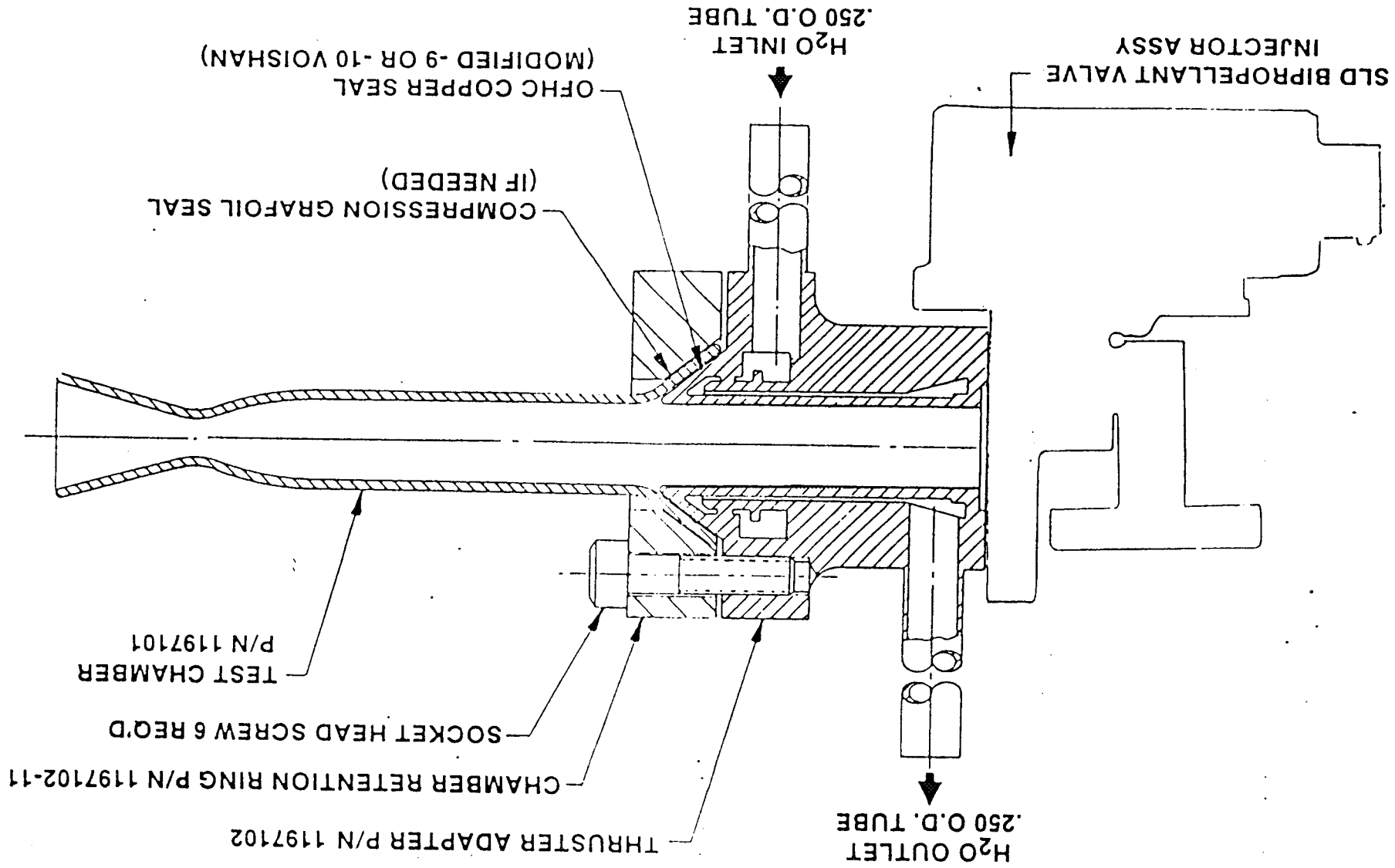


Figure 1. Chamber Material Tester

TABLE I
Aerojet High Temperature Rocket Materials Test Data Base

Material	Source	Chamber Type S/N	Thrust lbF	Temp Range, F	MR, NTO/MMH	Total Burn Time, Sec	Full Thermal Cycles	Total Starts	Throat ID Change, In.	Contract
Rhenium	SFL	85001	5	1,940 - 3,700	0.8 - 1.65	1,762	24	8,889	.028**	IR&D
Rhenium	SFL	85002	5	2,730 - 3,720	0.8 - 1.72	9009	34	1,207	0.002**	IR&D
Rhenium	Ultramet	85003	5	1,550 - 3,730	1.1 - 1.51	575	10	12	0.000	IR&D
Ir-Re	Ultramet	86001	5	3,400 - 4,200	1.2 - 2.18	31,363	37	3,638	Hole	IR&D
Ir-Re	Ultramet	86002	5	3,500 - 4,000	1.4 - 1.7	13,018	14	14	Hole	IR&D
HfO ₂ -Ir-Re	Ultramet	86005	5	3,540 - 4,100	1.4 - 1.6	1,232	5	5	HfO ₂ Spalled	IR&D
Ir-Re	Ultramet	86003	5	4,010 - 4,300	1.4 - 1.7	28,426	74	157	Hole	NASA
Ir-Re	Ultramet	86004	5	4,000 - 4,070	1.55 - 2.0	54,431	70	2,701*	0.000	NASA
Ir-Re***	Ultramet	86009	5	3,920	1.4	926	9	10	0.000	SBIR
Ir-Re	Ultramet	—	100	3,200 - 3,500	1.5 - 1.7	3,381	30	30	0.000	JPL
Ir-Re	Ultramet	88001	5	2,500 - 3,500	1.6	6,774		100,000	0.000	NASA
Ir-Re	Ultramet	—	100	3,200 - 3,500	1.5 - 1.7	15,000	33	33	0.000	JPL
Ir-Re***	Ultramet	—	5	2,000 - 3,000	1.8 - 2.8	7,800	29	29	0.004	IR&D
Ir-Re	Ultramet	—	5	Not tested						IR&D
ODS Pt	Englehard	—	5	Not tested						IR&D
ODS Pt	Englehard	—	5	2,000	1.8 - 2.8	3,000	15	15	0.000	IR&D
ZGSPt	JM****	85004	5	2,600 - 3000	0.8	1,011	5	5	0.000	IR&D
ZGSPt	JM****	86005	5	2,600 - 3,000	0.8 - 2.0	2,237	25	43,158	0.000	IR&D
ACC4CC	Vought	86006	5	1,625 - 2,375	1.4 - 1.5	327	4	4	Hole	IR&D
ACC4CC	Vought	86007	5	Not tested						IR&D
HfC-CC	Ref Comp Inc	87001	5	2,860	1.59	105	1	1	Mechanical	IR&D
SiC K-Karb	Midland Mat	85006	5	1,340 - 1,800	1.4 - 1.7	222	3	3	0.0025	IR&D
C-103/R512E	HiTempco	86008	5	2,200 - 2,610	0.8 - 2.1	4,170	16	16	0.001	IR&D
C-103	Thermocore	Heatpipe	5	2,000	0.7 - 1.65	905	4	4	0.000	SBIR
Rhenium	Ultramet	—	25	2,000 - 4,000	O ₂ /H ₂ O ₂ /CH ₄	6,840 360	192 6	192 6	0.000 0.007	Test @ JPL

*Cycled 3,500 to 4,000 F

** Material Loss Encountered in Pulsing and When Operated at MR>1.5

***Iridium Thickness Two Times Nominal .002 in.

****Johnson Matthey

log 88.716

3.0 Improvement of Materials

Potential advancements in material systems relative to the Ir/Re baseline fall into six categories. These are listed in Table II and discussed in this section.

TABLE II
MATERIAL IMPROVEMENTS

- 1) Cost reduction
- 2) Quality improvement
- 3) Longer life
- 4) Higher operating temperatures
- 5) Reduced weight
- 6) Improved oxidation margin

3.1 Improvement Options

1) Cost Reduction This option addresses material systems or fabrication approaches providing the same temperature and life capabilities as the baseline which can be produced at lower cost. This would include (a) improving the CVD fabrication process efficiency which has a 50-80% material loss rate or the use of other more efficient fabrication processes, and (b) improving material structural properties so that smaller quantities of costly materials are required.

2) Quality Improvement The CVD fabrication process control is not sufficiently developed at this time to allow flight-qualified components to be fabricated. Optimization of the CVD process, or use of a post-deposition HIP or other possible fabrication methods, represents another type of advancement in material technology that will be required before proceeding into a flight system.

3) Longer Life Extending the operating life beyond 15 hr at 4000 F represents another improvement. This could be accomplished by use of thicker iridium layers and possibly by the use of a diffusion barrier between the iridium and rhenium

layers. Improvement in the high-temperature creep properties of rhenium and thicker iridium deposits would also be required.

4) Higher Operating Temperature Increasing the operating temperature above 4000 F could be useful as the combustion products of other propellants, such as O_2/H_2 and O_2/CH_4 , are ~ 600 F hotter than the storable $N_2O_4/CH_3N_2H_3$ propellants used in the Aerojet Material Tester.

5) Reduced Weight Weight reduction provides another useful form of material improvement. The iridium and rhenium materials are very dense, resulting in heavy parts. A high cantilevered chamber mass makes it necessary to reinforce the chamber head to withstand anticipated vibration loads. This, in turn, makes thermal isolation of the hot chamber more difficult and can limit operational flexibility. Potential methods of reducing weight include alloying with lower density materials, and/or the use of dispersion strengthening or grain stabilization to improve high-temperature creep strength.

6) Improved Oxidation Margin Iridium is lost at a slow rate at high temperature even under mild oxidation conditions. Most small thrusters normally operate fuel rich, so this is not a major problem. A significant loss of material, however, can result from a poor injector design, a partially obstructed or misaligned fuel element, or a faulty tank pressurizing system. The addition of an oxide coating over the iridium could provide improved design margin.

3.2 Technical Approach to Options

The various possible technical approaches that can be employed to attain the six types of improvements are discussed in this section.

3.2.1 Cost Reductions

Options include:

- o Optimize CVD process

- o Provide multiple fabrication sources (competition)
- o Investigate more efficient processes
 - plasma spray
 - casting
 - powder metallurgy + HIP
 - wire preforms + HIP
- o Lower cost materials
 - alloys of W-Re, Re-Mo, Re-Nb
 - grain-stabilized Re (stronger, therefore, less required)
 - replace iridium

3.2.2 Weight Reduction

Options include:

- o Rhenium alloys, higher strength
 - Mo-Re (lower density)
 - Nb-Re (lower density)
- o Improve high-temperature creep strength (thinner walls), dispersion strengthen, grain stabilize
- o Monolithic ceramics

3.2.3 Longer Life

Options include:

- o Thicker iridium
- o Diffusion barrier between iridium and rhenium

3.2.4 Higher Temperatures

Options include:

- o Other material systems, mixed carbides

3.2.5 Improved Oxidation Margin

Options include:

- o Oxide overcoat on iridium, i.e., stabilized HfO_2

3.2.6 Better Quality

The most direct approach to better quality is to optimize the CVD process. This includes adding control specifications on the process parameters, and raw material composition, and the use of in-process diagnostics, i.e., monitor O_2 content, etc. NASA has funded Ultramet to perform this task under Contract NAS 3-25792.

It can be noted that certain approaches have multiple benefits. For example, increasing high-temperature creep strength of rhenium can reduce both cost and weight. Alternate fabrication processes which provide thicker, higher quality iridium could improve life and reduce cost compared to CVD which is only 50% efficient at best.

4.0 Ranking of Priorities and Possible Options

Two factors were considered in ranking the six possible improvement categories relative to the long range NASA goals. One was the importance of the improvement relative to the present contract, the other was the degree of risk, i.e., the probability of success within the program resources. When evaluated by the importance to risk ratio, it was concluded that developing the fabrication process controls for flight-qualified components of the baseline material system was number one. There is little question that the process can be improved and the work is essential if flight systems are to be produced. It was also concluded that this important task was not in accord with our scope of work.

Next in importance were reduced weight and improved oxidation margin. These were ranked equally important. Reducing the weight was seen as essential to both the thermal management (reduced heat soak) and vibration design criteria. The oxidation margin improvement was seen as being required for the cryogenic propellants which burn hotter and therefore contain a greater mole fraction of HO^+ and O^- than the storable propellants. Space station applications may require operation at higher mixture ratios, i.e., 8:1 for O_2/H_2 .

Reducing cost was ranked third, mostly because of the low risk rather than great importance.

Longer life and higher temperature systems were lowest in ranking for different reasons. The 15 hr demonstrated at 4000 F without failure appears more than adequate for the foreseeable applications. An effort to increase life is not required at this time. The iridium is now operating within 400 F of its melting point ($T_m=4436$ F). It is not considered prudent to increase the operating temperature. Introduction of a new material system designed for operation at higher temperatures is very important, but is accompanied by a very high probability of failure and, therefore, could be either nonproductive or consume resources which are planned for use in the diagnostic tasks. Investigation of an all-new system, i.e., carbon-carbon ceramic, is not in the best interest of the program.

5.0 Discussion of Material Options

5.1 Improvement of High-Temperature Strength-to-Weight Ratio

Increasing the material creep strength at high temperature will reduce the required chamber wall thickness, and therefore, reduce the chamber thermal energy storage and cantilevered chamber mass. In combination, these will minimize the thermal heat soak, provide greater pulse mode duty cycle capabilities, and enable the thruster to withstand the imposed vibration requirements. It must be cautioned that any changes or modification of the substrate material (rhenium) must be compatible with the iridium liner concept.

The first material selection criteria is melting temperature and density. Figure 2 provides a comparison of the melting temperatures and density of candidate metallic materials. Tungsten ($T_m=6128$ F) is the only metal having a melting temperature higher than rhenium ($T_m=5755$ F). Rhenium was selected over lower-cost tungsten for our baseline design because of its excellent low-temperature ductility (Figures 3 and 4). Tungsten and molybdenum are noted to be brittle at room temperature. The only other metal worthy of consideration for 4000 F structural member is tantalum ($T_m=5395$ F) which is also ductile at low temperatures.

The second criteria for substrate material selection is expansion coefficient relative to iridium. Based on the data of Figure 5, the order of preference of the materials is tantalum, rhenium, and tungsten.

The third criteria is strength at elevated temperature. Standard methods of improving the high-temperature strength of elemental metals are alloying, dispersion strengthening, and/or the addition of a grain stabilizing agent to provide retention of a fine-grain morphology during extended operating periods at elevated temperature. It is well known that the structural properties of molybdenum, tungsten, and platinum can be significantly enhanced by combinations of these standard methods. Another method to be considered is the use of composite structures.

5.1.1 Rhenium Alloys An investigation of published data indicates that alloying of pure rhenium results in a decrease of the high-temperature rupture strength. Figure 6 provides a comparison of the time-to-rupture at 2200 C (3991 F) of rhenium, tungsten, molybdenum, and various alloys of these materials. The addition of molybdenum, which is less than half the density of rhenium, 10.2 vs. 21 gm/cc, results in a less favorable strength-to-weight ratio than pure rhenium. The common alloys of tungsten-rhenium, used to reduce cost, appear to provide no structural improvement.

5.1.2 Tantalum Tantalum and its alloys were investigated and, as shown in Figures 7 through 10, pure tantalum has significantly lower high-temperature creep strength than rhenium. Some of the more important tantalum-base alloys which have been developed are:

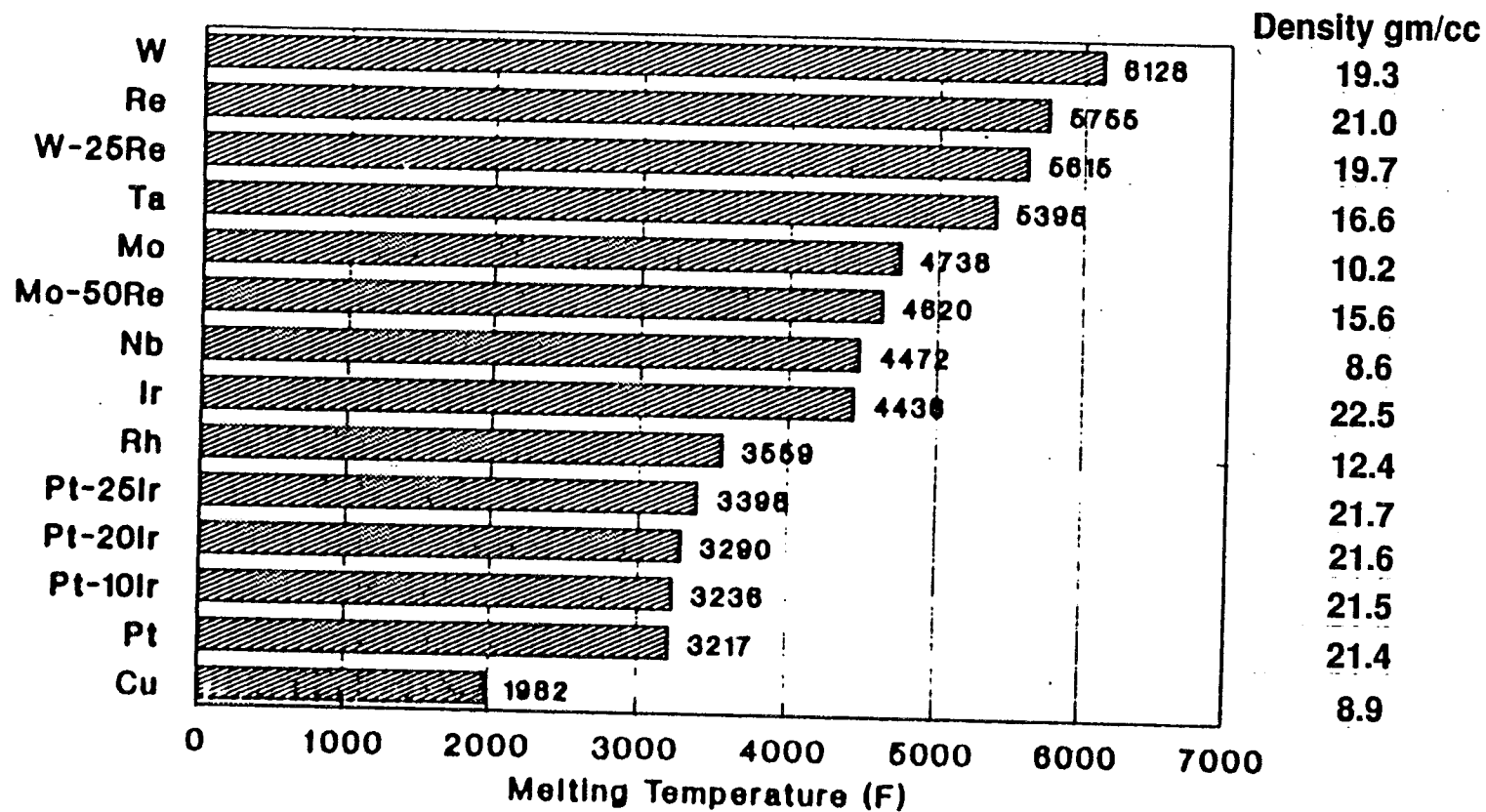
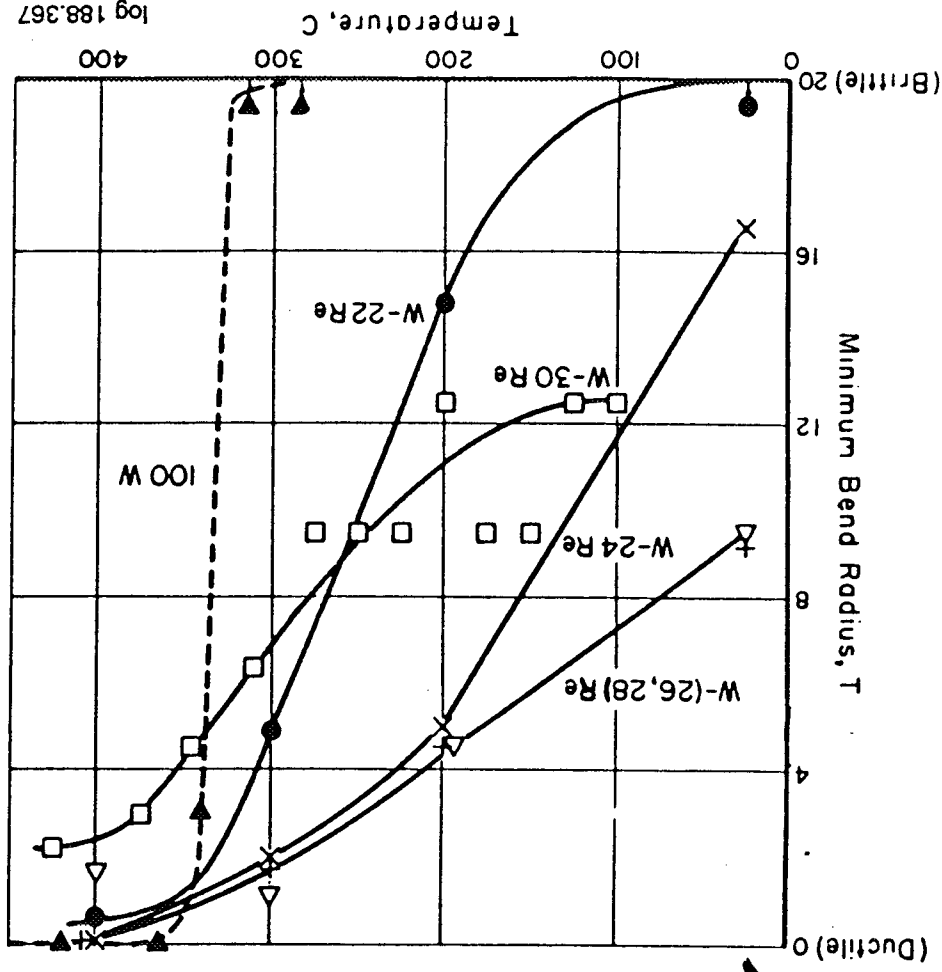


Figure 2. Comparison of Melting Temperatures and Density of High Temperature Chamber Materials

Figure 3. The Addition of Rhenium to Tungsten Improves the Ductile-to-Brittle Transition Temperature



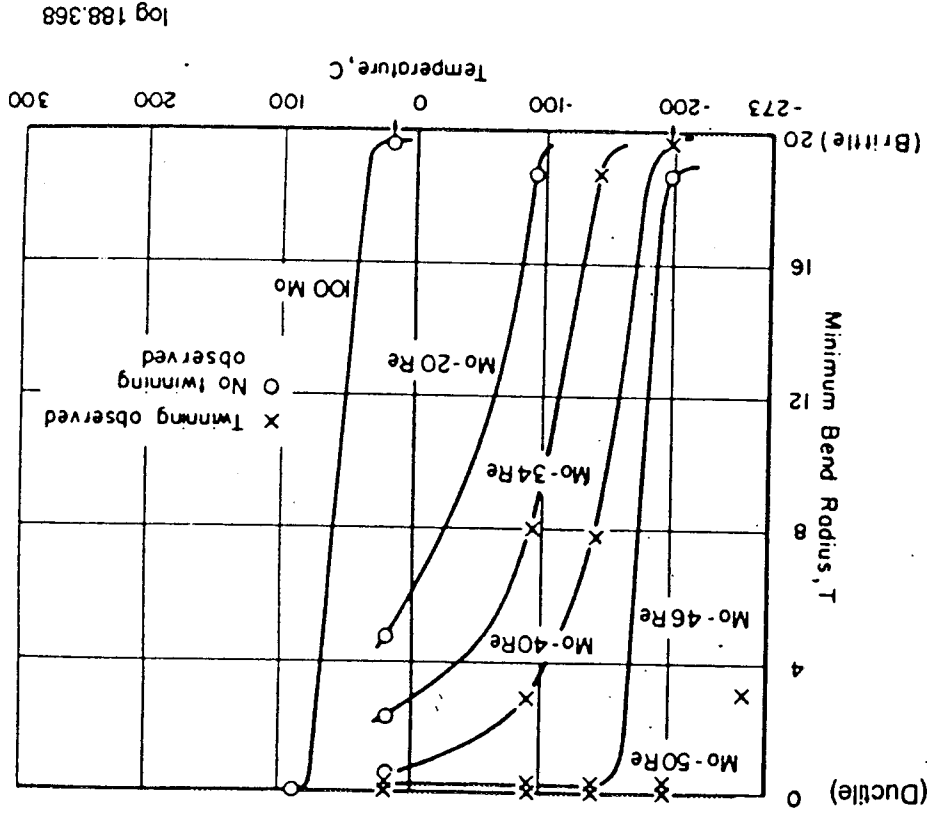
Pure Rhenium

RHENIUM AND PLATINUM-GROUP METALS

433

0.020 in. Thick crystallized Strip

Figure 4. The Addition of Rhenium to Molybdenum Improves the Ductile-to-Brittle Transition Temperature



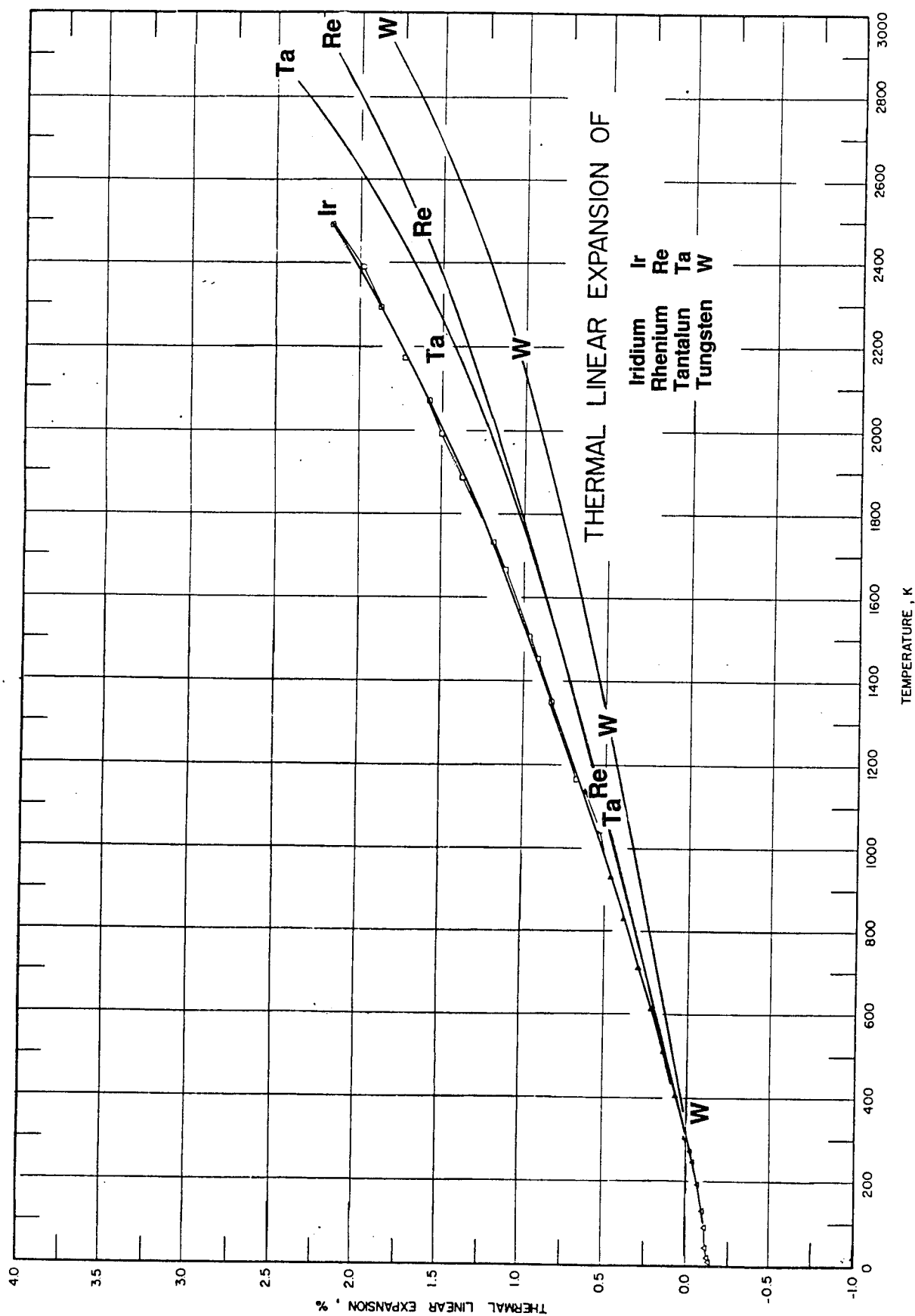
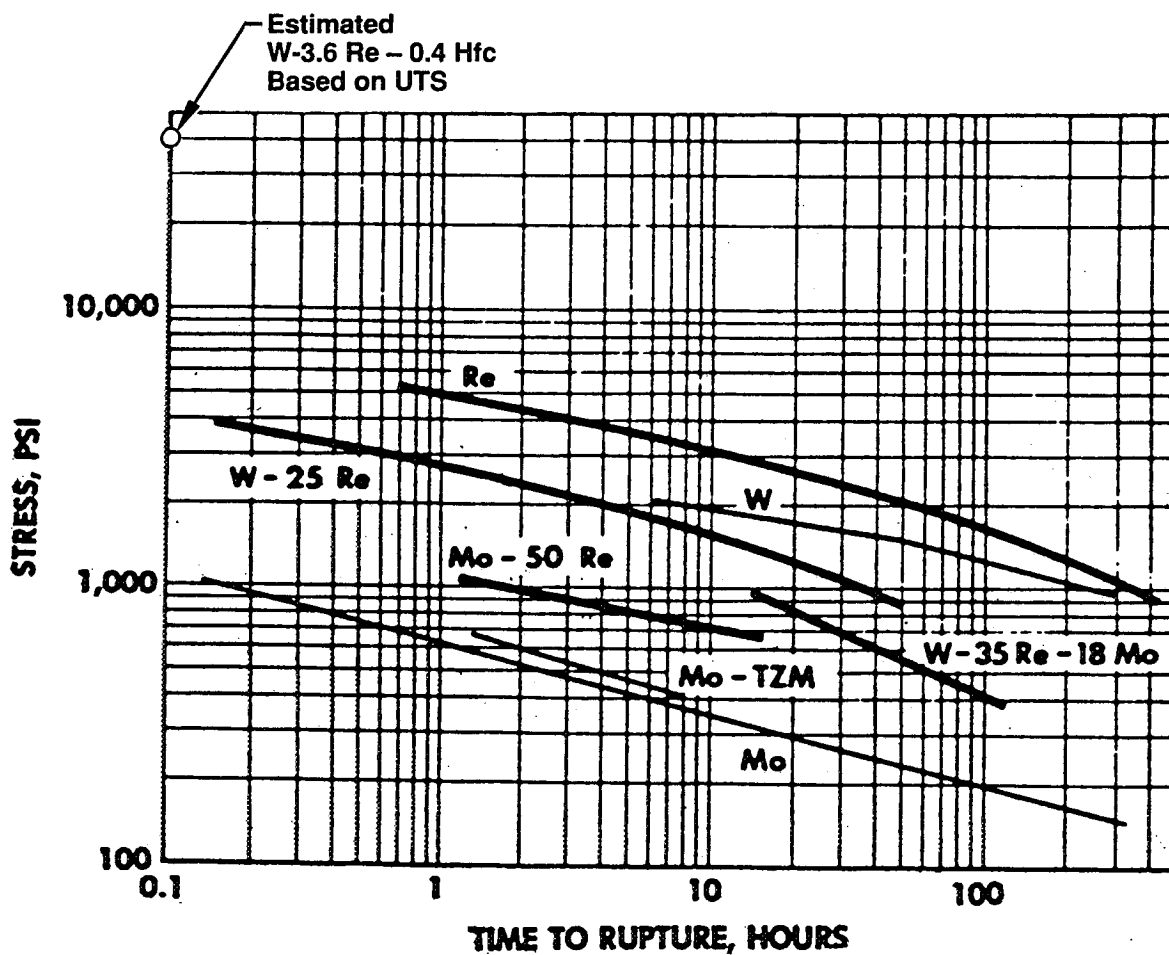


Figure 5.



Stress-Rupture Characteristics of Rhenium and Rhenium Alloys Compared to Those of Molybdenum Molybdenum-TZM, Tungsten at 2200°C (3991°F)

	Density gm cm ³	S100/P
Mo	10.2	19.6
Re	21.0	80.9
W	19.3	67

Figure 6. Mechanical Properties – High-Temperature Stress-Rupture Data

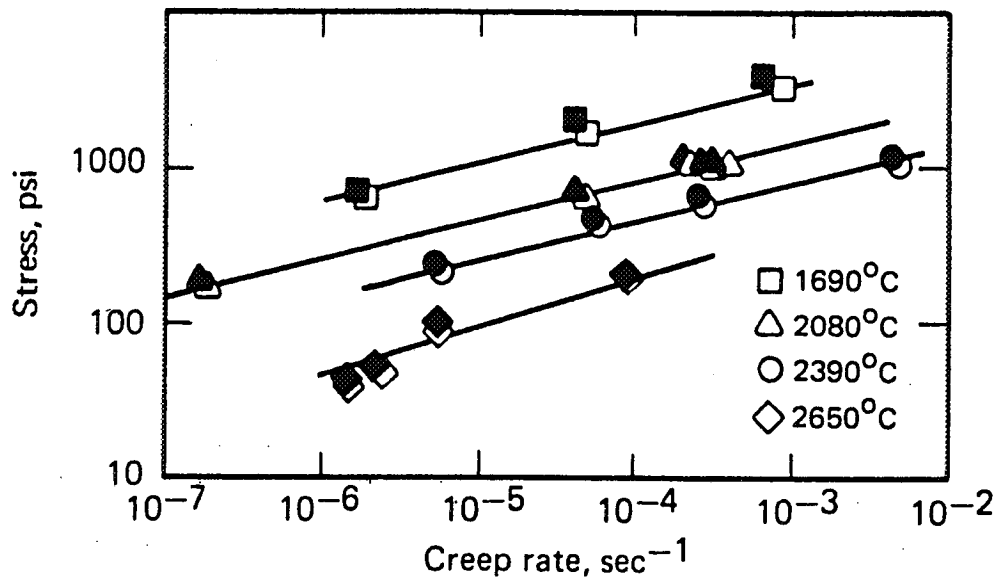


Figure 7. Creep Rate Data for Electron-Beam-Melted Tantalum Tested in Helium. (Filled Points Represent True Creep Stresses Corresponding to Minimum True Creep Rates; Open Points Represent Engineering Stress vs Linear Creep Rate.)

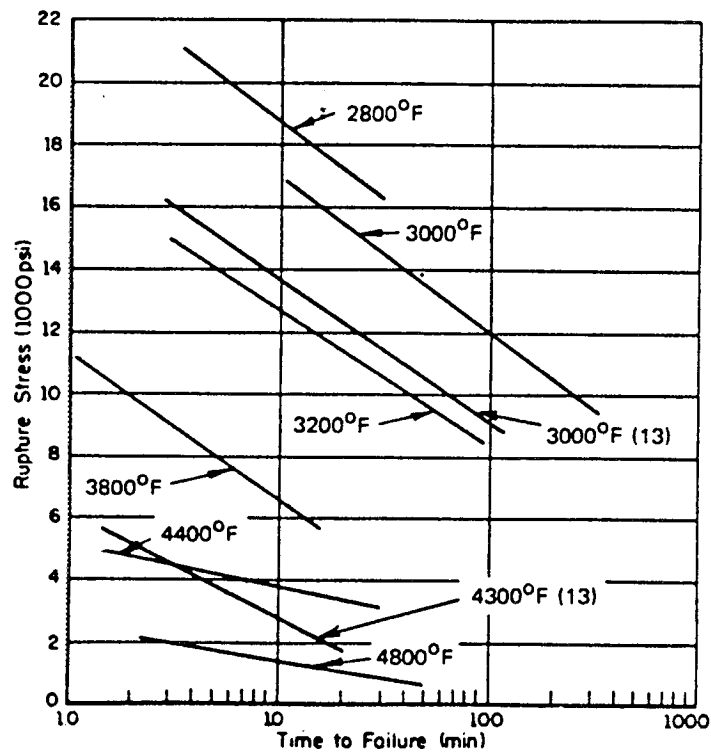
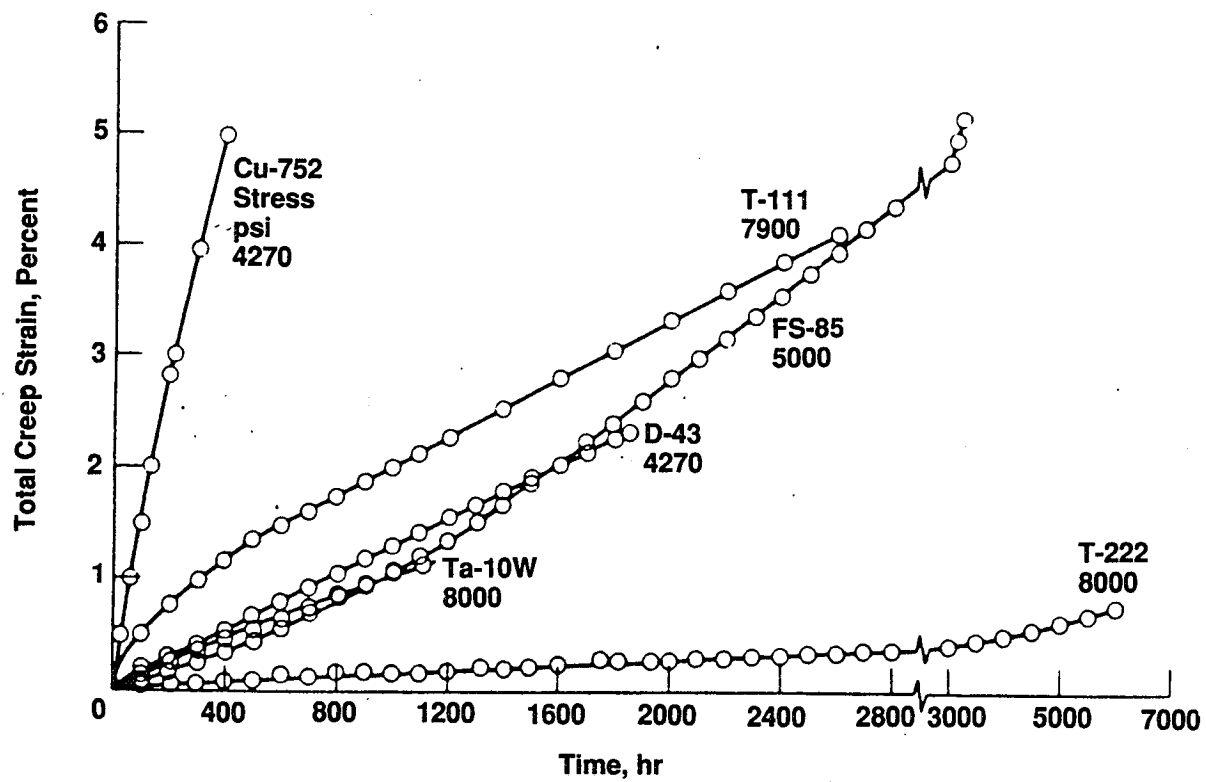


Figure 8. Stress-Rupture Data for Electron-Beam-Melted Ta-10W Sheet Tested in Vacuum (Data From Conway, Ref. 5)



(b) Test Temperature, 2200°F; Common Stress-to-Density Ratio, 1.3×10^4 Inches

Figure 9. Comparison of the Creep Behavior of Several Tantalum and Niobium Alloys Tested in Vacuum (Data From Conway, Ref 5)

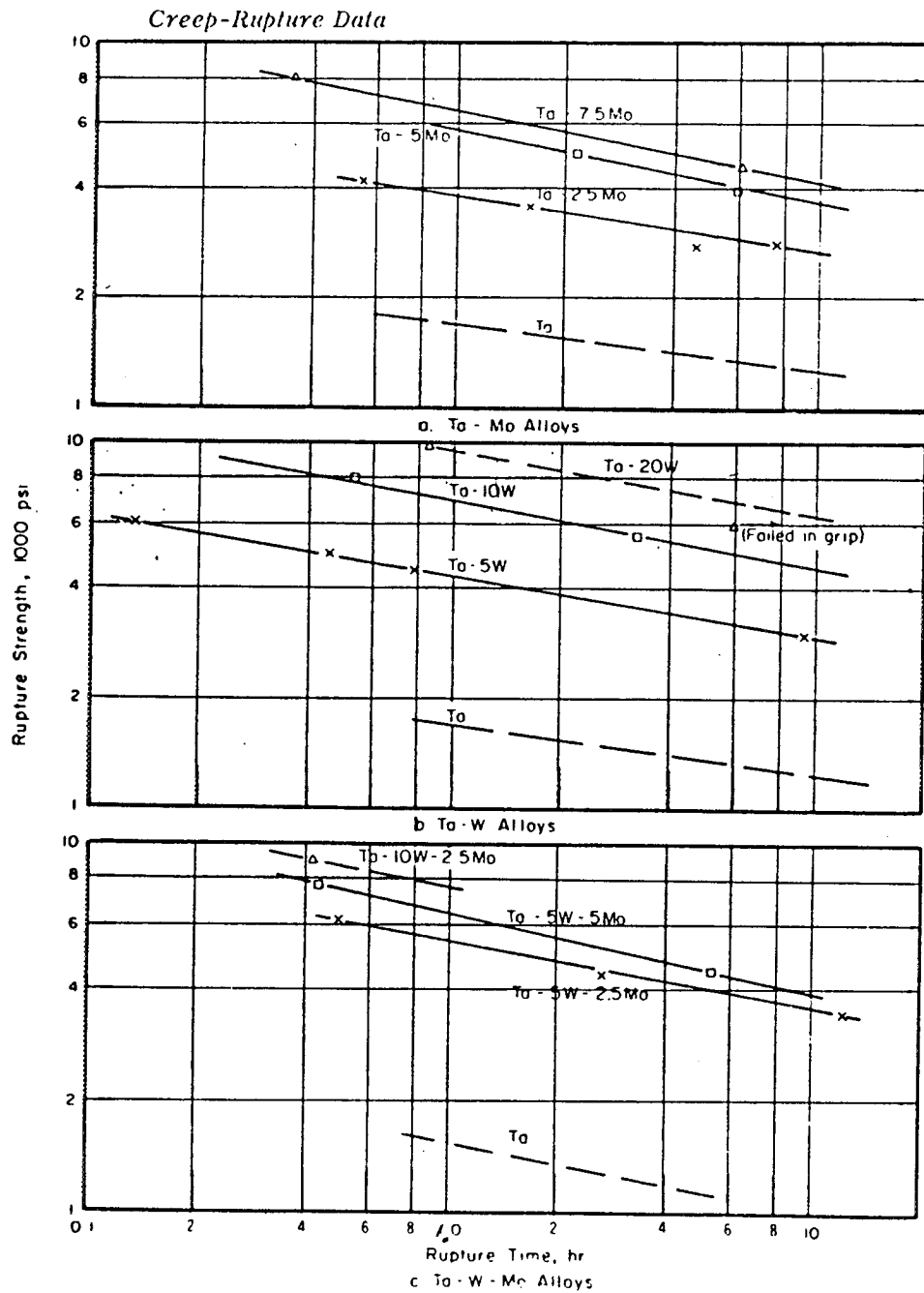


Figure 10. Stress-Rupture Data at 3500°F for Various Ta-W-Mo Alloys Tested as Recrystallized Sheet in Vacuum (Ref. 5)

Ta-10 W*	Commercial
Ta-20 W*	Experimental
Ta-8 W-1 Hf (T-111)	Experimental
Ta-9.5 W-2.5 Hf-0.01 C (T-222)	Experimental
*Weight percent.	

Creep-rupture data for these prominent compositions and for some other tantalum alloys which have been studied to only a limited extent are presented in the following sections.

Figure 8 provides creep rupture strength for Ta-10 W which is a commonly available alloy. This data is ambiguous at 4000°F and comparison with unalloyed Rhenium data suggests lower strength (15 to 75%).

Figure 9 from Conway (Reference 5) compares the strain of Ta-10 W with the T-111 and T-222 at 2200 F, the highest temperature for which comparable data could be found. These data show a significant improvement in high-temperature creep strength for T-222 compared to the other alloys shown.

Figure 10 from the same reference provides creep rupture data for Ta-20 W at 3500 F compared to Ta-Mo and Ta-W-Mo alloys. The two-hour rupture strength of the Ta-20 W, based on one data point, is estimated to be slightly higher than 8000 psi. Insufficient data were found for a direct comparison with rhenium at 4000 F.

Figure 11, showing the stress-to-density ratio of a range of alloys was employed to project how rhenium compares to these tantalum-based alloys. The comparison was made on 0.5% total creep. The results, based on very limited data, indicate that rhenium has a higher creep strength-to-density ratio at high temperatures.

Thus far, it appears that there are no commercially available tantalum or tungsten alloys which are structurally more favorable than pure rhenium.

5.1.3 Alloys of Tungsten and Rhenium Hafnium and Carbon The literature investigation has revealed that extensive work has been conducted by NASA for

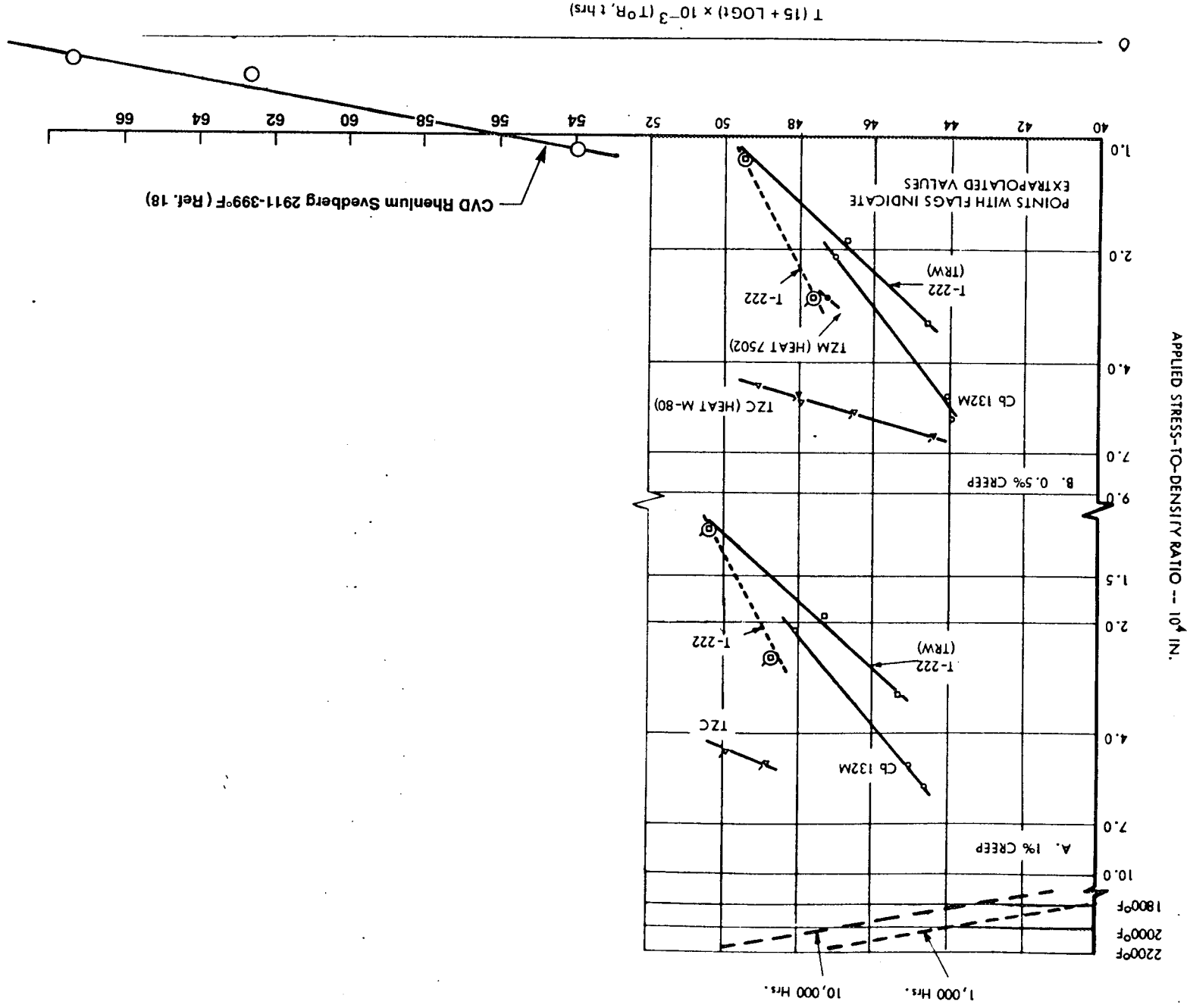


Figure 11. Larson Miller Parameter Plot Comparing Creep Strength of Various Alloys in Terms of Stress-to-Density Ratio From Ref. 5

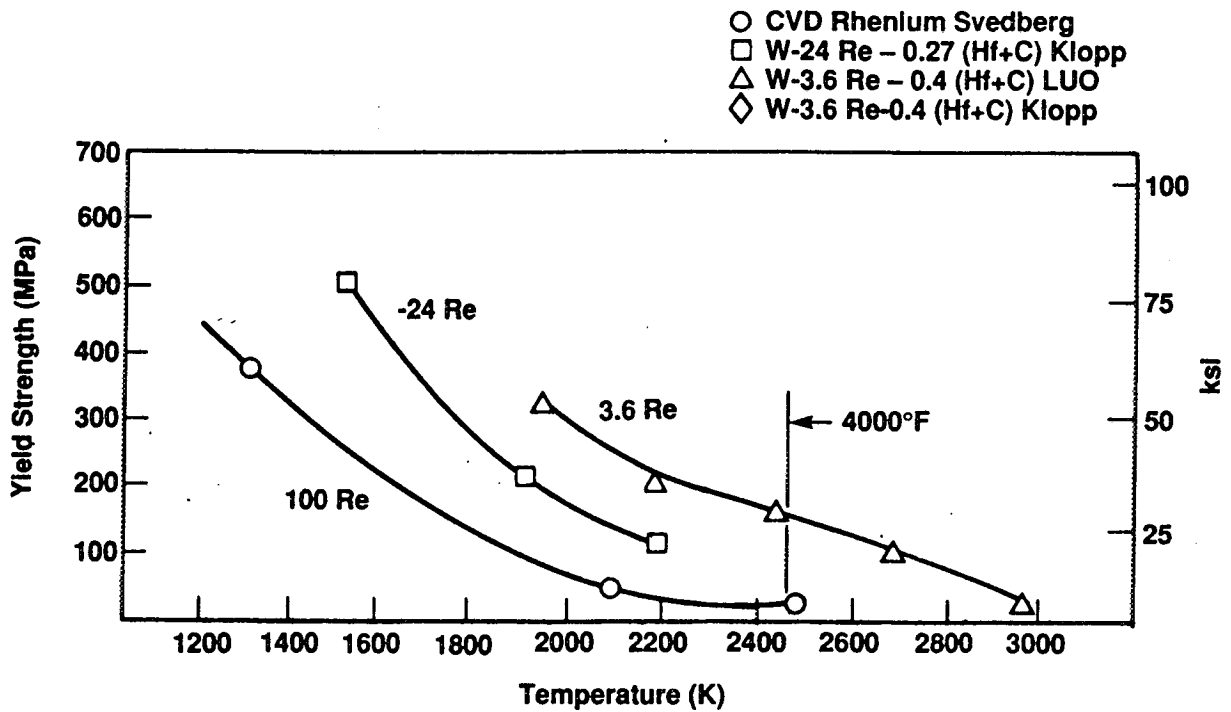
the past 20 years on an experimental dispersion strengthened alloy comprised of W-Re-CHf, References 6 through 15. Two alloys are presently under additional investigation under NASA/Lewis contract. These are W-23.4 Re-0.27 (Hf+C) and W-3.6 Re-0.4 (Hf+C). A comparison of the high-temperature yield and ultimate tensile strength on these two materials with CVD rhenium is provided in Figure 12.

Dr. A. Lou (Reference 16) of Arizona State conducted tensile tests of the W-3.6 Re-0.4 Hf+C alloy at temperatures between 1900-3000 C. The tests conducted in 1988 were based on a 1-in.-dia rod fabricated by Westinghouse for NASA/LeRC in ~1970-1975, Reference 17. His results at 2200 C are comparable with properties of recrystallized material reported earlier by Klopp (Reference 10). At an operating temperature of 2473 K (4000 F), this alloy provides a yield strength of 180 Mpa (26,000 psi) compared to 38 MPa (5500 psi) reported by Svedberg, Reference 18) for Ultramet CVD rhenium. This improves the strength-to-weight ratio by nearly a factor of 5. Furthermore, the cost of tungsten is an order of magnitude less than rhenium. Figure 13 compares the linear creep rates of CVD rhenium with the W-3.6 Re-0.4 (Hf+C) alloy. The strength advantage in creep is greater than 400% at 3500 F. Figure 14 shows this material also has a more favorable high-temperature ductility than CVD rhenium. Unfortunately, the material ductile-to-brittle transition temperature is above ambient temperature, as shown in Figure 15. This is a concern for cold starts in space. The use of a metal matrix composite design, such as shown in Figure 16, could provide a design solution to this limitation. As represented by the data provided in the appendix, this material is sufficiently well characterized to allow preliminary designs to be established.

The alloy having the higher (24%) rhenium content results in a more favorable ductile-to-brittle transition temperature, Figure 15, but exhibits a much lower tensile strength at the high temperatures of interest.

The fabrication status of these materials was determined by personal communications with the technical staff at NASA/LeRC, Westinghouse, and Phillips Elmet. Both alloys have been prepared by vacuum arc melt at Westinghouse,*

*Personal communication with Mr. B. Buckman.



Comparison of Yield Strength of CVD Rhenium With Advanced W-Re Hf+C Alloys

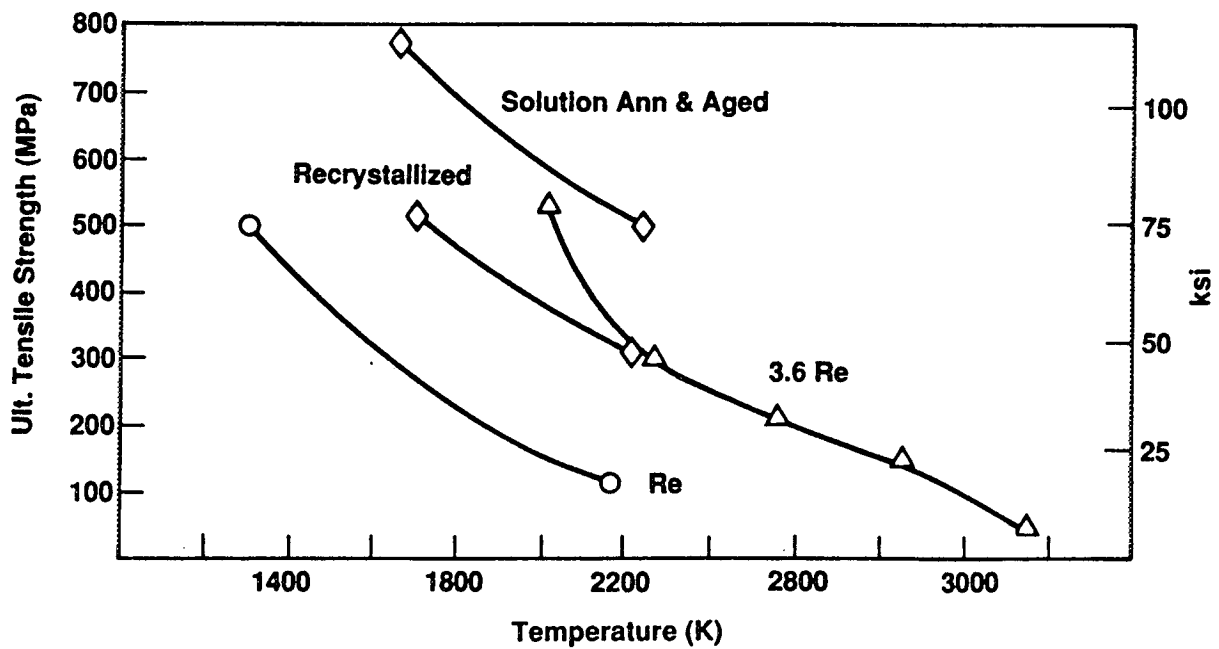
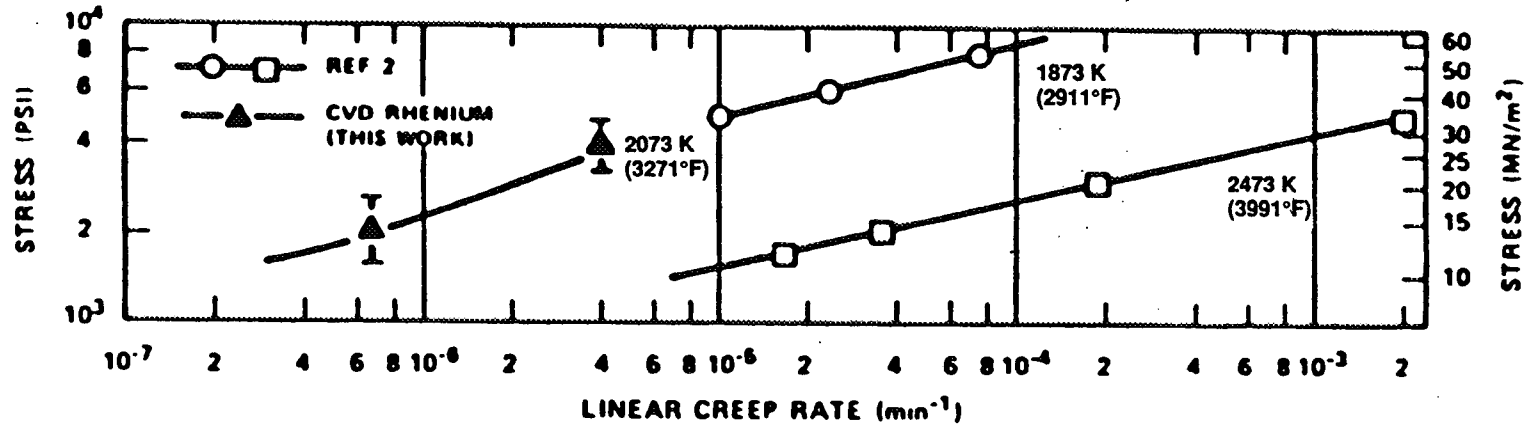


Figure 12. Comparison of Ultimate Tensile Strength of CVD Rhenium With Advanced W-Re (Hf+C) Alloys



Typical Properties Ultramet CVD Rhenium (Ref 18)

(Ref 18)

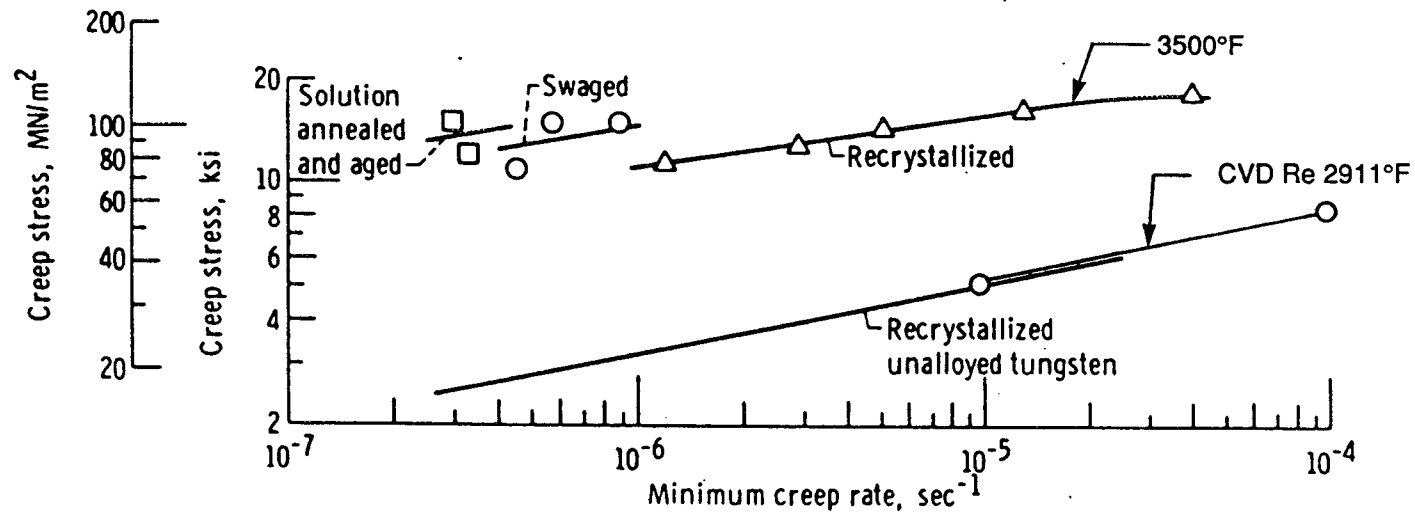


Figure 13. Creep Rates for Alloy W-3.6 Re-0.4 (HP + C) at 3500°F (1927°C) in as-Swaged, Recrystallized, and Solution-Annealed Conditions. Unalloyed Tungsten is Included for Comparison (Ref 10)

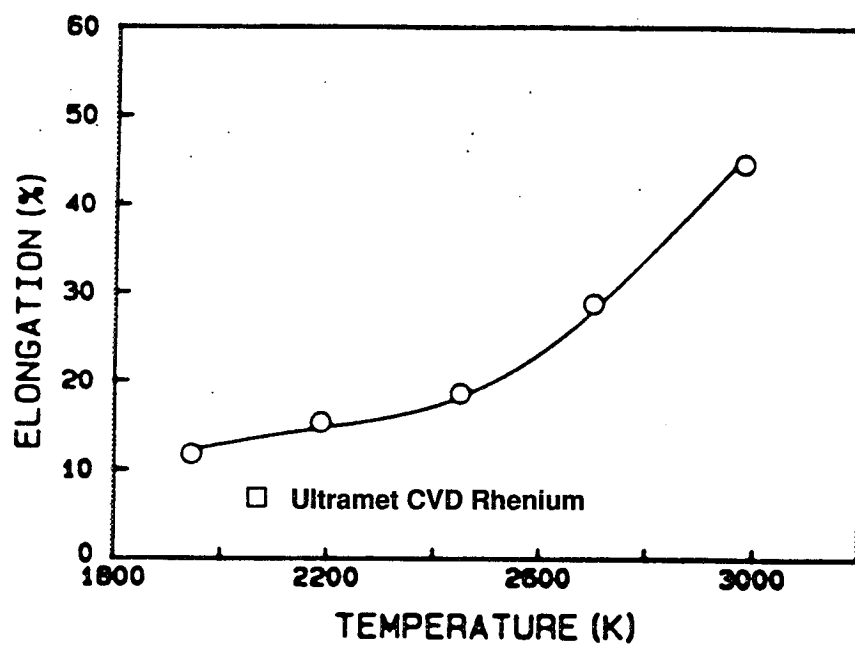
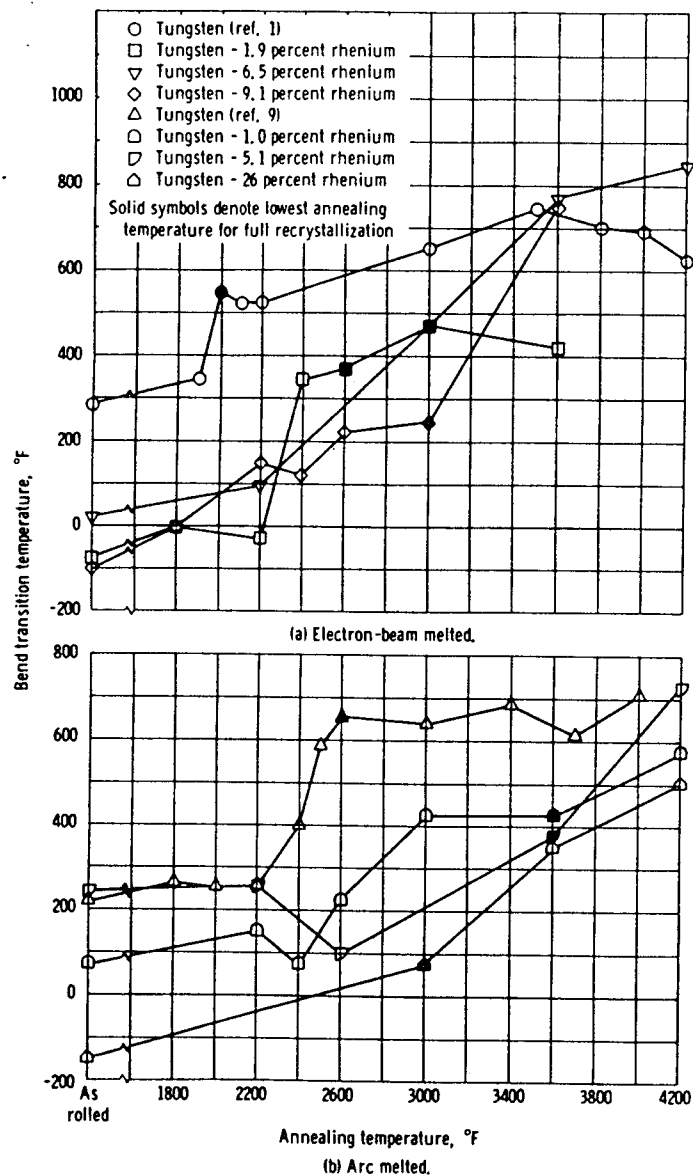
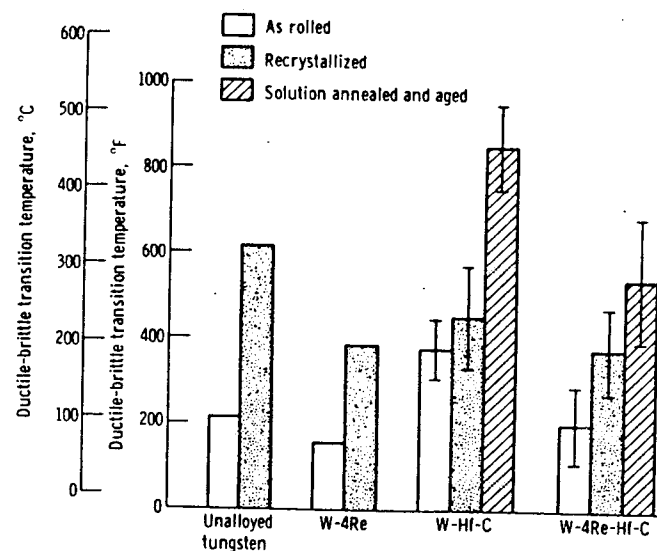


Figure 14. Effect of Temperature on the Tensile Elongation of W-3.6Re-0.4HfC (Ref. 16)



Bend transition temperature of electron-beam- and arc-melted tungsten and tungsten-rhenium alloys as rolled and after annealing for 1 hour at various temperatures. (Ref. 7)



Ductile-brittle transition temperatures for arc-melted tungsten, W-4Re, W-Hf-C, and W-4Re-Hf-C. Average values are shown for tungsten and W-4Re, while median values and average differences from median are shown for W-Hf-C and W-4Re-Hf-C. (Ref 10)

Figure 15. Low Temperature Ductility Properties of W-Re-Hf+C Alloys

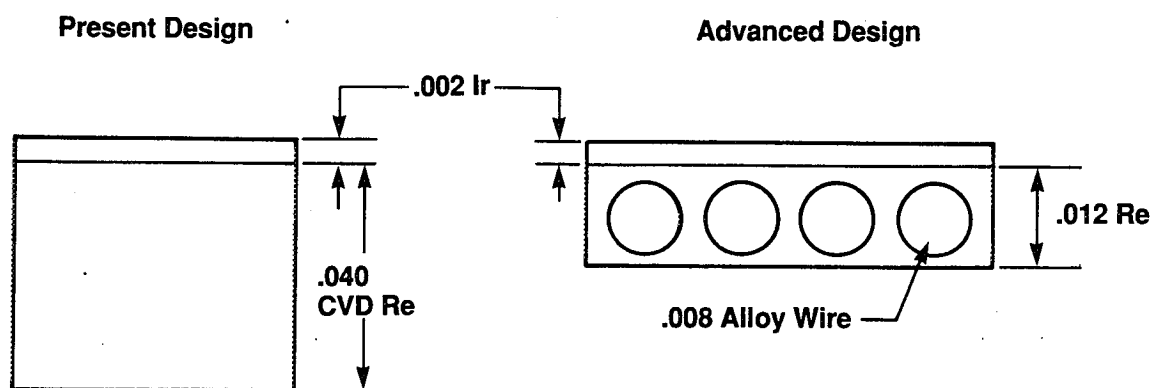


Figure 16.

swedged to bar at Oakridge, and shipped to Phillips for wire fabrication. The NASA goal is to produce 0.015-in.-dia wire near-term and 0.008-in.-dia wire as a final product. The availability of this material could reduce the wall thickness of the present 5-lbF thrust rhenium chamber from 0.040 in. to ~0.012 in., as shown by the sketch in Figure 16. Due to technical difficulties in the final wire drawing, in combination with funding limitations, the NASA project engineer could make no assurances that the material would become available in wire form in the next 18 to 24 months. Apparently, material is presently in bar and rod shapes in sufficient size to fabricate a small chamber.

5.1.4 Oxide Dispersion Strengthening

The addition of small quantities (<1%) of finely dispersed oxides, such as ThO_2 , ZrO_2 , and Y_2O_3 , to elemental metals such as tungsten and platinum can provide significant improvements in high-temperature properties. Figure 17 displays the increase in UTS that can be attained in platinum by the addition of 0.5% zirconia to Pt and to Pt-10 Rh. The zirconia grain-stabilized material is designated by the ZGS prefix.

A comprehensive literature investigation revealed no commercially available oxide grain-stabilized rhenium materials. The only documentation of the fabrication of this material was by Barr, References 19 and 20, for the NASA. This material was produced by slip casting. Photomicrographs presented in the documentation revealed excess porosity indicating further process development is required. No mechanical property data for this material were presented.

Discussion with W. D. Klopp, Reference 21, material consultant and a co-developer of the W-Re-Hf-C alloy revealed that oxide dispersion-strengthened rhenium was not considered during the development of these high-temperature alloys because of the high cost of rhenium and the large quantities required. Poor nuclear adsorption characteristics also made the alloy undesirable in previous applications. Discussion with several other long-time refractory metal experts indicated no known published work on thorium stabilized unalloyed rhenium. Most agreed that an approach of this type could have a high payoff and should be investigated further.

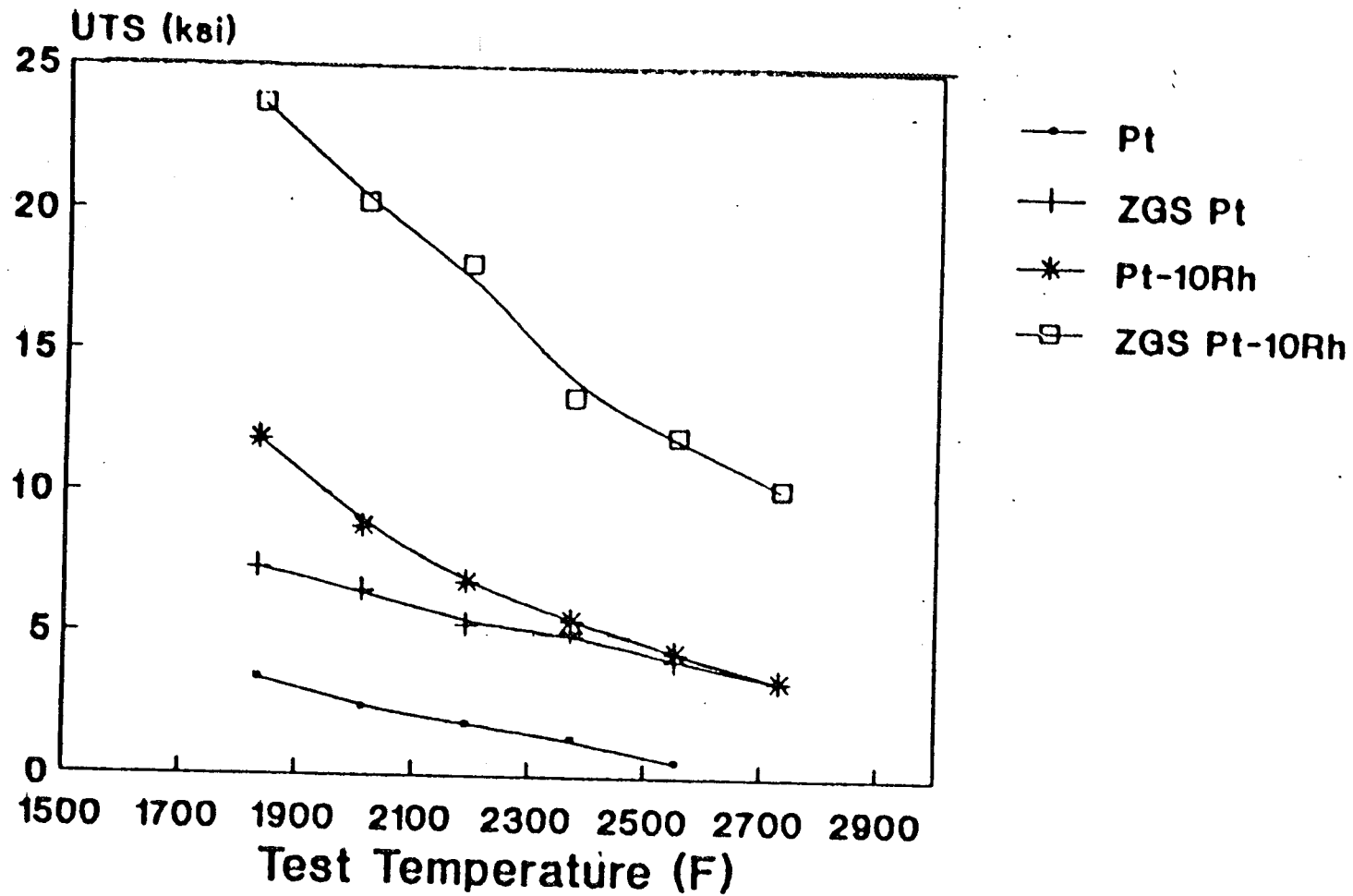


Figure 17. Platinum Alloys Provide Improved Tensile Strength at High Temperatures

Discussion with Fred Foyle of Rhenium Alloys, Inc., revealed that oxide dispersion-strengthened rhenium had been fabricated by his company in the past for a special application. Residual material containing 1% ThO₂ is available in wire dia of 0.005, 0.010, and 0.025 inch. No mechanical properties data were available from the manufacturer. Small samples have been requested for examination of the microstructure. If the material appears sound, sufficient quantities are available to conduct tensile and creep characterization tests.

5.2 Improved Oxidation Resistance

The availability of high-temperature, oxidation-resistant materials other than iridium was investigated. These fall into three groupings as follows.

- 1) Other platinum group metals
- 2) Metal oxides
- 3) Other non-oxide refractories

5.2.1 Platinum Group Metals

A comparison of the melting temperature and relative oxidation rates of the platinum group metals is shown in Table III Figure 18, respectively. Of these, only platinum and rhodium are more oxidation resistant than iridium. These two elements can be added to iridium to improve its oxidation resistance. However, as shown in the Phase Diagrams in Figure 17A, this reduces the melting temperature significantly. Platinum, grain-stabilized platinum, platinum-10 rhodium, and platinum-(5 to 30) Ir should be considered the preferred oxidation-resistant materials for temperatures up to ~3000 F. The only member of the platinum group metals which has a higher melting temperature than iridium is osmium, T_m=3300 K (5480 F). As shown in Figure 18, the oxidation resistance of osmium is significantly lower than the other members of this family of elements. Alloys of platinum-iridium with up to 30% iridium are commercially available from Johnson Matthey, Inc. The addition of 30% iridium to platinum increases the melting temperature, 1770 C (3217 F), to 1885 C (3424 F), while reducing the oxidation resistance. The alloy, however, is significantly more oxidation resistant than pure iridium. The difficulty in fabricating the Pt-30Ir alloy discourages its use except where

TABLE III
Melting Points of the Platinum Group Metals

Element	Melting Point	
	°C	°F
Os	3055	5530
Ir	2440	4423
Ru	2310	3207
Rh	1956	3552
Pt	1770	3217
Pd	1552	2825

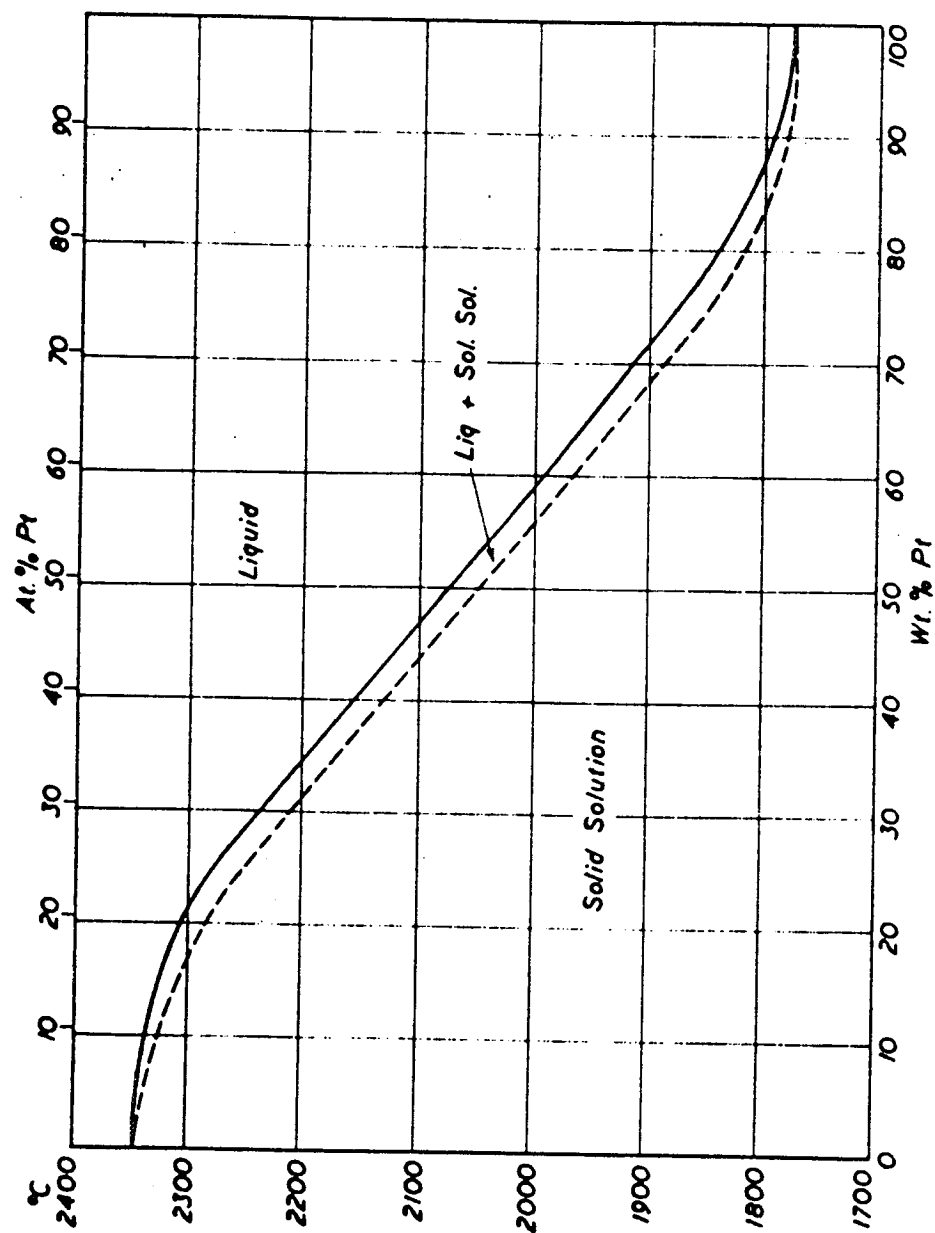
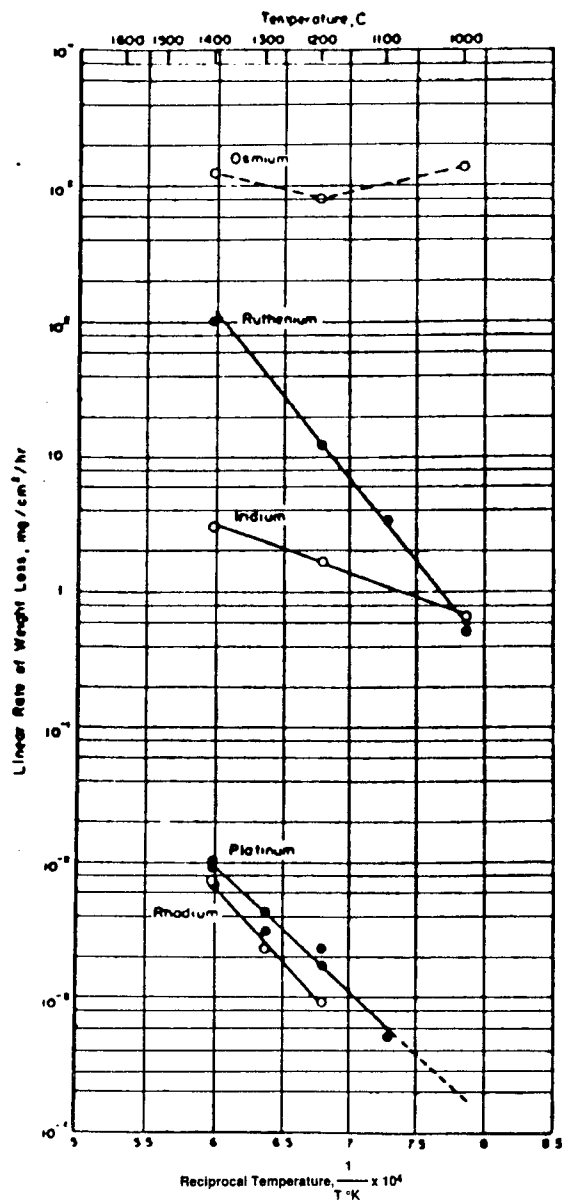


Figure 17A



Variation With Temperature of the Rate of Weight Loss In Air of the Platinum Group Metals, From Reference 4.

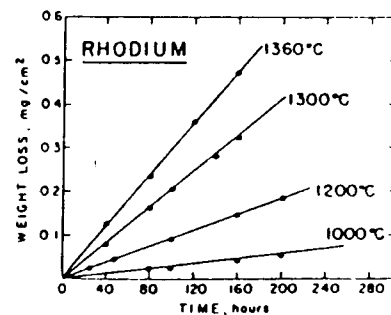
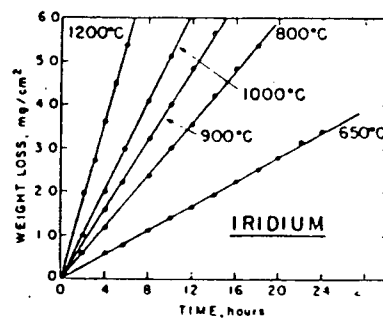
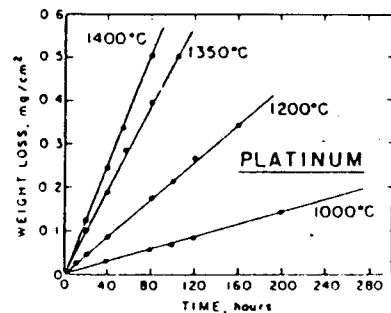
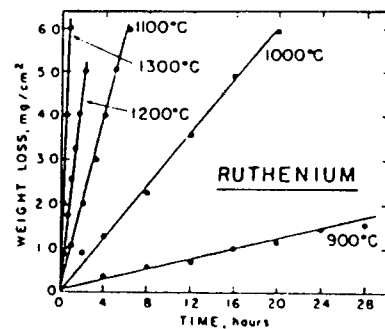
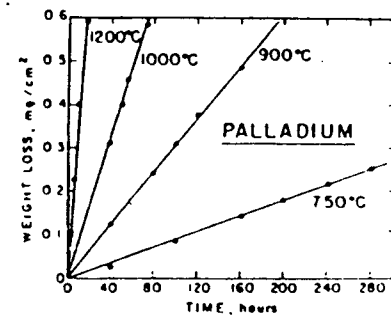
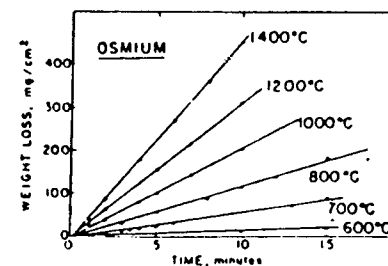


Figure 18. Weight Loss vs. Time for the Platinum Group Metals in Air, From Reference 4

absolutely necessary for extra thermal margin. The Ir-Pt Phase Diagram in Figure 17A indicates higher iridium alloy content is theoretically possible. These higher alloys however are not fabricable by standard methods because of very poor ductility.

The addition of 40% rhodium to iridium was examined in References 4 and 22. Similar difficulties in fabrication were reported. The Ir-40 Rh alloy has a melting temperature of 2250 C (4081 F). Experimental data from Reference 4 indicates that the addition of 40% Rh reduces the air oxidation of iridium at 3000 F by a factor of ~4. This is in good agreement with the data of Dickson, Reference 22, who tested Ir-30 Rh in air at 3860 F. Dickson evaluated the oxidation resistance of a number of alloys and cermets which included Ir, Rh, Re, Os, Ta, and a number of oxides. In his experiments, candidate coating alloys were subjected to plasma-arc oxidation at 3860 F in a simulated air environment. The coatings were found to have the following order of increasing surface recession rates:

- o Ir-30 Rh
- o Ir-5 vol% ThO₂-5 vol% Ta₂O₅
- o Ir-10 vol% HfO₂
- o Ir-10 vol% SiO₂
- o Ir-10 vol% Al₂O₃
- o Ir-10 vol% ThO₂
- o Unalloyed iridium
- o Ir-15 Os
- o Ir-10 vol% MgO
- o Hf-25 Ta

Table IV provides the actual material loss rates. The above ranking indicates that the addition of ThO₂, Ta₂O₅, and HfO₂ can provide improvements in oxidation resistance compared with unalloyed iridium. The addition of ThO₂ and HfO₂ were noted to be beneficial. The further addition of Ta₂O₅, which has a melting temperature below the test temperature (see Table V), was found to be second only to the Ir-30 Rh alloy. SiO₂ and Al₂O₃ would ordinarily not be used

TABLE IV
Oxidation in Plasma-Arc Rig at 3860°F For 1 Hour

Composition	Oxygen Ingression Rate ⁽¹⁾ (mil/hr)*
Arc Melt	
Ir, No. 1	9.1
Ir, No. 2	6.1
Ir, No. 2	6.4 ⁽²⁾
Ir-30 wt% Rh, No. 1	1.3
Ir-30 wt% Rh, No. 2	4.1
Ir-30 wt% Rh, No. 2	4.4 ⁽²⁾
Ir-15 wt% Os	7.6
Hf-25Ta ⁽⁴⁾	390.0
Powder Metallurgy	
Ir	8.3
Ir-10 vol% HfO ₂	5.9
Ir-10 vol% MgO	7.8
Ir-10 vol% SiO ₂ ⁽³⁾	6.4
Ir-10 vol% ThO ₂	6.7
Ir-10 vol% Al ₂ O ₃	6.5
Ir-5 vol% ThO ₂ -5 vol% Ta ₂ O ₅	5.6
1. Average of three micrometer readings 2. Rerun of specimen immediately above referenced specimen 3. Oxide melts at temperature <3860 F 4. 8-minute test; specimen surface temperature >>3860 F because of temperature gradient through oxide layer	

*Should Read cm x 10⁻³ /hr

Dickson AFML TR 66-317
 Ref 22

TABLE V
Melting Temperature and Evaluation of High Temperature Ceramic Oxides

<u>Material Oxides</u>	<u>MP °C (°F)</u>	<u>Thermal Shock Resistance</u>	<u>Oxidation Resistance</u>	<u>Comments</u>
Ta ₂ O ₅	1872 (3401)	Bad	Good	Low Melting Temperature
MgO	2825 (5116)	Bad	Good	Easily Reduced
ZrO ₂	2715 (1918)	Bad	Good	(Decomposes in contact with (C, N, or H at 2200C;
HfO ₂	2844 (5150)	Bad	Good	(Stability Problem, also with HfO ₂
ThO ₂	3220 (5827)	Bad?	Good	Radioactive

because of their low melt temperature; however, in these tests, the results were favorable.

Brimhall (Reference 23) of the Battelle Pacific Northwest Laboratory investigated the behavior of pure iridium with and without an HfO_2 coating at 1500 C (2731 F). His conclusions, based on data in Figure 19, were that a dense, defect-free coating of HfO_2 inhibits the oxidation of iridium. However, localized oxidation of the iridium was found to accelerate at cracks in the coating. Dickson (Reference 22) had the same results when he tested a hafnia-coated iridium wire at 4035 F for 110 minutes. Both data sets indicate that a thin, continuous HfO_2 coating over the iridium was beneficial in reducing the oxidation rate of iridium.

Aerojet has tested an $\text{HfO}_2/\text{Ir}/\text{Re}$ chamber at 3500-4100 F for 1232 sec, Reference 24, using the material tester shown in Figure 1. Testing was terminated when small spots of the HfO_2 spalled. There was no visible effect of the spalling on the integrity of the underlying iridium and the chamber, in fireable condition, was returned to Ultramet.

Based on the data provided in Table IV, a coating of $\text{Ta}_2\text{O}_5 + \text{ThO}_2$ may be even more effective than pure HfO_2 , and using a combination of HfO_2 and Ta_2O_5 as a surface coating should also be considered to avoid the mild radioactivity of the ThO_2 .

6.0 Conclusions and Recommendations

Development of more advanced materials should proceed in accord with the following plan.

6.1 Gas-Side Compatibility Experiments

The most essential activity is to fully characterize and understand the oxidation/reduction limits of the baseline materials and their operating limits. The baseline materials are defined as those used in the rocket engine demonstration tests of Contract NAS 3-24643, Reference 4, i.e., unalloyed platinum, rhenium, and iridium.

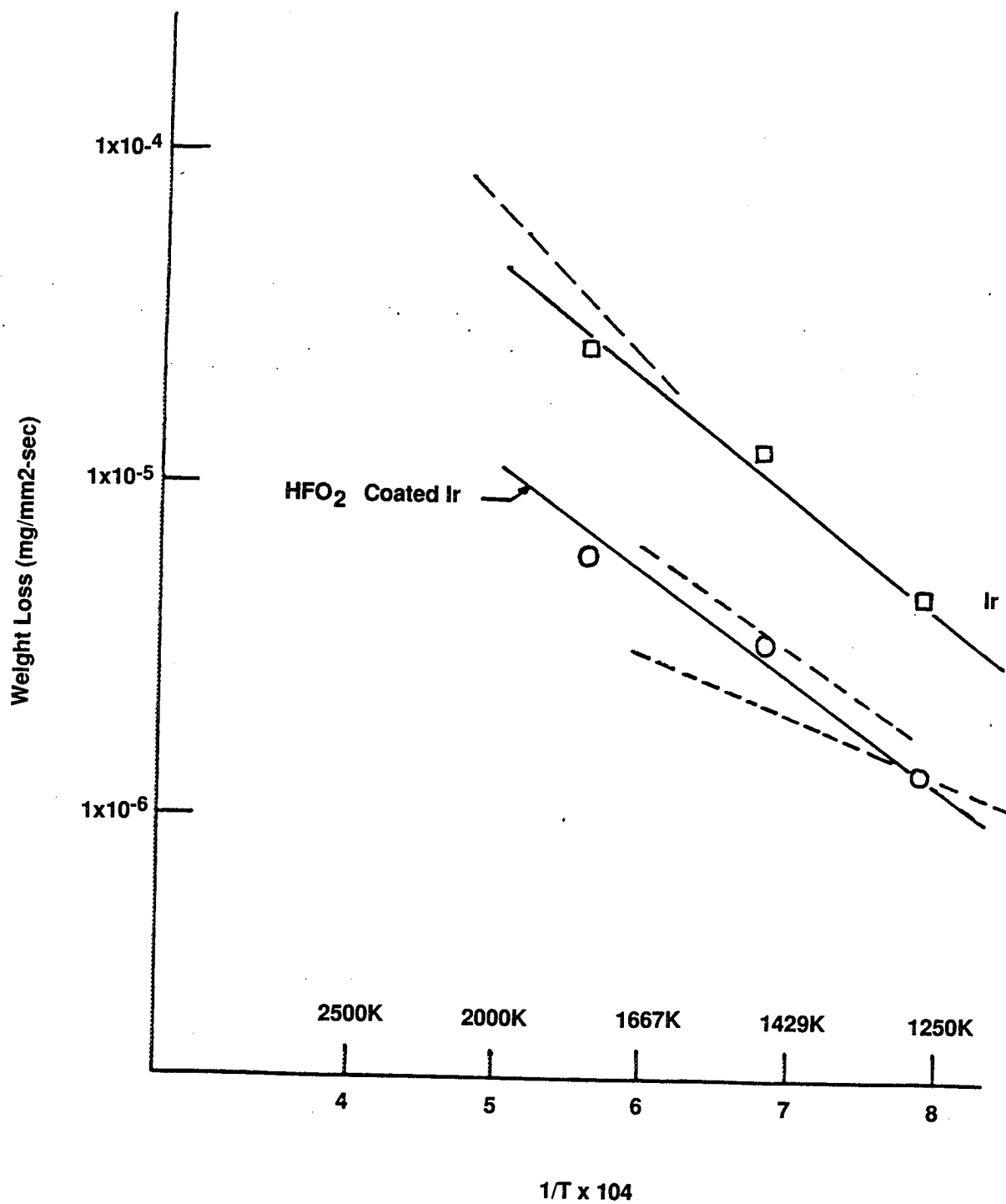


Figure 19. Recession Rate of Iridium as a Function of Temperature. Data of Ref. 22 is for a Gas Flow of $\sim 6 \times 10^4$ mm/sec (12000 ft/min)

This should be followed, in Phase II, by comparable tests using the higher strength-to-weight, grain-stabilized platinum + 10 rhodium alloy, a higher strength, grain-stabilized rhenium, and two types of coated iridium. The first is unstabilized HfO_2 applied as a very thin surface coating. The second is a thin, stabilized HfO_2 with a TBD stabilizer. These tests should be conducted in the diagnostic thruster over a wide range of propellant chemistries, fuel-rich to oxidizer-rich.

6.2 Substrate Weight Reduction

Dispersion-strengthened rhenium should be characterized for creep strength and grain growth at 4000 F. The material should be evaluated in both bar and wire form, bar for outside-in fabrication and wire for inside-out fabrication. The use of a wire-wound iridium-coated mandrel would allow the efficient fabrication of much larger thrust chambers. A typical fabrication sequence would be as follows:

- o Deposit the stabilized HfO_2 on the mandrel
- o Deposit the iridium over the HfO_2
- o Deposit a thin layer, 0.002-0.005 in., of rhenium
- o Wire wrap the structure to the thickness required for hoop loading
- o Vapor deposit or plasma spray a seal coat of rhenium
- o HIP the assembly
- o Remove the mandrel

When the higher-strength W-3.6 Re - 0.4 (Hf + C) wire becomes available, this material should be employed to further reduce the weight and cost of the basic design.

6.3 Diffusion Studies

Concurrent with the compatibility work discussed in Section 6.1, simple diffusion experiments should be conducted to determine if stabilizing media in the high-strength alloys has any influence on the mechanical properties affecting life of the iridium. The additives of interest are ThO_2 , HfO_2 , Hf, C, and HfC. These should be subject to 4000 F environment for

at least 10 hr and then examined to determine if they adversely impact the ductility of the iridium layer.

The best combination of materials should be selected and a representative thrust chamber built and hot-fire tested.

References

1. L. Schoenman, *Advanced Cooling Concepts*, ATS IR&D Report 7484-04, March 1985.
2. P. T. Lansaw, *Material Evaluation Hot-Fire Testing*, Aerojet IR&D, June 1988.
3. D. K. Berkman, et al., *Advanced Materials and Processes*, ATS IR&D Report 85-02, July 1986.
4. P. T. Lansaw, *High-Temperature, Oxidation-Resistant Thruster Research*, Final Report Contract NAS 3-24643, NASA-CR-185233, February, 1990.
5. J. B. Conway and P. N. Flagella, *Creep Rupture Data for the Refractory Metals to High Temperature*, Gordon & Breach, 1971.
6. W. D. Klopp and P. L. Raffo, NASA Tech. Note D-2503, Cleveland, Ohio (1964).
7. W. D. Klopp, W. R. Witzke, and P. L. Raffo, NASA Tech. Note D-3483, Cleveland, Ohio (1966).
8. L. S. Rubenstein, NASA Tech. Note D-4379, Cleveland, Ohio (1968).
9. P. L. Raffo, *J. Less-Common Metals*, 17, 133 (1969).
10. W. D. Klopp and W. R. Witzke, NASA Tech. Note D-5348, Cleveland, Ohio (1969).
11. W. D. Klopp, P. L. Raffo, and W. R. Witzke, *J. Metals* 6, 27 (1971).
12. J. R. Stephens and W. R. Witzke, *J. Less-Common Metals* 23, 325 (1971).
13. W. D. Klopp and W. R. Witzke, *J. Less-Common Metals* 24, 427 (1971).
14. W. R. Witzke, *Metall. Trans.* 5, 499 (1974).
15. W. D. Klopp, *Space Nuclear Power Systems*, Orbit Book Co. (1985), Eds. Ms. El Genk and M. D. Hoover, Ch. 42.
16. A. Luo, et al., *Tensile Properties of Tungsten-3.6% Rhenium-0.4% Hafnium Carbide Above 0.5 Tm*, *Metallurgica*, Vol. 23, 1989.
17. B. Titran, NASA LeRC, personal communication.
18. R. C. Svedberg and W. W. Bowen, *High-Temperature Creep and Tensile Properties of Chemically Vapor Deposited Rhenium*, Hanford Engineering Development Laboratory, SA2695FD, and Process Technology Conference, San Diego, CA, April 1982.
19. F. A. Barr and R. J. Page, *Slip Casting and Extruded Shapes of Rhenium with Metal Oxide Additives*, NASA CR 174970, April 1986.
20. F. A. Barr and R. J. Page, *Slip Casting and Extruding of Rhenium with Metal Oxide Additives*, NASA CR 180 851, November 1987.
21. W. D. Klopp personal communication.
22. D. T. Dickson, R. T. Wimber, and A. R. Stetson, *Very High Temperature Coatings for Tantalum Alloys*, AFML TR-66-317.
23. J. L. Brimhall, *Oxidation Behavior of HfO₂-Coated Iridium*, Battelle Pacific Northwest Laboratory Internal Report, February 1989.
24. L. Schoenman, *Rocket Engine Test Report, HfO₂-Lined Ir/Re Chamber*, Aerojet IR&D Report, 25 June 1986.

APPENDIX SUPPLEMENT

HIGH-TEMPERATURE PROPERTIES OF RHENIUM AND RHENIUM ALLOYS

Creep Behavior of Electron-Beam-Melted Rhenium

WALTER R. WITZKE AND PETER L. RAFFO

Creep deformation in electron-beam-melted polycrystalline rhenium sheet was evaluated at 2200° to 4200°F (1477° to 2588°K) and 4 to 40 ksi (28 to 276 MN per sq m). Comparisons were made with powder metallurgy rhenium under similar conditions. Changes in creep-rupture behavior resulting from electron beam melting of rhenium were greater ductility, higher primary creep rate, and longer rupture life, especially at lower temperatures. The activation energy for creep was 72 kcal per mole for electron-beam-melted rhenium and 64 kcal per mole for powder metallurgy rhenium.

THE potential usefulness of rhenium as an aerospace material can be expressed in terms of its refractory character, stiffness, and low temperature ductility. Rhenium has a hcp crystal structure and a melting point of 5750°F (3450°K), the second-highest of the metals. Its modulus of elasticity at room temperature approximates 67×10^6 psi (4.6×10^5 MN per sq m) and it has enough ductility to be fabricable at room temperature. Although it is costly and scarce, rhenium and its alloys can be expected to be used in specialized design applications.

The mechanical properties of unalloyed rhenium have not been investigated in as much detail as those of the other refractory metals, W, Mo, Cb(Nb), and Ta. Literature reviews of rhenium up to 1960^{1,2} indicate a small amount of data on the tensile and stress-rupture properties of powder metallurgy wire as the only information available on the high temperature properties of rhenium. Since that time, additional mechanical property data including creep and stress rupture data on powder metallurgy sheet at high temperatures have been reported.³⁻⁵

Because electron beam melting has shown improved properties in other metals due to purification, this vacuum melting process could possibly render improvements in rhenium also. In general, electron-beam melted materials have been described as having superior ductility to arc-cast or sintered stock.⁶

The objective of the present study was to characterize the high temperature creep deformation of polycrystalline rhenium sheet rolled from an electron-beam-melted (EB) ingot. Creep rupture, step-load, and step-temperature creep tests were performed in the temperature range 2200° to 4200°F (1477° to 2588°K, 0.43 to 0.75 T_m) at stresses ranging from 4 to 40 ksi (28 to 276 MN per sq m). These data are compared with similar test data on commercial powder metallurgy (PM) rhenium sheet and with previous data.

EXPERIMENTAL PROCEDURE

Materials

Commercial rhenium powder having a minus-200 mesh particle size was used in preparing the EB rhenium. The supplier's analysis of the powder is given

WALTER R. WITZKE is Research Metallurgist, Lewis Research Center, NASA, Cleveland, Ohio. PETER L. RAFFO, deceased, was Assistant Professor, Illinois Institute of Technology, Chicago, Ill, and was formerly associated with Lewis Research Center, NASA.

Manuscript submitted February 22, 1971.

in Table I. PM rhenium sheet 0.040-in. (0.10-cm) thick was obtained commercially and used for comparison testing. A small amount of the PM rhenium sheet was rolled to a thickness of 0.020 in. (0.050 cm).

Melting

In preparation for electron beam melting, 9 lb (4.1 kg) of rhenium powder were hydrostatically pressed at 30 ksi (208 MN per sq m) into a 1.25-in. (3.2-cm) diam bar and sintered in dry hydrogen at 4000°F (2477°K) for 3 hr. Melting was performed in a commercial 150 kw electron beam furnace previously described in Ref. 7. The rhenium metal was double melted into a 2-in. (5-cm) diam mold at a power level of 80 to 100 kw with the chamber pressure maintained at 5×10^{-5} torr. The average Vickers hardness (10 kg load) across the diameter of the double-melted ingot near its top was 225 Dph. Taken in several

Table I. Rhenium Analyses

Impurity Element*	Impurity Content, ppm		
	Commercial Powder (Supplier Analysis)	Commercial Powder Metallurgy Sheet	Electron-Beam-Melted Sheet
Ag	ND		
Al	<1	3.0	5.0
Ca	<1		
Co		0.2	<0.2
Cr	<1	6.0	3.0
Cu	<1		
Fe	8	30.0	15.0
Mg	<1		
Mn	ND	0.5	<3.0
Mo	<1	0.2	<0.2
Na	<1		
Nb		0.6	<0.2
Ni	<1	2.0	0.7
Si	<1		
Sn	ND		
Ta		2.0	1.0
Ti	ND	0.3	0.2
V	ND		
W	ND	5.0	<0.2
Zr	ND	1.6	0.5
C	59	8	11
N	40	5	4
O	2700	6	8
H	42		

*Elements other than interstitials determined by emission spectrograph.

*ND = not detected.

grains of varying crystallographic orientations, 18 hardness indentations ranged in value from 181 to 270 Dph. This large spread reflects the extreme hardness anisotropy typical of hcp metals.

Fabrication

The fabrication of the EB rhenium ingot was accomplished by first extruding at 3800°F (2366°K) and then by rolling at room temperature with intermediate recrystallization anneals. The extrusion step is unique in rhenium fabrication. Rhenium is seldom worked above room temperature because of embrittlement due to hot shortness problems. The hot shortness is thought to be due to the melting of a Re_2O_7 oxide normally situated at the grain boundaries.⁸ Hot shortness was avoided in the present work by extruding the rhenium in an evacuated and sealed container. Rhenium is also characterized by rapid work hardening. The high extrusion temperature was chosen so that the deformation would occur above the work-hardening temperature range.

Preparations for extrusion involved grinding of the ingot surface, sealing the billet in 0.01-in. (0.025-cm) thick tantalum sheet using TIG and EB welding, and canning in powder metallurgy Mo-25 wt pct W alloy. The purpose of the claddings was to prevent the formation of low-melting Re_2O_7 and to facilitate the extrusion.

The clad rhenium was successfully extruded at 3800°F (2366°K) and a reduction ratio of 8:1. The extrusion speed was about 5 ips (13 cm per sec) with a breakthrough pressure of 118 ksi (814 MN per sq m). Thus, with suitable precautions to avoid hot short and work-hardening characteristics, the extrusion of rhenium at high temperatures has been shown to be feasible. (This general extrusion procedure was suggested by Dr. Fred J. Rollfinke of Cleveland Refractory Metals, Solon, Ohio.)

The resultant flat bar was ground to remove the cladding. The extruded rhenium was fully recrystallized with an average grain diameter of 66 μm . The average Vickers hardness (10 kg load) was 176 Dph.

Room temperature rolling was required to bring the rhenium to a final 0.020-in. (0.050-cm) thickness. Reductions of 8 to 10 pct were made per rolling pass. Due to the rapid work-hardening rate of rhenium, after each 15 to 20 pct total reduction the sheet was recrystallized by annealing in hydrogen for 5 min at 3000°F (1922°K). The final as-rolled sheet was approximately 60 pct recrystallized with an average Vickers hardness (200 g load) of 536 Dph.

TESTING

Creep test specimens were cut from EB and PM rhenium sheet materials by electrospark machining. The specimens were 3.25-in. (8.25-cm) long by 0.63-in. (1.60-cm) wide with a 1.0-in. (2.54-cm) long by 0.25-in. (0.64-cm) wide test section. Prior to testing all specimens were annealed in a hydrogen atmosphere for 1 hr at 3000°F (1922°K). Both materials were fully recrystallized by the treatment, see Fig. 1, and had average grain diameters of 37 μm for the EB rhenium sheet and 47 μm for the PM rhenium sheet.

Creep testing was performed in vacuum [10^{-5} to 10^{-7} torr (10^{-3} to 10^{-5} N per sq m)] under constant load.

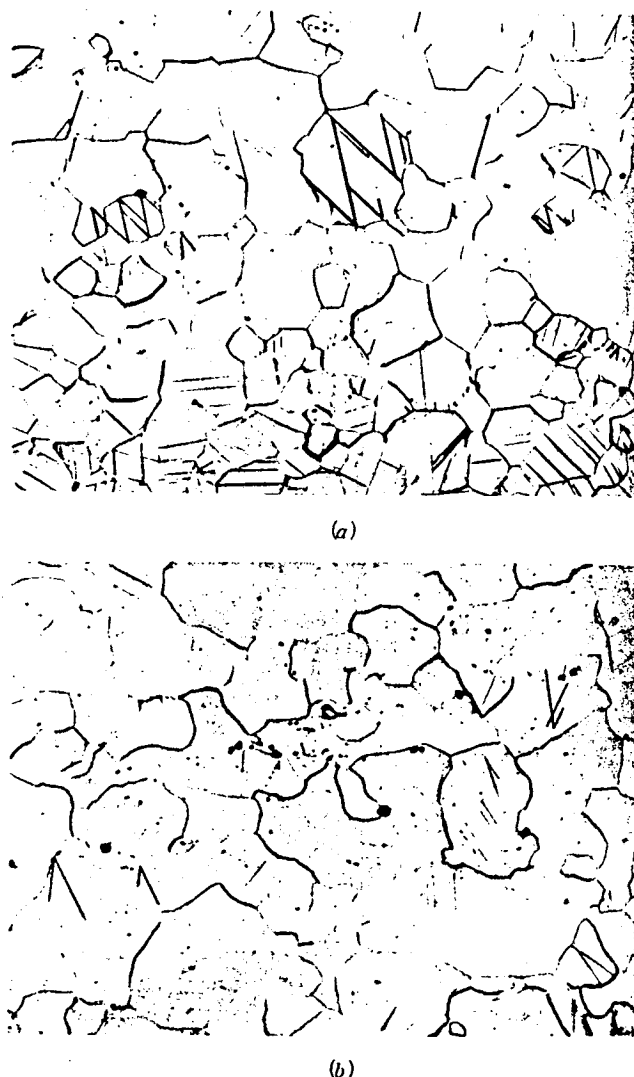


Fig. 1—Microstructure of rhenium sheet annealed 1 hr at 3000°F (1922°K) in hydrogen. Magnification 210 times. (a) Electron-beam-melted (EB) rhenium. (b) Powder-metalurgy (PM) rhenium.

Deformation was recorded during the creep tests from load train displacement measurements. Strains were determined on the basis of this measurement and the assumption that all of the creep occurred in the gage length. The minimum creep rates were determined graphically.

The majority of the creep tests consisted of applying a constant load and permitting the material to elongate to rupture. Other tests that were conducted for determining secondary creep rates under varying conditions consisted of changing the load (steploading) or temperature (step temperature) periodically. Step changes were made as the creep rate approached a minimum.

Chemical Analysis

The EB and PM rhenium sheet materials were analyzed to determine impurity contents. A comparison of the emission spectrographic analysis given in Table I suggests only small differences in impurity levels between the EB and PM sheet. Both materials were of very high purity, namely >99.99 pct Re. The content level of most of the metallic and interstitial impurities

are unfortunately at or near the present quantitative limits of detection. The values of analyzed impurity content, therefore, may not present a true picture of the differences between the EB and PM rhenium materials. Indirect evidence of the higher purity of the EB-melted rhenium is presented later under results and discussion.

Metallography

Standard optical microscopy techniques were used in examining the rhenium specimens. The microstructure of the mechanically polished sections were best revealed by etching with Murakami's etchant and through use of polarized light. Grain diameter measurements were made by the line intercept method.

RESULTS

Grain Growth Observations

Indirect evidence of the higher purity of EB-melted rhenium compared to the PM rhenium material was afforded both by the results of annealing studies and observations of the grain size of specimens after creep testing. As shown in Fig. 2, the powder metallurgy rhenium sheet was remarkably resistant to grain growth during annealing. Specimens recrystallized at 3000°F (1922°K) showed essentially no grain growth in 1 hr anneals at temperatures as high as 4000°F (2477°K). On the other hand, the EB rhenium exhibited grain growth beginning at approximately 3200°F (2033°K). We believe this difference in grain growth behavior reflects the higher purity of the EB rhenium, since small quantities of impurities can have a pronounced effect on the grain boundary migration rate.⁹

This difference in grain growth behavior may account for some of the observed differences in creep behavior of the two types of rhenium at temperatures

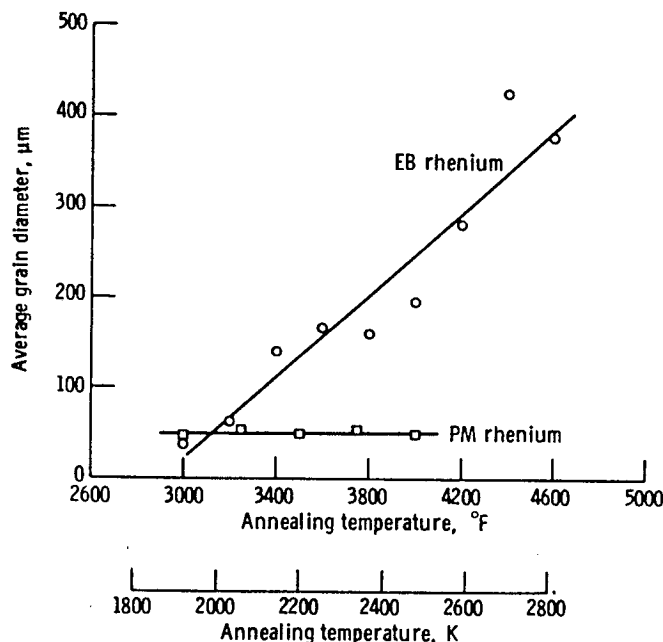


Fig. 2—Effect of 1-hr annealing temperature on grain size in electron-beam-melted (EB) and powder-metallurgy (PM) rhenium sheet.

above 3000°F (1922°K), as will be indicated later. Observations made on the unstrained portions of the test specimens indicated that the grain size of the EB rhenium increased during tests at 3000°F (1922°K) and above while that of the PM rhenium remained constant.

Creep-Rupture Life and Ductility

The results of the creep tests conducted on the EB and PM rhenium sheet are illustrated in Figs. 3 to 8. Creep curves for both types of rhenium at 2200°F (1477°K), 3000°F (1922°K), and 4000°F (2477°K) are compared in Fig. 3. The most striking differences in behavior were the much greater rupture ductility and longer rupture life of the EB rhenium at 2200°F (1477°K), Fig. 3(a), and 3000°F (1922°K), Fig. 3(b). For example, at 2200°F (1477°K) at a stress of 20 ksi (138 MN per sq m), the elongation at rupture for the EB rhenium was 22 pct while that of the PM rhenium was only 4 pct. The higher ductility of the EB rhenium appears to be responsible for its much longer rupture life, 721 hr as compared to 32.2 hr for the PM rhenium under the test conditions noted above. These large differences are not attributable to differences in grain size of the two materials, for the grain sizes were very comparable and stable during these lower temperature tests.

At 4000°F (2477°K), Fig. 3(c), where differences in grain growth behavior might be expected to influence the test results, the differences in rupture life and ductility were much smaller than at the lower temperatures. Under the test conditions illustrated in Fig. 3(c), there appeared to be a significant effect of specimen thickness on the rupture life and ductility of the PM rhenium sheet. The 1.0-mm thick sheet appeared to be significantly less ductile and exhibited a shorter rupture life than the 0.5-mm sheet. Unfortunately this variable was not explored in EB rhenium sheet or at test temperatures of 3000°F (1922°K) or lower, so the extent to which a size effect may influence the results at lower temperatures is unknown.

Secondary Creep Behavior

The temperature dependence of the secondary (minimum) creep rate $\dot{\epsilon}_s$ is shown for EB and PM rhenium in Fig. 4 for stress σ levels ranging from 4 to 40 ksi (28 to 276 MN per sq m). The activation energy for creep Q_c for EB rhenium was determined from this plot to have an average value of 72 kcal per mole and was relatively independent of stress. The Q_c for the PM rhenium was previously reported by the authors as 64 kcal per mole.⁵ Vandervoort and Barmore have determined Q_c for PM rhenium as 60 kcal per mole.⁴

A least squares treatment of the data indicated a stress exponent of 3.7 for EB rhenium and 3.5 for PM rhenium. These relatively low exponent values are in agreement with the work of Vandervoort and Barmore⁴ who observed a value of 3.4 for PM rhenium. However, a log-log plot of $\dot{\epsilon}_s$ vs σ at constant temperature for the EB rhenium data suggested a possible increase in n to 4.3 above 3400°F (2144°K). Insufficient information was available to determine the validity or possible causes of a higher stress exponent.

Fig. 5 shows the stress dependence of the temperature compensated creep rate, $\dot{\epsilon}_s \exp(Q_c/RT)$ where

Q_c for the composite data is 69,000 cal per mole. EB rhenium is 3.6 for almost the entire stress range, whereas for PM rhenium the stress dependence ranges from 2.2 at low stresses to 4.8 above 10 ksi (69 MN per sq m). In the high temperature creep of most pure metals n is observed between 4 and 6.¹⁰

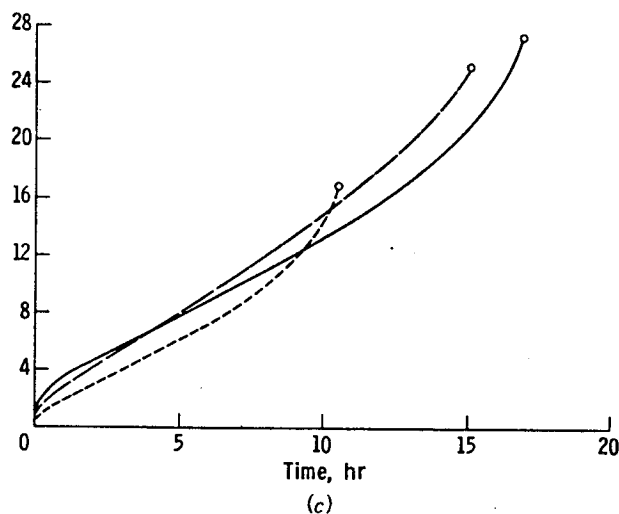
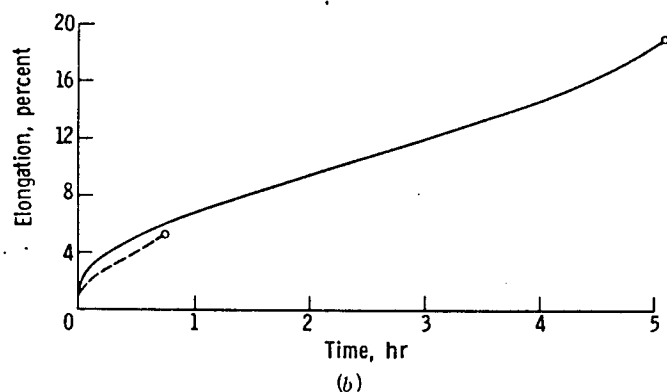
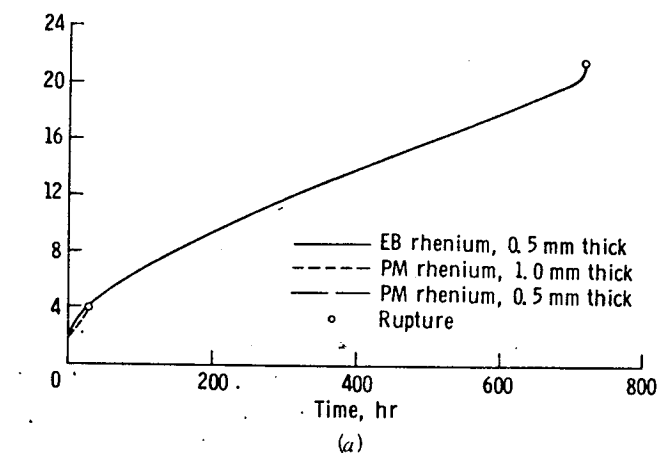


Fig. 3—Creep curves for electron-beam-melted (EB) and powder-metallurgy (PM) rhenium under various temperature and stress conditions. (a) Test temperature, 2200°F (1477°K); load stress, 20 ksi (138 MN per sq m). (b) Test temperature, 3000°F (1922°K); load stress, 15 ksi (103 MN per sq m). (c) Test temperature, 4000°F (2477°K); load stress, 4 ksi (28 MN per sq m).

Primary Creep Behavior

Primary creep rates were determined according to the Andrade $t^{1/3}$ law using the expression

$$\epsilon = \beta t^{1/3} + \dot{\epsilon}_s t$$

where the measured strain ϵ at time t consists of strain components related to the primary creep rate β and the secondary creep rate $\dot{\epsilon}_s$.

The temperature dependencies of the primary creep rates for EB and PM rhenium are shown in Fig. 6. Activation energies determined from these plots averaged 87 kcal per mole for EB rhenium and 78 kcal per mole for PM rhenium. These values are about 20 pct higher than the activation energies determined for secondary creep. Previous studies have indicated that the activation energy remains relatively constant during primary and secondary creep provided no change in deformation mode occurs.¹⁰

The relation between the primary and secondary creep of rhenium was examined. This is shown in Fig. 7 where β is plotted against $\dot{\epsilon}_s$ for the EB and PM rhenium creep-rupture tests. The data for the two materials do not coincide but the slopes of the least squares determinations were nearly identical and indicated the relation

$$\beta = k(\dot{\epsilon}_s)^{0.4}$$

The magnitudes of the primary creep rates for EB rhenium were greater than for PM rhenium by a factor slightly less than 3.

Rupture Life Behavior

The effect of creep stress on rupture life at constant temperature is shown by means of a log-log plot in Fig. 8 for three temperature levels. The slopes of the stress-rupture life data for the various temperatures for each sheet material have been drawn parallel to each other. At 4000°F (2477°K) the effect of stress for both EB and PM rhenium sheet materials can be described by a single line. However, as the test temperature was decreased, a difference in stress-rupture life behavior of the two materials became more apparent. Although EB rhenium had approximately the same life as PM rhenium at 4000°F (2477°K), at 3000°F (1922°K) EB rhenium had about three times the life of PM rhenium, while at 2200°F (1477°K) EB rhenium lasted over 20 times longer than PM rhenium. The stress for a 100-hr rupture life at 2200°F (1477°K) was 30 ksi (207 MN per sq m) for EB rhenium, almost twice that for PM rhenium.

Rupture data from Ref. 3 for PM rhenium (Lot 1) at 2912° and 3969°F (1873° and 2473°K) are also shown in Fig. 8 for comparison. A difference in stress dependency can be noted. The rhenium materials from this study had a stress dependency coefficient of -4.8 compared to -3.7 for the data from Ref. 3.

DISCUSSION

Considerable differences have been observed in the properties of electron-beam-melted (EB) rhenium sheet compared to powder metallurgy (PM) sheet. Relative to PM rhenium the results of this study have shown that EB rhenium had a) greater ductility,

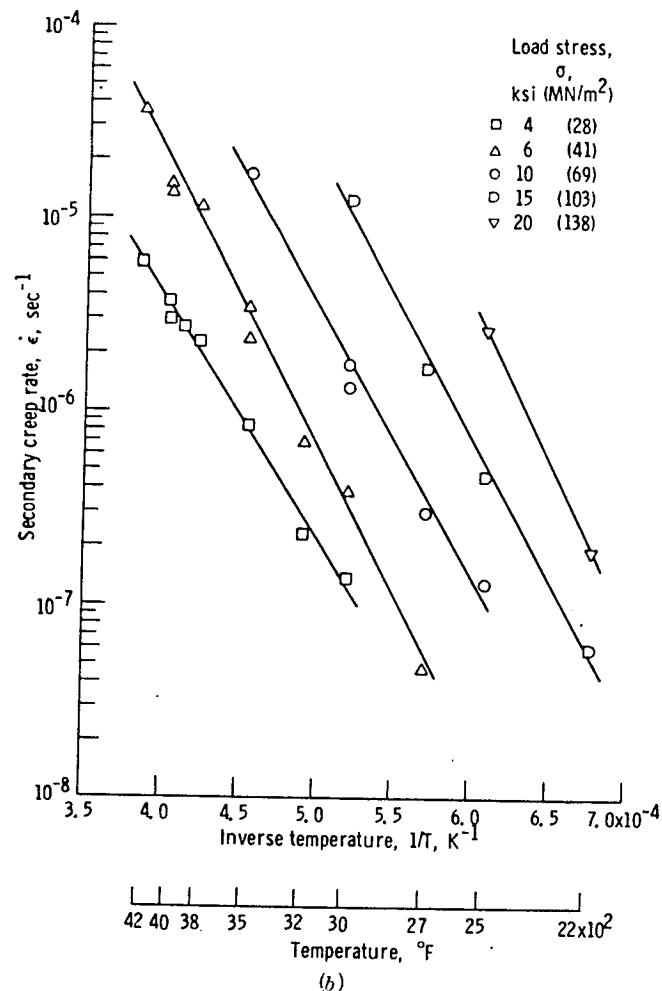
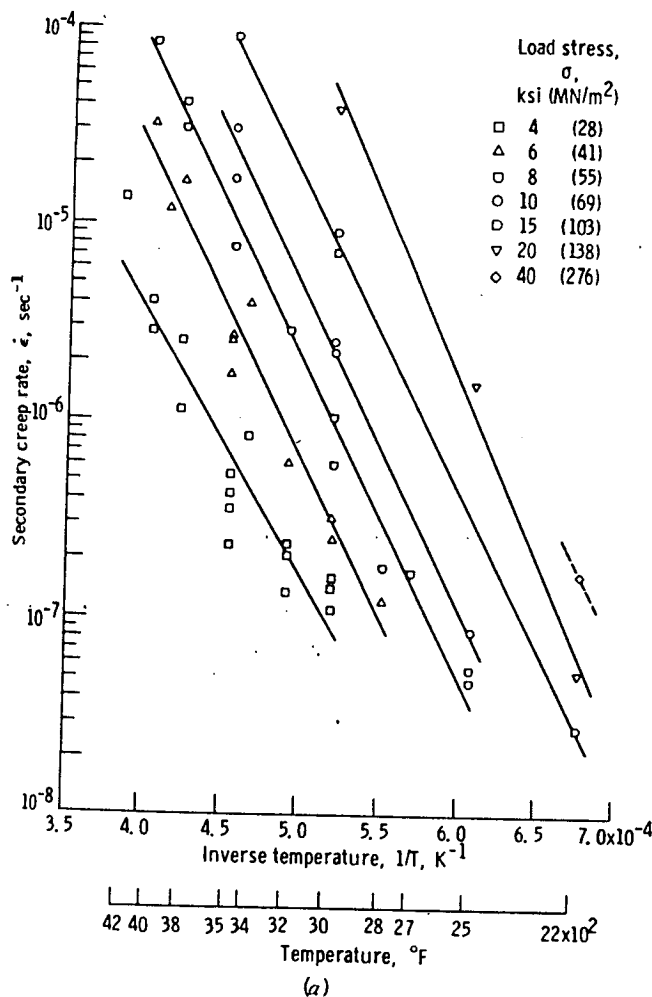


Fig. 4—Temperature dependence of secondary creep rate in rhodium for constant load stresses of 4 to 40 ksi (28 to 276 MN per sq m). (a) Electron-beam-melted rhodium sheet. (b) Powder-metallurgy rhodium sheet.

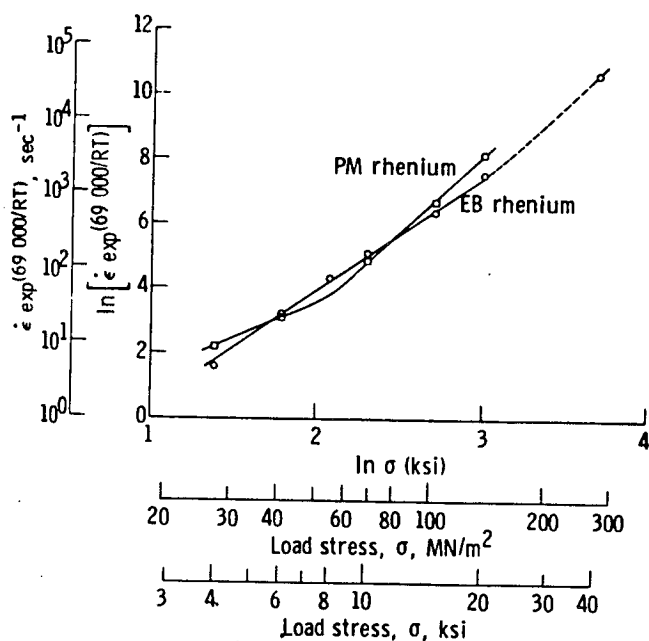


Fig. 5—Stress dependency of temperature-compensated secondary creep rate for recrystallized electron-beam-melted (EB) and powder-metallurgy (PM) rhodium.

b) longer rupture life, c) higher primary creep rates, d) similar secondary creep rates, and e) grain growth initiating at a much lower temperature.

With the essential difference in processing being the additional steps of melting and extruding one can assume that the changes listed above are mainly due to melting. An accepted consequence of melting refractory metals under good vacuum conditions is the generally increased purity of the product. That this might occur in the electron beam melting of already high purity rhodium powder compacts was not known. However, as shown in Fig. 1, the melting was beneficial in preparing a material with relatively few voids. Also indirect evidence suggesting increased purity was noted in the grain growth characteristics of the two materials. The lowering of impurities and voids can reasonably account for the greater ductility (as measured by total elongation) and longer rupture life of EB rhodium.

Void formation during creep testing was observed in both EB and PM rhodium, as shown in Fig. 9. Voids at the grain boundaries were larger in the PM rhodium at 2 pct elongation where rupture occurred than in the EB rhodium at 9 pct elongation where the test was interrupted.

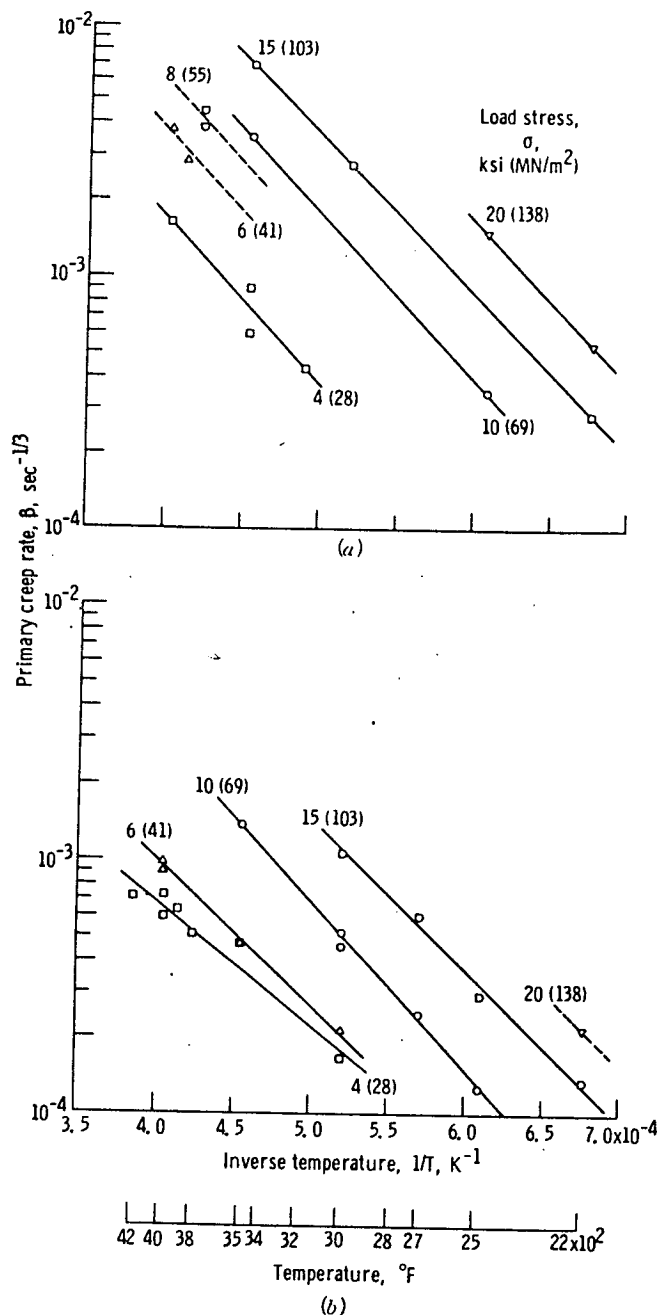


Fig. 6—Temperature dependency of primary creep rates of rhenium sheet at stresses of 4 to 20 ksi (38 to 138 MN per sq m). (a) Electron-beam-melted rhenium. (b) Powder-metallurgy rhenium.

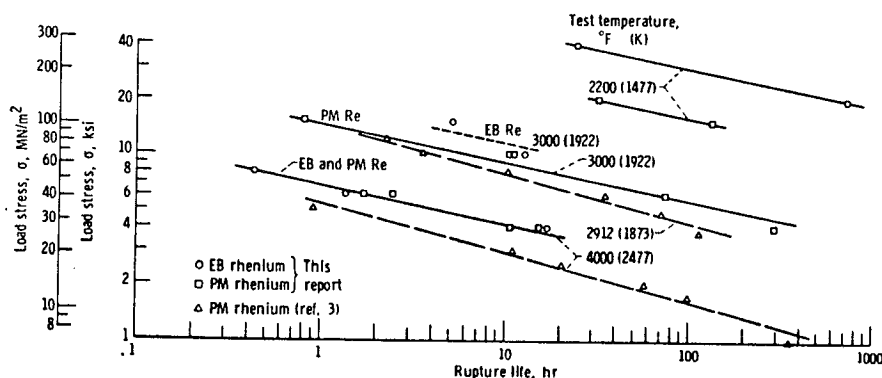


Fig. 8—Effect of creep stress on rupture life at constant temperature for electron-beam-melted (EB) and powder-metallurgy (PM) rhenium sheet at three temperature levels.

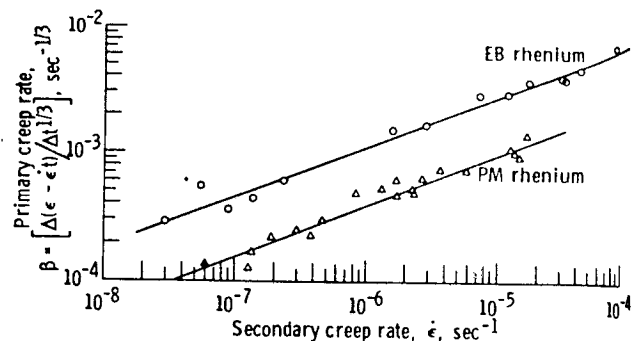


Fig. 7—Relation of primary and secondary creep rates of electron-beam-melted (EB) and powder-metallurgy (PM) rhenium at 2400° to 4200°F (1477° to 2588 K). $\beta = k(\dot{\epsilon})^{0.40}$.

Tertiary creep has been associated with the development of voids at the grain boundaries.¹¹ Resnick and Seigle¹² have shown that the removal of impurities which catalyze void formation during diffusion also decreases the tendency for grain boundary void formation during creep and thereby significantly improves the stress-rupture life of the material. The existence of voids in the grain boundaries before creep testing probably account for the lower strain values observed in PM rhenium prior to tertiary creep compared to EB rhenium and thereby served to reduce rupture life.

Under the same test conditions the secondary creep rates of the two rhenium materials were similar, but, as observed in Fig. 6, the primary creep rates of the EB rhenium were higher than those for PM rhenium. For a given secondary creep rate, the primary creep rate for EB rhenium was shown in Fig. 7 to be greater by a factor of three. This is consistent with the greater ease of dislocation movement that would be expected with increased purity.

The activation energy for creep in pure metals above half the absolute melting temperature has been shown in a large number of investigations to be nearly equal to the activation energy for self diffusion.¹³ Experimentally determined values of the activation energy for self diffusion in rhenium are not available, but estimates based on the melting point suggest values ranging from 117 to 131 kcal per mole. The apparent activation energies for creep determined in this investigation, however, are approximately half the estimated values for self diffusion, indicating the creep behavior of rhenium in this temperature range (0.43 to 0.75 T_m) is not controlled by dislocation climb. As would be expected, the activation energies resulting from this in-



Fig. 9—Voids in microstructure following creep at 2500°F (1644°K) and 20 ksi (138 MN per sq m). Magnification 420 times. (a) Electron-beam-melted (EB) rhenium after 9 pct total elongation (broke in grip). (b) Powder-metallurgy (PM) rhenium after 2 pct total elongation rupture.

vestigation are somewhat higher than those experimentally evaluated for surface diffusion of rhenium¹⁴ ranging from 48.4 to 53.0 kcal per mole depending on crystal orientation.

Vandervoort and Barmore⁴ observed that creep deformation in rhenium took place by dislocation motion within the grain and that no subgrain formation occurred. This ruled out grain boundary and subbound-

ary diffusion. In accord with Vandervoort and Barmore's conclusions and with those previously proposed by the authors⁵ the rate-controlling process in the high temperature creep of rhenium is associated with dislocation pipe diffusion.

SUMMARY OF RESULTS

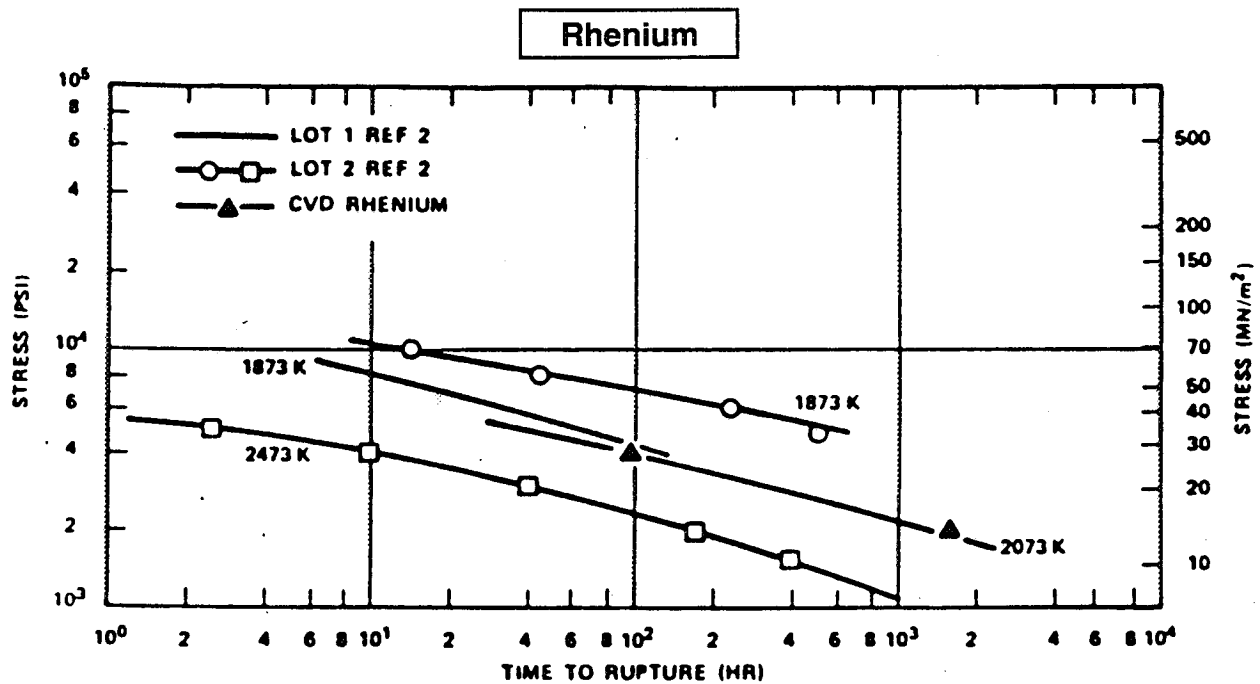
The creep properties of rhenium sheet prepared from electron-beam melted and extruded material were compared with sheet prepared by commercial powder metallurgy methods. The results of this study in the temperature range of 0.43 to $0.75T_m$ were as follows:

1) EB rhenium, compared to PM rhenium, had greater ductility (total elongation), longer rupture life, and higher primary creep rates. For example, at 2200°F (1477°K) EB rhenium had 5.5 times the total elongation and 20 times the rupture life exhibited by PM rhenium. These differences decreased as temperature increased. Secondary creep rates were comparable. We believe that the improved creep and rupture properties of EB rhenium can be attributed to the reduction in impurities and voids by vacuum melting.

2) Activation energies for creep between 2200° and 4200°F (1477° and 2588°K) ranged from 72 kcal per mole for EB rhenium to 64 kcal per mole for PM rhenium. The rate-controlling process in this temperature range is associated by the authors with dislocation pipe diffusion.

REFERENCES

1. C. T. Sims, E. N. Wyler, G. B. Gaines, and D. M. Rosenbaum: Battelle Memorial Inst., WADC-TR-56 319, June, 1956.
2. *Rhenium*: B. W. Gonser, ed., Elsevier Publishing Co., 1962.
3. J. B. Conway and P. N. Flagella: General Electric Co., GEMP-G85, March, 1969.
4. R. R. Vandervoort and W. L. Barmore: *Trans. TMS-AIME*, 1969, vol. 245, p. 825.
5. P. L. Raffo and W. R. Witzke: *Trans. TMS-AIME*, 1969, vol. 245, p. 889.
6. *Introduction to Electron Beam Technology*: R. Bakish, ed., John Wiley & Sons, Inc., 1962.
7. W. R. Witzke, E. C. Sutherland, and G. K. Watson: *NASA TN D-1707*, 1963.
8. G. Lebert: in *Rhenium*, B. W. Gonser, ed., p. 126, Elsevier Publishing Co., 1962.
9. P. Gordon: in *Energetics in Metallurgical Phenomena*, vol. I, W. M. Mueller, ed., p. 205, Gordon and Breach Science Publishers, 1965.
10. F. Garofalo: *Fundamentals of Creep and Creep-Rupture in Metals*, The Macmillan Co., New York, 1965.
11. P. W. Davies and R. W. Evans: *Acta Met.*, 1965, vol. 13, p. 353.
12. R. Resnick and L. Seigle: *J. Metals*, 1957, vol. 9, p. 87.
13. J. E. Dorn: in *Seminar on Creep and Recovery*, p. 225, ASM, 1957.
14. P. C. Bettler and G. Barnes: *Surface Sci.*, 1968, vol. 10, p. 165.



Typical Properties for Ultramet CVD Rhenium (Ref 18)

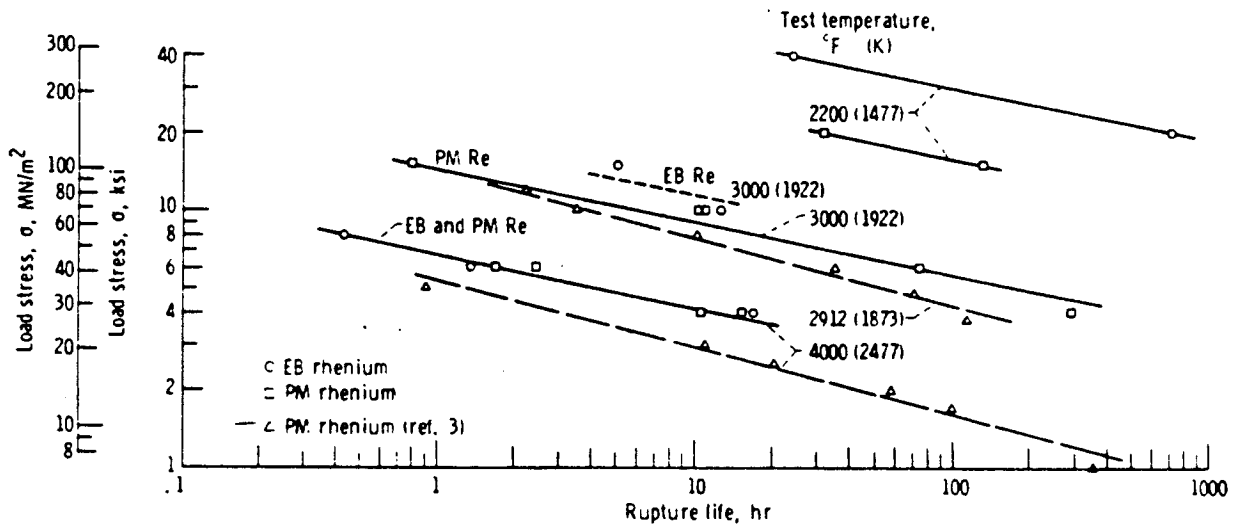
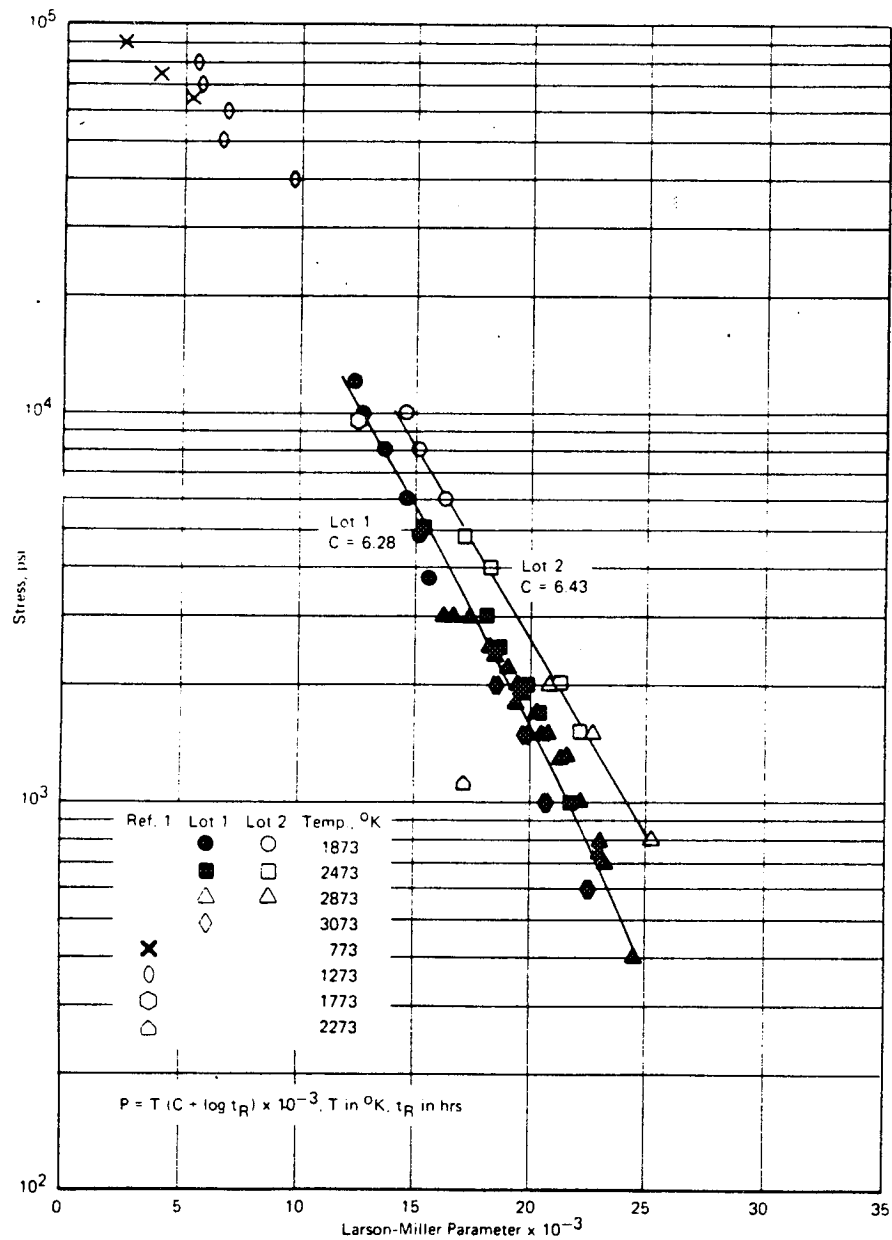


Figure 21. Typical Properties for Electron Beam EB Melted and Powder Metallurgy PM Rhenium (Wityke and Roffo, *Met. Trans.*, 9/71)

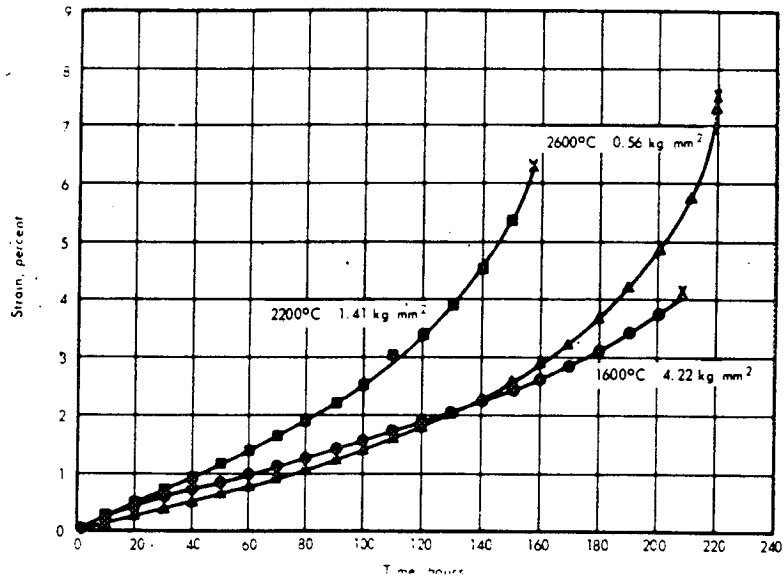
Rhenium



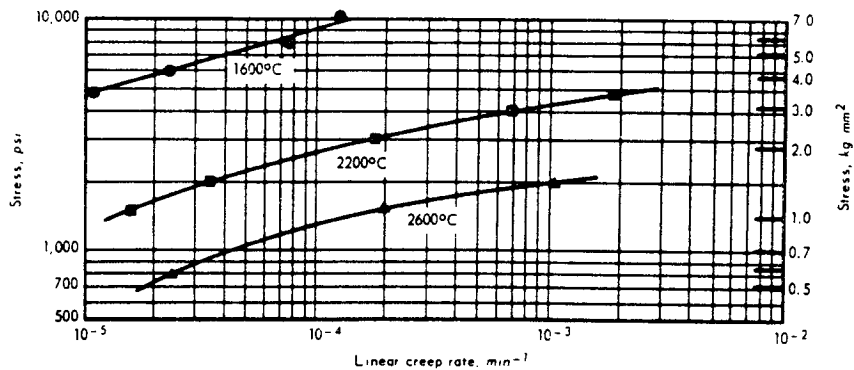
Source Conway and Flagella (Ref 5)

Larson-Miller Parameter Plot of Rupture Data for Rhenium

Rhenium

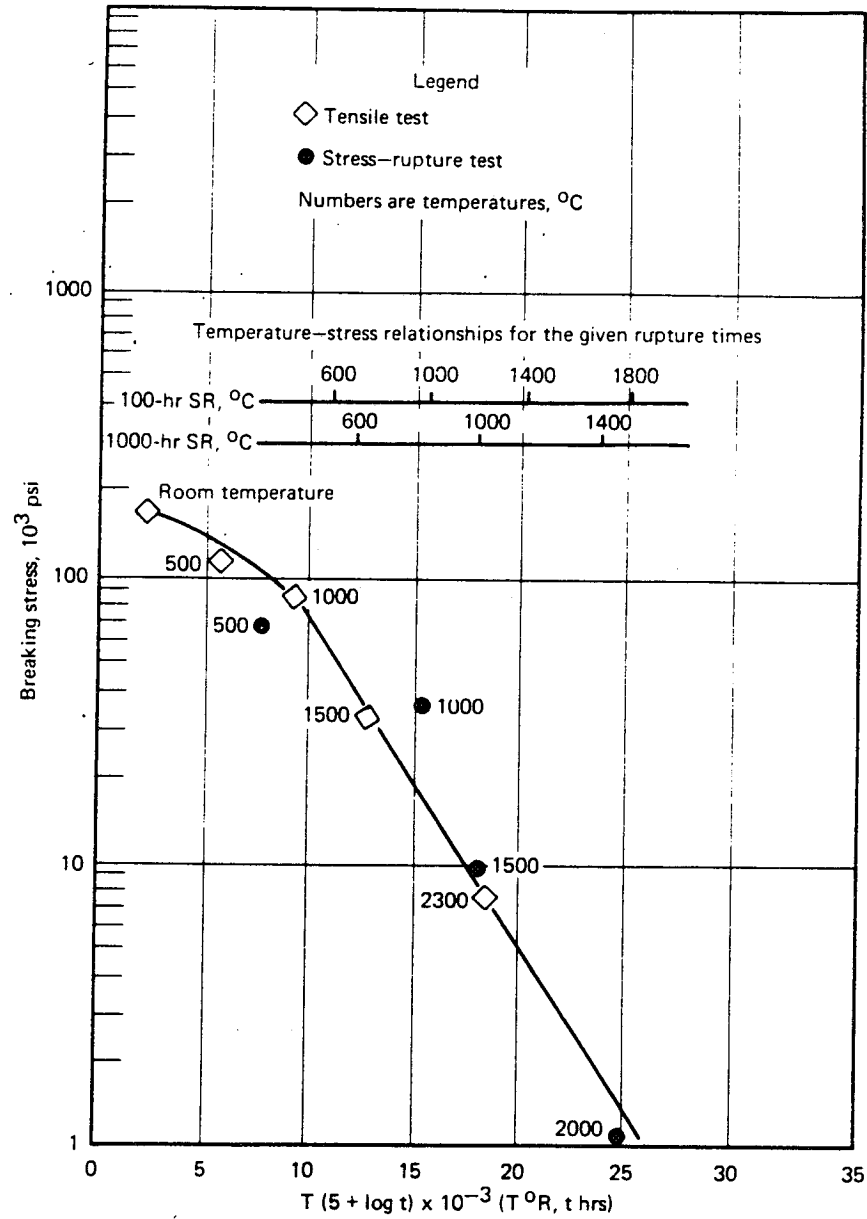


Typical Creep Curves for Powder Metallurgy Rhenium Tested in Hydrogen



Stress Versus Linear Creep Rate Data for Powder Metallurgy Rhenium Tested in Hydrogen

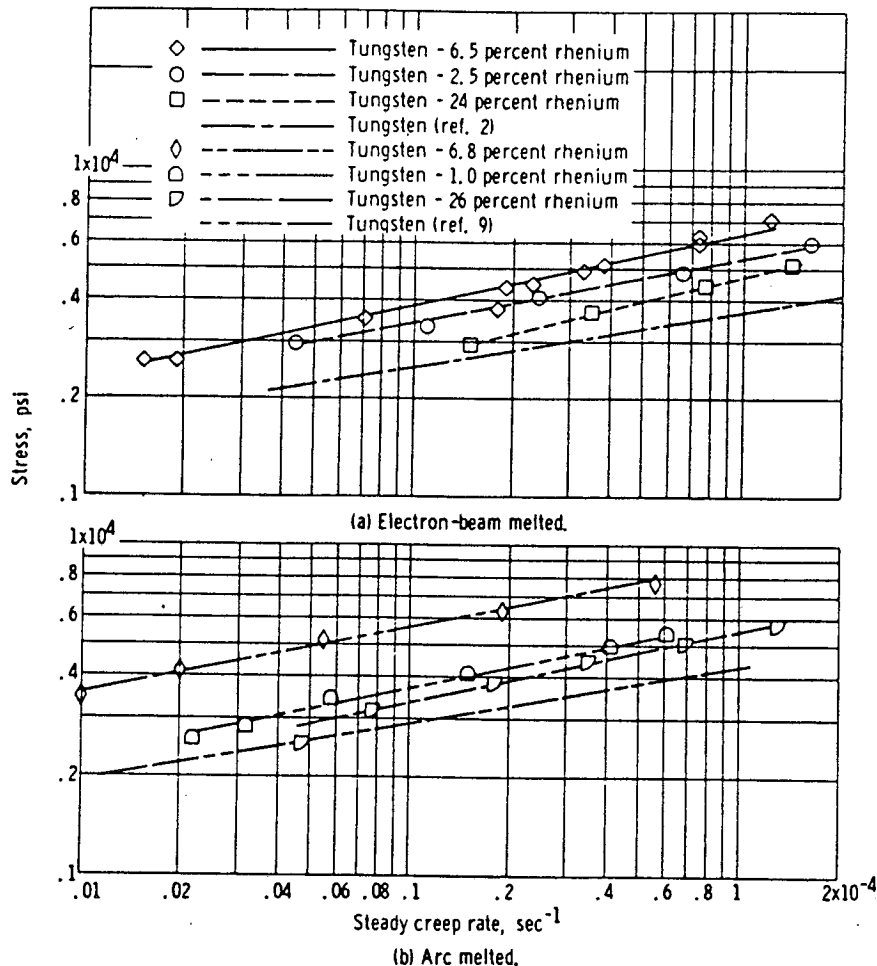
Rhenium



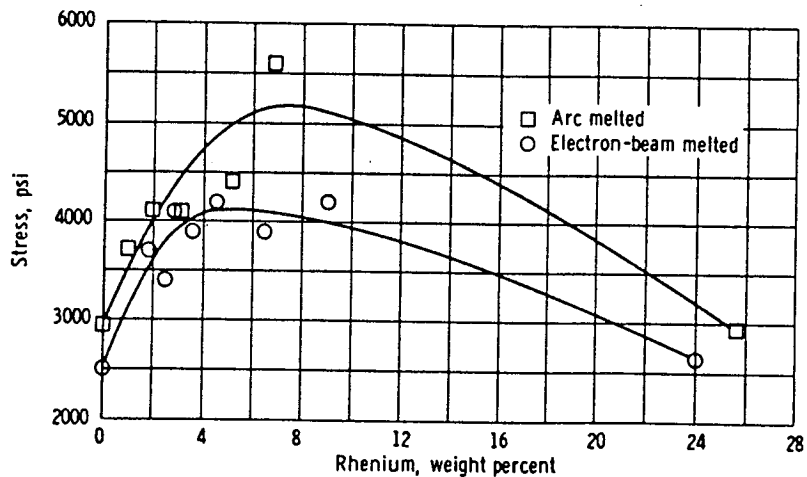
Larson-Miller Parameters Plot for Sintered Rhenium Wire Data (Ref 5)

Rhenium Alloys

W-Re



Representative Creep Rate Data for Electron Beam- and Arc-Melted Tungsten and Tungsten-Rhenium Alloys at 3500°F

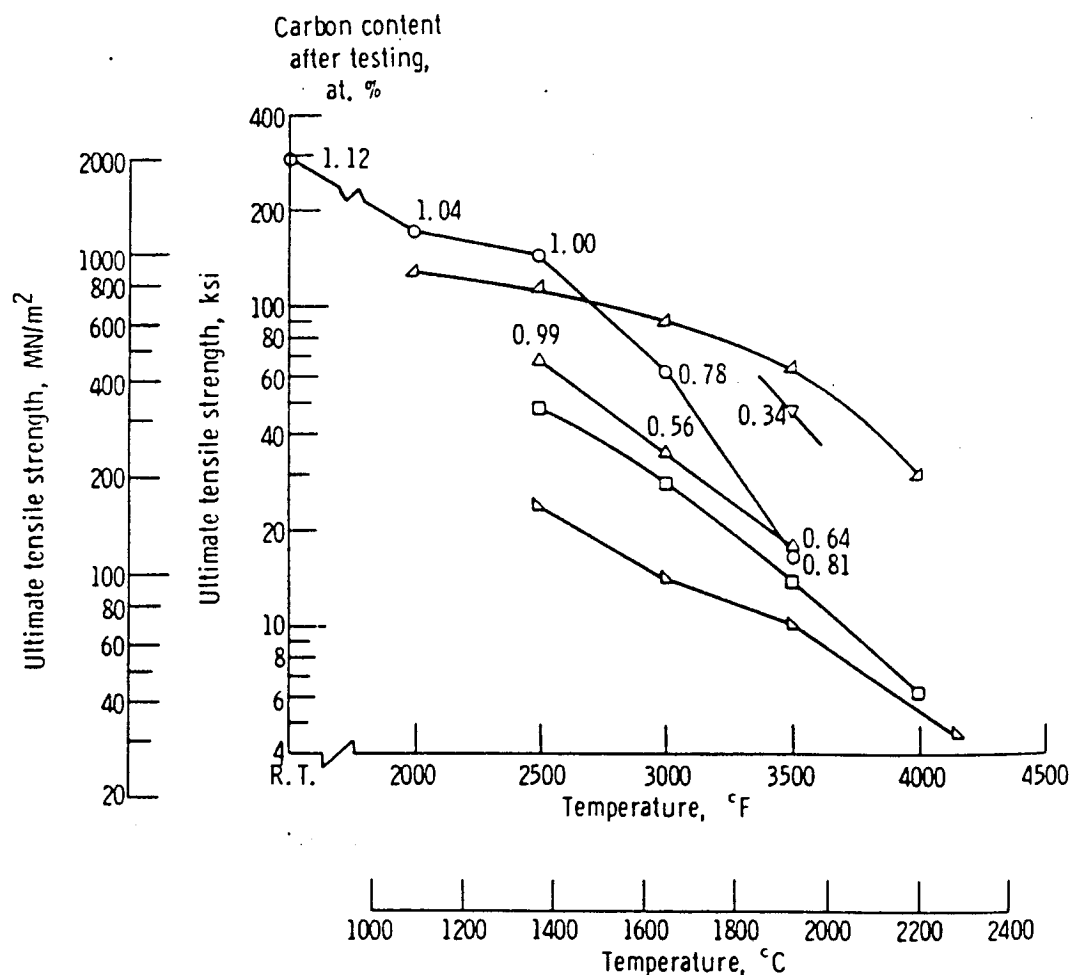


Effect of Rhenium on Strength of Tungsten-Rhenium Alloys. Steady Creep Rate, 10^{-6} per Second; Temperature, 3500°F (Corresponds Approximately to Rupture Life of 50 hrs) (Ref 7)

Rhenium Alloys

W-Re-(Hf + C)

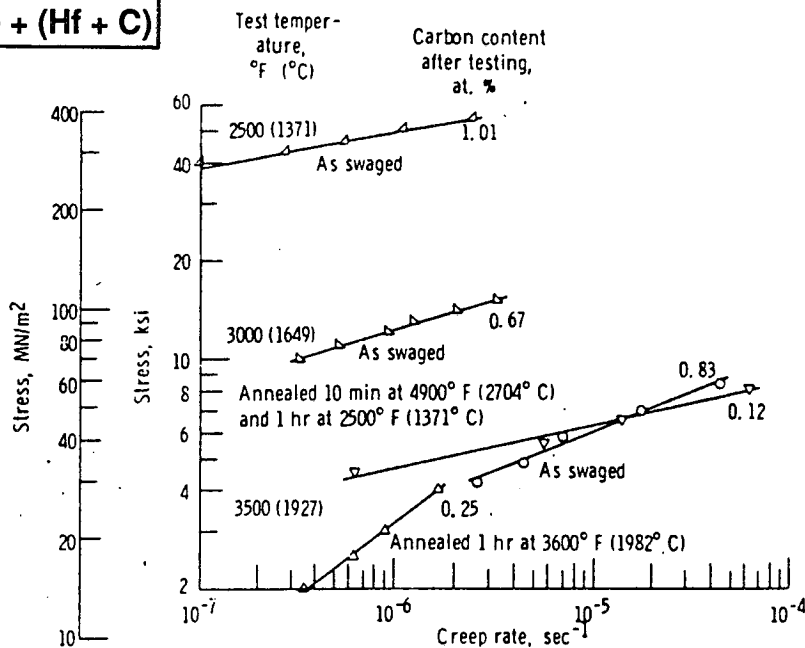
- W-23.4 Re-Hf-C, as swaged
- △ W-23.4 Re-Hf-C, annealed 1 hr at 3600° F (1982° C)
- ▽ W-23.4 Re-Hf-C, annealed 10 min at 4900° F (2704° K) and 1 hr at 2500° F (1371° C)
- W-24 Re, annealed 1 hr at 3600° F (1982° C)
- ▴ 100 W, annealed 1 hr at 2800° F (1538° C) (ref. 7)
- ◀ W-3.9 Re-0.41 Hf-0.51 C, as swaged



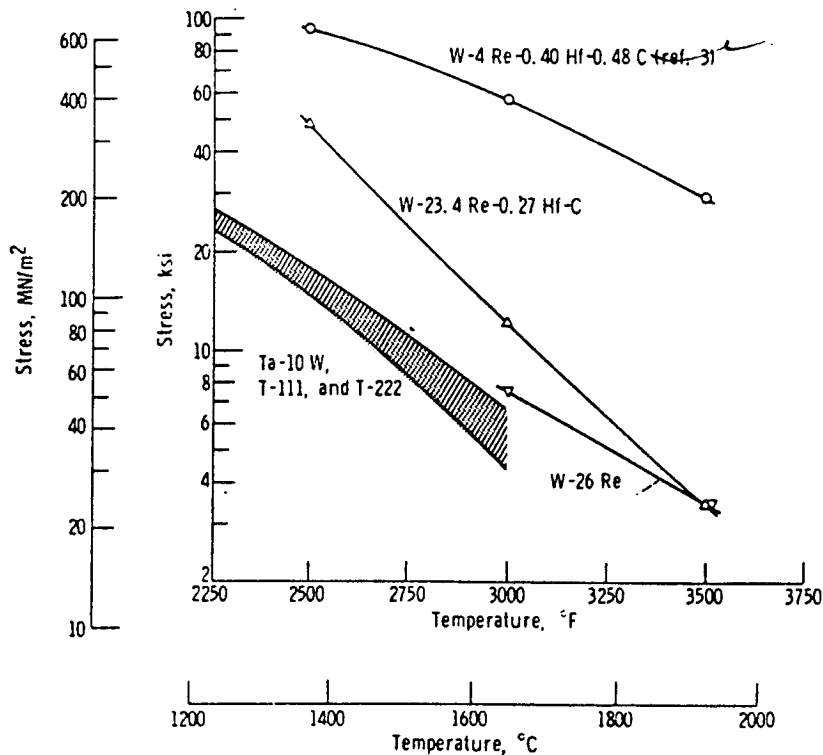
Tensile Strengths of W-23.4Re-Hf-C and Other Tungsten Alloys at Elevated Temperatures

Rhenium Alloys

W + Re + (Hf + C)



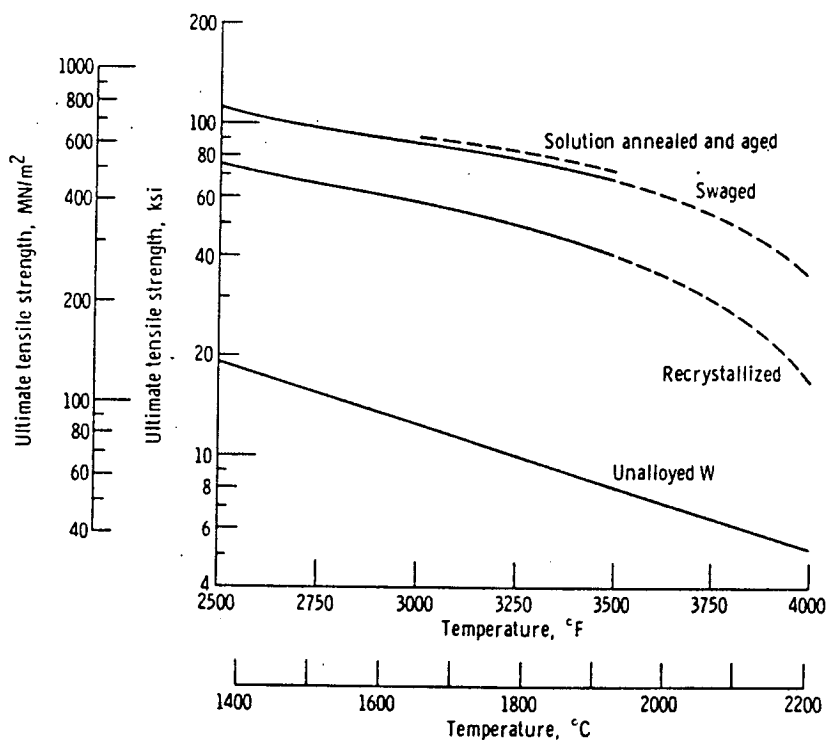
Creep Behavior of W-23.4Re-Hf-C at 2500°-3500°F (1371°-1927°C). Carbon Content of Each Specimen After Step-Load Testing is Indicated



Creep Strength at Creep Rate of 10⁻⁶/sec for Swaged W-23.4Re-0.27Hf-C Compared to Swaged W-4Re-0.40Hf-0.48C and High-Strength Tantalum Alloys at Elevated Temperatures (Ref 12)

W-Re-(Hf + C)

Rhenium Alloys

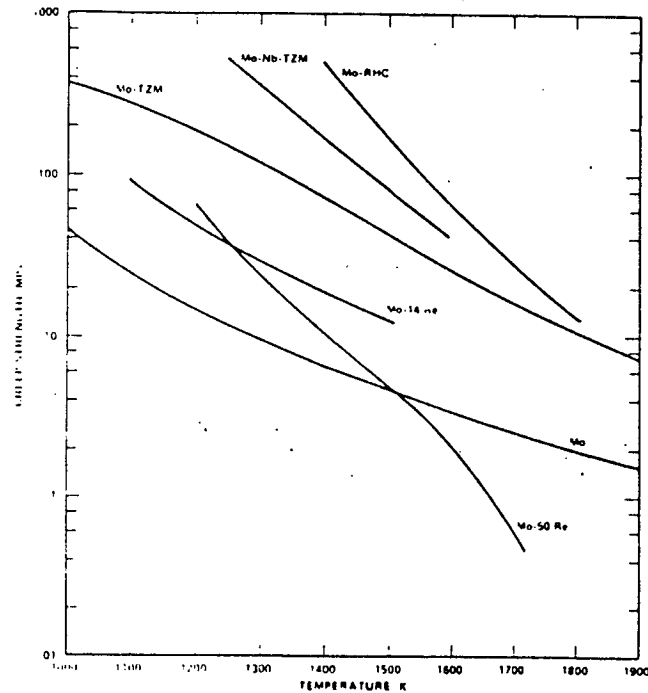


Tensile Strength of Optimum Alloy Composition W-4Re-0.35Hf-0.35C (Taken From Fig 1) Compared With Strength of Unalloyed Tungsten at 2500° to 4000°F (1371° to 2214°C)

Source W-D. Klopp NASA TN 5348 Mech. Prop. W-Pe HfC Alloys

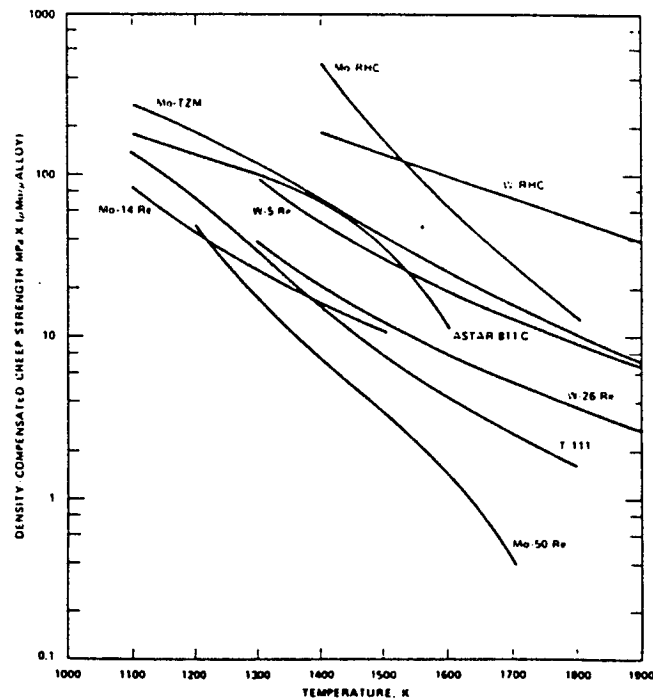
Rhenium Alloys

Mo-Re



Extrapolated Stress for 1 Percent Creep Strain in 61,000 Hours as a Function of Temperature for Molybdenum and Molybdenum Alloys.

Mo-Re
Ta-Re
W-Re
W-Re-HfC



Density-Compensated Stress for 1 Percent Creep Strain in 61,000 Hours as a Function of Temperature for Selected Alloys, Corrected to Density of Molybdenum.

Source: W.D. Klopp Space Nuclear Power Systems 1984 (Ref. 15)

PROPELLANT COMBUSTION PRODUCT COMPOSITION

APPENDIX B

- B-1 Combustion Temperature versus Mixture Ratio for Oxygen/Hydrogen at 1, 5 and 10 atm
- B-2 Mole Fraction versus Mixture Ratio of Oxygen/Hydrogen at 1 atm
- B-3 Mole Fraction versus Mixture Ratio of Oxygen/Hydrogen at 5 atm
- B-4 Mole Fraction versus Mixture Ratio of Oxygen/Hydrogen at 10 atm
- B-5 Combustion Temperature and Specific Impulse for Oxygen/Hydrogen at 5 atm
- B-6 Combustion Temperature and Specific Impulse for Oxygen/Hydrogen at 10 atm
- B-7 Combustion Temperature versus Mixture Ratio for Oxygen/Methane at 1, 5 and 10 atm
- B-8 Mole Fraction versus Mixture Ratio for Oxygen/Methane at 1 atm
- B-9 Mole Fraction versus Mixture Ratio for Oxygen/Methane at 5 atm
- B-10 Mole Fraction versus Mixture Ratio for Oxygen/Methane at 10 atm
- B-11 Combustion Temperature and Specific Impulse for Oxygen/Methane at 5 atm
- B-12 Combustion Temperature and Specific Impulse for Oxygen/Methane at 10 atm
- B-13 Combustion Temperature versus Mixture Ratio for Nitrogen Tetroxide/Hydrazine at 1, 5 and 10 atm
- B-14 Mole Fraction versus Mixture Ratio for Nitrogen Tetroxide/Hydrazine at 1 atm
- B-15 Mole Fraction versus Mixture Ratio for Nitrogen Tetroxide/Hydrazine at 5 atm
- B-16 Mole Fraction versus Mixture Ratio for Nitrogen Tetroxide/Hydrazine at 10 atm
- B-17 Combustion Temperature and Specific Impulse Versus Mixture Ratio for Nitrogen Tetroxide/Hydrazine at 5 atm
- B-18 Combustion Temperature and Specific Impulse versus Mixture Ratio for Nitrogen Tetroxide/Hydrazine at 10 atm
- B-19 Combustion Temperature versus Mixture Ratio for Nitrogen Tetroxide/Monomethylhydrazine at 1, 5 and 10 atm
- B-20 Mole Fraction versus Mixture Ratio for Nitrogen Tetroxide/Monomethylhydrazine at 1 atm
- B-21 Mole Fraction versus Mixture Ratio for Nitrogen Tetroxide/Monomethylhydrazine at 5 atm
- B-22 Mole Fraction versus Mixture Ratio for Nitrogen Tetroxide/Monomethylhydrazine at 10 atm

- B-23 Combustion Temperature and Specific Impulse versus Mixture Ratio for Nitrogen Tetroxide/Monomethylhydrazine at 1 atm
- B-24 Combustion Temperature and Specific Impulse versus Mixture Ratio for Nitrogen Tetroxide/Monomethylhydrazine at 5 atm
- B-25 combustion Temperature and Specific Impulse versus Mixture Ratio for Nitrogen Tetroxide/Monomethylhydrazine at 10 atm
- B-26 Exhaust Gas Temperature versus Nozzle Expansion Ratio for O_2/H_2 , O_2/CH_4 , N_2O_4/N_2H_4 and $N_2O_4/N_2H_3CH_3$

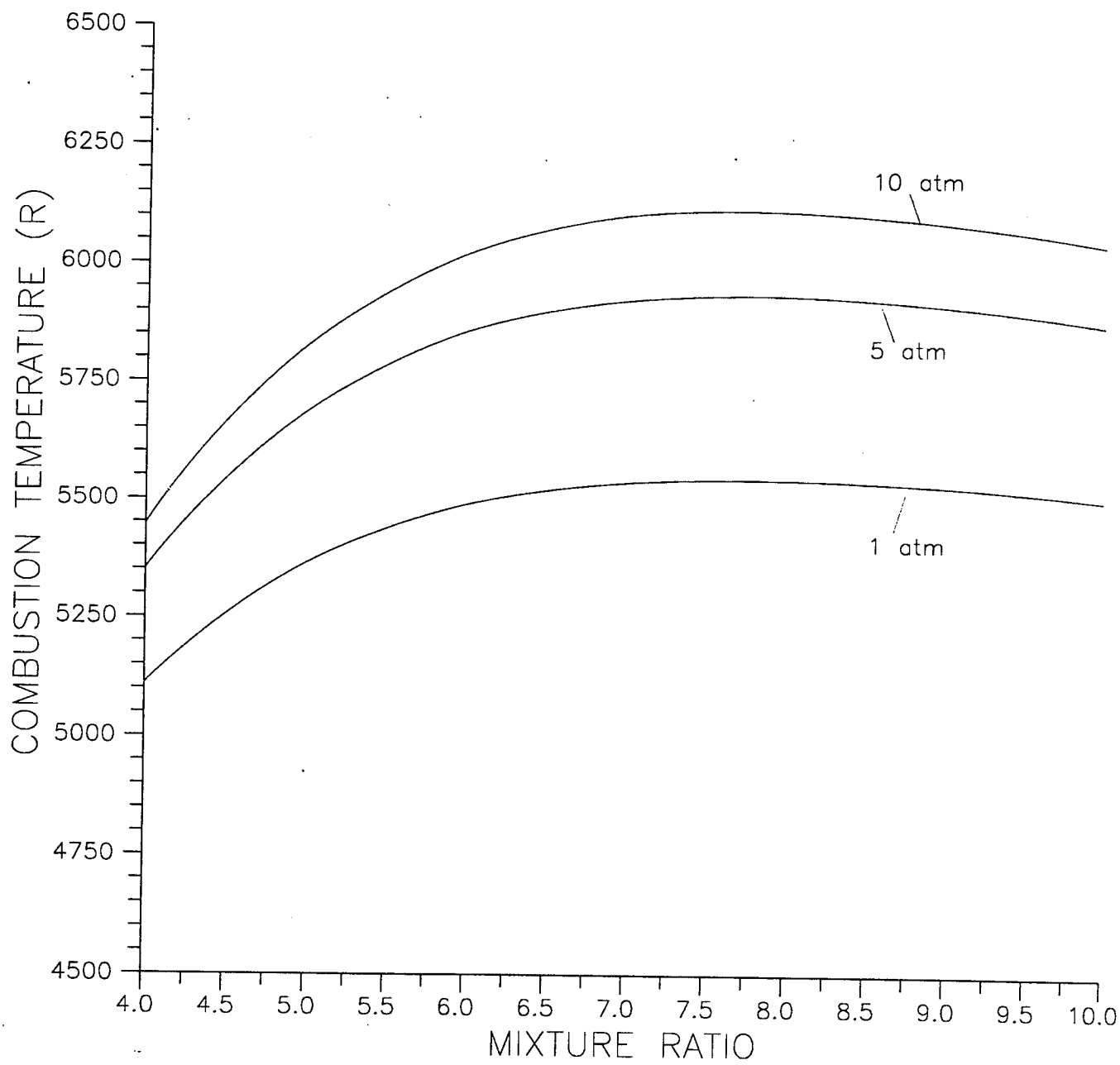


**Figure B-1. Combustion Temperature Versus Mixture Ratio
for Oxygen/Hydrogen at 1, 5, and 10 atm**

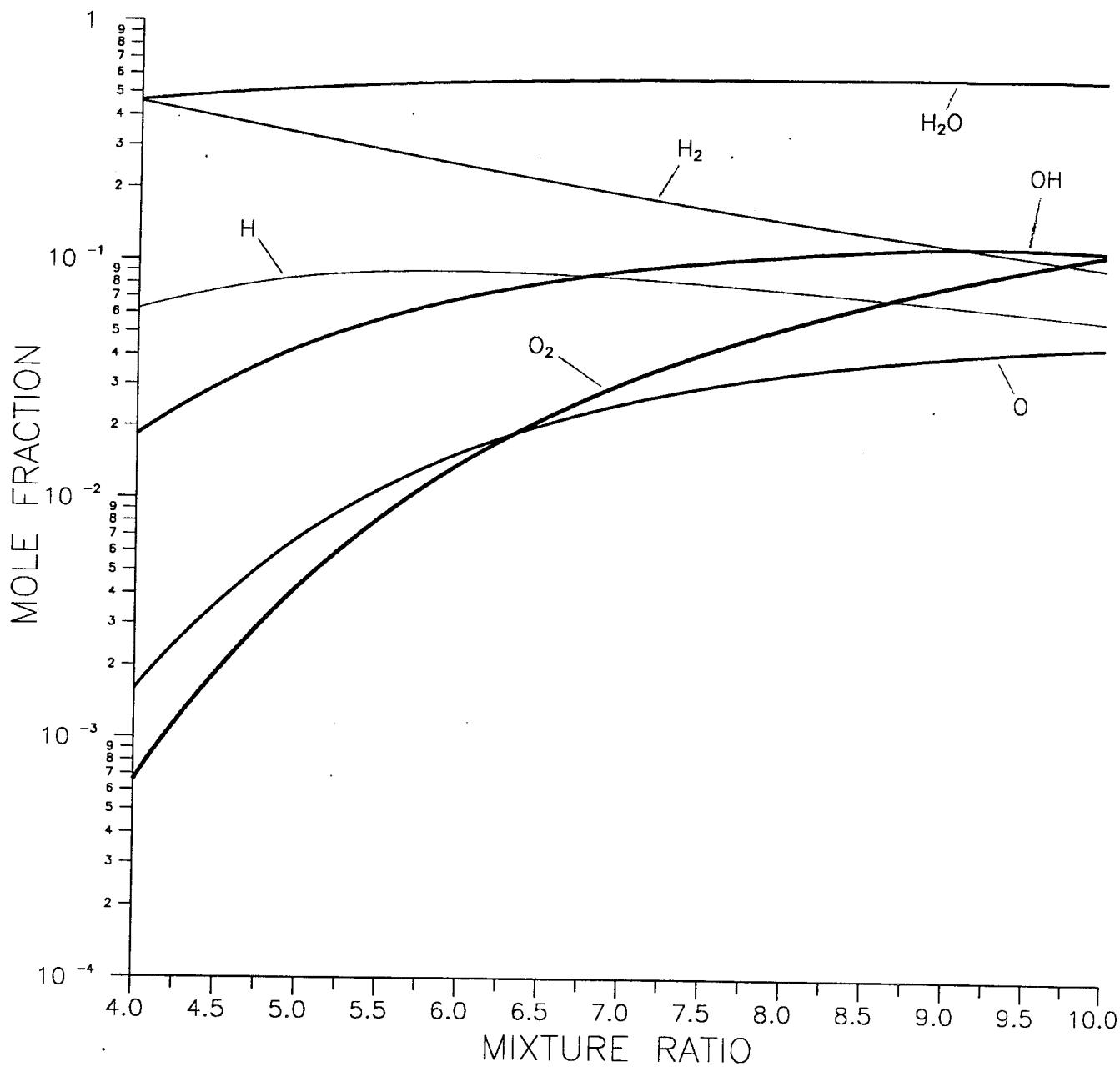


Figure B-2. Mole Fraction Versus Mixture Ratio of Oxygen/Hydrogen at 1 atm

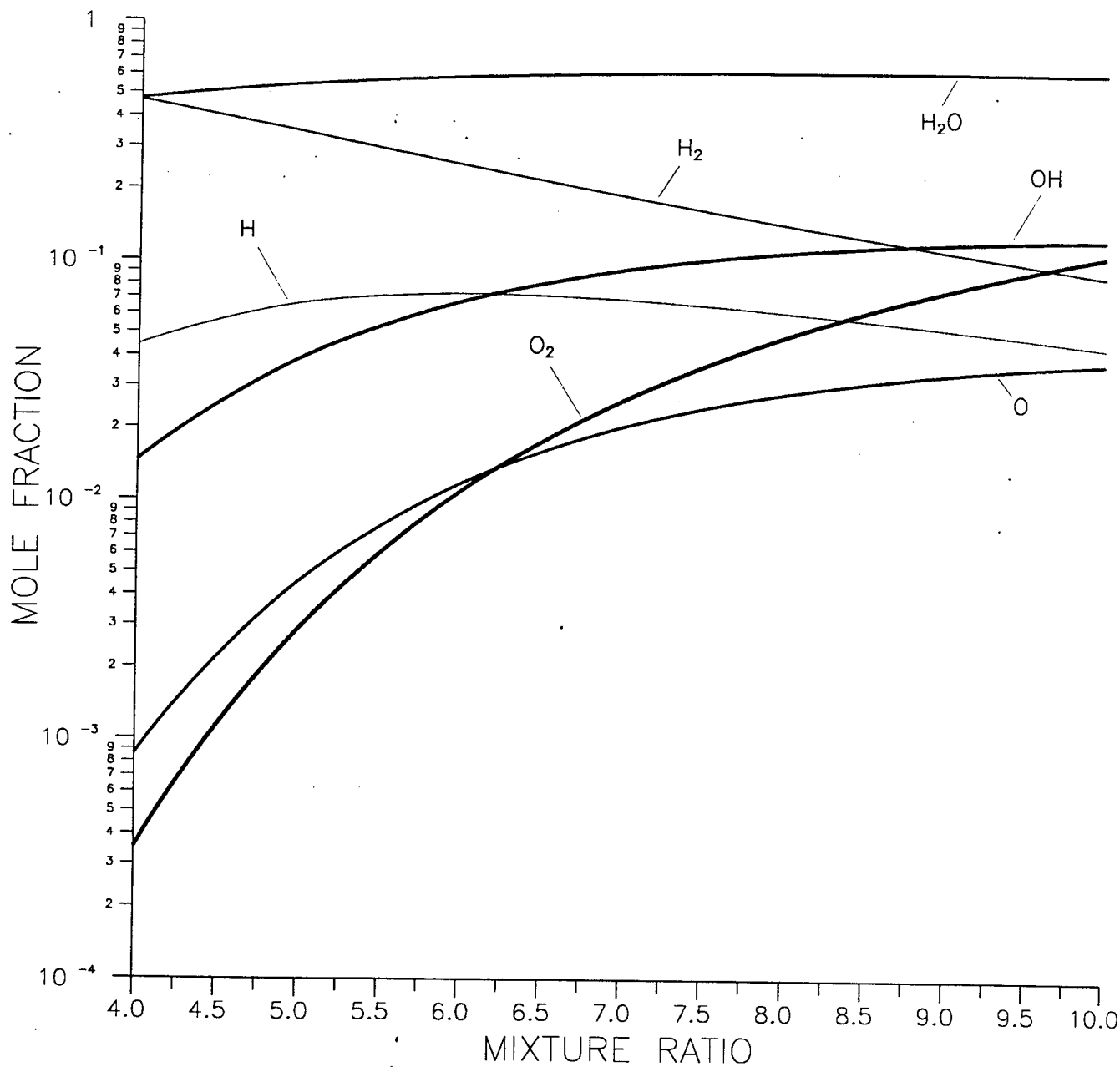


Figure B-3. Mole Fraction Versus Mixture Ratio of Oxygen/Hydrogen at 5 atm

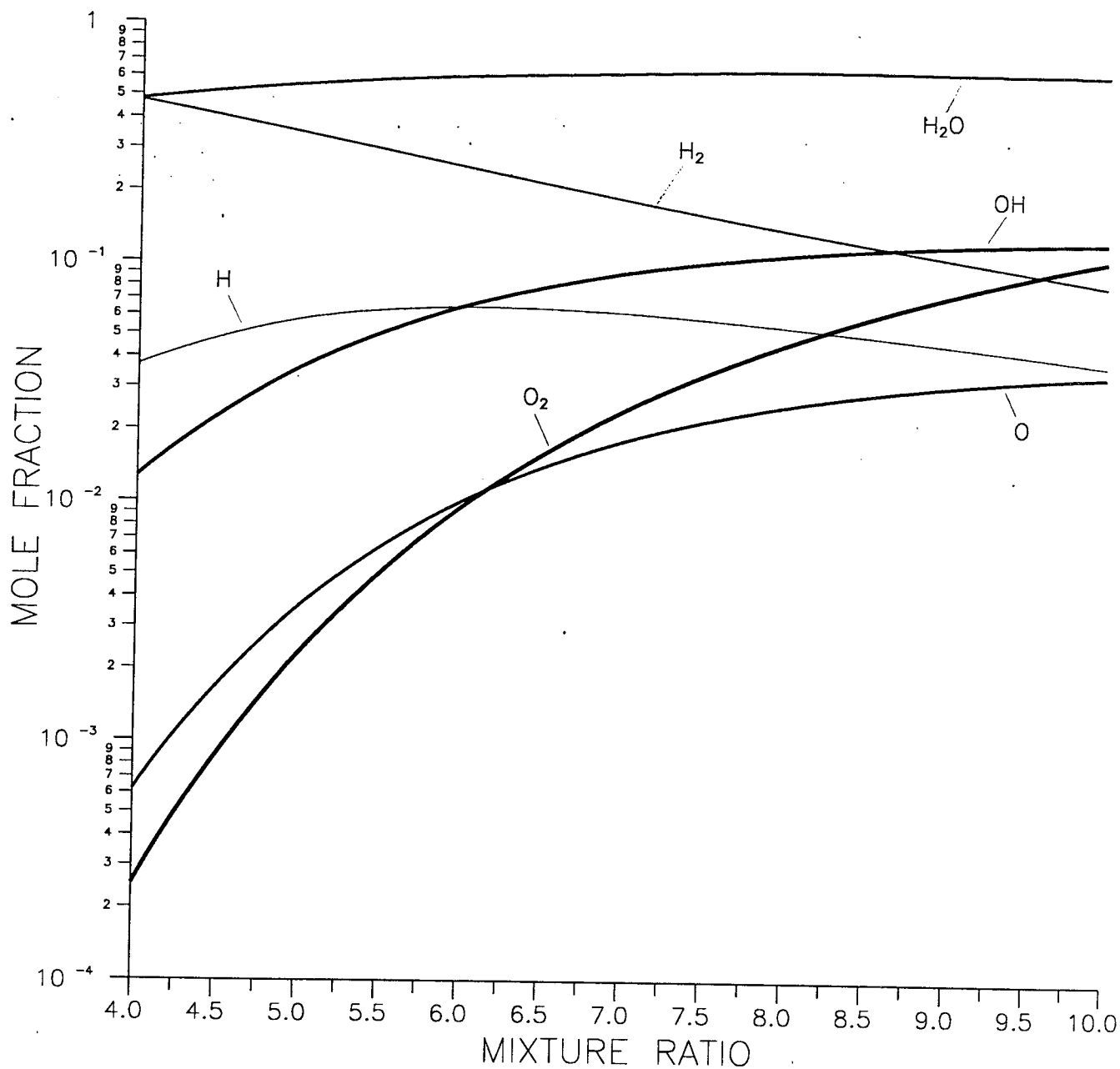


Figure B-4. Mole Fraction Versus Mixture Ratio of Oxygen/Hydrogen at 10 atm

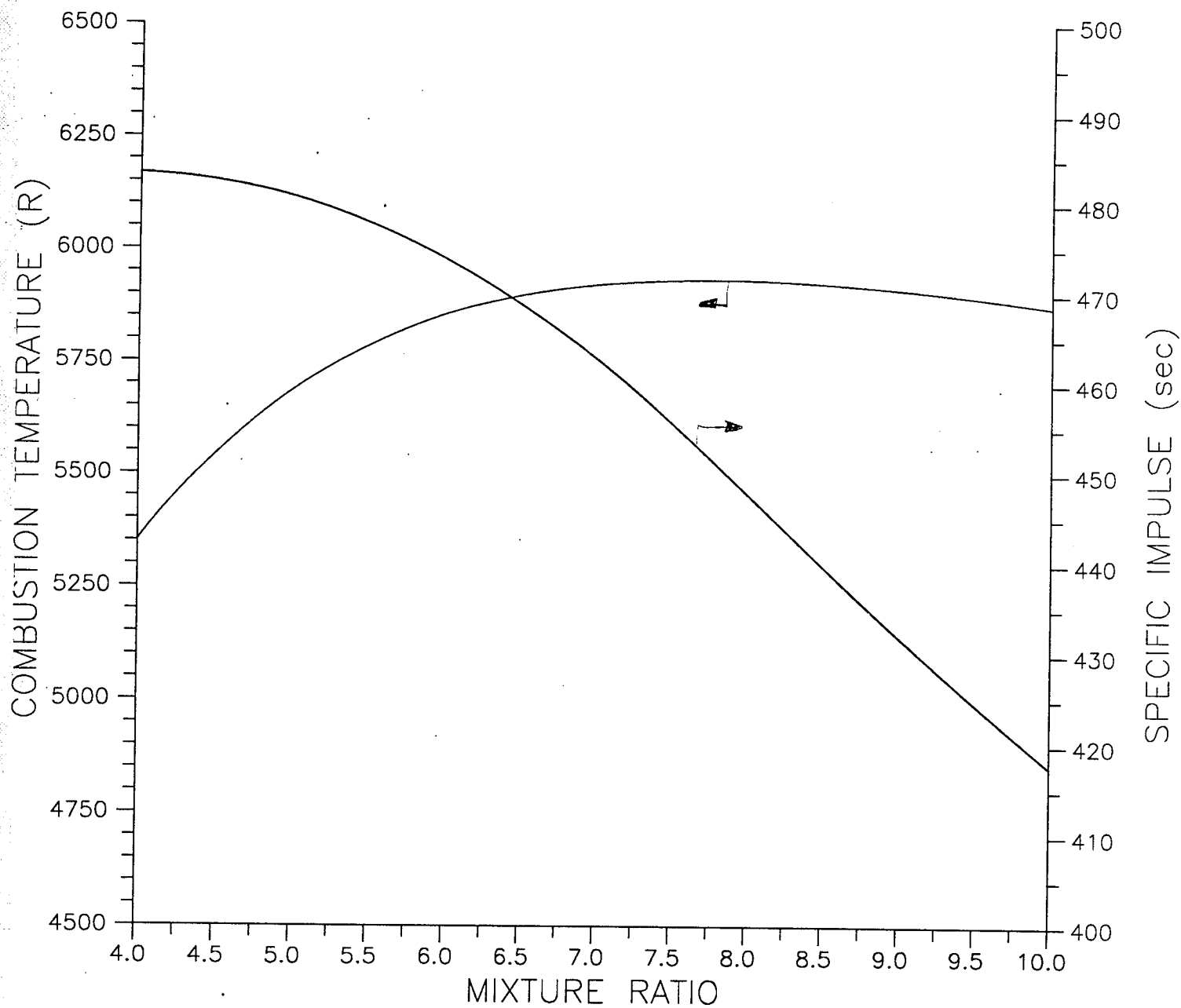


Figure B-5. Combustion Temperature and Specific Impulse for Oxygen/Hydrogen at 5 atm

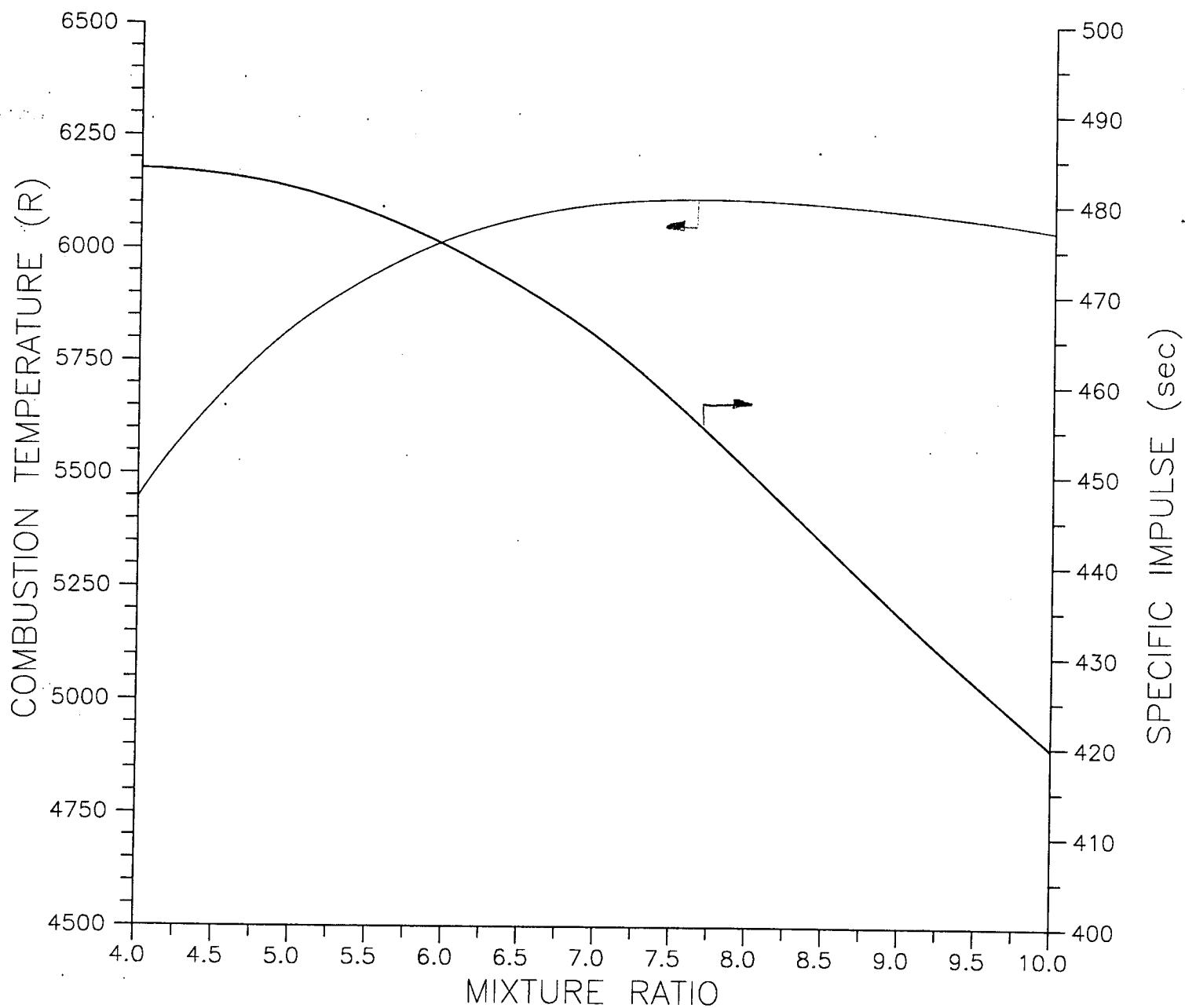
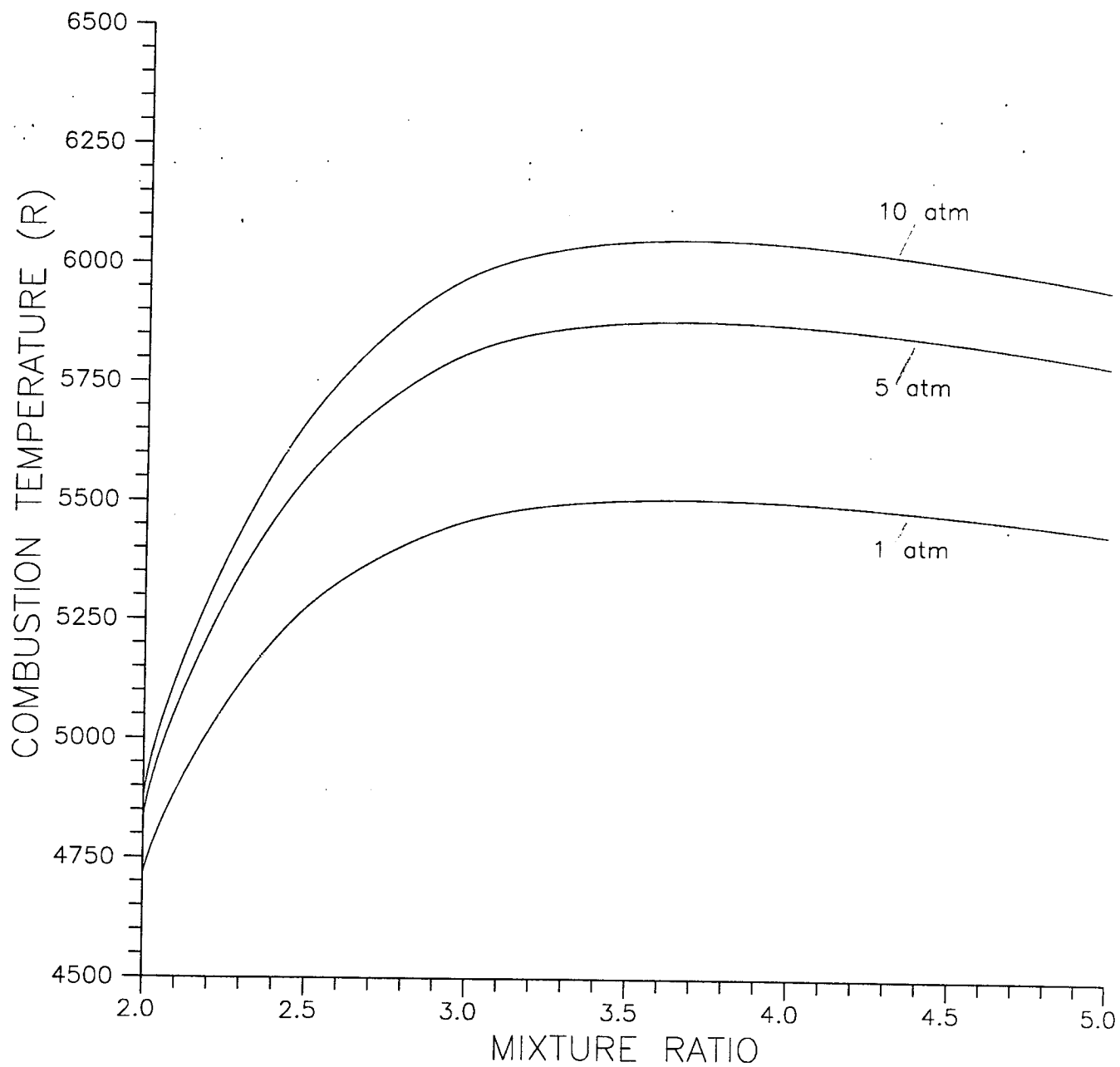


Figure B-6. Combustion Temperature and Specific Impulse for Oxygen/Hydrogen at 10 atm



**Figure B-7. Combustion Temperature Versus Mixture Ratio
for Oxygen/Methane at 1, 5 and 10 atm**

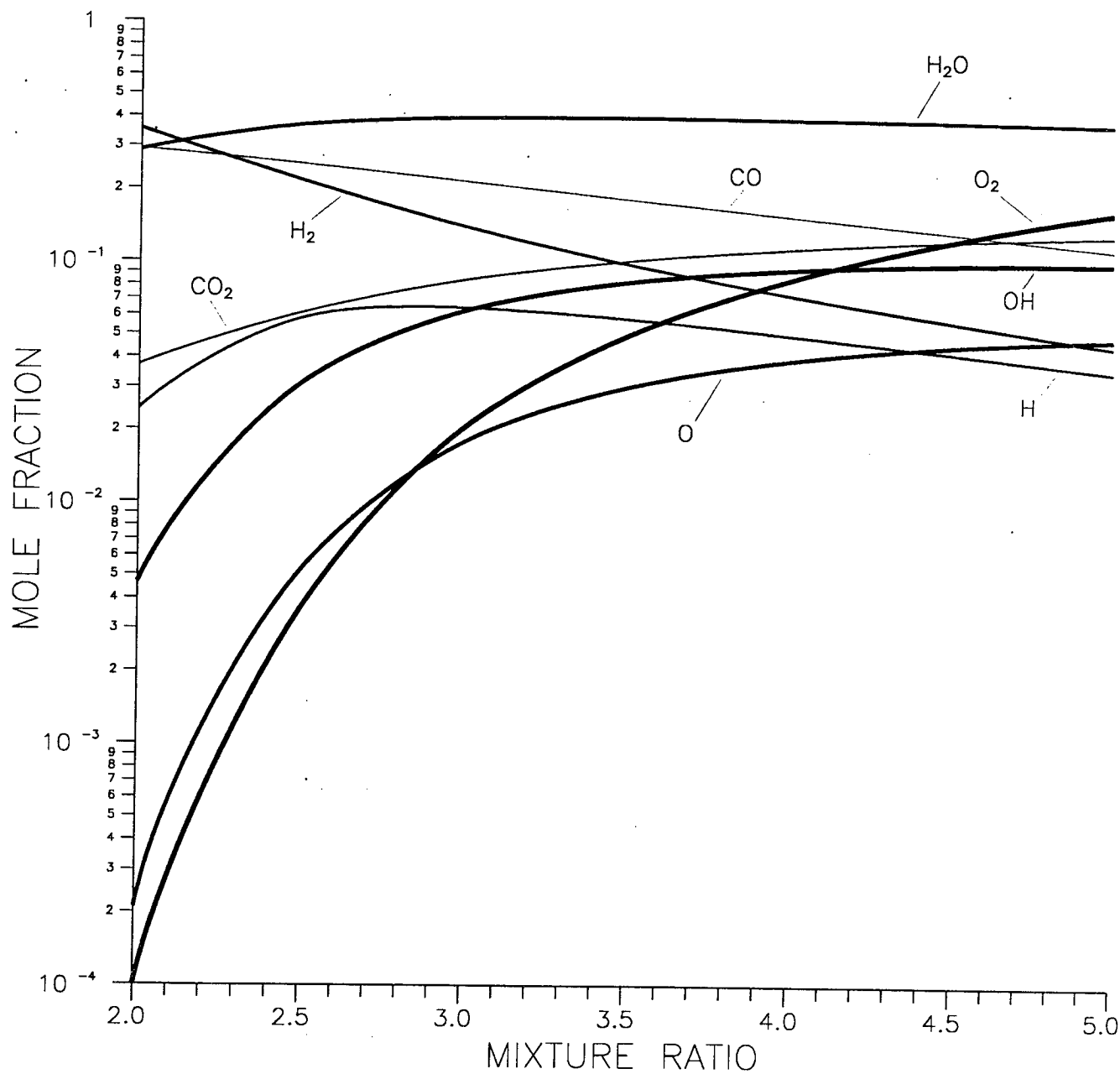


Figure B-8. Mole Fraction Versus Mixture Ratio for Oxygen/Methane at 1 atm

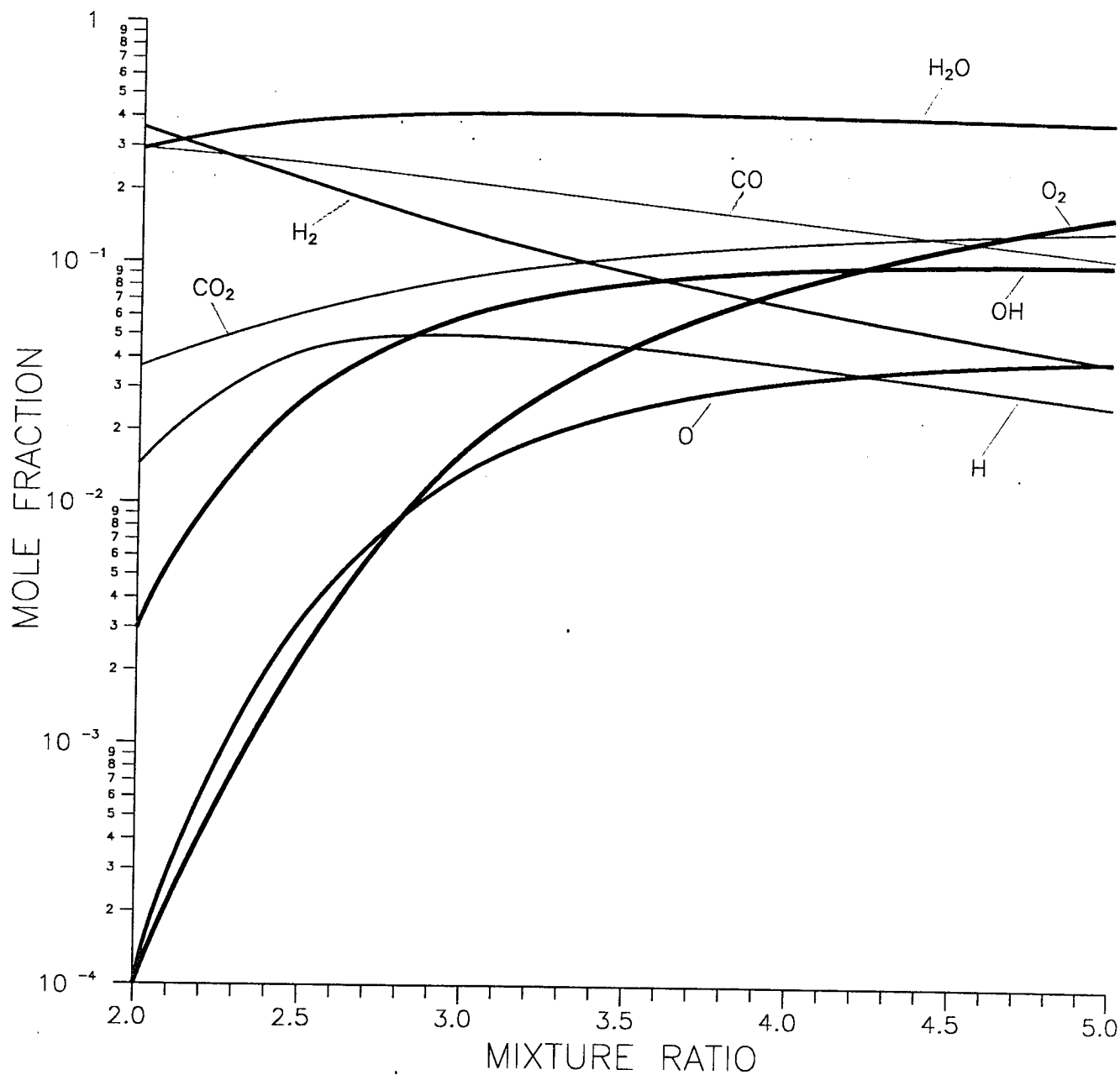


Figure B-9. Mole Fraction Versus Mixture Ratio for Oxygen/Methane at 5 atm

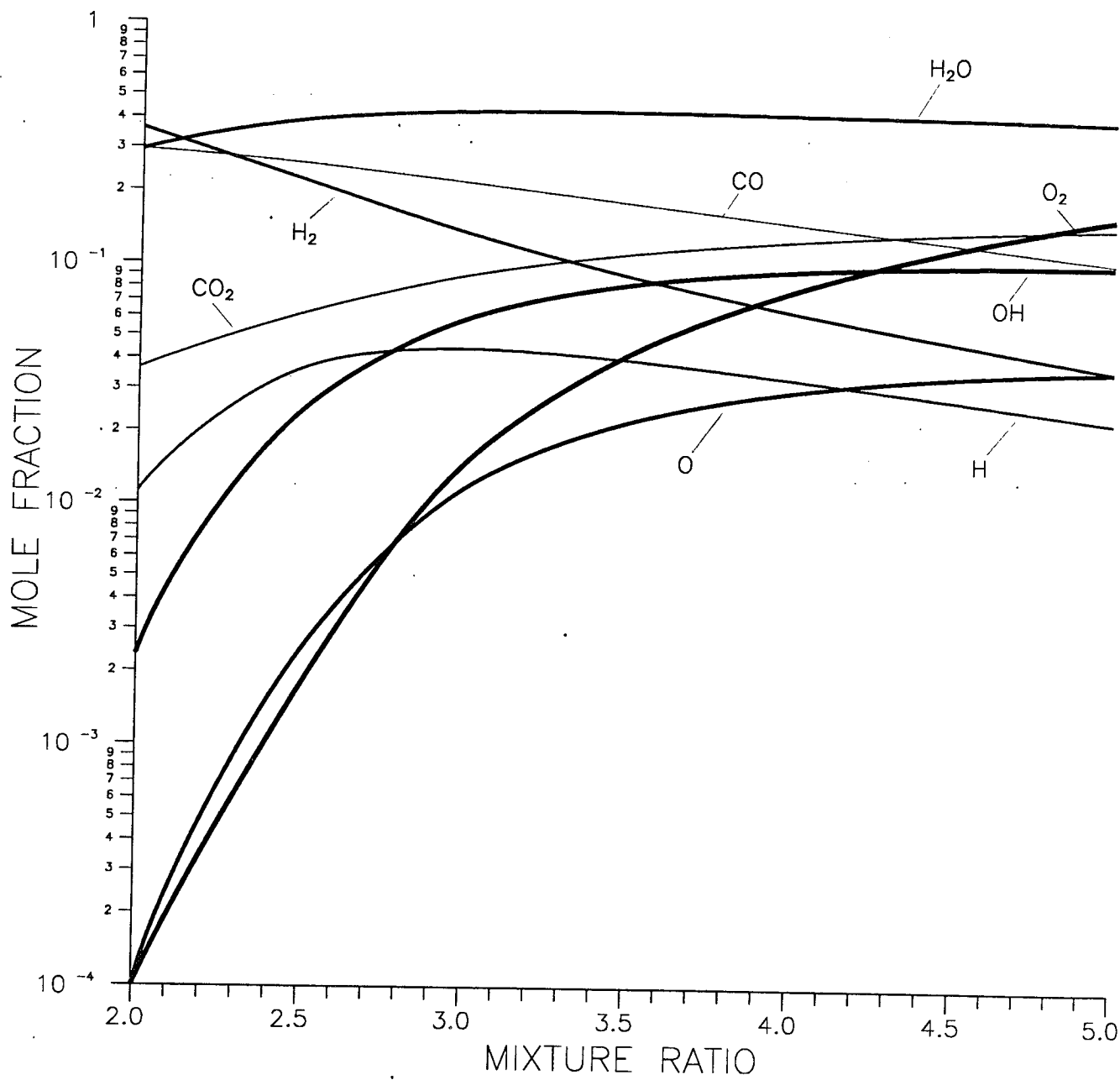


Figure B-10. Mole Fraction Versus Mixture Ratio for Oxygen/Methane at 10 atm

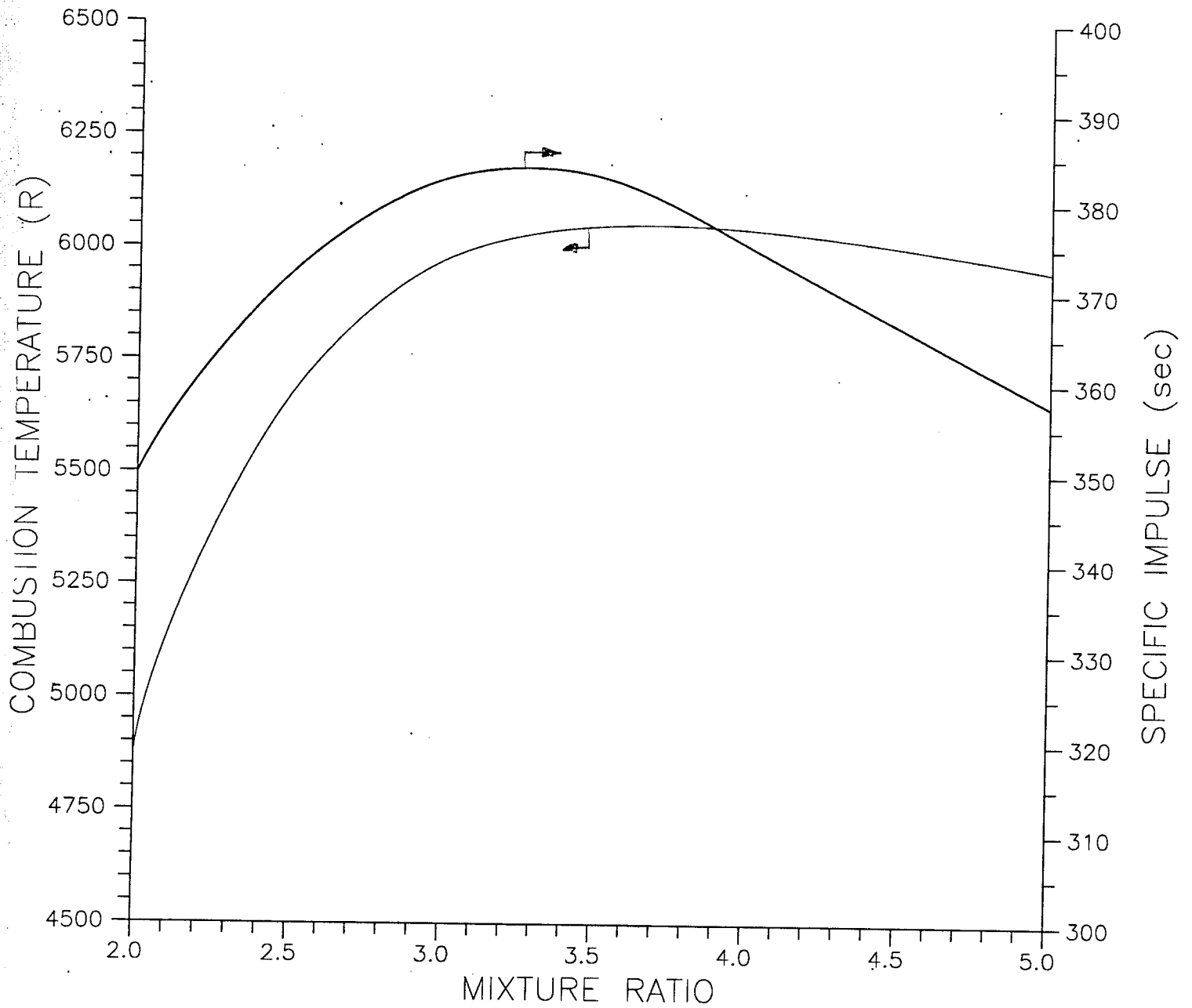


Figure B-11. Combustion Temperature and Specific Impulse for Oxygen/Methane at 5 atm

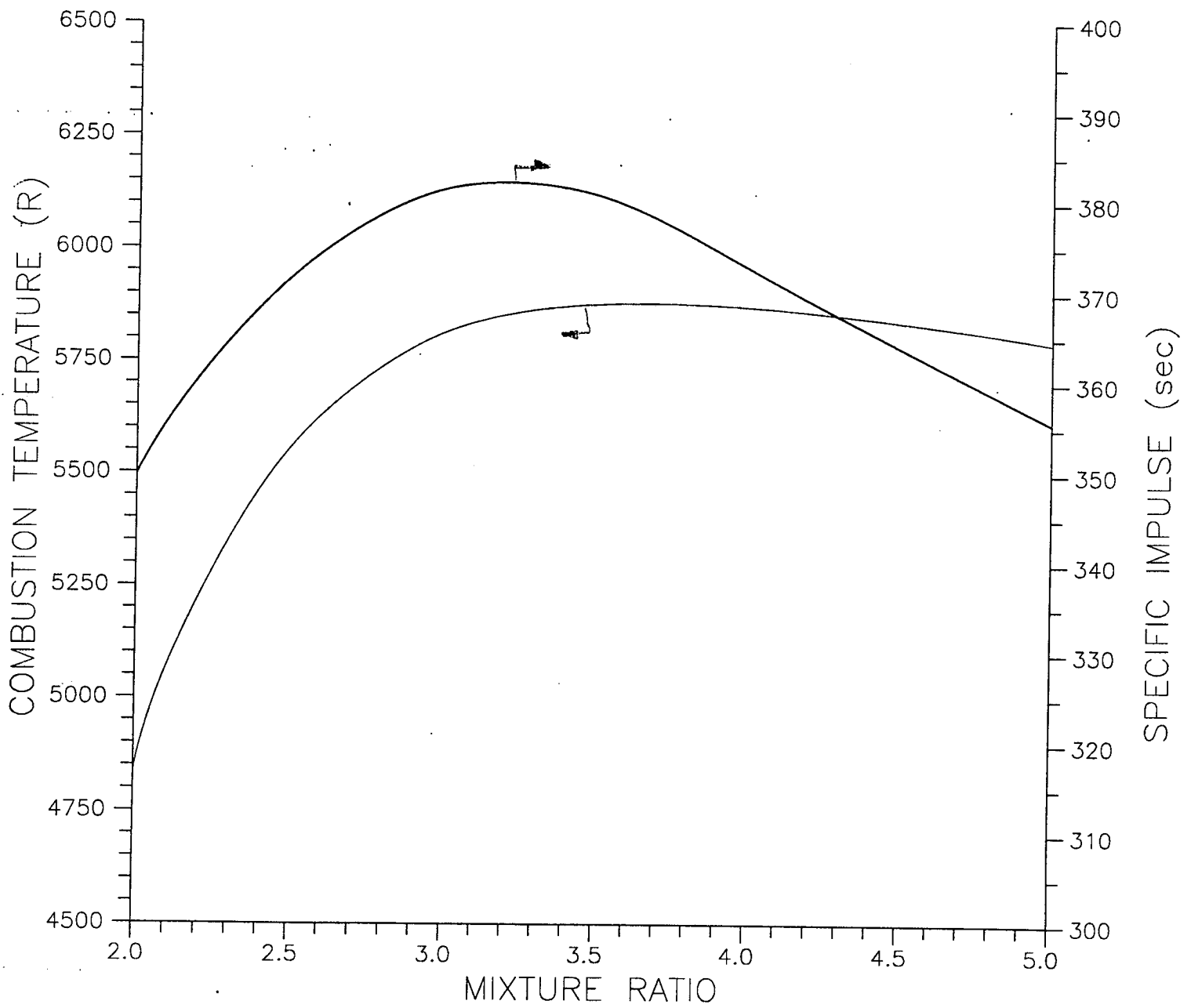


Figure B-12. Combustion Temperature and Specific Impulse for Oxygen/Methane at 10 atm

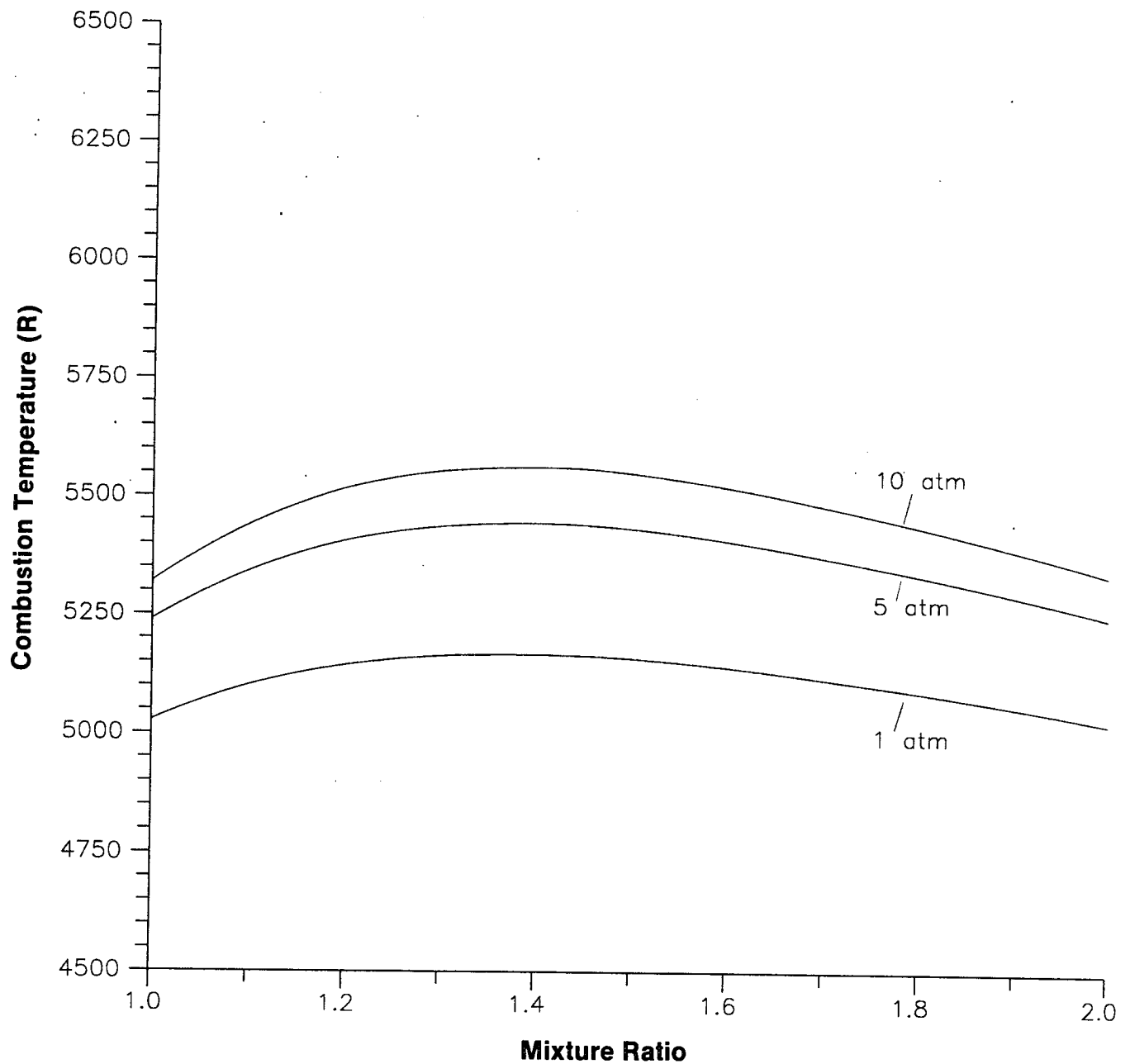


Figure B-13. Combustion Temperature Versus Mixture Ratio for Nitrogen Tetroxide/Hydrazine at 1, 5, and 10 atm

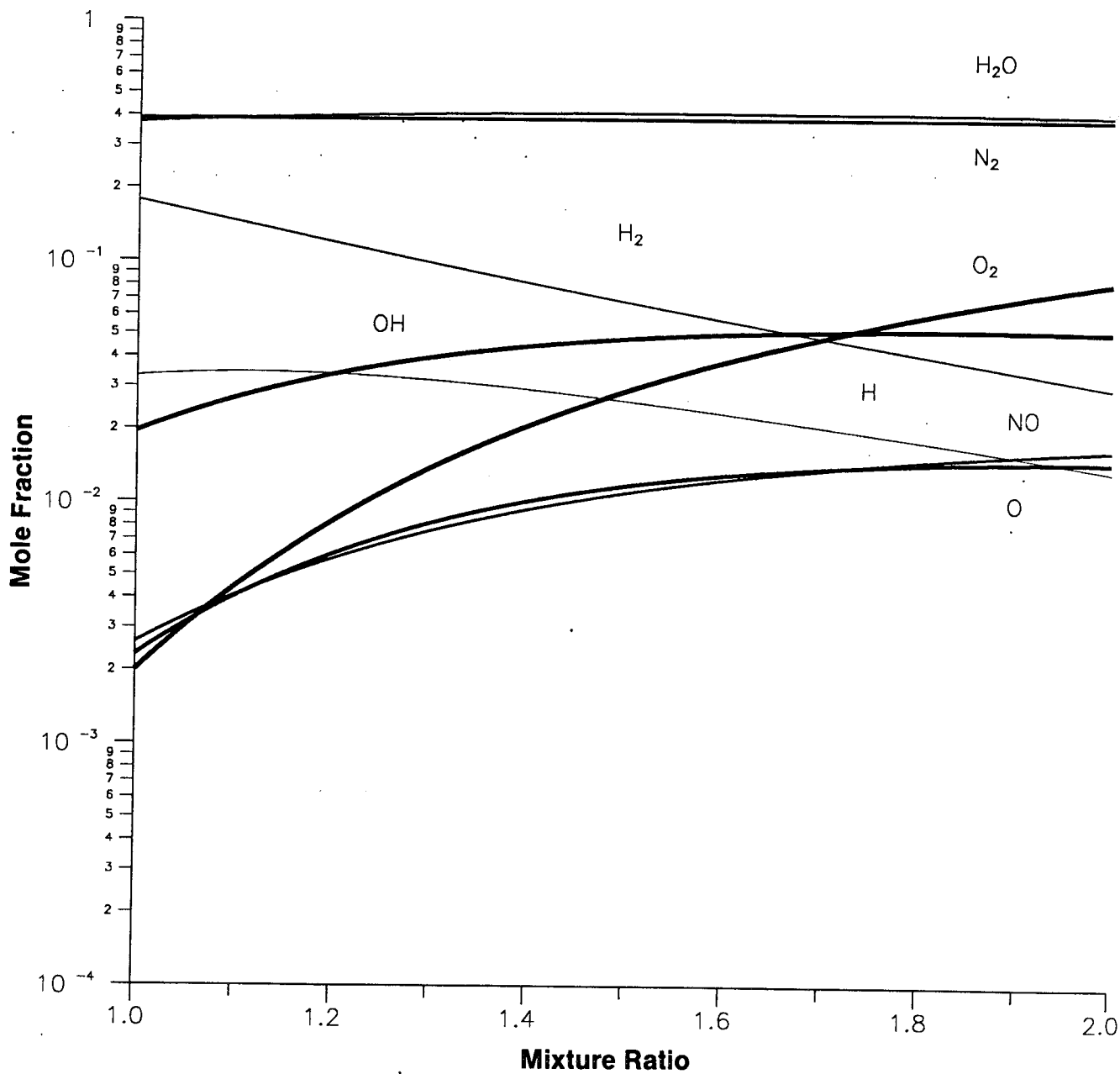


Figure B-14. Mole Fraction Versus Mixture Ratio for Nitrogen Tetroxide/Hydrazine at 1 atm

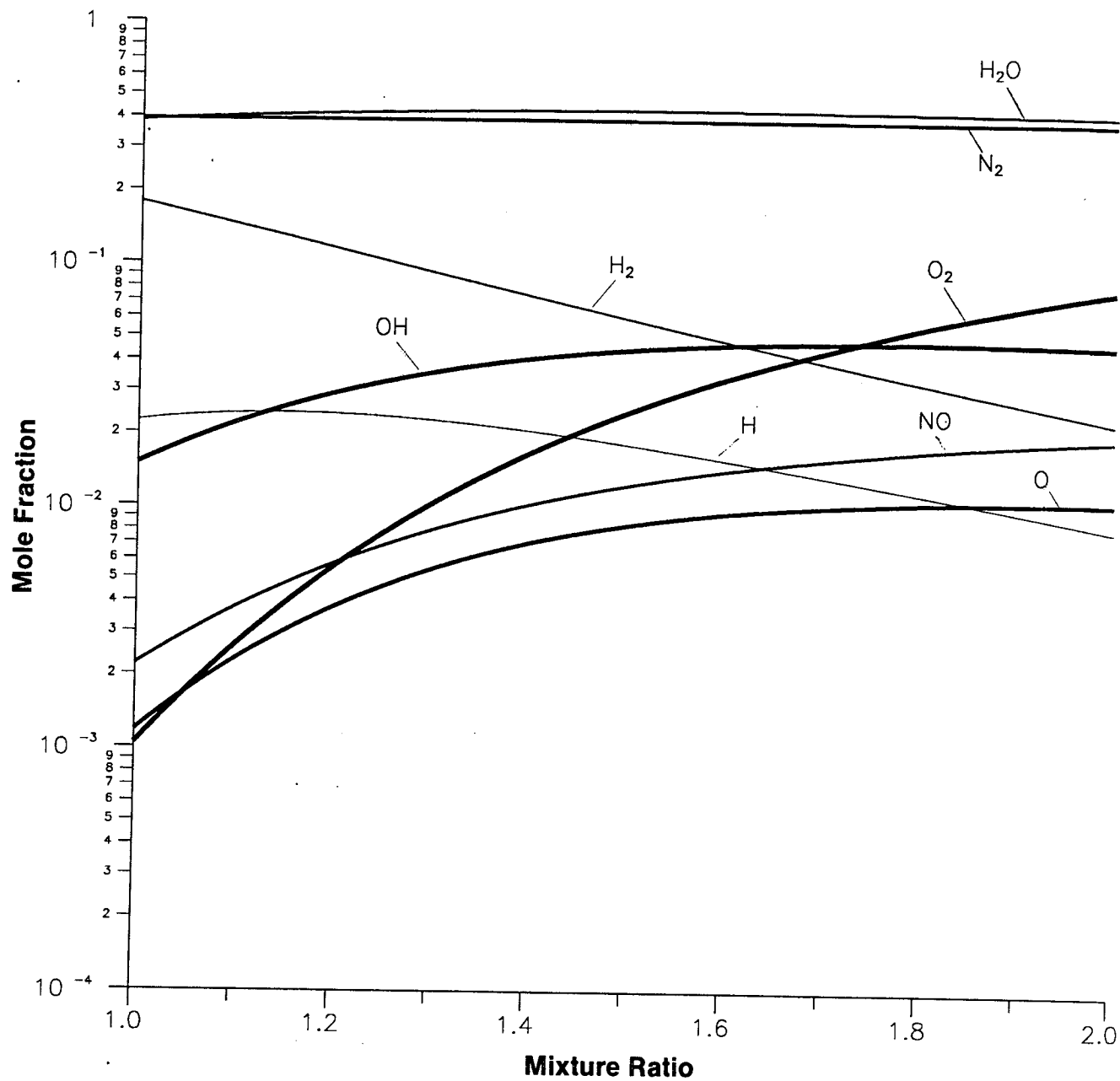


Figure B-15. Mole Fraction Versus Mixture Ratio for Nitrogen Tetroxide/Hydrazine at 5 atm

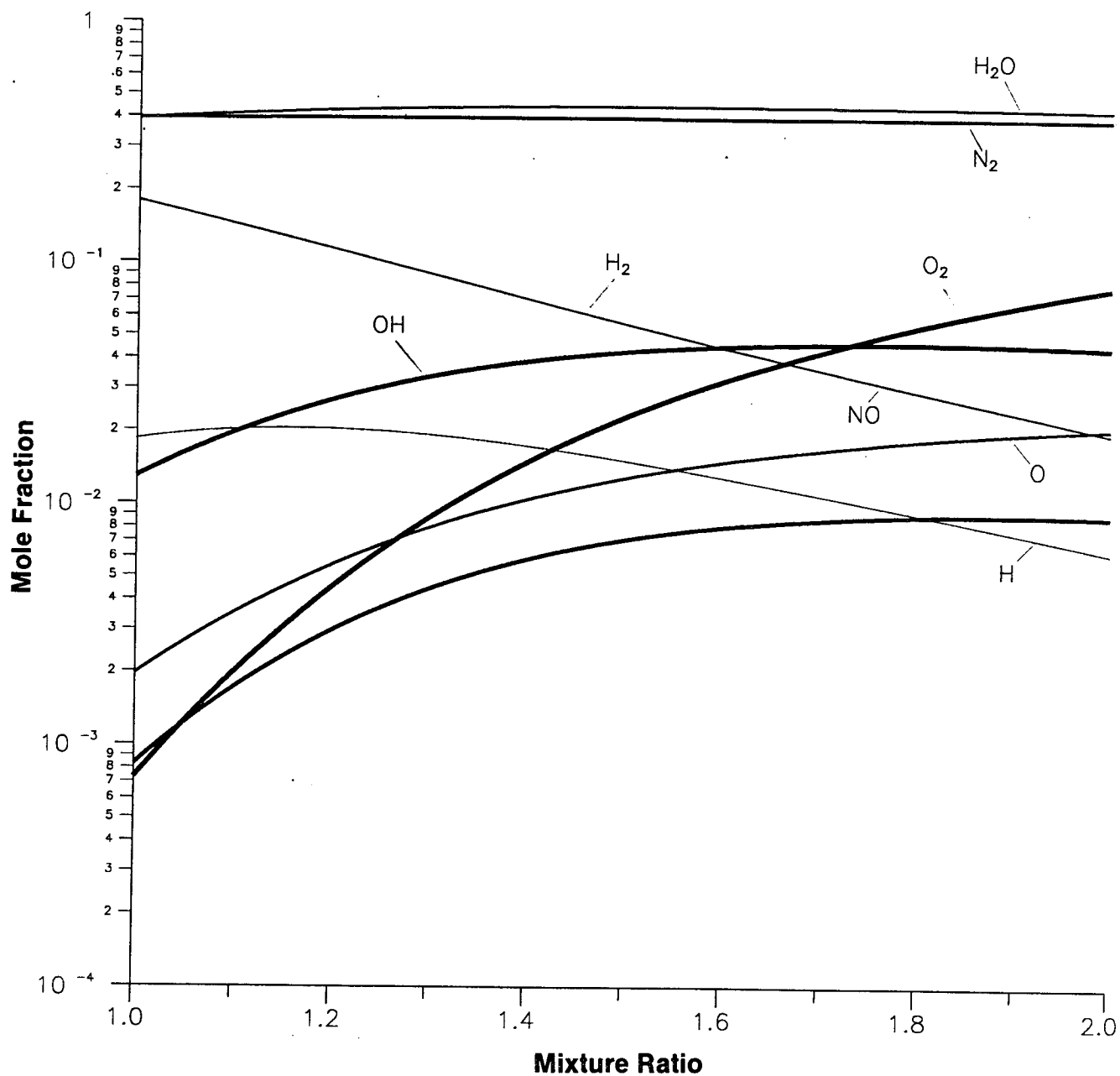


Figure B-16. Mole Fraction Versus Mixture Ratio for Nitrogen Tetroxide/Hydrazine at 10 atm

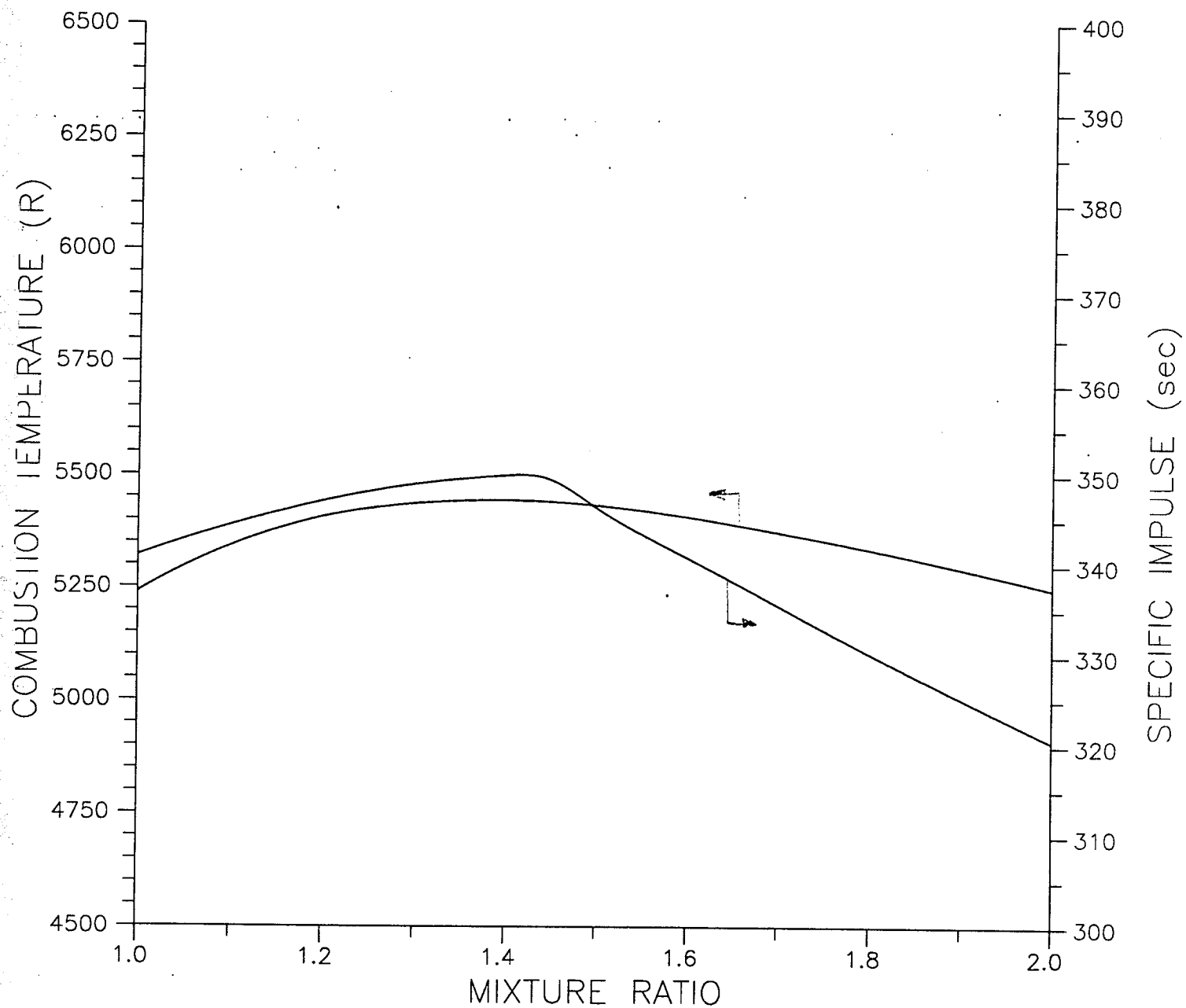


Figure B-17. Combustion Temperature and Specific Impulse Versus Mixture Ratio for Nitrogen Tetroxide/Hydrazine at 5 atm

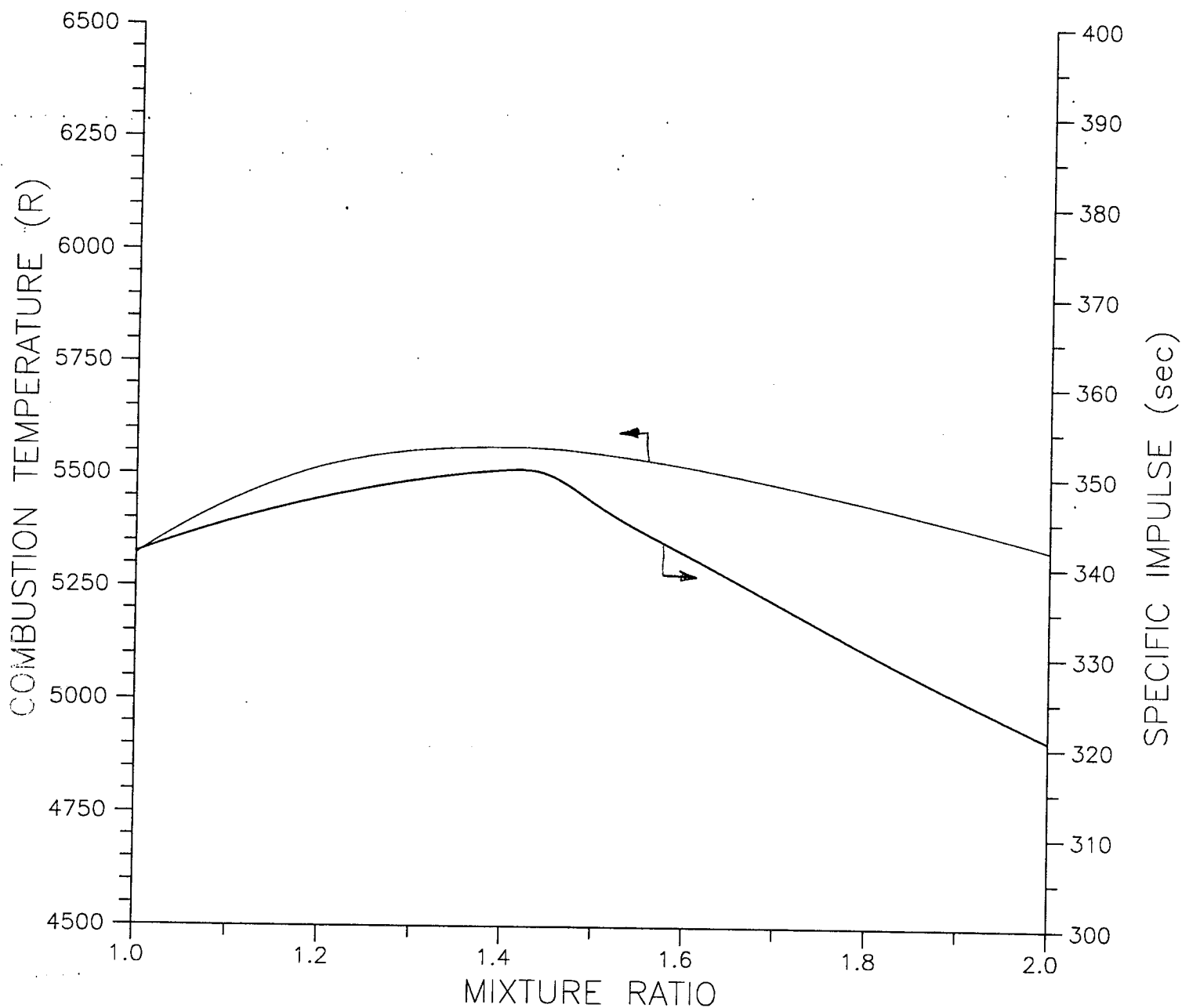


Figure B-18. Combustion Temperature and Specific Impulse Versus Mixture Ratio for Nitrogen Tetroxide/Hydrazine at 10 atm

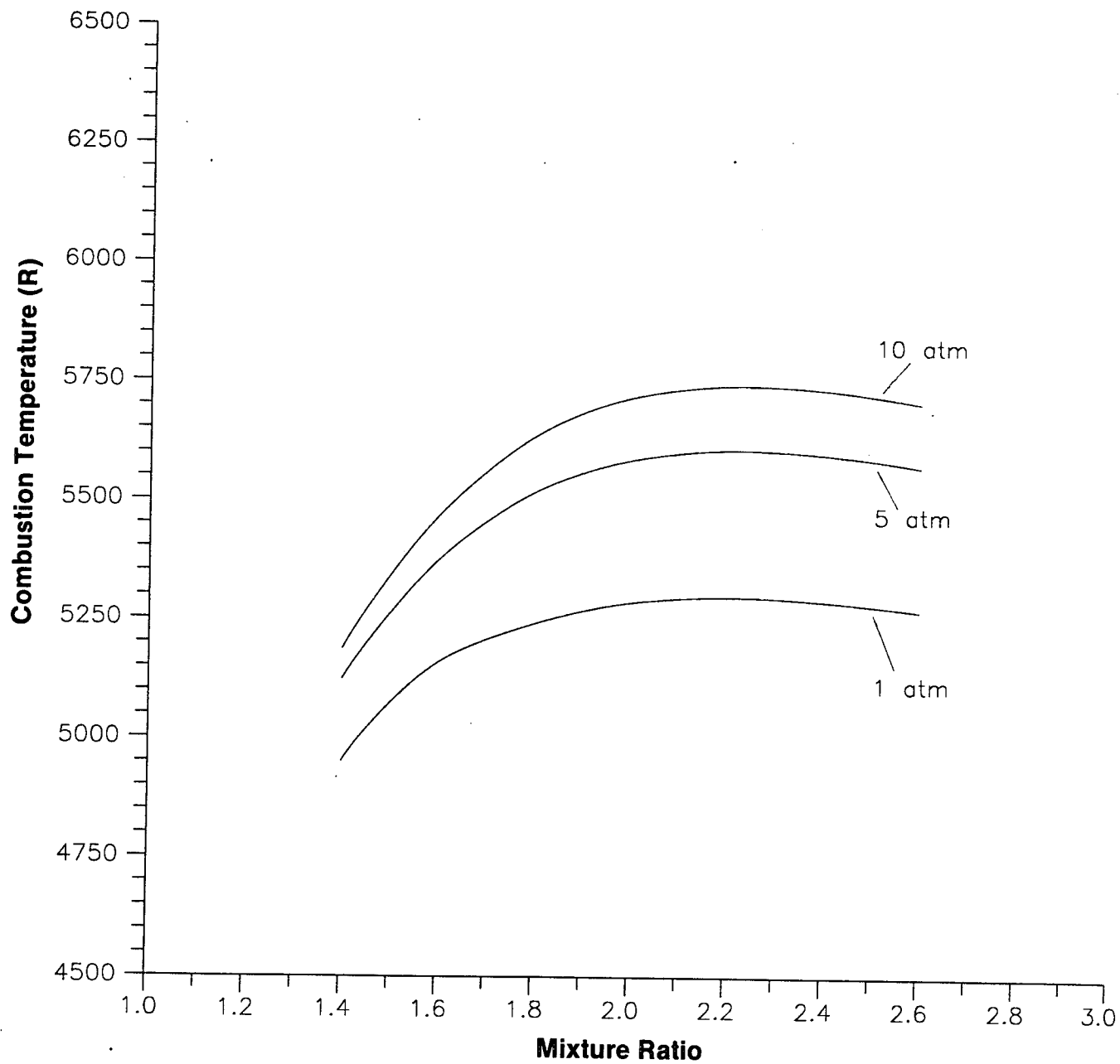


Figure B-19. Combustion Temperature Versus Mixture Ratio for Nitrogen Tetroxide/ Monomethylhydrazine at 1, 5 and 10 atm

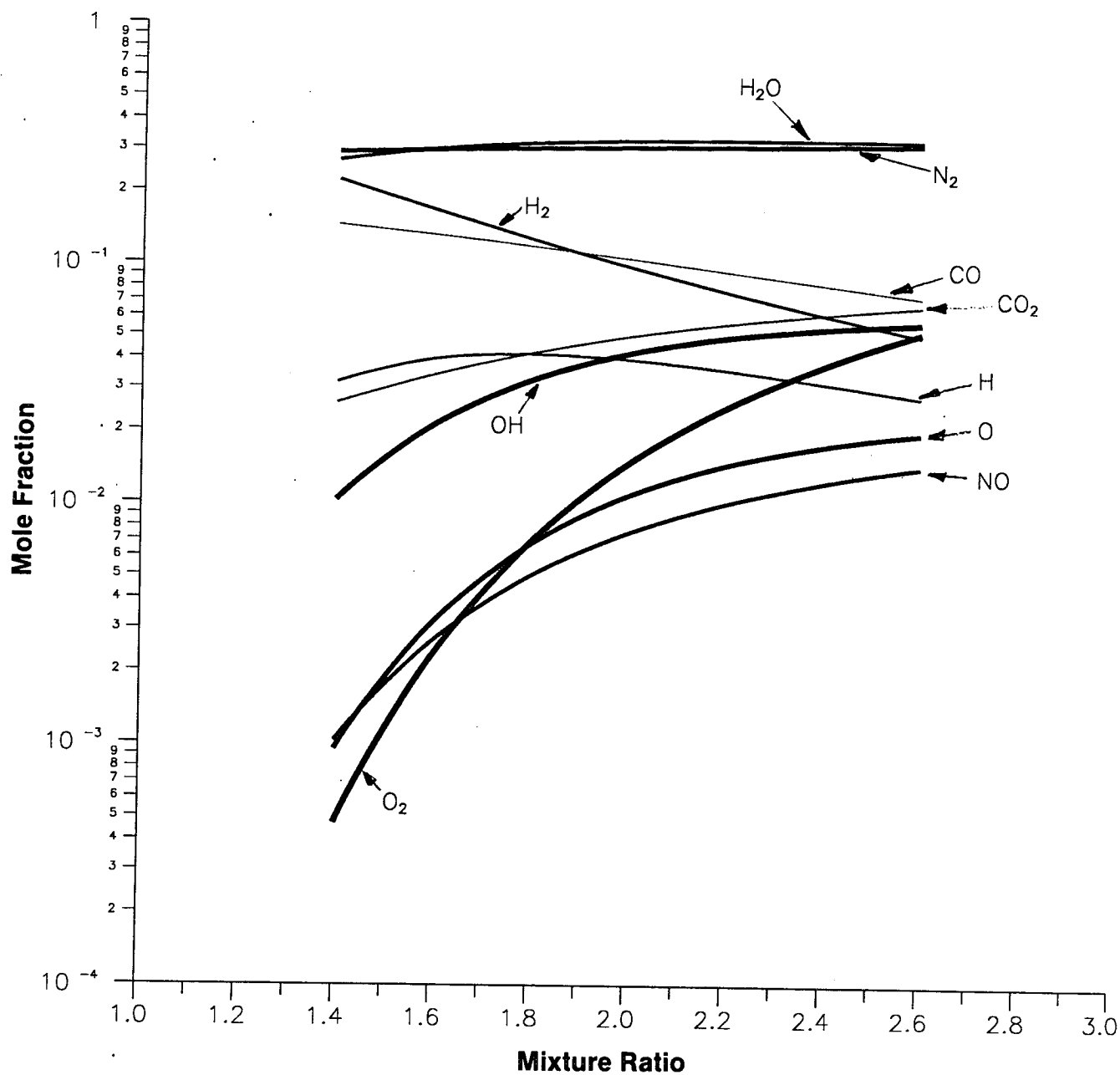


Figure B-20. Mole Fraction Versus Mixture Ratio for Nitrogen Tetroxide/Monomethylhydrazine at 1 atm

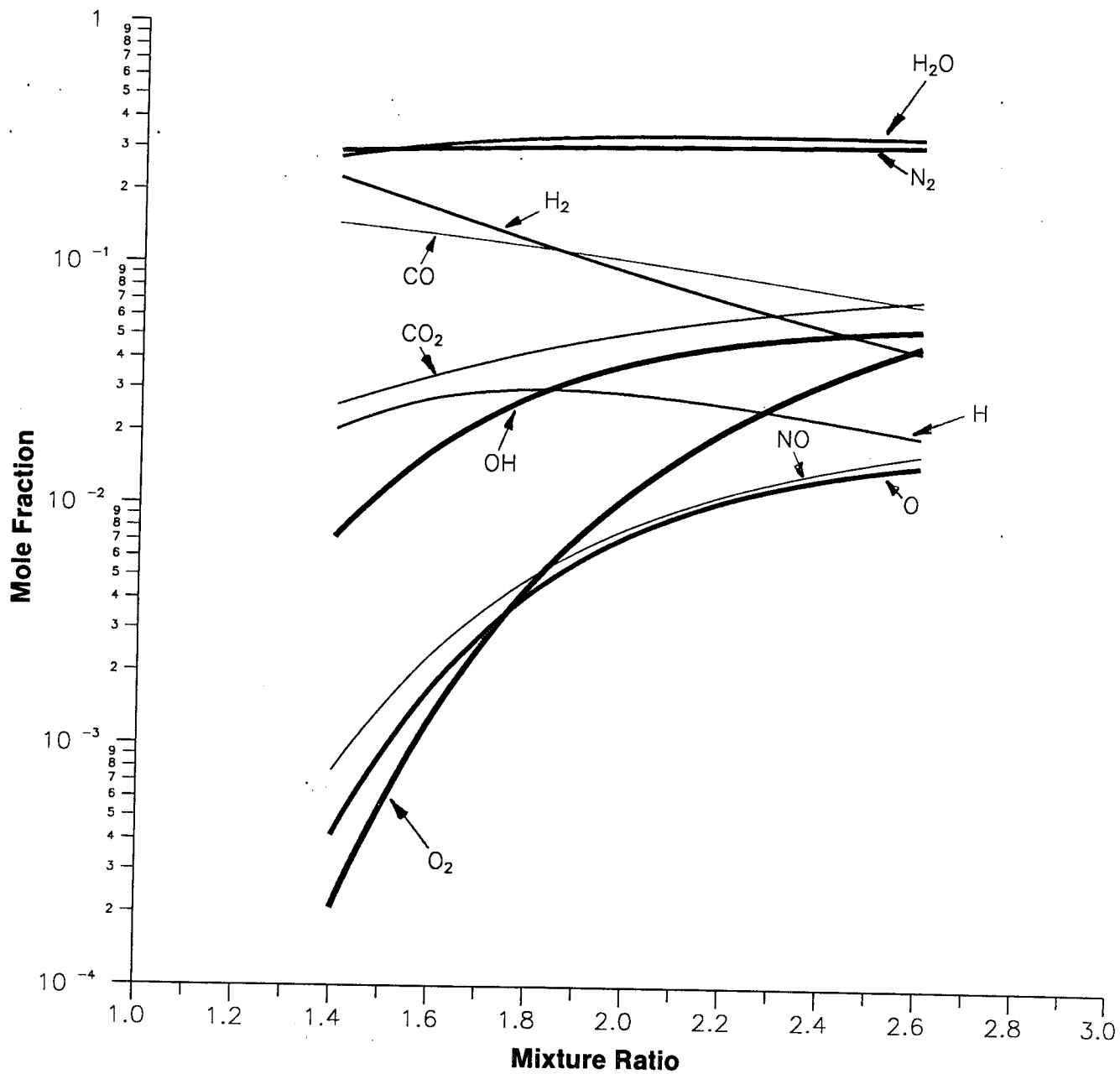


Figure B-21. Mole Fraction Versus Mixture Ratio for Nitrogen Tetroxide/ Monomethylhydrazine at 5 atm

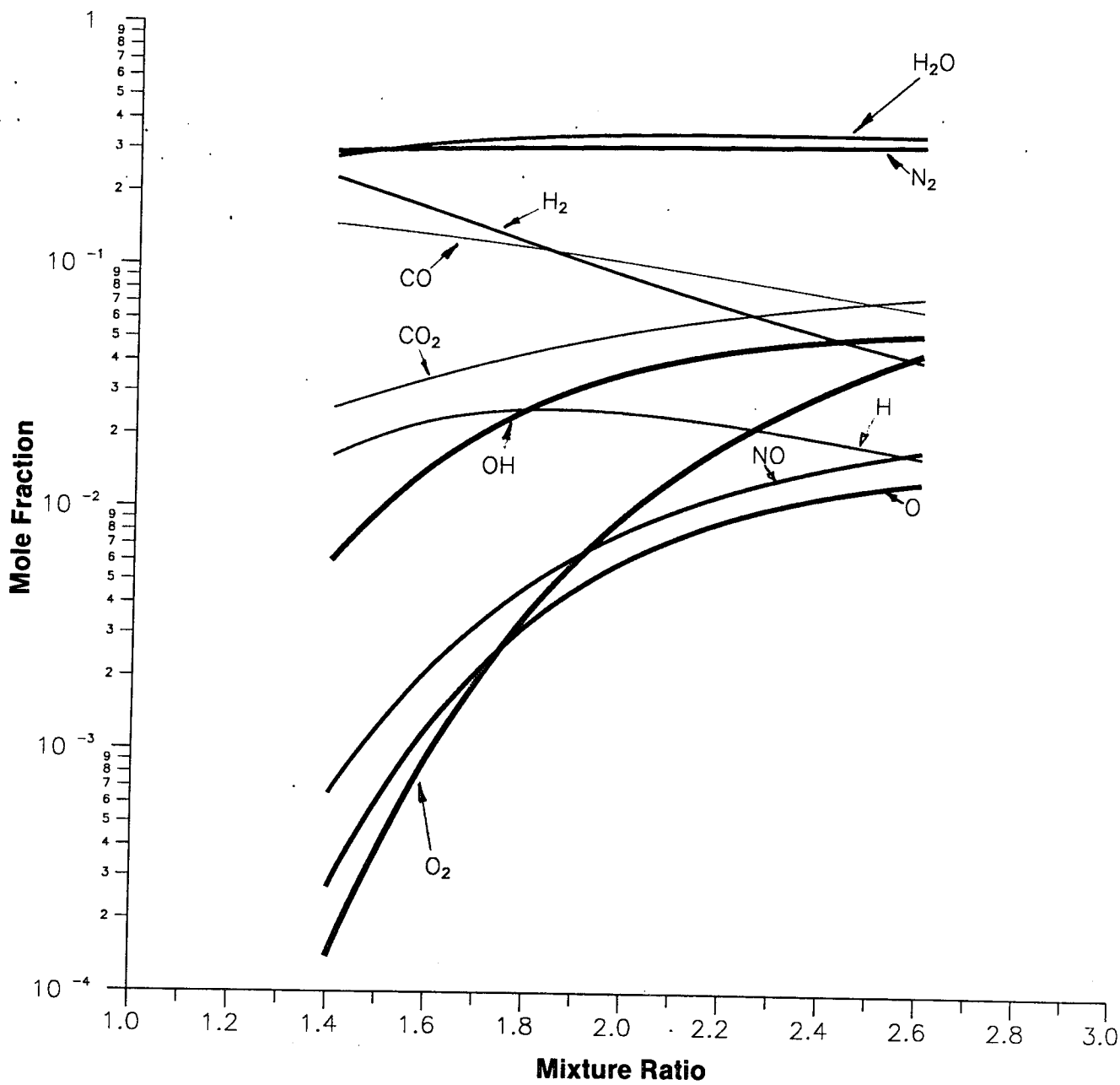


Figure B-22. Mole Fraction Versus Mixture Ratio for Nitrogen Tetroxide/
Monomethylhydrazine at 10 atm

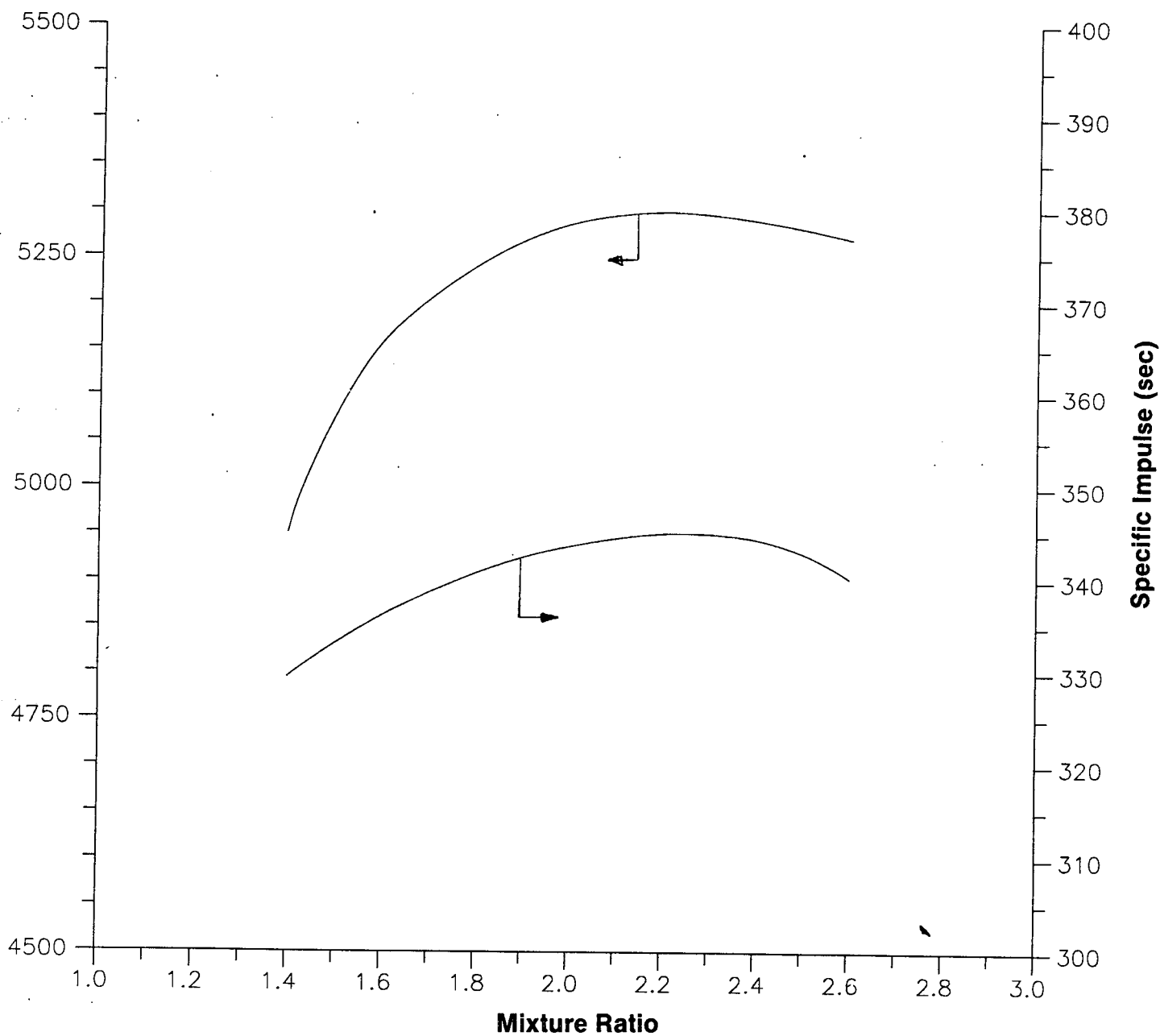


Figure B-23. Combustion Temperature and Specific Impulse Versus Mixture Ratio for Nitrogen Tetroxide/ Monomethylhydrazine at 1 atm

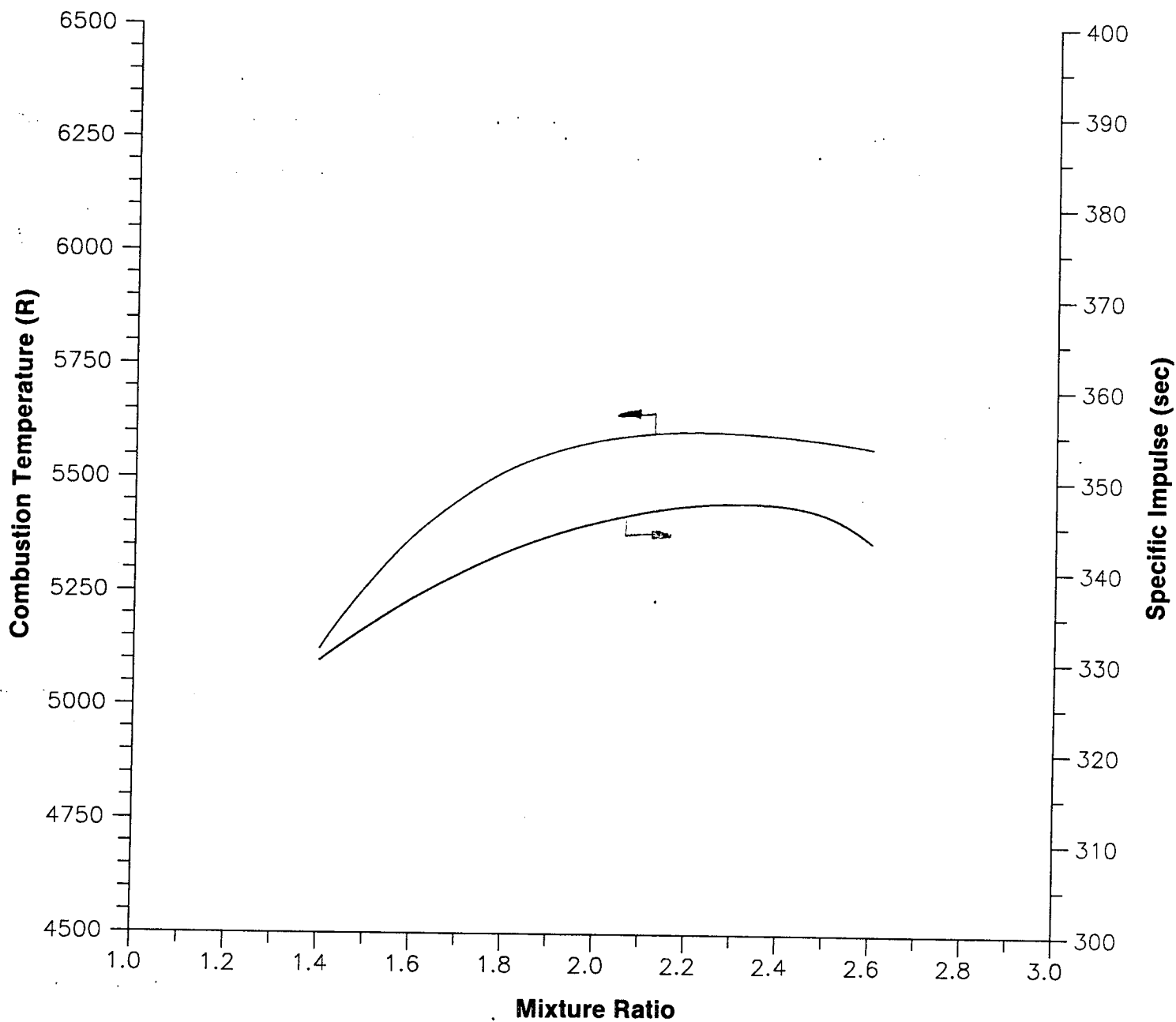


Figure B-24. Combustion Temperature and Specific Impulse Versus Mixture Ratio for Nitrogen Tetroxide/ Monomethylhydrazine at 5 atm

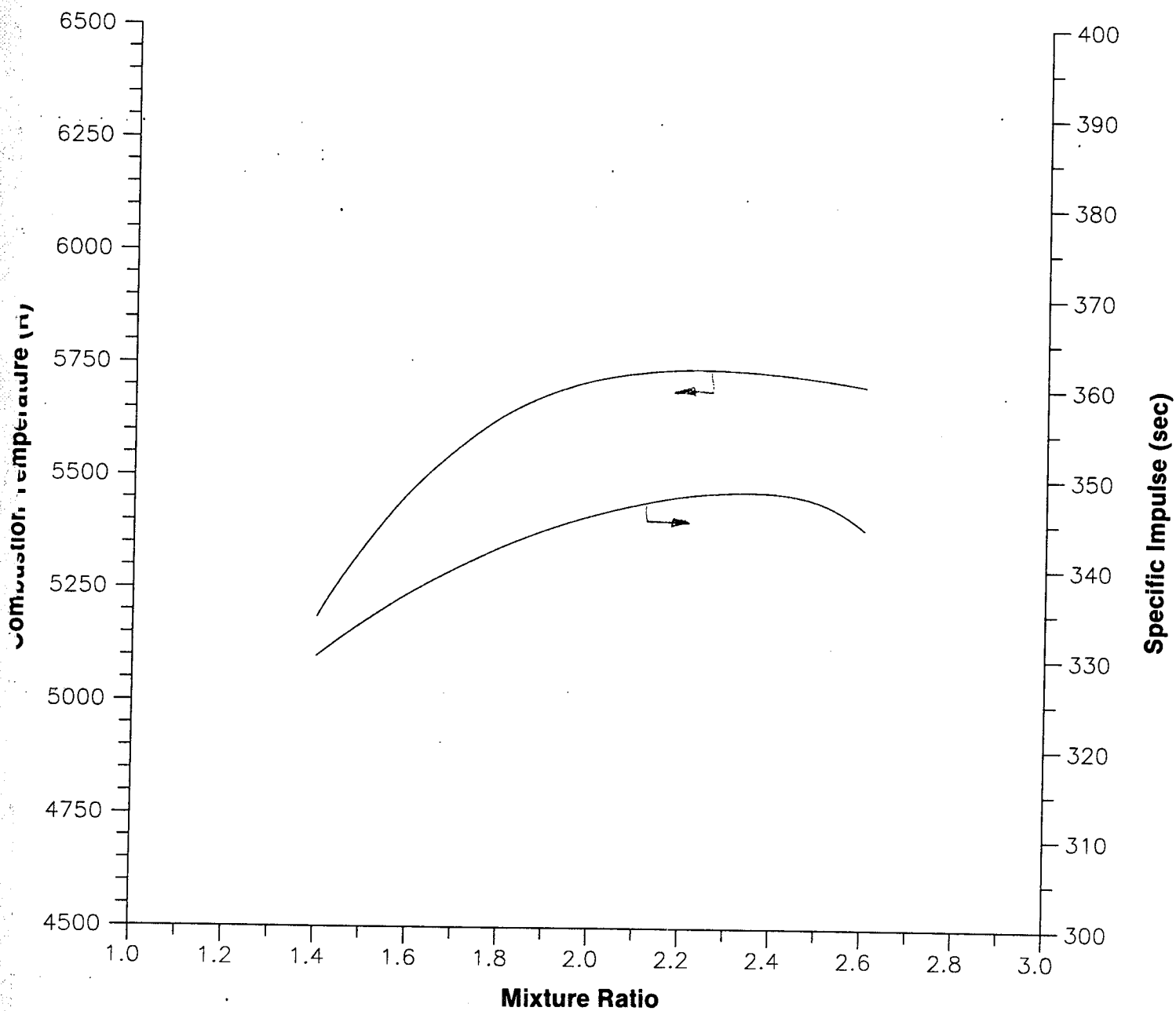


Figure B-25. Combustion Temperature and Specific Impulse Versus Mixture Ratio for Nitrogen Tetroxide/Monomethylhydrazine at 10 atm

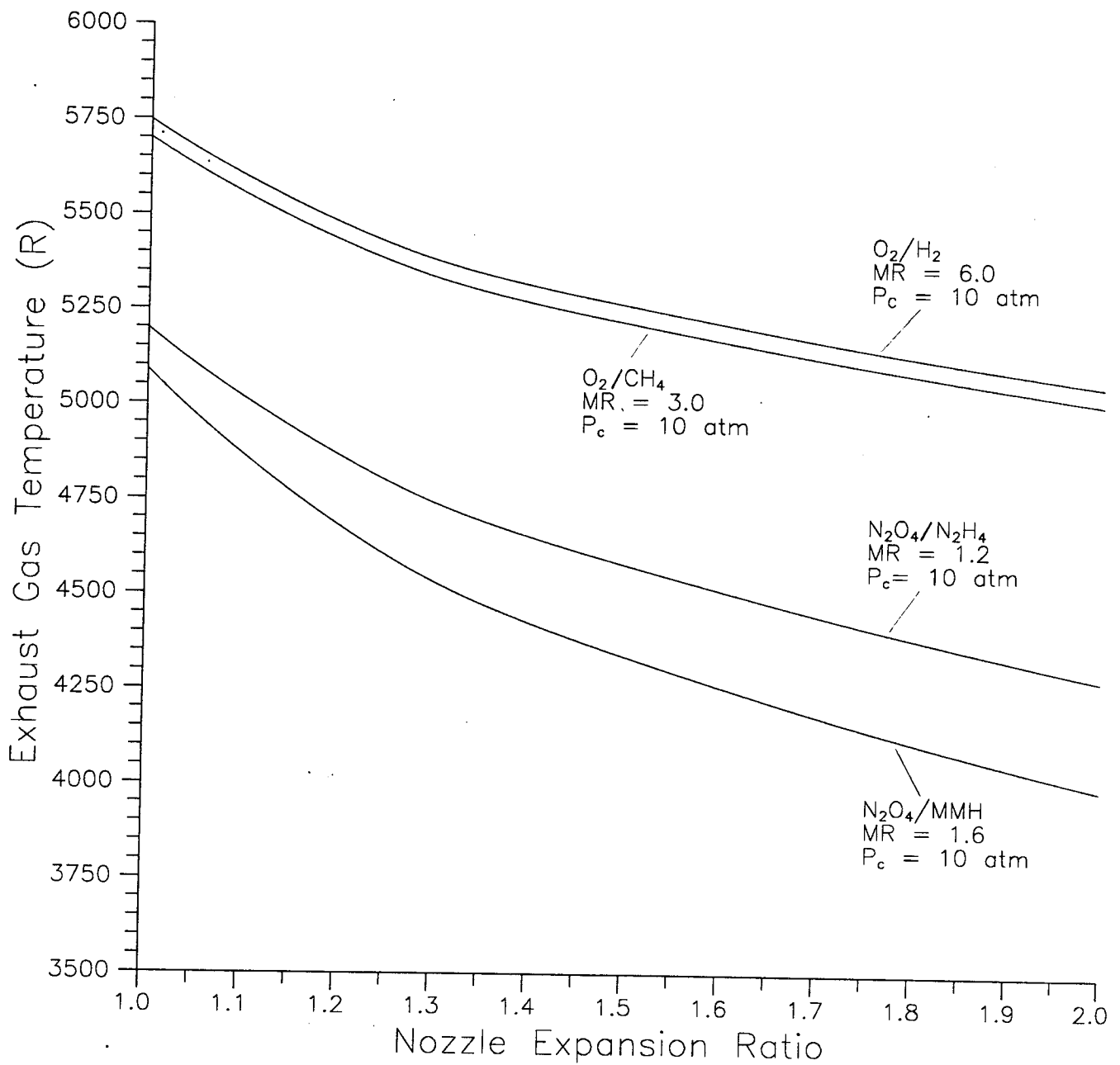


Figure B-26. Exhaust Gas Temperature Versus Nozzle Expansion Ratio for O_2/H_2 , O_2/CH_4 , N_2O_4/N_2H_4 and $N_2O_4/N_2H_3CH_3$

TABLE B-1.
Tabulation of Bipropellant Performance and Combustion Gas Composition, Sheet 2 of 4

O₂/CH₄ 1 atm

MR	CO	CO ₂	H	HCO	HO ₂	H ₂	H ₂ O	H ₂ O ₂	O	OH	O ₂	TEMP	Isp
2.0	0.29130	0.03711	0.02435	0	0	0.35423	0.28808	0	0.00021	0.00466	0.00007	4716	349.5
2.5	0.25398	0.06140	0.05829	0	0	0.21620	0.36970	0	0.00531	0.03142	0.00369	5277	370.6
3.0	0.21535	0.08403	0.06442	0	0.00001	0.13954	0.39572	0	0.01788	0.06254	0.02050	5461	378.7
3.5	0.18222	0.10107	0.05825	0	0.00002	0.09814	0.39807	0	0.03023	0.08247	0.04952	5506	375.7
4.0	0.15467	0.11348	0.04983	0	0.00003	0.07306	0.39178	0	0.03920	0.09305	0.08490	5502	367.2
4.5	0.13170	0.12249	0.04189	0	0.00004	0.05643	0.38216	0	0.04486	0.09766	0.12278	5475	358.6
5.0	0.11245	0.12896	0.03503	0	0.00004	0.04470	0.37129	0	0.04792	0.09858	0.16104	5437	350.7

O₂/CH₄ 5 atm

MR	CO	CO ₂	H	HCO	HO ₂	H ₂	H ₂ O	H ₂ O ₂	O	OH	O ₂	TEMP	Isp
2.0	0.29386	0.03653	0.01446	0	0	0.35951	0.29257	0	0.00008	0.00297	0.00003	4836	349.8
2.5	0.25821	0.06169	0.04279	0	0	0.21927	0.38571	0	0.00322	0.02683	0.00229	5556	371.8
3.0	0.21744	0.08742	0.05021	0	0	0.13667	0.41767	0	0.01349	0.06055	0.01653	5814	381.6
3.5	0.18150	0.10732	0.04547	0	0.00004	0.09287	0.42042	0.00001	0.02460	0.08318	0.04460	5878	381.0
4.0	0.15171	0.12168	0.03836	0	0.00006	0.06727	0.41282	0.00001	0.03272	0.09494	0.08043	5873	373.0
4.5	0.12716	0.13189	0.03170	0	0.00007	0.05079	0.40153	0.00001	0.03769	0.09975	0.11941	5839	364.1
5.0	0.10684	0.13902	0.02602	0	0.00009	0.03945	0.38905	0.00001	0.04018	0.10033	0.15901	5790	355.6

O₂/CH₄ 10 atm

MR	CO	CO ₂	H	HCO	HO ₂	H ₂	H ₂ O	H ₂ O ₂	O	OH	O ₂	TEMP	Isp
2.0	0.29470	0.03636	0.01116	0	0	0.36128	0.29409	0	0.00005	0.00234	0.00002	4878	349.9
2.5	0.25987	0.06192	0.03649	0	0	0.22050	0.39270	0	0.00246	0.02429	0.00176	5673	372.2
3.0	0.21803	0.08934	0.04434	0.00001	0.00002	0.13506	0.42812	0	0.01160	0.05877	0.01469	5974	382.7
3.5	0.18059	0.11082	0.04024	0	0.00005	0.09012	0.43120	0.00001	0.02210	0.08268	0.04219	6049	383.1
4.0	0.14965	0.12620	0.03373	0	0.00008	0.06436	0.42292	0.00001	0.02982	0.09501	0.07822	6044	375.4
4.5	0.12435	0.13697	0.02763	0	0.00010	0.04805	0.41076	0.00001	0.03448	0.09990	0.11774	6004	366.4
5.0	0.10357	0.14437	0.02248	0	0.00120	0.03695	0.39745	0.00001	0.03673	0.10032	0.15800	5950	357.6

Tabulation of Bipropellant Performance and Combustion Gas Composition, Sheet 3 of 4

[illegible]

MR	H	H02	H2	H20	H202	NO	NO2	N2	O	OH	O2	TEMP	1 st
1.0	0.01839	0	0.17946	0.39135	0.00196	0	0.39437	0.00083	0.01290	0.00073	0.00075	5320	341.2
1.1	0.02020	0	0.14366	0.41254	0.00352	0	0.39667	0.00172	0.01967	0.00199	0.00452	5317	347.4
1.2	0.02038	0.00001	0.11366	0.42799	0.00585	0	0.39797	0.00298	0.02689	0.00452	0.00452	5317	347.4
1.3	0.01925	0.00001	0.08949	0.43807	0.00798	0	0.39940	0.00444	0.03336	0.00878	0.00878	5354	349.4
1.4	0.01734	0.00002	0.07056	0.44376	0.01046	0	0.39817	0.00589	0.03897	0.01494	0.01494	5363	350.6
1.4375	0.01652	0.00002	0.06462	0.44763	0.01137	0	0.39795	0.00639	0.04060	0.01774	0.01774	5362	350.5
1.5	0.01512	0.00002	0.05939	0.44569	0.01284	0	0.39748	0.00713	0.04283	0.02292	0.02292	5351	347
1.6	0.01291	0.00003	0.04468	0.44516	0.00001	0.0198	0.39654	0.00806	0.04520	0.03242	0.03242	5322	341.4
1.8	0.00909	0.00003	0.02920	0.43910	0.00001	0.01835	0.39432	0.00896	0.04638	0.05452	0.05452	5339	330.6
2.0	0.00627	0.00004	0.01962	0.42934	0.00001	0.02056	0.39209	0.00887	0.04446	0.07873	0.07873	5338	320.8

TABLE B-1.
Tabulation of Bipropellant Performance and Combustion Gas Composition, Sheet 4 of 4

N2O4/MMH 1 atm

MR	CH4	CO	CO2	H	HNO	HO2	H2	H2O	H2O2	N	NO	NO2	N2	O	OH	O2	T (R)	Isp
1.4	0	0.14516	0.02620	0.03192	0	0	0.22327	0.26968	0	0	0.00103	0	0.29097	0.00095	0.01035	0.00047	4951	329.5
1.6	0	0.13178	0.03417	0.03984	0	0	0.16730	0.30008	0	0	0.00267	0	0.29756	0.00318	0.02110	0.00233	5159	336.2
1.8	0	0.11821	0.04221	0.04179	0	0	0.12647	0.31761	0	0	0.00500	0	0.30250	0.00676	0.03253	0.00690	5241	340.8
1.9	0	0.11162	0.04603	0.04116	0	0	0.11079	0.32277	0	0	0.00627	0	0.30451	0.00878	0.03766	0.01039	5268	342.5
2.0	0	0.10526	0.04966	0.03985	0	0.00001	0.09759	0.32615	0	0.00001	0.00756	0	0.30628	0.01079	0.04218	0.01465	5286	343.7
2.2	0	0.09331	0.05626	0.03614	0	0.00001	0.07692	0.32910	0	0.00001	0.01004	0	0.30931	0.01449	0.04924	0.02517	5299	345.1
2.4	0	0.08247	0.06196	0.03191	0	0.00001	0.06172	0.32865	0	0.00001	0.01228	0	0.31185	0.01746	0.05391	0.03777	5290	344.5
2.5	0	0.07746	0.06449	0.02980	0	0.00001	0.05559	0.32760	0	0	0.01330	0	0.31298	0.01865	0.05548	0.04464	5281	343.0
2.6	0	0.07271	0.06682	0.02775	0	0.00001	0.05023	0.32614	0	0	0.01423	0	0.31405	0.01963	0.05663	0.05179	5270	340.3

N2O4/MMH 5 atm

MR	CH4	CO	CO2	H	HNO	HO2	H2	H2O	H2O2	N	NO	NO2	N2	O	OH	O2	T (R)	Isp
1.4	0	0.14689	0.02590	0.02049	0	0	0.22757	0.27690	0	0	0.00078	0	0.29353	0.00042	0.00731	0.00021	5124	329.9
1.6	0	0.13348	0.03435	0.02765	0	0	0.16905	0.31219	0	0	0.00236	0	0.30110	0.00171	0.01682	0.00128	5373	336.8
1.8	0	0.11915	0.04343	0.03027	0	0	0.12494	0.33350	0	0.00001	0.00493	0	0.30665	0.00423	0.02833	0.00456	5517	341.9
1.9	0	0.11200	0.04790	0.03010	0	0.00001	0.10789	0.33984	0	0.00001	0.00645	0	0.30879	0.00581	0.03382	0.00738	5558	343.8
2.0	0	0.10500	0.05220	0.02926	0	0.00001	0.09362	0.34398	0	0.00001	0.00805	0	0.31061	0.00745	0.03878	0.01103	5585	345.3
2.2	0	0.09177	0.06009	0.02644	0	0.00001	0.07161	0.34743	0	0.00001	0.01121	0	0.31355	0.01057	0.04665	0.02066	5607	347.2
2.4	0	0.07977	0.06688	0.02304	0	0.00002	0.05586	0.34667	0	0.00001	0.01411	0.00001	0.31584	0.01313	0.05183	0.03283	5598	347.3
2.5	0	0.07426	0.06987	0.02134	0	0.00002	0.04965	0.34528	0	0.00001	0.01541	0.00001	0.31684	0.01414	0.05354	0.03963	5587	346.2
2.6	0	0.06907	0.07259	0.01969	0	0.00003	0.04429	0.34343	0	0.00001	0.01663	0.00001	0.31775	0.01497	0.05475	0.04679	5572	343.2

N2O4/MMH 10 atm

MR	CH4	CO	CO2	H	HNO	HO2	H2	H2O	H2O2	N	NO	NO2	N2	O	OH	O2	T (R)	Isp
1.4	0	0.14750	0.02581	0.01636	0	0	0.22912	0.27962	0	0	0.00066	0	0.29447	0.00027	0.00604	0.00014	5187	330.0
1.6	0	0.13410	0.03447	0.02294	0	0	0.16967	0.31723	0	0	0.00214	0	0.30256	0.00123	0.01471	0.00093	5466	337.0
1.8	0	0.11942	0.04408	0.02571	0	0	0.12408	0.34057	0	0.00001	0.00475	0	0.30848	0.00330	0.02596	0.00364	5634	342.2
1.9	0	0.11197	0.04889	0.02572	0	0.00001	0.10637	0.34759	0	0.00001	0.00637	0	0.31073	0.00466	0.03154	0.00612	5684	344.2
2.0	0	0.10465	0.05356	0.02508	0	0.00001	0.09158	0.35218	0	0.00001	0.00809	0	0.31260	0.00612	0.03665	0.00946	5716	345.8
2.2	0	0.09073	0.06216	0.02264	0	0.00002	0.06894	0.35595	0	0.00001	0.01158	0	0.31551	0.00897	0.04487	0.01860	5742	348.0
2.4	0	0.07813	0.06953	0.01961	0.00001	0.00003	0.05298	0.35503	0	0.00001	0.01482	0.00001	0.31769	0.01134	0.05029	0.03052	5734	348.4
2.5	0	0.07236	0.07275	0.01809	0.00001	0.00003	0.04676	0.35347	0.00001	0.00001	0.01628	0.00001	0.31861	0.01227	0.05207	0.03728	5722	347.4
2.6	0	0.06695	0.07566	0.01661	0.00001	0.00003	0.04144	0.35140	0.00001	0.00001	0.01763	0.00001	0.31944	0.01304	0.05331	0.04444	5706	344.4